Lecture Notes in Civil Engineering

Han-Yong Jeon *Editor*

Proceedings of the International Conference on Geosynthetics and Environmental Engineering

Springer

Lecture Notes in Civil Engineering

Volume 374

Lecture Notes in Civil Engineering (LNCE) publishes the latest developments in Civil Engineering—quickly, informally and in top quality. Though original research reported in proceedings and post-proceedings represents the core of LNCE, edited volumes of exceptionally high quality and interest may also be considered for publication. Volumes published in LNCE embrace all aspects and subfields of, as well as new challenges in, Civil Engineering. Topics in the series include:

- Construction and Structural Mechanics
- Building Materials
- Concrete, Steel and Timber Structures
- Geotechnical Engineering
- Earthquake Engineering
- Coastal Engineering
- Ocean and Offshore Engineering; Ships and Floating Structures
- Hydraulics, Hydrology and Water Resources Engineering
- Environmental Engineering and Sustainability
- Structural Health and Monitoring
- Surveying and Geographical Information Systems
- Indoor Environments
- Transportation and Traffic
- Risk Analysis
- Safety and Security

To submit a proposal or request further information, please contact the appropriate Springer Editor:

– Pierpaolo Riva at pierpaolo.riva@springer.com (Europe and Americas);
– Swati Meherishi at swati.meherishi@springer.com (Asia—except China, Australia, and New Zealand);
– Wayne Hu at wayne.hu@springer.com (China).

All books in the series now indexed by Scopus and EI Compendex database!

Han-Yong Jeon
Editor

Proceedings of the International Conference on Geosynthetics and Environmental Engineering

Springer

Editor
Han-Yong Jeon
Department of Chemical Engineering
Inha University
Michuhol-gu, Incheon, Korea (Republic of)

ISSN 2366-2557 ISSN 2366-2565 (electronic)
Lecture Notes in Civil Engineering
ISBN 978-981-99-4228-2 ISBN 978-981-99-4229-9 (eBook)
https://doi.org/10.1007/978-981-99-4229-9

Organizing Committee

Conference Chair

Prof. Han-Yong Jeon

Program Committee Chair

Prof. Song Feng

Publicity Chair

Assoc. Prof. Haoliang Wu

Proceedings Guest Editors

Prof. Han-Yong Jeon, Inha University, South Korea

Technical Program Committees

Prof. Herbert Klapperich, TU Bergakademie Freiberg, Germany
Prof. Zhanping You, Michigan Technological University, USA
Prof. Szeto, Wai Yuen, The University of Hong Kong, China
Prof. Mohammed J. K. Bashir, University of Tunku Abdul Rahman, Malaysia

Prof. Zhijian Zhang, Zhejiang University, China
Prof. Yanjun Du, Southeast University, China
Prof. Jamal Khatib, University of Wolverhampton, UK
Prof. Yewei Zheng, Wuhan University, China
Prof. LIM, C. W., City University of Hong Kong, China
Prof. Antonio Caggiano, TU Darmstadt, Germany
Prof. Boronbaev Erkin, Kyrgyz Republic
Prof. Wei Gao, Hohai University, China
Prof. Iwona Cieslak, University of Warmia and Mazury in Olsztyn, Poland
Assoc. Prof. Chaminda Gallage, Queensland University of Technology, Australia
Assoc. Prof. Kai Gu, Nanjing University, China
Assoc. Prof. Paulo Barreto Cachim, University of aviro, Portugal
Assoc. Prof. Xiaohui Sun, Shenzhen University, China
Assoc. Prof. Katarzyna Pietrucha-Urbanik, Rzeszow University of Technology, Poland
Assoc. Prof. Cheng Lin, University of Victoria, Canada
Assoc. Prof. Triantafyllos Makarios, Aristotle University of Thessaloniki, Greece
Assoc. Prof. Luigi Coppola, University of Bergamo, Italy
Assoc. Prof. Payam Shafigh, University of Malaya, Malaysia
Assist. Prof. Hubert Anysz, Warsaw University of Technology, Poland
Assist. Prof. Amin Mojiri, Hiroshima University, Japan
Assist. Prof. Chae, Wonseok, University of Wuppertal, Germany
Assist. Prof. Arshad Ullah, National University of Sciences and Technology, Islamabad, Pakistan

Preface

We are delighted to present the proceedings of 2023 the International Conference on Geosynthetics and Environmental Engineering (ICGEE2023), which was held successfully on Jeju Island, South Korea, from March 30–31, 2023. We hope you will find it useful, interesting, and encouraging.

The proceedings contain papers submitted to ICGEE2023, which is organized by Inha University, ASGES, and co-organized by the Korean Geosynthetics Society. The conferences's main objective is to bring together leading academic scientists, researchers, and research scholars to exchange and share their experiences and research results in all geosynthetics and environmental engineering. It also provides a premier interdisciplinary platform for researchers, practitioners, and educators to present and discuss the latest innovations, trends, and concerns, as well as practical challenges encountered and solutions adopted in the field of geosynthetics in geotechnical, civil, and environmental engineering.

This conference proceedings collect the accepted papers and represent an interesting outcome of this conference, which covers geosynthetics applications and sustainability, civil and structural engineering, environmental engineering, and science.

We would like to extend our heartfelt appreciation to everyone who contributed to the success of ICGEE2023. We are grateful for the invaluable support of each individual and institution that played a significant role in making the conference a grand success. We also express our sincere gratitude to the organizing committee for their valuable guidance on the conference organization and peer review of the papers.

We are confident that ICGEE2023 has provided an excellent forum for discussion, fostering new ideas and collaborative research. We believe that these proceedings will serve as an essential research reference and knowledge source that will help

advance scientific and engineering innovations and foster the development of new products and processes.

Michuhol-gu, Incheon, South Korea

Prof. Han-Yong Jeon
ICGEE General Chair
On behalf of ICGEE2023 committee

Contents

An Innovative Technology for Overloading Microshoots in the in Vitro

Suleimen Kaimov, Talgat Kaiym, Abylay Kaimov, Amandyk Tuleshov, Aidarkhan Kaimov, Zarina Saurova, Nurzhan Aimbetov, Kalimagul Bakhyieva, Orken Mamyrbayev, Maksat Kalimoldayev, and Ualikhan Karymsakov

Abstract Industrial development of cities is the main cause of destruction and degradation of natural resources around the world. Urbanization negatively affects the species composition of plants, the atmosphere, and the land cover in the populated areas of the world's major cities. Tree plantations are the main mechanism for stabilizing the ecological situation in large cities and arid areas in countries around the world. To obtain a large number of genetically identical plants through micropropagation, it is necessary to automate the main stages of this technological process. The result of the study is the creation of a robotic complex with a phalanx pincer to automate the technological process of transshipment operations in the microclonal propagation of a plant. This will have a positive impact on solving the urgent problem of greening large cities and arid areas not only in the Republic of Kazakhstan, but also in other countries of the world, and represents a fundamentally new approach to solving the environmental problems of the Earth (Kaimov et al. Eastern-European Journal of Enterprise Technologiesthis link is disabled, 2022, 1(7–115), pp. 48–58). In the article, different variants of the structural-kinematic schemes of the robot

S. Kaimov (✉) · A. Kaimov · A. Kaimov · K. Bakhyieva · O. Mamyrbayev · M. Kalimoldayev
Kazakh National University Named After Al-Farabi, Almaty, Kazakhstan
e-mail: kayim.suleimen@gmail.com

T. Kaiym
Military Engineering Institute of Radio Electronics and Communications of the Ministry of Defense of the Republic of Kazakhstan, Almaty, Kazakhstan

A. Tuleshov
Institute of Mechanics and Engineering Named After U. A. Joldasbekov, Almaty, Kazakhstan

Z. Saurova
Kazakh Medical University of Continuing Education, Almaty, Kazakhstan

N. Aimbetov
Halyk Bank of Kazakhstan, Almaty, Kazakhstan

U. Karymsakov
International Educational Corporation, Almaty, Kazakhstan

H.-Y. Jeon (ed.), *Proceedings of the International Conference on Geosynthetics and Environmental Engineering*, Lecture Notes in Civil Engineering 374,
https://doi.org/10.1007/978-981-99-4229-9_1

gripper are justified taking into account the stochastic conditions of its interaction with the loaded object. Currently, we have introduced 280 seedlings. Since 2019, we have been working to increase the size of the planting material that we began to grow in the field. Thanks to this technology, we have planted 6,102 seedlings in the forest nursery (Kaimov et al. Eastern-European Journal of Enterprise Technologiesthis link is disabled, 2022, 1(7–115), pp. 48–58).

Keywords Microshoots · Microsprouts · Robotic complex · Kalman coefficient · Adaptive gripper

1 Introduction

As you know, in December 2015, a United Nations conference was held in Paris, where all the countries of the world were recommended to adopt their national programs to reduce greenhouse gas emissions into the earth's atmosphere in order to improve the climate and solve the urgent modern problem of improving the climate. As you know, planting trees is one of the ways to improve the environmental situation in the settlements of big cities and arid areas of the countries of the world [1].

In the last 15–20 years, active greening of urban areas has been carried out in large cities and arid areas of countries around the world. For example, in the Re-public of Kazakhstan alone, a large-scale greening of areas is planned by 2025: the planting of two billion trees in forests and 15 million in large cities and dry settlement areas. The green massif will not only improve the ecological situation in the country, but also make Kazakhstan more aesthetically attractive, both for tourists and for the citizens of the country itself [1].

It is known that micropropagation of plants has a number of advantages: high multiplication factor; restoration; the possibility to work throughout the year and plan the release of plants until a certain date; preservation of valuable genotypes; obtaining homogeneous clones [1].

Currently, in Kazakhstan, the technological process of microclonal propaga-tion of plants is carried out with human manual labor, which makes large-scale land-scaping in large cities and in areas with dry soils in the Republic of Kazakh-stan impossible. The effect of micropropagation of plants on an industrial scale depends on the degree of automation of the transfer of the microsprouts of plants from the transport container in vitro to the working container with soil [1].

In this context, the article proceeds from the solution of an extremely urgent task, namely, automation of the main stages of the technological process of mi-croclonal propagation of plants to solve the problem of landscaping of settlement areas in the Republic of Kazakhstan and other countries of the world. The study deals with the development of an innovative robotic complex of a manipulation device with a gripper for automating the handling processes of plants during their microclonal propagation. Mathematical methods for selection and justification of geometrical, structural-kinematic and dynamic parameters of grippers for over-loading of plant

microshoots and their 3D computer models were developed. Different variants of structural-kinematic schemes of the gripper of this robot were justified taking into account the stochastic conditions of its interaction with an overloaded object. Software for modeling the operation of a remote-controlled prototype of a mobile robot with an adaptive gripper for overloading plant microshoots from a transport container into a loading tank was developed [1].

Please note that the first paragraph of a section or subsection is not indented. The first paragraphs that follows a table, figure, equation etc. does not have an indent, either. Subsequent paragraphs, however, are indented [1].

Please note that the first paragraph of a section or subsection is not indented. The first paragraphs that follows a table, figure, equation etc. does not have an indent, either. Subsequent paragraphs, however, are indented [1].

2 Proposal for Problem Solution

The aim of the study is to create a robotic complex with a phalanx tong to automate the technological process of handling operations of micropropagation of plants. To achieve this goal, the following tasks must be solved:

- selection and justification of the concept of a robotic complex with a phalanx tong for automating the transfer operations of plant micropropagation shoots from a transport container to a working container with soil;
- selection and justification of the structural parameters of the actuator of the phalanx gripper of the robot;
- determination of the parameters of the gripper taking into account the stochastic conditions of its interaction with the microshoot surface;
- experimental studies of the prototype of an innovative robot with a phalange gripper.

3 Proposal for Problem Solution

Selection and justification of the concept of a robotic complex with a phalanx pincer for automating the transfer of plant microshoots from a transport container to a working container with soil.

Selection and justification of the general concept of a robot complex of a manipulation device with a phalanx gripper for automating the transfer operations of microsprouts from a transport container to a working container with soil in the microclonal propagation of plants.

The technological process of plant microcloning consists of the steps shown in Table 1. In vitro introduction; animation of plant microsprouts; rooting of plant microsprouts; adaptation of plant microsprouts in soil; obtaining plant seedlings and

miniature plants of plants. Currently, they are carried out with human manual labor, which makes it impossible to solve the urgent problem of greening settlements in many parts of the world. In this context, a solution to this problem is proposed by creating a robotic complex consisting of a manipulation device with a gripper for transporting plant microshoots from an in vitro transport container to a working container with soil [3].

Figure 1 shows the conceptual image of an innovative robotic complex of a manipulation device with a phalanx gripper for transporting plant microshoots from an in vitro transport container to a working container with soil at the stage of their adaptation in the soil during microclonal propagation [1].

The functioning of this robotic complex is described in the articles [2–5].

Table 1 The main stages of plant microcloning

Time	Stages	
15 days	Introduction to in vitro culture to obtain the main shoot from the auxiliary bud	Introduction to in vitro culture
40 days	Animation of microshoots (10 plants in one jar). From one microshoot, on average, 20 additional microshoots are formed	Microshoots cartoon
50 days	Rooting of microshoots (10 plants in one jar) on average, 10 additional microshoots are formed	Rooting microshoots
30 days	Adaptation of microshoots in the soil	Adaptation of microshoots
90 days	Adaptation seeding 25–50 cm	Obtaining seeding up to 50 cm
90 days	Adaptation seeding 50–150 cm	Seeding up to 150 cm
Total	It takes 315 days to obtain seeding up to 150 cm	

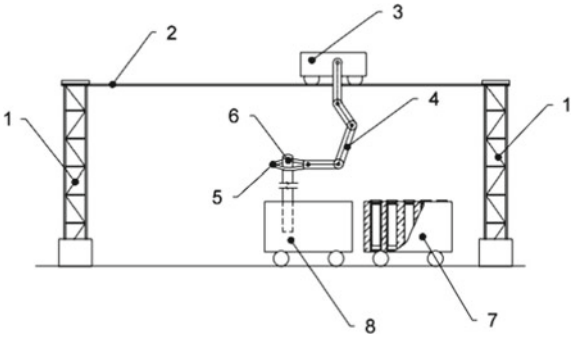

Fig. 1 Scheme of transshipment of plant sprouts from a shipping container into a cargo container with soil using an innovative phalanx gripper of an industrial robot manipulator: 1—support post; 2—horizontal crossbar; 3—vehicle; 4—manipulator; 5—innovative phalanx tong; 6—plant microshoot; 7—transport container; 8—cargo container with soil

3.1 Selection and Justification of the Structural Parameters of the Actuator of the Phalangeal Gripper of the Robot

A model of a thin-walled ring, which most accurately represents the outer "sensitive" surface of a plant microsprout, was used to investigate all major methods of possible grasping options for elastic and fragile thin-walled manipulation objects. When grasping plant microsprouts, the limitations on the magnitude of the grasping forces imposed by the conditions for ensuring the required reserves of grasping safety and the insignificance of the elastic movements at the points of contact of the grasping jaws of the phalangeal gripper with the area of the outer surface of the plant microsprout must be taken into account.

An increase in the number of working elements of the handle leads to a widening of the range of allowable values of gripping forces of a large diameter ring under the conditions of absence of deformation and tension in the contact area of the working element of the phalange handle with a plant microsprout. Therefore, in this study, cases of grasping the ring-shaped structural element of a plant microsprout at four, six, and eight contact points of the inner surface of the working element of the phalanx grasp with the outer surface of the plant microsprout are considered. In [1, 2], the following formulas for calculating the maximum and minimum allowable values of the gripping force of a thin-walled ring were justified from the conditions for ensuring the reliability of the grip and the insignificance of the values of elastic displacements at the points of contact of the working element of the gripper with the ring.

The value of the contact force of the outer inner surfaces of each phalanx 3–5 with the retaining teeth 8 of each gripper lever attached to them on the outer boundary surface of the upper part of the plant microsprout body 10 (Fig. 1) is determined by the formula:

$$P_{\max} = \frac{\sigma_{\partial} l t^2}{0.3967}, \tag{1}$$

and

$$P_{\min} = \frac{G + F_I}{8f}, \tag{2}$$

where P_{max} the value of the maximum permissible gripping force of the gripper ring when performing minor elastic movements at the points of contact of the working element of the gripper with the ring; σ_{add}—the value of the allowable normal voltage of an object having an annular cross section; l and t are the width and thickness of the ring; P_{min} the value of the minimum allowable gripping force on the outer surface of the ring for reliable retention of the plant microshoot; G is the weight of the ring and F_I—the magnitude of the inertial force acting on the ring (Fig. 2).

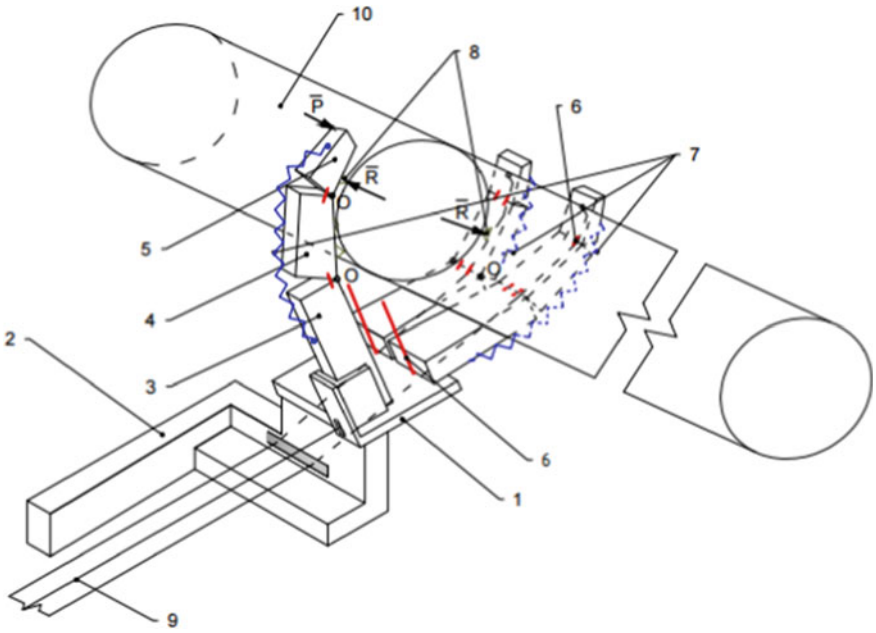

Fig. 2 Three-phalange adaptive gripper of the robot manipulator for reloading plant microshoots from the transport container into the working container with soil: 1—tile-base for attaching the main phalanx of the gripper lever; 2—mounting arm of the manipulator; 3—main phalanx; 4—middle phalanx; 5—pointed phalanx; 6—hinge for fastening adjacent phalanxes to each other; 7—tightening spring; 8—gripping sponge; 9—flexible traction element, 10—plant microshoot

The rotation of the phalanges of the grapple levers should be done using the two most effective options for the placement of the retaining teeth of the phalanges of the grapple levers near the upper part of the plant microsprout body [6]:

- Fig. 3a shows two gripping jaws located on the inner surface of the phalanges of the gripper levers, located on one side of the outer surface of the plant microshoot body section, one retaining tooth, located on the outer inner surface of the gripper phalanx, is located near the opposite side of the outer surface of the body section plant microshoot;
- Figure 3b shows two gripping jaws located on the outer inner surface of the phalanges of the gripper lever, located on йone side of the outer surface of the plant microshoot body section and two retaining teeth located on the outer inner surfaces of the phalanges of the gripper lever, located near the opposite side of the outer surface part of the plant microshoot body.

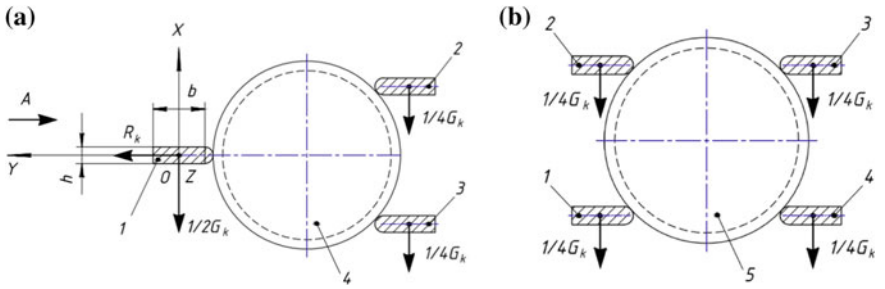

Fig. 3 Different options for capturing an object: **a** variants of the scheme of loading the gripping jaws of the phalanxes of the gripper lever (view along the longitudinal axis of the gripping jaw); **b** when clamping a part of the plant microshoot body from above and below with gripping sponges. 1, 2, 3, 4—gripping jaws; 5—plant microshoot b is the length of the holding tooth; h is the width of the gripping jaw

3.1.1 Determination of Gripper Parameters Taking into Account Stochastic Conditions of Its Interaction with the Microshoot Surface

The magnitude of the force P, i.e. Pk, with which the gripper interacts with the upper part of the body of the captured object, is determined from the following system of equations:

$$\begin{cases} P_{k+1} = P_k + u_k + \gamma_k \\ z_k = P_k + \delta_k \end{cases}, \tag{3}$$

where P_k—the magnitude of the force P, determined taking into account the random error of its deviation in the "ideal model"; $x_k + 1$—the magnitude of the force P, determined taking into account the random error of its deviation in the "ideal model" in a different time interval; u_k—the magnitude of the force P, which controls the evolution of the state matrix of its change, with which the gripper interacts with the surface of the upper part of the body of the manipulated object, which is determined analytically by formula (1) or (2); z_k—the magnitude of the force P, determined experimentally, taking into account the systematic error caused by the accuracy of the measuring instruments; γ_k and δ_k—accordingly, the errors of the mathematical model of the analytical calculation and experimental determination of the magnitude of the force P, measured by technical means of measurement, and the analytical values of the force P are determined by (1) or (2).

In this case, random errors caused by the deviation of the designed three-phalanx adaptive gripper of the manipulator from its "ideal" model are determined by statistical moments M_{γ_i} whose values and their distribution laws do not depend on time (iteration numbers i); mean error values are zero: $M_{\gamma_i} = M_{\delta_i} = 0$. The law of distribution of random variables of the force of grasping an object with a gripper may not be known, but their dispersions are known σ_γ^2 and σ_δ^2. It is assumed that all random

errors in determining the magnitude of the gripping force of an object with a gripper are independent.

It is assumed that at the i-th step the filtered value from the sensor is found P_i^{opt}, which approximates the true coordinate of the system Pi. The unknown value P_{i+1} is determined by the formula:

$$P_{i+1} = P_i + u_i + \gamma_i, \tag{4}$$

where u_i is the value that controls the evolution of the state matrix of the change in force P.

Therefore, having not yet determined the value of the grasping force of the gripper object from the sensor, it is assumed that at step i + 1 the system evolves according to this law and the sensor will show the grasping force of the object by the gripper close to the value $P_i^{opt} + u_i$. Simultaneously with this circumstance, at step i + 1, there is an inaccurate reading from the sensor z_{i+1}. The idea is that in order to get the best approximation to the true coordinate x_{i+1} the so-called "golden" mean between the indication z_{i+1} source from the sensor and $P_i^{opt} + u_i$ being his prediction. The sensor reading is given a Kalman weight K, and the predicted value (1 − K) is given a value P_{i+1}^{opt} is determined by the formula:

$$P_{i+1}^{opt} = K \cdot z_{i+1} + (1 - K) \cdot (P_i^{opt} + u_i), \tag{5}$$

where K is the value of the Kalman weight coefficient, which is chosen such that the resulting optimal value of the coordinate P_{i+1}^{opt} P_{i+1}^{opt} would be closest to the value of the true coordinate P_{i+1}. For example, if it is known that the readings from the sensor are very accurate, then the degree of confidence in it will be greater and the value will have a greater weight (K is close to one). If the sensor is estimated with significant errors, then it is necessary to focus more on the theoretically predicted value $P_i^{opt} + u_i$. In general, to find the exact value of the Kalman coefficient, it is necessary to minimize the magnitude of random and systematic errors γ_k and δ_i.

To determine the exact value of the Kalman coefficient, it is necessary to minimize the value e_{i+1}, which is the mathematical expectation of the square of the error:

$$e_{i+1} = P_{i+1} - P_{i+1}^{opt}, \tag{6}$$

After substituting formula (4) into Eq. (5), it turns out:

$$e_{i+1} = (1 - K) \cdot (e_i + \gamma_i) - K \cdot \delta_{i+1} \tag{7}$$

The average value of the mathematical expectation from the squared error is minimized:

$$M(e_{i+1}^2) \to \min. \tag{8}$$

The mathematical expectation of the value of the square of the error in determining the force P of interaction of the adaptive three-point gripper of the industrial robot with the object to be manipulated during transfer from the transport container to the work container is determined by the formula:

$$M(e_{i+1}^2) = (1 - K)^2(Me_i^2 + \sigma_\gamma^2) + K^2\sigma_\delta^2. \quad (9)$$

According to formula (9), the minimum value of the mathematical expectation of the squared error is determined under the condition:

$$K_{i+1} = \frac{Me_i^2 + \sigma_\gamma^2}{Me_i^2 + \sigma_\gamma^2 + \sigma_\delta^2}. \quad (10)$$

To determine the value of the Kalman weight coefficient, it is necessary to calculate the values of the statistical moments of the random errors of the mathematical model and the systematic errors in the measurement of the gripping force P of the adaptive three-point gripper of the robot when interacting with the upper part of the manipulated object. Thus, the algorithm for solving the developed mathematical model, for estimating the stochastic system of the dynamic process of interaction of the adaptive three-halanx gripper of the manipulator with the object to be manipulated is implemented using an iterative formula for calculating the value of the Kalman weight coefficient.

During an experimental study of the operation of pressing each phalanx of the gripper, with the gripping jaws of each gripper lever attached to each of them, to the surface of the upper section of the object of manipulation, an experimental relationship was obtained between the value of the force P and the length of each phalanx. The found Kalman coefficient made it possible to reduce the errors in the indication of the grip force sensor. The maximum and minimum errors of the sensor in estimating the value P of the gripping force of the phalangeal tong were respectively $\varepsilon_{max} = 5{\cdot}10^{-2}$ and $\varepsilon_{min} = 0{,}09{\cdot}10^{-2}$ [1].

3.1.2 Experimental Studies of the Prototype of an Innovative Robot with a Phalangeal Gripper

The prototype three-finger gripper was tested in several different gripping events, e.g., with the tennis ball and the ripe tomato. Figures 4, 5, 6, 7, 8 and 9 show the results of experimental studies of tested grippers on the amount of gripping force and energy consumed, measured by FSR sensors, e.g., for a tennis ball, immature tomatoes, and ripe tomatoes. These graphs show the time history of the gripping force measured by each sensor and the energy consumed, which is obtained by multiplying the measured current by the supply voltage of 6 V. The time was taken from the internal clock of the Arduino Nano and measured in milliseconds.

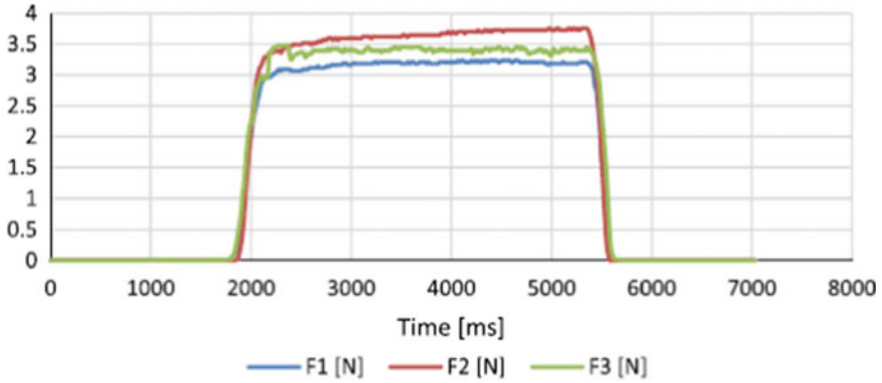

Fig. 4 Grip force test results measured by FSR sensors for a tennis ball [2]

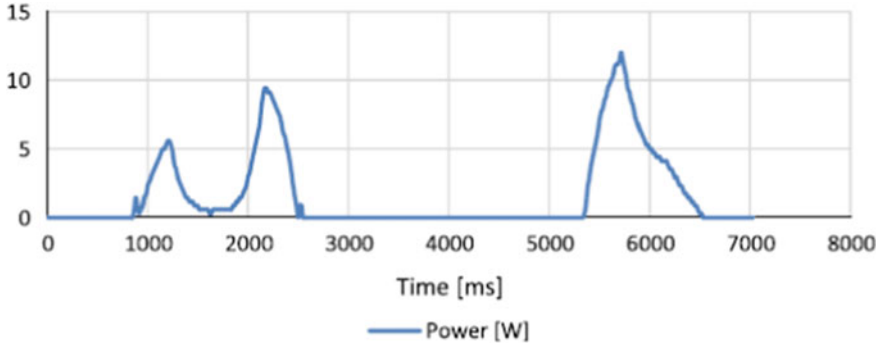

Fig. 5 Results of testing the power consumption [W] for a tennis ball [2]

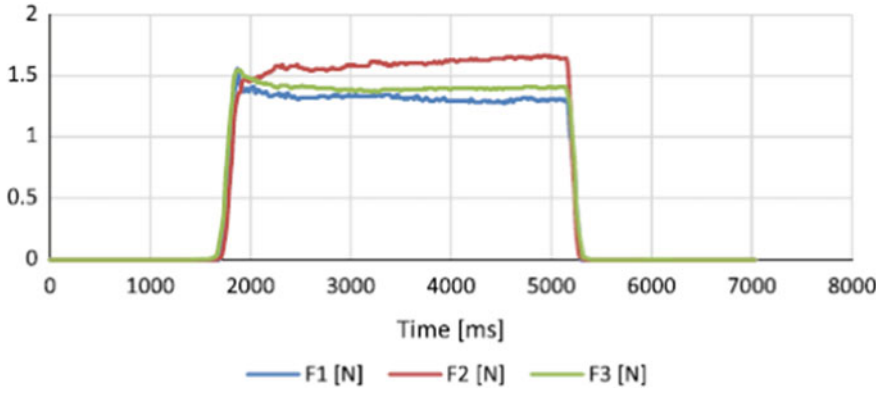

Fig. 6 Results of a test of change in grip force measured by FSR sensors for an immature tomato [2]

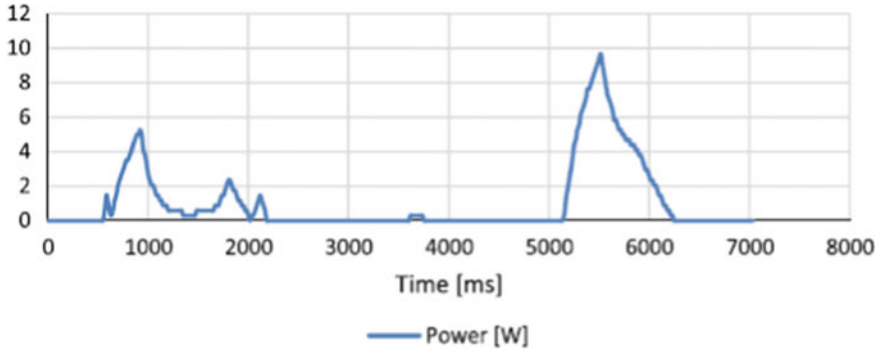

Fig. 7 Test results of the power consumption [W] for an unripe tomato [2]

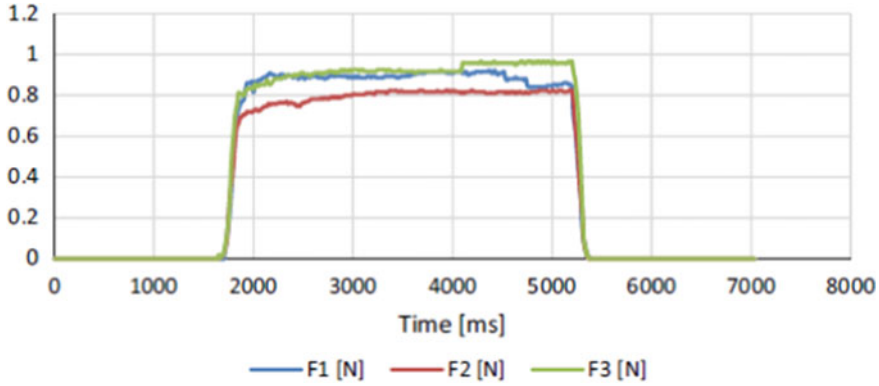

Fig. 8 Results of the grip force test, measured by FSR sensors for a ripe tomato [2]

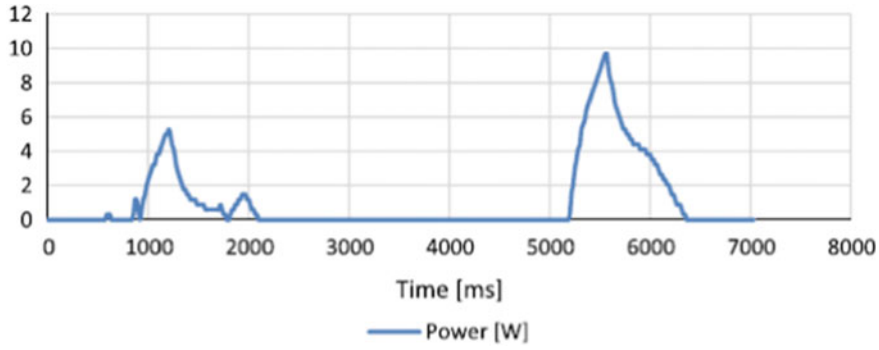

Fig. 9 Test results of the power consumption [W] for a ripe tomato [2]

Figures 4, 5, 6, 7, 8 and 9 show the results of experimental studies of tested grippers on the amount of gripping force and energy consumed, measured by FSR sensors, e.g., for a tennis ball, immature tomatoes, and ripe tomatoes. These graphs show the time history of the gripping force measured by each sensor and the energy consumed, which is obtained by multiplying the measured current by the supply voltage of 6 V. The time was taken from the internal clock of the Arduino Nano and measured in milliseconds [2].

Figures 4 and 6 show the change in grip force during the test, for example, for a tennis ball and an unripe tomato. The shape of the function again approximates a square wave, with the average gripping force for a tennis ball and an unripe tomato being 3.25 N and 1.42 N, respectively. The evolution of energy consumption is shown in Figures 4, 5, 6, 7, 8 and 9. For a tennis ball and an immature tomato, the maximum energy consumption is 12.8 and 9.8 watts, respectively, at the peak of release. Thus, the value of the force is approximately constant during the grip and averages 3.12 N (Fig. 5). The power consumption is characterized by three peaks, as shown in Fig. 6: the first peak during the gripping process, the second peak at the end of the gripping process when the stop switch is triggered, and the last peak when the gripper releases the object. The value of the maximum power consumption is 12.1 W [7].

4 Conclusions

1. In this article, an innovative robotic complex with a pincer for automating the transloading process of plant microsprouts of the technological process of their microcloning was created. Different variants of structural-kinematic schemes of the robot gripper and its structural elements for overloading a plant microsprout were selected and justified. Mathematical methods for selection and justification of geometrical, structural-kinematic and dynamic parameters of structural elements of phalanx grapple are presented.
2. The formulas for calculating the maximum and minimum permissible values of the gripping force of a thin-walled ring are derived from the conditions for ensuring the reliability of the grip and the insignificance of the values of elastic displacements at the contact points of the working element of the gripper with the ring. On the basis of these requirements, the geometrical parameters and the strength parameters of the structural elements of the pincers of the gripper—the gripping jaws—and their positioning on the upper part of the microsprout body of the plant were determined. The rotation of the pincers of the grapple levers should be carried out using the two most effective options for the location of the pincers of the grapple levers near the upper part of the plant microsprout body. According to the variants of the loading scheme of the gripping sponges of the pincers of the gripping levers when they pinch a part of the plant microsprout body.

3. A mathematical method was developed to increase the reliability of the evaluation of the main parameters of the structural elements of the gripper of a robot for automating the overloading of a plant microsprout. Analytical and experimental studies were conducted to determine the relationship between the gripping forces of the phalanx pincers and their geometric parameters. During the experimental studies, errors were found between the values of the gripping force measured by three sensors in each test. These errors are due to the need to improve the accuracy of the estimation of the gripping force parameters of the gripped object by the robotic gripper. The obtained experimental data were refined by determining the Kalman coefficient, which ensured an increase in the accuracy of the estimate of the gripping force parameter of the robot gripper.
4. A prototype of a three-manipulated robotic gripper was developed to automate the handling of various objects, such as a tennis ball or a ripe tomato. It was tested under laboratory and production conditions at the International Scientific Center in Cassino (Italy). The obtained empirical results were refined based on the developed method for selecting and reasoning about the geometrical, structural-kinematic and dynamic parameters of the adaptive gripper, taking into account the stochastic conditions of its operation. Software was developed to simulate the operation of a remotely controlled prototype of a mobile robot with adaptive gripper for overloading a plant microshell.

Based on the research conducted, an innovative robotic complex with a phalanx gripper was created to automate the technological process of transloading plant microsprouts during their microclonal reproduction. These stages of the technological process are currently carried out manually or using complex robotic gripping systems in a number of countries around the world, including the Republic of Kazakhstan, resulting in higher product costs. The concept of creating a perspective image of a controlled mobile robot with a gripper for automating reloading operations. The concept of creating a perspective image of a controlled mobile robot with a gripper for automation of reloading operations and a method of improving the accuracy of estimation of geometric, structural-kinematic and dynamic parameters of an adaptive gripper taking into account the stochastic environment of its operation are new, of scientific and practical interest and can be directly applied in engineering not only in the Republic of Kazakhstan, but also in other countries of the world.

Acknowledgements This research has been/was/is funded by the Science Committee of the Ministry of Education and Science of the Republic of Kazakhstan (**project AP14870662**)

References

1. Kaimov S, Kaimov A, Kaiym T, Syrgaliev Y, Kaimov A, Primbetova A, Tuleshov A (2022) Creation of an innovative robot with a gripper for moving plant microshoots from the in vitro transport tank to the working tank with soil ground at the stage of their adaptation in soil ground during microclonal reproduction. East Eur J Enterp Technol Link Disabl 1(7–115):48–58. http://journals.uran.ua/eejet/article/view/253135
2. Russo M, Ceccarelli M, Corves B, Hüsing M, Lorenz M, Cafolla D, Carbone G (2017) Design and test of a gripper prototype for horticulture products. Robot Comput-Integr Manuf 44:266–275. https://doi.org/10.1016/j.rcim.2016.09.005)
3. Zhu W, Piedboeuf J, Gonthier Y (2002) Emulation of a space robot using a hydraulic manipulator on ground. In: Proceedings of the 2002 IEEE international conference on robotics and automation. Washington, DC. https://www.researchgate.net/profile/Wen-Hong-Zhu/publication/3955354_Emulation_of_a_space_robot_using_a_hydraulic_manipulator_on_ground/links/0a85e5370739caf8e3000000/Emulation-of-a-space-robot-using-a-hydraulic-manipulator-on-ground.pdf
4. Petcovic D, Pavlovic ND (2012) A new principle of adaptive compliant gripper. In: Lovasz EC, Corves B (eds) Machanisms, transmissions and applications. Mechanism and machine science, vol 3. https://doi.org/10.1007/978-94-007-2727-4_13. Springer, London, New York, pp 143–150. https://link.springer.com/book/10.1007%2F978-94-007-2727-4
5. Ivanov KS (2013) Creation of adaptive-mechanical continuously variable transmission. In: 5th international conference on advanced design and manufacture (ADM). Valencia, Spain, pp 63–70. https://www.researchgate.net/publication/272608525_Dynamic_Synthesis_of_Adaptive-Mechanical_CVT
6. Ceccarelli M, Kaimov S, Kaiym T, Kaimov A, Temirbekov E (2019) Grasps of robot manipulator when overloading solid high-radioactive elements and their calculation. Mech Mach Sci 68:316–323. https://link.springer.com/chapter/10.1007%2F978-3-030-03320-0_34
7. Ivanov KS, Tultayev B (2016) Adaptive hydraulic drive of manipulator. Appl Mech Mater 841:215–220. https://doi.org/10.4028/www.scientific.net/AMM.841.215

Investigation into Mechanical Behaviour of Tin Tailing Considering Incremental Loading Oedometer

Ismail Adeniyi Okewale and Hendrik Grobler

Abstract Due to tremendous engineering applications of tin worldwide, tin ores are mined and processed, and these processes generate a left-over materials called tin tailings. Tailing dam failures have led to studies on some tailings because of their adverse environmental, social and economic implications. However, there is hardly any study investigating the mechanical behaviour of tin tailings and the knowledge about these materials is few and very scanty. Here, the mechanical behaviour of tin tailing was investigated through one-dimensional compression. In addition to carrying out of series of oedometer tests, index and physical, microstructural, chemical and mineralogical analyses were also conducted. Tin tailings are poorly graded in nature. The microstructure is characterised by agglomeration of particles to form continuous clusters with few inter and intra-cluster pores. The fabric is heterogeneous. Cassiterite, ilmenite and quartz dominate the mineralogy. The compression paths are parallel and the normal compression lines are not unique. The mode of behaviour in tin tailing is transitional in nature and the behaviour is therefore initial state dependent.

Keywords Tailing · Tin · Fabric · Non-convergent · Regularity

1 Introduction

Tin ores are mined in order to obtain pure tin for various industrial and engineering applications. In order to obtain the end products, tin ore minerals are mined and processed, and these processes produced the inevitable unwanted materials called tailings. Due to these processes, the materials vary widely in their mineralogy and grading. Tailings are stored in tailing dams or dumps and due to previous failures in tailing dams, the importance of investigations into their mechanical behaviour have received more attention [1–5]. Furthermore, the stability of tailing dams and their

I. A. Okewale (✉) · H. Grobler
Department of Mining Engineering, University of Johannesburg, Johannesburg, South Africa
e-mail: iaokewale@futa.edu.ng

H.-Y. Jeon (ed.), *Proceedings of the International Conference on Geosynthetics and Environmental Engineering*, Lecture Notes in Civil Engineering 374,
https://doi.org/10.1007/978-981-99-4229-9_2

susceptibility to failure have been investigated [6–10]. This is because the run out of tailings from dam is fast and mortally fatal. In fact, more than 240 incidents of catastrophic tailing dam's failure were reported between 1912 and 2014 [5]. The most recent incident is diamond tailing dam failure in South Africa in 2022. Therefore, it is very crucial to obtain more intuition into the mechanical characteristics of tailings.

Although, some tailings (e.g., iron, gold) mechanical characteristics has been studied, the knowledge about this material is still limited. For example, there is hardly any study investigating the characteristics of tin tailings. Mechanical behaviour of tin tailings is presented in this study. Series of oedometer tests were conducted in conjunction with physical and index tests, microstructural and chemical analyses and mineralogical analysis. The work is new for tin tailing and it is also novel the manner in which the features of tin tailings are compared with other tailings. It is also interesting the way in which the evolution of shape descriptors with effective vertical stress is investigated.

2 Materials and Methods

Disturbed tin tailings were the materials used. The samples were collected from Kuza tailings dump in Bauchi State, North East Nigeria. The coordinate of sample location is 10° 58′ 11.8″N and 9° 53′ 55.8″E. However, natural grading was used for the samples tested. Grading of the specimens was determined using a combination of wet sieving and sedimentation technique [1]. A Phenom ProX scanning electron microscope (SEM) equipped with an energy dispersive spectrometer (EDS) was used for the microstructure and geochemical analyses. For the EDS analysis, air-dried and pulverized specimens were placed in specimen holder for testing [11].

A Shimadzu XDS 2400H diffractometer that was equipped with JCPDFWIN software was used for the mineralogy test [1]. The minerals were recognized within $5° \leq 2\theta \leq 90°$ with Cu-Kα radiation and the machine operated at 40 kV and 55 mA. The powdered form specimens were scanned at an interval of 0.02°/0.30 s. Sphericity (S), roundness (R) and regularity (ρ, arithmetic mean of S and R) were the shape descriptors used. They were estimated from the specimen's image from the petrographic microscope. The values for different particle shapes were determined using empirical chart proposed by Krumbein and Sloss [12]. However, fifty particles were selected randomly and observed under an optical microscope to determine the repeatability of the particle shape for different samples.

The compression behaviour of the specimens was investigated using a conventional front loading oedometer. The closed base confining ring of height 20 mm was utilized. Incremental loading was adopted and the maximum load was 65 kg. Dry compaction (DC), wet compaction (WC) and slurry (SL) were the sample preparation methods used. The specimens were mixed and then vibrated for about 1 h for air bubbles to escape. Specimens were then placed in the oedometer ring and height carefully taken under a small surcharge load. To allow for saturation, the specimens were flooded for about 12–24 h.

Different measurements were taken to determine the specific volume ($v = e + 1$, e is void ratio). To improve the confidence, several methods were used [13–15]. Initial height, diameter, water content and specimen mass were used to estimate initial v. Final height, diameter and water content were utilized for confirmation by back-calculating the initial v using the vertical strains obtained. Similar to other studies, different equations were used [16–18].

3 Results and Discussions

Figure 1 shows the grading of the specimen. The specimen is poorly graded in nature and it is characterised by horizontal tail in the earlier section followed by almost vertical which constitutes the substantial part. This feature is comparable to what was found by similar studies [1, 5, 19]. The grading characteristics in terms of coefficients of uniformity (Cu) and curvature (Cc), mean particle size (D_{50}), grain size index (I_{GS}), fines content (Fc) and clay fraction (CF) are given in Table 1. The D_{50} is 0.23 and this is similar to other tailings [1, 5, 8]. However, the value is higher than some tailings [3, 8] and this indicates that tin tailing is coarser. The Cu and Cc are 1500 and 540 respectively and these seem to show that the specimen is well-graded but this results from long tail and vertical section in the grading curve. The I_{GS} value of 0.002 is similar to other studies [3, 8].

The CF of 14.80 is very low which shows the tailing is non-clayey material similar to other materials [1, 3, 5, 20, 21]. The Fc is 22 and in comparison to other tailings, the value is very small and this further confirms the coarser nature of the sample.

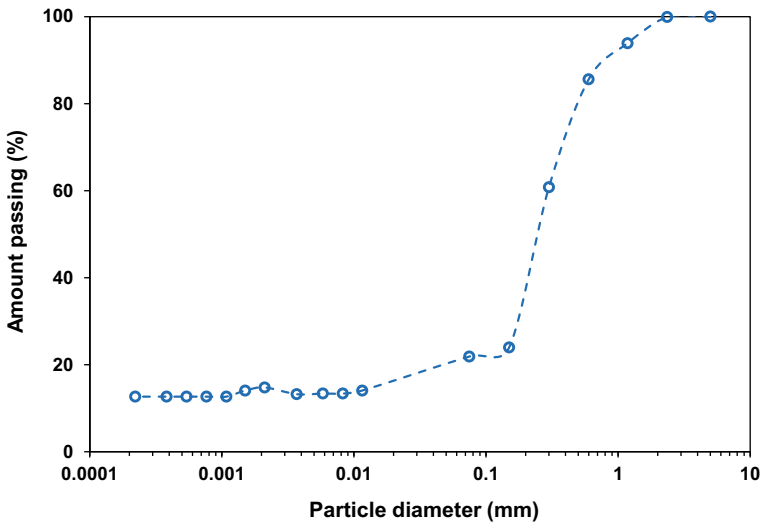

Fig. 1 Grading of the sample

Table 1 Characteristics of different samples

Sample	D_{50} (mm)	C_u	C_c	I_{GS}	CF (%)	F_c (%)	LL (%)	References
Tin	0.23	1500	540	0.002	14.8	22	–	This paper
Iron top1	0.22	27	2.1	0.008	10	28	–	Okewale and Grobler [1] and Okewale et al. [2]
Iron base1	0.9	112	68	0.008	8	18	–	Okewale and Grobler [1] and Okewale et al. [2]
Iron top 2	0.31	84	19	0.003	10	18	21.7	Okewale et al. [2]
Iron middle 2	0.26	70	6.7	0.003	10	14	19.8	Okewale et al. [2]
Iron base 2	0.25	55	9. 9	0.004	10	18	20.3	Okewale et al. [2]
Iron (UB)	0.22	10.4	2.6	0.021	1	16	–	Li et al. [5], Li and Coop (2019)
Iron (MB)	0.035	10	1.1	0.003	2	62	–	Li et al. [5], Li and Coop (2019)
Iron (PO)	0.023	6.7	2.2	0.003	2	92	–	Li et al. [5], Li and Coop (2019)
Gold	0.065	7.0	2.3	0.009	4	68	–	Bedin et al. [4]
Gold	0.011	7.3	1.4	0.001	10	94	–	Li et al. [5]
Gold (UB)	0.096	24.1	2.2	0.003	7	33	–	Chang et al. (2011)
Gold (MB)	0.053	10.5	0.8	0.005	3	53	–	Chang et al. (2011)
Gold (PO)	0.006	2.6	1.6	0.002	8	98	–	Chang et al. (2011)
Copper	0.031	5.1	1.5	0.006	2	92	–	Li et al. [5]
Fluorite sand	0.180	2.5	1.1	0.072	–	–	–	Carrera et al. [8]
Fluorite silt	0.026	9.7	2.6	0.002	8	92	–	Carrera et al. [8]

C_u coefficient of uniformity, C_c coefficient of curvature, D_{50} mean particle size, I_{GS} grain size index, F_C fines content, CF clay fraction, LL liquid limit, UB upper beach, MB middle beach and PO pond

Figure 2 shows the microstructure of the sample with the field of view of image of 200 μm. Fabric is dominated by agglomeration of particles to form clusters. The particles are fairly angular with intra-particle and inter-particle pores. The fabric is isotropic and heterogeneous. Table 2 shows the details of the chemical composition of the specimen. This is dominated by silica followed by heamatite and alumina. Also available is titania and other oxides. Table 3 presents the mineralogy of the sample and the spectrum is presented in Fig. 3. This comprises quartz, cassiterite, ilmenite, pyrite, mullite and xenotime.

Figure 4 presents the oedometer test data for the specimens. One-dimensional compression behaviour of dry compacted (DC) specimens is presented in Fig. 4a. The compression curves of the DC specimens are stiff and they are diverging from a unique line, similar to other studies [1]. The paths of the wet compacted (WC) specimens (Fig. 4b) are variable but unlike DC specimens, the curves are slightly steeper but, the paths are diverging. Figure 4c shows the compression paths of the

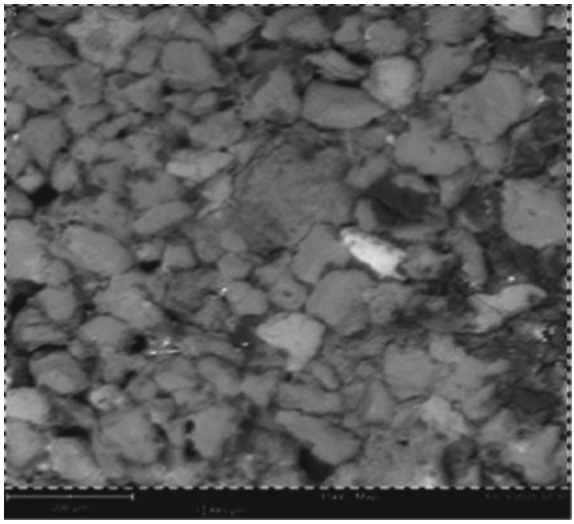

Fig. 2 Microstructure of the sample

Table 2 Chemical compositions

Oxide symbol	SiO_2	Fe_2O_3	Al_2O_3	TiO_2	K_2O	SO_2	Ag_2O	Nb_2O_5	CaO	MgO	Na_2O
Weight (%)	54.2	14.5	7.2	6.5	2.8	3.7	1.2	1.2	0.7	0.3	0.2

Table 3 Details of mineralogy

Minerals	Quartz	Cassiterite	Ilmenite	Pyrite	Mullite	Xenotime
Amount (%)	9.16	58.52	19.12	16.41	4.06	6.48

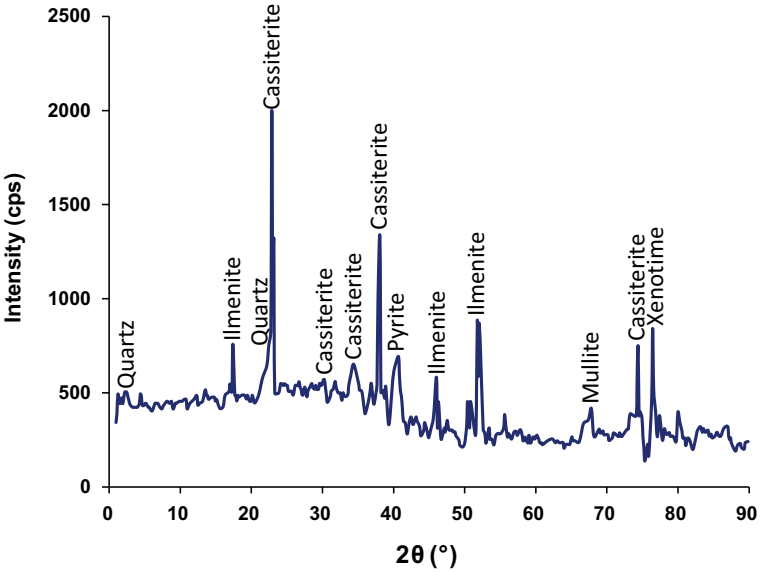

Fig. 3 Spectrum of the sampler showing the mineralogy

slurry (SL) specimens and it can be seen that the curves are less steep than the WC specimens. Again, the compression curves are diverging from a unique line. This indicates that the samples with different initial specific volumes are not converging to a unique line. This feature has been termed transitional mode of behaviour and it is present in tin tailing, similar to other tailings [5].

Figure 5 presents the overall degree of convergence. This was estimated using the parameter m proposed by Ponzoni et al. [22]. The m value of 0.79 shows that the degree of transitionalty in the specimen is very strong.

Figure 6 presents the evolution of particle shape of specimens from natural to the compressed. For the original specimen (Fig. 6a), the values of sphericity, roundness and regularity are 0.66, 0.64 and 0.65 respectively. This shows that the specimen is fairly angular which also confirms what was seen in the fabric. Furthermore, the shape of the specimen after compression to 8237 kPa is presented in Fig. 6b. Again, the values of sphericity, roundness and regularity are 0.66, 0.58 and 0.62 respectively. The particle shape is again fairly angular and very close in value and similar to original specimen. This also shows that the particle breakage in the specimen is insignificant.

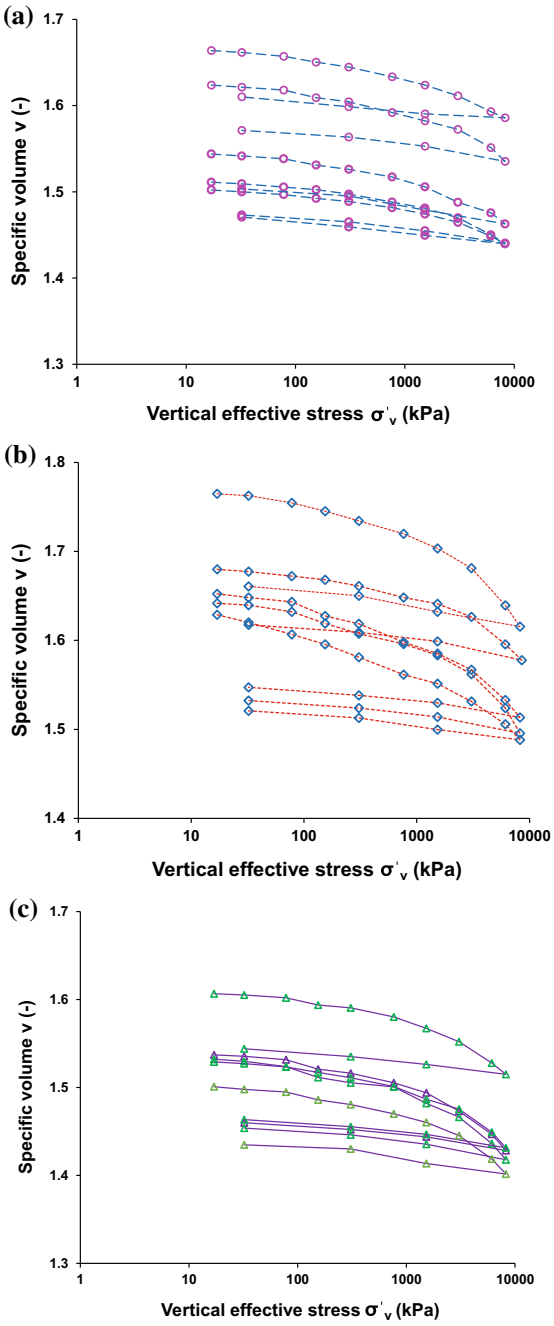

Fig. 4 Figure 4 Oedometer test results of the samples; **a** Dry Compaction, **b** Wet compaction and **c** Slurry

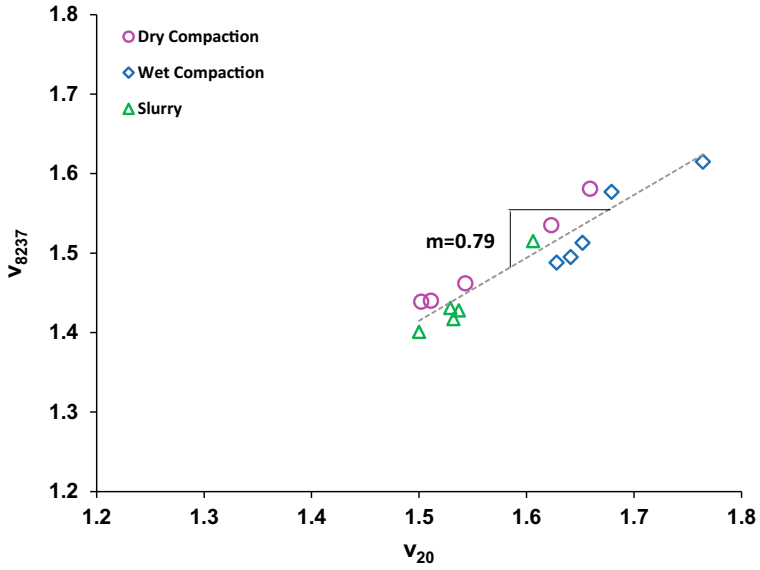

Fig. 5 Overall degree of convergence

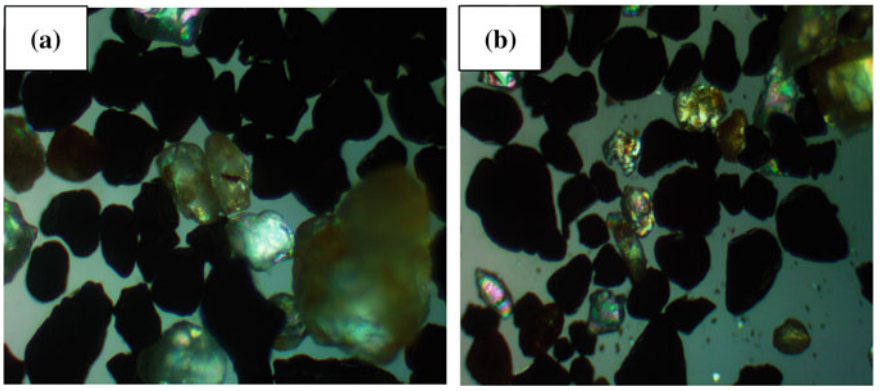

Fig. 6 Evolution of particle shape; **a** original shape and **b** shape after compression

4 Conclusions

Mechanical behaviour of tin tailing has been studied by conducting oedometer tests, physical and index tests, chemical and microstructural analyses, mineralogy and particle shape analyses. Specimens were prepared using wet compaction, dry compaction and slurry methods. The specimen is poorly graded and non-clayey in nature. The fabric is characterised by particle agglomeration, heterogeneity, isotropic and variable inter and intra particle voids. Silica, heamatite and alumina dominate the

chemical composition and the mineralogy is dominated by cassiterite and quartz. The compression behaviour shows that the specimen has transitional mode of behaviour. At different initial states, the specimens do not converge to a unique line and this could be linked to heterogeneous fabric. The shape of the particles are fairly angular and no significant particle breakage in the specimens.

References

1. Okewale IA, Grobler H (2022) Mechanical and microstructural properties of iron tailings. Environ Geotech 1–13
2. Okewale IA, Coop MR, Grobler H (2022) On the one-dimensional compression behaviour of iron tailings. Submitted Geomech Eng
3. Chang N, Heymann G, Clayton C (2002) The effect of fabric on the behaviour of gold tailings. Géotechnique 61:187–197
4. Bedin J, Schnaid F, da Fonseca AV, Costa Filho LDM (2012) Gold tailings liquefaction under critical state soil mechanics. Géotechnique 62:263–267
5. Li W, Coop MR, Senetakis K, Schnaid F (2018) The mechanics of a silt-sized gold tailing. Eng Geol 241:97–108
6. Fourie AB, Blight GE, Papageorgiou G (2001) Static liquefaction as a possible explanation for the Merriespruit tailings dam failure. Can Geotech J 38:707–719
7. Zandarin MT, Oldecop LA, Rodriguez R, Zabala F (2009) The role of capillary water in the stability of tailing dams. Eng Geol 105:108–118
8. Carrera A, Coop M, Lancellotta R (2011) Influence of grading on the mechanical behaviour of Stava tailings. Géotechnique 61:935–946
9. Schnaid F, Bedin J, Viana da Fonseca AJP, de Moura Costa Filho L (2013) Stiffness and strength governing the static liquefaction of tailings. J Geotech Geoenviron 139:2136–2144
10. Zhang Q, Yin G, Wei Z, Fan X, Wang W, Nie W (2015) An experimental study of the mechanical features of layered structures in dam tailings from macroscopic and microscopic points of view. Eng Geol 195:142–154
11. Okewale IA, Grobler H (2021) Mechanics of compression in talc considering sample quality. Arab J Geosci 1–13
12. Krumbein WC, Sloss LL (1963) Stratigraphy and sedimentation. 2nd edn. Freeman and Company, San Francisco
13. Okewale IA, Grobler H (2020) The effects of structure of Nigeria clay in one-dimensional compression. In: The 2020 world congress on advances in civil, environmental, and materials research (ACEM20) GECE. Seoul, Korea, pp 1–10
14. Okewale IA, Grobler H (2020) Mechanics of compression behaviour in shale. In: The 2020 world congress on advances in civil, environmental, and materials research (ACEM20) GECE. Seoul, Korea, pp 1–10
15. Okewale IA, Grobler H (2021) Inherent complexibilities in weathered rocks: a case of volcanic rocks. Rock Mech Rock Eng 1–22
16. Okewale IA (2020) On the intrinsic behaviour of decomposed volcanic rocks. Bull Eng Geol Env 79:1311–1322
17. Okewale IA (2020) Compressibility and the effects of structure of tropical clay in incremental loading oedometer tests. Geotech Geol Eng 79(38):5355–5371
18. Okewale IA (2019) Influence of fines on the compression behaviour of decomposed volcanic rocks. Int J Geo-Eng 10:1–17
19. Li W, Coop MR (2019) Mechanical behaviour of Panzhihua iron tailings. Can Geotech J 1–16
20. Okewale IA, Grobler H (2021) Influence of fabrics on compression mechanics of iron tailings. Emerging technologies and applications for green infrastructure, Lecture notes in civil engineering. pp 1113–1120

21. Okewale IA, Grobler H (2021) Investigations into grading characteristics of tailings. Emerging technologies and applications for green infrastructure, Lecture notes in civil engineering. pp 1121–1127
22. Ponzoni E, Nocilla A, Coop MR, Colleselli F (2014) Identification and quantification of transitional modes of behaviour in the sediments of Venice Lagoon. Géotechnique 64:694–708

An Alternative Scheme to Estimate Displacement from Earthquake-Induced Acceleration for Building Structures

Shieh-Kung Huang

Abstract Story drift plays an important role in the safety assessment of building structures as well as the rapid assessment after a seismic event once structural displacement can be properly measured or estimated. For structural health monitoring (SHM), considering their cost, accelerometers are generally used to measure the responses instead of using displacement meters. During the past decade, different techniques have been developed to provide displacement estimation using integration but the conventional integration scheme relies on baseline correction methods to have a reasonable result and none of these techniques can properly estimate the residual displacement. Nevertheless, few of them can have great performance on the structural responses. This study proposes a combination of singular spectrum analysis (SSA) and an integration scheme to estimate the structural displacement directly from the recorded acceleration. Moreover, the proposed method is verified by using the roof responses of the RC specimen recorded during the shaking table test. SSA decomposes the acceleration measurement into approximation and detail parts; the first part are used as weighting factors, and the detail part are integrated twice to have the temporary displacement. Finally, the structural displacement is correctly estimated as well as the induced residual displacement during earthquake excitation.

Keywords Residual deformation · Displacement estimation · Inter-story drift · Singular spectrum analysis · Damage assessment

1 Introduction

In damage assessment of building structures under earthquakes, story drift plays an important role once structural displacement can be measured or estimated. Accordingly, three performance levels regarding drift limits for reinforced concrete (RC) structures and steel structures are addressed in the Prestandard and Commentary

S.-K. Huang (✉)
National Chung-Hsing University, Taichung 40227, Taiwan
e-mail: skhuang@nchu.edu.tw

H.-Y. Jeon (ed.), *Proceedings of the International Conference on Geosynthetics and Environmental Engineering*, Lecture Notes in Civil Engineering 374,
https://doi.org/10.1007/978-981-99-4229-9_3

for the Seismic Rehabilitation of Buildings from the Federal Emergency Management Agency (FEMA 356), including immediate occupancy, life safety, and collapse prevention [1]. Although story drift serves as a guideline for a safety assessment of building structures as well as a rapid assessment after a seismic event, direct measurement of structural displacement is inaccessible in most field applications and, therefore, structural acceleration is suggested as an alternative. Furthermore, considering the cost, displacement meters are generally replaced by accelerometers to collect the structural responses for building seismic monitoring. As the result, estimation of structural displacement using acceleration measurement can be helpful for a rapid assessment.

The displacement estimation through the recorded acceleration directly is a challenging topic. In the conventional integration scheme, the recorded acceleration is integrated twice to estimate displacement; however, a trend is always induced (in the integrated velocity and displacement) and baseline correction methods are required all the time to have a reasonable estimation. For example, in the field of seismology, Housner suggests a correction scheme while integrating ground displacement from the acceleration [2]. Then, Berg and Housner further discuss the integrated velocity and displacement during a strong ground motion to improve the scheme [3]. Later, in the field of structural engineering, a successive study pointed out that the displacement error obtained through the double integration of the linear acceleration response can be as low as 5% of the peak value; however, the one for a nonlinear acceleration response might be higher than 12% [4]. Recently, Liao et al. try to improve the displacement estimation by using the complementary filter [5]. In recognition of the importance of the structural displacement associated with assessing structural conditions, some novel sensors designed for directly measuring the relative displacement of a building structure through the composition of a laser light source and a phototransistor array have been developed [6]. With advances in optics and electronics, several displacement measurements have been also proposed [7].

Despite the advances of those novel sensors, signal processing techniques are developed correspondingly and the conventional integration scheme is still promising. Although baseline correction methods, such as lowpass filter, can be adopted to eliminate the undesirable trends, the residual displacement (or drift as well) that is inherent in the uncorrected data is inevitably wiped out [4]. Other signal processing techniques are developed to correct the baseline drift under some assumptions and limitations [8–11]. Since the residual displacement after a seismic event describes very useful information for damage assessment of building structures, a different approach needs to be developed to estimate a reliable displacement without the lack of residue.

In this study, the scheme combining the techniques of singular spectrum analysis (SSA) and the double integration is developed to estimate the structural displacement directly from the recorded acceleration. In the proposed method, SSA is implemented to decompose the recorded acceleration into approximation and detail parts and the structural displacement, as well as the residual displacement, can be correctly reproduced by fusing the information. The performance of the proposed scheme is verified by using the seismic responses of specimens recorded during the shaking table

test. In the meanwhile, the effects of the parameters are studied to provide reliable displacement estimation. Finally, the study is summarized and a brief conclusion is drawn.

2 Estimation of Structural Displacement

In the conventional integration scheme, a trend always appears in the integrated displacement due to unknown initial conditions, errors aggravated with an increase of time, transducer noise, and, especially mechanical or electrical hysteresis of the sensors. Iwan et al. have introduced the hysteresis problem within the accelerometers and the occurrence of baseline drift as a small step function [8]. Besides the accelerometers, the baseline drifts can also be observed from the geophones and seismometers, so the displacement estimation through the recorded acceleration directly is a difficulty both in the field of structural engineering and earthquake engineering.

2.1 Singular Spectrum Analysis (SSA)

The baseline shifts in the recorded data produce trends after integration. Hence, SSA is implemented in this study to extract the shifts which are so small to extract using conventional signal processing techniques. It is a novel technique for time series analysis incorporating the elements of classical time series analysis, multi-variate statistics, multi-variate geometry, dynamic systems, and signal processing [12–14].

The basic procedure of SSA consists of four steps: (1) embedding Hankel matrix, (2) applying singular value decomposition (SVD), (3) grouping, and (4) reconstructing signal [15]. Generally, the first two steps are considered as decomposition stage and the last two steps are named as reconstruction stage.

$$\mathbf{X} = \mathbf{U}\mathbf{S}\mathbf{V}^{*} \tag{1}$$

where $\mathbf{U}$ is a $L \times L$ unitary matrix, $\mathbf{S}$ is a $L \times K$ diagonal matrix with non-negative real numbers on diagonal, and $\mathbf{V}^{*}$ (the conjugate transpose of $\mathbf{V}$) is a $K \times K$ unitary matrix. The diagonal entries of $\mathbf{S}$ are known as singular values of matrix. L columns of $\mathbf{U}$ and K columns of $\mathbf{V}$ are called left singular vectors and right singular vectors of matrix, respectively. Furthermore, by applying SVD, it is possible to write the Hankel matrix, $\mathbf{X}$, as a sum of L elementary matrices, $\mathbf{X}_n$, which are composed of the left singular vectors and the principal components of the time delay series.

Grouping is the first step in the reconstruction stage. This procedure partitions the above-mentioned elementary matrices into several subsets as

$$\mathrm{X} = \overline{\mathrm{X}}_1 + \overline{\mathrm{X}}_2 + \ldots + \overline{\mathrm{X}}_D \tag{2}$$

The question about how to group the elementary matrices depends on the targets of SSA. For example, if one wants to extract non-periodic trends, the elementary matrices can be grouped into two subsets where the first subset only includes only the first elementary matrix. After the subsets are grouped, the k-th element of the time series, x_n, can be reconstructed by skew-diagonal averaging of each elementary matrix

$$x_k = \text{s.d.a.}\{\mathbf{N}_k\} = \begin{cases} \frac{1}{k}\sum_{j=1}^{k} \mathbf{N}_{k-j+1,j} & \text{for } 1 \le k < K \\ \frac{1}{K}\sum_{j=1}^{K} \mathbf{N}_{k-j+1,j} & \text{for } K \le k \le L \\ \frac{1}{K+L-k}\sum_{j=k-L+1}^{K} \mathbf{N}_{k-j+1,j} & \text{for } L < k \le N \end{cases} \tag{3}$$

where L is assumed to be larger than K. Equation (3) refers to average the matrix elements along the anti-diagonal direction (or positive sloping skew-diagonals). For K is larger than L, the expression is analogous; the only changes are the substitution $L \leftrightarrow K$ and the use of the transposition of the matrix, $\mathbf{X}$. The reconstructed time series produced by the elementary grouping is called elementary reconstructed series.

These components can be further used to identify trends, smooth data, extract periodic signals, detect cycles, forecast tendency, and so on and so forth. A possible application is the removal of the trend appeared in the integrated responses.

2.2 Trend Removal via SSA

To remove the trend that appears in the integrated velocity and displacement, a constant, c, is added to amplify the small shifts included in the recorded acceleration. The constant and can be assigned by multiplying the peak amplitude with an amplification factor, c_a, as

$$c = c_a \max\{|x_n|\} \tag{4}$$

Then, SSA is implemented to extract the added constant as well as the amplified distortion (baseline shifts). Because the combination is significant, the extraction can simply select the largest singular value during the third and fourth steps.

The reconstructed acceleration using the largest singular value is called approximation part, x_{approx}, while the one using the rest of singular values is called detail part, x_{detail}. Hence, a temporary displacement can be integrated from the detail part since most of the distortion is decomposed through SSA. Repeat the works iteratively by using the ascending size, L, each temporary displacement, which corresponds to each size of Hankel matrix, can be obtained. To generate the estimated displacement, the temporary displacements are summed up with the weighting factor, w_i, which is the linear correlation between the uncorrected acceleration and the approximation part.

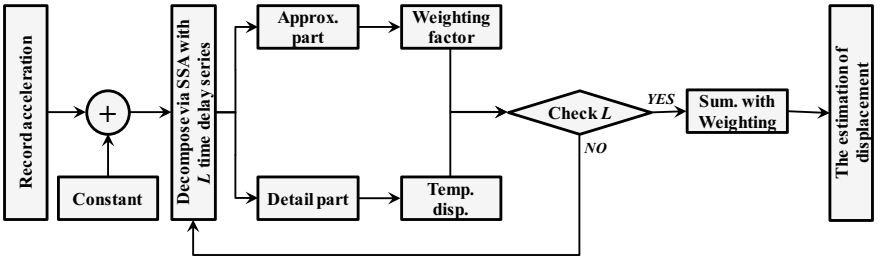

Fig. 1 Flowchart of the displacement estimation using recorded acceleration

$$c_i = \mathrm{corr}\{x_n, x_{\mathrm{approx},i}\} \tag{5}$$

$$w_i = \frac{c_i}{\sum c_i} \tag{6}$$

where c_i is the correlation coefficient, corr{,} denotes as linear correlation operator, and i is the number of the size It is important to note that by using a smaller L in the Hankel matrix, the approximation part, x_{approx}, reconstructed contains not only the distortion (the combination of the small shifts and the added constant) but also the waveform of the dominant frequency in the recorded acceleration; therefore, the correlation between xn and $x_{\mathrm{approx},i}$ is stronger. On the contrary, when using a larger L to reconstruct the approximation part, only the added constant is extracted. Finally, the estimation of the displacement can be calculated as

$$d_n = \sum w_i \, d_{\mathrm{detail},i} \tag{7}$$

where $d_{detail,i}$ is the temporary displacement integrated from the detail part.

Figure 1 shows the flowchart on estimating the displacement using the recorded acceleration. Obviously, some key parameters are needed to produce a realistic estimation. For example, the amplification factor, c_a, the sizes of the Hankel matrix, i, the necessary number of the detail parts, and so on. Fortunately, the effects of those parameters are examined and studied in the previous study [16].

3 Verification Using Recorded Acceleration

In an ideal world, integrating acceleration could be simple and easy to deal with; however, it is a complex one in the real measured data. Many researchers proposed different schemes to correct the baseline drifts, trying to avoid serious trends for the integrals of velocity and displacement [11, 17–20]. Nevertheless, few of them can have great performance on the structural responses. And, the baseline correction

applied to the estimated displacement, generally, may remove some critical information, which then leads to missing some of the displacement components, particularly the low-frequency components (or residual displacement) of the structural response. In this study, the SSA scheme is proposed to estimate the displacement via integration. To verify the proposed schemes, a shaking table test is conducted to simulate seismic events.

3.1 Experimental Setup

A series of shaking table tests were conducted at National Center for Research on Earthquake Engineering (NCREE) to verify the estimation of structural displacement using acceleration measurement during earthquake excitation. Four identical specimens are tested on the shaking table, as shown in Fig. 2, and they are subjected to the same earthquake excitations with different intensities to produce different damage as well as residual displacement.

The input of the shaking table is scaled from 1999 Taiwan Chi-Chi earthquake at station TCU082 and the target excitation levels are selected as 600 gal, 840 gal, 1100 gal, and 1300 gal (named RCF6, RCF2, RCF4, and RCF3, respectively). Those intensities can provide different structural behaviors from no damage to severe damage according to the numerical simulation before the formal tests. As the result, the specimens can generate different displacements; consequently, the severely damaged one could leave a larger residual displacement and the final displacement of the no damaged one could return initial position. Furthermore, several accelerometers and linear variable differential transformers (LVDTs) are installed to measure the acceleration and displacement responses on the structural roof and the shaking table. Those structural responses are digitalized and collected by the default DAQ system of the shaking table system with a sampling rate of 200 Hz.

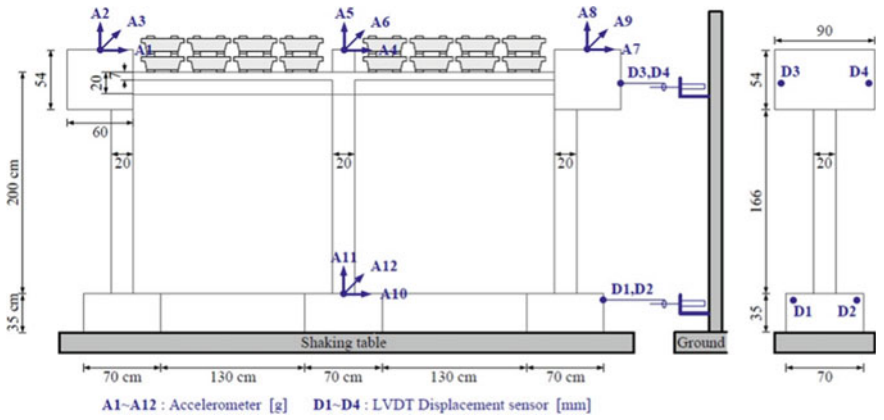

Fig. 2 Sketch of the test specimen for the shaking table test

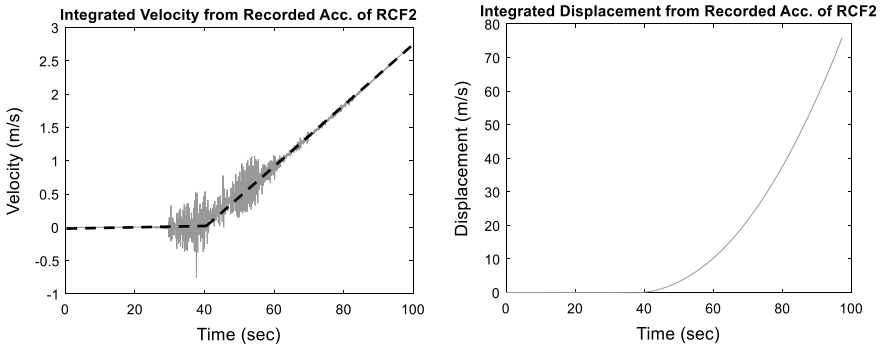

Fig. 3 Integrated velocity and displacement from recorded acceleration

3.2 Preliminary Analysis

Since the inter-story drift is a relative response, the relative acceleration in between the structural needs to be calculated first instead of using absolute acceleration directly measured from the accelerometers. Even so, the structural velocity and displacement cannot be integrated from the relative acceleration directly. For example, Fig. 3 shows the integrated results from the relative acceleration between the structural roof and the shaking table during the test of RCF2. Obviously, Fig. 3a contains two straight lines intersected around 40 s and produces a second-order polynomial line in Fig. 3b. This observation indicates some baseline shifts within the recorded acceleration.

The baseline shifts are non-periodic signals and the assumption suggested by Iwan and Boore works well [8–10], especially for the acceleration measured from the test of RCF2. Figure 4 shows the extracted shifts and displacement estimation using Iwan and Boore's scheme. The threshold used in this figure is the one proposed by Iwan et al. and the optimized interval is the best fit for the filtered acceleration. Indeed, the threshold removes some baseline shifts, resulting that the corrected velocity is around zero near the end of the recorded acceleration. However, as shown in Fig. 4d, the optimized interval provides even better performance and the well-corrected velocity seems to remove all the shifts successfully. But none of them produce a realistic estimation of displacement. This scheme fails because the baseline shifts brought by hysteresis aren't simple step functions, as shown in Fig. 4c, e.

3.3 Proposed Method

The estimation of the shaking table test is generated following the flowchart shown in Fig. 1. To evaluate the estimation, the absolute errors of the overall displacement, the peak displacement, and the residual displacement are provided, as shown in Fig. 5,

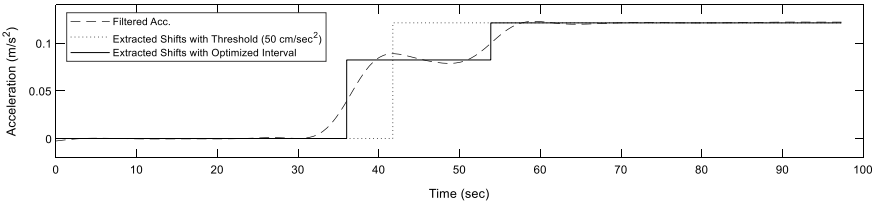

(a) comparison between filtered acceleration and extracted shifts

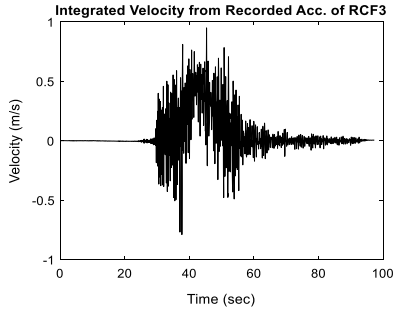

(b) integrated velocity with threshold

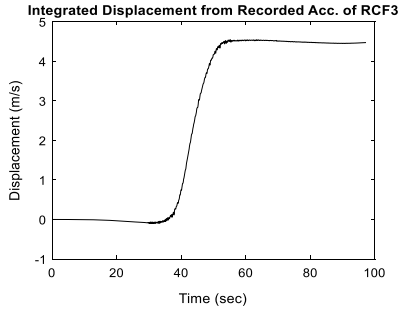

(c) integrated displacement with threshold

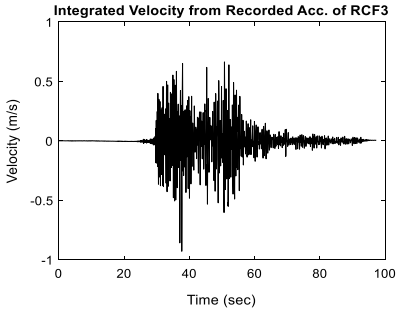

(d) integrated velocity with optimized interval

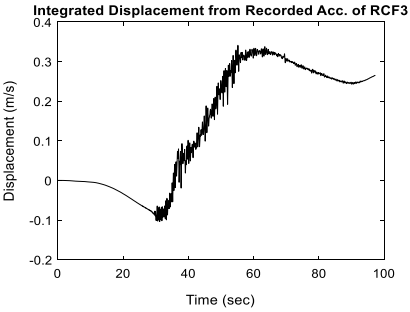

(e) integrated displacement with optimized interval

Fig. 4 Extracted shifts and displacement estimation using Iwan and Boore's scheme

and the performance of the proposed procedure is excellent. First, the absolute errors of the overall displacement are calculated by using the root mean square (RMS) value and the removal of the baseline shifts using SSA performs quite well. The errors ranged only from 1.6 to 4.0 mm. Then, if the inter-story drift is considered for building seismic monitoring, the absolute errors of the peak displacement demonstrate that this procedure can provide a good index. The peak displacement of the four tests is 27.00 mm, 48.59 mm, 65.62 mm, and 89.06 mm, respectively; however, the absolute errors only range from 6.2% to 12.6%. On the other hand, the absolute errors of the residual displacement exhibit that the estimated displacement can include the permanent deformation for the damage assessment of building structures. In the four tests, the residual displacement is 0.84 mm, 8.45 mm, 18.03 mm, and 41.69 mm,

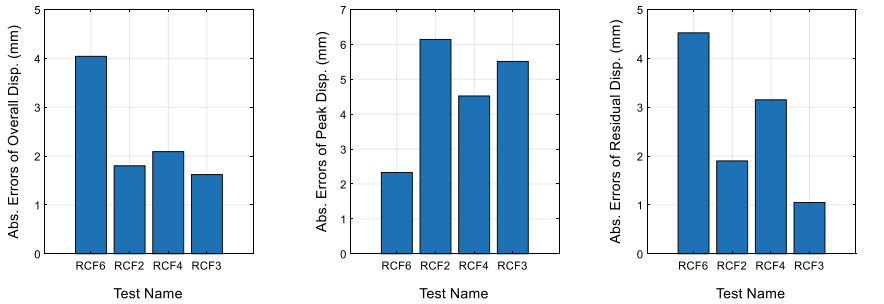

(a) Absolute Errors of Overall Displacement

(b) Absolute Error of Peak Displacement

(c) Absolute Error of Residual Displacement

Fig. 5 Errors of displacement under different earthquake excitations

respectively. The absolute errors are 22.5, 17.5, and 2.5% for RCF2, RCF4, and RCF3. In RCF2, the absolute error of the residual displacement is slightly larger because the residual displacement is relatively small.

To compare the estimated and measured displacement under different earthquake.

To compare the estimated and measured displacement under different earthquake excitations, the similarity is also studied using correlation coefficient and Euclidean distance. The minimum correlation coefficient which is up to 93% displays that the estimation is consistent well with the measurement, especially the response phase. The maximum Euclidean distance is down to 0.6 and most of them are under 0.3, meaning that the response amplitude fused by SSA scheme is accurate even the structural displacement contains residue. Figure 6 shows the estimated displacement of the four tests. It's clear that the residual displacement increases as the intensities, meaning that different damages are generated to the specimens. From the shaking table test of the four RC specimens, it is verified that a good estimation of the inter-story drift can be obtained using the proposed method. The relative displacement, as well as the residual displacement, can be correctly reproduced by fusing the approximation and detail parts.

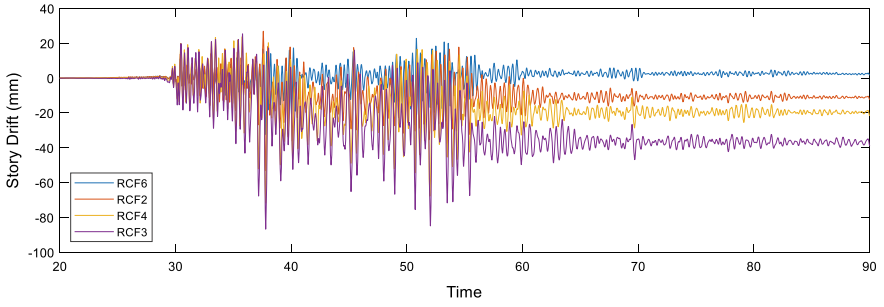

Fig. 6 Estimated displacement for the shaking table test

4 Conclusions

Estimating displacement by using recorded acceleration directly is useful to investigate the inter-story drift or roof drift of a building during earthquakes, allowing for a rapid assessment of building structures. In this regard, the undesired baseline shifts within the recorded acceleration are the major difficulty if the conventional integra-tion scheme is applied. In this study, SSA scheme for the estimation using the record-ed acceleration was proposed and verified using the shaking table test. The results prove the proposed method for estimating the relative displacement and residual displacement during earthquakes. For comparison, Iwan and Boore's scheme was also applied to estimate displacement; however, it fails because the baseline shifts brought by hysteresis aren't simple step functions. For field application, the type of multi-story structures and the combination of complex noises are still challenging, so seismic response data, especially the responses of inter-story drift or roof drift, is needed to further verify this proposed scheme.

References

1. ASCE (2000) FEMA 356 Prestandard and commentary for the seismic rehabilitation of buildings. American Society of Civil Engineers (ASCE) for the Federal Emergency Management Agency, Washington, D.C
2. Housner GW (1947) Ground displacement computed from strong-motion accelerograms. Bull Seismol Soc Am 37(4):299–305
3. Berg GV, Housner GW (1961) Integrated velocity and displacement of strong earthquake ground motion. Bull Seismol Soc Am 51(2):175–189
4. Skolnik DA, Wallace JW (2010) Critical assessment of interstory drift measurements. J Struct Eng 136(12):1574–1584
5. Liao Y, Kiremidjian A, Rajagopal R, Loh CH (2017) Experimental validation of an improved dynamic displacement estimation method using accelerometer and gyroscope. Struct Health Monit
6. Kanekawa K, Matsuya I, Sato M, Tomishi R, Takahashi M, Miura S, Ohdomari I (2010) An experimental study on relative displacement sensing using phototransistor array for building structures. IEEJ Trans Electr Electron Eng 5(2):251–255
7. Park JW, Moon DS, Yoon H, Gomez F, Spencer BF Jr, Kim JR (2018) Visual–inertial displacement sensing using data fusion of vision-based displacement with acceleration. Struct Control Health Monit 25(3):e2122
8. Iwan WD, Moser MA, Peng CY (1985) Some observations on strong-motion earthquake measurement using a digital accelerograph. Bull Seismol Soc Am 75(5):1225–1246
9. Boore DM (1999) Effect of baseline corrections on response spectra for two recordings of the 1999 Chi-Chi, Taiwan, earthquake. US Department of the Interior, US Geological Survey. p 37
10. Boore DM (2001) Effect of baseline corrections on displacements and response spectra for several recordings of the 1999 Chi-Chi, Taiwan, earthquake. Bull Seismol Soc Am 91(5):1199–1211
11. Huang JY, Wen KL, Li XJ, Xie JJ, Chen CT, Su SC (2013) Coseismic deformation time history calculated from acceleration records using an EMD-derived baseline correction scheme: a new approach validated for the 2011 Tohoku earthquake. Bull Seismol Soc Am 103(2B):1321–1335
12. Broomhead DS, King GP (1986) Extracting qualitative dynamics from experimental data. Physica D 20(2–3):217–236

13. Vautard R, Ghil M (1989) Singular spectrum analysis in nonlinear dynamics, with applications to paleoclimatic time series. Physica D 35(3):395–424
14. Vautard R, Yiou P, Ghil M (1992) Singular-spectrum analysis: a toolkit for short, noisy chaotic signals. Physica D 58(1–4):95–126
15. Golyandina N, Nekrutkin V, Zhigljavsky AA (2001) Analysis of time series structure: SSA and related techniques. CRC press
16. Huang SK, Loh CH (2022) Estimation of residual deformation of building structures using singular spectrum analysis for a safety assessment. In: Sensors and smart structures technologies for civil, mechanical, and aerospace systems, vol 12046. SPIE, pp 193–202
17. Graizer VM (1979) Determination of the true ground displacement by using strong motion records. Izv. USSR Acad Sci Phy Solid Earth 15:875–885
18. Chiu HC (1997) Stable baseline correction of digital strong-motion data. Bull Seismol Soc Am 87(4):932–944
19. Boore DM, Stephens CD, Joyner WB (2002) Comments on baseline correction of digital strong-motion data: examples from the 1999 Hector Mine, California, earthquake. Bull Seismol Soc Am 92(4):1543–1560
20. Wang GQ, Boore DM, Igel H, Zhou XY (2003) Some observations on colocated and closely spaced strong ground-motion records of the 1999 Chi-Chi, Taiwan, earthquake. Bull Seismol Soc Am 93(2):674–693

The Determination of Plumb Line Deviation Using Satellite/Levelling Technique

Murat Gazizovich Mustafin and Hiba Moussa

Abstract The article deals with adopting the GNSS/levelling technique to calculate the plumb line deviation. The topic focuses on the possibility of determining normal heights using satellite measurements. Even though there are many local algorithm models of plumb line deviation, finding the model parameters is not an easy task, especially for large coverage areas, and the calculation accuracy is hard to be attained as well. The distance between any two baselines, the azimuth and geodetic height differences can be easily obtained using GNSS relative positioning technology; while the normal height difference can be obtained using precise trigonometric leveling method. Therefore, it is an ideal way to use GNSS/levelling technique to determine the deviation along the plumb line in small study areas. This technique is mostly suitable for countries where a local geodetic network doesn't exist, which in turns prevents finding a full-fledged solution of many practical engineering problems. An example of testing the described methodology in Lebanon is presented, where the results show the superiority of GNSS/levelling technique as it is applicable to calculate accurately the influence value of error affected by the plumb line deviation.

Keywords Satellite leveling · Plumb line deviation · Geodetic networks

1 Introduction

Currently, global navigation satellite systems (GNSS) play a vital role in the wide field of human life security. In principle, GNSS is introduced in almost every area of human activity systems such as mining, energy or construction, etc. However, its vast applications could be restricted by certain constraints where in urban canyons the traditional positioning techniques could become a necessity to enhance the quality of GNSS that was affected or blocked by multipath effect. Moreover, there are some applications where GNSS observations have to be integrated with traditional geodetic

M. G. Mustafin (✉) · H. Moussa
Saint Petersburg Mining University, 199106 St. Petersburg, Russia
e-mail: Mustafin_m@mail.ru

H.-Y. Jeon (ed.), *Proceedings of the International Conference on Geosynthetics and Environmental Engineering*, Lecture Notes in Civil Engineering 374,
https://doi.org/10.1007/978-981-99-4229-9_4

measurements, such as underground engineering surveying. In order to integrate the GNSS observations with traditional measurement techniques, it is necessary to obtain the value of plumb line deviation.

However, in regions where gravitational information are unknown, it makes it more challenging to obtain the plumb line deviation using gravitational method. Lebanon, one of these regions, lacks such gravitational information which in turn forms many obstacles in the way of estimating the vertical deflection along the plumb line, thus the whole reliance will be on the use of geometric methods. [1–3].

The deflection of the vertical is an angle that describes the deviation of the true vertical, as defined by the direction of Earth's gravity vector, with respect to some reference direction. The reference direction may be defined purely geometrically or physically. The classic geometric definition of the reference direction identifies it as the perpendicular to an ellipsoid (a geodetic datum) that approximates the geoid, either locally or globally. The deflection of the vertical has two components: north–south component or meridional component (ξ) and east–west component or prime vertical component (η) [4–6]. The meridional component (ξ) component is positive when the astronomical zenith is north of the geodetic zenith, and the prime vertical component (η) is positive when the astronomical zenith is east of its geodetic zenith. The vertical deflection is classified as absolute when it refers to a geocentric ellipsoid and relative when it refers to a local ellipsoid (Figs. 1 and 2).

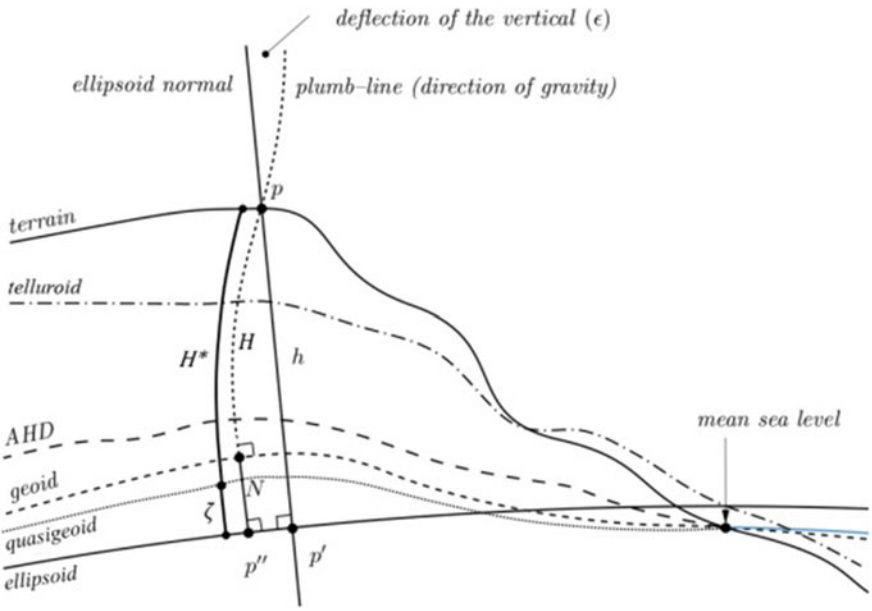

Fig. 1 Physical height systems and Deflection of the Vertical along the Plumb Line. https://www.icsm.gov.au/sites/default/files/2021-04/AVWS%20Technical%20Implementation%20Plan_V1.5.pdf

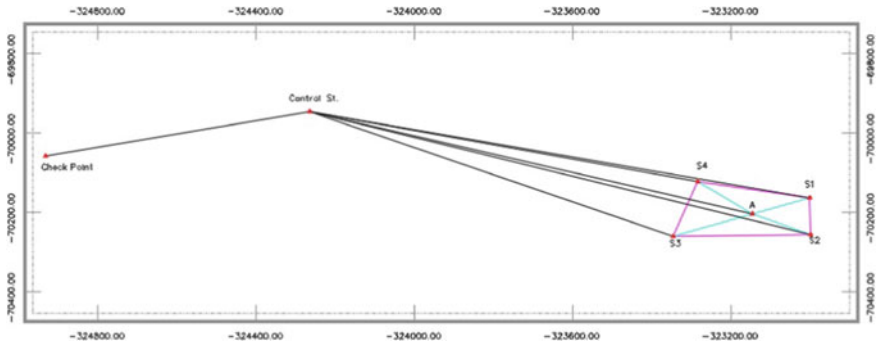

Fig. 2 Control Point, check point, and stations distribution. [contributed by authors]

Historically, determination of deflection of the vertical was an astronomic or gravimetric geodesy application. This has not been a problem for the typical land surveyor until the recent introduction of the Global Navigation Satellite Systems (GNSS). Now, surveyors must integrate the geodetic coordinate system used by GNSS with the astronomic coordinate system from traditional terrestrial observations.

Astrogeodetic method is the foremost method for determining the components of the Deflection of Vertical, it is based on the comparison between astronomical coordinates and geodetic coordinates at a point. However, gravimetric method is based on the using of worldwide gravity measurements to compute the deflection of the vertical. The surface gravity measurements are reduced into free-air gravity anomalies to take into account the elevation at which a measurement is made. The first paper that discussed the expansion of GNSS applications towards estimating the deflection of vertical was published by Tomas Soler who experimented the determination of deflection of the vertical using geodetic coordinates and orthometric heights in the year 1989. He has supported his study by comparing the Geometric method with Astrogeodetic method [7–10].

2 Research Methodology

The study area included a control point with auxiliary stations located in Beqaa Valley, Lebanon, where the covered area was 36,700 m^2.

The variations of the gravitational field on the specified area will be priori small. At the same time, the methodological aspect is important, which can be extended to large areas. In addition, for certain tasks, for example, irrigation or high-rise construction, it is very important to refine the picture of the distribution of normal heights. As seen (Fig. 3), the points are well distributed over the four quadrants.

The GNSS observations were performed using four receivers and carried out in static mode with two receivers fixed at the control and the central stations. The main

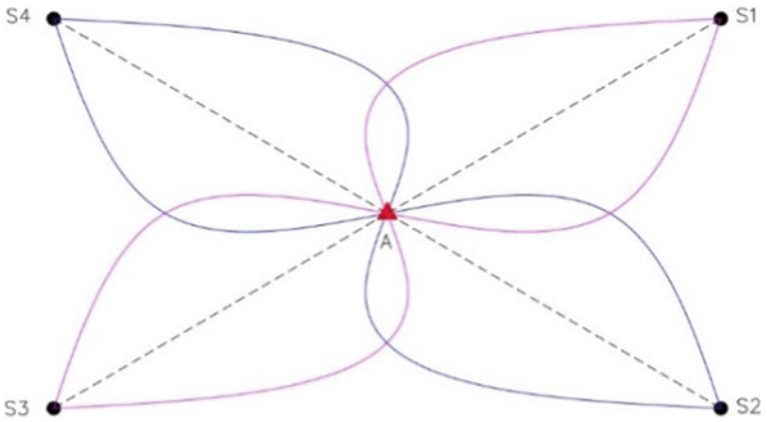

Fig. 3 The three measured leveling routes. [contributed by authors]

purpose of GNSS Observations is to obtain Azimuth, position, ellipsoidal height and distance for the central and the auxiliary stations with their variances.

In contrast, a leveling network was created to determine the orthometric height differences for the allocated stations. Double-run leveling was initiated along the leveling routes. The irregular mass distribution inside the earth leads to uneven gravitational pull, because of these variations in gravitational force, the geoid undulation is always changing, moving up and down in response to gravity. So, in order to indicate whether there is a noticeable change in geoid undulation or not and determine if gravitational measurements are required, measurements between each two points were accomplished along three different routes then the elevation differences were compared [11–13]. The systematic errors, that can't be sufficiently controlled by instrumentation or observational techniques, were minimized by applying appropriate corrections to the observed data in order to achieve the highest possible accuracy.

The Raw data obtained from GNSS static observations have been transferred from the receivers to the computer. After that the data was processed and adjusted to obtain the geodetic coordinates, geodetic azimuth, ellipsoidal height, ellipsoidal distance and variances of the stations [14–19]. The fully constrained adjustment was performed using the control points. Fixing the control points led to shifting the observations to the correct location within the chosen datum. Subsequently, the adjusted coordinates for all other points in the network can be determined with respect to the project datum (Tables 1, 2 and 3).

The leveling misclosures of the double run level routes were compared with the Standards and Specifications for Geodetic Control Networks, FGCC, 1984 to identify the leveling order of each section and the results are shown in the charts below (Fig. 4).

An adjustment was done to the leveling sections to minimize systematic errors. The Corrections in mm of the collimation error (CE), atmospheric refraction and earth curvature (AREC), and rod temperature (RT) were applied to the raw observations to

Table 1 The adjusted geodetic coordinates of the stations. [contributed by authors]

Station	Φ	λ	h in m
S1	N33°31′04.23088″	E35°40′19.02209″	879.954
S2	N33°31′01.24131″	E35°40′19.23139″	881.054
S3	N33°31′00.71578″	E35°40′05.80162″	885.348
S4	N33°31′05.25177″	E35°40′08.02764″	885.476
A	N33°31′01.69385″	E35°40′13.54181″	882.446

Table 2 Geodetic Azimuth and ellipsoidal distance of the baselines. [contributed by authors]

Baseline	Geodetic Azimuth	Ellipsoidal distance (m)
A–S1	61°04′22″	161.593
A–S2	95°25′25″	147.495
A–S3	261°25′21″	202.016
A–S4	307°36′21″	179.628

Table 3 Check point coordinates (I47). [contributed by authors]

Axis	True coordinates (m)	Calculated coordinates (m)	Difference (cm)
X	−324,931.79	−324,931.834	4.4
Y	−70,058.13	−70,058.085	−4.5
Z	1001.9	1001.941	−4.1

indicate the adjusted elevation difference between the central point and the auxiliary stations [20, 21] (See Table 4).

The orthometric height differences obtained using high-precision leveling were compared with data from the Earth model EGM2008. The results are close to each other, the differences are within 1–2 mm. Thus, based on the results presented in the chart below, it is not necessary to include gravity measurements in the local areas where this project was carried out (Fig. 5).

The components of the vertical deflection of the study area were calculated based on theoretical models using the MATLAB software. In addition, the residuals, posterior variance, posterior standard deviation, and standard deviation of each of the unknown components were calculated based on theoretical models calculated using MATLAB software. The following formulas were used in MATLAB:

The components of vertical deflection at the surface of the Earth and in direction of the prime vertical η and meridian ξ are defined as following:

$$\eta = -\frac{1}{(N+h)cos\varphi} \cdot \frac{\partial N}{\partial \lambda} \xi = -\frac{1}{(M+h)} \cdot \frac{\partial N}{\partial \varphi} \tag{1}$$

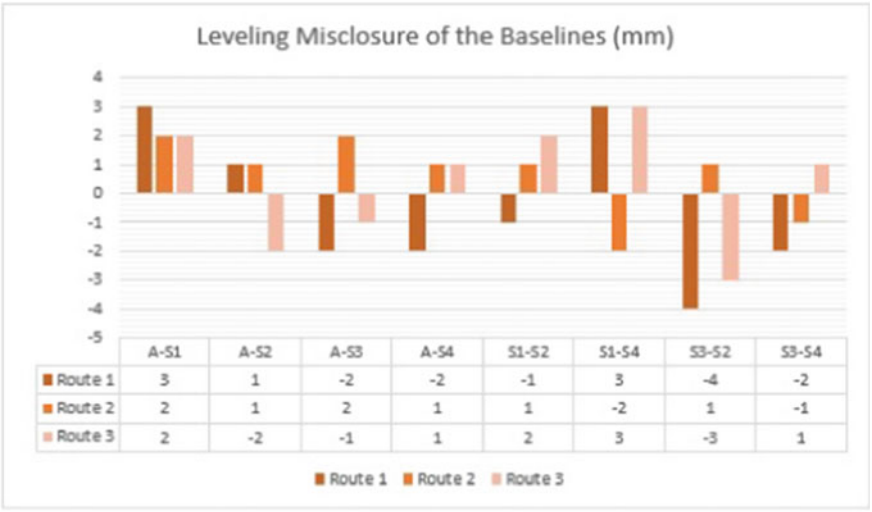

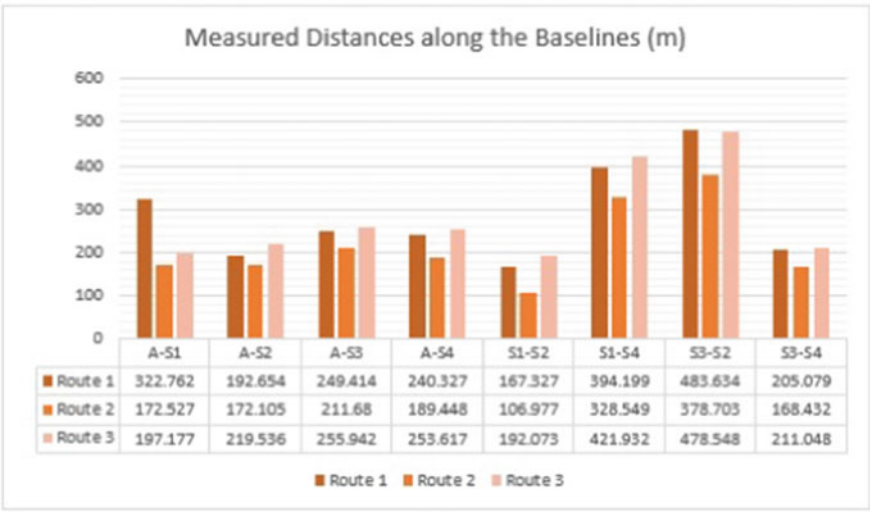

Fig. 4 Calculated misclosure and distances for the baselines along the three measured routes. [contributed by authors]

where (φ, λ) are the geodetic coordinates, N is the geoid undulation, N is the prime vertical radius of curvature, M is the meridional radius of curvature and h is the ellipsoidal height.

The deflection of the vertical ($\mathfrak{E}$) along a geodetic azimuth direction α, is defined as following:

$$\varepsilon = \xi \cdot Cos\alpha + \eta \cdot Sin\alpha \tag{2}$$

Table 4 Applied corrections to the elevation differences. [contributed by authors]

Section	Route	CE	AREC	RT	Adjusted ΔE	Average	LS adjustment
A–S1	1	0.046	0.026	−0.548	−2.499	−2.500	−2.501
	2	0.161	0.058	−0.595	−2.500		
	3	0.506	0.181	−0.799	−2.500		
A–S2	1	0.176	0.069	−0.247	−1.401	−1.401	−1.401
	2	0.653	0.218	−0.467	−1.400		
	3	0.482	0.172	−0.248	−1.401		
A–S3	1	−0.083	0.002	0.436	2.912	2.913	2.913
	2	0.0189	−0.003	0.596	2.914		
	3	0.191	0.036	0.970	2.913		
A–S4	1	−0.089	−0.018	0.754	3.037	3.037	3.038
	2	0.041	0.015	0.607	3.037		
	3	0.267	0.057	1.095	3.038		
S1–S2	1	0.127	0.040	0.241	1.100	1.100	1.100
	2	−0.037	−0.01	0.262	1.099		
	3	0.202	0.052	0.352	1.102		
S2–S4	1	−0.196	−0.056	0.975	5.540	5.540	5.539
	2	0.147	0.065	1.845	5.539		
	3	0.17	0.059	0.979	5.540		
S3–S2	1	0.075	0.038	−0.645	−4.313	−4.314	−4.314
	2	0.068	0.038	−0.883	−4.315		
	3	−0.178	−0.089	−1.437	−4.313		
S3–S4	1	0.058	0.023	0.031	0.123	0.124	0.124
	2	−0.011	0.009	0.025	0.124		
	3	0.154	0.064	0.045	0.125		

where α is the geodetic azimuth, ξ (xi) is the north–south component (meridional component) and η (eta) is the east–west component (prime vertical component).

The differential relationship between geoid height and deflection of the vertical at the surface of geoid is defined through the following formula:

$$\varepsilon = -\frac{dN}{dS} \tag{3}$$

where dN is the variation in geoid height and dS is the ellipsoidal distance (Tables 5 and 6).

After combining these formulas, the result is as follows:

$$-\frac{dN}{dS} = \xi \cdot \mathrm{Cos}\alpha + \eta \cdot \mathrm{Sin}\alpha \tag{4}$$

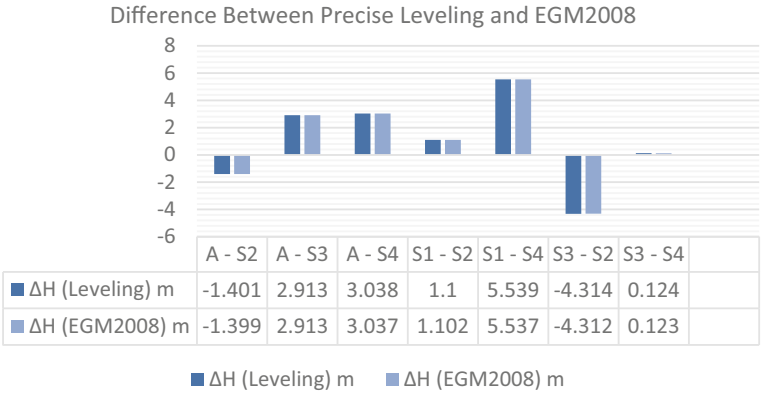

Fig. 5 Difference between measured orthometric height and EGM08 orthometric height. [contributed by authors]

Table 5 DOV components at the surface of earth and the surface of geoid. [contributed by authors]

DOV components	Earth surface (s)	Geoid surface (s)	Difference (ms)
ξ	-3.4138 ± 0.1163	-3.4144 ± 0.1163	0.6
η	-10.7876 ± 0.0487	-10.7886 ± 0.0487	1.8

Table 6 DOV at the surface of earth and the surface of geoid. [contributed by authors]

DOV components	Earth surface (s)	Geoid surface (s)	Difference (ms)
ε	11.3149	11.3160	1.1

After computing the components, the magnitude of the vertical deflection can be computed as follows:

$$\varepsilon = \sqrt{\xi^2 + \eta^2} \tag{5}$$

3 Results

As for the check point (I47), the difference between the true and calculated coordinates are in centimeters because of the lack of updates on the Lebanese state geodetic network, for instance the control point 8F3Z is established in 1951, without any later updates, thus the effect of continental drift alone can be responsible for such difference.

The vertical deflection was calculated relative to the local ellipsoid (Clarke, 1880), so it is classified as a relative value. Both the meridional component ξ and the main vertical component η are negative, so the astronomical zenith is south-west of the geodesic zenith. The resulting standard deviations of the vertical components are within fractions of an arc second, allowing it to be used in theodolites and total stations with high angular accuracy (0.5 inches), so it can be used in projects requiring high accuracy. The results obtained are consistent with the topography of the study area. The summit of the mountain is located about 1150 m west of the central station. The negative value of the η component indicates that the plumb line is attracted towards the mountain. This lateral pull is due to the gravitational pull of the mountain.

4 Conclusion

The obtained results showed that leveling according to the program of classes I and II in combination with one-hour GNSS observations is sufficient to calculate the exact values of the vertical deviation components. If high-resolution quasi-geoid models doesn't exist in the region under consideration, the presented approach allows the determination of heights [22, 23]. The geometric method can be applied to a geodetic network by solving for all stations having normal heights. However, since long baselines are common in GNSS surveys, it is not always desirable to have every normal height station computed for vertical deviation components or included in other station solutions. Stations outside the allowable limits of the model should be removed or a weighting function should be used to give the most influence to the closest stations.

Determining the vertical deviation components is important for a country like Lebanon due to the lack of a high-resolution quasi-geoid model. Thus, this method can be used to determine the marks, as well as to check: the unevenness of the field of normal heights (differences in reference surfaces). It is necessary to emphasize the importance of determining deviations from the plumb line, which is of high practical importance. For example, the definition of slopes for supplying water to arid regions, or in high-rise construction. In this case, the absolute marks of the quasi-geoid may not be so important, but the deviation from the vertical is extremely important. In fact, during the construction of various objects, we rely on the results of geometric leveling, which ensures the verticality of the marks [24–28].

References

1. Albayrak et al (2020) Quality assessment of global gravity field models in coastal zones: a case study using astrogeodetic vertical deflections in Istanbul, Turkey. Studia geophysica et geodaetica 64:306–329

2. Basil DD et al (2021) Determination if the veritcal components: implications on terrestrial geodetic measurement. World J Geomats Geosci
3. Ceylan A, Baykal O (2013) Precise height determination using simultanuous-reciprocal trignometric levelling
4. Dai D et al (2014) An improved method for dynamic measurement of deflections of the vertical based on the maintenance of attitude reference. Sensors 14(9):16322–16342
5. Dvulit P et al (2019) Determination of plumb lines with using trigonometric levelling and GNSS measurements. Geod Cartogr Aer Photogr 89:12–19
6. Featherstone WE, Goyal R (2022) Digitisation and analysis of historical vertical deflections in India. Surv Rev 1–6
7. Featherstone WE, Olliver JG (2013) Assessment of EGM2008 over Britain using vertical deflections, and problems with historical data. Surv Rev 45(332):319–324
8. Karpik AP, Kanushin VF, Ganagina IG, Goldobin DN, Kosarev NS, Kosareva AM (2018) Determination of plumb-line deflection components in the territory of western siberia by numerical differentiation. Vestnik SSUGT 6
9. Shin MS et al (2016) Determination of the deflection of vertical components via GPS and leveling measurement: a Case Study of Chunchoen Gangwon-do. J Ind Technol 36:65–69
10. Soler T, Yu-Han J (2021) Rapid prediction of vertical deflections and their statistics for surveying and mapping applications: three case studies. J Surv Eng
11. Vittuari L, Tini MA, Sarti P, Serantoni E, Borghi A, Negusini M, Guillaume S (2016) A comparative study of the applied methods for estimating deflection of the vertical in terrestrial geodetic measurements. Sensors 16(4):565
12. Wang J et al (2023) Height connection across sea by using satellite altimetry data sets, ellipsoidal heights, astrogeodetic deflections of the vertical, and an earth gravity model. Geod Geodyn
13. Wijesiriwardhana H, Rathnayake R, Prasanna H, Welikanna D (2017) Calculation of deflection of the vertical components: analyzing the GPS, levelling measurements and their distribution geometry
14. Balandin VN, Bryn MYa, Menshikov IV, Firsov UG (2014) Calculation of flat rectangular coordinates, convergence of meridians and Gaussian projection scale in a 6-degree zone using geodetic coordinates. Geod Cartogr (2):11–13. (In Russian)
15. Balandin VN, Bryn MYa, Menshikov IV, Firsov UG (2013) Algorithm for calculating flat rectangular coordinates, convergence of meridians and Gaussian projection scale in a 6-degree zone using geodetic coordinates. Notes of the Mining Institute. T.204. Saint Petersburg. p S.24-26. (In Russian)
16. Vizgin AA (2004) Reducing the accuracy of geodetic networks caused by errors. Vestnik SSGA 9:52–54 [In Russian]
17. Kanushin VF, Ganagina IG, Goldobin DN, Mazurova EM, Kosarev NS, Kosareva AM (2017) Modern global quasi-geoid models: accuracy characteristics and resolution. Vestnik SGUGiT (Sib State Univ Geosystems Technol) 22(1):30–49 [In Russian]
18. Gura DA, Ryzhkova AA, Boloban TI, Bolgova AS, Cherepanov AS, Kashaev BR (2016) Basic geodetic works in construction. Science Technique Technol (Polytech Bull) 2:133–137 (In Russian)
19. Zagretdinov RV (2014) Satellite positioning systems. Lecture notes. Kazan, Kazan Federal University, p 148. (In Russian)
20. Kovyazin VF, Xuan NT, Bogolyubova AA (2017) Land use transformation in the north and south of Vietnam. Geogr Environ Living Syst (4):95–110. (In Russian)
21. Kornilov YN (2008) Geodesy.: topographic surveys: a textbook. SPB.: St. Petersburg State Mining Institute, p 145. (In Russian)
22. Mazurov BT, Mustafin MG, Panzhin AA (2019) A method for assessing the divergence of vector fields of deformations of the earth's surface in the development of mineral deposits. Notes Min Inst 238:376–382 (In Russian)
23. Manukhov VF, Shpak DD, Erfurt VS (2021) The use of global positioning systems in engineering surveys. Ogaryov-Online 5(158):2 (In Russian)

24. Mikhalenko EB, Belyaev ND, Bogolyubova AA (2014) Engineering geodesy. Use of modern equipment for solving geodetic problems. St. Petersburg: St. Petersburg State Polytechnic University, p 98. (In Russian)
25. Popov AB (2019) A system for determining deviations of a plumb line. (In Russian)
26. Pavlov NS, Zubov AV (2013) Evaluation of the stability of supporting and deformation mine surveying and geodetic networks/Mine Surveying. Bulletin 2:21–23 (In Russian)
27. Sergeev OP (2004) Geodetic work on the construction of a cable-stayed bridge across the Neva in St Petersburg. Notes Min Inst 156:217–218 (In Russian)
28. Trushko VL, Dyakov BN (2009) Topological reliability of mine surveying geodesic networks. Notes Min Inst 180:198–202 (In Russian)

Efficiency of Digitalization of Housing and Communal Services and Construction in Kazakhstan

Shalbolova Urpash, Junussova Ainur, and Salykov Azamat

Abstract This article shows the results of research on the use of digital technologies in urban areas of Kazakhstan. Digitalization has become quite a new technology for the country and it has become widespread in the last 6–7 years. The implementation of the government digitalization program in Kazakhstan affects all areas of the national economy and the life of the main population. Nowadays, it is not possible to imagine a country with no usage of digital technologies. The results of the author's research are shown in the form of an analytical review of the digitalization of urban facilities, in particular, the housing and communal sector of the country. Programs for the use of digital technologies in construction have also been considered since the construction industry creates the majority of the country's housing stock. The effectiveness of digitalization of housing and communal services is given in a predictive assessment. The effectiveness of the introduction of digitalization in energy supply is given in the context of the main cities of Kazakhstan, whereas the effectiveness of digitalization of the water supply sector is regarded for the country as a whole. These two utility sectors have quite a few problematic issues, which have also been disclosed in this article. The results of research on the implementation of the Smart city concept are presented. Rating estimates are given for the areas of urban economy before and after the use of digital technologies.

Keywords Smart city · Digitalization · Urban economy · Housing and communal services · Construction · Efficiency

S. Urpash (✉) · S. Azamat
L.N. Gumilyov, Eurasian National University, Kazhymukana Streettreet,11, Astana City, Kazakhstan
e-mail: Shalbolova_Uzh@enu.kz; Urpash.Shalbolova@astanait.edu.kz

S. Urpash · J. Ainur
Astana IT University, Mangilik Ate, 55/11, Astana City, Kazakhstan

H.-Y. Jeon (ed.), *Proceedings of the International Conference on Geosynthetics and Environmental Engineering*, Lecture Notes in Civil Engineering 374,
https://doi.org/10.1007/978-981-99-4229-9_5

1 Introduction

The modern world nowadays is represented by cities that have been rapidly developing in the recent years. According to the United Nations, by 2050, urbanization will reach about 70% [1]. The migration of the population to the large cities is increasingly causing various problems related to the provision of housing and the effective management of the urban economy, mainly housing and communal services. Preserving the comfort of living in the city, ensuring the availability of all the social needs of the population today is possible thanks to the use of Smart city elements. The use of digital technologies allows to provide the progressive development of the cities in Kazakhstan.

It is known that in the next 10–15 years, Smart city elements will accompany residents of Kazakhstan cities everywhere. First of all, it applies to public transportation, to the social sphere (hospitals, educational institutions, sports, culture, recreation), parking areas, housing and communal services, retail outlets and other facilities. But today, residents of the country widely use various universal city applications, by using which they save time and increase the level of comfort of their lives.

However, there are still a lot city management and urban construction areas, where innovative digital technologies could be used. For example, in the cities of Kazakhstan, it is planned to use smart outdoor lighting, which is currently in its initial stage. There are some significant problems with the disposal of municipal solid waste, because so far, there are no "smart points" for garbage collection anywhere. A small number of fire detectors installed in private housing stock leads to frequent fires, especially during heating periods. Moving wireless networks and data transmission through visible light are still new, not implemented digital technologies for Kazakhstan.

But, nevertheless, digitalization is dynamically developing in Kazakhstan, and almost all residents of the country are in contact with it. Digital technologies are increasingly taking their place in many areas of the population's daily lives. There is also a place for technology transfer. Kazakhstan is trying to adopt the experience of Seoul, Singapore, San Francisco, Barcelona, Singapore, Amsterdam, Tianjin and other developed megapolises. According to the Smart centers index—SCI 6 rating, in 2022, Astana, the capital of Kazakhstan, ranks 64th and is considered as an attractive city for investing in digital technologies [2].

A lot of scientists, researchers, authors have been turning to the topic of Smart city in the last decade. The results of research in various areas of science, such as engineering, information technology, architecture, jurisprudence, natural sciences, various areas of social sciences have been published. Many works are devoted to managing a smart city, raising the social level of city residents, and city security. The authors present achievements in the implementation of the global Smart city concept in a particular country or city.

The Smart city concept appeared at the end of the last century, relatively recently in history. The emerging problems of urban overcrowding, environmental disasters, rising poverty, social inequalities have led to the ideas of using digital technologies.

An analysis of various concepts of Smart city is given in the studies of Cocchia A., where two concepts "Digital city" and "Smart city" are substantiated [3]. Kummitha and Crutzen revealed the processes of Smart city formation in the Indian economy [4]. Some aspects of the Smart city that need to be taken into account when planning and implementing a smart city, what risks may be in the operation of smart cities are given in the work of Reem and Shaligram [5]. Leonidas Anthopoulos determines the future of cities, analyzes 10 precedents—cities for the title of Smart city [6]. The influence of the Smart city on the ecology of the city, the desire for low-carbon, economical consumption of resources through the use of "smart technologies" on the example of China are analyzed in the work of Shuping Wu [7]. Quite a lot of Chinese scientists are addressing various issues of development and implementation of the Smart city concept, since this country is now one of the leaders in technological development [8, 9]. Bitkom collected a whole atlas of Smart city in Germany, considering the advantages and disadvantages of each city [10].

The main directions of digitalization in the sector of housing and communal services are presented in the article by Bannykh and Kozhevnikova, who define the range of applied technologies for automating various processes in this urban sector [11]. The problems of the functioning of the housing and communal services sector, digitalization at the level of individual areas of the city's public utilities are explored by Voevodkin [12]. Dmitrieva, Ganchenko, and Bodrov have also devoted their works to digitalization in housing and communal services [13, 14]. A review of the literature provides a considerable number of research results in this area. But the effects of the introduction of digital technologies in the development of the Smart city, the digitalization of urban sectors are practically not reflected in the scientific literature.

The purpose of this article is to present the effectiveness (efficiency) of using individual elements of the Smart city in the urban economy of Kazakhstan, namely, in housing and communal services; to show what digitalization programs are being implemented to transform the construction industry, in particular, in the construction of housing in Kazakhstan, since the study of digitalization of housing and communal services and the housing stock should be carried out in conjunction.

2 Results

The introduction of digital technologies in the urban economy, firstly, allows creating a work transparency and providing a comfortable environment for the urban population. The benefits of using digital technologies in urban management will also help to increase the level of production of enterprises serving the city itself.

The digitalization of housing and communal services has several goals: cost reduction, financial management efficiency, ensuring transparency for public monitoring, lowering rates by creating a competitive environment, and improving the quality of public services. In addition, there are opportunities to increase the attraction of investment resources to expand the digitalization of urban housing and communal services.

The authors conducted various studies in the field of modernization and application of innovative technologies in the housing and communal services of Kazakhstan. Table 1 presents selected urban and construction digitalization programs in Kazakhstan.

Programs for the introduction of digital technologies, given in Table 2, are practically working today in most of Kazakhstan. In addition to the functioning of these programs, residents of Kazakhstan use only digital format to make all types of payments for housing and communal services, Internet communications and public transportation. Many types of public services, including queuing for concessional financing (obtaining a mortgage) for the purchase of an apartment under state housing programs for providing the population with affordable housing, for obtaining a rental apartment from the state housing stock, for receiving subsidies for paying rental housing to individual categories of the population, to obtain a land plot for private housing construction are currently carried out in digital format on-line through the official websites of organizations or through the platform of the "E-gov" program—the Electronic Government of the Republic of Kazakhstan.

A review of the state of the housing and communal and urban economy in Kazakhstan revealed a number of significant problems (see Fig. 1). Despite the development of technologies, the urban economy in Kazakhstan, housing and communal services are still the weakest links in the national economy. Many networks for the supply of heat, electricity, water is simply worn out. In recent years, as part of the implementation of modernization programs, work has been carried out on reconstruction, the creation of new communal infrastructure facilities using the latest materials and the installation of innovative, information technologies for control and accounting.

Among all utilities, one of the most expensive ones is the provision of electricity. One of the ways to solve problems in the housing and communal and urban sectors is the installation of smart sensors, which can save up to 40% of electricity. Table 2 presents a forecast for a decrease in energy consumption with the maximum digitalization of this sector of the economy for the main cities of Kazakhstan.

The widespread installation of electronic sensors for water consumption by the population also gives a reduction in payment, since information is transferred aromatically from the consumer to the water supply organization through the cloud system. Forecast performance indicators as a result of digitalization of water supply are given in Table 3.

In Kazakhstan, all "Smart Homes" and high-class luxury housing houses have automatic water transfer sensors that allow, in case of sudden pipe damage, to protect apartments from water leakage, thereby preventing flooding, damage to furniture, carpets and other household items. Thus, these sensors act as savings, since after the flood, additional repairs often have to be carried out.

Another problem in urban areas in Kazakhstan is outdoor lighting. For example, in the capital of Kazakhstan, more than 200,000 outdoor lighting points have been installed, of which only about 50,000 are energy efficient. In many developed countries of the world, 100% of urban spaces are equipped with inefficient street lighting.

Table 1 Separate areas of digitalization of housing and communal services and the construction sector of Kazakhstan

Program	Contractor	Efficiency
Creation of a single platform for digitalization of housing and communal services	JSC Kazakhtelecom, JSC "Kazakhstan Center for Modernization and Development of Housing and Communal Services"	1. Increase the installation of base stations—up to 400 units. 2. In Kazakhstan, the level of installation of IT devices—information transmission sensors are 45% (8000 devices in the country), to install at least 60 thousand devices. 3. The presence of common house meters reduces the cost of utilities by 36%. 4. Long Range technologies have been introduced in the cities of Astana, Almaty and Aktobe
"E-Shanyraq" intelligent information system	JSC "Kazakhstan Center for Modernization and Development of Housing and Communal Services"	1. Implementation of a unified system of intelligent management of apartment buildings. 2. Self-monitoring by residents: general income and expenses at home, the activities of the management company, the correctness of calculations and charges for utility bills
"Open source" program-project	JSC "Kazakhstan Center for Modernization and Development of Housing and Communal Services"	1. Management of an apartment building 2. Information system for centralized collection and storage of electronic resources in the housing sector
Republican situational center using Big Data	JSC "Kazakhstan Center for Modernization and Development of Housing and Communal Services"	The state will be able to control the problems of housing and communal services, respond in a timely manner to the accident rate of utility networks, depreciation of the housing stock, the condition of infrastructure facilities

(continued)

Table 1 (continued)

Program	Contractor	Efficiency
The electronic program on the "I-Qala" portal—an element of the "Smart Astana" program	Astana city government body (capital of Kazakhstan)	The program is up and running. Through a single window, individuals and legal entities can conclude contracts for the receipt of 134 different services (mainly housing and communal services) around the clock on the website www.iqala.kz
"BI-Ecosystem" program	"BI Group" construction company	1. BI Click is the first online real estate store in Kazakhstan. 2. BIG App provides all the necessary services for a comfortable life from paying household bills to calling an electrician or plumber. 3. A platform for partners of the BI-Partners company for the purchase of raw materials and materials in digital format
"E-Qurylys" system—"State Bank of Information Models" system	Ministry for Investment and Development of the Republic of Kazakhstan	1. Modeling of building objects in online format. 2. Application of information modeling technologies—BIM technologies. 3. Monitoring of all stages of the construction of the facility online 4. Transparency of payments for construction works—out through the Blockchain platform

Note Compiled by the authors according to sources [15–18]

Table 4 gives a forecast of the effectiveness of installing digital technologies on street lighting in the capital of Kazakhstan, in the city of Astana.

The analysis of survey data from the "Smart city" internet portal, which was carried out a parts of research, allowed the authors to identify the main directions for the development of the "Smart City" (Table 5).

In the process of selecting innovative projects or forming a portfolio of projects for the implementation of the Smart City program in various regions of Kazakhstan, it is recommended to use indicators of the level of the project's rating indicator.

Table 2 The effectiveness of the introduction of digital technologies for energy supply in the cities of Kazakhstan (forecast)

№	City	Year 2021 before the introduction of digital technologies (kW × h/m^2 × year)	Year 2022 (forecast) after the introduction of digital technologies (kW × h/m^2 × year)	Economy growth rate (%)
1	Almaty	253,38	207,28	77,75
2	Astana	285,95	229,40	75,34
3	Karaganda	251,05	175,10	56,62
4	Atyrau	284,03	194,25	53,78
5	Oskemen	321,82	234,38	62,69
6	Aktobe	325,77	265,63	77,35
7	Oral	340,39	234,86	55,06
8	Kyzylorda	191,24	119,62	40,12
9	Taldykorgan	201,21	108,02	13,72
10	Kokshetau	300,98	220,80	63,68
11	Kostanay	308,65	196,50	42,92
12	Shymkent	205,73	114,74	20,69
13	Turkestan	204,90	116,87	24,67
14	Petropavl	298,84	210,83	58,25
15	Taraz	220,60	173,95	73,18
16	Aktau	254,62	169,80	50,04
17	Pavlodar	333,53	265,17	74,22
	Total	269,57	190,42	58,43

Note Compiled by the authors according to the source [19]

The implementation index of the Smart City project can be determined by the following method:

$$I = S_i / \sum N_i \tag{1}$$

where:

I—"Smart City" project implementation index, S_i—number of implemented projects in Kazakhstan, $\sum N_i$—total number of implemented projects for each direction of digitalization of the urban economy (urban environment).

Of course, a project is selected for investment, which has the largest areas of digitalization with rating indicators.

Not too far from the capital of Kazakhstan (100 km) in 2005, the first "Smart City" was created—Smart Aqkol, with 14 thousand population. All information is sent to a single digital platform for city management. You can view all the information in hospitals, schools, businesses, roads, public utilities in an online format. The main implementers of the project are the Tengri Lab IT company together with

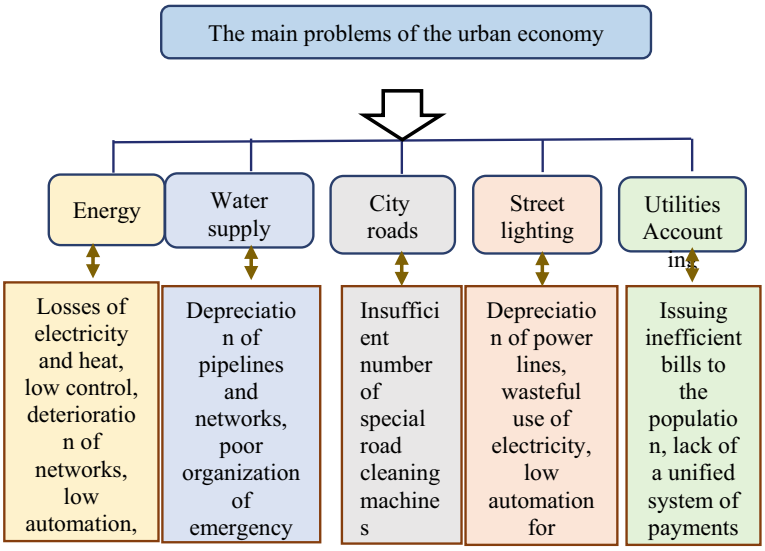

Fig. 1 Problematic areas of urban economy in Kazakhstan. *Note* Compiled by the authors

Table 3 Efficiency from the introduction of digital technologies in water supply in Kazakhstan (forecast)

1 $м^3$ water usage	The cost of water per 1 m^3 (in KZT)			
	Year 2021	Year 2022	Year 2023	Year 2024
Individuals	44,81	44,14	43,48	42,82
Legal entities	195,60	192,66	189,78	186,93

Note Compiled by the authors according to the source [19]

Table 4 Efficiency from the introduction of digital technologies for street lighting in the city of Astana

Funding amount (bln.KZT)			
Year 2021	Year 2022	Year 2023	Year 2024
1,7	1,66	1,632	1,60

Note Compiled by the authors

Kazakhtelecom, ERG, BTS Digital, the Akmola Electricity Distribution Company and the leadership of the Akmola region [20]. Smart water meters (4,500 units) and smart electricity meters (6,000 units) have been installed in buildings and residential buildings. Outdoor lighting is equipped with 250 automatic lamps. Digital recognition cameras, fire alarm sensors, transport tracking systems, health care and school performance monitoring systems are installed everywhere. The whole city is covered by 4G networks on LoRaWasn.

Table 5 The main directions of development of the "Smart city" in Kazakhstan

Direction of digitalization	Number of the implemented projects	Share of the implemented projects (%)	Implementation plan for the most effective projects, number	"Smart city" projects implementation index (%)	"Smart city" projects implementation rating, quality and rating number
Energy saving	41	11.3	140	3,41	High (1)
Digital city and information systems	180	49,5	87	0,48	Low (9)
Transport	40	11,0	20	0,5	Low (8)
Municipal solid waste	5	1,4	10	2,0	High (2)
Heat supply	11	3,0	7	0,64	Low (7)
Construction	6	1,6	2	0,33	Low (10)
Water supply	14	3,9	25	1,79	High (3)
Ecology	10	2,7	12	1,2	Average (5)
Safety	47	12,9	43	0,91	Average (6)
Power supply	10	2,7	15	1,5	High (4)
Total	364	10	361	–	–

Note Compiled by the authors

3 Conclusion

The results of the study showed that the introduction of digitalization in energy supply in Kazakhstan as a whole can save energy consumption above 50%, the installation of smart meters for monitoring water supply can lead to a decrease in the cost of water supply services. According to rating indicators, energy supply and water supply have high scores, which shows the effectiveness of digitalization.

The annual growth of investment in digitalization projects makes Astana, the capital of Kazakhstan, even more attractive for inviting external investors. Digitalization is also on the same level in other large cities like Almaty, Shymkent, Aktobe, Karaganda.

In Kazakhstan, Smart Aqkol is the first experimental area, where smart city smart systems are used to the maximum.

The first author has been conducting research on this topic for a long time. In addition, two co-authors, PhD students, are working on doctoral dissertations on the digitalization of urban farms and the construction industry. Research on this topic will continue in the future.

Acknowledgements This research has been funded by the Science Committee of the Ministry of Science and Higher Education of the Republic of Kazakhstan (Grant No. AP09260210).

References

1. Smart city: concept, technology, examples. Information on https://trasscom.ru/blog/umnyj-gorod
2. Astana entered the rating of smart cities for the first time. Information on https://profit.kz/news/64107/Astana-vpervie-voshla-v-rejting-intellektualnih-gorodov/
3. Cocchia A (2014) Smart and digital city: a systematic literature review. Progress in IS. pp 13–43
4. Kummitha RKR, Crutzen N (2019) Smart cities and the citizen-driven internet of things: a qualitative inquiry into an emerging smart city. Technol Forecast Soc Chang 140:44–53. https://www.sciencedirect.com/science/article/abs/pii/S0040162518308011
5. AlSharif R, Pokharel S (2022) Smart city dimensions and associated risks: review of literature. Sustain Cities Soc 77:103542. https://www.sciencedirect.com/science/article/pii/S2210670721008088
6. Anthopoulos L (2017) Smart utopia VS smart reality: learning by experience from 10 smart city cases. Cities 63:128–148. https://www.sciencedirect.com/science/article/abs/pii/S0264275116305157?via%3Dihub
7. Wu S (2022) Smart cities and urban household carbon emissions: a perspective on smart city development policy in China. J Clean Prod 373:133877. https://www.sciencedirect.com/science/article/abs/pii/S0959652622034515
8. Zhu S, Li D, Feng H (2019) Is smart city resilient? Evidence from China. Sustain Cities Soc 50:101636. https://www.sciencedirect.com/science/article/abs/pii/S2210670718325794
9. Yu Y, Zhang N (2019) Does smart city policy improve energy efficiency? Evidence from a quasi-natural experiment in China. J Clean Prod 229:501–512. https://www.sciencedirect.com/science/article/abs/pii/S0959652619314131?via%3Dihub
10. Bitkom EV (2019) Smart-City-Atlas. Bundesverband Information swirtschaft, Telecommunication und neue Median e. V. Albrechtstraße 10:194
11. Bannykh GA (2021) Digitalization of municipal-private partnership projects in the housing and communal services. Strategies for the development of social communities, institutions and territories: materials of the VII International scientific and practical conference.T.1. pp 302–306. https://elar.urfu.ru/handle/10995/103490
12. Voevodkin N (2019) Features of the functioning of the sphere of housing and communal services in the context of digitalization. Econ Bus 1:35–39
13. Dmitrieva E (2021) Digitalization of the housing and communal services: development prospects. E3S Web of Conferences 263:04037. https://www.sciencedirect.com/science/article/abs/pii/S0959652619314131?via%3Dihu
14. Ganchenko DN, Bobrov AA (2019) Digitalization of housing and communal services in the context of new industrialization. In: Proceedings of the 1st international scientific conference "Modern management trends and the digital economy: from regional development to global economic growth" (MTDE). pp 192–197. file:///C:/Users/urpash/Downloads/125908817.pdf
15. Kazakhtelecom plans to create a single platform for the digitalization of the housing and communal services sector (2018) Information on https://kz.kursiv.media/2018-11-29/kazakhtelekom-planiruet-sozdat-edinuyu-platformu-dlya-cifrovizacii-sfery/
16. Digitization of the housing and communal services sector is convenient (2020) Information on https://www.zakon.kz/5045251-otsifrovka-sfery-zhkh-udobna-glava.html
17. Digitization in construction makes housing more affordable (2021) Information on https://forbes.kz/process/technologies/tsifrovizatsiya_v_stroitelstve_delaet_jile_dostupney/

18. How digitalization helps regulate the construction market in Kazakhstan. Information on https://www.inform.kz/ru/kak-cifrovizaciya-pomogaet-regulirovat-stroitel-nyy-rynok-v-kazahstane_a3879001
19. Agency for Strategic Planning and Reforms of the Republic of Kazakhstan. Official website of the Bureau of National Statistics. Information on https://stat.gov.kz/
20. Smart city Aqkol. Information on (rodestech.com)

Experimental Investigation of Sand Seam Effects on Consolidation Behavior of Vertical Drain-Installed Soft Soils

Chau Phuong Ngo, Kien-Tai Do, Daeho Yun, Yun-Tae Kim, and Ba-Phu Nguyen

Abstract Thin-layered sand seam in soft deposits can be formed artificially or naturally. It affects significantly the consolidation behavior of subsoil. To investigate the consolidation settlement of soft deposits with thin-layered sand seam, a series of consolidation tests of the layered soft soil-sand systems improved by prefabricated vertical drain (PVDs) is performed. To estimate the effects of thin sand layers, three cases of consolidation tests are carried out as follows: in Case 1, the PVD-soil column is tested without thin sand layer; one and two thin sand layers were placed between the soft soil layers in Case 2 and Case 3, respectively. The experimental results indicate that the rate of consolidation settlement of PVD-installed soft deposit with the thin sand layers is faster than that of the case without sand seam, because the thin sand layers can provide a shorter drainage path for consolidation of the soft soil. As expected, this result is obviously appeared in Case 3. However, the final settlement of PVD-installed soft soil with thin sand layers is smaller than that of the case without sand seam. It can be seen that the existence of thin sand layers interbedded with soft soil layer can improve the strength of soft soil.

Keywords Geosynthetics · Soft soil · Sand seam · Consolidation · Settlement · Vertical drain

C. P. Ngo
Campus in Ho Chi Minh City, University of Transport and Communications, No. 450−451 Le Van Viet Street, Tang Nhon Phu A Ward, Thu Duc City, Ho Chi Minh City 700000, Vietnam

K.-T. Do · B.-P. Nguyen (✉)
Department of Civil Engineering, Industrial University of Ho Chi Minh City, Ho Chi Minh City 700000, Vietnam
e-mail: nguyenbaphu@iuh.edu.vn

D. Yun · Y.-T. Kim
Department of Ocean Engineering, Pukyong National University, Busan 608−737, Korea

H.-Y. Jeon (ed.), *Proceedings of the International Conference on Geosynthetics and Environmental Engineering*, Lecture Notes in Civil Engineering 374,
https://doi.org/10.1007/978-981-99-4229-9_6

1 Introduction

Due to the rapid economy development and booming population, more land is required to develop the systems of infrastructure, residential and commercial buildings, railways and airport. In the land reclamation projects, the layer clay-thin sand model was typically applied as an alternative to the conventional full sand reclamation model as a result of the reduction of usage intensity of natural sand. The thin sand layers have been applied for horizontal drains in reclaimed lands with clay fill and in clay fill embankment [1–4]. These sand layers provide lateral drainage for the soft soil in the consolidation process. Based on the field observation of land reclamation project using the clay-sand systems, Lee et al. [3] indicated that provision of horizontal thin layers of sand between sedimented marine clay layers will make the later settle faster and gain strength more rapidly. The consolidation coefficient estimated using the field settlement of layer clay-sand scheme was larger than that of soft clay from the laboratory consolidation test. Specifically, the consolidation coefficient estimated using the field settlement readings ranges from 7–18 m^2/year, where these values from consolidation test for soft clay ranged from 0.5–4 m^2/year. The field test also presented that the field settlement was smaller obviously than settlement of soft clay calculated from compression data of laboratory consolidation test. With sufficient discharge, the sand seam layers can change the hydraulic gradient of vertical flow of pore water in the soft soil. This results in the complex coupled behavior of the consolidation of clay and horizontal drainage of discharge pore water in the thin sand layers [5]. Therefore, the estimation of effects of sand layer discharge capacity on consolidation behaviors is required in practice.

Moreover, the thin-layered sand seam in soft deposits can be also formed naturally in glacial lakes and postglacial clays, which were often formed with a varved or layered structure due to seasonal variation in deposited particle size [5–7]. In practice engineer, the thin sand seam which is embedded in soft ground can be identified by Piezocone test or using sampler [8]. The piezocone penetration test (CPTu) can detect the sand same based on the results obtained from this test. Some characteristics of thin sand seam embedded in soft clay from CPTu test is as increase of cone resistance and decreases of friction ratio and pore water pressure, can help us to evaluate the thickness of those sand seams [8].

Generally, sand seam embedded in soft clay layer may affect consolidation settlement. In an ordinary soil exploration, a thin sand seam sometimes goes unnoticed. However, if the sand seam allows free drainage, this overlooking causes a great error in settlement-time prediction [9]. Asaoka [9] assumed that the settlement of the layer clay-thin sand seam was equal to total settlement of each clay layer. The average degree of consolidation can calculate simply by average mathematical procedure. However, this is just simple estimation in engineering practice, because consolidation rate and deformation of soft clay with embedded sand seams depends on hydraulic conductivity, stiffness and thickness of those thin sand layers. Therefore, these effects should be considered to predict consolidation behavior of sand seam embedded in soft deposits.

Nowadays, the prefabricated vertical drains (PVDs) are typically applied in soft soil improvement in the land reclamation projects with soft soil. PVDs were typically used to accelerate the consolidation phase for the soil improvement. In the combination of PVDs and horizontal drains (i.e., thin sand seam, prefabricated horizontal drains), the role of horizontal drains is to discharge the pore water in soft soil to vertical drains and the pore water can then squeeze out [10]. Moreover, as thin sand seam layers are deposited naturally in soft soil such as marine clay. Generally, the horizontal drains in soft ground require some means to take the collected water out. Therefore, a combination of PVDs and horizontal drains is a favorable condition for increasing consolidation process in soft deposits.

The prediction of consolidation settlement behavior of PVD-improved soft deposits is still difficult and challenging problem in geotechnical engineering. Moreover, the consolidation settlement behavior of PVD-installed soft deposits is affected by many factors [7]. Therefore, performance of vertical and horizontal drain systems (e.g., thin sand layers) in soft deposits has to be investigated through the experimental and field tests. Although the layered clay-thin sand model of land reclamation has been successfully tested in a small field trial conducted at Palau Tekong Basar [3], the experimental test with the number of thin sand layers have not been attended. In the previous studies [7, 11], the experimental test of PVD-improved soft deposit consolidation was performed on a single stage to investigate the effects of factors on behavior of soil consolidation process. These parameters, such as smear zone, discharge capacity, non-Darcian flow, artesian pressure, was then determined by the back analysis approach. Deng et al. [11] carried out the laboratory model tests for soft soil deposits with and without PVD to consider the consolidation and long-term performance of PVDs. The settlement consolidation behavior of soft deposits and excess pore water pressure were then estimated using a general back-analysis method. When subsoils are a layered inhomogeneous medium as the layered clay-thin sand systems, it is very difficult to develop analytical solutions for its consolidation behavior. Thus, the experimental investigation of consolidation settlement behavior of the layered clay-thin sand systems should be performed.

The aim of this paper is to carry out a series of consolidation tests of the layered clay-thin sand systems to investigate the effects of thin sand layer on the consolidation behavior. Three consolidation tests of the soil column with thin sand seam are performed, in which the one and two of thin sand layer is embedded in first and second column test, respectively. The another one is carried out without thin sand layer.

2 Experimental Test

2.1 Test Program

In this test program, three acrylic columns with the same dimensions were designed for the experimental tests. This is convenient to compare the consolidation behavior of soft deposits. The cases of experiment test are design as follows: Case 1 without thin sand layer; Case 2 and Case 3 with one and two of thin sand layer, respectively. Figure 1 presents a test set-up using a large one-dimensional (1-D) column equipment. The inside diameter of the columns was 0.16 m, and the length of the columns was 0.5 m. Because of high stiffness of acrylic columns, it was ensured that the horizontal deformation was fixed to create one dimension (1-D) deformation model. Soil layers consisted of top sand with 0.05 m thick and soft clay with 0.45 m thick. The soft soils were poured to bottom of column; therefore, the drainage boundary at bottom of column is impervious. The top sand layer was to provide a drainage boundary of consolidation model. The thin sand seam layer with 0.01 m thick was embedded in soft soils. The soft soil and sand layers were separated by filter papers, which can prevent intrusion of sand into soft soil. In this experiment, the external load is a dead load system which was made by plate cuprum. Settlement was measured by a vertical displacement sensor (LVDT) at the top of the loading system.

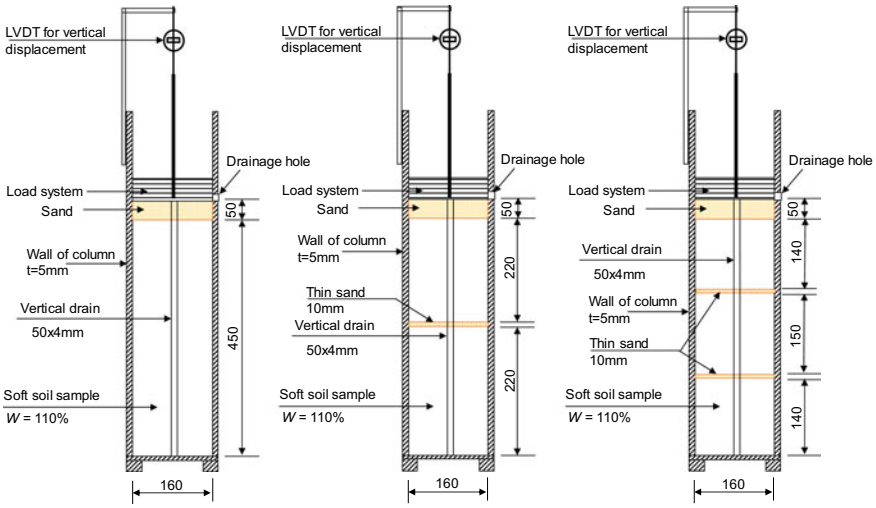

Fig. 1 Layered soft soil-thin sand model: **a** without sand seam; **b** with one sand seam layer and **c** with two sand seam layers (Unit: mm)

Table 1 Geotechnical characteristics of the soft soil using in the experimental test

Properties	Symbol/unit	Values
Field water content	%	88.3
Void ratio	e_0	2.369
Unit weigh	kN/m^3	14.5
Specific gravity	G_s	2.59
Atterberg limit	*LL (%)*	73.4
	PL (%)	45.4
	PI	28

2.2 Materials Using in the Experimental Tests

The soft soil samples used in this experimental test were taken from a depth of 3–5 m from the Kenh 2 bridge at Km 18 + 850, Ho Chi Minh City 3rd Ring Road project, Vietnam. The geotechnical properties of the soft clay samples are presented in Table 1. Because the soft soil samples contained many crushed shell fragments, the soft clay was prepared as homogeneous clay. After preparation, the water content of the soft soil using in the experimental tests was set at 110%. The sand material was applied as a drainage material. It was placed above the soft clay layer. This sand material had a unit weight of 20 kN/m^3 and hydraulic conductivity of 1 m/day. The sand passed through a No. 4 (4.75 mm). This means that the grain-size limit of sand is 4.75 mm. The prefabricated vertical drains used in this study were of the harmonica type with the actual size of 100 mm wide and 4 mm thick. However, the diameter of test column is relatively small. Therefore, the original size of PVD was reduced down to the used size with 50 mm wide, 4 mm thick, and 0.5 m long for each column test.

2.3 Method and Procedure of Test

After setting up the necessary apparatus of test program, the soft soil and sand material were poured sequentially into the test columns. In the first step, the soft soils were filled carefully into the test column using a 0.1 m diameter tube. To reduce any air trapped during pouring process, the lower end of the tube should be immersed in the soft soils. After the soft soil had been placed in the column, the prefabricated vertical drains were installed in the columns center with a small-diameter rod of high stiffness. The top sand layer with 50 mm thick was then poured on top of the clay layer. Before carrying out the 1-D consolidation test for soil columns, the period with 2 weeks were given to wait for self-weight consolidation of the prepared soft soil. Three soil columns with the same conditions except existing the thin sand layer for Case 2 and Case 3. For Case 2, one of thin sand layer was embedded at middle of soft soil layer. For Case 3, two of thin sand layers were embedded in the soft soil layer,

as shown in Fig. 1. The filter papers were used to prevent intrusion of sand into soft soil. Three step loadings were applied: 1.492, 2.984, and 4.476 kPa. These loading values are used to ensure that the hydraulic gradients in the experimental test always less than 1. This is due to the initial discharge capacity of PVD was performed under hydraulic gradients of 1 [12]. The duration of consolidation process was 7 days for the first and second loading phases, and 20 days for the third phase. This ensures that the consolidation settlement process of soft soil in columns can completely occurred. During the experimental tests, the settlement data was observed by LVDT. After consolidation test, the water contents of soft soil were also investigated.

3 Experimental Results and Discussion

In the soft soil improvement engineering, the settlement is an important factor to investigate in consolidation characteristics in soft soil deposits. In this study, the settlement results were measured by the LVDT during consolidation. The settlement due to the self-weight consolidation settlement before loading phases was neglected in the observation process. Moreover, the compression properties of sand layers due to external loading were neglected. This means that the observed results of settlement in experimental tests were just considered for soft soil layers. Figure 2 shows the variation in the measured results of settlement of soft soil in the three cases. According to these experimental results, the observed settlement of soft soil without sand seam layer (Case 1) was larger than that with existence of thin sand seam layers (i.e., Case 2, 3). The final settlement in Case 1, Case 2 and Case 3 was 10.25 cm, 10 cm and 9.75 cm, respectively. The experimental results show that the long-term settlement of soft soil without the sand seam layer was larger than that of soft soil with sand seam layer because the thin sand same layers contributed to the increase of foundation stiffness. Generally, these results are completely consistent with the previous studies [3, 5]; however, the rate of consolidation of the subsoils depend on the drainage efficiency provided by the sand layers. Moreover, the settlement rate of soft soil with sand seam layers in early stage is faster than that without sand seam layer. It could be explained that the thin sand layer can play a role as drainage boundary in soft soil; forcedly, this depend on the characteristics of thickness and hydraulic conductivity of thin sand layers which will be discussed in next study.

4 Summary and Conclusion

This paper presents a series of experimental tests of the layered clay-thin sand systems to investigate the effects of thin sand layers on the consolidation settlement behavior of soft soil deposits. The results obtained from the experimental test show that the rate of consolidation settlement (vertical deformation) of vertical drain-installed soft soil deposits with the thin sand layers is faster than that of the case without sand seam,

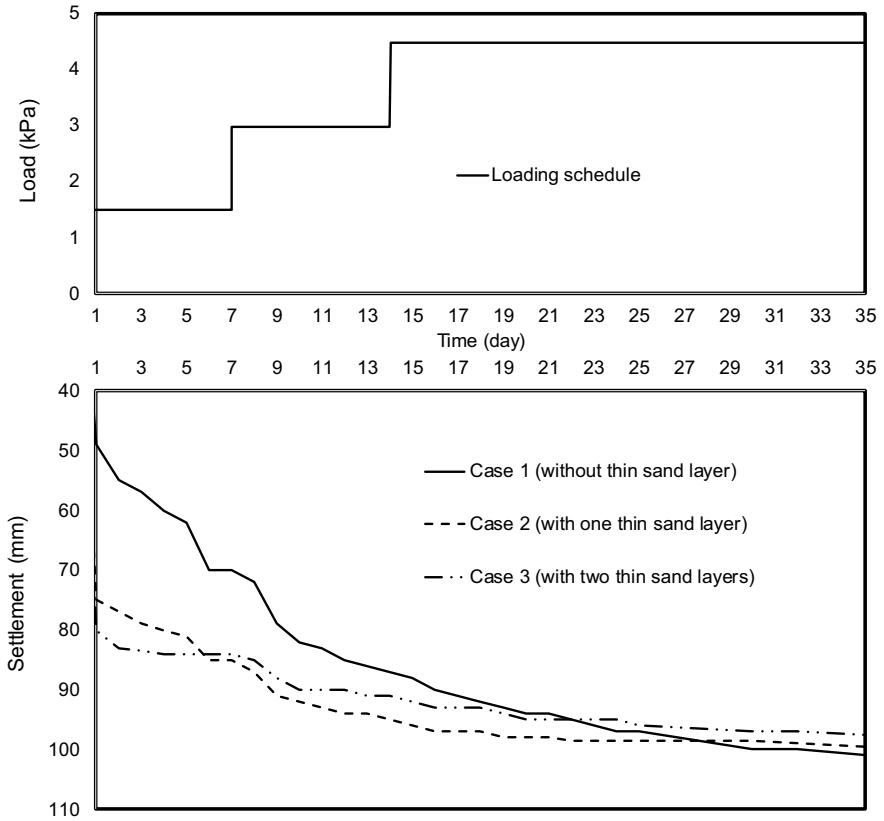

Fig. 2 Loading schedule and observed data of settlement during consolidation process

because the thin sand layers can provide a shorter drainage path for consolidation of the soft soil. The stiffness of soft soil ground is improved and increased due to the existence of thin sand layers. Therefore, the final settlement of vertical drain-installed soft soil in the cases with thin sand layers is reduced, comparing with the case without sand seam.

Acknowledgements The first author would like to thank Students in IUH (Mr. Đinh Van Phuong, Mr. Vo Huu Vinh, Mr. Le Hoang Tuan and Mr. Nguyen Tran Anh Tuan) who performed carefully the experimental test.

References

1. Gibson RE, Shefford GC (1968) The efficiency of horizontal drainage layers for accelerating consolidation of clay embankments. Géotechnique 18:327–335
2. Watari Y (1984) Reclamation with clayey soil and method of earth spreading on the surface. In: Proceedings Seminar on Soil Improvement and Construction Technique in Soft Ground, Japanese Society of SMFE. pp 103–119.
3. Lee SL, Karunaratne GP, Young KY, Ganeshan V (1987) Layered clay-sand scheme of land reclamation. J Geotech Engrg 113(9):984–995
4. Karunaratne GP, Young KY, Tan TS, Liang KM, Lee SL, Vijiaratnam A (1990) Layered clay-sand scheme reclamation at Changi south bay. In: Proceedins of the 10th Southeast Asian Geotechnical Conference, Southeast Asian Society of SMFE, pp 71–76.
5. Nogami T, Maoxin L (2002) Consolidation of system of clay and thin sand layers. Soils Found 42(4):1–11
6. Kim SK (2008) Characterization of deltaic deposits in the Nakdong river mouth, Busan, keynote/theme notes. In: Proceedings of the International Symposium on Geotechnical and Geophysical Site Characterization. Taylor & Francis, London
7. Kim YT, Nguyen BP, Yun DH (2018) Effect of artesian pressure on consolidation behavior of drainage-installed marine clay deposit. J Mater Civ Eng 30(8):04018156
8. Yoon H-K, Jung S-H, Kim R-H, Lee J-S (2010) Cone resistivity penetrometer for detecting thin-layered soils. J Korean Geotech Soc 26(8):15–25
9. Asaoka A (1978) Observational procedure of settlement prediction. Soils Found 18(4):87–101
10. Nguyen BP, Kim YT (2019) Radial consolidation of PVD-Installed normally consolidated soil with discharge capacity reduction using large-strain theory. Geotext Geomembr 47(2):243–254
11. Deng YB, Liu GB, Indraratna B, Rujikiatkamjorn C, Xie K (2017) Model test and theoretical analysis for soft soil foundations improved by prefabricated vertical drains. Int J Geomech 17(1): 04016045.
12. Bergado DT, Manivannan R, Balasubramaniam AS (1996) Proposed criteria for discharge capacity of prefabricated vertical drains. Geotext Geomembr 14(9):481–505

Research on the Treatment Process of Fracturing Flowback Fluid

Xiong Feng, Wang Xue-Qiang, L. I. U. Yang, Chen Long, Zhao Zhi-Hong, Yang Hao, H. U. Jing-Yu, L. I. Ding, and Ming Shuang

Abstract With the continuous advancement of global industrialization, the demand for energy in various countries is increasing year by year. In order to meet this challenge, various development technologies came into being. As one of the important stimulation and transformation measures, hydraulic fracturing technology is widely used in conventional and unconventional oil and gas reservoirs such as shale oil and gas reservoirs, tight oil and gas reservoirs and coalbed methane reservoirs to improve the recovery of oil and gas reservoirs. After hydraulic fracturing, the fracturing fluid is gradually discharged along with other impurities such as formation water. The fracturing flowback fluid has a large amount and complex components. The flowback fluid generally has the characteristics of high salinity, high hardness, high bacterial content, high COD value, high suspended solids content, high viscosity, oil and so on. Flowback fluid treatment is a difficulty and challenge for major oilfield units around the world. In order to avoid pollution, the local laws of various countries have formulated relevant laws and regulations on the reinjection and discharge of oil and gas field flowback liquid. Due to the characteristics of flowback liquid, its treatment cost is high and it is difficult to discharge. In order to reduce the treatment cost of flowback liquid, various universities, scientific research institutes and oil and gas field units have carried out various research on flowback liquid treatment technology, and various physical, chemical and biological treatment methods came into being. This paper investigates the treatment technology of fracturing flowback fluid in various oilfields at home and abroad, expounds various treatment processes of fracturing flowback fluid, and finally prospects the treatment method and direction of fracturing flowback fluid, which can be used as a reference for scholars in the industry.

Keywords Fracturing · Fracturing flowback fluid · Processing technology

X. Feng (✉) · W. Xue-Qiang · L. I. U. Yang · C. Long · Z. Zhi-Hong · Y. Hao · H. U. Jing-Yu · L. I. Ding · M. Shuang
Engineering Technology Research Institute of Petrochina Southwest Oil and Gas Field Company, Chengdu, China
e-mail: 136525528@qq.com

H.-Y. Jeon (ed.), *Proceedings of the International Conference on Geosynthetics and Environmental Engineering*, Lecture Notes in Civil Engineering 374,
https://doi.org/10.1007/978-981-99-4229-9_7

1 Fracturing Flowback of Oil Fields Around the World

With the rapid development of economy and the increasing demand for energy, the reserves of conventional oil and gas reservoirs and backward exploitation and development methods can no longer meet the needs of countries [1]. The exploration of various unconventional oil and gas reservoirs has become an indispensable part of the sources of oil and gas resources in the world. Among them, unconventional gas reservoirs represented by shale gas, shale oil, tight gas and tight oil are important targets for oil and gas exploration and development in various countries, mainly distributed in North Africa, China, Central Asia, Latin America, the Middle East, North America and Russia [2]. Sand fracturing has become an effective development method for such reservoirs with low permeability and strong heterogeneity. Among them, shale gas development in North America and shale gas and tight gas development in China are the largest and most representative. Around 2012, the United States basically realized large-scale commercial production of shale gas, shale oil and gas, tight oil and gas and other resources in China are gradually being exploited, and the scale of fracturing construction is increasing year by year [3]. The research shows that for unconventional gas reservoirs such as shale gas and tight gas, the water required for fracturing construction of a well is about 4000−3000m3, and the flowback liquid rate is about 10−80% [4]. Every 10000m^3 of flowback liquid contains about 60t of benzene, methanol, fungicide, oxidant, reducing agent, polymer and other chemicals, with a salinity of about 5 to 10 times that of seawater. Fracturing flowback fluid in various countries, blocks and reservoirs is characterized by large amount and complex composition [5, 6].

1.1 Analysis on the Backflow of Fracturing Fluid in North America and the Quality of Backflow Fluid

Under the background of industrialization promotion and technological change in the upstream of energy production, North America has witnessed a shale gas revolution, and its shale gas output has grown rapidly in the past 30 years [7]. Currently, fracturing means in North America are mainly used for shale gas development. By about 2020, shale gas production in the United States will account for about 40% of its natural gas production [8].

According to the statistics of the US Environmental Protection Agency, the water consumption of shale gas single wells in North America is generally 7000−27000m3, and the flowback rate is 15−80% [9]. The fracturing backflow fluid in North America is mainly shale gas fracturing backflow fluid, accounting for more than 70% of the backflow fluid. Many shale gas blocks in North America are represented by Barnett, Woodford, Fayetteville, Haynesville and Marcellus gas fields. The annual flowback volume of shale gas fracturing in North America is more than 2 million m3. Taking Marcellus and Barnett shale gas flowback fluid as examples, the water quality of

Table 1 Overview of water quality indicators of main flowback fluid in Marcellus shale area and Barnett shale area in the United States

Water quality index	Fluid flowback in marcellus shale area on the 14th day		Fluid flowback in Barnett shale area in the 10th to 12th days	
	Range	Median value	Range	Median value
pH	4.9–6.8	6.2	6.5–7.2	7.1
Total alkalinity	26.1–121	85.2	215–1240	725
Total suspended solids content	17–1150	209	120–535	242
Chloride content	1670–181,000	78,100	9600–60,800	34,700
Total dissolved solids content	3010–261,000	120,000	16,400–97,800	50,550
Total organic carbon content	1.2–509	38.7	6.2–36.2	9.75
Oil content	7.4–103	30.8	88.2–1430	163.5
Sulfide content	1.6–3.2	2	Not measured	Not measured
Sulphate content	0.078–89.3	40	120–1260	709
Total barium content	133–4220	1440	0.93–17.9	3.6
Total strontium content	1220–8020	3480	48–1550	529
Total calcium content	8500–24,000	18,300	1110–6370	1600
Total magnesium content	933–1790	1710	149–755	255
Total iron content	69.7–158	93	12.1–93.8	24.9
Total manganese content	2.13–9.77	4.72	0.25–2.20	0.86
Total boron content	13–145	25.3	7.0–31.9	30.3

flowback fluid is analyzed. The composition of flowback fluid from each well in North America varies greatly, and the content of each component fluctuates greatly with time. Table 1 lists the water quality indicators of the backflow fluid of Marcellus and Barnett shale gas, and the specific parameters are shown in the table below.

1.2 Domestic Fracturing Backflow Fluid Drainage and Water Quality Analysis

The largest fracturing scale and the largest water consumption areas in China are Sichuan Basin and Ordos, accounting for more than one-third to half of the fracturing wells in China. The backflow rate of shale fracturing in China is extremely low. In most areas, the backflow rate of fracturing fluid is less than 50%, some even less than 5%, and the backflow rate of tight gas is about 30 to 80% [10].

At present, unconventional natural gas fracturing fluids such as shale gas and tight gas mainly include slippery water and gel fluid, which are mainly composed of thickener, drag reducer, anti swelling agent, surfactant, gel breaker, etc. [11]. Sampling and water quality analysis of flowback fluid from some domestic shale gas wells and unconventional fracturing wells in Zhongyuan Oilfield (Table 1), its

Table 2 Water quality analysis of shale gas and tight gas flowback fluid in China

Test items	1#	2#	3#	4#	5#
pH	6	7	7	6	8
Calcium ion content/(mmol L−1)	4.60	5.20	12.31	45.26	53.21
Magnesium ion content/(mmol L−1)	0.68	0.84	3.23	6.26	8.52
Aluminum ion content/(mmol L−1)	0.04	0.10	1.16	0.09	0.24
Sodium ion content/(mmol L−1)	89.41	63.20	113.02	58.19	97.36
Chloride ion content/(mmol L−1)	152.20	72.54	93.13	412.58	341.07
Sulfate ion content/(mmol L−1)	1.81	1.38	1.52	20.00	23.00
Barium ion content/(mmol L−1)	0.30	0.40	0.35	52.00	64.00
Total iron content/(mmol L−1)	0.03	0.18	0.08	0.45	0.52
TSS/(mg L−1)	65	73	56	23	31
Turbidity/NTU	189	165	≥ 200	≥ 200	≥ 200
SRB/(pet ml)	700	2500	1600	3600	4100
TGB/(pet ml)	1200	8500	3600	12,000	15,000
FB/(pet ml)	2500	4300	2900	11,000	12,000

basic characteristics are high turbidity, high salinity, high solid content and high bacterial content [12]. Table 2 lists the specific indicators of water quality analysis of flowback fluid from several domestic shale gas and tight gas wells, and the parameters are shown in the table below.

2 Treatment Technology and Status Quo of Fracturing Flowback Fluid in North America

The disposal of fracturing flowback fluid in North America mainly includes the following methods. It mainly includes deep well injection, discharge after treatment by municipal sewage treatment plant, reuse or discharge after treatment by on-site or central plant [13]. Among them, the U.S. Environmental Protection Agency stipulates that only the second type of injection wells that meet the requirements can be used for reinjection of fracturing flowback fluid. By the end of 2020, the reinjection proportion of shale gas produced water in deep wells in the United States has reached 95%, among which Barnett has more than 20,000 reinjection wells, and Marcellus has only more than 10 reinjection wells [14]. There are two types of efflux: ① efflux after treatment by municipal sewage treatment plant. With the improvement of sewage discharge standard, the flowback liquid simply treated by municipal sewage treatment system can no longer meet the relevant requirements, so this method is no longer applicable to the treatment of fracturing flowback liquid; ② After the site or treatment center is built and treated, it will be discharged. The one-time investment of this method is large, but the treated flowback liquid that cannot be reinjected can meet the

discharge standard [14]. With the expansion of unconventional oil and gas reservoir development scale, the improvement of environmental protection requirements and the shortage of water resources, the reuse of flowback fluid is becoming a new trend [14].

2.1 Ozonix Water Treatment Technology

Hydrozonix water treatment vehicle adopts Ozonix water treatment technology, which combines four technologies of hydraulic cavitation, ozone, ultrasonic cavitation and electro oxidation to treat wastewater in a synergistic way [15]. The four treatment mechanisms of hydraulic cavitation, ozone, ultrasonic cavitation and electro oxidation work together in the main reactor to generate efficient free radicals to degrade pollutants in water, precipitate hard salts and suspend them in the form of nano particles. The treated water in the main reactor flows through a set of static mixers and electrodes for further purification, and finally is discharged from the water outlet at the tail of the treatment truck to complete the purification treatment of fracturing flowback fluid [15].

From its establishment in 2011 to 2020, Hydrozonix will process about 20 million cubic meters of water on site [15]. The bactericidal efficiency of Hydrozonix water treatment vehicle reaches 99%, and the water treatment speed during construction is 12.8m^3/min, and the device has excellent scale inhibition performance. It is also found in field application that Hydrozonix treatment water has better resistance reduction performance [16].

2.2 CLEANWAVETM Processing Technology

The mobile CLEANWAVETM water treatment system developed by Halliburton Company adopts water quality regulation-electro flocculation process-fine filtration and other processes. The treatment flow can reach 4m^3/min, which can remove 99% of the total suspended solids and 99% of the total iron, and adapt to the inlet water quality with a total dissolved solids content of 100−300000 mg/L [17]. Combined with the company's CleanStreamTM ultraviolet sterilization process equipment, it can form a full set of technical solutions for treatment and reuse of shale gas fracturing flowback fluid, which has been applied in the Haynesville shale area and other unconventional natural gas fields. The Multiflo technology provided by Veolia can simultaneously complete suspended particle removal and chemical softening. The treatment flow can reach 4.5m3/min, the effluent hardness is less than 20 mg/L, and the turbidity is less than 10NTU. It meets the actual needs of most treatment and reuse. It is one of the main providers of fracturing flowback fluid treatment services in shale areas such as Marcellus [17].

3 Treatment Technology and Status Quo of Fracturing Flowback Fluid in Domestic Oilfields

In early China, fracturing flowback fluid was treated as waste fluid from oil and gas fields. Generally, oilfield waste fluid refers to waste fluid from drilling, acidizing, fracturing, well washing and other operations. In fact, these waste fluids have different properties [18]. In recent years, technical research on fracturing flowback fluid treatment has begun. The treatment process of flowback liquid is different due to different objectives. There are four disposal methods of fracturing flowback fluid in China: external discharge, reinjection, reinjection and reuse [18]. Among them, efflux is to treat the effluents until all indicators meet the national or local discharge standards. At present, there are 69 effluent quality indicators, and the water meeting the standards can be directly discharged into the environment, which is the most difficult and costly; There is no technical difference between reinjection and tank reinjection. Reinjection is to treat the flowback fluid to the oil and gas field water injection standard. There are only 7 reinjection standard indicators. The water meeting the standard is directly injected into the reservoir for oil production or gas production; For reinjection, the treated water is directly injected into non oil and gas reservoirs, which has nothing to do with oil production and gas production. It is just to find a formation with good water absorption for special disposal of sewage [19]. Reuse is to use the treated water for the next fracturing fluid preparation, which can make full use of the useful components in the flowback fluid. This is the most ideal treatment method, but there is no recognized water quality standard for fracturing fluid preparation. Before using the fracturing fluid, 16 indicators such as standard base fluid density, apparent viscosity, cross-linking time, temperature resistance, shear resistance, viscoelasticity, fluid loss, permeability damage rate, gel breaking performance, slag content and resistance reduction rate need to be tested. The fracturing fluid can be used after passing the test [19].

3.1 Sinopec Coagulation Sedimentation Fine Filtration Membrane Advanced Treatment Fracturing Flowback Fluid Treatment Process

The Environmental Protection Technology Service Company of Sinopec Jianghan Petroleum Engineering Co., Ltd. treats COD, suspended solids, petroleum, bacteria, iron, magnesium, calcium and other high valence cations in fracturing flowback fluid through the process of coagulation sedimentation fine filtration membrane advanced treatment. According to the treatment process of fracturing flowback fluid, four treatment modules are designed, namely, coagulation unit, inclined plate sedimentation unit, fine filtration unit and membrane advanced treatment unit, The whole unit is designed as a truck mounted skid with a processing capacity of 20~30m3/h, which can flexibly meet the fracturing flowback fluid treatment requirements of different well locations [17].

3.2 Northeast Oil and Gas Field Mobile Sewage Treatment Unit

Fracturing flowback fluid contains a large number of complex components such as sludge, suspended solids, oil, organic matter and soluble salts. Northeast Oil and Gas Field has designed and developed a mobile sewage treatment device for the recovery and reuse of fracturing flowback fluid [20]. The unit is composed of three operation containers: high-efficiency destabilizing device (treatment agent: destabilizing agent, alkalizing agent, bridging agent), solid–liquid separation device and deep purification device. After treatment, the removal rate of solid particles in the flowback liquid reaches more than 99%, and the transparency of the treatment liquid is significantly improved [18].

3.3 Changqing Oilfield Calcium Ion Treatment Agent

PetroChina Changqing Oilfield has developed a treatment agent capable of complexing free Ca^{2+} to form water-soluble chelates and eliminate the influence of metal ions on the solubility of hydrophobically associated polymers [15]. The treatment agent is compounded with sodium hydroxyethylidenedipho sphonate (HEDP · Na4) and polyaspartic acid (PASP) as the chelating agent and triethanolamine as the stabilizer. Its chelating agent molecule has a number of atoms that can provide coordination lone pair electrons, high complexing capacity and large complexing stability constant. After $Ca^{2+}$is complexed, a stable water-soluble chelate is formed, thus eliminating the influence of Ca^{2+}on the swelling and viscosity of hydrophobic association polymer [15]. It has been applied in 15 wells in Changqing Oilfield, and the treated fluid has been recovered 3900 m^3 [15].

4 Conclusion

The fracturing flowback fluid, as the product of reservoir fracturing, is difficult to be treated and expensive due to its characteristics, which seriously restricts the efficiency of modern oil and gas field development. According to its characteristics and local laws and regulations, various countries and regions have carried out research on different treatment processes of fracturing flowback fluid, and also carried out research and development on treatment equipment for impurities with different components in the flowback fluid. The treatment methods of fracturing flowback fluid at home and abroad can be roughly divided into three categories: treated efflux, treated reinjection and treated reuse. In North America, fracturing flowback fluid is discharged after treatment and reinjected after treatment. However, due to the increasing production of fracturing flowback fluid year by year and the continuous

revision of local laws, these two methods become increasingly unsuitable for the exploitation of unconventional oil and gas reservoirs such as shale gas. After treatment, reuse becomes the most popular and promising treatment method. In China, fracturing construction started late, but developed rapidly. The fracturing flowback fluid is also the first choice for major domestic oilfields to reuse after treatment. The main idea for reuse after treatment is to remove impurities in fracturing flowback fluid, such as suspended solids, oil, salts and bacteria. To sum up, it is basically no more than physical, chemical, biological and other methods. By comparing the treatment methods of fracturing flowback fluid at home and abroad, there is no efficient, systematic and universal treatment method and equipment in China. Most of the domestic treatment methods focus on each indicator, and no mature fracturing flowback fluid treatment technology has been developed. In the future, domestic research in this field is needed to reduce the difficulty of fracturing flowback fluid treatment in major oil and gas fields, reduce the treatment cost and improve the treatment effect.

References

1. Lewis A (2012) Wastewater generation and disposal from natural gas wells in Pennsylvania[D]. Duke University, Durham
2. Lu H, Bian X (2016) Challenges and countermeasures of shale gas development environment in North America [J]. Nat Gas Ind 36(007):110–116
3. Warner NR, Christie CA, Jackson RB, Vengosh A (2013) Impacts of shale gas wastewater disposal on water quality in western Pennsylvania[J]. Environ Sci Technol 47(20):11849–11857
4. Delaware Riverkeeper Network. Natural gas well drilling and production in the upper Delaware River Watershed[R/OL]. (2010–05–10)[2016–03–20].
5. Liu F, Pan D, Qin Y (2015) Discussion on recovery and treatment technology of fracturing flowback fluid in shale gas reservoir [J]. Drill Prod Technol 38(3): 4
6. Howarth RW, Santoro R, Ingraffea A (2012) Venting and leaking of methane from shale gas development: response to Cathles et al[J]. Clim Change 113(2):537–549
7. Wang Y (2020) Research status of shale gas flowback liquid treatment technology [J]. J Jianghan Pet Staff Univ 33(5): 3
8. Gorody AW (2012) Factors affecting the variability of stray gas concentration and composition in groundwater[J]. Environ Geosci 19(1):17–31
9. Earthworks TML Oil & Gas Accountability Project. Pennsylvania Department of Environmental Protection inadequate enforcement guarantees irresponsible oil and gas development in Pennsylvania[R/OL]. (2012–9–12)[2016–03–20].
10. Song L, Zhang X, Wang Y et al (2014) Progress and prospect of shale gas fracturing flowback fluid treatment technology in the United States [J]. J Environ Eng (11):5
11. Alkouh AB, Mcketta SF, Wattenbarger RA (2013) Estimation of fracture volume using water flowback and production data for shale gas wells[C]. In: SPE Annual Technical Conference and Exhibition, 30 September-2, October 2013 New Orleans, Louisiana, USA. https://doi.org/10.2118/166279-MS
12. Liu F, Yang Z, Luo Z et al (2019) North American shale gas development fracturing flowback fluid ozonix water treatment technology [J]. Chem Manag (34):3
13. Intergovernmental Panel on Climate Change. Fifth Assessment Report (AR5) [R/OL]. (2015–06–10)[2016–03–20].
14. Ying X, Ying X, Youquan L et al (2016) Study on main factors affecting the reuse of shale gas fracturing flowback fluid and treatment technology [C]

15. Chunguo MOU, Kuang D, Yi D etc (2018) Recoverable fracturing fluid technology and its application in Sulige gas field [J]. Low Permeability Oil Gas Fields (1): 5
16. Wei L (2021) Research and application of new technology for reusing guanidine gel fracturing flowback fluid [J]. Guangdong Chem Ind
17. Xiao D, Zhou Z, Yin L (2015) Reuse technology of fracturing fluid flowback fluid [J]. Oil Prod Eng (2):5
18. Liu Y, Chen P, Wu W et al (2013) Reuse technology of slick water flowback fluid for sand fracturing [J]. Petroleum and Natural Gas Chemical Industry
19. Liu P, Zhang X, Zhao Y et al (2018) Micro eddy current coagulation treatment test of well pad measure waste liquid [J]. Environ Prot Oil Gas Fields 28(4): 5
20. Frohlich C, Potter E, Hayward C, Stump B (2010) Dallas-fort worth earthquakes coincident with activity associated with natural gas production[J]. Lead Edge 29(3):270–275
21. Révész KM, Breen KJ, Baldassare AJ, Burruss RC (2010) Carbon and hydrogen isotopic evidence for the origin of combustible gases in water-supply wells in north-central Pennsylvania[J]. Appl Geochem 25(12):1845–1859

Exploratory Application of Bacteria: A Self-Healing Concrete Review

Eunice R. Berina and Orlean G. Dela Cruz

Abstract Self-healing concrete is one of the practical and effective ways to intelligently respond to cracks and lessen or even completely fix the crack. This method aids in crack repair by generating calcium carbonate crystals from bacteria that obstruct the pores and microcracks in concrete. A critical review of the self-healing technique will narrow down the different methods and approaches to utilizing this technique which is the objective of this paper. The family Bacillus genera are the most used bacteria in the literature review. It is utilized by the method of direct application and immobilized encapsulation. Therefore, various types of experiments on specimens of varying sizes have been used by various researchers for their study of bacterial concrete in comparison to conventional concrete. However, the self-healing technique is still new due to a lack of introduction and exposure in the civil engineering industry. Therefore, the proper procedure or standard should be established for proper application in practical engineering.

Keywords Self-healing · Bacteria · Construction · Building materials · Crack

1 Introduction

Concrete is still the most famous building material in the world. However, they are relatively brittle and must be applied appropriately to avoid cracking when movements due to drying shrinkage or thermal changes are restrained [1]. To solve the cracking problem in civil engineering, researchers present the biological approach as

E. R. Berina
National University Laguna, Km. 53 Pan-Philippine Hwy., 4027 Calamba City, Laguna, Philippines
e-mail: eunicerberina@iskolarngbayan.pup.edu.ph

E. R. Berina · O. G. Dela Cruz (✉)
Graduate School, Polytechnic University of the Philippines, 1016 Sta. Mesa, Metro Manila, Philippines
e-mail: ogdelacruz@pup.edu.ph

H.-Y. Jeon (ed.), *Proceedings of the International Conference on Geosynthetics and Environmental Engineering*, Lecture Notes in Civil Engineering 374,
https://doi.org/10.1007/978-981-99-4229-9_8

an environmentally benign and alternative method for ensuring the long-term durability of concrete structures [2]. The self-repairing technique based on microbial mineralization provides unique advantages because microbial spores have exceptional resistance to hostile environments and may be kept for an extended period which is the primary goal in the application of bacteria as self-healing concrete which is to enhance the longevity of structures because cracks may shorten the lifespan of concrete structures [3]. The paper aims to review the performance of different bacteria as crack remediators that the re-searchers have explored in self-healing concrete to identify the most frequent, easy-to-use, and effective remediators of cracks. In the realm of civil engineering, researchers present the biological approach as an environmentally benign and alternative method for ensuring the long-term durability of concrete structures. Bio-healing materials are based on the field of bacteriology, which is a subset of microbiology. Providing bacteria with nutrients and acquiring precipitated calcium carbonate as a result of metabolic processes such as photosynthesis, sulfate reduction, and urea hydrolysis generation is one method for bacterial healing.

2 Methodology

The objective was to determine the self-healing concrete trends in research. The following research questions were developed and applied to each identified publication to guide this goal:

- (RQ1): What bacteria are used for self-healing?
- (RQ2): What specific methods apply bacteria as self-healing concrete?
- (RQ3): What are bacteria's possible effects on concrete compressive strength?
- (RQ4): What is the performance of bacteria as crack remediators?
- (RQ5): What are the gaps in the study of applying bacteria as self-healing concrete?

Peer-reviewed bibliographic databases were looked at utilizing a three-step process: (1) exploratory search, (2) systematic selection, and (3) classification to answer the research questions of this study. To record this technique, the PRISMA (Preferred Reporting Items for Systematic Reviews and Meta-Analyses) procedure was used (see Fig. 1).

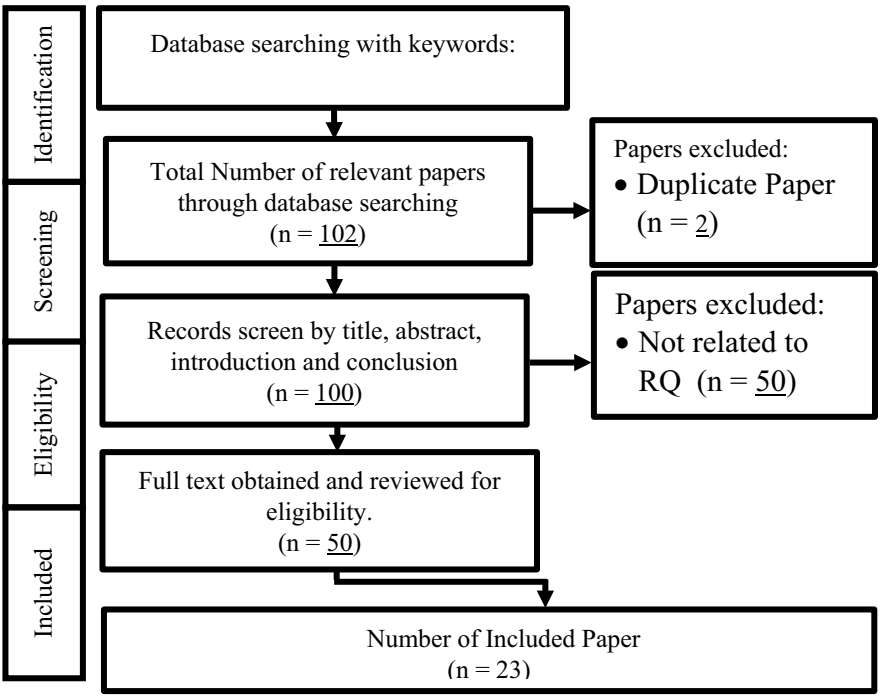

Fig. 1 Literature selection following preferred reporting item for systematic reviews and meta-analyses (PRISMA) guidelines

3 Discussion

3.1 Different Bacteria Are Used for Self-Healing

Microorganisms can grow anywhere, such as in soil, acidic springs, water, oil reservoir, etc., to fill the cracks and voids of concrete. However, bacteria of strain are the most effective for self-healing concrete because of their ability to precipitate certain beneficial chemicals to be used in designing self-healing concrete. The calcium Ca^{2+} concentration, the concentration of dissolved inorganic carbon, the pH (pK2(CO) = 10.3 at 25 OC), and the availability of nucleation sites are all simple chemical processes that should be present in bacteria [4]. Table 1 lists the bacteria that are frequently employed in research. *Bacillus sphaericus* produces carbonic anhydrase, which catalyzes the conversion of CO_2 to HCO_3, which subsequently reacts with Ca^{2+} in mortar cracks to precipitate $CaCO_3$, which was observed using Scanning Electron Microscopy (SEM) [5–7]. *Bacillus pasteurii* in Recycled Coarse Aggregates (RCA) showed that the microbial-induced precipitates in the crack were $CaCO_3$ [8]. According to X-ray diffraction (XRD) and scanning electron microscopy (SEM) data, the precipitate mineral was calcium carbonate in the calcite phase, and Bacillus

Table 1 Types of bacteria used as a self-healing remediator

Bacteria name	Application	References
Bacillus sphaericus	Direct and encapsulation	Erşan et al. [5–7]
Bacillus pasteurii	Encapsulation	Liu et al. [8]
Bacillus subtilis	Direct and encapsulation	Feng et al. [4, 7, 9–11]
Bacillus megaterium	Encapsulation	Su et al. [13]
Deinococcus radiodurans	Direct	Mondal and Ghosh [10]
Sporosarcina pasteurii	Direct	Amer Algaifi et al. [12, 14, 15]
Bacillus cohnii	Encapsulation	Rauf et al. [7, 16–18]
Lysinibacillus sphaericus	Direct	Amer Algaifi et al. [12, 19]
Bacillus pseudofirmus	Direct and encapsulation	Erşan [5]

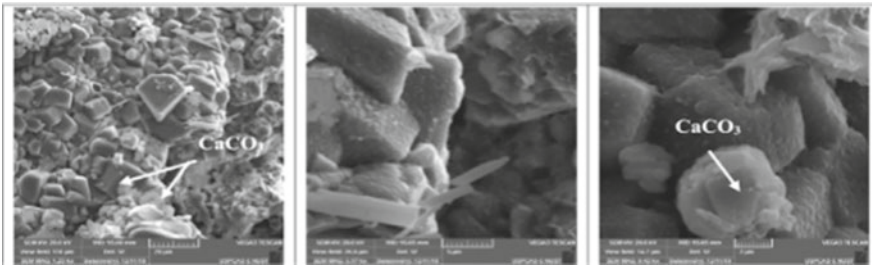

Fig. 2 $CaCO_3$ in concrete scanned using scanning electron microscopy (SEM) [7]

subtilis was employed for the biomineralization test. It was discovered that calcite is the dominating mineral phase, with some bacterial fingerprints on the crystal surface [4, 7, 9–11]. In the series with Ca^{2+} concentrations of 50 mM, *Sporosarcina pasteurii* hydrolyzed around 40% of the urea, and after seven days, all urea was hydrolyzed entirely [12] (Fig. 2).

3.2 Methods of Applying Bacteria as Self-Healing Concrete

Microorganisms are included in concrete in various ways, including microbial broth in freshly formed concrete, spores, immobile form on silica gel, encapsulation, and direct application, according to the literature. Comparing the performance of *Bacillus sphaericus* using direct and encapsulation [6]. The vegetative cell-dropping (direct) method was more effective than immobilized microencapsulated bacterial spores for mortar repair. Even by using *Bacillus subtilis,* where the comparison between direct and immobilization of bacteria by using Bentonite nano/microparticles (BNMP), shows that the direct induction of bacteria in concrete healed the cracks up to 0.44 mm compared to healing efficiency up to 0.2 mm by immobilization using BNMPs [11].

However, the microencapsulation method in UK field applications to evaluate its self-healing performance on-site is already applied [20]. The researchers also highlighted the challenges and improvements in producing next-generation microencapsulate-based self-healing systems. Even the tunnel project at Qianhai, Shenzhen, which uses encapsulation, was investigated through field and laboratory tests [21]. The results indicated that this self-healing technology is feasible and is expected to improve the durability of concrete structures, especially in coastal civil engineering [21]. Also, it highlighted that one obstacle that impedes the direct application of bacteria in concrete is its harsh environment, i.e., high shear strength and temperature during mixing, high alkalinity (pH > 12), and minimal space (pore size < 0.1 μm) after hardening [15]. Unprotected bacteria cells could not survive directly mixed with fresh concrete. Thus, protective carriers must be used along with bacteria. In short, bacteria should be wrapped in encapsulation materials. Recycled coarse aggregates (RCA) were useds an encapsulation for bacteria, and after 28 days of healing, the crack of the concrete prepared was healed [8]. *Bacillus pseudofirmus* bacteria spores and nutrients were encapsulated using polyurea without affecting its chemical reaction. It was found to be a practical approach to protecting bacteria included in cementitious material for self-healing [22]. Expanded Perlite (EP) wrapped with various materials as a bacterial and nutrient carrier and found to enhance the healing process of mixing with concrete [16, 18]. In particular, the crack-healing of concrete peaked when EP particles immobilized with bacterial spores were wrapped with a low-alkaline material (potassium magnesium phosphate cement). This result was also validated by the water permeability experiments [10]. EP is a low-cost material; thus, it can be used as a bacterial carrier for large-scale self-healing concrete applications. Moreover, the study on the effects of the core–shell bacterial carriers showshat the batch-prepared carrier has good quality stability, can achieve strong growth, has low porosity and small pore size, and can significantly extend the survival time of microorganisms [23].

3.3 Effects of Bacteria on Properties of Concrete Compressive Strength

The compressive strength test is the most essential of the various tests performed on concrete since it provides information about the concrete's qualities. It shows the capacity of concrete to withstand loads before failure. The application of bacteria based on calcite precipitation has influenced the strength of structural concrete. Using *Bacillus sphaericus* bacteria by direct applying bacteria cells and nutrients results in 46% more strength than specimens without bacteria [6]. It was also supported by bacteria *B. subtilis* and *D. radiodurans,* which after 28 days of curing the mortar samples increased their compressive strength by 29% and 45%, respectively, with 10^3 cells/ml of bacterial concentration where the bacteria were sterilized by autoclaving for 30 min at a temperature of 130 °C. The bacteria were inoculated in the nutrient

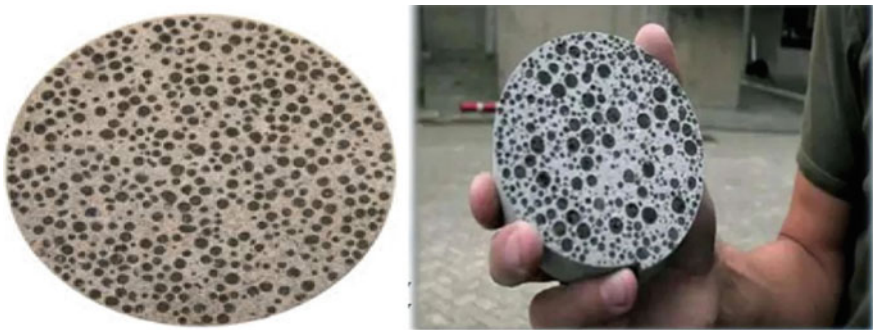

Fig. 3 Example of self-healing concrete with the use of bacteria

broth inside a laminar flow chamber after chilling to ambient temperature (27 C). About 10μ from each culture medium were taken on a hemocytometer after 5–6 days of inoculation. And the number of bacterial cells was counted under a microscope [10]. With a cell concentration of 2×10^7 cells/mL, the *L. sphaericus* and *S. pasteurii* enhance strength by 15 and 11% compared to control concrete by incorporating bacteria by direct application [12]. *Sporosarcina pasteurii* gives the highest results in compressive strength recovery, which is over 87% of the original value [24]. Higher compression strength values also indicate that healing processes were not restricted to the surface but occurred in deeper parts of the cracks. This result was due to the precipitation of microbial calcium carbonate inside the concrete, which was proven using a Scanning Electron Microscope (SEM) [6, 9, 10, 12, 24]. Evaluating the effects of multi-varied atmospheric curing conditions on the compressive strength of bacteria *Bacillus Subtilis*, finding that higher temperatures, relative humidity, and the wind speed increased compressive strength [9]. See Fig. 1 as an example of the Self-repairing technique using bacteria (Fig. 3).

3.4 Performance of Bacteria as Crack Remediator

The most common method for designing self-healing concrete in the literature is bacterial calcium carbonate precipitation utilizing *ureolytic* bacteria. The urease enzyme from bacteria catalyzes the hydrolysis of urea to carbon dioxide and ammonia. According to the microbiological pathway for calcium carbonate precipitation, urea must be present in the self-healing concrete to activate the necessary biochemical events. To detect the biological calcite precipitation needed in self-healing concrete, X-ray diffraction (XRD) is commonly used.

Bacillus subtilis is the most frequently used in the related literature. With a cell concentration of 105 cells/ml of concrete in direct application, calcite was the most predominant mineral phase of calcium carbonate in precipitation, which was proven by a Scanning Electron Microscope (SEM) [4, 10]. However, the healing decreases

as times go by [4]. With 5.9L/m3 of cell concentrate, it can heal cracks up to 1.2 mm widths if incorporated by encapsulation/immobilization using iron oxide nano/microparticles (INMPs) [11]. The presence of calcium carbonate ($CaCO_3$) is also observed in the bacteria *Bacillus sphaericus* with 106 cell/mL cell concentration which is dropped directly at the surface of cracks twice a day for seven days, and 100% of cracks are healed [6]. *Bacillus conhii* can also be immobilized in these fibers, where massive rhombohedral crystals of size more than 20 μm can be seen using SEM, indicating that *Bacillus conhii* integrated with concrete mix has adequate bacterial activity for crack healing [18].

Using Expanded Perlite (EP) [25], where *Bacil lus conhii* is encapsulated with 3.9×109 cell/cm^3 completely healed crack width up to 1.24 mm after 28 days [16]. *Bacillus conhii* degrades organic molecules into CO_2 and H_2O, which results in the formation of $CaCO_3$ [16]. *Bacillus pseudofirmus* was also encapsulated at Expanded Perlite (EP), where calcium carbonate was detected using Fourier transform infrared spectroscopy (FTIR) with 4.1×109 spores per g, and healing occurred after 165 days [26]. However, heat (45 °C for 4 h) and pH (12.9 for 4 h) treatments of the bacteria had a significantly lower impact on the viability and urea hydrolysis using *Sporosarcina pasteurii* [14]. Tables 2 and 3 summarize a few researchers' previous research on self-healing concrete.

4 Conclusion

This review paper examines the biological approach's potential to create biologically self-healing concrete by employing microorganisms that can precipitate calcite. Understanding the application of urease-producing bacterium isolates, such as those from the Bacillus species, in the repair of concrete fractures is crucial to our effort. The study examined various bacterial species that can be employed to repair cracks. The proposed assortment in this study helps the researchers better understand the self-healing concrete road map. The realization paves the way for future studies on developing biological techniques for self-healing concrete on the amount of *Bacillus subtilis* to be applied in concrete mixture using direct application of bacteria's urea.

Table 2 Summary of direct method used by researchers

Bacteria	Cell concentration	Compresive strength	Effectiveness as crack remediation	Machine used	References
Bacillus sphaericus	10^6 cells/mL	46% more	100% cracked areas	SEM and EDS	Intarasoontron [6]
Bacillus subtilis	0.055/cu.m	Flexural by 14%	Micro-cracks were healed 28d	SEM	Erşan [5]
Deinococcus radiodurans	10^5 cells/ml	42% increase	Cracks precipitations at 28 days	SEM and EDS	Mondal [10]
Bacillus subtilis		26% increase			
Bacillus subtilis	10^9 cells/ml	130.6%	Improves the compressive	–	Abdulkareem [9]
Sporosarcina pasteurii	10^9 cells/m	–	450 μm in 120 days	Image-pro plus	Xu [15]
Sporosarcina pasteurii	$2x10^7$ cells/mL	15% increase	0.4 mm crack achieved after 70s	X-ray μCT scanning	Amer Algaifi et al [12]
Lysinibacillus sphaericus		11% increase	Cracked mended in 70d		
Lysinibacillus sphaericus	10^7 cells/mL	–	Cracked mended in 70d	VP-SEM with EDX	Algaifi et al.[19]

Table 3 Summary of encapsulation method used by researchers

Bacteria	Cellconcentration	Encapsulation material	Compresive strength	Effectiveness as crack healing	Machine use to verify crack width	References
Bacillus subtilis	3×10^8 cells/m^3	Lightweight aggregate (LWA) abd graphite nanoplatelets (GNP)	Improvement of 12% (LWA) and 9.8% (GNP)	GNP early age healing LWA consistent healing efficiency	XRD analysis (SEM) analysis	Algaifi et al. [19]
Bacillus megaterium	–	Low alkali calcium sulphoaluminate (CSA) cement	–	4000 μm	XRD and SEM are with an EDS.	Su et al. [13]
Bacillus cohnii	12.5×10^{10} cfu	Aerated concrete granule w/carbonated mortar	–	Fill the crack for up to 84 days	Leica M205C light microscope, SEM w/ EDX	Tan et al. [17]
Bacillus cohnii	3.9×10^9cell/cm^3	Expanded perlite (EP)	–	1.24 mm width after 28 days	KLN-CBY501 Image microscope CAM-MS	Jiang et al. [16]
Bacillus cohnii	5.2×10^8cell/ cm^3	Expanded perlite (EP)	–	Crack widths were up to 0.79 mm after 28 days	FESEM and and XRD	Zhang et al. [18]
Bacillus pseudofirmus	–	Polyurea polymer	–	–	TGA, EDX, FTIR, and XRD	Zamani et al. [22]
Bacillus pseudofirmus	4.1×10^9 spores/g	Expanded perlite (EP)	–	165 days for healing to occur.	FTIR	Alazhari et al. [26]

References

1. Kim R, Woo U, Shin M, Ahn E, Choi H (2022) Evaluation of self-healing in concrete using linear and nonlinear resonance spectroscopy. Constr Build Mater 335:127492. https://doi.org/10.1016/j.conbuildmat.2022.127492
2. Xu J, Tang Y, Wang X, Wang Z, Yao W (2020) Application of ureolysis-based microbial $CaCO_3$ precipitation in self-healing of concrete and inhibition of reinforcement corrosion. Constr Build Mater 265:120364. https://doi.org/10.1016/j.conbuildmat.2020.120364
3. Vijay K, Murmu M, Deo SV (2017) Bacteria based self healing concrete–a review. Constr Build Mater 152:1008–1014. https://doi.org/10.1016/j.conbuildmat.2017.07.040
4. Feng J, Chen B, Sun W, Wang Y (2021) Microbial induced calcium carbonate precipitation study using Bacillus subtilis with application to self-healing concrete preparation and characterization. Constr Build Mater 280:122460. https://doi.org/10.1016/j.conbuildmat.2021.122460
5. Erşan YÇ, Da Silva FB, Boon N, Verstraete W, De Belie N (2015) Screening of bacteria and concrete compatible protection materials. Constr Build Mater 88:196–203. https://doi.org/10.1016/j.conbuildmat.2015.04.027
6. Intarasoontron J, Pungrasmi W, Nuaklong P, Jongvivatsakul P, Likitlersuang S (2021) Comparing performances of MICP bacterial vegetative cell and microencapsulated bacterial spore methods on concrete crack healing. Constr Build Mater 302:124227. https://doi.org/10.1016/j.conbuildmat.2021.124227
7. Rauf M, Khaliq W, Khushnood RA, Ahmed I (2020) Comparative performance of different bacteria immobilized in natural fibers for self-healing in concrete. Constr Build Mater 258:119578. https://doi.org/10.1016/j.conbuildmat.2020.119578
8. Liu C, Zhang R, Liu H, Xu X, Lv Z (2021) Experimental and analytical study on the flexural rigidity of microbial self-healing concrete based on recycled coarse aggregate (RCA). Constr Build Mater 285:122941. https://doi.org/10.1016/j.conbuildmat.2021.122941
9. Abdulkareem M, Ayeronfe F, Majid MZA, Mohd Sam AR, Kim JHJ (2019) Evaluation of effects of multi-varied atmospheric curing conditions on compressive strength of bacterial (bacillus subtilis) cement mortar. Constr Build Mater 218: 1–7. https://doi.org/10.1016/j.conbuildmat.2019.05.119.
10. Mondal S, Ghosh AD (2021) Spore-forming bacillus subtilis vis-à-vis non-spore-forming deinococcus radiodurans, a novel bacterium for self-healing of concrete structures: a comparative study. Constr Build Mater 266: 121122. https://doi.org/10.1016/j.conbuildmat.2020.121122.
11. Shaheen N, Khushnood RA, Khaliq W, Murtaza H, Iqbal R, Khan MH (2019) Synthesis and characterization of bio-immobilized nano/micro inert and reactive additives for feasibility investigation in self-healing concrete. Constr Build Mater 226:492–506. https://doi.org/10.1016/j.conbuildmat.2019.07.202
12. Amer Algaifi H et al (2020) Insight into the role of microbial calcium carbonate and the factors involved in self-healing concrete. Constr Build Mater 254: 119258. https://doi.org/10.1016/j.conbuildmat.2020.119258.
13. Su Y, Zheng T, Qian C (2021) Application potential of bacillus megaterium encapsulated by low alkaline sulphoaluminate cement in self-healing concrete. Constr Build Mater 273:121740. https://doi.org/10.1016/j.conbuildmat.2020.121740
14. Williams SL, Kirisits MJ, Ferron RD (2017) Influence of concrete-related environmental stressors on biomineralizing bacteria used in self-healing concrete. Constr Build Mater 139:611–618. https://doi.org/10.1016/j.conbuildmat.2016.09.155
15. Xu J, Tang Y, Wang X, Wang Z, Yao W (2020) Application of ureolysis-based microbial precipitation in self-healing of concrete and inhibition of reinforcement corrosion. Constr Build Mater 265:120364. https://doi.org/10.1016/j.conbuildmat.2020.120364
16. Jiang L, Jia G, Jiang C, Li Z (2020) Sugar-coated expanded perlite as a bacterial carrier for crack-healing concrete applications. Constr Build Mater 232:117222. https://doi.org/10.1016/j.conbuildmat.2019.117222

17. Tan L, Reeksting B, Ferrandiz-Mas V, Heath A, Gebhard S, Paine K (2020) Effect of carbonation on bacteria-based self-healing of cementitious composites. Constr Build Mater 257:119501. https://doi.org/10.1016/j.conbuildmat.2020.119501
18. Zhang J et al (2017) Immobilizing bacteria in expanded perlite for the crack self-healing in concrete. Constr Build Mater 148:610–617. https://doi.org/10.1016/j.conbuildmat.2017.05.021
19. Algaifi HA, Bakar SA, Mohd Sam AR, Abidin ARZ, Shahir S, AL-Towayti WAH (2018) Numerical modeling for crack self-healing concrete by microbial calcium carbonate. Constr Build Mater 189: 816–824. https://doi.org/10.1016/j.conbuildmat.2018.08.218
20. Al-Tabbaa A, Litina C, Giannaros P, Kanellopoulos A, Souza L (2019) First UK field application and performance of microcapsule-based self-healing concrete. Constr Build Mater 208:669–685. https://doi.org/10.1016/j.conbuildmat.2019.02.178
21. Wang X et al (2019) Laboratory and field study on the performance of microcapsule-based self-healing concrete in tunnel engineering. Constr Build Mater 220:90–101. https://doi.org/10.1016/j.conbuildmat.2019.06.017
22. Zamani M, Nikafshar S, Mousa A, Behnia A (2020) Bacteria encapsulation using synthesized polyurea for self-healing of cement paste. Constr Build Mater 249:118556. https://doi.org/10.1016/j.conbuildmat.2020.118556
23. Zhang X, Jin Z, Li M, Qian C (2021) Effects of carrier on the performance of bacteria-based self-healing concrete. Constr Build Mater 305:124771. https://doi.org/10.1016/j.conbuildmat.2021.124771
24. van der Bergh JM et al (2020) Preliminary approach to bio-based surface healing of structural repair cement mortars. Constr Build Mater 248:118557. https://doi.org/10.1016/j.conbuildmat.2020.118557
25. Kim R, Woo U, Shin M, Ahn E, Choi H (2022) Evaluation of self-healing in concrete using linear and nonlinear resonance spectroscopy. Constr Build Mater 335:127492. https://doi.org/10.1016/j.conbuildmat.2022.127492
26. Alazhari M, Sharma T, Heath A, Cooper R, Paine K (2018) Application of expanded perlite encapsulated bacteria and growth media for self-healing concrete. Constr Build Mater 160:610–619. https://doi.org/10.1016/j.conbuildmat.2017.11.086

Shear and Flexural Performance of Reinforced Concrete Beams with Modified Shear Reinforcement: A Literature Review

Bonjoebee R. Bello and Orlean G. Dela Cruz

Abstract Shear failure is undesirable to any structural engineer due to its occurrence without warning. Such loss must be avoided in the design of any structure. Consequently, there has been a significant urge to improve and strengthen the behavior of RC beams. Researchers have innovated various approaches, encompassing additives, partial or full replacement of fundamental concrete materials and explorations into size effects. Conversely, changing the con-figurations of the typical stirrups emerges as a new and promising technique for improving the strength of RC beams. This paper reviewed different literature on modifying beams' shear reinforcement in terms of geometry, inclination, and spacing. The literature revealed that RC Beams with spiral and truss reinforcement increased shear capacity by 18.148%, flexural capacity by 13.08%, and reduced deflection by 80mm to 150mm. Due to challenges and gaps, this area of research is still an open field for study. Therefore, to further study this area, it is recommended to use FEM as an alternative to design complex FE models and analyze complicated structural members to obtain safe and accurate results with less cost and time. This paper may contribute to future studies to evaluate the best design demonstrating exemplary performance for RC beams' shear and flexural behavior.

Keywords Shear reinforcement configurations · Spiral stirrups · Truss reinforcement system · Finite element method · RC beam

B. R. Bello
Tarlac State University, Romulo Blvd., San Vicente, Tarlac City, 2300 Tarlac, Philippines
e-mail: brbello@tsu.edu.ph

B. R. Bello · O. G. Dela Cruz (✉)
Graduate School, Polytechnic University of the Philippines, 1016 Sta. Mesa, Metro Manila, Philippines
e-mail: ogdelacruz@pup.edu.ph

H.-Y. Jeon (ed.), *Proceedings of the International Conference on Geosynthetics and Environmental Engineering*, Lecture Notes in Civil Engineering 374,
https://doi.org/10.1007/978-981-99-4229-9_9

1 Introduction

Shear failure is the most dangerous and complex failure mode on reinforced concrete (RC) beams [1]. It is unfavorable for engineers because of its sudden occurrence with a brittle failure approach [2, 3]. Furthermore, such failure would lead to the crushing [4] of concrete before the tensile reinforcement yields, making it critical and unsafe for the occupants of any structures.

Modifying the traditional steel reinforcement of RC beams regarding the geometry, inclination, and spacings is a promising technique to improve their strength [5−11]. Various researchers have studied and shown the effectiveness of using the modified configuration of shear reinforcement in beams' shear and flexural behavior.

Most of the studies about shear reinforcement modification are experimental approaches that use additional laboratory testing that is costly and not immediately accessible [12] to researchers. This problem makes the research expensive and time-consuming. However, the Finite Element Method (FEM) uses less effort and budget to evaluate and understand the RC beams' behavior [13].

FEM is one of the most precise and efficient advances to analyze complicated structural engineering problems like reinforced concrete, which gives a convenient and flexible tool for solving the difficulties related to the RC members' analyses [14]. This study aims to identify different designs of modified configurations of shear reinforcement that significantly affect RC beams' shear and flexural behavior. Moreover, this study reviews how useful FEM is in analyzing the effect of modified shear reinforcement in beams. Finally, this study seeks to find gaps and challenges that may need to address in the future by conducting a review.

2 Methodology

A comprehensive literature review (refer to Fig. 1) has been done to collect and present data by the following procedures: (1) collecting of published journals by searching thru keywords such as shear reinforcement configurations; (2) screening of relevant journals by title, abstract, introduction and conclusion; and (3) evaluating the eligibility of the collected literature. Forty-seven published journals were collected and selected for screening to acquire four topics.

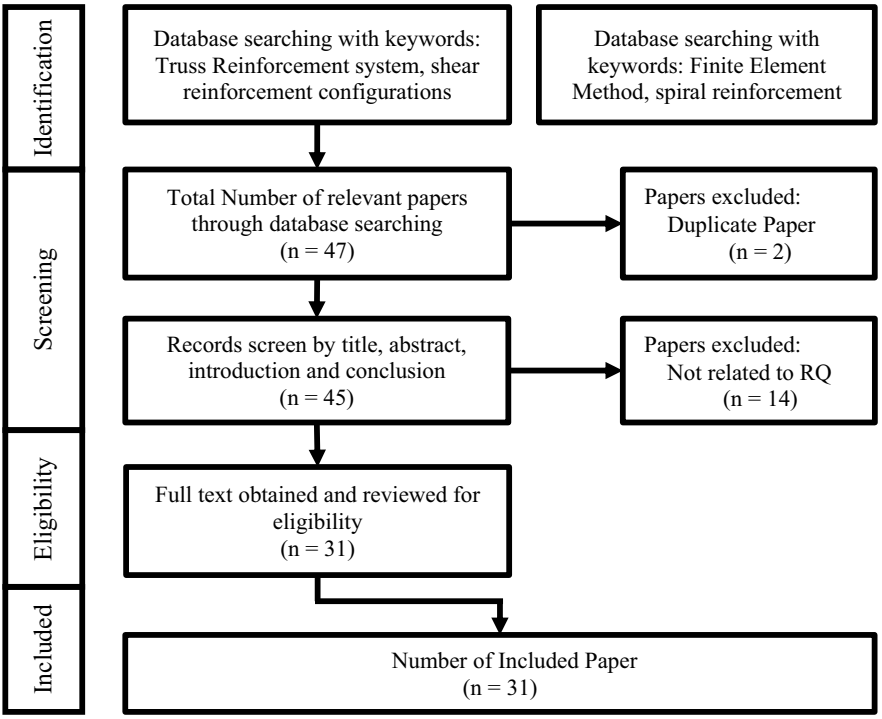

Fig. 1 Systematic review flow chart

3 Discussion

3.1 Shear Reinforcement Modification of RC Beams

RC beams need shear reinforcement, and theoretically, it is required when an external force exceeds the member's design shear resistance. Nevertheless, minimum shear reinforcement is necessary to avoid brittle failure [7]. Shear failure is brittle and, therefore, must be avoided in the design of RC beams [15]. Many researchers modified the conventional stirrups into spiral and truss reinforcement to address such failure.

Spiral Stirrups. Spiral reinforcements are closely spaced continuous spirals that encircles the main bars in the forms [16]. It is not new in reinforced concrete members, as columns have already used this reinforcement. These columns provide greater load-bearing capacity since the energy transfers continuously in the spiral reinforcement, making it more malleable and flexible [17]. In RC beams, vertical stirrups are replaced by spiral reinforcement to increase flexural and shear carrying capacity and in the ductile behavior of beams [18].

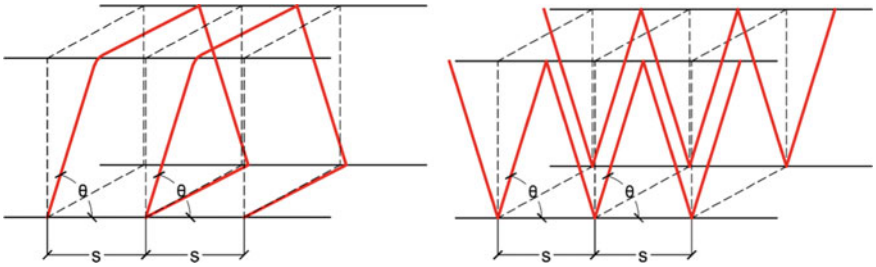

a. Spiral Reinforcement b. Truss Reinforcement System

Fig. 2 Sample design of modified shear reinforcement

RC beams with spiral reinforcement are designed according to the following: beam dimension, material properties, stirrup geometry, stirrup diameter, stirrup inclinations, and spacings (refer to Fig. 2a). The beams have rectangular cross-sections with different compressive strengths ranging from 25 to 60 MPa [7, 8, 10, 15, 19, 20]. The stirrups are continuous rectangular & circular spiral reinforcement ranging from 3 to 6 mm∅ in diameter [7, 8, 10, 15, 19, 20] with yield strength going from 290 to 540 MPa [8, 10, 20].

The spacing of the spiral stirrups varies from a minimum of 14 mm to a maximum of 200 mm [7, 8, 10, 15, 19, 20]. If the stirrup's size is 8 or 10 mm∅, the spacing should be 250 or 400 mm to acquire a desirable transverse reinforcement ratio but should not exceed 0.75d [21, 22]. More importantly, the design of the beams with spiral reinforcement that shows a significant effect on the beams' behavior is the inclination [10], and the tendency used differs from 72.5° to 85° concerning the horizontal axis [7, 8, 10].

Truss Stirrups. A truss is a triangulated arrangement of straight, slender members linked together [23]. Many researchers adopted the conceptual design of the truss to replace the shear reinforcement to strengthen the load-carrying capacity of beams. A special steel–concrete composite beam known as Hybrid Steel Truss Concrete Beams (HSTCBs) was recently introduced in the construction industry, with prefabricated truss reinforcement embedded into the concrete [24−27].

RC beams with truss reinforcement are designed according to the following: beam dimension, material properties, stirrup geometry, steel type and sizes, and stirrup inclination and spacings (refer to Fig. 2b). The beams have rectangular cross-sections with different compressive strengths ranging from 18.5 MPa to 38.83 MPa [28−32]. The stirrups are truss reinforcement composed of round bar, 8 mm [28−31] and 16 mm in diameter [32], and steel strips, 2 mm thick and 14, 25, and 40 mm wide [29] with yield strength ranging from 300 to 479 MPa [28−32].

The spacing of the different truss stirrups varies from 83 to 450 mm [28−32]. Some designs in spacing are based on 25, 50, and 75% of the adequate depth of the beam [28]. Moreover, the inclination is based on the spacings of the truss stirrups.

The closer the spacing, the stiffer the tendency of the stirrups.

3.2 Finite Element Method

The experimental approach to evaluating the mechanical behavior of RC beams is considered helpful in developing results [13]. However, this approach has disadvantages in terms of time and budget, as laboratory testing is costly and not immediately accessible [12] to researchers and requires more labor. The numerical method, in contrast, expends less cost and time and can also assist in obtaining an excellent understating of the behavior of RC beams [13].

The Finite Element Method, or FEM, is a numerical analysis methodology that provides approximate solutions to various engineering problems. It gives a nonlinear analysis of the system of equations to the finite element (FE) model problems [33]. FEM has made significant promises in several mechanical applications associated with civil engineering structural modeling [12]. The core premise of FEM is a solution zone that can be analytically described by replacing discrete elements known as discretization. Furthermore, these components can be combined to create highly complicated geometrical shapes or forms [33]. These features of FEM help any researcher to design complex FE models. It is one of the most precise and effective ways to analyze complicated structural engineering issues like reinforced concrete; moreover, it provides a straightforward and adaptable tool for resolving RC member analysis difficulties [14]. Comparing the available experimental and numerical data with the analytical calculation reveals that a proposed model from FEM can provide a safe and reasonably accurate evaluation of the RC beam behavior [34].

Six leading companies offer commercial software for finite element analyses, such as ABAQUS, ANSYS, SDRC-Ideas, RASNA, and MSC/NASTRAN [33]. ABAQUS [13, 35] and ANSYS [36, 37] are used by various researchers for modeling and studying the effect of spiral and truss reinforcement in RC beams.

3.3 Effects of Modified Shear Reinforcement

The products of modified shear reinforcement in RC beams are presented based on the shear, flexural strength, and midspan deflection. These results are reviewed based on the relations with the inclinations and spacings of stirrups.

Spiral Stirrups. RC beams with spiral reinforcement are setups (refer to Fig. 3a and b) in three-point [20] and four-point bending tests [7, 8, 10, 15, 19]. These testing exhibited an average 18.148% increase in shear capacity [7, 8, 10, 15]. It is shown that the most remarkable difference between the beams tested with spiral reinforcement configurations is the ability to sustain the shear force for more considerable deflections [20]. Moreover, spirals with spacing ranging from 80 to 120 mm showed these positive results [12, 13, 17, 18, 20], and 85° being the optimum angle that presents optimum performance [10].

Truss Stirrups. For the beams with truss reinforcement, the three-point [32] and four-point bending tests [28−31] are used. These testing exhibited an average of

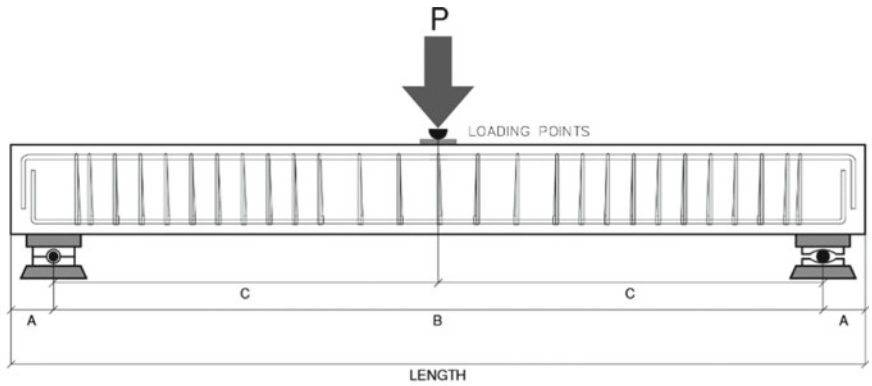

a. Three-Point Bending Setup

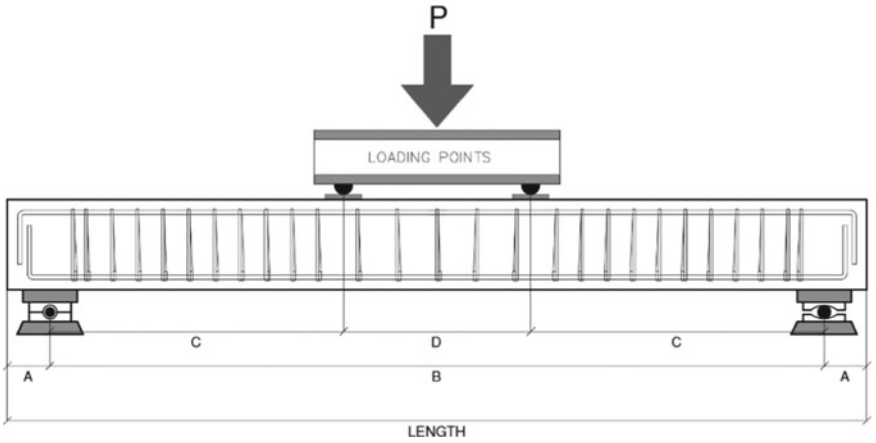

b. Four-Point Bending Setup

Fig. 3 Testing setup

13.08% increase in flexural capacity [28–30]. It is also shown that the beams with truss reinforcements sustain remarkable deflection [30]. Moreover, truss stirrups with spacing ranging from 83 to 150 mm showed these positive results [28−32].

Modified Stirrups in FEM. FE models are designed in numerical software and tested through three-point [34, 35, 37, 38], and four-point bending tests [13, 36]. After the testing, it is shown that ultimate shear strength increased compared to control beams [13, 35, 36]; the load carrying capacity of the model with inclined stirrups is increased by 28 to 83% [37]. In addition, all RC beams using embedded steel angle trusses showed a reduction in deflection [13, 37].

3.4 Effectiveness of Modified Shear Reinforcement

The strength of any structural member, such as beams, must be enough to resist all the effects caused by loadings during its lifetime without failure [10]. Most structural design specifications suggest RC beams' ductile failure to guarantee structures' safety [39].

Replacing traditional stirrups with spiral reinforcement showed a promising result in the RC beams' behavior. Beams reinforced with rectangular spiral stirrups are more effective than regular and circular spiral stirrups [15]. Spirals are recommended in beams because they improve the shear capacity and ductility of beams [7, 8, 10, 19] and minimize construction time and costs [10]. Test findings demonstrate that introducing rectangular spiral reinforcement improves the tested beams' bearing capacity and shear performance [8].

Meanwhile, beams with truss reinforcement systems also demonstrated a positive conclusion about the RC beams' behavior. Beams reinforced with trussed steel strips had higher shear performance in both ultimate capacities and developed significant shear crack width than beams reinforced with equivalent trussed bars. This is due to the larger surface area of the internal trussed strips compared to round bars, that reinforced beam could keep the concrete core within the section, reducing the primary shear fracture width and increasing the final strength of the reinforced concrete beam [29]. Flexural capacity [28, 30, 31], shear capacity [28, 31], and stiffness [30] of the concrete beams increased compared to the standard steel reinforced concrete beam. It is also noticeable that an increase in the shear capacity of beams can be achieved by using inclined stirrups in a suitable direction and arrangement [32].

In FEM, favorable results from the RC beams' behavior are also found. The embedment of steel trusses in RC beams improved the structural behavior of RC beams [13]. Beams with embedded trusses or providing inclination to the vertical stirrups significantly increased the ultimate shear strength [13, 37] and increased ductility [34] compared with traditional RC beams. Furthermore, the shear reinforcement has a negligible effect on the failure and midspan deflection of the RC beam by using steel trusses [13]. Therefore, truss reinforcement is comparatively more significant than conventional beams [35].

4 Challenges and Gaps

The literature revealed that modifying the traditional shear reinforcement into spiral and truss systems increased RC beams' shear and flexural behavior. However, it is also shown that designs in the shear reinforcement's geometry, inclination, and spacings are limited to continuous rectangular or circular spiral and truss systems.

Promising results are obtained by using spiral and truss systems in beams. Nevertheless, authors do not often compare the behavior of RC beams between these two technologies.

Most studies only focused on either the shear or flexural performances of RC beams with modified reinforcement.

The FEM is a beneficial approach to obtaining and understanding the results of any structural analysis due to its safe and accurate outcomes. But authors in experimental and descriptive studies only compared data between the control and independent specimens.

References	Challenges and Gaps Imposed
[7, 8, 10, 15, 19, 20, 28–32]	Limited design in stirrup modifications
[7, 8, 10, 13, 15, 19, 20, 34–38]	Lack of research in comparing different spiral, truss, and other designs of stirrup modification
[8, 10, 13, 19, 20, 28–32, 35–37]	Limited research in evaluating both shear and flexure
[7, 8, 10, 13, 15, 19, 20, 34–38]	Lack of statistical analysis in result assessment

5 Conclusions

The effects of using modified shear reinforcement in RC beam's shear and flexural behavior have been well-reviewed. The change in the stirrups' geometry, inclination, and spacings significantly affected RC beams' shear and flexural capacity and reduced deflection. Although this promising technique tends to increase the beam's load-carrying capacity, several gaps and challenges still exist, such as limited designs in the modification of shear reinforcement, lack of research in comparing different spiral, truss, and other design of stirrup modification, limited research in evaluating both shear and flexure, and lack of statistical analysis in result assessment.

Consequently, this area of research is still an open field for study. Therefore, to further study this area of research, FEM is an alternative and a very useful tool to design complex FE models and analyze complicated structural members to obtain safe and accurate results with less cost and time.

To conclude this paper, exploring the modification of beams' shear reinforcement in terms of geometry, inclination, and spacing is significant and recommended since this will help future studies to evaluate the best design that shows relative improvement in RC beams' capacity. Moreover, assessment and comparisons of the outcomes between spiral, truss, and other modification designs are necessary to show which method demonstrates significant strength for beams. Furthermore, it is vital to study both the shear and flexural performances of beams since beams may fail both in flexure and shear [39]. Finally, investigation and assessment of the results through statistical analysis are essential to describe the significance of modifying the shear reinforcement in RC beams since the statistical analysis helps the researcher understand the results to provide confident recommendations and conclusions.

References

1. Jin L, Wang T, Jiang X, Du X (2019) Size effect in shear failure of RC beams with stirrups: simulation and formulation. Eng Struct 199:109573 https://doi.org/10.1016/J.ENGSTRUCT.2019.109573
2. Mansour W, Tayeh BA (2020) Shear behaviour of RC beams strengthened by various ultrahigh performance fibre-reinforced concrete systems. Adv Civ Eng 2020(3):1–18. https://doi.org/10.1155/2020/2139054
3. Li Y, Wu M, Wang W, Xue X (2021) Shear behavior of RC beams strengthened by external vertical prestressing rebar. Adv Civ Eng 2021:1–12. https://doi.org/10.1155/2021/5483436
4. Fritih Y, Vidal T, Turatsinze A, Pons G (2013) Flexural and shear behavior of steel fiber reinforced SCC beams. KSCE J Civ Eng 17(6):1383–1393. https://doi.org/10.1007/s12205-013-1115-1
5. Shahrooz BM, Forry ML, Anderson NS, Bill HL, Doellman AM (2016) Continuous transverse reinforcement—behavior and design implications. ACI Struct J 113(5):1085–1094. https://doi.org/10.14359/51689154
6. Karayannis CG (2015) Mechanics of external RC beam-column joints with rectangular spiral shear reinforcement: experimental verification. Meccanica 50(2):311–322. https://doi.org/10.1007/S11012-014-9953-6
7. de Corte W, Boel V (2013) Effectiveness of spirally shaped stirrups in reinforced concrete beams. Eng Struct 52:667–675. https://doi.org/10.1016/j.engstruct.2013.03.032
8. Karayannis CG, Chalioris CE (2013) Shear tests of reinforced concrete beams with continuous rectangular spiral reinforcement. Constr Build Mater 46:86–97. https://doi.org/10.1016/j.conbuildmat.2013.04.023
9. Shatarat N, Katkhuda H, Abdel-Jaber M, Alqam M (2016) Experimental investigation of reinforced concrete beams with spiral reinforcement in shear. Constr Build Mater 125:585–594. https://doi.org/10.1016/j.conbuildmat.2016.08.070
10. Shatarat N, Mahmoud HM, Katkhuda H (2018) Shear capacity investigation of self compacting concrete beams with rectangular spiral reinforcement. Constr Build Mater 189:640–648. https://doi.org/10.1016/j.conbuildmat.2018.09.046
11. Chalioris CE, Karayannis CG (2013) Experimental investigation of RC beams with rectangular spiral reinforcement in torsion. Eng Struct 56:286–297. https://doi.org/10.1016/j.engstruct.2013.05.003
12. Bhat FZ (2022) Application of finite element analysis. In: Application of Finite Element Analysis. Accessed 07 Aug 2022. [Online]. https://www.researchgate.net/publication/352017598_Application_of_Finite_Element_Analysis
13. Arafa M, Alqedra MA, Salim R (2018) Performance of RC beams with embedded steel trusses using nonlinear FEM analysis. Adv Civ Eng 2018. https://doi.org/10.1155/2018/9079818
14. Yang SH, Woo KS, Kim JJ, Ahn JS (2021) Finite element analysis of RC beams by the discrete model and CBIS model using LS-DYNA. Adv Civ Eng 2021. https://doi.org/10.1155/2021/8857491
15. Karunanidhis (2019) Investigation on spiral stirrups in reinforced concrete beams. Int J Nov Res Civ Struct Earth Sci 6(3):14–28. Accessed 03 Aug 2022. [Online]. www.noveltyjournals.com
16. Hamakareem MI (2021) How to design axially loaded circular RC columns as per ACI 318–19? | Example Included. The Constructor. Accessed 12 Feb 2023. https://theconstructor.org/structural-engg/design-axially-loaded-circular-columns/551968/
17. Bhople A (2021) Difference between tied column and spiral column | What is spiral column | What is tied column. Accessed 03 May 2022. https://civiljungle.com/tied-column-and-spiral-column/
18. Pathan H (2018) Effect of spiral reinforcement in beams and columns. Int Res J Eng Technol (IRJET) 05(01):264–267
19. Joshy V, Faisal KM (2017) Experimental study on the behaviour of spirally reinforced SCC beams. Int J Eng Res Gen Sci 5(3):96–105

20. Mas B, Cladera A, Ribas C (2016) Experimental study on concrete beams reinforced with pseudoelastic Ni-Ti continuous rectangular spiral reinforcement failing in shear. Eng Struct 127:759–768. https://doi.org/10.1016/J.ENGSTRUCT.2016.09.022
21. General Rules and Rules for Buildings. in Eurocode 2 (EC2–04), 2004th ed.
22. Greek Code for Concrete Structures (2000) Earthquake Planning and Protection Organisation. Athens.
23. Trusses-SteelConstruction.info. https://www.steelconstruction.info/Trusses. Accessed 21 Sep 2022.
24. Tesser L, Scotta R (2013) Flexural and shear capacity of composite steel truss and concrete beams with inferior precast concrete base. Eng Struct 49:135–145. https://doi.org/10.1016/J.ENGSTRUCT.2012.11.004
25. Yasser Y, Parung H, Tjaronge MW, Djamaluddin R (2013) Studi on the efficiency using nature materials in the structural elements of reinforced concrete beam-Neliti. In: 2nd International Conference on Engineering and Technology Development 2013.
26. Deshpande VS, Fleck NA (2001) Collapse of truss core sandwich beams in 3-point bending. Int J Solids Struct 38(36–37):6275–6305. https://doi.org/10.1016/S0020-7683(01)00103-2
27. Trentadue F, Mastromarino E, Quaranta G, Petrone F, Monti G, Marano GC (2014) Bending stiffness of truss-reinforced steel-concrete composite beams. Open J Civ Eng 04(03):285–300. https://doi.org/10.4236/OJCE.2014.43024
28. Hamkah H (2021) Improving flexural moment capacity of concrete beam by changing the reinforcement configuration. Int J Geomate 20(79):161–167. https://doi.org/10.21660/2021.79.j2042
29. Etman EE, Afefy HM, Baraghith AT, Abuelwafa M (2021) Shear behavior of RC beams reinforced with internal trussed steel strips at shear span zone. Structures 32:1734–1751. https://doi.org/10.1016/J.ISTRUC.2021.03.093
30. Djamaluddin R, Frans PL, Irmawati R (2017) Flexural capacity of the concrete beams reinforced by steel truss system. MATEC Web Conf 138:1–8. https://doi.org/10.1051/MATECCONF/201713802003
31. Djamaluddin R, Bachtiar Y, Irmawati R, Akkas AM, Latief RU (2014) Effect of the truss system to the flexural behavior of the external reinforced concrete beams. Int Sci Index 8(6): 938–942.
32. Colajanni P, la Mendola L, Mancini G, Recupero A, Spinella N (2014) Shear capacity in concrete beams reinforced by stirrups with two different inclinations. Eng Struct 81(1):444–453. https://doi.org/10.1016/j.engstruct.2014.10.011
33. Jagota V, Sethi APS, Kumar K (2013) Finite element method: an overview. Walailak J 10(1):1–8. https://doi.org/10.2004/wjst.v10i1.499
34. Campione G, Colajanni P, Monaco A (2016) Analytical evaluation of steel–concrete composite trussed beam shear capacity. Mater Struct /Materiaux et Constructions 49(8):3159–3176. https://doi.org/10.1617/S11527-015-0711-6
35. Chiriki SS, Sri Harsha G (2020) Finite element analysis of RC deep beams strengthened with I-section and truss reinforcement. Mater Today Proc 33: 156–161 https://doi.org/10.1016/J.MATPR.2020.03.579
36. M MB, Vedic N (2018) Shear capacity of RC beams with different patterns of spiral reinforcements. Int J Eng Res & Technol 6(6). https://doi.org/10.17577/IJERTCONV6IS06017
37. Dinesh D, A P (2017) Numerical study of hybrid steel trussed concrete beam. Int Res J Eng Technol (IRJET) 4(5).
38. Ballarini R, la Mendola L, Le J-L, Monaco A (2017) Computational study of failure of hybrid steel trussed concrete beams. J Struct Eng 143(8):04017060. https://doi.org/10.1061/(ASCE)ST.1943-541X.0001792
39. Kim S-W (2021) Prediction of shear strength of reinforced high-strength concrete beams using compatibility-aided truss model. Appl Sci 11(22):10585. https://doi.org/10.3390/app112210585

Mechanical Coupler as an Alternative Rebar Splicing: A Review

Jhun M. Jacinto, Felix Paul C. Rabago, Antonio D. Bolivar III, Ernie D. Tombado, and Orlean G. Dela Cruz

Abstract The world is searching for innovative technologies that can lessen the hardship of traditional work. Construction is one of the industries in search of new technology that can be used in every aspect of its operations, as well as cutting-edge technology for a wide range of construction materials. Using a mechanical coupler is one of the advancements in building materials. Utilizing mechanical couplers in construction is a creative and potentially industry-altering innovation. By generating a more robust and practical link between reinforcing bars, these devices could increase the safety and durability of construction projects. Furthermore, since there is a limited length of available reinforcing bars on the market, the mechanical coupler provides an alternative to the traditional splicing method. One of the study's goals is to determine the benefits and disadvantages of using this mechanical coupler in the building. In addition, this paper illustrates a discussion of the many applications and types of mechanical couplers.

J. M. Jacinto · F. P. C. Rabago
School of Engineering, Aurora State College of Technology, Brgy. Zabali, Baler, Aurora, Philippines
e-mail: jhun.jacinto05@gmail.com

F. P. C. Rabago
e-mail: felixpaul.fpr@gmail.com

A. D. Bolivar III
School of Industrial Technology, Aurora State College of Technology, Brgy. Zabali, Baler, Aurora, Philippines
e-mail: bolivarantonio101@gmail.com

E. D. Tombado
Laguna Lake Development Authority, National Ecology Center, East Ave. Diliman Quezon City, Metro Manila, Philippines
e-mail: dtombado.ernie@gmail.com

E. D. Tombado · O. G. Dela Cruz (✉)
Graduate School, Polytechnic University of the Philippines, Sta. Mesa Manila, 1016 Metro Manila, Philippines
e-mail: ogdelacruz@pup.edu.ph

H.-Y. Jeon (ed.), *Proceedings of the International Conference on Geosynthetics and Environmental Engineering*, Lecture Notes in Civil Engineering 374,
https://doi.org/10.1007/978-981-99-4229-9_10

Keywords Mechanical coupler · Innovative material · Construction · Lap splicing · Rebar splicing

1 Introduction

The world is continuing to expand and progress. It accompanies the technological advancement of different everyday materials. The challenge of water supply shortage has been addressed, as well as the shortage of food. The use of innovative materials and modern technology in construction is in high demand due to the world's increasing population and limited resources. Whenever load path continuity is essential in prominent members such as beams, slabs, and columns, lap splicing has become the standard way of connecting two steel reinforcing bars [1]. Due to bar length constraints, splicing of reinforcing bars is unavoidable in reinforced concrete (RC) structures [2]. Within standards, codes of practice, and regulations that set parameters for the dimensioning of structural elements in reinforced concrete, the steel bar splicing zone is always given particular attention [3]. Lap splicing is a conventional method of transferring load, tension, moment, and shear stresses between steel reinforcing bars used in concrete structures [4]. Lap splices are ineffective for longer spans, are not regarded as reliable under cyclic pressure, and have a lot of hidden expenses [1]. Rebar congestion at the lap zone is increased by lap splicing. It is one of the most common reasons for forming rock pockets and voids in concrete. There are a few other hidden costs associated with providing lap splices: the time spent preparing lap splices, the necessity for additional transverse reinforcement, the tools used in forming the lap splice, and the cost of rebar replacement [4]. Due to this reason, the contractor and engineers turn to use mechanical couplers to address the apparent issues of bar length limitations. The steel bar splicing zone is always given special consideration in guidelines, codes of practice, and standards that set parameters for dimensioning structural elements in reinforced concrete [5]. Due to the mechanical joint, spliced rebar operates like continuous reinforcement as opposed to lapping, which is dependent on the concrete; this prevents mistakes brought on by providing the incorrect lap length, decreasing the grade of the concrete, problems with compaction or segregation, deterioration of the concrete over time, or due to an immediate impact that reduces the strength of the lap joint [6]. Couplers, particularly threaded ones, can simplify the design, constructing with reinforced concrete and utilizing less reinforcement required [5].

The design and arrangement of anchorages and splices in any reinforced concrete structural design require a unique combination of art and science. Well-designed splices are an essential component of every well-executed strategy. In terms of design and implementation, the usage of laps might be time-consuming because of the higher number of rebar used; the installation can generate more congestion within the concrete [5]. When seismic detailing requirements combine with the issue of reinforcement congestion, mechanical reinforcement couplers can provide significant constructional and financial advantages over traditional techniques of lap splicing

[7]. Mechanical couplers, an alternative to lapping rebars, are cylindrical elements that link the two revolving edges of reinforcing bars. The coupler's grade should be the same as the reinforcing bars to ensure maximum load stress distribution from one bar to the next.

2 Methodology

The section of this research study focuses on the outline of journal results obtained from a website such as Scopus and Google Scholar on the relevance of the research topic. Figure 1 shows the systematic procedure for finding and choosing the relevant articles and journals needed in this review. Google Scholar and Scopus support Boolean syntax, a search strategy that enables users to integrate keywords using operators such as "and," "not," and "or" to generate more precise findings from research papers and publications [8]. It tracks citation data for other journals and provides access to the system's databases for its journal impact measures (SNIP and SJR) [9]. The Boolean Syntax keywords used to find a theme or journal are mechanical couplers and the design of mechanical couplers. These keywords help supply different papers and journals related to the researcher's topic of interest. The main goal of this literature review is to figure out and tell the researcher's questions which are summarized as follows:

RQ 1: What are the advantages and disadvantages of using a mechanical coupler for building structures?

RQ 2: What quality testing is required to ensure a mechanical coupler is a reliable alternative to conventional lap splicing?

RQ 3: What are the different types and usages of mechanical couplers? (Fig. 1)

3 Discussion

3.1 Advantages and Disadvantages of Using Mechanical Coupler

Mechanical Rebar connections are increasingly being specified instead of lap splices by engineers. Mechanical connections, they have discovered, provide a level of uniformity and reliability that lap splicing cannot match. The design process assumes that a mechanical splice between two reinforcing bars will not reduce the spliced bar's structural strength, stiffness, or ductility. Guidelines, codes of practice, and norms that set requirements for dimensioning structural elements in reinforced concrete always pay special attention to the steel bar splicing zone. These splices must be done in a way that does not conflict with the structural element's original intended

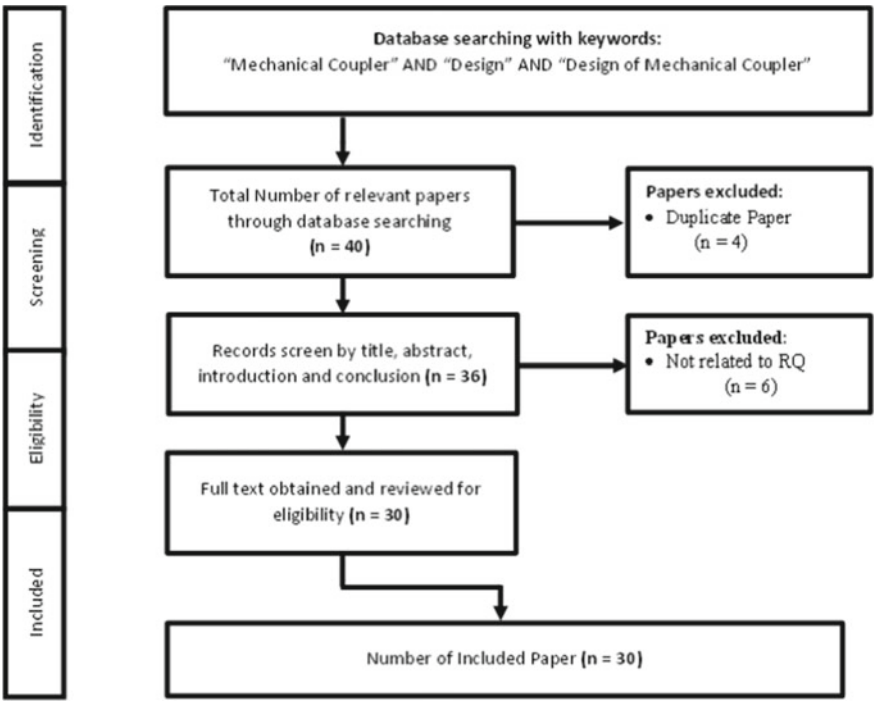

Fig. 1 Systematic related literature selecting process

behavior in the region where they are present [3]. Table 1 shows the different advantages and disadvantages of using a mechanical coupler. With tabulated benefits and drawbacks, most engineers now use this innovation in the construction industry.

3.2 Mechanical Testing Requirement

Because there are no national standards regulating coupler behavior, we relied on other international standards such as AC133, ISO 15835:2009, and IS 16172:2014, as well as published consultant requirements. In addition, couplers should be made of a material that meets the minimum strength requirement (125 percent of the rebar yield strength) [1]. Couplers are typically mild steel; however, other metal alloys can be utilized in specific instances.

Table 1 Common advantages and disadvantages of the mechanical coupler

Reference	Advantages	Disadvantages
Jain et al. [1–3, 5–7, 10–16]	– It is a practical and economical alternative to lap bars	– There is a possibility of misalignment in the connection of two shafts which can cause excessive force on the coupling, shaft, and bearing that may cause them to fail prematurely
	– Reduce the dependency on the concrete for load transfer	– Availability of couplers in the local market for above 32 mm diameter
	– Easy to install and assemble; no torque wrench is required	– It may create structural damage if the coupler grade is not equivalent to the reinforcing bars
	– Shorten construction schedule and offers greater structural integrity	– Skilled personnel are required in the assembling process
	– It eliminates the reinforcement congestion and thus reduces the material cost by eliminating the length of laps	
	– Larger diameter rebar in a smaller column while minimizing congestion	

3.2.1 Strength Test

The ACI 318–2008 code is the most referenced code for mechanical couplers. It is a performance-based code that divides splicing into two categories: Type 1 and Type 2. A Type 1 joint must reach a minimum of 1.25Fy, while a Type 2 joint must meet both the 1.25Fy criterion and the rebar's stipulated tensile strength [6]. Table 2 summarizes the test result conducted for the mechanical coupler strength test.

3.2.2 Sip Test

The average slip must be 0.25 mm for bars with 25 mm diameter and more minor and 0.75 mm above 25 mm diameter bars. In addition, the reference points must be established with a distance of 10 and 40 mm from the coupler to connecting bars [17]. To ensure that the protocol used was reliable, the methodology laid out in ISO 15835:2009 was used, and took the slip reading at the end of the third cycle of 0.6fy. Table 3 shows the summary of the test results.

Table 2 Control bar test [18]

Bar dia (mm)	Yield range to comply with ASTM a706 (MPa)	Actual yield from the test (MPa)	Min ultimate tensile strength to comply with ASTM a706 (MPa)	Actual max stress from test (MPa)	Min elongation to comply with ASTM a706 (%)	Definite elongation (%)	Pass or fail
25	420–550	460	550	611	12	22.5	PASS
28	420–550	469	550	620	12	19.8	PASS
32	420–550	439	550	639	12	9.4[a]	PASS
36	420–550	466	550	642	12	11.4[a]	PASS

[a] These bars ruptured the gauge length, so the ductile necking phase was not recorded, only the elongation at maximum load (Agt). The actual extension was much higher and most likely complied with the requirements of ASTM a716

Table 3 Slip test requirement [18]

Bar Dia (mm)	Test Number	Max allowable slip	Actual slip after three cycles	PASS/FAIL
25	1	0.2	0.047	PASS
	2	0.2	0.05	PASS
28	1	0.2	0.2	PASS
	2	0.2	0.017	PASS
32	1	0.2	0.197	PASS
	2	0.2	0.019	PASS
36	1	0.2	0.057	PASS
	2	0.2	0.083	PASS

3.2.3 Cyclic Fatigue Test

The reverse cyclic elastic test of 100,000 load cycles with a stress range of −173 to + 173 MPa determines fatigue suitability. To accommodate available test equipment, the maximum frequency may vary depending on ASTM E466, "Standard Practice for Conducting Force Controlled Constant Amplitude Axial Fatigue Tests of Metallic Materials," or ASTM E606M, "Standard Test Method for Strain-Controlled Fatigue Testing". [17]

In the study conducted by Pochara Kruavit, Anat Ruangrassamee, and Qudeer Hussain, Experimental and Analytical Study on Reinforcing Steels with Threaded Mechanical Couplers under Monotonic and Cyclic Loadings [19]. The cyclic loading test was carried out according to the loading scheme shown in Fig. 2 and 3 after test specimens failed because of low-cycle fatigue fracture. Figure 2 depicts the hysteretic loops for each model. The buckling of reinforcing bars causes the compression strength to be decreased. In addition, explicit pinching behavior occurred during

the transition from tension to compression. For bars with a larger L/D, the hysteretic loop is smaller.

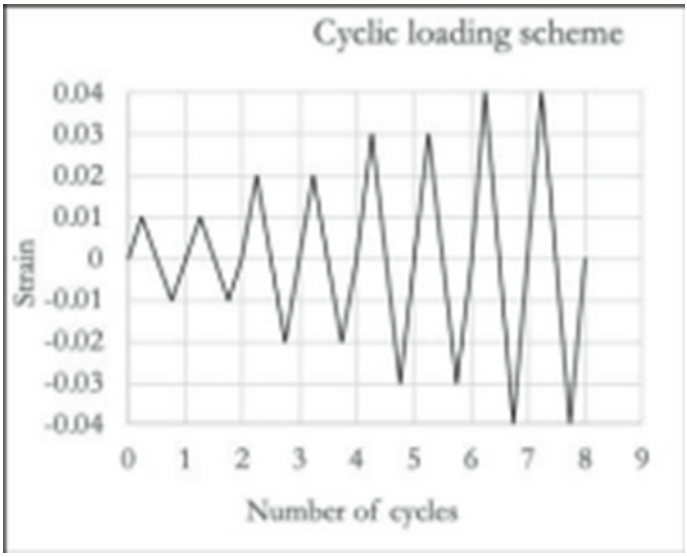

Fig. 2 Cyclic loading scheme

Fig. 3 Fracture failure

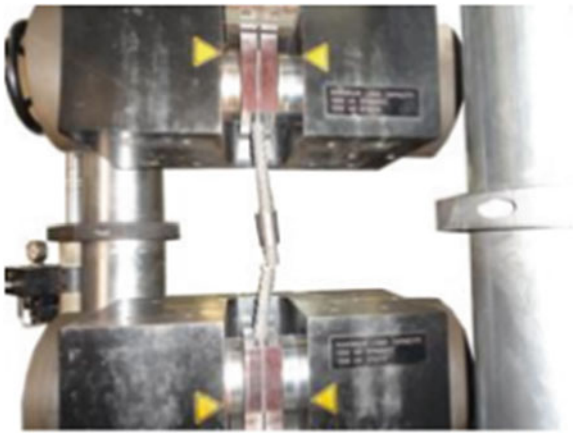

Table 4 Summary of types and usage of the mechanical coupler

Item no	Type of mechanical coupler	Usage	References
1	Shear screw couplers	To shear off at a specified torque	Himanshu [6, 10]
2	Headed bar couplers	Alternative to hooks and long development length	Himanshu [6, 10]
3	Grouted sleeve couplers	Precast connection	Himanshu [6, 11–13]
4	Threaded couplers	Connect two threaded bars	Jain [1, 6, 10, 12, 14–18]
5	Swaged couplers	Produce mechanical interlock	dela Cruz [10, 12]
6	Taper threaded couplers	To account for the defects in rebar	dela Cruz [10, 12, 16, 18–20]

3.3 Mechanical Coupler Types and Usage

When working with smaller diameter reinforcing bars, more significant column dimensions may be required to accommodate more bars. Therefore, structural engineers can use larger diameter rebars in the smaller column while limiting congestion using mechanical splices. In concrete construction, mechanical splices connect reinforcing bars by establishing a mechanical connection between two pieces of reinforcing steel. Mechanical splices are divided into three categories: tension–compression, compression-only, and tension-only. The mechanical splicing attaches various and secures the joined rebar ends in an in-line connection that satisfies the splice specifications. There are several types of mechanical couplers available on the market. However, only a specific mechanical coupler can be used as an alternative to lap splicing. Table 4 shows the summary of recent research and study regarding the types and usage of mechanical couplers.

3.4 Mechanical Coupler for Splicing Precast Member

Precast concrete's adaptability allows for practically any shape element, including curved and radial portions, and freedom in connecting points and load routes. Compared to other structural systems, prestressed concrete structural elements provide great load-carrying capacity, allowing for smaller sections, longer spans, or both. Using precast members provides for a rapid, long-lasting, and labor-saving construction approach [20]. The connection of the structural system, the linkages, and the individual components all play a role in the design of precast, prestressed concrete structures. Each element must consider the others and the practical limitations of the building's intended purpose. Mechanical reinforcement couplers (MRCs) are one of the critical options for strengthening the strength and energy absorption

in the precast connection zone [14]. Prefabricated elements are frequently united by splicing or coupling steel reinforcement. Mechanical splicers/couplers can join prefabricated elements [20]. Because of its distinct advantages, such as lowering construction time, cutting costs, reducing energy consumption, and boosting the quality of the members due to higher quality control, precast concrete (PC) structures outperform traditional concrete buildings [16]. By applying different approaches categories: (a) shear screw couplers, (b) headed bar couplers, (c) grouted sleeve couplers, (d) threaded couplers, and (e) swaged couplers. The most effective used method of splicing precast members is the grouted sleeve. Different grouting defects, insufficient grout strength, the bonding strength between the steel bar and grout, the bonding strength between the grout and the inner surface of the sleeve of the steel pipe or coupler, embedded length of steel bar inside the sleeve, and the alignment of a bar in a splice connector in-line or adjacent leading to the offset of the steel bar are all factors that can affect the performance of the grouted sleeve [16].

3.5 Mechanical Coupler for Reinforcement

Steel reinforcement has been extensively utilized in constructing concrete structures to transfer tension and shear pressures [5]. If needed to reinforce a structure, lap splicing has become the conventional way of connecting two steel reinforcing bars to provide load path continuity; prominent elements such as beams, slabs, and columns are used [1]. Couplers, precisely threaded ones, could make the design process more accessible and reduce the reinforcement needed in reinforced-concrete construction; the coupler system is designed to rapidly and easily join two pieces of rebar in the field [5]. Mechanical splices like threaded couplers can be particularly effective since they simplify design parameters, are simple to install, and lower the required reinforcement, resulting in maximum cost savings [1]. The design assumes that a mechanical splice between two reinforcing bars will not reduce the spliced bar's structural strength, stiffness, or ductility [3]. Increasing the embedding bar length will improve the couplers' ultimate tensile load capacity [16]. It can be determined that using a tube coupler to attach rebars in compression members, such as columns, is more successful than lap splicing in carrying greater axial loads [21]. In the construction industry, couplers have recently been utilized to ensure compliance with structural strength and ductility criteria; it is required to keep proper checks on this product [6].

4 Research Gap

Reinforced Concrete (RC) structures, such as buildings and infrastructure, consume a lot of concrete and rebar during construction. Steel bars are deformed bars, plain bars, wire, and steel products, all of which help concrete carry more tensile and

Table 5 Challenges and limitations of the study

Challenges and limitations	References
Lack of reliable information on their inelastic performance	Dahal and Tazarv [2, 3, 7, 13, 15]
Testing standards currently do not specify any requirements to explore the post-yield cyclic behavior of couplers	Chiari [3, 6, 11, 16]
The behavior of couplers is mainly unknown in the plastic hinge region of RC ductile members in the high seismic zone	Dahal and Tazarv [2, 11, 14]

compressive stress. The steel reinforcing is also critical in concrete construction crack control [10] (Table 5).

As previously stated, couplers gained appeal in the building industry after the sharp increase in steel reinforcing prices. On the other hand, the mechanical splice consists of the coupler and the spliced rebar to establish the connection. The performance of the coupler is affected by several factors: (1) rebar grade, (2) ductility of the rebar, (3) size and shape of the rebar, and (4) under-sizing of the rebar for threading or rib size. Therefore, another consideration is to have a group of competent personnel uses these threading machines to ensure that the joints are prepared within the permitted tolerances, as well as a group of fitters familiar with splice installation on the project [6].

5 Conclusion

It has been observed that limited resources and studies support the mechanical coupler's capacity and structural integrity. This literature review reveals many advantages and disadvantages to using the mechanical coupler as an alternative for lap splicing. A comprehensive study should provide a national code and precise method and approach to designing the mechanical coupler concerning its location, strength, and behavior. Furthermore, detailed research on how well the mechanical coupler will react to different loading and forces when applied to the structure—an innovative and comprehensive approach in load application testing. Moreover, combining other structural materials with the mechanical coupler enhances its capability.

References

1. Jain SB, Naik N, Andelimath M, Hosagoudar VS, MH G 5 Student (2017) Use of mechanical threaded coupler in steel reinforcement. [Online] http://ijesc.org/
2. Dahal PK, Tazarv M (2020) Mechanical bar splices for incorporation in plastic hinge regions of RC members. Constr Build Mater 258. https://doi.org/10.1016/j.conbuildmat.2020.120308
3. Chiari VG, Junior ALM (2018) Experimental evaluation of coupler behavior for mechanical rebar splices in reinforced concrete structures. Revista IBRACON de Estruturas e Materiais 11(6): 1326–1353. https://doi.org/10.1590/s1983-41952018000600009

4. Hasan A, Maharaj SI, Kibria MG, Hasan FMM (2017) Performance evaluation of MS tube coupler on axial load capacity of column. Int J Recent Technol Eng (IJRTE) 6(4).
5. Himanshu SK Reinforcement couplers as an alternative to lap splices: a case study. [Online]. www.ijert.org
6. Mechanical Splicing Couplers for Reinforcement. [Online]. www.masterbuilder.co.in
7. Bompa DV, Elghazouli AY (2017) Ductility considerations for mechanical reinforcement couplers. Structures 12:115–119. https://doi.org/10.1016/j.istruc.2017.08.007
8. dela Cruz OG, Ongpeng JMC (2022) Building information modeling on construction safety: a literature review. pp 89–102. https://doi.org/10.1007/978-3-031-11232-4_8.
9. Lasda Bergman EM (2012) Finding citations to social work literature: the relative benefits of using web of science, scopus, or google scholar. J Acad Libr 38(6). https://doi.org/10.1016/j.acalib.2012.08.002
10. Raju G, Selvi MK An experimental investigation on splicing of reinforcement in reinforced concrete beam by car coupler.
11. Shokrzadeh MR, Nateghi-Alahi F Behavior considerations for mechanical rebar couplers. [Online]. https://www.researchgate.net/publication/349772249
12. Kwon K, Kim D, Kim S (2021) Cutting waste minimization of rebar for sustainable structural work: a systematic literature review. Sustainability (Switzerland) 13(11). MDPI AG. https://doi.org/10.3390/su13115929.
13. Bompa DV, Elghazouli AY Ductility of reinforced concrete members incorporating mechanical splices.
14. Mobedi E, Parastesh H, Khaloo A (2020) AUT journal of civil engineering effects of mechanical coupler on cyclic behavior of wet connection in precast concrete frame. Civil Eng 4(1):3–16. https://doi.org/10.22060/ajce.2019.15680.5547
15. Phares B, Lee YS, Hosteng TK, Nelson J (2021) Investigation of grouted coupler connection details for accelerated bridge construction. Transp Res Rec 2675(8). SAGE Publications Ltd, pp. 562–569. https://doi.org/10.1177/0361198121999393.
16. Ghayeb HH, Razak HA, Sulong NHR, Mo KH, Abutaha F, Gordan M (2021) Performance of mechanical steel bar splices using grouted couplers under uniaxial tension. J Build Eng 34. https://doi.org/10.1016/j.jobe.2020.101892
17. Republic of the Philippines department of public works and highways office of the secretary subject: DPWH standard specification for item 737-mechanical couplers for reinforcing steel.
18. Genenral product Brochure testing of barbreak RT coupler systems.
19. Kruavit P, Ruangrassamee A, Hussain Q (2020) Experimental and analytical study on reinforcing steels with threaded mechanical couplers under monotonic and cyclic loadings. Eng J 24(3):61–70. https://doi.org/10.4186/ej.2020.24.3.61
20. Khedmatgozar Dolati SS (2021) Review of mechanical bar couplers for splicing precast concrete members. Sci J Res & Rev 3(1). https://doi.org/10.33552/sjrr.2021.03.000551
21. Ameri F, Shoaei P, Reza Musaeei H, Alireza Zareei S, Cheah CB (2020) Partial replacement of copper slag with treated crumb rubber aggregates in alkali-activated slag mortar. Constr Build Mater 256. https://doi.org/10.1016/j.conbuildmat.2020.119468

Behavior of Two-Tiered Mechanically Stabilized Earth Retaining Wall with Bamboo Reinforcement Under Isolated Footing Load

Jlxeondyke Drie L. Ifurung, Matthew Travis M. Alcantara, and Giancarlo P. Ventura

Abstract A numerical analysis was conducted to determine the behavior of a two-tiered MSE wall subjected to an isolated footing load with varying tier offset distances and reinforcement types. A displacement-based footing load was performed to evaluate the wall's response at the serviceability limit state of the varied design parameters. Moreover, the viability of bamboo reinforcements was determined by comparing how they performed at the allowable and ultimate settlement of the footing against commercially available reinforcements. In terms of serviceability, the bamboo reinforcements were at par with the chosen commercially available reinforcements since none of the bamboo reinforcements yielded from the 1 inch (25 mm) allowable settlement of the footing proving that it can be used as a support for resisting vertical loads from a footing in a two-tier MSE wall. The results suggested that bamboo reinforcements exhibit brittle behavior due to their high tensile modulus but still displayed sufficient performance with regards to allowable settlement and footing settlement before initial reinforcement yielding. Increasing offset distance reduced the reinforcement loads in the lower tier by 12% from no offset to 1.2 m.

Keywords Two-tier MSE wall · Isolated footing · Failure mechanism · Bamboo reinforcement · Tier offset distance

1 Introduction

MSE walls are widely used due to their advantages under static and dynamic loading, cost-effectiveness, ease of construction, and aesthetics. These are built with soil reinforcements which increase the load-bearing capacity and overall stability of

J. D. L. Ifurung · M. T. M. Alcantara (✉) · G. P. Ventura
Institute of Civil Engineering, University of the Philippines Diliman, Quezon City, Philippines
e-mail: mmalcantara@up.edu.ph

H.-Y. Jeon (ed.), *Proceedings of the International Conference on Geosynthetics and Environmental Engineering*, Lecture Notes in Civil Engineering 374,
https://doi.org/10.1007/978-981-99-4229-9_11

the retaining structure [1]. It is also able to sustain large horizontal and vertical displacements.

Increasing the wall height increases the tensile stresses experienced by the lower layers of reinforcements which requires decreasing the spacing between reinforcements to reduce tensile stresses at the bottom of the wall [2]. Consequently, this raises the cost of construction due to the necessity for more reinforcements. Tiering of walls addresses this issue as it can alleviate the tensile stresses on lower reinforcements.

Unlike conventional geosynthetic reinforced soil retaining walls which are typically used for earth retention, geosynthetic reinforced soil retaining walls for bridge abutments or any other applied loading from an overlaying structure are subjected to higher surcharge loads. Thus, the allowable bearing pressure and resulting deformations are crucial considerations for design [3]. Producing a proper design for support of footings on walls, such as bridge abutment design, provides a cheaper alternative compared to conventional pile-supported design and is able to reduce differential settlements between bridge and approach embankments [4].

A study by Xiao et al. [5] analyzed the relationship between different wall design parameters, including footing width and location. It was observed that a transition in the failure mechanism and the lateral deformation was greatly influenced by the offset distance of the footing.

Bamboo is an abundant plant in the Philippines, which is easily accessible and versatile with numerous possible applications. It is a traditional source of construction materials, wherein five bamboo species in the Philippines have been documented for empirical use in construction [6]. Recently, sustainable and natural materials such as bamboo drew the attention of soil engineers since it is deemed to be very effective as a reinforcement because of its mechanical and engineering properties [7]. Ahirwar and Mandal [8] were also able to prove that bamboo-reinforced soil significantly improved the bearing capacity and reduced the settlement of soil with improvement in the bamboo reinforcement with changes in aperture shape, placement depth, and width of reinforcement. Due to its easy workability, it is simple for bamboo to be modified for a specific purpose such as soil reinforcements weaved as grids, meshes, and mats.

MSE walls have numerous parameters for consideration in design which consequently raises uncertainties in the relationship of these parameters. In addition, the behavior and failure mechanisms are heavily dependent on footing and MSE wall parameters. Current two-tier design guidelines are also considered to be conservative and overestimate surcharge load-induced strains [9–12]. MSE walls are generally used as soil retaining structures, but the performance of the wall is of concern when used as a structure to resist loading from vertical loads with great surcharge.

The performance of bamboo reinforcements is generally analyzed in small-scale laboratory tests [7, 8, 13]. Studies with MSE walls using bamboo reinforcements are scarce and bamboo may have different responses and performance when installed in this type of structure and when subjected to high surcharge loading. Lastly, the utilization of eco-friendly materials such as bamboo for an alternative reinforcement will greatly benefit the economic factors and environmental impact in design considerations.

The general objective of this paper is to numerically analyze the behavior and associated failure mechanisms of a two-tiered bamboo reinforced MSE wall subjected to a surcharge load from an isolated footing. This paper aims to (1) develop a 2D model following the Mohr–Coulomb soil constitutive model that captures the behavior of an MSE wall subjected to surcharge loading from an isolated footing load; (2) determine the suitability of bamboo reinforcements as a viable alternative by the comparison of reinforcement loads and failure mechanisms at allowable and ultimate settlement with commercially available reinforcements; and (3) conduct a parametric study to analyze the effects of the variation of upper tier offset distance with regards to its serviceability limits.

2 Methodology

The numerical simulation of the behavior of the two-tiered MSE wall was performed using the program RS2 by Rocscience. Prior to carrying out the simulation, a model verification phase was performed using RS2 by attempting to replicate the results of Damians et al. [16] in terms of the behavior of a reinforced wall which used PLAXIS. This allows a layer of model validation in the absence of a physical model or an in situ MSE wall. The verification phase resulted in a general agreement in the results in terms of facing displacements and reinforcement loads. The results of which are omitted in this paper.

The parametric study was performed using the test cases shown in Table 1. The parameters that were varied for this study were the reinforcement type and the tier offset distance. The offset distance was measured from the front of the lower tier wall facing until the front of the upper tier wall facing. The tier offset distances were based on the study by Bhattacharjee and Amin [2] while following AASHTO's guidelines of tiered MSE walls such that the cases suppose that the tiers are not independent of each other. The reinforcements were collected from commercial brands of geogrids.

Table 1 Test cases for the study

Parameter	Case			
	1	2	3	4
Reinforcement type	Bamboo	ACEgrid GG 40-I	Maccaferri paragrid 30/5	Tencate miragrid GX 110/30
Offset distance (m)	0	1.2	2.0	3.0

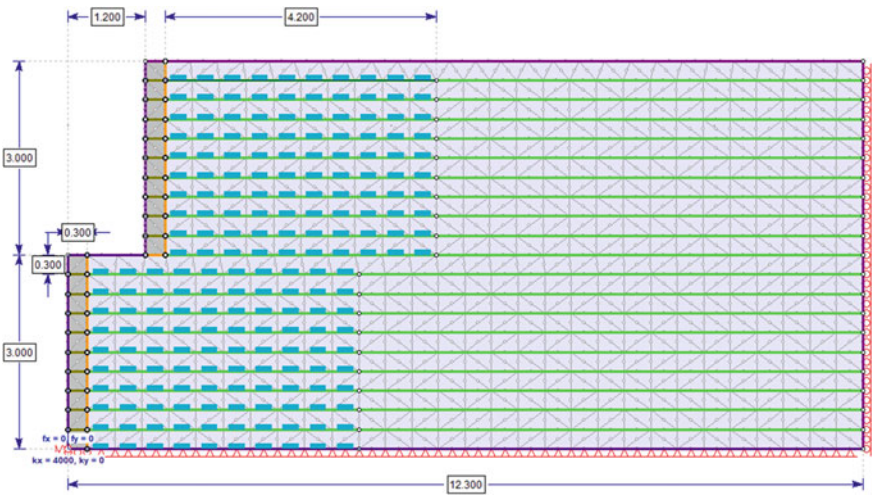

Fig. 1 Base model

2.1 Wall Geometry and Construction

The base model is a 6 m high MSE wall with 3.0 m high tiers as shown in Fig. 1. It was constructed with 45 stages of bottom-up construction for the trials with a footing displacement of 1-inch. The first 20 stages were for the wall construction with an 8 kPa compaction load while the remaining 25 stages were for surcharge loading. Additional stages were included for surcharge loading for the model to fail depending on the maximum allowable footing load displacement until the reinforcements yield and show a clear failure surface. A total of 19 reinforcements layers at length of 4.2 m each, vertically spaced at 0.3 m, with 9 reinforcements in the lower tier and 10 reinforcements in the upper tier were installed.

2.2 Footing Geometry and Load Application

The surcharge load application was applied as displacement controlled with uniform settlement along the bottom of the footing. Its width was 1.5 m and was located 1.65 m from the facing of the upper tier.

A set displacement of 1-inch was programmed for the footing and was chosen as Terzaghi [14] mentioned that settlements of shallow footings are generally limited to 25 mm only. Therefore, the service state of these models is being tested and analyzed. For the test on the reinforcement types which aim to reach failure, additional stages were added with 10 mm footing displacement per stage to find the displacement of the footing that caused reinforcement yielding and formation of the failure surface.

Table 2 Reinforcement strength parameters

Type	Tensile modulus (kN/m)	Ultimate tensile strength (kN/m)
Bamboo grid	865	28
ACEGrid GG 40-I	444.44	40
Maccaferri paragrid 30/5	333.33	30
TenCate miragrid 110/30	1049.52	110.2

2.3 Material Properties

The bamboo reinforcement properties were taken from a study by Ahirwar and Mandal [8]. Bamboo strips were collected from Dadar, Mumbai which were then interwoven together to form reinforcements with an orthogonal and hexagonal aperture. On the other hand, the geosynthetics used in this paper were collected from the library of RS2. The summary of the material properties of the reinforcements is shown in Table 2.

The soil backfill was clean washed sand with $D_{50} = 0.34$ mm, coefficient of curvature $C_c = 2.25$, and coefficient of uniformity $C_u = 1.09$. The constitutive model used was the linear elastic-perfectly plastic Mohr–Coulomb model.

The wall facing was constructed using commercially available solid masonry concrete blocks. The properties were obtained from a study by Damians et al. [16].

Huang et al. [17] provided interface properties for soil-block, block-block, and backfill-reinforcement as summarized in Table 3. The reinforcement backfill interface possessed a high value of adhesive strength to prevent slipping. In this study, the reinforcement-soil interface was assumed to be perfectly bonded, and no slip would occur.

3 Results and Discussion

3.1 Reinforcement Types at Allowable Settlement

On the loading of 1 inch footing settlement, bamboo reinforcements were observed to have the second least maximum facing displacement which was due to the high tensile modulus of the bamboo reinforcements. A higher tensile modulus requires more force for the material to deform since it is less flexible compared to those with a lower tensile modulus. Additionally, walls with bamboo reinforcement did not exceed the FHWA limit for facing displacement equal to 50 mm. The facing displacements are shown in Fig. 2.

No yielding of reinforcements occurred for the allowable settlement of the footing. Moreover, no clear failure surface was defined in this loading case. From a serviceability standpoint, bamboo reinforcements are suitable to be used as a support in an

Table 3 Wall material properties

Material	Parameter	Value
Soil backfill	Unit weight (kN/m^2)	16.8
	Young's modulus (MPa)	40
	Poisson's ratio	0.3
	Friction angle (°)	44
	Dilatancy angle (°)	11
	Cohesion (kPa)	0.2
Block facing	Young's modulus (MPa)	23,000
	Poisson's ratio	0.15
	Unit weight (kN/m^3)	22
Soil-block interface properties	Friction angle (°)	44
	Cohesion (kPa)	0
	Normal stiffness (MPa/m)	100
	Shear stiffness (MPa/m)	1

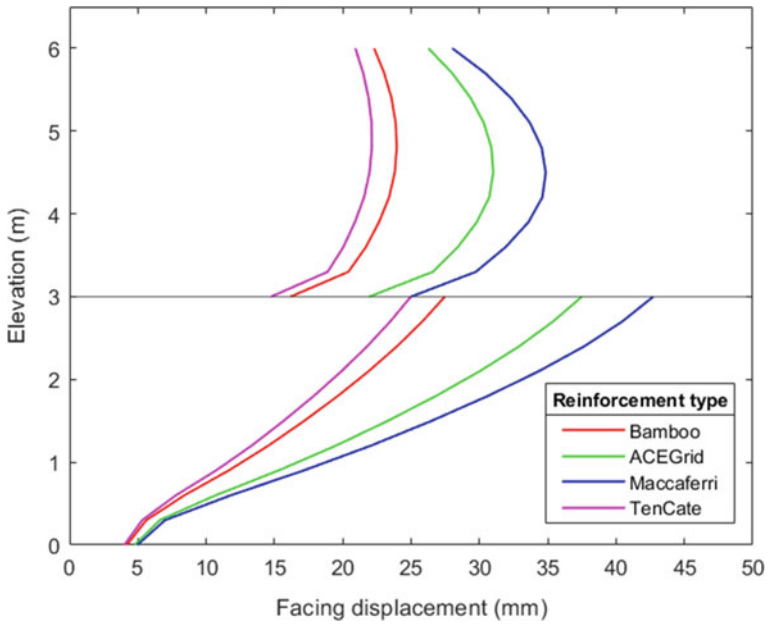

Fig. 2 Facing displacements for each reinforcement type

Table 4 Maximum reinforcement load at allowable load

Reinforcement type	Max reinforcement load (kN)	% of ultimate tensile load (%)
Bamboo	6.77	24
ACEGrid	5.10	13
Maccaferri	4.61	15
TenCate	7.54	7

MSE wall to resist vertical loading from an isolated footing using only a fraction of the tensile strength in carrying the required reinforcement load as shown in Table 4.

3.2 Reinforcement Types at Failure

The ultimate settlement of the footing was tested to analyze the performance of the bamboo reinforcements as the MSE wall approached yielding. In this case, failure is identified by yielding of any portion of the wall reinforcements.

Figure 3 shows the maximum shear strain contour plots during the first stage of reinforcement yielding. The red portion on the reinforcement denotes the reinforcement elements that yielded. The footing settlements when the first set of reinforcements yielded are given in Table 5. Hence, bamboo reinforcements started to yield at the lowest reported footing displacements from the other 3 reinforcements. For all cases, the yielded reinforcements would first appear at the farther edge of the footing.

The top layers of the reinforcement always yielded first as they carry the most reinforcement loads. Reinforcements with higher tensile modulus (i.e. bamboo and TenCate) tended to yield multiple layers simultaneously. The yielded reinforcements of these types already reached the lower tier. On the other hand, reinforcements with

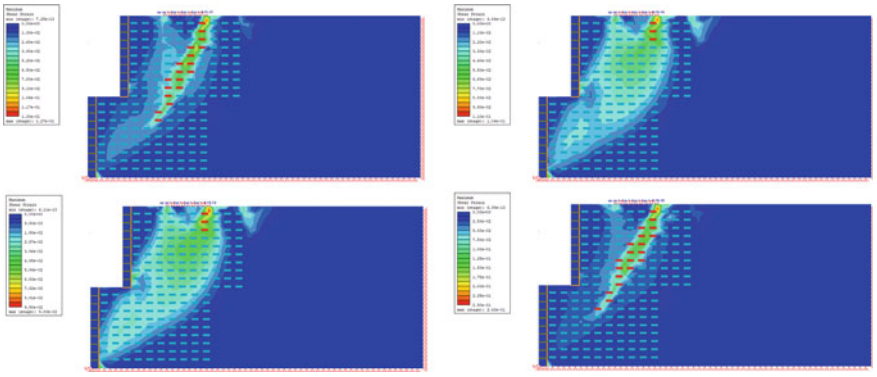

Fig. 3 Maximum shear strain contour plots at failure

Table 5 Footing settlement at yield

Reinforcement type	Footing settlement at first yield (mm)	Ultimate footing settlement
Bamboo	110	130
ACEGrid	140	200
Maccaferri	130	200
TenCate	190	210

lower tensile modulus (i.e. ACEGrid and Maccaferri) only had yielded reinforcements at the top 3 layers of the wall. The strains were already concentrated where the reinforcements failed for bamboo and TenCate while the strains for ACEGrid and Maccaferri were still distributed throughout the wall.

Further increase in the footing load was performed to see higher strains to reach wall failure. All the failure shapes that developed for all the reinforcement types resulted in a log-spiral failure. The properties of the reinforcements, specifically the tensile modulus and ultimate tensile strength, did not seem to affect what failure shape developed. Bamboo reinforcements yielded at the lowest reported footing displacement and reached the ultimate settlement at the lowest reported footing displacement compared to the commercially available reinforcements. The difference between ultimate settlement to allowable settlement for bamboo, TenCate, ACEGrid, and Maccaferri reinforcements are 105 mm, 185 mm, 175 mm, and 175 mm, respectively. Bamboo reinforcements exhibit the lowest gap between the allowable and the ultimate footing displacement.

The step by step loading also showed brittle failure in reinforcements with higher tensile moduli. Reinforcements with lower tensile modulus had about 1.5 times greater plastic strength allowance compared to reinforcements with lower tensile modulus.

3.3 Offset Distance at Allowable Settlement

The variation of offset distance and the resulting facing displacements are shown in Fig. 4. It is noticeable that tiering reduces the facing displacement of an MSE wall. Additionally, all offset distances were acceptable since all the resulting displacements conformed to the FHWA standards which required the maximum allowable facing displacement to be less than or equal to 50 mm.

A decrease in the maximum upper tier facing displacement occurred until the 2.0 m offset distance since an increase was noticed for the 3.0 m offset. The following are the percentage difference in the displacement between the offset distances, 32% decrease from no offset to 1.2 m, 3% decrease from 1.2 to 2.0 m, and 1% increase from 2.0 to 3.0 m. After the 1.2 m offset, the displacements of the upper tier of the walls with offset distances started to behave similarly to a wall with no offset. This was observed in the trend of the graphs and where the maximum displacement occurred. The 1.2 m

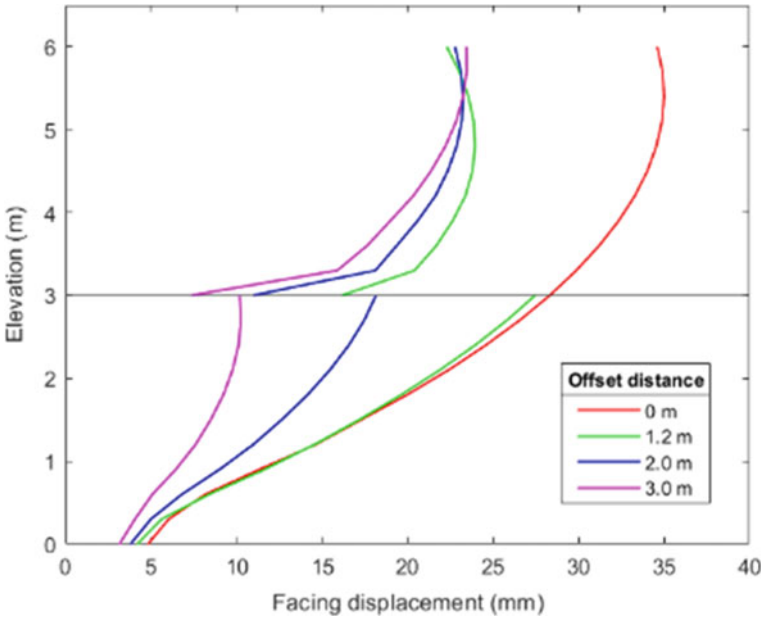

Fig. 4 Facing displacement at different offset distances

offset would have its upper tier maximum displacement occurring approximately in the middle of the facing while the 2.0 and 3.0 m offset occurred at higher elevations of the wall, similar to the wall with no offset.

A continuous flow of strain from the footing until the toe of the lower reinforcement was observed for the model with no offset and 1.2 m offset (Fig. 5). On the other hand, the strain was discontinuous from the upper tier to the lower tier for the 2.0 m offset and 3.0 m offset. The strain flow for the greater offset distances is

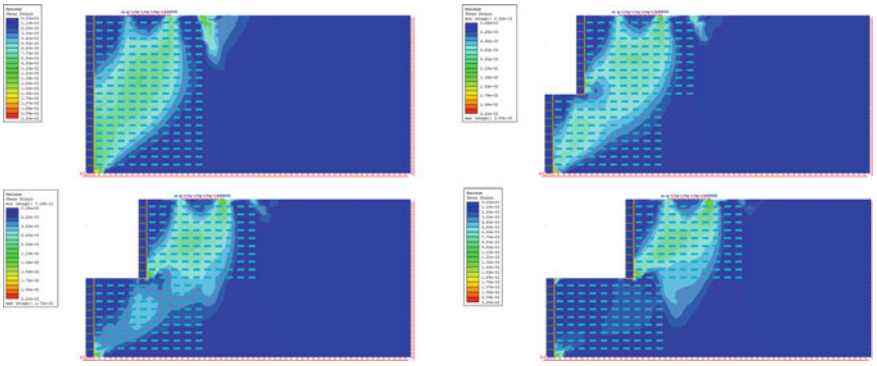

Fig. 5 Shear strain plots at allowable settlement (offset distance)

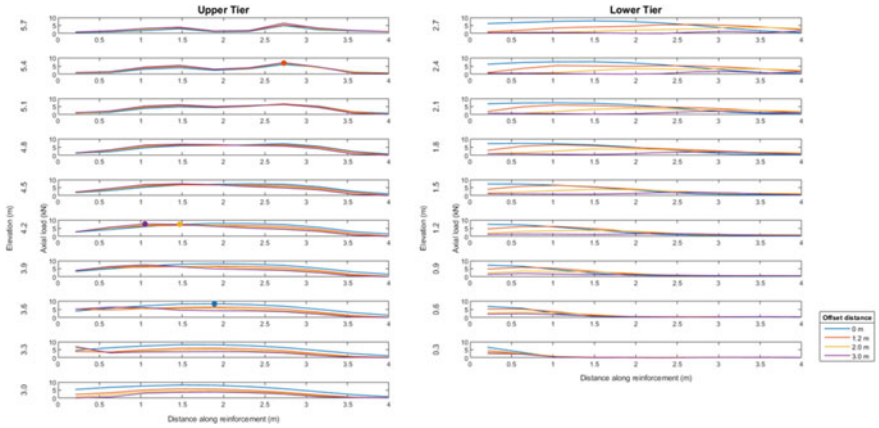

Fig. 6 Reinforcement load distribution at different offset distances

Table 6 Maximum reinforcement load at allowable load (offset distance)

Offset distance (m)	Max reinforcement load (kN)	% of tensile strength (%)
0	8.25	29
1.2	6.77	24
2.0	7.38	26
3.0	7.58	27

directed towards to toe of the upper tier instead of the lower tier which was the case for 0 m offset and 1.2 m offset. Following AASHTO's guidelines, two tiers that are 3.10 m apart will act as independent walls.

Greater offset distances resulted in less reinforcement load experienced by the reinforcements in the lower tier. Tiering was beneficial for walls as no offset to 1.2 m offset decreased the maximum reinforcement load by 18%. (Fig. 6) An increase was observed, however, for the offset distance from 1.2 to 2.0 m. This may be due to the underutilization of the lower tier reinforcements in helping carry the load induced by the footing (Table 6).

4 Conclusions

The behavior and failure mechanism of a two-tiered bamboo reinforced MSE retaining wall subjected to an isolated footing load was evaluated using a numerical approach by utilizing the 2D finite element program RS2. The following conclusions are drawn from the results of the study:

1. Reinforcements with higher tensile modulus such as bamboo and TenCate exhibited somewhat of a brittle failure as observed from its rapid or sudden failure after a small footing settlement from initial reinforcement yielding to wall failure. The opposite was true for reinforcements with smaller tensile modulus such as ACEGrid and Maccaferri which yielded slower as footing settlement depth increased. Generally, reinforcements with lower tensile modulus are safer since there is more allowance before the structure fails, meaning larger footing settlements must occur after initial reinforcement yielding before failure.
2. All reinforcement types developed a log-spiral shape of the failure plane. This was observed when the slip began at the farther edge of the footing which exited through a critical point on the wall facing. Reinforcement properties, specifically the tensile modulus and ultimate tensile strength, did not affect the failure shape that occurred, at least for the geometry and properties of the wall in this study.
3. Initial bamboo reinforcements yielded at the lowest reported footing displacement and reached the ultimate settlement at the lowest reported footing displacement Bamboo reinforcements were able to withstand the allowable footing settlement without any reinforcements yielding and no development of failure surface. From a serviceability standpoint, bamboo reinforcements are viable to be used as a support for resisting footing loads since the bamboo garnered more than a 100 mm difference from allowable settlement to ultimate settlement.
4. Tiering is beneficial for MSE walls for a range of offset distances. Introduction of an offset reduces the load carried by the upper reinforcements, distributing the strains throughout the wall in a log-spiral distribution. At greater offset distances, the load reduction effect gradually lessens with each tier acting as its own MSE wall.

References

1. Srivastava A, Chauhan VB (2020) Numerical studies on two-tiered MSE walls under seismic loading. SN Appl Sci 2(10):1625
2. Bhattacharjee A, Amin MU (2019) Behaviour of two-tiered geosynthetic-reinforced soil walls. INAE Lett 4(2):91–100
3. Zheng Y, Fox PJ (2016) Numerical investigation of geosynthetic-reinforced soil bridge abutments under static loading. J Geotech Geoenviron Eng 142(5):04016004
4. Abu-Hejleh N, Zornberg JG, Wang T, Watcharamonthein J (2002) Monitored displacements of unique geosynthetic-reinforced soil bridge abutments. Geosynth Int 9(1):71–95
5. Xiao C, Han J, Zhang Z (2015) Experimental study on performance of geosynthetic-reinforced soil model walls on rigid foundations subjected to static footing loading. Geotext Geomembr 44(1):81–94
6. Rojo J, Roxas C, Pitargue F, Briñas C (2000) Philippine erect bamboos—a field identification guide, forest products research and development institute. Los Banos, Laguna, Philippines
7. Akhil KS, Sankar N, Chandrakaran S (2020) Use of bamboo mat as a potential soil reinforcement material—an experimental study. Mater Today: Proc 31
8. Ahirwar SK, Mandal JN (2018) Behaviour of bamboo grid-reinforced soil bed. Int J Geotech Eng 15(7):1–10

9. Mohamed SBA, Yang K-H, Hung W-Y (2014) Finite element analyses of two-tier geosynthetic-reinforced soil walls: comparison involving centrifuge tests and limit equilibrium results. Comput Geotech 61:67–84
10. Mohamed SBA, Yang K-H, Hung W-Y (2013) Limit equilibrium analyses of geosynthetic-reinforced two-tiered walls: calibration from centrifuge tests. Geotext Geomembr 41:1–16
11. Leshchinsky D, Han J (2004) Geosynthetic reinforced multitiered walls. J Geotech Geoenviron Eng 130:1225–1235
12. Yoo C, Kim S-B (2008) Performance of a two-tier geosynthetic reinforced segmental retaining wall under a surcharge load: full-scale load test and 3D finite element analysis. Geotext Geomembr 26(6):460–472
13. Hegde A, Sitharam TG (2015) Use of bamboo in soft-ground engineering and its performance comparison with geosynthetics: experimental studies. J Mater Civ Eng 27(9):04014256
14. Terzaghi K, Peck RB, Mesri G (1996) Soil mechanics in engineering practice, 3rd edn. Wiley
15. Berg RR, Christopher BR, Samtani NC (2009) Design and construction of mechanically stabilized earth walls and reinforced soil slopes, vol I. FHWANHI-10-024. Federal Highway Administration, Washington, D.C.
16. Damians IP, Bathurst RJ, Josa A, Lloret A (2013) Comparison of finite element and finite difference modelling results with measured performance of a reinforced soil wall. In: Paper presented at the 66th Canadian geotechnical conference, Montreal, Quebec
17. Huang B, Bathurst RJ, Hatami K (2009) Numerical study of reinforced soil segmental walls using three different constitutive soil models. J Geotech Geoenviron Eng

A Review of the Effect of Mixing Water Quality on Concrete

Francis Cayanan, Orlean G. Dela Cruz, Aldrine Paul P. Bornales, Romeuel M. Domalaon, and Janecca B. Marbella

Abstract In many developing nations worldwide, building disasters have occurred over time, resulting in lost lives and property. However, most investigations on the reasons for construction collapses have pointed to poor design, insufficient monitoring, and the use of substandard materials as the causes of the disasters. This study examined how various water sources affected the concrete's properties. Different water sources that are being considered as possible alternative mixing water in concrete production have been explored in this review. Many beneficial and detrimental effects were discovered in the literature presented. Therefore, it is imperative to carefully examine the elements in the water to be used in mixing concrete, especially if it is not recommended for drinking water. First, the permitted chemical and physical contaminants and their evolution methodology are gathered. Next, each alternative water source's beneficial and detrimental effects (aside from the suggested

F. Cayanan · O. G. Dela Cruz (✉) · A. P. P. Bornales · R. M. Domalaon · J. B. Marbella
Graduate School, Polytechnic University of the Philippines, Manila, Philippines
e-mail: ogdelacruz@pup.edu.ph

F. Cayanan
e-mail: engrkikocayanan2@gmail.com

A. P. P. Bornales
e-mail: aldrine.bornales09@gmail.com

R. M. Domalaon
e-mail: domalaonrom@gmail.com

J. B. Marbella
e-mail: janecca45@gmail.com

F. Cayanan
Don Honorio Ventura State University, Bacolor, Philippines

R. M. Domalaon
Municipal Engineering Office - Local Government Unit of Daraga, Daraga, Philippines

J. B. Marbella
Department of Social Welfare & Development V, Legazpi, Philippines

H.-Y. Jeon (ed.), *Proceedings of the International Conference on Geosynthetics and Environmental Engineering*, Lecture Notes in Civil Engineering 374,
https://doi.org/10.1007/978-981-99-4229-9_12

potable water) were thoroughly examined. Finally, the challenges and gaps encountered by the existing studies were compiled to guide future research in searching for potential substitutes for mixing water amid rising global difficulties in supply.

Keywords Mixing · Water quality · Fresh concrete · Potable water · Slump test · Water standard

1 Introduction

Concrete is the material used in construction the most widely [1]. Cement (typically Portland cement and other cementitious materials like fly ash and slag cement), aggregate (typically a coarse aggregate made of gravels or crushed rocks like limestone or granite plus a fine aggregate such as sand), water, and chemical admixtures make up the construction material concrete [2]. Hence, the mixing water used for concrete production must have a quality that will remain the preferred performance.

A significant amount of freshwater appears to be utilized by the building sector, even though freshwater is Earth's most often used natural resource [3]. According to global data, compared to other industries, concrete manufacturing uses the most water [4]. Approximately 2.15 to 2.6 billion tons of water are used in concrete manufacturing annually [5]. As everyone is aware, water is a crucial component of concrete since it chemically combines with cement (hydration) to give the material the desired qualities [6]. Water is used in the building sector for the following reasons: (a) Because cement paste attaches to aggregate surfaces more rapidly and satisfactorily when they are wet than when they are dry, it is necessary to wet the surface of the aggregates to promote adhesion, (b) creating a plastic mixture of the various materials and giving concrete workability to make positioning it in the correct position more accessible, and (c) For the cementing ingredients to set and solidify during the curing process, water is also required for hydration [7]. According to ASTM C1602, combining "potable" water without testing or verification is allowed in structural and non-structural concrete.

In concrete manufacture, non-potable sources of water can also be used, provided that the source does not negatively affect the qualities of concrete [6]. The type of water used and its quantity in the concrete mix are believed to impact the concrete's rates significantly. However, the effects of several alternative water sources still need to be understood. Many water types unsuitable for drinking, such as well water, may be satisfactorily utilized in concrete when potable water is not readily available. Based on Hassan et al. (2014), it was determined as a possible choice to use well water as mixing water in concrete after fulfilling concrete mixing-water requirements by evaluating it chemically and comparing it with the specification [8].

Similarly, using seawater to mix concrete is considered to have potential benefits from a sustainability standpoint [9]. The recovered washout water that batch plants already utilize as concrete mixing water is also gaining popularity. Water used onsite for various tasks, such as washing truck agitator bowls, moistening aggregate, and

runoff, is known as recycled washout water. Allowing washout water to be reused in successive batches of concrete affects the strength qualities of the concrete. Therefore, reducing wash water as a waste product is a practical way. Comparatively, it was discovered in a different study that the compressive strength of concrete is significantly impacted by sewage water. This impact is evident after 7, 14, and 28 days and the values obtained are almost one-third lower than those found for a concrete constructed with drinking water [10].

The market for ready-mixed concrete worldwide was estimated at USD 451.1 billion in 2021. Furthermore, it is anticipated over the forecast period (2022–2028) to have grown to USD 571.46 billion, with a CAGR of 4.6%, as SkyQuest Technology Consulting Pvt reported. Ltd.; consequently, an increase in the need for mixing water used in concrete production is expected; therefore, this literature review searches the recommended quality of possible alternative mixing water and their effect on the concrete properties. Furthermore, to search for ways to improve the sustainability of the environment, this paper is anticipated to become a reliable reference for construction industry professionals in selecting their next possible option.

2 Methodology

This literature review's objective is to compile all of the studies that have been done on the impact of Mixing Water Quality on Concrete Properties. Science, technology, medicine, social sciences and humanities research are covered by the multidisciplinary, peer-reviewed journal article database ScienceDirect. The database's "Keyword" feature was used to search. The following keywords were used to obtain the most relevant articles: "reinforced concrete," "properties," "water type," "mixing," and "effect." There are 91 documents found; 27 publications were found relevant by manually reading the abstracts and some of the full articles. Additional 14 papers were found using Google Scholar. Figure 1 shows the selection process flowchart, which follows the PRISMA (Preferred Reporting Items for Systematic Reviews and Meta-Analyses) procedure. PRISMA is an evidence-based minimum set of items for reporting in systematic reviews and meta-analyses that primarily focuses on the reporting of studies evaluating the effects of interventions but can also be used as a basis for writing systematic reviews with objectives other than evaluating interventions (e.g., assess an etiology, prevalence, diagnosis or prognosis). Table 1, on the other hand, shows the summary of all Reviewed Papers and Outcomes Measured.

Software called NVivo is used for mixed-methods and qualitative research. In particular, it is used to analyze the unstructured text, audio, video, and image data from sources such (but not restricted to) interviews, focus groups, surveys, social media, and journal articles. One of the advantages of this software is the use of Word Frequency queries, which are valuable for identifying potential themes, especially in the early stages of a project, and for examining the most commonly used terms in specific demography. The software can also generate visuals after the query that could be useful for writing, such as a Word Cloud (also known as a tag cloud or text

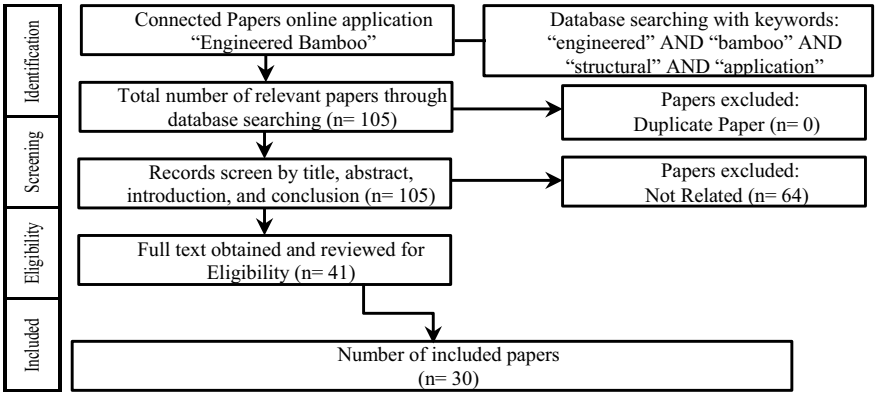

Fig. 1 Systematic related literature selecting process

cloud), which is a graphic representation of a text in which the words are sized up according to how frequently they are used in the collection of articles. The Word Cloud shown in Fig. 2 can be used as a guide in selecting the possible themes to be emphasized in the study.

3 Effect of Mixing Water Quality on Concrete Properties

High demand for and continuous mismanagement of water resources has exacerbated widespread hazards of water stress. Water stress occurs when the need for water exceeds the available amount. This stress frequently happens during a specific time or when the water quality is low, limiting safe water usage [29]. Water is a crucial resource for human existence, but potable water is scarce in some places [6]. A cement paste is created when water and a cementitious substance are combined during hydration [2]. Water suitable for human consumption, often potable, is typically acceptable for mixing water [6]. However, Ojo (2019) has found that water from sources other than potable water can make concrete [17]. Table 2 below shows the World Health Organization (WHO) drinking Water Standards Table, which contains some parameters' highest desirable and maximum permissible levels.

3.1 Fresh Concrete

Concrete Slump (Workability). A study carried out by Asadollahfardi et al. [30], where 300, 350, and 400 denote the kg/m^3 of cement in one cubic meter of concrete and A300, A350, and A400 labels were used to identify the concrete samples created and cured by drinking water as the control samples.

Table 1 Reviewed paper and outcomes measured

Source	Year	Outcomes measured	
Nikhil et al. [7]	2011	• Compressive strength at 7, 14, and 28 days	
Mama et al. [11]	2019	• Compressive strength of concrete	
Kokoszka [10]	2019	• Consistency • Compressive strength after 7, 14, and 28 days • Density	
Awoyera et al. [12]	2020	• Fresh properties of concrete, such as setting time and slump • The hardened properties of concrete, such as strength and durability	
Younis et al. [9]	2018	• Slump flow • Density • Yield • Air content • Setting time • Compressive strength	• Splitting tensile strength • Shrinkage • Rapid chloride permeabil-ity • Chloride migration • Water absorption
Kumar [13]	2000	• Strength of concrete exposed to seawater attack	
Emmanuel et al. [14]	2012	• Compressive strength of concrete cast with fresh water, ocean water, and lagoon water	
Farid et al. [15]	2019	• Compressive, tensile, and flexural strength	
Mangi et al. [16]	2020	• Effects of natural seawater on the properties of concrete	
Ojo [17]	2019	• Compressive strength of concrete	
Meena and Luhar [18]	2019	• Compressive strength • Flexural strength • Chloride penetration resistance	• Carbonation resistance • Abrasion resistance
Su et al. [19]	2002	• Compressive strength • Setting times	• Workabil-ity
Saputra and Sulistyo [20]	2018	• Strength of concrete after 28 days • The strength of concrete after 90 days	
Shafaq Bazaz [21]	2020	• Compressive strength of concrete cubes	
Tarak and Saxena [22]	2022	• Compressive strength • Setting time • Workability • pH value	• Strength • Sieve analysis • W/C ratio
Al-Jabri et al. [23]	2011	• Compressive strength • Tensile strength	• Flexural strength • Initial surface absorption
Shafaq Bazaz [21]	2014	• Compressive strength • Concrete	• Mixing water
Ganesh Naidu et al. [4]	2019	• Workability • Compressive strength	
Gupta et al. [3]	2022	• Compressive and tensile strength of hardened cement cubes • Compressive strength of concrete cubes	

(continued)

Table 1 (continued)

Source	Year	Outcomes measured	
Kucche et al. [24]	2015	• Setting time • The compressive strength • The softening of concrete	
Moinul Islam et al. [25]	2012	• Compressive strength of concrete when mixed with seawater • Compressive strength of concrete when cured with seawater	
Chatveera et al. [26]	2006	• Properties of dry sludge powder • The properties of fresh concrete	• The mechanical properties of concrete • The durability aspects of concrete
Ojo [17]	2021	• Compressive strength properties of concrete	
Dhondy et al. [27]	2020	• Heat of hydration • Shrinkage	• Compressive strength • Modulus of elasticity
Hasan et al. [28]	2020	• Compressive strength of concrete	

Fig. 2 Word cloud showing the most commonly used terms in the reviewed literature

The concrete examples made with drinking water and cured with wastewater treatment were given the B300, B350, and B400 labels. To depict the concrete samples made and cured using treated wastewater, C300, C350, and C400 labels were utilized. As shown in Table 3, compared to concrete prepared with drinking water, the workability of concrete made with treated wastewater remained relatively high [30]. On

Table 2 World Health Organization (WHO) drinking water standards

Parameter	Highest desirable level	Maximum permissible level
Total solid	500	1500
Color (pt co)	5	50
Taste	Unobjectionable	–
Odour	Unobjectionable	–
Turbidity (NTU)	5	25
Chlorine	200	600
Iron	0.1	1
Manganese	0.05	0.5
Copper	0.05	1.5
Zinc	5	15
Calcium	75	200
Magnesium	30	150
Sulphate	200	400
Total hardness ($CaCO_3$)	100	500
Nitrate	45	500
Ammonium	–	–
pH (unit)	7–8	Min 6.5 Max 9.2

the other hand, according to Farid et al. (2019), groundwater or tap water produced a shear slump, while wastewater and surface water had true slumps for both mix proportions [15].

Setting Time. When seawater was used in concrete, there was a noticeable decrease in workability, workability retention, and initial setting time assessments. The initial setting time of the fresh concrete was decreased by around 30% by the addition of seawater. These findings may be explained by the seawater-induced acceleration of cement hydration, which reduces slump, slump retention, and setting time [9]. Additionally, treated wastewater raised the initial time setting compared to drinking water. As a result, the final setting time for samples made with drinking was 180

Table 3 Slump test results [30]

Water	Slump (mm)
A300	110
C300	99
A400	90
C400	82
B350	117
C350	105

min, while the last time for samples made with treated wastewater was 240 min. The samples from treated waste also required a more extended final setting period [30]. Moreover, Tarak et al.'s research findings in 2022 support this, where groundwater samples from various districts demonstrate that the water quality used to mix concrete significantly impacts cement's initial and final setting times [22].

3.2 Hardened Concrete

Compressive Strength. Significantly, it was found by Nikhil et al. (2019) that the compressive strength of concrete made using potable water increased by 33.34% compared to concrete made with sewage water [7]. Additionally, when comparing the compressive strength of concrete built with drinking water to that made with sewage water after 7, 14, and 28 days, it was discovered that the compressive strength had decreased by 29.8%, 25%, and 33.4%, respectively [10].

Further research utilizing seawater in concrete produced a similar impact to sewage water. It initially caused a slight rise in the compressive and tensile strength of the hardened concrete until Day 7 after mixing. After 28 days, there was a 7–10% decline in the compressive and tensile strength results of Mix B compared to Mix A. (Mix A represents the conventional concrete mixed with fresh water and is considered as a reference. Mix B is made with the use of seawater) [9]. The overall compressive strength behavior for both concrete mix ratios was compared using line graph analysis. It can be shown that wastewater significantly impacted concrete compressive strength compared to groundwater and surface water [15]. Moreover, the Compressive Strength of concrete built using rainwater grew with age at 7 and 14 days. Still, it dramatically decreased at the 28-day mark, indicating no solid assurance of the long-term strength of concrete made with this water source [11]. Meaning the tests shows that Sewage water, in general, consistently decreases the capacity of the concrete in terms of compression in almost the same amount concerning the results of two independent experiments presented.

Tensile Strength. According to several studies, concrete made with potable water has a 14.89% higher split tensile strength than concrete made with sewage water [7]. In contrast, the impact of water type on the tensile strength of concrete at intervals of 7–28 days concerning both of the experiment's concrete mix ratios. The graph's general trend shows that using wastewater and surface water in equal amounts improved the tensile strength of concrete; however, wastewater demonstrated a tremendous improvement in tensile strength compared to the other two types [15]. Interestingly, the tensile strength of cement made using treated sewage water is 1.63% higher than that of freshwater-made cement [3]. It shows that sewage water, in its nature, usually harms concrete properties, but effective treatment can offer a positive benefit.

Flexure Strength. When compared to concrete made using sewage water, it was found by Mama et al. (2019) that the flexural strength of concrete made with potable water increased by 11.12% [11]. Another study shows flexure strength increased

when wastewater and surface water were used instead of groundwater [15]. Another finding from another study is that the proportion of sludge water used to substitute tap water tends to reduce the compressive strength, flexural strength, and elastic modulus of concrete [26].

4 Research Gap and Further Studies

Currently, only comparison tests have been devised to determine the acceptability of mixing water. In most comparison tests, it is necessary to compare the strength of the concrete made with the unknown water to the power of the concrete made with water that is known to be suitable [22]. Because potable water is scarce, it is advised that additional water sources be used to mix concrete to lessen the strain on the insufficient water supply. However, before casting, the water supply utilized to make concrete should be investigated and approved by the appropriate authorities [17]. In 2001, Mehta et al. mentioned that the concrete consumption rate had not changed significantly during the past 30 years. It is believed that the current consumption of substantial worldwide during those times is of the order of 55 billion tons every year [1] (Table 4).

Table 4 Challenges to mixing water quality

References	Challenges/gap
Olugbenga [2]	Long term performance and durability of concrete made from alternative mixing water used
Younis et al. [9]	Permeability
Kokoszka [10]	Durability and porosity
Asadollahfardi et al. [30]	Parameters and acceptable limits to be acquired when treating wastewater
Farid et al. [15]	Impact analysis of changes in the chemical Parameters of water samples on the development of concrete
Tarak and Saxena [22]	Different mix design
Awoyera et al. [12]	Compacting factor, hydration mechanism, mineralogical changes, crack integration, porosity
Al-Jabri et al. [23]	Durability
Moinul Islam et al. [25]	The extent of strength deterioration of concrete in seawater environment
Hasan et al. [28]	Impact of the greywater on other important characteristics of concrete and the consequent changes in the phase-structural parameters of the material

5 Conclusion

This review explores various water sources that could serve as alternative mixing water in concrete production. The literature presented reveals multiple beneficial and detrimental effects associated with these sources, highlighting the need to carefully evaluate the water's constituent elements, primarily if it is not intended for drinking. Based on the findings, it is clear that the quality of water used significantly affects the workability, setting time, compressive strength, tensile strength, and flexure strength of the concrete. For example, drinking water remains the optimal choice to meet standard slump requirements. At the same time, seawater reduces the initial setting time of the concrete, making it ideal for faster setting times, meaning we can take advantage of this effect for conditions that require a quicker setting time. However, the effects of salt on other properties need further study. In addition, potable water is the best option for achieving the expected compressive strength, while wastewater acquires more tensile strength than other alternatives. Finally, flexure strength decreases when additional water sources, except potable, are used.

References

1. Kumar Mehta PJMMP (2001) Microstructure, properties, and materials. Statewide agricultural land use baseline 2015, vol 1, p 684
2. Olugbenga A (2011) Civil and environmental research. Civ Environ Res 6(3): 39–43. https://www.iiste.org/Journals/index.php/CER/article/view/11701
3. Gupta A, Dhruw A, Sinha GK, Sahu NK, Sahu P, Saxena T (2022) Effect of treated wastewater on properties of concrete. Ymer 21(5):1376–1382. https://doi.org/10.37896/YMER21.05/F1
4. Ganesh Naidu G, Sri Durga Vara Prasad M, Upendra Varma U, Sandhya S (2019) Effect of R.O. waste water on properties of concrete. Int J Recent Technol Eng 8(3): 2806–2808. https://doi.org/10.35940/ijrte.C5201.098319
5. Vahit A, Jain J, Ravikumar D, Mccandlish L, Decristofaro N (2016) Technologies that reduce water use in cement and concrete help global industry address mounting concerns of water scarcity. Solidia Technol 1–8
6. NRMCA (2017) TIP 10 - Mixing Water Quality for Concrete This TIP outlines qualification tests and documentation for use of non-potable water as mixing water. Technol Pract 10
7. Nikhil TR, Sushma R, Dr. Gopinath SM, Dr. Shanthappa BC (2011) Impact of water quality on strength properties of concrete. Ind J Appl Res 4(7): 197–199. https://doi.org/10.15373/2249555x/july2014/60
8. Hassan IH, Abdul-Kareem OM, Shihab AY (2014) Effect of using well water as mixing water in concrete. AL-Rafdain Eng J (AREJ) 22(5):166–177. https://doi.org/10.33899/rengj.2014.101015
9. Younis A, Ebead U, Suraneni P, Nanni A (2018) Fresh and hardened properties of seawater-mixed concrete. Constr Build Mater 190:276–286. https://doi.org/10.1016/j.conbuildmat.2018.09.126
10. Kokoszka W (2019) Impact of water quality on concrete mix and hardened concrete parameters. Civ Environ Eng Rep 29(3):174–182. https://doi.org/10.2478/ceer-2019-0033
11. Mama CN, Nnaji CC, Onovo CJ, Nwosu ID (2019) Effects of water quality on strength properties of concrete. Int J Civ, Mech Energy Sci 5(2):7–13. https://doi.org/10.22161/ijcmes.5.2.2

12. Awoyera P, Adesina A, Olalusi OB, Viloria A (2020) Reinforced concrete deterioration caused by contaminated construction water: an overview. Eng Fail Anal 116(July): 104715. https://doi.org/10.1016/j.engfailanal.2020.104715.
13. Kumar S (2000) Influence of water quality on the strength of plain and blended cement concretes in marine environments. Cem Concr Res 30(3):345–350. https://doi.org/10.1016/S0008-8846(99)00263-X
14. Emmanuel AO, Oladipo FA, Olabode O (2012) Investigation of salinity effect on compressive strength of reinforced concrete. J Sustain Dev 5(6). https://doi.org/10.5539/jsd.v5n6p74
15. Farid H et al (2019) Impact analysis of water quality on the development of construction materials. Processes 7(9):1–13. https://doi.org/10.3390/pr7090579
16. Mangi SA, Makhija A, Raza MS, Khahro SH, Jhatial AA (2021) A comprehensive review on effects of seawater on engineering properties of concrete. SILICON 13(12):4519–4526. https://doi.org/10.1007/s12633-020-00724-7
17. Ojo OM (2019) Effect of water quality on compressive strength of concrete. Eur Sci J ESJ 15(12). https://doi.org/10.19044/esj.2019.v15n12p172
18. Meena K, Luhar S (2019) Effect of wastewater on properties of concrete. J Build Eng 21:106–112. https://doi.org/10.1016/j.jobe.2018.10.003
19. Su N, Miao B, Liu FS (2002) Effect of wash water and underground water on properties of concrete. Cem Concr Res 32(5):777–782. https://doi.org/10.1016/S0008-8846(01)00762-1
20. Saputra A, Sulistyo D (2018) Effect of water content and water type on the physical properties of concrete. J Phys Sci 29(August 2020): 159–173. https://doi.org/10.21315/jps2018.29.s2.12
21. Shafaq Bazaz M (2020) Experimental study on the effect of water quality on strength of concrete case study: dal lake water. Int J Eng Appl Sci Technol 5(5): 241–248. https://doi.org/10.33564/ijeast.2020.v05i05.041
22. Tarak Y, Saxena T (2022) Effect of different district water sources on compressive strength on concrete. Ymer 21(5):1026–1034. https://doi.org/10.37896/YMER21.05/B7
23. Al-Jabri KS, Al-Saidy AH, Taha R, Al-Kemyani AJ (2011) Effect of using wastewater on the properties of high strength concrete. Procedia Eng 14:370–376. https://doi.org/10.1016/j.proeng.2011.07.046
24. Kucche KJ, Jamkar SS, Sadgir PA (2015) Quality of water for making concrete: a review of. Int J Sci Res Publ 5(1): 1–10. ISSN:2250-3153
25. Moinul Islam M, Saiful Islam M, Al-Amin M, Mydul Islam M (2012) Suitability of sea water on curing and compressive strength of structural concrete. J Civ Eng (IEB) 40(1): 37–45
26. Chatveera B, Lertwattanaruk P, Makul N (2006) Effect of sludge water from ready-mixed concrete plant on properties and durability of concrete. Cem Concr Compos 28(5):441–450. https://doi.org/10.1016/j.cemconcomp.2006.01.001
27. Dhondy T, Xiang Y, Yu T, Teng JG (2021) Effects of mixing water salinity on the properties of concrete. Adv Struct Eng 24(6):1150–1160. https://doi.org/10.1177/1369433220965272
28. Hasan MM, Pial MA, Arafat MS, Miah MJ, Miah MS (2020) Influence of raw greywater on compressive strength of concrete. Mag Civ Eng 100(8):6–12. https://doi.org/10.18720/MCE.100.10
29. Biswas AK (2003) Water availability and use. Water Resour North Am (April 2018): 163–174. https://doi.org/10.1007/978-3-662-10868-0_19
30. Asadollahfardi G, Delnavaz M, Rashnoiee V, Fazeli A, Gonabadi N (2016) Dataset of producing and curing concrete using domestic treated wastewater. Data Brief 6:316–325. https://doi.org/10.1016/j.dib.2015.12.020

A Review on Processing Techniques and Building Methods of Engineered Bamboo

Francis Cayanan, John Robert D. Gabriel, Carlito H. Pantalunan, Orlean G. Dela Cruz, and Irene R. Roque

Abstract The unstoppable growth of civilization and the unending process of the Industrial Revolution led people to search for high-strength materials that are strong enough to build skyscraper infrastructures and different venues, leaving the traditional Bamboo behind the innovations. Moving faster towards a more futuristic environment, we feel the negative impacts of harmful chemicals, non-eco-friendly materials, and pollution-emitting activities worldwide. That is why, Engineers, Architects, Builders, Scientists, and Researchers revisit the materials and methods that will lessen the greenhouse gas and carbon emissions we produce. Bamboo has several advantages and provides both strength and aesthetic value. Even though it was evident that there is still a long way to the perfection of Engineered Bamboo (EB) application in many construction fields, especially in structural engineering, the tireless effort being exerted by the researchers interested in its development is considered contributing and substantial. This paper will describe and summarize the current and related information on using engineered Bamboo as a construction material.

Keywords Engineered bamboo · Bamboo · Structural bamboo · Building method

F. Cayanan · J. R. D. Gabriel · O. G. Dela Cruz (✉)
Graduate School, Polytechnic University of the Philippines, Manila, Philippines
e-mail: ogdelacruz@pup.edu.ph

F. Cayanan
e-mail: engrkikocayanan2@gmail.com

J. R. D. Gabriel
e-mail: gabrielsteelconcrete1707@gmail.com

F. Cayanan · J. R. D. Gabriel · I. R. Roque
Don Honorio Ventura State University, Bacolor, Philippines
e-mail: edocardelacruz@gmail.com

C. H. Pantalunan
Aurora State College of Technology, Baler, Aurora, Philippines
e-mail: carlitopantalunan@gmail.com

H.-Y. Jeon (ed.), *Proceedings of the International Conference on Geosynthetics and Environmental Engineering*, Lecture Notes in Civil Engineering 374,
https://doi.org/10.1007/978-981-99-4229-9_13

1 Introduction

The majority of modern construction materials require a lot of energy and environmental harm to make. They must be mined, processed, heated, or given various chemical treatments [1]. Greater than one-fourth of primary resource extraction, around 20% of CO_2 emissions, and 35% or so of the world's electrical use are all related to manufacturing. Reducing the materials used in construction (or using reasonably priced low-carbon substitutes) could lower building costs and reduce emissions during manufacturing [2]. Although timber is a low-cost building material, deforestation and rising urbanization have exhausted tropical resources. Timber forests need 30 to 50 years, with European oak requiring up to 80 years [3]. The projection is that oil, bauxite, iron, and copper will become scarce within this century, and soon after, there will be a shortage of tropical hardwood [4]. Due to rapid urbanization's growing demand for sustainable building materials, Bamboo has gained more attention and has been developed for use in modern construction [3].

Bamboo's mechanical strength, usability attributes, and anatomical features stabilize and develop in 3–5 years, making it appropriate for various uses [5]. According to test results, Bamboo may replace wood in structural applications from a load-carrying perspective because its strength and stiffness are comparable [6]. However, despite having natural qualities relatively similar to wood, Bamboo's original geometrical shape makes it challenging to use in modern construction [7]. Additionally, because Bamboo has an irregular cross-section and is not perfectly straight, it has problems with squeaky joints and thermal bridges [6]. Reduced variability of the natural material is the goal of Engineered Bamboo (EB) [8]. It represents bamboo products processed primarily to create a uniform, straight-edged building components from rounded, asymmetrical culms. It is a terminology that refers to a wide variety of reconstituted composite products made by cutting the complete element into smaller pieces, known as furnishing, and then fusing them together to make composite panels or shaped lumber stock using modern adhesives used in the wood industry [9]. Engineered bamboo products have the advantage of allowing for the creation of standard sections for members and connections and the reduction of variability within a single member [8].

Analysts anticipate that the bamboo market will increase between 2022 and 2030, at a Compound Annual Growth Rate (CAGR) of 4.5% after being valued at USD 59.30 billion in 2021, as stated by Grand View Research. This paper investigates the literature published regarding the improvements of EB as a building material through its manufacturing processes and construction methods. Furthermore, related applications, challenges to standardization, and future studies recommendations are to be discussed.

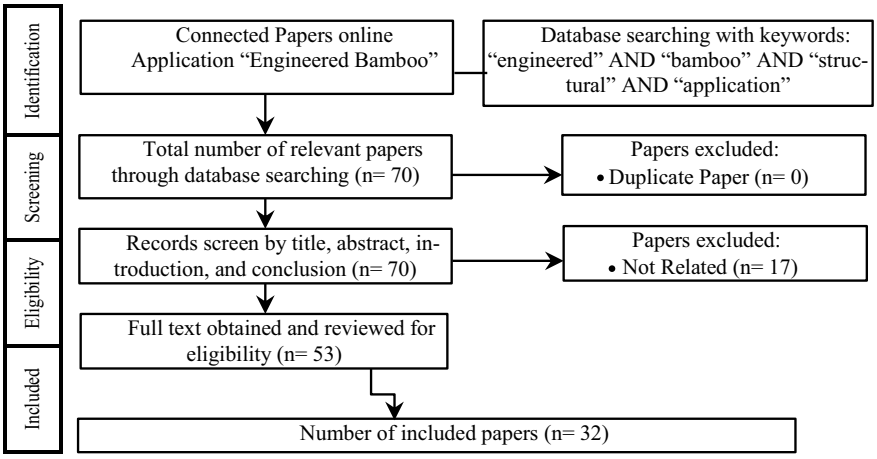

Fig. 1 Systematic method for selecting relevant literature

2 Methodology

The keywords used to find an article or journal are engineered, Bamboo, structural, and application. To determine the full potential of Bamboo as an innovative construction material.

The researcher uses the online application "Connected Papers" to answer the above-stated research questions. First, after reading the abstract to filter the papers directly connected to the topic, documents were searched using different online sources. Secondly, Fig. 1 shows the Systematic related literature selection process. Lastly, Fig. 2 shows the Topic Modelling of all related literature using Orange Data Mining Software, which shows the most used words from all the documents.

3 Discussion

3.1 Bamboo Physical and Mechanical Properties

Bamboo has different mechanical properties in the transverse, longitudinal, and radial directions because it is an anisotropic material. A large grass with hollowed culms and horizontal fibers oriented within lignin arrays split by solid diaphragms (nodes) makes up the raw material for bamboo. The bamboo fibers, vary within the wall of the culm, becoming less dense as they advance within, and the thickness, likewise, decreases from the bottom to the top [10]. Depending on its age, bamboo can be utilized for a variety of purposes, including: (a) eating (less than thirty days), (b) It takes six to nine months, to make a basket, (c) Making bamboo boards or laminations

Fig. 2 Topic modelling from selected related kinds of literature

Table 1 Properties of bamboo, wood, concrete, and steel

Property	Bamboo [12]	Wood [13]	Concrete	Steel
Density (kg/m^3)	620	–	2240–2400	7800–8000
Compressive strength (MPa)	51–56	43	20–40	≈172
Tensile strength (MPa)	150–264	89	2–5	350–420
Young's modulus (GPa)	11.219–	11	14–41	200
Poisson's ratio	–	–	0.20–0.21	0.25

takes two to three years, (d) Three to five years, for Construction use, (e) Bamboo rapidly loses strength from 6 to 12 years old (if not harvested). It's interesting that it can compete with steel in terms of tensile strength while outperforming wood, brick, and concrete in terms of compressive strength [11]. Some of the mechanical and physical features of bamboo, wood (spruce), steel, and concrete are included in Table 1.

3.2 Structural Grade Bamboo Species

Although there are more than 1200 species of Bamboo around the globe, the variety in geometric and mechanical qualities restricts the use of complete culm bamboo construction [10]. Table 2 shows the bamboo species with Structural Grade under the "Heavy Construction" category selected from an article by Stéphane Schröder.

Table 2 Structural grade bamboo species

Species	ML	MD	CW	Species	ML	MD	CW
B. balcooa	25	15	v.thk	D. peculiaris	18	15	Thick
B. bambos	30	18	v.thk	D. sikkimensis	18	13	Thick
B. polymorpha	25	15	Thick	D. sinicus	30	30	Thick
B. spinosa	25	12	Thick	D. xishuangbannaensis	28	22	Thin
B. valida	16	12	Thin	D. yunnanicus	25	18	Thin
D. asper	30	20	Thick	Gi. levis	20	13	Thin
D. barbatus	18	15	Thick	Gi. pruriens	15	12	Thin
D. brandisii	33	20	Thick	Gi. scortechinii	20	12	Thin
D. copelandii	30	25	Thin	Gu. aculeata	25	18	Thick
D. dianxiensis	28	18	Thick	Gu. amplexifolia	20	10	Solid
D. giganteus	30	30	Thick	Gu. angustifolia	25	15	Thin
D. hamiltonii	23	18	Thick	Gu. chacoensis	20	15	Thin
D. hookeri	20	15	Thick	Gu. superba	20	15	Thick
D. jianshuiensis	18	12	Thin	P. edulis	23	18	Thin
D. latiflorus	25	20	Thick				

*ML—Maximum length (in meters); *MD—Maximum diameter (in centimeters); *CW—Culm wall; B—Bambusa; D—Dendrocalamus; Gi—Gigantochloa; Gu—Guadua; P—Phyllostachys; v—very; thk—thick

3.3 Common Types of Engineered Bamboo

Bamboo is gaining popularity in contemporary buildings and bridge structures as part of the sustainable development trend [7]. Bamboo boards, reconstituted densified bamboo, and laminated bamboo are the three main categories of EB products [9].

Glue Laminated Bamboo (Glubam). The "thin layer bamboo strips" are laminated into mats using Glubam or ply bamboo sheets, which use the original method of plywood production [7]. A "strip" is a split that has been solidified into a rectangular cross-section after being dried out. After the outer and inner culm wall layers are removed, it is only three(3) to ten(10) millimeters thick in the circumferential(radial) direction and up to twenty-five(25) millimeters wide in the tangential direction [9]. In the main fiber direction, according to a recent study, Glubam has an average compression value of 51 MPa and a tension strength of 82 MPa, while, a 10,400 MPa Elastic Modulus is recorded. Also, it was found that Glubam has a parallel to the grain mean shear strength of about 7.2 MPa, a Modulus of Rupture of 9400 MPa, and a mean static bending strength of 99 MPa according to the results of the bending test [7]. An insightful study used the well-known Hankinson's equation to try to estimate the off-axis tensional strength of Glubam with a longitudinal and transverse fiber ratio of 4 to 1. Yet, the model continually overpredicts the results

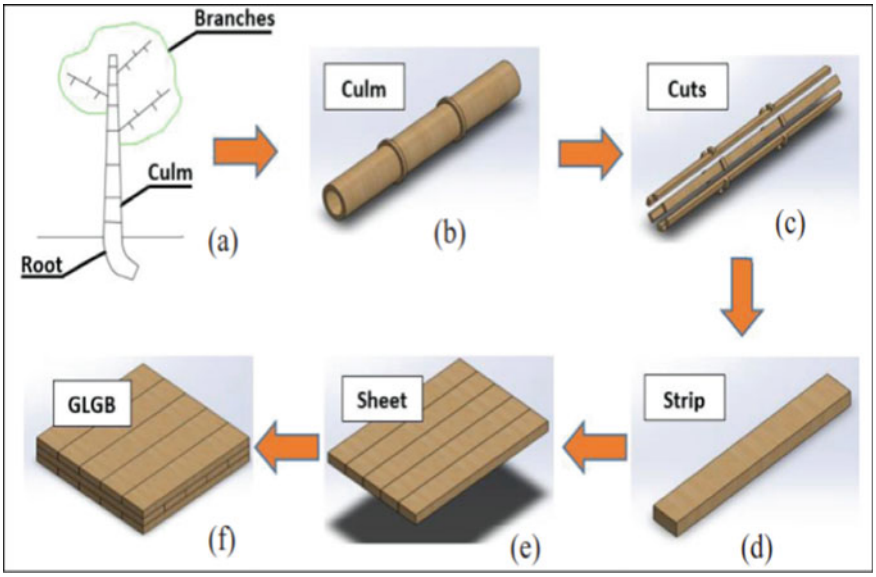

Fig. 3 Process of glued laminated (Guadua) bamboo [16]

regardless of the variations of the characteristic coefficient "n" proving that the original version of Hankinson's equation cannot correctly predict the strength of the material [14]. Typically, organized bamboo strips in a way called 4:1 sheets, with 80% of the strips oriented longitudinally and 20% oriented transversely. Bamboo curtains typically have 15 layers or fewer, with a 2 mm thickness between each layer [15]. Figure 3 shows the Glubam production process [16].

Laminated Bamboo Lumber (LBL). One of the most innovative composite materials is created by binding thin and flat bamboo culms next to each other [18]. The bamboo plant's stem, or "culm," is made up of several segments (internodes) that are spaced apart by diaphragms (nodes) [9]. Because LBL possesses the mechanical properties of bamboo yet can be made with well-defined shapes, similar to the available commercial wood products, it has drawn the interest of both academics and practitioners in particular [6]. Brittle tensile failure, which begins at the tensional face of the beam, is what causes LBL beams to fail. Moreover, stress concentrations in areas where defects are present can affect its tensile strength [18]. Figure 4 shows the LBL production process [17].

Reconstituted Densified Bamboo—(Scrimber). Bamboo Scrimber (BS), often referred to as parallel-strand bamboo or strand-woven bamboo, is created from crushed fibers which have been pressed into a solid mass after being soaked with resin [10]. Cold molded, hot cure, and high-temperature pressing are the three primary forming processes [19]. Fiber Bundles are the pieces of crushed culm walls that can be gathered and used to make reconstituted lumber. In the scrimber process,

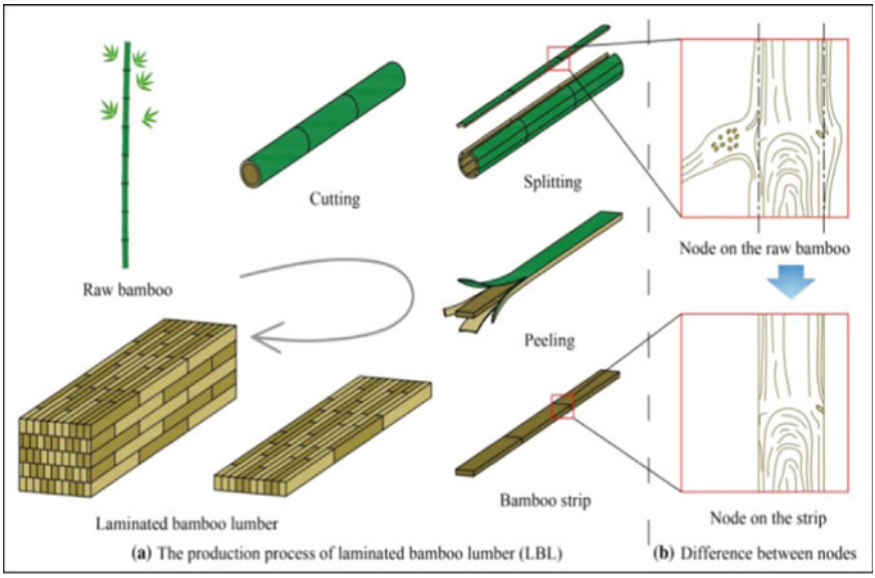

Fig. 4 Laminated bamboo lumber (LBL) [17]

these are made by roughly splitting the culm wall with chopper-rolling, crushing it through a series of closely spaced rollers, and brooming (for elements with smaller diameter) [9]. The unprocessed culm of bamboo was turned into EB scrimber, a laminated (with resin which is thermosetting) or crushed product with a density of 800–1200 kg/m^3 [20]. A separate experiment found that the bending specimen resin did not experience compression failures, but the bamboo scrim material did. This outcome might have been influenced by the resin's tendency to be more rigid than Bamboo when fully cured, even at 4% resin loading [19]. Figure 5 illustrates the BS manufacturing process [21], while, Fig. 6 presents the detailed process of mechanically rolled bamboo fibers [22].

3.4 Adhesives

Any organic material, whether natural or artificial, containing a viscous liquid or non-crystalline is referred to as resin. Natural resins are often transparent or translucent organic materials with a yellowish-to-brown appearance that is combustible and fusible. A broad category of synthetic products with some physical features of natural resins but different chemical compositions are referred to as synthetic resins. Plastics and synthetic resins cannot be distinguished with certainty. Glubam sheets are made using phenol–formaldehyde, just like plywood in North America [15]. An experiment showing superior technical properties for the bamboo scrimber made from

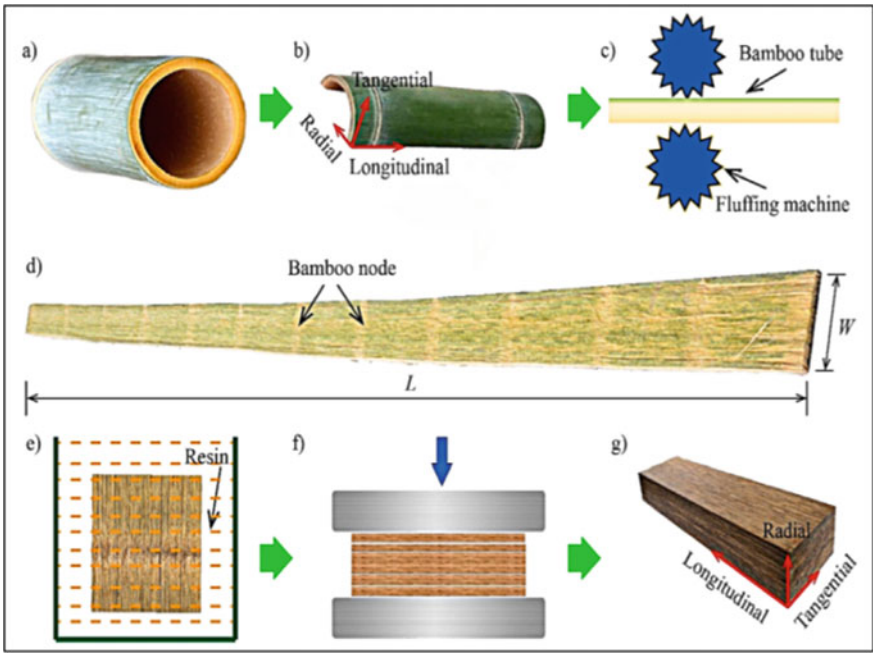

Fig. 5 Manufacturing process from full-culm rolled Bamboo to BS [21]

processed bamboo bundles (180 °C), combined dry air treatment and 18% PF resin loading, yielded favorable results. The binding performance of the bamboo scrimber slightly increased with greater PF resin loading, whether or not it underwent heat treatment [19]. Moreover, another notable result showed that other than the modulus of bending, which was not greatly impacted by density, practically all parameters enhanced with higher resin amounts and densities [23]. Table 3 contains the resins used by the recent studies.

3.5 Existing Structural Elements or Structures Made of EB

At Nanjing Forestry University, a three-story office building with LBL was constructed in 2017 as depicted in Fig. 7a [28]. Second, in Fig. 7b, from one study, the industry is adopting a new trend of creating new bamboo products to broaden the present application from surfaces to structures [3]. Lastly, Fig. 7c proves that due to the unique flexibility of the material slats and laminated planks, curved bamboo arcs preserve the original performance of Bamboo, making them an excellent choice for structural columns or posts for tiny house frames that can carry a specific amount of weight.

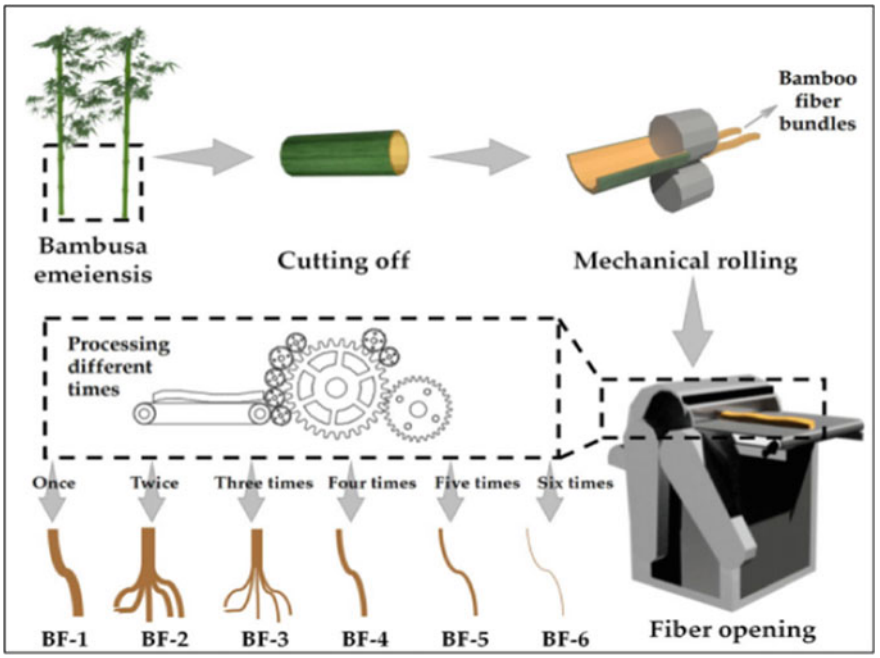

Fig. 6 Process for preparing mechanically bamboo fibers [22]

Table 3 Resins used in recent studies

Resin	Refs.	
PF	Yu et al. [19]	Note: PF—Phenol Formaldehyde; UF—Urea–Formaldehyde; E—Epoxy; I—Isocyanate; PRF—Phenol-Resorcinol Formal dehyde
UF	Correal et al. [24]	
E	Verma and Chariar[25], Verma et al. [26]	
I	Sinha et al. [27]	
PRF	Sinha et al. [27]	

3.6 Standardization

Construction stakeholders' coordinated participation is necessary for standardization, which they do by collectively promoting and accelerating the process. International coding and standards would promote structural and engineered Bamboo as a sustainable building material globally [3]. Table 4 compiles the Material Testing standard used and the description of each.

Fig. 7 Existing structural elements or structures made of EB

Table 4 Material testing used by some recent studies

Material testing used	Description	Refs.
ASTM D-1037	Standard test method for evaluating properties of wood-base fiber and particle panel materials	[19, 23]
ASTM D143-94	Standard test methods for small clear specimens of timber	[7]
ASTM D198	Standard test methods of static tests of lumber in structural	[18]
ASTM D2334	Short-beam strength testing of polymer matrix Composite materials	[19, 23]
GB/T 30,364–2013	Bamboo scrimber flooring	[29]
GB/T 50,329–2012	Standard for test methods of timber structures	[18]

It can be observed from the description that most of the studies about Bamboo use the relevant codes primarily intended for Timber or Wood and that the engineered bamboo composites currently need to be described by standards or codes [20].

4 Challenges and Limitations

The challenges from the reviewed materials are summarized in Table 5. Addressing the issues listed in Table 5 is important for the future development of the engineered bamboo and the discipline as a whole. The insights shown in this Table 5 will lead us in the appropriate path for improving the quality and dependability of using engineered bamboo as construction material. These recommendations, drawn from previous experiments' lessons, have an opportunity to provide significant and accurate information that will substantially aid in the ongoing advancement of the engineered bamboo studies.

Table 5 List of future research recommendations

Refs.	Challenges and limitations
[30]	Processing-related changes to Bamboo's characteristics and those of its numerous derivative materials in structural applications
[10]	Full-scale specimens testing
[15]	Possibility of combining bamboo with different materials like wood, steel, and FRP
[19]	Dimensional stability while preserving the bamboo bundles' mechanical qualities
[31]	Applying lateral pressure to layers to better understand how it affects the strength characteristics
[14]	Failure characteristics of Glubam; Glubam with various fiber ratios and complex stress states
[32]	Thermal treatment effects

5 Conclusions

The market can accept engineered Bamboo as a competitive product. Bamboo has several advantages and provides strength and aesthetic value compared to other materials. Although developing a thorough codification of structural bamboo products may be necessary soon, the process will be slow and useless without coordinated cooperation from relevant parties. The engineering quantification of mechanical properties will determine future structural applications. Through experimentation and analysis, academic research should seek to inform how industry leaders and policy-makers can work to lay the groundwork for standardization. Even though it was evident that there is still a long way to the perfection of EB application in many construction fields, especially in structural engineering, the tireless effort being exerted by the researchers interested in its development is considered contributing and substantial.

References

1. Low impact building: housing using renewable materials. Wiley, vol 1 (2013)
2. Chrysanidis T, Mousama D, Tzatzo E, Alamanis N, Zachos D (2022) Study of the effect of a seismic zone to the construction cost of a five-story reinforced concrete building. Sustainability (Switzerland) 14(16). https://doi.org/10.3390/su141610076
3. Gatóo A, Sharma B, Bock M, Mulligan H, Ramage MH (2014) Sustainable structures: bamboo standards and building codes. Proc Inst Civ Engineers: Eng Sustain 167(5):189–196. https://doi.org/10.1680/ensu.14.00009
4. Burroughs S, Růžička J (2019) The use of natural materials for construction projects-social aspects of sustainable building: case studies from Australia and Europe. IOP Conf Ser Earth Environ Sci 290(1). https://doi.org/10.1088/1755-1315/290/1/012009
5. Lee CH, Chung MJ, Lin CH, Yang TH (2012) Effects of layered structure on the physical and mechanical properties of laminated moso bamboo (Phyllosachys edulis) flooring. Constr Build Mater 28(1):31–35. https://doi.org/10.1016/j.conbuildmat.2011.08.038

6. Mahdavi M, Clouston PL, Arwade SR (2011) Development of laminated bamboo lumber: review of processing, performance, and economical considerations. J Mater Civ Eng 23(7):1036–1042. https://doi.org/10.1061/(asce)mt.1943-5533.0000253
7. Xiao Y, Yang RZ, Shan B (2013) Production, environmental impact and mechanical properties of glubam. Constr Build Mater 44:765–773. https://doi.org/10.1016/j.conbuildmat.2013.03.087
8. Sharma B, Gatoo A, Bock M, Mulligan H, Ramage M (2015) Engineered bamboo: state of the art. Proc Inst Civ Engineers: Constr Mater 168(2):57–67. https://doi.org/10.1680/coma.14.00020
9. Liu X et al (2016) Engineered bamboo nomenclature
10. Sharma B, Gatóo A, Bock M, Ramage M (2015) Engineered bamboo for structural applications. Constr Build Mater 81:66–73. https://doi.org/10.1016/j.conbuildmat.2015.01.077
11. Raj D, Agarwal B (2014) Bamboo as a building material and its processing methods. J Civ Eng Environ Technol 1(3): 56–61. https://www.krishisanskriti.org/vol_image/03Jul201502074415.pdf
12. Masdar A, Siswosukarto S, Suryani D (2020) Implementation of connection system of wooden plate and wooden clamp on joint model of bamboo truss structures. Int J GEOMATE 17(59): 15–20. https://doi.org/10.21660/2019.59.4589
13. Gutu T (2013) A study on the mechanical strength properties of bamboo to enhance its diversification on its utilization. Int J Innov Technol Exploring Eng (IJITEE) 5:314–319
14. Yang RZ, Xiao Y, Lam F (2014) Failure analysis of typical glubam with bidirectional fibers by off-axis tension tests. Constr Build Mater 58:9–15. https://doi.org/10.1016/j.conbuildmat.2014.02.014
15. Xiao Y (2016) Engineered bamboo. In: Nonconventional and vernacular construction materials, Elsevier, pp 433–452. https://doi.org/10.1016/b978-0-08-100038-0.00015-9
16. Castaneda H, Bjarnadottir S (2016) Analysis of the bolted connection of a bamboo composite i-shaped beam subjected to bending. Procedia Eng 145(December):796–803. https://doi.org/10.1016/j.proeng.2016.04.104
17. Wang Z et al (2021) Bamboo node effect on the tensile properties of side press-laminated bamboo lumber. Wood Sci Technol 55(1):195–214. https://doi.org/10.1007/s00226-020-01251-9
18. Li H-T, Deeks AJ, Zhang Q-S, Wu G, Flexural performance of laminated bamboo lumber beams
19. Yu Y, Zhu R, Wu B, Hu Y, Yu W (2015) Fabrication, material properties, and application of bamboo scrimber. Wood Sci Technol 49(1):83–98. https://doi.org/10.1007/s00226-014-0683-7
20. Kumar A et al (2016) Engineered bamboo scrimber: Influence of density on the mechanical and water absorption properties. Constr Build Mater 127:815–827. https://doi.org/10.1016/j.conbuildmat.2016.10.069
21. Luo X, Wang X, Ren H, Zhang S, Zhong Y (2022) Long-term mechanical properties of bamboo scrimber. Constr Build Mater 338(February): 127659. https://doi.org/10.1016/j.conbuildmat.2022.127659
22. Zhao W, Zhang J, Zhang W, Wang J, Wang G (2022) Changes in the structural composition and moisture-adsorption properties of mechanically rolled bamboo fibers. Materials 15(10). https://doi.org/10.3390/ma15103463
23. Yu Y, Liu R, Huang Y, Meng F, Yu W (2017) Preparation, physical, mechanical, and interfacial morphological properties of engineered bamboo scrimber. Constr Build Mater 157:1032–1039. https://doi.org/10.1016/j.conbuildmat.2017.09.185
24. Correal JF, Echeverry JS, Ramírez F, Yamín LE (2014) Experimental evaluation of physical and mechanical properties of Glued Laminated Guadua angustifolia Kunth. Constr Build Mater 73:105–112. https://doi.org/10.1016/j.conbuildmat.2014.09.056
25. Verma CS, Chariar VM (2012) Development of layered laminate bamboo composite and their mechanical properties. Compos B Eng 43(3):1063–1069. https://doi.org/10.1016/j.compositesb.2011.11.065

26. Verma CS, Sharma NK, Chariar VM, Maheshwari S, Hada MK (2014) Comparative study of mechanical properties of bamboo laminae and their laminates with woods and wood based composites. Compos B Eng 60:523–530. https://doi.org/10.1016/j.compositesb.2013.12.061
27. Sinha A, Way D, Mlasko S (2014) Structural performance of glued laminated bamboo beams. J Struct Eng 140(1). https://doi.org/10.1061/(asce)st.1943-541x.0000807
28. Chen G, Yu Y, Li X, He B (2020) Mechanical behavior of laminated bamboo lumber for structural application: an experimental investigation. Eur J Wood Wood Prod 78(1):53–63. https://doi.org/10.1007/s00107-019-01486-9
29. He S, Xu J, xing Wu Z, Yu H, he Chen Y, gang Song J (2018) Effect of bamboo bundle knitting on enhancing properties of bamboo scrimber. Eur J Wood Wood Prod 76(3): 1071–1078. https://doi.org/10.1007/s00107-017-1263-y
30. Sharma B, Shah DU, Beaugrand J, Janeček ER, Scherman OA, Ramage MH (2018) Chemical composition of processed bamboo for structural applications. Cellulose 25(6):3255–3266. https://doi.org/10.1007/s10570-018-1789-0
31. Mahdavi M, Clouston PL, Arwade SR (2012) A low-technology approach toward fabrication of laminated bamboo lumber. Constr Build Mater 29:257–262. https://doi.org/10.1016/j.conbuildmat.2011.10.046
32. Sharma B, Gatóo A, Ramage MH (2015) Effect of processing methods on the mechanical properties of engineered bamboo. Constr Build Mater 83:95–101. https://doi.org/10.1016/j.conbuildmat.2015.02.048

Experimental Study on Mechanical Properties of Fiber Reinforced Concrete Under Traffic Disturbance Environment

Meng Lian, Licun Yu, Zhaohua Yuan, Li Pang, and Ding Chang

Abstract In order to explore the mechanical properties of bridge widening joint materials under vehicle-bridge coupling vibration environment. Based on the reconstruction and expansion project of Shenzhen Airport to He'ao Section of Shenhai Expressway (Ji-He Expressway), this paper first conducts field tests on the vehicle-bridge coupling vibration characteristics of typical bridges, and obtains the maximum vibration velocity of 18 mm/s and the maximum vibration frequency of 5.62 Hz. Then, the conventional vibration environment and limit vibration environment were set, and the mechanical properties of fiber reinforced cement matrix composite 50(FRCM50) at different ages under vibration environment were tested through laboratory tests. The results show that the vibration environment has a certain influence on the mechanical properties of FRCM50, but there is no definite rule. In general, the vibration environment has an adverse effect on the disturbance period, cube compressive strength and flexural strength of FRCM50. It has a beneficial effect on elastic modulus; it has little effect on the splitting tensile strength. Moreover, the vibration environment increases the discreteness of FRCM50 mechanical property test results.

Keywords Engineering material · Mechanical properties · Experimental research · Field test · FRCM50 · Vehicle—bridge coupling vibration

M. Lian
Shenzhen Expressway Co., Ltd., Shenzhen, China

L. Yu (✉) · Z. Yuan · L. Pang · D. Chang
CCCC First Highway Consultants Co., Ltd., Xi'an, China
e-mail: 727705858@qq.com

L. Yu
School of Highway, Chang'an University, Xi'an, China

H.-Y. Jeon (ed.), *Proceedings of the International Conference on Geosynthetics and Environmental Engineering*, Lecture Notes in Civil Engineering 374,
https://doi.org/10.1007/978-981-99-4229-9_14

1 Introduction

The existing bridge widening project often adopts the method of interrupting traffic to carry out the construction of post-cast joints, so as to ensure the construction quality of widening joints. However, interruption of traffic construction will produce a lot of economic losses and negative social impacts. Therefore, the study of bridge widening technology without interrupting traffic state is of great significance. The study of mechanical properties of early age joint materials under vehicle-bridge coupling vibration environment is of great significance to the design and construction of bridge widening without interruption.

The vehicle-bridge coupling vibration will accompany the whole process of concrete strength formation without interrupting the construction of wide joint of traffic bridge. Vibration has a certain impact on the mechanical properties of concrete [1], and the addition of fibers in concrete can effectively improve the vibration resistance of concrete [2].

Domestic and foreign scholars have conducted some studies on the forming effect of concrete under vehicle-bridge coupled vibration environment. Wei Jianjun [3] found that the tensile strength of concrete changed little when the low-frequency vibration amplitude was less than 3 mm, but when the amplitude was greater than 5 mm, the tensile strength of concrete decreased to a certain extent. Dunham and Rush [4] found that the vibration environment increased the compressive strength of concrete, but decreased the splitting tensile strength. Dunham [5] found through the test that the concrete vibrated within 4 h after pouring, and the strength increased by about 14%. However, after 5~6 h after pouring, the concrete strength is reduced to a certain extent.

In the existing studies, the influence of the vibration environment on the mechanical properties of concrete is still not conclusive, and there are few studies on the influence of vibration on fiber reinforced concrete. In this paper, combined with the field test and the laboratory test, the mechanical properties of FRCM50 in early age under the vibration environment are studied by simulating the vehicle-bridge coupling vibration environment using a shaking table.

2 Mix Proportion and Test Design

2.1 Raw Material

FRCM50 is obtained in proportion to the formulation. Among them, 18 portions of ordinary Portland cement; Shandong Yingrun sulphoaluminate cement 8 parts; 45 quartz sand; gravel diameter 5–10 mm; Beijing Zhongxin Nanotechnology Co., Ltd. heavy calcium stone powder 8 Longbin Lide company anti-cracking agent 0.7; 0.015 portions of basalt fiber; Beijing Zhongxin Nanotechnology Co., Ltd. Early Strength Agent 12.5; sika WR-9 water reducing agent 1.3 parts; 13 water.

2.2 Vibration Frequency and Peak Vibration Velocity

In the existing research, there are two main ways to simulate the FRCM50 vibration environment:1. vehicle-bridge coupling vibration frequency and vehicle-bridge coupling vibration amplitude [6–9]. Vehicle-bridge coupled vibration frequency and vehicle-bridge coupled vibration peak velocity (ppv) [10–16]. In this paper, vehicle-bridge coupling vibration frequency and vehicle-bridge coupling vibration peak velocity are used as parameters of vibration environment. In the existing research, the vibration frequency and amplitude parameters of the bridge are shown in Table 1.

The analysis shows that the vibration frequency and vibration velocity of existing scholars are quite different, and no conclusion has been formed. In order to obtain more accurate vibration parameters, field measurement was carried out on four typical bridges in the reconstruction and expansion project of locomotive-load high-speed, and the vibration environment parameters are shown in Table 2.

Table 1 Vibration environment in related literature

Reference	Vibration frequency (Hz)	PPV (mm/s)
Furr a ingram [10]	6.7	–
Howard [11]	4	36
Müller-Roch holzand Weber [12]	5, 12	30
Brandl and Günzle [13]	5, 20, 35	20
Silfwerbrand [14]	4	≤7
		≤24
Cusson and Repette [15]	3.5	–
Sungnam Hong and Sun-Kyu Park [16]	5	3
		4.5
		6
		10

Table 2 Field measured vibration parameters

Structural style	Span (m)	Vibration frequency (Hz)	Ppv (mm/s)
Pre-stressed concrete hollow slab bridge	20	5.62	11
Cast-in-situ reinforced concrete continuous box girder bridge	25	5.156	7
Simply supported prestressed concrete ‘I’ beam bridge	30	5.219	18
Simply supported prestressed concrete ‘I’ beam bridge	30	5.125	14

Because the measured results are still random, according to the measured results, the conventional vibration environment 5 Hz, 25 mm/s (Fig. 1); limit vibration environment 10 Hz, 50 mm/s (Fig. 2). The frequency and velocity of the shaking table will decay when propagating to the surface of the sample, so the measured surface velocity of the sample is the standard.

Fig. 1 Conventional vibration environment

Fig. 2 Extreme vibration environment

2.3 Test Scheme

The test steps were as follows: cement, quartz sand, early strength agent, short-cut fiber and heavy calcium powder were fully stirred according to the above proportion. After mixing evenly, water and water reducer were added for slurry mixing, and the time was controlled in 5~8 min. After stirring, the fiber FRCM50 material was loaded into the test model of the corresponding mechanical test.

In this experiment, three replicate groups were set for each test item to test the mechanical properties of FRCM50 at different ages under different vibration environments. The vibration environment includes conventional vibration environment (5 Hz, 25 mm/s) and limit vibration environment (10 Hz, 50 mm/s). The test items include initial and final setting time, cube compressive strength, flexural strength, elastic modulus and splitting tensile strength; the test time was 1 h, 2 h, 3 h and 28d after final setting except splitting tensile strength. The mechanical properties of splitting tensile strength were tested for 6 and 24 h. The corresponding mechanical property tests are carried out in accordance with the test procedure in regulation.

3 Experimental Results and Analysis

3.1 Effect of Initial/Final Coagulation Time and Disturbance Period

According to Refs. [17, 18], the disturbance period of concrete is the time from initial setting to final setting. This test is carried out according to the procedure [19]. In this experiment, three replicate groups were made.

(1) Non-vibration conditions: 60 min initial setting, 15~20 min difference between initial setting and final setting. (2) Conventional vibration conditions (>5 Hz, > 25 mm/s): 65 min initial setting, initial setting and final setting difference of 20~25 min. (3) Limit vibration conditions (>10 Hz, >50 mm/s): 65 min initial setting, initial setting and final setting difference of 20~25 min.

Comparing the test results, it can be found that for fiber reinforced concrete, the vibration environment increases the initial setting time of concrete by 5 min, but the initial setting time of conventional vibration environment is consistent with that of limit vibration environment. The vibration environment increases the time difference between initial setting and final setting of concrete by 5 min, but the initial setting time of conventional vibration environment is consistent with that of limit vibration environment. The test results show that the vibration environment will increase the susceptibility period of FRCM50.

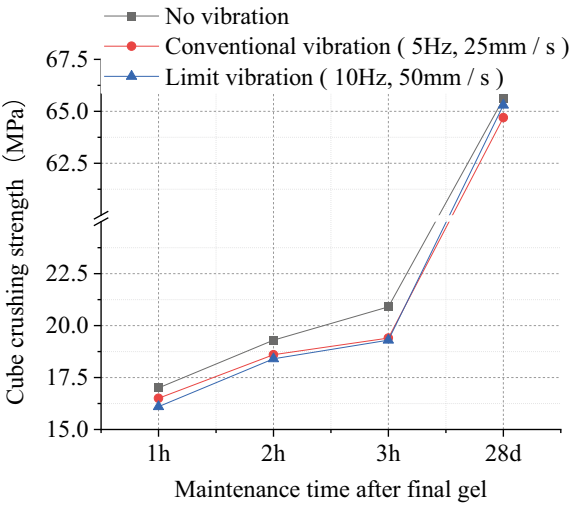

Fig. 3 Average compressive strength of cube at different ages

3.2 Influence of Cube Compressive Strength

The standard size of specimen was (150 × 150 × 150) mm. From Fig. 3, it can be seen that the cube average compressive strength of FRCM50 in vibration environment decreases at all ages compared with that in non-vibration environment. With the increase of vibration environment, the reduction of average cube compressive strength under ultimate vibration environment is greater than that under conventional vibration environment at 1, 2 and 3 h after final setting. However, at 28d, the reduction of average cube compressive strength under ultimate vibration environment is less than that under conventional vibration environment. The range can represent the dispersion degree of test results to a certain extent. It can be seen from Fig. 4 that the stronger the vibration environment is, the greater the dispersion of FRCM50 cube compressive strength is.

3.3 Influence Analysis of Flexural Strength

The standard size of specimen was (150 × 150 × 550) mm. Figure 5 shows that the flexural strength of FRCM50 under conventional vibration environment is less than that under non-vibration environment, and the reduction is between 2.67 and 14.29%. In the extreme vibration environment, the flexural strength of FRCM50 was smaller than that in the non-vibration environment before 3 h after final setting, and the decrease was 4~9.52%. After 3 h, it was larger than that in the non-vibration

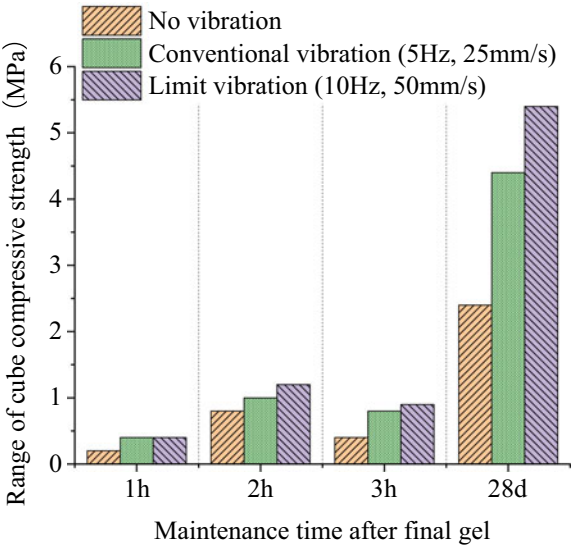

Fig. 4 Extreme compressive strength of cubes at different ages

environment, and the increase was 0~2.67%. It can be seen from Fig. 6 that the dispersion degrees of flexural strength in different vibration environments from large to small are limit vibration environment, non-vibration environment and conventional vibration environment.

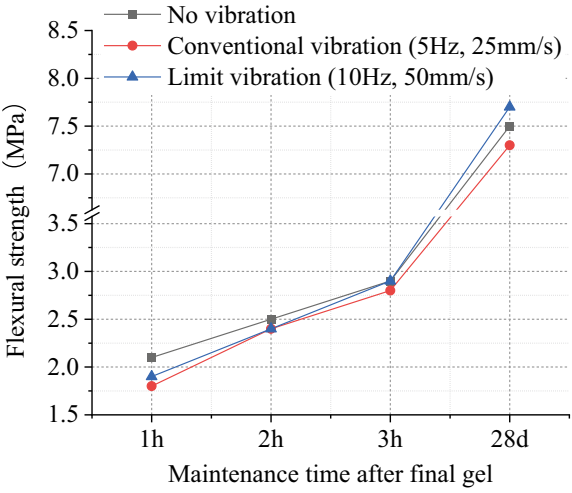

Fig. 5 Average flexural strength at different ages

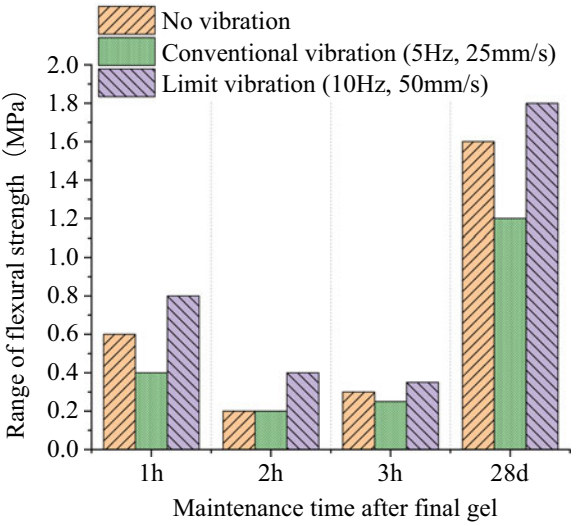

Fig. 6 Extremely poor flexural strength at different ages

3.4 Elastic Modulus Influence Analysis

The standard size of specimen was (150 × 150 × 300) mm. It can be seen from Fig. 7 that the elastic modulus of FRCM50 in the vibration environment is greater than that in the non-vibration environment except for the time point 1 h after final solidification. Among them, the elastic modulus of FRCM50 decreased by 0.73% and 2.19% respectively in conventional vibration environment and ultimate vibration environment at 1 h after final setting. In the test, the elastic modulus of the vibration environment at the time point increased by 0.56~2.74% in the conventional vibration environment and 1.24~5.08% in the limit vibration environment. In general, the vibration environment increases the elastic modulus of FRCM50. It can be seen from Fig. 8 that, in general, the dispersion degree of FRCM50 elastic modulus from large to small is the limit vibration environment, the conventional vibration environment and the non-vibration environment, respectively. The dispersion degree of elastic modulus in the limit vibration environment is small at 3 h.

3.5 Influence Analysis of Splitting Tensile Strength

The standard size of the specimen is (150 × 150 × 150) mm. Due to the large dispersion of the axial tensile test results of concrete, this study explores the influence of vibration environment on the tensile strength of fiber reinforced concrete by splitting tensile test.

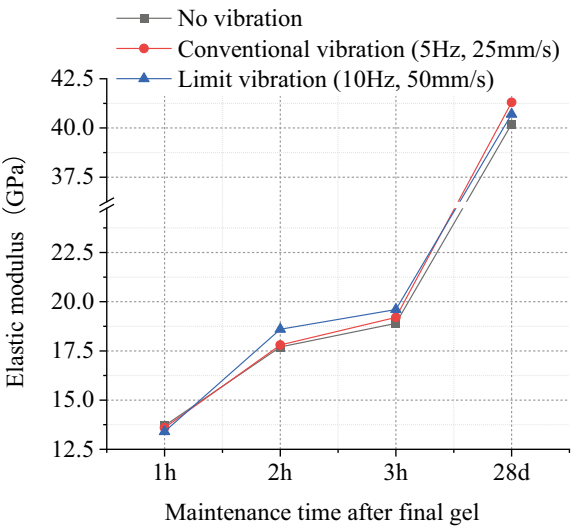

Fig. 7 Average elastic modulus at different ages

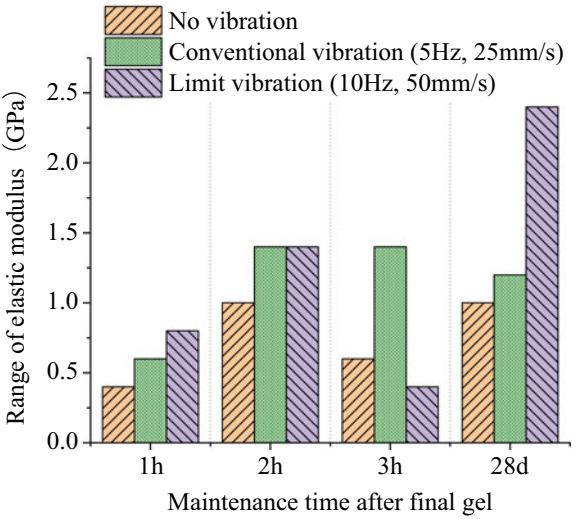

Fig. 8 Elastic modulus range of different ages

Figure 9 shows that different vibration environments within 24 h after final setting have little effect on the splitting tensile strength of FRCM50, and there is no obvious enhancement or weakening phenomenon. However, the splitting tensile strength of FRCM50 in the vibration environment at 28 d is greater than that in the non-vibration environment, and the ultimate vibration environment is greater than that in the conventional vibration environment. Among them, the splitting tensile strength of FRCM50 in the vibration environment is higher than that in the non-vibration environment, namely, there is an increase and a decrease, and there is no obvious

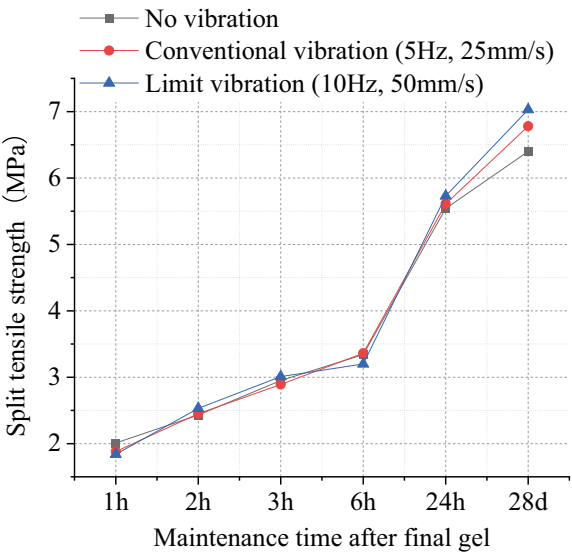

Fig. 9 Average splitting tensile strength at different ages

rule. Compared with the conventional vibration environment and the limit vibration environment, that is, there is a situation where the impact of the limit vibration environment is greater than that of the conventional vibration environment, and there is a contrary situation, and there is no obvious rule. It can be seen from Fig. 10 that the range of splitting tensile strength did not exceed 0.5in the first 6 h, and the range of splitting tensile strength was 0.86~3.12 MPa at 1d and 28d. In vibration environment, the splitting tensile strength of non-vibration environment is higher than that of vibration environment at 1 h, 2 h, 6 h and 24 h. 3 h and 28d are the discrete degree of vibration environment is greater than non-vibration environment. The results show that the vibration environment has no obvious regularity on the dispersion degree of FRCM50 splitting tensile strength.

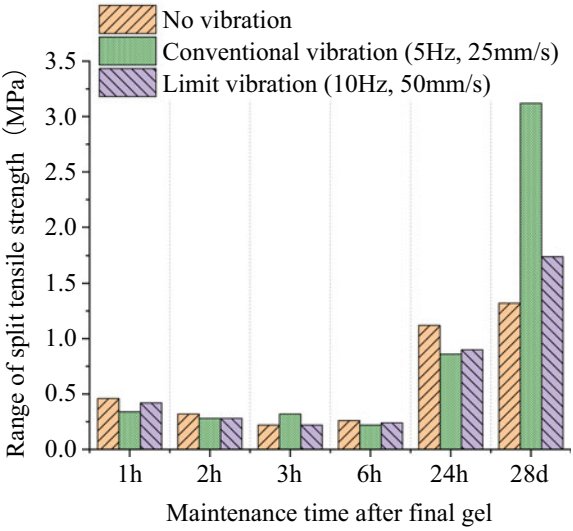

Fig. 10 Splitting tensile strength range of different ages

4 Conclusion

In this paper, the parameters of vehicle-bridge coupling vibration environment are obtained by the field test, and the mechanical properties of FRCM50 at different ages under the vibration environment are obtained by laboratory test. After analysis, the following conclusions are obtained which can be summarized like this:

1. Through the field test of the typical bridge, the maximum vibration frequency of the typical bridge is 5.62 Hz, 18 mm/s. Based on the principle of partial safety, the conventional vibration environment is 5 Hz, 25 mm/s and the limit vibration environment is 10 Hz, 50 mm/s.
2. By testing and analysing, the mechanical properties of FRCM50 at different ages in the vibration environment, it is found that the vibration environment increases the time of the susceptible period of FRCM50, reduces the cube compressive strength, and reduces the flexural strength, which has a negative impact on FRCM50 as a splicing joint. However, the vibration environment increases the elastic modulus of FRCM50, which has a favorable impact on FRCM50 as a splicing width joint. The vibration environment has no effect on the splitting tensile strength of FRCM50.
3. By analyzing the discreteness of the data, it is found that the overall vibration environment increases the discreteness of the mechanical properties of FRCM50.

References

1. Zhou L, Yongjuan Z (2008) Feasibility analysis of repairing concrete for uninterrupted traffic bridges. Guangdong Build Mater 6:56–28
2. Jing Z, Xinhua C, Hejun J (2007) Effect of hybrid fiber on early cracking behavior in concrete. J Harbin Inst Technol 2:232–234
3. Wei J, Xing J, Fu Z (2010) Effect of traffic load induced bridge vibrations on concrete tensile properties. J Southeast Univ (Natural Science Edition) (5): 1058–1060
4. Issa MA, Ovitigala T, Ibrahim M (2015) Shear behavior of basalt fiber reinforced concrete beams with and without basalt FRP stirrups. J Compos Constr 20(4):04015083
5. Dunham MR, Rush AS, Hanson JH et al (2007) Effects of induced vibrations on early age concrete. J Perform Constr Facil 21:179–184
6. Huang W, Xi L, Yi J, Ling Y (2018) Research on vehicle vibration influence on the mechanical properties of fresh concrete. Concrete (07): 37–41+45
7. Bu L (2011) The research on influence of the post-casting section of continuous rigid bridge suffered vibration of train. Hunan University
8. Ye D, Shang S, Fan Y (2011) Research on construction of continuous beam bridge over railway under influence of vibration caused by running train. Highway (09): 20–24
9. Shang S, Ye D (2002) Experimental study on concrete strength, grip strength and shear strength of restrained beams with post-cast segment under long-term vibration, Special Invitation Report of the eleventh national conference on structural engineering. Engineering Mechanics Supplement. Beijing, pp 54–56
10. Furr HL, Ingram L (1972) Concrete overlays for bridge deck repair. Highway research record no. 400. highway research board, national academy of sciences. Washington DC, pp 93–104
11. Furr HL, Fouad FH (1982) Effect of moving traffic on fresh concrete during bridge-deck widening. Transportation research record no 860, pp 28–36
12. Müller-Rochholz JFW, Weber JW (1986) Traffic vibration of a bridge deck and hardening of lightweight concrete. Concr Int 11:23–26
13. Brandl H, Günzler J (1989) Einfluss von Erschütterungen im frühen Erhürtungsstadium von Beton auf den Haftverbund mit Stahl. Bauplanung-Bautechnik 43:13–16
14. Silfwerbrand J (1992) Influence of traffic vibration on repaired concrete bridge deck. In: Proceeding of the 3th international workshop on bridge rehabilitation. Darmstadt, Germany, pp 415–422
15. Cusson D, Repette WL (2000) Early-age cracking in reconstructed concrete bridge barrier walls. ACI Mater J 97(04):438–446
16. Sukaswang N, Nassif H (2012) Impact of adjacent lane traffic on the serviceability of concrete bridge decks. Special Publication 284:1–14
17. Yueran Z, Yongjuan Z, Xiong Z (2009) Study on anti-disturbance performance of concrete in hardening stage. China Concr Cem Prod 05:1–3
18. Yongjuan Z, Yueran Z, Xiong Z (2011) Three techniques to improve disturbance resistance of concrete. J Build Mater 14(01):26–29
19. Ministry of communications of the People's Republic of China (2005). Testing methods of cement and concrete for highway engineering JTG 3420-2020. Beijing, China Communications Publishing and Media Management Co., Ltd.

Engineering Cementitious Composite as Seismic Isolation: A Review of Its Application as Bendable Concrete

Francis Cayanan, Orlean G. Dela Cruz, Jhun M. Jacinto, Abdurauf I. Sawadjaan, and Abdurahman A. Hawari

Abstract By using high-ductile matrix material instead of just adding more reinforcement, Engineered Cementitious Composites (ECC) offers an alternate method of improving the ductility of structural components. The evolution of ECC over the years is outlined in this article through a critical review. To adequately assess the properties of ECC to perform identical functions of an earthquake resistance device, in particular, the Base Isolator (BI), ECC and BI were examined along with their most widely used types and fundamental characteristics. Engineers and researchers interested in employing ECC for seismic isolation in structures will find this paper valuable. This paper's abundance of knowledge could support the development of innovative applications and enhance the safety and longevity of building structures. In addition, the challenges for both ECC and BI were compiled as a guide for future research. The vast amount of valuable data presented in this paper can help with the future seismic isolation use of ECC.

F. Cayanan · O. G. Dela Cruz (✉) · A. I. Sawadjaan · A. A. Hawari
Graduate School, Polytechnic University of the Philippines, Manila, Philippines
e-mail: ogdelacruz@pup.edu.ph

F. Cayanan
e-mail: engrkikocayanan2@gmail.com

A. I. Sawadjaan
e-mail: sbduraufsawadjaan@gmail.com

A. A. Hawari
e-mail: abdurahmanhawari@gmail.com

F. Cayanan
Don Honorio Ventura State University, Bacolor, Philippines

J. M. Jacinto
Aurora State College of Technology, Baler Aurora, Philippines
e-mail: jhun.jacinto05@gmail.com

A. I. Sawadjaan · A. A. Hawari
Hawari Construction Corporation, Zamboanga, Philippines

H.-Y. Jeon (ed.), *Proceedings of the International Conference on Geosynthetics and Environmental Engineering*, Lecture Notes in Civil Engineering 374,
https://doi.org/10.1007/978-981-99-4229-9_15

Keywords Engineered cementitious composite · Seismic isolation · Base isolation · Construction materials · Bendable concrete

1 Introduction

A significant fraction of the world's population resides in areas at risk from earthquakes of different severity and frequency [1, 2]. One of nature's most significant threats is an earthquake, which historically has resulted in considerable human casualties and severe property destruction, especially to man-made buildings [3–5]. Massive seismic vibrations result from an abrupt release of energy in the Earth's crust, which causes seismic waves to flow through bedrock [4, 6]. The historical earthquake data gives sufficient proof of how various types of structures behave in different seismic events and thus have become a topic of study for engineers and scientists [7], which resulted in them to start paying more attention to reducing the damage caused by earthquakes [8]. In today's society, reinforced concrete is a crucial building component for civil infrastructure. Concrete technology has advanced quickly during the past decade [9]. In the present time, many buildings have asymmetrical elevation and plan arrangements, which in the future, could eventually experience disastrous shocks [10]. Numerous efforts to develop "anti-seismic structures" or structures that can endure seismic threats and provide some ground resistance during earthquakes have not produced satisfactory results [11]. An extremely efficient earthquake-resistance technique is the base-isolation system [12]. These are reliable solutions for strengthening structures' resilience capacity and seismic protection [13]. Its system's fundamental idea is to create a flexible interface between a structure's base and foundation [14]. A famous example to explain this is when a structure is resting on frictionless rollers; as the earth shakes, the rollers move freely, but the building above remains stationary [15], but unfortunately, there are yet no seismic isolation devices that can meet the stringent conditions necessary for their widespread use in practice [16]. Engineered Cementitious Composite (ECC) materials, a special kind of high-performance FRC (Fiber Reinforced Concrete) composite, have seen fast development in recent years [16, 17]. A particular requirement of concrete structures is an enhancement of a more efficient material, which results in the evolution of an ECC, also known as "Bendable concrete," that belongs to the ductile concrete family. A bendable concrete's ingredients include cement, fine aggregate, fiber, and chemical additive [18–21]. The ECC composition does not include coarse aggregate since it tends to develop wider cracks likely to harm its ductile behavior [19, 22]. According to research, ECC holds great potential as a novel structural technology for earthquake protection and disaster reduction [23, 24]. The commonly occurring localized fracture modes, such as dynamic spall ejection (under impact), bond splitting, surface spalling, shear fracture, and punching, are also prevented [25]. Furthermore, it can enhance concrete bending performance to increase service life while reducing the building's maintenance costs; thus, it significantly impacts the long-term sustainability of infrastructure development [26]. This study intends to critically evaluate

the prior research findings on the ECC and utilize them to discover its possible use as a novel material for an innovative earthquake-resistance technique, specifically in base isolation (as bearing).

2 Methodology

Figure 1 shows the systematic procedure for finding and choosing the relevant articles and journals that needed to include on this literature review. The researcher use websites to obtained research articles and journals such as Google Scholar, Scopus and Science Direct these website support Bolean Syntax. The keywords used in this review are engineered cementitious composite seismic, base isolation and concrete buildings. Most documents' method for retrieving literature is based on Elicit.org search results (Elicit: The AI Research Assistant). Elicit is a research assistant that automates some of the operations of researchers using language models like GPT-3. The primary workflow of Elicit at the moment is a literature review. If you ask a question, Elicit will display pertinent documents and concise summaries of essential details about those documents in a simple table [27] (Fig. 1).

3 Discussion

3.1 Base Isolation

Shifting the structure's fundamental frequency away from the dominant frequencies of seismic excitations and from the fundamental frequency of the fixed bases is one of the objectives of seismic isolation [28]. The isolators are commonly designed to absorb energy and give the system an added damping [29]. The most well-known base isolation systems used in existing structures are friction pendulums and elastomeric bearings [30]. However, a deeper understanding of the bearing-type earthquake-resisting system will only be aimed because it represents the possible application of ECC as a substitute material with high ductility and energy dissipation, matched with the properties of a suitable base isolator. The most common seismic base isolation technique is laminated rubber bearings because of their reliability and economic effectiveness [14, 31]. The elastomeric Lead Rubber Bearing (LRB), which is typically used for base isolation of structures, is made up of a central lead core, multiple layers of alternating rubber and steel shims, and two steel fastening plates at the top and bottom [32], with lead core, sizes varying from 15 to 33% of the bearing's bonded diameter [3]. The lead core's energy dissipation through yielding allows for an equivalent viscous damping coefficient of up to 30%, double that of high-damping elastomeric isolators [28, 33].

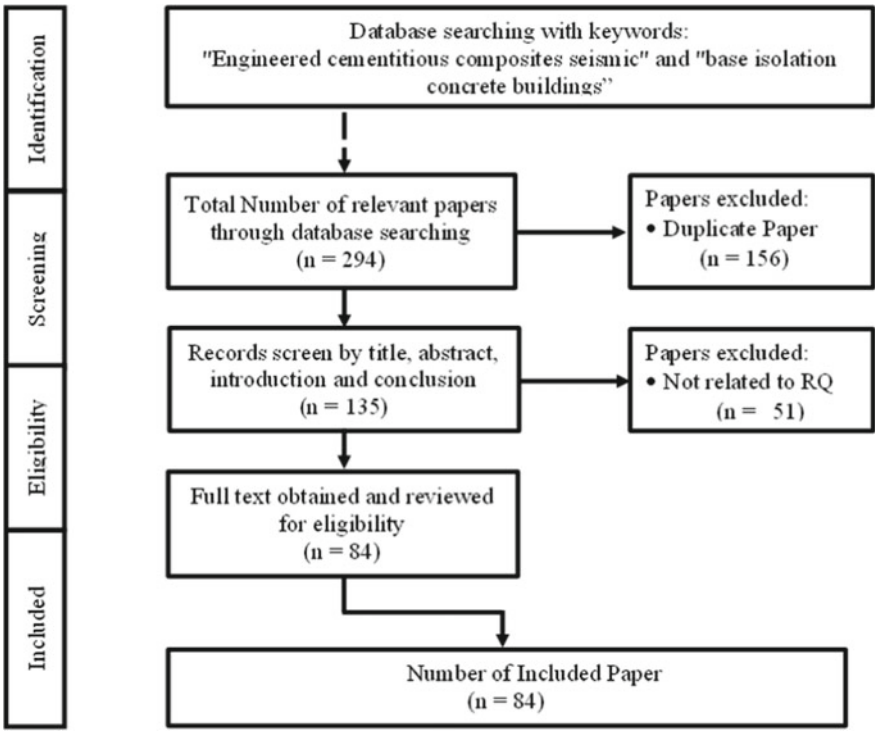

Fig. 1 Systematic related literature selection process

Similarly, the research of Gupta et al. (2014) also corroborated this conclusion, mentioning that the corresponding viscous damping caused by the hysteresis depends on displacement and typically falls between 15 and 35% [34]. Additionally, it is discovered that the LRB offers stiffness under service loads and energy dissipation under high lateral forces [7]. Given all the advantages of employing LRB that have been highlighted, it is essential to note that Gyawali et al. (2020) research concluded that, compared to fixed base buildings, the base shear value of LRB buildings had been lowered by 45 to 50% [2]. Furthermore, the outcomes discovered by Kabeer et al. (2014) found that using lead rubber bearings can result in a 20% reduction in the needed reinforcement [35].

3.2 ECC Properties

Lack of ductility and strain capacity is a significant problem for normal concrete [19]. At the same time, ECC can reach very high curvature at increasing loads similar to a ductile metal plate yielding [22], in addition to the highly narrow crack width (often

less than 80 μm) [9]. The material can demonstrate significantly increased flexibility since the tensile strain capacity of ECC can range from 3 to 5%. Compared to normal concrete and fiber-reinforced concrete, this results in 300–500 times the tensile strain capacity [19]. Concrete has good compression strength but is weak in tension [22]. Normal concrete has a tensile strength of only 10% of its compressive strength, and brittle concrete will crack when exposed to tensile forces [36]. Concrete's tendency to break easily has been addressed by the development of Engineered Cementitious Composites (ECC), also known as "Bendable Concrete" [19]. In a study conducted by Kumar et al. [37], Ordinary Portland Cement, Fly Ash (mainly Class F-ASTM C618), Ground Granulated Blast-furnace Slag (GGBS), Silica fume and sand, Super Plasticizers, and PVA (Polyvinyl alcohol) fibers are all utilized in the proportion of the ECC mix. The outcome demonstrates that the UHP (ultra-high performance)-ECC's compressive strength reached 150 MPa after 28 days of standard curing, while the tensile strength and strain capacity was 18 MPa and 8%, respectively [37].

Similarly, Kumar et al. (2021) also noted an improvement in compressive strain capacity where ECC acquired 0.45–0.65 percent [37]. Generally, it is said that ECC technology focuses more on increasing the flexural strength and does not significantly increase the compressive strength of the concrete [19]. It is one of the subject matters that will be recommended for further studies. Deshpande et al. (2016) research summary also mentioned that, although the compressive strength of ECC and normal concrete is about the same in their experiment, the flexural strength of ECC is 60% greater than that of conventional [20]. In the same manner, ECC specimen beams produced more flexural strength than traditional concrete beams would typically produce, as s concluded from a study by Bins et al. [19]. Under the principles of performance-based engineering, applications of ECC to energy absorption devices and damage-tolerant structural parts are considered to meet the performance criteria of structures [24]. ECC increased overall energy dissipation for non-seismic beam-column sub-assemblages by about 76% [17]. In addition, the ECC/RC composite frame exhibited increased equivalent damping ratio, absolute displacements, and decreased inter-story drifts and roof acceleration. These findings show that the ECC/RC composite frame outperforms the RC frame regarding damage resistance, less stiffness reduction, deformation capacity, and energy dissipation [38]. The ECC/RC composite frame requires fewer stirrups in beam-to-column connections than the RC frame [38]. It was also discovered that specimens with ECC had significantly higher ultimate loads (indicating inter-story shear) [39]. Similarly, the ECC considerably improved the short-span beam's shear performance under cyclic loading [21]. In the joint zones, it exhibits fewer flexural-shear cracks. In the ECC/RC composite frame, no major macrocracks or ECC spalling were found. Therefore, ECC can dramatically reduce structural damage and increase shear resistance [38].

3.3 ECC and Its Potential Seismic Isolation Application

The unique properties of ECC, such as high ductility, flexibility, strain capacity, energy dissipation, and shear strength, among others, matched with the fundamental characteristics of a base isolator, make it a candidate for an alternative, low-cost and innovative type of material.

The exemplary performance of ECC under different loading conditions, both in gravity and lateral loads, done by previous researchers, can motivate the further improvement of the study. Experimentation may start with low-rise buildings, especially those located in seismic-prone areas, and as the technology progresses, an application may extend even to medium and high-rise structures. Tables 1 and 2 shows the tabulation of selected studies and the outcomes measured about ECC and BI over the years.

Table 3 shows the study conducted wherein a lead rubber bearing with steel rings known as RRB is devised and used in three to six-story steel and concrete structures, and the outcomes are contrasted with those of fixed base, and base-isolated using LRB [80]. The same categories were compared against the performance of ECC in various research types. Although the authors did not indicate the numerical values in most of the selected reviewed articles, the descriptive conclusions at the end of each study reveal that using ECC had demonstrated better performance and positive benefits to the system. Many sources used graphical illustrations to emphasize the comparison of the variables; unfortunately, the scale is of large intervals, and specific values of significant points are not annotated in the image or figures. Nevertheless, it can be seen that the affirmative results derived from the earlier studies about the ECC show equal or better performance in comparison to the improvements acquired from using BI, such as LRB and RRB. Although it has been proven many times that ECC has high ductility, strain capacity, energy dissipation, and others, further studies about the best mix design and its specific application in the structure to acquire the most excellent performance, specifically, its use as a base isolator still needs to be done.

4 Research Gaps

Future Research Recommendations in ECC and Base Isolation are summarized. For ECC, it will be (1) Relaxing the ratio of column flexural moment to beam flexural moment is a possibility; Plastic Hinges [17], (2) Replacement of conventional concrete: Fully or Partially [57, 80], (3) Seismic performance of buildings (Level of collapse); Material properties and design [24], (4) Corrosion Testing, [46, 57, 81, 82], (5) Dimension stability; Alternate type of aggregates [82], (6) Numerical simulation and Theoretical analysis [62], (7) Cost [20, 22], (8) Poisson's Ratio; Shear resistance [20, 22] While for BI, (9) Cost [82], (10) Construction aspects [31]. It can be seen

Table 1 ECC developments over the years

Refs.	Year	Outcomes measured	
Yao et al. [20]	2013	• Strain hardening property	• The strain capacity
Dehghani et al. [47]	2014	• Flexural strength	• Flexural toughness
Gencturk et al. [48]	2015	• Lateral strength and energy absorption capacity of the infilled frame • The prevention of brittle failure modes in the infill wall • The provision of a reasonable system overstrength	
Li and Kanda [21]	2016	• Ductile and properties of regular concrete	
Sun et al. [51]	2017	• Development and study of Engineered Cementitious Composites using High Volume Fly Ash and Polyvinyl Alcohol Fiber	
Hosseini and Gencturk [52]	2018	• Hysteretic behavior, ductility, stiffness, energy dissipation, damping characteristics, and cracking patterns of HPFRCC beam-column joint connections	
Han et al. [53]	2018	• Failure modes • Peak stress • Peak strain • Elastic modulus • Toughness index stress–strain curves	
Wu et al. [26]	2019	• Delayed failure • Limited degradation in structural function during the load event	• Rapid recovery of structural functions post events
Cho et al. [54]	2019	• Lateral strength • Shape of the hysteresis curves	• Permanent deformation • Post-peak degradation
Sasi and Varghese [55]	2019	• Tensile performance	• Crack resistance
Cementitious [55]	2019	• Applicability of the high ductile fiber cementitious composite to develop seismically improved reinforced concrete columns • The seismic capacity of the column • The minimization of flexural and shear cracks in the bending critical region of the column	
Dong et al. [57]	2020	• Stiffness • Ductility	• Drift capacity • Overall strength
Lv et al. [58]	2020	• HPFRCC bridge columns' large-scale seismic behavior	
Crack-free engineered cementitious composites to overcome durability [59]	2020	• Probability of the frame structure under various damage states	

(continued)

Table 1 (continued)

Refs.	Year	Outcomes measured			
Etman et al. [60]	2020	• Fluidity • Bonding strength • Flexural strength	• Tensile strength • Strain capacity • Compressive strength • Fracture energy		
Chen et al. [61]	2020	• Strain capacity of the Engineered Cementitious Composites			
Deshpande and Murnal [20]	2021	• Compressive strength	• Flexural strength		
Dadkhah and Tulliani([62]	2021	• Splitting tensile strength	• Cracking width	• Flexural strength	
Stiemer and Barwig [63]	2022	• Failure mod		• Hysteretic behave	• Crack pattern
		• Energy dissipation capacity			• Stiffness degradation
		• Displacement ductility			
Ferritto [64]	2022	• Ability of ECC to partly replace transverse reinforcements and enhance the joint shear resistance, the energy absorption capacity, and the cracking response of concrete structures in seismic areas			

Table 2 BI development over the years

Refs.	Year	Outcomes measured
Minal et al. [29]	2013	• Maximum floor acceleration • Inter storey drifts • Storey shear forces
Dhawade [1]	2013	• Seismic performance of base-isolated and fixed based RC frame structures
Hu [77]	2013	• Minimum displacements • Minimum base shear forces • Minimum accelerations
Sorace and Terenzi [78]	2014	• Reduction in seismic responses
Talikoti and Thorat [11]	2014	• Size of the building components
Yuan et al. [79]	2014	• Base shear • Inter-story drifts
Şahmaran and Li[36]	2014	• Displacement • Moment • Shear
Li and Maleej [80]	2014	• Most significant example of a base-isolated “artificial ground” ever built in Italy

Table 3 Comparative analysis of base isolated (LRB and RRB) versus fixed-base structures by [80] and ECC performance in various studies

	LRB	RRB	Fixed	ECC
The average effective parameters reduction in structural design				
Acceleration reduction (average %)	28.33	48.62	–	[a]Reduced [38]
Displacement reduction (average %)	23.53	49.87	–	[b]Superior damage tolerance [41]
Shear reduction (average %)	32.87	49.21	–	–
Period of fixed base and isolated structures (seconds) (3-25-C) 3-story concrete structure with 25 columns	1.775	1.784	0.658	–
The damping ratio of structures (average %)	18.44	47.02	–	[a]17.92% [38]
Story drift reduction (average %)	23.53	49.87	–	[b]Improved [56]

[a]With respect to the separate structure analyzed in the study
[b]No detailed numerical data was provided, but it concluded descriptively

that for both ECC and Base Isolation, the "Cost" is the standard item. However, it should be made clear that the "cost" being mentioned for ECC is that which is compared to standard concrete, while, for Base Isolation, it is that which is being compared to the traditional lateral force-resisting frame. However, if the subsequent studies can develop an ECC with the same character as the Base Isolation bearings, a save percentage in multiple hundreds can be acquired as ECC will undoubtedly be cheaper in many ways than Base Isolation.

5 Conclusion

This comprehensive review paper synthesizes existing literature on the ECC and Base Isolation. ECC is a new product that can replace the existing materials of widely used base isolation (bearing type) systems. However, a long way to its complete perfection lies ahead. Nevertheless, based on the investigations, the following conclusions can be drawn: The current developments in the properties of ECC are considered significant because some characteristics are already acquiring near or almost equivalent strengths necessary for a good base isolation material. Using ECC as an alternative material for base isolation is feasible for engineering structures such as low to medium-rise buildings. The results acquired from the experiments show an excellent load-carrying capacity, flexibility, and energy dissipation, which are some of the vital requirements to sustain the gravity and lateral loads experienced by the isolator. This proposal promises to provide a low-cost alternative material for base isolation use, which can benefit the community, especially those in the area of high seismic hazard.

References

1. Dhawade SM (2014) Comparative study for seismic performance of base isolated and fixed based RC frame structure. Int J Civ Eng Res 5(2):183–190
2. Gyawali S, Thapa D, Bhattarai TR (2020) Effect of base isolation in multistoried RC regular and irregular building by using response spectrum analysis. Saudi J Civ Eng 4(5):77–84. https://doi.org/10.36348/sjce.2020.v04i05.004
3. Nassani DE, Abdulmajeed MW (2015) Seismic base isolation in reinforced concrete structures. Int J Res Stud Sci, Eng Technol 2(2):1–13
4. Shaikh OK (2018) Analysis and seismic response reduction of 10, 15, 20 storey building using base isolation. Int J Res Appl Sci Eng Technol 6(1):2802–2805. https://doi.org/10.22214/ijraset.2018.1385
5. Rajput G, Mishra V (2022) Seismic performance of multi story building with different base isolators. Int J Res Appl Sci Eng Technol 10(8):1259–1264. https://doi.org/10.22214/ijraset.2022.46403
6. Keerthana S, Sathish Kumar K, Balamonica K (2015) Seismic response reduction of structures using base isolation. IJISET-Int J Innov Sci, Eng Technol 2(2): 33–40. www.ijiset.com
7. Swathirani KS (2015) Eatrhquake response of reinforced cocrete multi storey building with base isolation. Int J Res Eng Technol 04(10):158–167. https://doi.org/10.15623/ijret.2015.0410028
8. Sun HL, Li Q (2010) Research and development of seismic base isolation technique for civil engineering structures. In: 2010 international conference on E-product E-service and E-entertainment, ICEEE 2010. https://doi.org/10.1109/ICEEE.2010.5660364
9. Şahmaran M, Li VC (2010) Engineered cementitious composites: can composites be accepted as crack-free concrete? Transp Res Rec 2164:1–8. https://doi.org/10.3141/2164-01
10. Beeraiah B, Sekhar GC, Earthquake response of reinforced concrete multistory building with base isolation 2(18): 149–154
11. Talikoti RS, Thorat VR (2014) Base isolation in seismic structural design 3(7): 863–868
12. Hu X, Zhou Z (2020) Seismic analysis of a reinforced concrete building isolated by high damping rubber bearings using deformation history integral type model. Struct Des Tall Special Build 29(18):1–13. https://doi.org/10.1002/tal.1811
13. Lopez-Almansa F, Piscal CM, Carrillo J, Leiva-Maldonado SL, Moscoso YFM (2022) Survey on major worldwide regulations on seismic base isolation of buildings. Adv Civ Eng 2022. Hindawi Limited. https://doi.org/10.1155/2022/6162698
14. Sabu SK, Chore HS, Patil SB, Effectiveness of lead rubber base isolators, for seismic resistance of buildings, supported on different soil stratas 1
15. Barbat AH, Bozzo LM (1997) Seismic analysis of base isolated buildings. Arch Comput Methods Eng 4(2):153–192. https://doi.org/10.1007/BF03020128
16. Banović I, Radnić J, Grgić N, Matešan D (2018) The use of limestone sand for the seismic base isolation of structures. Adv Civ Eng 2018. https://doi.org/10.1155/2018/9734283
17. Lee SW, Tan KH, Yang EH (2018) Seismic behaviour of interior reinforced-concrete beam-column sub-assemblages with engineered cementitious composites. Mag Concr Res 70(24):1280–1296. https://doi.org/10.1680/jmacr.17.00359
18. Alyousif A, Anil O, Sahmaran M, Lachemi M, Yildirim G, Ashour AF (2016) Comparison of shear behaviour of engineered cementitious composite and normal concrete beams with different shear span lengths. Mag Concr Res 68(5):217–228. https://doi.org/10.1680/jmacr.14.00336
19. Bins SR, Kumar CS, Togi S, George M (2021) A study of engineered cementitious composites by investigating its compressive and flexural strength 1–12
20. Deshpande UL, Murnal PB (2016) Ductile concrete using engineered cementitious composites. Issue: Special 3(5): 756–760
21. Li VC, Kanda T, Engineered cementitious composites for structural applications
22. Dhawale AW, Joshi VP (2013) Engineered cementitious composites for structural applications. Int J Appl Innov Eng M0anage (IJAIEM) 2(4): 198–205

23. Yao S, Zhang J, Tu Y (2011) Application of engineered cementitious composites for earthquake resistance and disaster mitigation of structures. Adv Mat Res 168–170:1665–1669. https://doi.org/10.4028/www.scientific.net/AMR.168-170.1665
24. Fukuyama H, Sato Y, Matsuzaki Y, Mihashi H (2000) Ductile engineered cementitious composite elements for 12 Wcee 2000, 1–8
25. Li VC (2019) Resilience of engineered cementitious composites (ECC) structural members. https://doi.org/10.1007/978-3-662-58438-5_6
26. Wu Y, Sun Q, Li W (2012) Improved bending strength and early crack-resistance performance of engineered cementitious composites reinforced by hybrid-fiber. Appl Mech Mater 174–177:1047–1050. https://doi.org/10.4028/www.scientific.net/AMM.174-177.1047
27. What is Elicit? (2022). https://elicit.org/faq
28. Santhosh HP (2013) Seismic analysis of low to medium rise building for base isolation. Int J Res Eng Technol 02(13): 1–5. https://doi.org/10.15623/ijret.2013.0213001
29. Minal M, Somwanshi A, Pantawane RN (2015) Seismic analysis of fixed based and base isolated building structures. Int J Multidisc Curr Res 3:747–757
30. Briman V, Ribakov Y (2008) Seismic isolation columns for earthquake-resistant structures. Struct Des Tall Special Build 17(1):99–116. https://doi.org/10.1002/tal.321
31. Amin A, Islam M, Ahamed MJ (2020) Base isolation of multi-storied building using lead rubber bearing. ITEGAM- J Eng Technol Indus Appl (ITEGAM-JETIA) 6(26): 52–60. https://doi.org/10.5935/jetia.v6i26.697
32. Andrade L, Tuxworth J (2009) Seismic protection of structures with modern base isolation technologies. Concrete Solutions Paper 7a-3, 1: 1–10
33. Ivan Skinner Trevor Kelly RE, Robinson B, Seismic isolation for designers and structural engineers. www.rslnz.com
34. Gupta N, Sharma D (2014) State of art review-base isolation for structures. Int J Sci Eng Res 5(5). http://www.ijser.org
35. KI SAK, Sanjeev Kumar KS (2014) Comparison of two similar buildings with and without base isolation. Int J Adv Res 1(1)
36. Şahmaran M, Li VC (2009) Engineered cementitious composites: an innovative concrete for durable structure. In: Proceedings of the 2009 structures congress - don't mess with structural engineers: expanding our role, pp 2219–2231. https://doi.org/10.1061/41031(341)243
37. Kumar PGSMN, Kumar KS (2021) A review on fundamentals of engineered cementitious composite (bendable concrete). Int J Sci Res Eng Trends 7(4): 1–4
38. Xu L, Pan J, Leung CKY, Yin W (2018) Shaking table tests on precast reinforced concrete and engineered cementitious composite/reinforced concrete composite frames. Adv Struct Eng 21(6):824–837. https://doi.org/10.1177/1369433217733759
39. Qudah S, Maalej M (2014) Application of engineered cementitious composites (ECC) in interior beam-column connections for enhanced seismic resistance. Eng Struct 69:235–245. https://doi.org/10.1016/j.engstruct.2014.03.026
40. Banthia N, Chokri K, Ohama Y, Mindess S (1994) Fiber-reinforced cement based composites under tensile impact. Adv Cem Based Mater 1(3):131–141. https://doi.org/10.1016/1065-7355(94)90044-2
41. Canbolat BA, Parra-Montesinos GJ, Wight JK, Paulay T (2005) Experimental study on seismic behavior of high-performance fiber-reinforced cement composite coupling beams. ACI Struct J 102(6):909–912
42. Rossi P (2005) Development of new cement composite materials for construction. Proc Inst Mech Engineers, Part L: J Mater: Des Appl 219(1):67–74. https://doi.org/10.1243/146442005X10193
43. Wang S, Li VC (2007) Engineered cementitious composites with high-volume fly ash. ACI Mater J 104(3):233–241. https://doi.org/10.14359/18668
44. Spagnoli A (2009) A micromechanical lattice model to describe the fracture behaviour of engineered cementitious composites. Comput Mater Sci 46(1):7–14. https://doi.org/10.1016/j.commatsci.2009.01.021

45. Cho C-G, Lim H-J, Yang K-H, Song J-K, Lee B-Y (2012) Basic mixing and mechanical tests on high ductile fiber reinforced cementless composites. J Korea Concr Inst 24(2):121–127. https://doi.org/10.4334/jkci.2012.24.2.121
46. Halvaei M, Jamshidi M, Latifi M (2014) Application of low modulus polymeric fibers in engineered cementitious composites. J Ind Text 43(4):511–524. https://doi.org/10.1177/1528083712465881
47. Dehghani A, Nateghi-Alahi F, Fischer G (2015) Engineered cementitious composites for strengthening masonry infilled reinforced concrete frames. Eng Struct 105:197–208. https://doi.org/10.1016/j.engstruct.2015.10.013
48. Gencturk B, Kaymaz I, Hosseini F (2016) Derivation of seismic design parameters for ECC and multi-material special moment-resisting frames. J Earthquake Eng 20(7):1054–1076. https://doi.org/10.1080/13632469.2016.1138161
49. Santhosh CH (2017) Engineered cementitious composites using high volume fly ash and PVA fibers for the sustainable development in construction industry. J Eng Res Appl 7(2): 35–39. https://doi.org/10.9790/9622.www.ijera.com
50. hossein Saghafi M, Shariatmadar H (2018) Enhancement of seismic performance of beam-column joint connections using high performance fiber reinforced cementitious composites. Constr Build Mater 180: 665–680. https://doi.org/10.1016/j.conbuildmat.2018.05.221
51. Sun L, Hao Q, Zhao J, Wu D, Yang F (2018) Stress strain behavior of hybrid steel-PVA fiber reinforced cementitious composites under uniaxial compression. Constr Build Mater 188:349–360. https://doi.org/10.1016/j.conbuildmat.2018.08.128
52. Hosseini F, Gencturk B (2019) Structural assessment of bridge columns with engineered cementitious composites and Cu-Al-Mn superelastic alloys. Constr Build Mater 203:331–342. https://doi.org/10.1016/j.conbuildmat.2019.01.102
53. Han YD, Wang Q, Wang ZB, Yao BY (2019) Mechanical properties and crack resistance of sustainable high strength engineered cementitious composites. IOP Conf Ser Mater Sci Eng 587(1). https://doi.org/10.1088/1757-899X/587/1/012011
54. Cho CG, Moon HJ, Kim HY, Lee KS (2019) Seismic-improved reinforced-concrete composite column using a high-ductile fiber cementitious composite precast box. J Asian Architecture Build Eng 18(2):131–141. https://doi.org/10.1080/13467581.2019.1603108
55. Sasi A, Varghese SM (2020) Review on seismic strengthening using eco friendly ductile cementitious composites (May): 5–8
56. Cementitious HF (2020) High-performance fiber-reinforced cementitious composites for seismic design: a review of columns (September)
57. Dong F, Yu J, Zhan K, Li Z (2020) Seismic fragility analysis of two-story ultra-high ductile cementitious composites frame without steel reinforcement. Adv Struct Eng 23(11):2373–2387. https://doi.org/10.1177/1369433220912350
58. Lv L, Hong X, Ding Z, Ma X, Li H (2020) Preparation and characterization of calcium sulfoaluminate based engineered cementitious composites for rapid repairing of concrete member. Front Mater 7(September):1–11. https://doi.org/10.3389/fmats.2020.00282
59. Crack-free engineered cementitious composites to overcome durability (2020), 11(10): 1–12. https://doi.org/10.34218/IJARET.11.10.2020.001
60. Etman Z, Saafan M, Rokbah S (2021) Mechanical properties of engineered cementitious composite materials using different types of fibers. ERJ. Eng Res J 44(4): 433–446. https://doi.org/10.21608/erjm.2021.80561.1099
61. Chen W, Feng K, Wang Y, Cui S, Lin Y (2022) Seismic performance of a novel precast beam-column joint using shape memory alloy fibers-reinforced engineered cementitious composites. Buildings 12(9). https://doi.org/10.3390/buildings12091404
62. Dadkhah M, Tulliani JM (2022) Damage management of concrete structures with engineered cementitious materials and natural fibers: a review of potential uses. Sustainability (Switzerland) 14(7). https://doi.org/10.3390/su14073917
63. Stiemer SF, Barwig BB (1985) Seismic base isolation for steel structures. Can J Civ Eng 12(1):73–81. https://doi.org/10.1139/l85-008

64. Ferritto JM (1991) Studies on seismic isolation of buildings. J Struct Eng 117(11):3293–3314. https://doi.org/10.1061/(asce)0733-9445(1991)117:11(3293)
65. Jain SK, Thakkar SK (2004) Application of base isolation for flexible buildings. In: 13th world conference on earthquake engineering, no 1924
66. Kelly T, Me S (2004) Usage of seismic base isolation to reduce the ductility demand from prefabricated concrete structures. Holmes Consulting Group Limited. Wellington, New Zealand, pp 1–10
67. Kaplan H, Aydilek AH (2006) Seismic analysis of a low-rise base-isolated structural system. J Low Freq Noise Vibr Active Control 25(2):93–109. https://doi.org/10.1260/026309206778494328
68. Kalantari SM, Naderpour H, Vaez SRH (2008) Investigation of Base-isolator type selection on seismic behavior of structures including story drifts and plastic hinge formation. In: The 14th world conference on earthquake engineering. Beijing, China
69. Saiful Islam ABM, Jameel M, Uddin MA, Ahmad SI (2011) Simplified design guidelines for seismic base isolation in multi-storey buildings for Bangladesh National Building Code (BNBC). Int J Phys Sci 6(23): 5467–5486. https://doi.org/10.5897/IJPS11.795
70. Mahmoud S, Austrell PE, Jankowski R (2012) Non-linear behaviour of base-isolated building supported on flexible soil under damaging earthquakes. Key Eng Mater 488–489:142–145. https://doi.org/10.4028/www.scientific.net/KEM.488-489.142
71. Nanda RP, Agarwal P, Shrikhande M (2012) Base isolation by geosynthetic for brick masonry buildings. JVC/J Vibr Control 18(6):903–910. https://doi.org/10.1177/1077546311412411
72. Soleimanloo HS, Soleimanloo MS (2012) Advance model for seismic base isolation systems of building
73. Cancellara D, De Angelis F (2012) Seismical protection properties of high damping rubber bearing and lead rubber bearing base isolation systems for multi-storey RC buildings. Appl Mech Mater 234:90–95. https://doi.org/10.4028/www.scientific.net/AMM.234.90
74. Ashok SP, Mehta N, Padhiyar M, Samare A, Patil Y (2012) Response spectrum analysis of multi storeyed base-isolated building 1, 2(3): 66–75
75. Dănilă G (2013) Seismic isolation systems for buildings subjected to vrancea earthquakes, no Lxiii
76. Sabu SK, Chore HS, Patil SB (2014) Effectiveness of lead rubber base isolators, for seismic resistance of buildings, supported on different soil stratas. Int J Electr, Electron Comput Syst 2(4):53–59
77. Hu JW (2015) Response of seismically isolated steel frame buildings with sustainable lead-rubber bearing (LRB) isolator devices subjected to near-fault (NF) ground motions. Sustainability (Switzerland) 7(1):111–137. https://doi.org/10.3390/su7010111
78. Sorace S, Terenzi G (2014) Analysis, design, and construction of a base-isolated multiple building structure. Adv Civ Eng 2014. https://doi.org/10.1155/2014/585429
79. Yuan F, Pan J, Leung CKY (2017) Elastoplastic time history analysis of reinforced engineered cementitious composite or engineered cementitious composite-concrete composite frame under earthquake action. Adv Struct Eng 20(4):491–503. https://doi.org/10.1177/1369433216655809
80. Li M, Maleej VC (1995) Introduction of strain hardening engineered cementitious composites in design of reinforced concrete flexural members for improved durability. ACI Struct J 92(2): 167–176
81. Kesner K, Billington SL (2004) Tension, compression and cyclic testing of engineered cementitious composite materials. Mceer (July): 107. https://www.researchgate.net/publication/265821093
82. Beirami Shahabi A, Ahari GZ, Barghian M (2020) Base isolation systems-a state of the art review according to their mechanism. J Rehab Civ Eng 8(2): 37–61. https://doi.org/10.22075/JRCE.2019.16186.1306

Structural Equation Modelling (SEM) for Economically Resilient Metro Tunnels Based-Urban Underground Space (UUS) Spatial Planning and Development in Subsiding Coastal Megacities by 2035 BaU in Shanghai and Jakarta: COVID-19 Period Analysed

Muhammad Akmal Hakim bin Hishammuddin, Jianxiu Wang, Muhammad Azizol bin Ismail, Soheil Sabri, Hasanuddin Zainal Abidin, Chin Siong Ho, Xinlei Huang, Tianliang Yang, and Keng Yinn Wong

Abstract Coastal megacities are constantly challenged with nature-anthropogenic hazards e.g. land subsidence and climate change consequences. This research focuses on the promising metro tunnels-based UUS planning and development towards economic resilience at subsiding coastal megacities scale in Shanghai and Jakarta. Factors are studied through multiple regressions to understand the development extent via cause-effect relations. Five main determinant factors; surface loads, UUS construction, groundwater, climate change and land subsidence risks-related with six economic factors; land price, underground structures, infrastructure, buildings, properties and socio-economic are finalised. Year 1960, 2020 and 2035 are selected as

M. A. H. Hishammuddin (✉) · J. Wang
College of Civil Engineering, Tongji University, Shanghai 200092, China
e-mail: akmal_hkm@yahoo.com

M. A. Ismail · C. S. Ho
Faculty of Built Environment and Surveying, Universiti Teknologi Malaysia, 81310 Skudai, Malaysia

S. Sabri
Infrastructure Engineering, University of Melbourne, Parkville, VIC 3010, Australia

H. Zainal Abidin
Faculty of Earth Science and Technology, Institute of Technology Bandung (ITB), Bandung, Indonesia

X. Huang · T. Yang
Shanghai Institute of Geological Survey, Shanghai 200093, China

K. Y. Wong
Faculty of Engineering, Universiti Teknologi Malaysia, 81310 Skudai, Malaysia

H.-Y. Jeon (ed.), *Proceedings of the International Conference on Geosynthetics and Environmental Engineering*, Lecture Notes in Civil Engineering 374,
https://doi.org/10.1007/978-981-99-4229-9_16

study period. COVID-19 impact in year 2020–2021 are also analysed. SEM analysis is carried via IBM SPSS Amos. Findings are; first, 'Surface' and 'Natural' determined factors have 0.98 and 0.86 R squared values, whilst 'Groundwater' and 'UUS' have the least with −0.75 and −0.71, respectively in Shanghai with model fit summary of 130,855.510 CMIN. Second, highly impacted economic factors are land subsidence, district revenues, company's production, economic activities disruption and underground structure damage with 0.98, 0.97, 0.03, 0.02 and 0.006 values, respectively. Third, during COVID-19, a stagnant condition of underground tunneling leakage is observed. Fourth, for Jakarta, property prices, vulnerable population, reconstruction demand are among the highly impacted economic factors with 0.99, 0.96 and 0.93 R values respectively. Fifth, 90% of cause-impact changes in Shanghai are controlled with positive increment while 90% are negative economic impact losses in Jakarta. Both developed and developing megacities can learn from each other based on the contradictory findings.

Keywords Structural equation modelling · Land subsidence · Underground space

1 Introduction

Coastal megacities are constantly challenged with natural hazards e.g. constant land subsidence, and climate change e.g. sea level rise, flood and storm surge [1–3]. With further growing concerns of uncertain future, rapid urban growth and ambitious urban goals and targets, hence, understanding the mechanisms involved are important [4, 5]. There are many identified cause and effect factors related to the land subsidence. From natural to anthropogenic causes e.g. climate change, socio-economic development and many adverse environmental and socio-economic impacts e.g. buildings and infrastructure damage, loss of life and seawater intrusions as shown in Fig. 1. Being dubbed as a silent disaster [6], therefore, further continuous study of its mechanisms is important. The relations of land subsidence, urban development and the direct–indirect economic impact has also been discussed and outlined well in [4, 7]. The suggestion is to include land subsidence as consideration in urban spatial land use planning, groundwater regulation, building-infrastructure codes, flood management, seawater intrusion control and environmental conservation. As these factors will have huge impact on the urban development that will constantly buildup in urban areas along with population, socio-economic activities and groundwater extraction. The impact of land subsidence is diverse and include both direct and indirect e.g. building and infrastructure damages, tilting of buildings, widening of inundation areas, quality of life and possess high correlation with coastal megacities.

However, the spatial and temporal domains have still yet to be fully and extensively established e.g. detailed mapping of land subsidence impacts and modelling [7]. Kok and Costa [4] has also outlined land subsidence-economic impact framework which consists of the direct–indirect and market, non-market factors and suggests few economic cost assessment or valuation for each factor. However, the non-market

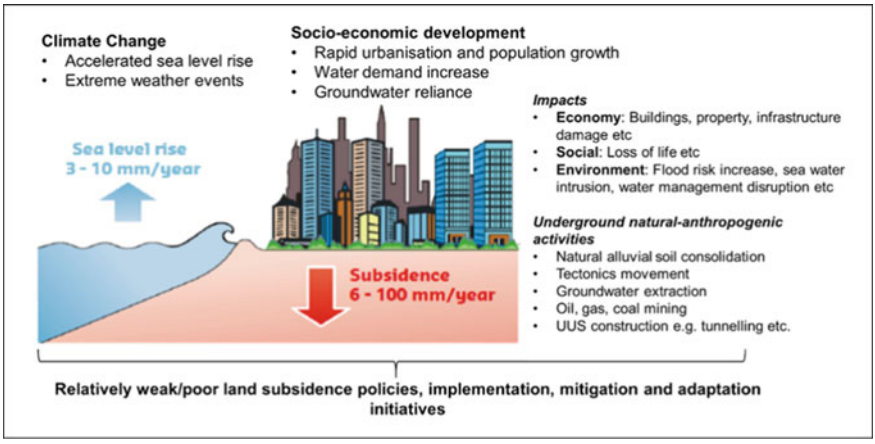

Fig. 1 Complex mechanisms of cause-effect relations in land subsidence (Modified from [2])

or social factors are taken out due to their abstract and complex measurability. This research tries to focus on the promising planning and development of metro tunnels-based urban underground space (UUS) in the coastal megacity by taking Shanghai and Jakarta as case studies. In meeting further development demands, within condensed and limited space in coastal megacities, stakeholders and engineers often pursue UUS as an ideal state to facilitate utility purposes, cross river tunnels, metro lines, basements, complexes, markets, and environmental deepening. Nevertheless, taking Shanghai as example, most metro tunnels based-UUS are developed in aquifers I and II [8, 9]. As UUS development and construction are two to ten times larger than surface structures, the post destruction cost and consequences are inevitable, hence, planning and decision-making of any UUS development must be conducted carefully [10–12]. Metro tunnels-based UUS is chosen to limit the broad context of UUS development itself, with 97% growth from 1960 by 2020 in Shanghai, it it expected to grow further with additional 60% by next thirty years with expansion of deeper excavation [9]. The purpose is to combine the previous micro-meso engineering-based research and comprehensively assess the regression relationships at macro coastal megacity scale. To clarify, this study presents the Business as Usual (BaU) scenario by 2035.

1.1 Coastal Megacity Geotechnical Profile

Shanghai, P.R China. Shanghai is located at alluvial plain of Yangtze River Delta and known for its challenging underground soft soil. Shanghai's underground soft soil consists of sandy and clay layers with high silt content, fifty metres thick of artesian aquifer and high groundwater level [3, 13]. The UUS development in Shanghai

is divided into three layers; shallow, middle and underground whereby, the shallow-middle layer is already compact and saturated [14]. Groundwater is determined as the primary challenge of UUS construction and development in Shanghai. The depth of metro tunnels and UUS development in Shanghai is usually 9–15 m at the first soft clay layer, which are below the utility's burial e.g. electric, gas, water and telecommunications. Other deeper underground layers include for sewerage and deep water pumping which are 15–40 m below at sand layers (see Fig. 2). However, there are metro tunnels built below the existing tunnels and crossing below the Huangpu River with the depth of 15–25 m at the second soft clay later e.g. Metro Line 3, 4 and 9 (29.7 m) with retaining wall constructed in depth of 62.9 m [15]. Hence, the regional groundwater withdrawal-recharge, deep foundation pit dewatering, urban planning and further deeper underground factors should be considered in the development of UUS in Shanghai as a coastal megacity.

Tunnels constructed before 1990s in Shanghai, have serious groundwater leakage with more than 1 L/m^2/day [3]. These are all cause by differential settlement, cracking of tunnel segments, inappropriate waterproofing materials and design which deteriorates and deform underground structure. This worsens with continuous land subsidence at macro scale e.g. catastrophic damage and failures of Shanghai Metro Line 4 in July 2003 [16], discomfort for users, environmental consequences and further catastrophic hazards. Nevertheless, latest tunnels built have had less than 0.1 L/m2/day leakage rate. In preventing ad-hoc conflict of engineering-nature disasters through differential settlement and even land subsidence at large coastal megacity,

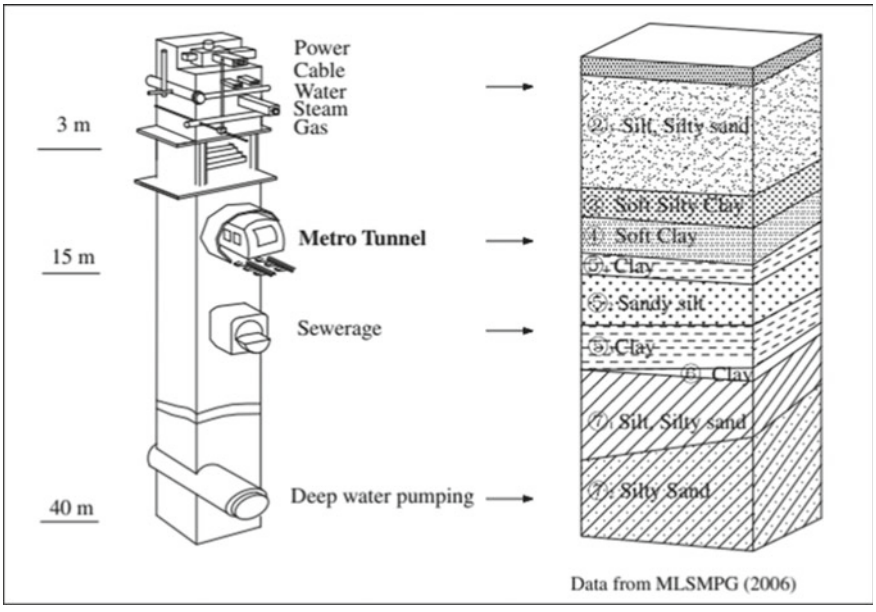

Fig. 2 Cross section of metro tunnels-based UUS development and soil layers in Shanghai [3]

urban spatial planning role is important in determining which areas possess high risks and potential for future adverse damage. A good spatial documentation and identification can further add values and assists future planning at macro scale thus, prevention countermeasures and adaptation strategies can be suggested. The planning, construction and engineering of metro tunnels-based UUS at large megacity scale in general shall be made advanced, sustainable and resilient based on population agglomeration, climate, geological condition, spatial constraint, risk management, geo-environmental protection, technological benefits e.g. Global Positioning System (GPS), Interferometric Synthetic Aperture Radar (InSAR), Geographic Information System (GIS), experience and construction information [1, 8, 17]. Since 1970s, United Nations (UN) and International Union of Geological Sciences (IUGS) have partnered together in delivering the International Geoscience Programme (IGCP) to further facilitate international scientific cooperation for geosciences and geo-hazards risk which include land subsidence in coastal megacities. Shanghai and Jakarta are both important cases which possess 'mainly in the past' and 'currently underway or active' land subsidence stages, respectively [18].

2 Research Method

Metro tunnels-based UUS development, subsidence-economic resilience and urban planning factors are studied using multiple regressions analysis to ultimately understand the extent development impact via cause-effect relations. The factors are referred, derived, integrated and simplified from various literatures and existing framework to suit the current research purposes e.g. [2, 4, 7, 14], Sustainable Development Goals 2030 (SDG 2030) and lastly, Shanghai Masterplan 2017–2035 (SM2035). Initially, there are 44 and 38 determined causing and economic impact factors, respectively. Study years of 1960 (first groundwater banning policies in Shanghai and 10 years earlier of the IGCP plan), 2020 (the year this study started, 10 years after Kyoto Protocol in 2015, 3 years after the execution of SM2035, 2035 (target year of SM2035, five years after SDG2030 targets) are selected. Coronavirus diseases 2019 (COVID-19) period is also discussed (2020–2021). To provide simplicity, straightforwardness and meeting this research's purposes, only sixteen causing and six economic impact key factors are finalised. The factors are combined selected and integrated from various reviews of existing frameworks, and localities and simplicity of data availability to reach the perfection and comprehensiveness of the model that this research trying to achieve as enlisted in Table 1. As well as trying to fulfil the sustainable development aspects of social, economic and environment aspects of paradigm. To provide further accuracy, the SEM is then carried by visualising and transferring datasets from IBM Statistical Package for the Social Sciences (SPSS) Statistics to IBM Amos SPSS Graphics Version 28. The procedures in IBM Amos SPSS are as follow;

Table 1 Determinant-economic factors

No	Determinant (causes, independent, *x*)	References
1	Surface: increasing surface load	Sustainable Development Goals 2030, [2, 14]
2	Groundwater: excessive groundwater extraction	Sustainable Development Goals 2030, [2]
3	UUS: urban underground space pre-during-post construction	[14], Shanghai Masterplan 2035 (SM2035)
4	Natural: natural or climate change disasters	[2, 4, 7]
No	Economic impact factors (Effect, dependent, *y*)	
1	Land development	
2	Underground structures	
3	Infrastructures	[4, 7]
4	Buildings or properties	
5	Socio-economic activities	
6	Land subsidence risks	

(1) Opening datasets: Select data > File Name > Select.sav file data > OK.
(2) Draw latent variable.
(3) Detailed further procedures can be referred to [19].

3 Research Results and Discussions

3.1 Correlations of Determinant-Economic Factors in Shanghai

Analysis results for Shanghai indicate, 'Surface' and 'Natural' determinant factors possess high correlations of 0.98 and 0.86 R squared values, respectively. Whereas, 'UUS' and 'Groundwater (GW)' have the least with −0.71 and −0.75, respectively (refer Fig. 3). The model fit summary of 'Surface' is statistically significant with Chi-square value (CMIN) of 130,855.510.

3.2 Minor Comparison Case: Jakarta's Situations

For Jakarta, the determined high regressed determinant-economic factors are different from Shanghai's which consists of residential construction investment, groundwater extraction-induced subsidence, underground metro tunnel construction and seawater level rise. The determinant factors are highly correlated with economic factors; vulnerable population, reconstruction demand and property prices, with 0.99,

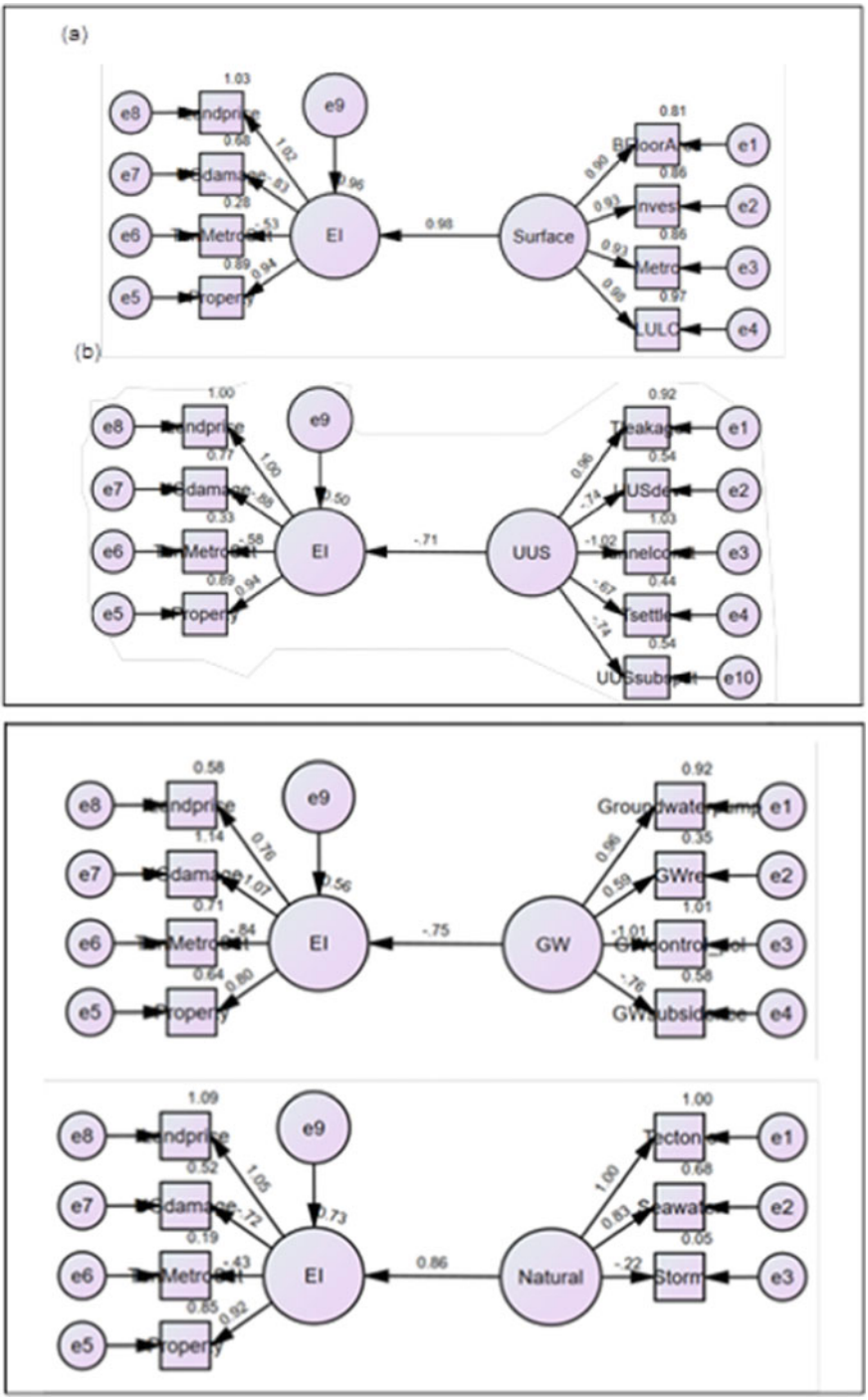

Fig. 3 Model for 'Surface', 'UUS', 'GW' and 'Natural'

Table 2 High regressed determinant-economic factors in Jakarta by 2035 BaU

Main determinant factors	Breakdown factors	R^2	Type of economic impact
Surface	Residential construction investment [$/year]	0.99	Indirect
Groundwater	Groundwater extraction-induced subsidence [mm/year)	0.96	Indirect
Natural	Seawater level rise [mm/year)	0.93	Indirect
UUS	Underground metro tunnel construction [km/year]	0.002	Indirect
Main economic factors	Breakdown Factors	R^2	Type of economic impact
Land	Number of vulnerable populations [Mill. / year]	0.96	Direct
Buildings	Average property prices [$/m^2/year)	0.99	Indirect
Infrastructure	Reconstruction demand [$/year)	0.93	Indirect
Buildings	Average property prices [$/m^2/year)	0.002	Indirect

0.96, 0.93, 0.002 R values, respectively. With Jakarta's category as a developing coastal megacity with on-going land subsidence-related issues, the determined high regressed factors somehow signify the adverse situation of the megacity was facing from 1960, 2010, 2020 and especially towards 2035 BaU. The following Table 2 describes the situation.

3.3 Direct–Indirect Economic Impact Changes

This section provides discussion on the direct–indirect economic impact changes with the focuses on the high regressed impacted economic factors towards the goal of this research. A coastal megacity may always deter the determinant factors however, reducing the negative impact especially the indirect economic factors are crucial in ensuring an economically resilient metro tunnels-based UUS planning and development. Based on both regression and SEM results, 90% of determinant-economic impact changes in a developed coastal megacity (Shanghai) are positive-controlled increment. Meanwhile for a developing coastal megacity (Jakarta), proven by 2035 BaU possess 90% of negative-economic impact losses. Significantly, both developed and developing coastal megacities possess similar 90% of indirect economic impact factors. This is in line with the known land subsidence impact in previous literatures as silent-indirect yet disastrous. On the other hand, the positive impacted (be it increase

Table 3 High regressed positive impacted economic factors in Shanghai

Positive economic factors		Changes (%)	Type
Land	Average land price [$/m^2/year]	94.45	Indirect
Buildings	Average property prices [$/m^2/year)	91.69	Indirect

Table 4 High regressed negative economic impact factors in Shanghai and Jakarta

Negative economic impact factors		Changes (%)	Type	Megacity
Underground	Underground structure damage and deformation [mm/year]	100	Indirect	Shanghai
Infrastructure	Metro tunnel settlement [mm/year]	84	Indirect	Shanghai
Land	Number of vulnerable populations [Mill./year]	92.10	Direct	Jakarta
Infrastructure	Reconstruction demand [$/year]	100.00	Indirect	Jakarta
Buildings	Average property prices [$/$m_2$/year)	100.00	Indirect	Jakarta

or decrease) economic factors e.g. increment of land and property prices, either direct or indirect must be supported, whilst negative impacted economic factors e.g. metro tunnels settlement and vulnerable populations, both direct–indirect must be avoided by providing significant countermeasures. Following Tables 3 and 4 tabulate the findings.

4 Conclusions and Further Research Suggestions

To emphasise, this paper presents the results and findings for 2035 BaU scenario of which factors are finalised based on existing subsidence-economic impact, metro based-UUS and urban spatial planning framework to provide inclusivity, locality, comprehensiveness and towards fulfilling SDGs spectrum of economic, social and environment. A significant stagnant correlation is observed during COVID-19 period which depicts consistent development with limited tunnel leakage and subsidence rate. Both developed-developing coastal megacity possess maximum surface built-environment and hence, opted further for the promising UUS development. Nevertheless, the determinant-economic relations for Shanghai as a 'developed' coastal megacity with 'mainly in the past' subsidence issues have mostly positive impacted economic factors. This is tremendously different from the case of a 'developing' coastal megacity like Jakarta with 'on-going' land subsidence, where most of the impacted economic factors are still adversely impacted and negative. Based on the results and discussions, there are a few outstanding discoveries and further research conduct to be proposed. In general, the developed and developing megacities can further control and plan their built environment physically and spatially based on the regression analysis. This can be fully accomplished by establishing a good

statistic-spatial relation through geostatistical study, especially to further locate the high regressed determinant-economic impact factors by avoiding further damage. A mere policies improvements and formulation based on statistical analysis alone is not enough. Improvements via estimation and projections and creating countermeasures, spatially with big data contributions are essentials in this challenging era. Further comprehensive and detailed study with countermeasure (CM) scenario can be conducted to counter the current BaU situation by 2035. Furthermore, a study with the expectation beyond 2035 is also needed, to model how Jakarta can replicate the current policies and implementation in Shanghai to achieve the positive outcomes of Shanghai by 2035BaU. The monitoring and assessment are needed especially for developing coastal megacity by 2050 to develop the same path as developed coastal megacity by 2035. Stakeholders such as local government, civil engineers, urban planners, academician and local communities must join ventures towards effective policies formulation and implementation.

Acknowledgements This research is sponsored by the Shanghai Municipal Science and Technology Project 39 (18DZ1201301; 19DZ1200900); Key Laboratory of Land Subsidence Monitoring and Prevention, Ministry of 40 Natural Resources of the People's Republic of China (No. KLLSMP202101), and International Geoscience 41 Programme (IGCP) Project (663-Land subsidence in coastal cities).

References

1. Deltares (2015) Sinking cities, an integrated approach towards solutions. https://www.deltares.nl/app/uploads/2015/09/Sinking-cities.pdf
2. Erkens G, Bucx T, Dam R, De Lange G, Lambert J (2015) Sinking coastal cities. Proc Int Assoc Hydro Sci 372(2016):189–198. https://doi.org/10.5194/piahs-372-189-2015
3. Oppenheimer M, Glavovic BC, Hinkel J, Van de Wal R, Magnan AK, Abd-Elgawad AR et al (2022) Sea level rise and implications for low-lying islands, coasts and communities. In: IPCC Special Report on the Ocean and Cryosphere in a Changing Climate. Cambridge University Press, Cambridge, UK and New York, NY, USA, pp 321–445. https://doi.org/10.1017/9781009157964.006
4. Kok S, Costa AL (2021) Framework for economic cost assessment of land subsidence. Nat Hazards. https://doi.org/10.1007/s11069-021-04520-3
5. Hishammuddin MAH, Wang JX (2021) Towards sustainable, resilient and adaptive urban underground space (uus) exploration, land subsidence and economic impact spatial model (usem) in Shanghai, p.r. China: systematic reviews, model framework, initial results and pre-determined challenges. IOP Conf Ser Earth Environ Sci 861:072033
6. Saputra E, Thomas H, Annelies Z, Tejo S (2017) Fighting the ignorance: public authorities' and land users' responses to land subsidence in Indonesia. Am J Clim Change 6(1)
7. Abidin HZ, Andreas H, Gumilar I, Wibowo IRR (2015) On correlation between urban development, land subsidence and flooding phenomena in Jakarta Geodesy Research Group, Institute of Technology Bandung, Jl. Ganesha 10, Bandung, Indonesia. Proc IAHS 370:15–20. https://doi.org/10.5194/piahs-370-15-2015
8. Huang Y, Yang Y, Li J (2015) Numerical simulation of artificial groundwater recharge for controlling land subsidence. KSCE J Civ Eng 19: 418–426. https://doi.org/10.1007/s12205-015-0505-y

9. Qiao YK, Fang-Le P, Soheil S, Abbas R (2019) Socio-environmental costs of underground space use for urban sustainability. Sustain Cities Soc 51:101757. https://doi.org/10.1016/j.scs.2019.101757
10. Kaliampakos D, Bernardos A, Mavrikos A (2016) A review on the economics of underground space utilisation. Tunn Undergr Space Technol 55:236–244
11. Bobyley N (2009) Mainstreaming sustainable development into a city's Master plan: a case of Urban Underground Space use. Land Use Policy 26:1128–1137. https://doi.org/10.1016/j.landusepol.2009.02.003
12. Qiao YK, Peng FL (2015) Lessons learnt from Urban Underground Space use in Shanghai—from lujiazui business district to hongqiao central business district. Tunnel Underg Space Technol. https://doi.org/10.1016/j.tust.2015.12.001
13. Wu HN, Huang RQ, Sun WJ, Shen SL, Xu YS, Liu YB, Du SJ (2014) Leaking behavior of shield tunnels under the Huangpu River of Shanghai with induced hazards. Nat Hazards. https://doi.org/10.1007/s11069-013-0863-,70:1115-1132
14. Zhang XH, Wang XW, Xu YS (2022) Groundwater environment and related potential engineering disasters of deep underground space in Shanghai. Bull Eng Geol Environ. https://doi.org/10.1007/s10064-022-02692-181,203
15. Wang J, Hu L, Wu L et al (2009) Hydraulic barrier function of the underground continuous concrete wall in the pit of subway station and its optimization. Environ Geol. https://doi.org/10.1007/s00254-008-1315-z57,447-453
16. Tan Y, Ye L, Dalong W (2021) Catastrophic failure of Shanghai metro line 4 in July, 2003: occurrence, emergency response, and disaster relief. J Perform Constr Facil Am Soc Civ Eng 5(1)
17. Chen B, Gong H, Li X, Lei K, Ke Y, Duan G, Zhou C (2014) Spatial correlation between land subsidence and urbanization in Beijing, China. Nat Hazards. https://doi.org/10.1007/s11069-014-1451-675(3),2637-2652
18. Guzy A (2020) Groundwater withdrawal-induced land subsidence groundwater withdrawal-induced land subsidence https://doi.org/10.32545/encyclopedia202008.0011.v2
19. Statistics and Theory, Structural equation modelling using AMOS. https://www.youtube.com/watch?v=CxJuHqyYVGk. Accessed 14 Aug 2022

Probability Density Distribution and Reliability Evaluation of Load Settlement Curve of PHC Pile in Deep Silt Area

Songting Zeng, Xiaoyun Ma, Zenghui Yu, and Jihui Ding

Abstract PHC pile has become one of the widely used foundation treatment methods in soft soil foundation. Taking a pile foundation project in Wenzhou as an example, the thickness of hydraulic fill and silt in the site is 27.20–33.60 m, and the length of PHC pile is mostly 43–50 m. In this paper, the load test results of 130 PHC compression piles detection in the project site are statistically analyzed by the method of probability regression parameters. The results show that the settlement value under all levels of load basically conforms to the normal distribution, and the goodness of fit is 0.80–0.90; The exponential, hyperbolic and power function are used for fitting, and the regression coefficient is statistically analyzed. The normal distribution function is used for fitting, and the goodness of fit is 0.85–0.99; On this basis, the relationship between the safety factor and reliability index of the ultimate bearing capacity of the PHC pile and the allowable settlement is analyzed. With the increase of the allowable settlement, the ultimate bearing capacity of the PHC pile increases, and the corresponding safety factor and reliability index increase. Among the three fitting curves, the reliability index calculated by the exponential function is the largest, and the reliability index is close to that of power function and hyperbolic function.

Keywords PHC pipe pile · Load test · Curve fitting · Probability density · Goodness of fit

S. Zeng · X. Ma · J. Ding
CCCC Road and Bridge Special Engineering Co., Ltd. Wuhan, Hubei, China

Z. Yu (✉)
China Construction Second Bureau Eighth Engineering Co., Ltd, Jinan, China
e-mail: 1976316086@qq.com

H.-Y. Jeon (ed.), *Proceedings of the International Conference on Geosynthetics and Environmental Engineering*, Lecture Notes in Civil Engineering 374,
https://doi.org/10.1007/978-981-99-4229-9_17

1 Introduction

Prestressed high-strength concrete pipe piles have the advantages of high bearing capacity, good bending resistance, stable quality, strong adaptability, etc. PHC piles are increasingly widely used in soft soil areas and densely populated large cities. The ultimate vertical compressive bearing capacity of a single pile is determined by the material strength of the pile itself and the strength of the foundation soil, which is the main factor determining the ultimate compressive bearing capacity of a single pile. Due to the spatial variability of the rock and soil layer through which the foundation pile passes, the ultimate compressive bearing capacity of a single pile at a site shows a certain degree of dispersion, which leads to a certain degree of dispersion of the load-settlement curve of the foundation pile on the site.

The probabilistic regression parameter method is to fit each test curve by linear or nonlinear regression, and then indirectly describe the dispersion between curves by constructing the joint distribution of multiple (or dozens of) regression parameters in the site[1–3]. Based on the typical test results of load deformation at the site level in the capital city and its environ, including bored piles, CFG piles and anchor bolts, the probability density distribution of the deformation value under the given load and the probability density distribution of the load value under the given deformation are discussed respectively [4–7]. In this paper, the probability regression parameter method is used to statistically analyze the load test of 130 PHC compression piles monitored in a development zone in Wenzhou City, Zhejiang Province, and then determine the reliability index of bearing capacity of the foundation piles to be relocated.

2 Statistical Analysis of Load-Settlement Curve

2.1 Project Overview

The project is located in a development zone in Wenzhou, Zhejiang Province, with a total land area of about 370,000 m^2. From top to bottom, the stratum of the project site is composed of artificial fill, silt-alluvial soft soil, lacustrine and marine general cohesive soil, which is divided into 8 engineering geological layers and 15 sub-layers. The adverse geological effect of the construction site is 27.20–33.60 m thick siltation (alluvium) soft soil and other adverse foundation soil, mainly including shallow artificial hydraulic fill, which is under-consolidated, with poor geological conditions and poor stability. The buried depth of groundwater level is 1.29–3.21 m. The buildings on the site are mostly steel frame structure (light steel structure), and partially reinforced concrete frame structure, without basement. The design pile length of the pile foundation is 43–49 m. The first two sections of the foundation pile are PHC-AB500 (125), and the last two sections are PC-AB500 (125) prestressed pipe piles. The concrete strength of the pile body is C80, the bearing layer of the pile

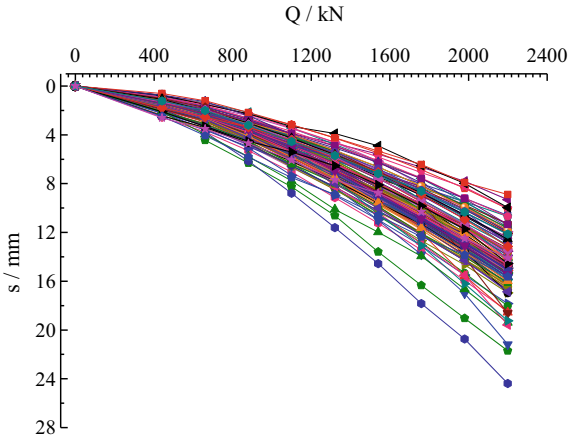

Fig. 1 Q-s curve of 130 PHC piles

end is 5–2 or 6–1 clay soil layer. The foundation pile is end-bearing friction pile, and the design value of the single pile bearing capacity is 1200 kN.

2.2 Statistical Analysis of Load-Settlement Curve

Figure 1 shows the Q-s curve of 130 compression PHC piles. It can be seen from Fig. 1 that the settlement value of the foundation pile under all levels of load is not a fixed value and is random. Table 1 shows the settlement statistics of 130 PHC piles under various loads. It can be seen from Table 1 that the coefficient of variation of settlement value under the first two levels of load is greater than 0.20 and less than 0.25, the load is 880–2200 kN, and the coefficient of variation of settlement value is 0.16–0.20. The variability of settlement value is mainly attributed to the variability of geometric parameters, including the pile length and the thickness of soil layer through which PHC piles pass, spatial variability of soil shear strength index. Figure 2 shows the probability distribution fitting curve of settlement under graded load. It can be seen from Fig. 2 that when Q = constant, the settlement value is a random variable and basically conforms to the normal distribution, and the goodness of fit of the distribution function is between 0.80 and 0.90.

2.3 Statistical Analysis of Fitting Parameters of Load-Settlement Curve

The current code for design of building foundation [8] points out that the loading level should not be less than 8, and the loading amount of each level should be 1/8 ~ 1/10 of the estimated limit load. In order to obtain the theoretical description under

Table 1 Statistical value of settlement under graded load

Q (kN)	Minimum (mm)	Maximum (mm)	Mean (mm)	standard deviation	Coefficient of variation	Goodness of fit
440	0.62	2.61	1.52053	0.37909	0.24932	0.88409
660	1.21	4.45	2.52221	0.56805	0.22522	0.86541
880	2.16	6.32	3.76504	0.74924	0.19900	0.86280
1100	3.17	8.79	5.21847	0.96137	0.18422	0.86871
1320	3.89	11.60	6.78786	1.22406	0.18033	0.85296
1540	4.90	14.56	8.50901	1.48567	0.17460	0.80634
1760	6.43	17.84	10.3363	1.74220	0.16855	0.80020
1980	7.81	20.73	12.3457	2.02778	0.16425	0.84583
2200	8.90	24.39	14.5838	2.37451	0.16282	0.89228

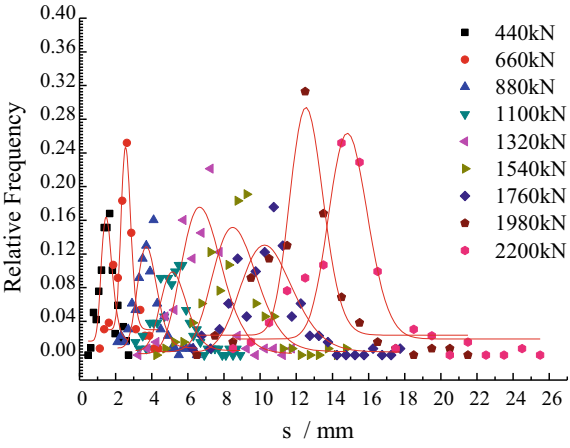

Fig. 2 Normal distribution function fitting curve

any value, the load and settlement test results can be nonlinear regression, and then the model expression of load and settlement can be constructed. The commonly used two-parameter regression forms include hyperbola, power function and exponential function [6, 7].

For the loading section of the PHC pile load-settlement curve of the field, exponential function, hyperbolic function and power function regression are used respectively:

$$Q = a_1(1 - b_1^s) \cdot \text{(Exponential, Box Lucas Model)} \tag{1}$$

$$Q = \frac{a_2 s}{b_2 + s} = \frac{a_2}{b_2/s + 1} \cdot \text{(Hyperbolic function)} \tag{2}$$

$$Q = a_3 s^{b_3} \cdot \text{(Power function)} \tag{3}$$

Table 2 Statistical value of regression coefficient of Q ~ s curve during loading

Coefficient	Min	Max	Mean	Standard deviation	Coefficient of variation	Goodnes of fit
a_1	4677.443	2244.812	2990.549	390.62077	0.13062	0.97759
b_1	0.97300	0.83243	0.90899	0.02723	0.02995	0.91481
a_2	8215.970	3005.304	4690.142	839.10503	0.17890	0.93958
b_2	40.08578	6.78929	16.92851	6.19499	0.36600	0.93643
a_3	545.8831	180.7947	360.3929	71.18320	0.19752	0.85572
b_3	0.90789	0.50014	0.68825	0.0611	0.08877	0.94933

The randomness of PHC pile settlement is mainly reflected in the randomness of the regression coefficient of Q-s fitting curve. The statistical parameters of regression coefficient of Q-s fitting curve are shown in Table 2. It can be seen from Table 2 that the dispersion of the regression coefficient of exponential fitting is the smallest, followed by the power function, while the deformation of the regression coefficient of hyperbolic function is the largest, and its coefficient of variation a_3 reaches 0.366. Assuming that the fitting parameters conform to the normal distribution, the goodness of fitting curve of the normal distribution is 0.85 ~ 0.99, and the fitting degree is high. The optimal distribution does not necessarily obey the normal distribution, but the difference between the normal distribution and the optimal distribution AIC (Akaike Information Criterion) is small, and the difference is mostly less than 10% [6, 7]. Therefore, normal distribution can be used for approximation for simplification.

Figure 3 shows the relationship between the regression coefficients of the three regression curves. As can be seen from Fig. 3, a_1 and b_1, a_2 and b_2 are positively correlated with each other. The correlation coefficients are respective 0.77945 and 0.85745. a_3 and b_3 are negatively correlated and correlation coefficients −0.81113.

3 Reliability Analysis Based on Probability Density Distribution

3.1 Limit State Equation

It can be seen from the above analysis that the bearing capacity (resistance Q_R) of the foundation pile is not a fixed value as a random variable due to the influence of pile length, stratum distribution, ultimate strength of soil layer, etc. The load (action Q_s) borne by the foundation pile is the actual (or design) load value. When the foundation pile is in a reliable state, the resistance Q_R is required to be greater than the action Q_s, and the corresponding limit state equation is:

$$Z = Q_R - Q_s = f(a_i, b_i, s_a) - Q_{sG} - Q_{sQ} \ (i = 1, 2, 3) \tag{4}$$

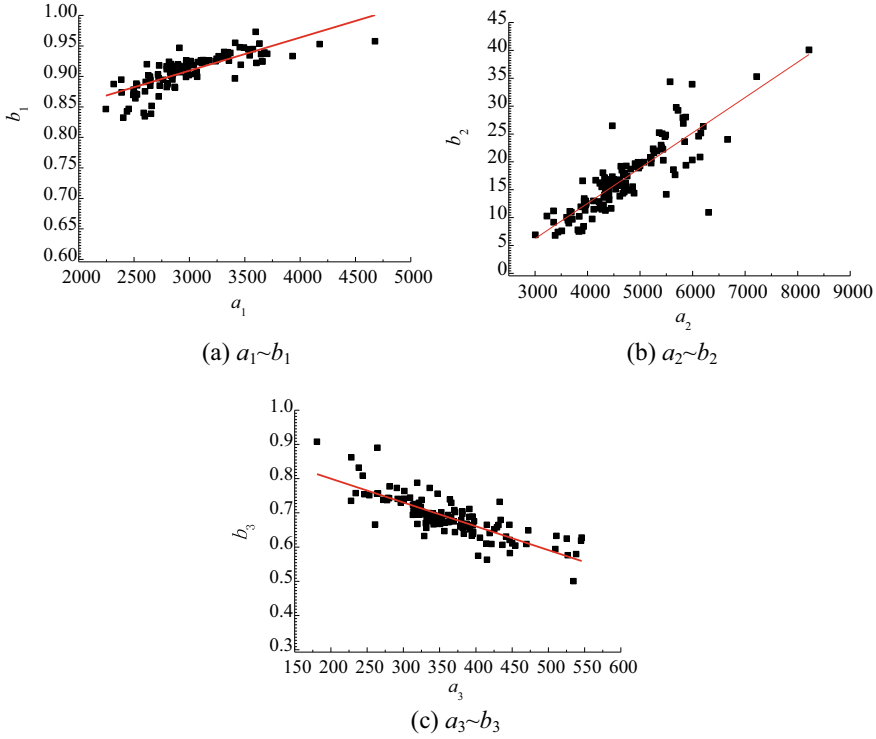

Fig. 3 Scatter plot of regression coefficient

The resistance Q_R in the above formula can be determined according to the given displacement tolerance value (s_a) of the fitting curve given above, and s_a can be given in advance. Since Q-s fitting curve coefficients (a_i, b_i) are random variables, Q_R is also a random variable. For foundation piles, the load value is mostly recommended by the engineer, and its value is estimated according to the characteristic load combination of the superstructure. For example, the vertical load can be composed of the weight of the structure (dead load or permanent load) and seismic activity (live load or variable load). The vertical load effect Q_s is equal to the sum of the vertical dead load effect Q_{sG} and the vertical live load effect Q_{sQ}. Once the random variables are determined, the reliability index can be calculated by random sampling method, one-time reliability method and geometric reliability method. The primary reliability method is used to calculate the reliability index as follows:

$$\beta = \frac{\mu_z}{\sigma_z} = \frac{\mu_R - \mu_S}{\sqrt{\sigma_R^2 + \sigma_S^2}} \tag{5}$$

The formula (5) does not explain the probability distribution of random variables Q_R and Q_s, but directly uses its mean and standard deviation. This method is suitable

for reliability analysis when the calculation accuracy is not high in practical application. This method is suitable for reliability analysis when the calculation accuracy is not high in practical application. If the probability density function of each random variable is known, the mean and standard deviation can be accurately calculated by Gaussian integration. If the function function (5) is nonlinear, Eq. (5) can be expanded into Taylor series and retained to the first term, then the approximate results of μ_z and σ_z can be given.

3.2 Reliability Index Analysis

The determination method of vertical ultimate bearing capacity of single pile in the current code [8]: (1) Make load-settlement (Q–s) curve and other curves required for auxiliary analysis. (2) When the steep descent section is obvious, take the load value corresponding to the starting point of the steep descent section; (3) When the Q–s curve is slowly changing, take the load value corresponding to the total settlement of the pile top s = 40 mm. When the pile length is greater than 40 m, the elastic compression of the pile body should be considered.

The maximum value of Q ~ s curve loading of 130 PHC piles in this project is 2200 kN, the design value of bearing capacity of foundation piles is 1100 kN (including dead load of 900 kN, variation coefficient of 0.09; live load of 200 kN, variation coefficient of 0.29), and its safety factor is 2.00. When the load is 2200 kN, the mean value of settlement is 14.58 mm, and the corresponding pile bearing capacity is calculated by fitting the Q-s curve, and then the corresponding safety factors of exponential function, hyperbolic function and power function are 2.04, 1.97 and 2.07, which are close to 2.0, and the corresponding reliability indexes are respectively 3.70, 2.22 and 2.56.

Figure 4 shows the relationship between the safety factor of PHC pipe pile and the allowable settlement of foundation pile. It can be seen from Fig. 4 that with the increase of allowable settlement from 14 to 40 mm, the safety coefficient calculated by using three fitting curves increases, the safety coefficient of exponential function increases from 2.00 to 2.66, the hyperbolic function increases from 1.93 to 3.00, and the power function increases from 2.01 to 4.15, and the safety coefficient of power function increases greatly.

Figure 5 shows the relationship between the reliability index of PHC pipe pile and the allowable settlement of foundation pile. With the increase of allowable settlement from 14 to 40 mm, the reliability index calculated by the three fitting curves increases, the reliability index coefficient of exponential function increases from 3.62 to 4.62, the hyperbolic function increases from 2.19 to 3.94, and the power function increases from 2.49 to 3.82. Among the three fitting curves, the reliability index calculated by exponential function is the largest, and the reliability index is close to that of power function and hyperbolic function.

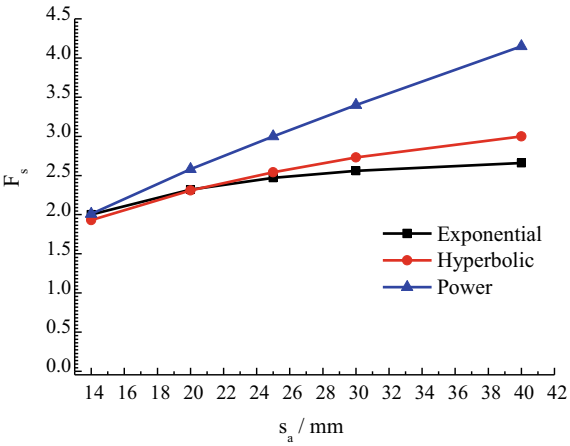

Fig. 4 Fafety factor (Fs) ~ s_a relationship

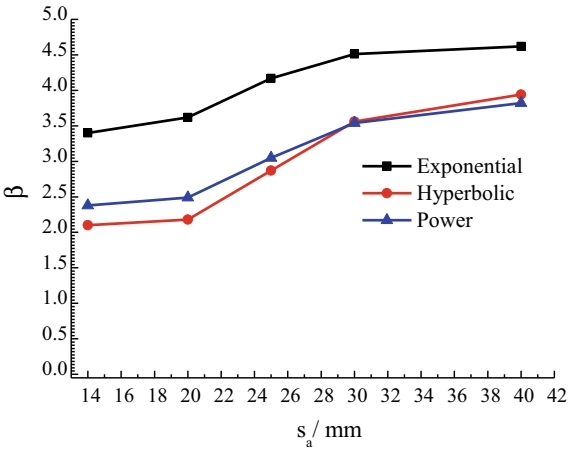

Fig. 5 Reliability index β ~ s_a relationship

4 Conclusion

(1) Based on the statistical analysis of the load test of 130 PHC compression piles in a development zone in Wenzhou, Zhejiang Province, the coefficient of variation of the settlement value under the first two levels of load is slightly larger, the load is 440–2200 kN, and the coefficient of variation of the settlement value is 0.16–0.25; The settlement under all levels of load basically conforms to normal distribution, and the goodness of fit is 0.80–0.90.

(2) The distribution of 130 load test results of 130 PHC piles at the site is fitted with exponential function, hyperbolic function and power function, and the regression coefficient is statistically analyzed. The dispersion of exponential fitting regression coefficient is the smallest, followed by power function, and

the deformation of the regression coefficient of hyperbolic function is the largest. The goodness of fit of the regression coefficient function is between 0.85 and 0.99, and the degree of fitting is high.

(3) Based on the limit state design of the bearing capacity of PHC piles, the relationship between the safety factor and reliability index of the ultimate bearing capacity of PHC piles and the allowable settlement is analyzed. With the increase of the allowable settlement, the ultimate bearing capacity of PHC piles increases, and the corresponding reliability index increases with the increase of the safety factor. Among the three fitting curves, the reliability index calculated by the exponential function is the largest, and the reliability index is close to that of power function and hyperbolic function.

References

1. Li DQ, Tang XS, Phoon KK et al (2013) Bivariate simulation using copula and its application to probabilistic pile settlement analysis. Int J Numer Anal Meth Geomech 37(6):597–617
2. Tang XS, Li DQ et al (2012) Probabilistic analysis of load-displacement hyperbolic curves of single pile using Copula. Rock Soil Mech 33(1):171–178
3. Jun-xia X, Xing-zheng W et al (2016) Copula-based analysis of load-displacement curves of cement-fly ash-gravel pile. Rock Soil Mech 37(S1):424–434
4. Wu X, Wang R et al (2017) Probability density distribution of load deformation curves of geotechnical structures at a specific site. Eng Qual 35(9):41–45
5. Wu XZ (2017) Implementing statistical fitting and reliability analysis for geotechnical engineering problems in R. Georisk 11(2):173–188
6. Wu XZ, Wang RK et al (2020a) Geometric reliability analysis of geotechnical structures at a specific site. Rock Soil Mech 41(6):1–11
7. Wu XZ, Wang RK et al (2020b) Simplified geometric reliability assessment of foundation piles under specific buildings based on limited test data. Rock Soil Mech 41(s2):1–9
8. GB 50007-2011 (2012) Code for design of building foundation. China Construction Industry Press, Beijing

Research on High Geothermal in Complex Deep Buried Tunnel Environment

Chenze Huang, Junzhou Huang, Haoyu Wu, and Qiang Wang

Abstract An effective and practical three-dimensional modeling method and analytical theory of high geothermal in complex deep buried tunnel environment based on voxel model and Kriging algorithm was proposed after considering the effects of spatial correlation, adaptation and accuracy of relevant parameters, which can accurately prevent and control the high geothermal disaster risk in complex deep buried tunnel environment. Compared with the results of classical tunnel models, it is found that the proposed three-dimensional modeling method and analytical theory of high geothermal in complex deep buried tunnel environment was effective. Secondly, the three-dimensional modeling method and analytical theory had a good application prospect in the field of high geothermal heat damage area, and can effectively reveal the spatial distribution characteristics of high geothermal heat damage area. Finally, the proposed method can provide theoretical foundation and thought innovation for precise prevention and control of high geothermal disaster risk in complex deep buried tunnel environment, and has good practical significance and scientific value.

Keywords Voxel model · Kriging algorithm · Three-dimensional modeling method · High geothermal

1 Introduction

With the implementation of a new round of western development strategy, more and more long-buried tunnel projects have begun to be planned and constructed. In the complex and dangerous areas in western China, high ground temperature is a common geological disaster that seriously affects operators and tunnel structures, and

C. Huang (✉) · H. Wu · Q. Wang
Gansu Probincial Engineering Laboratory for National Geographic State Monitoring, Lanzhou 730030, China
e-mail: 2011448918@qq.com

J. Huang
School of Civil Engineering, Hubei Engineering University, Hubei 432000, China

H.-Y. Jeon (ed.), *Proceedings of the International Conference on Geosynthetics and Environmental Engineering*, Lecture Notes in Civil Engineering 374,
https://doi.org/10.1007/978-981-99-4229-9_18

its precise prevention and control has become one of the challenges faced by tunnel construction [1]. Accurate analysis and evaluation of tunnel high geothermal risk is the foundation, involving multi-source heterogeneous data processing, including geological investigation and adjustment, drilling, geophysical exploration and remote sensing thermal infrared image, etc., the process includes first constructing a high-precision geo-geological environment model around the tunnel, and then associating and integrating 3D temperature field data on this basis to reveal the refined spatial and temporal distribution of high temperature thermal damage [2].

In the construction of three-dimensional temperature field, the common methods include numerical simulation, analytical and spatial interpolation, etc., while the large range of high-precision three-dimensional geothermal field often has the problem of non-convergence due to the large amount of calculation, which eventually leads to the failure of modeling [3]. Spatial interpolation algorithm takes into account spatial correlation between real data and statistical analysis data, physical characteristics of temperature and heat conduction, as well as modeling feasibility regardless of computational load and convergence [4], including inverse range-weighted interpolation (IDW) algorithm, radial basis neural network interpolation (RBF) algorithm and Kriging algorithm, in which, The accuracy of IDW algorithm is insufficient, and RBF algorithm is easy to lose key information. Kriging algorithm has shown good compatibility in overcoming the shortcomings of IDW algorithm and RBF algorithm, and has become one of the most extensive spatial statistical interpolation algorithms for processing borehole and section data [5–7].

The existed researches show that [8, 9], remote sensing thermal infrared images can fully reflect the surface temperature but lack the deep temperature information and elevation information, while the existing interpolation modeling of underground temperature field is usually based on limited geothermal borehole data, which are sparsely distributed and have obvious spatial incompleteness, so it is difficult to construct a three-dimensional model to fully and accurately reflect the geothermal field. However, the high-precision and multi-resolution voxel model with the help of multi-source data fusion technology can effectively improve the accuracy of modeling in the tunnel and its surrounding geographic and geological environment expression, as well as the integration of geothermal data and topographic data, and make up for the shortcomings of insufficient expression of a single type of temperature data [10].

Combining the advantages of high-precision and multi-resolution voxel model and Kriging algorithm, and considering the effects of spatial correlation, self-adaptation and the accuracy of related parameters, an efficient and practical three-dimensional modeling method and analysis idea of high ground temperature field in complex deep-buried tunnel environment are proposed, so as to realize the precise prevention and control of high ground temperature disaster risk in complex deep-buried tunnel environment.

2 Working Principle of Multi-resolution Voxel Model in Tunnel Environment with High Ground Temperature

2.1 Mechanism of High Ground Temperature Multi-source Data Fusion

The modeling of the temperature field in the high altitude tunnel environment must consider the fusion of multi-class and multi-source data [9], and the high-precision and multi-resolution voxel model of multi-source data fusion technology can make up for the deficiency of the expression of a single type of temperature data in the modeling of the tunnel and its surrounding geographical and geological environment expression, geothermal data and topographic data integration [10]. The accuracy of the 3D highland temperature field model is improved. Its working flow and principle are shown in Fig. 1. When the multi-resolution voxel model is adopted, the accuracy of collecting attribute feature points of the temperature field in the tunnel environment is extremely important. The feature points are mainly extracted from surface thermal infrared remote sensing images and high geothermal drilling holes. After adding elevation data, the tunnel model with three-dimensional distribution is reconstructed from measured feature points. Subsequently, the collected temperature field feature points of the tunnel environment were integrated into the semantic point set of high geothermal temperature, which was stored in the geographic information system (ArcGis) to realize the fusion of multi-source temperature feature points considering terrain.

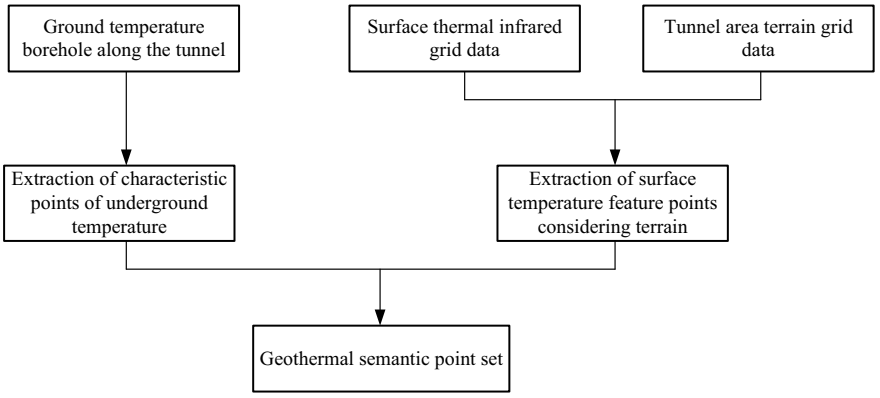

Fig. 1 Diagram of multi-source data fusion of high geothermal under tunnel environment

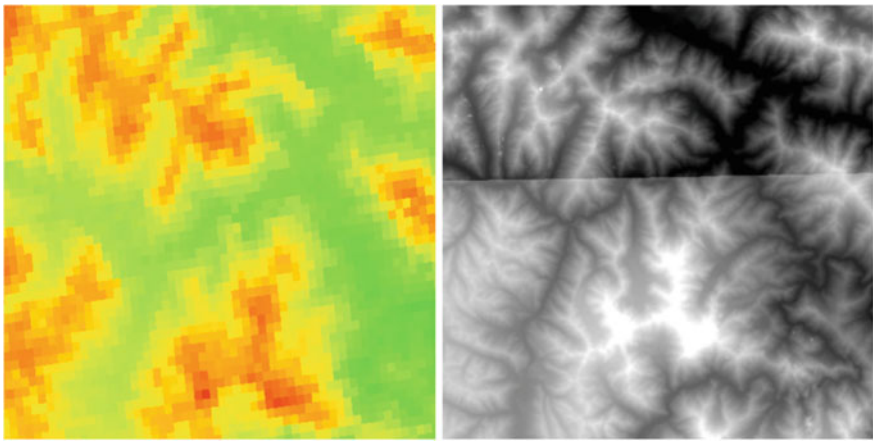

Fig. 2 Diagram of high geothermal and elevation distribution under tunnel environment

2.2 Extraction of Surface Thermal Infrared Feature Points

The extraction of surface temperature feature points is based on the surface thermal infrared remote sensing image, and the elevation and coordinate values of the feature points in the research area are extracted. By integrating the surface thermal infrared data and the terrain data of the tunnel area, the feature points of surface data can be obtained considering the terrain. The first is to match the accuracy of thermal infrared remote sensing interpretation image and topographic raster map (DEM) in the tunnel area. The problem of inconsistent data modal accuracy may occur in the fusion of multi-source data. By resampling DEM to match its accuracy with remote sensing image, all feature points in the study area are located after accuracy matching, and the image is transferred from raster file to point. The two-dimensional coordinates of evenly distributed temperature points are obtained and showed in Fig. 2, and then the surface temperature points in the tunnel buffer area are intercepted by combining the sampled DEM and surface temperature points. Finally, the feature points are converted into coordinate points by using the value extraction function. It is realized that the feature points fall on the DEM of tunnel area, and the 3D of the feature points of surface temperature is completed.

2.3 Extraction of Feature Points from High Geothermal Borehole

In the inversion of surface temperature and mountain gullies, it is suggested to lay high geothermal boreholes in the range of 10~100 m along both sides of the tunnel axis, and the data of temperature measurement boreholes mainly include the bottom

temperature of holes, the elevation of holes and temperature gradient, etc. [4]. The orifice elevation and borehole depth are usually determined by locating the location of each borehole. Combined with the borehole bottom temperature extracted from the borehole characteristic points of high geothermal temperature, the linear fitting with the high geothermal gradient is completed, and the effective data of the borehole characteristic points of high geothermal temperature are finally obtained.

2.4 High Ground Temperature Data Fusion Technology

In order to avoid the error caused by the change of coordinate system, a coordinate system must be adopted in the same tunnel environment, and the information of the characteristic points of high geothermal drilling, such as elevation, coordinate and temperature, must be established by reading coordinate points. According to Sect. 2.1, the obtained information of characteristic points of the temperature field in the tunnel environment is integrated into ArcGis into the location relationship between multi-source temperature data into the semantic point set of high geothermal temperature, thus forming a high geothermal data fusion technology suitable for complex deep-buried tunnel environment.

3 Parameter Adaptive Determination Basis and Accuracy Evaluation Method Considering Spatial Correlation

3.1 Modeling Area Voxelization

The voxel model is a three-dimensional model represented by a large number of regular voxels [1], and the minimum unit voxel assignment corresponds to the temperature value, which is used to express the distribution of high temperature field in the tunnel area, and the influence of the voxel unit size of the model on the interpolation effect cannot be ignored. In the modeling area, the average well spacing of the temperature characteristic points in the study area was taken as the standard to set the appropriate voxel size. The minimum voxel cell grid size was suggested to be $100 \times 100 \times 20$ m, and the depth of the modeling area was determined according to the elevation threshold of the tunnel area and the maximum borehole depth.

3.2 Parameter Determination of Adaptive Variogram

The analysis of adaptive variogram is a crucial step in modeling, and the fitting degree of variogram will directly affect the effect of subsequent interpolation. Therefore,

geo-statistical soft SGeMS with excellent effect was adopted in this study to complete the setting of variogram parameters. According to expert experience [11], the search radius is generally less than or equal to L/2 (where, L is the distance of the farthest data point in the research area), and the number of lag distance is calculated by the search radius and the minimum lag distance, as shown in Eq. (1).

$$n = \frac{R}{D} \tag{1}$$

where, n is the number of lag distance; R is the search radius; D is the minimum lag distance.

Among them, the hysteresis distance tolerance is generally half of the minimum lag distance in this direction (that is, $0.5D$), and bandwidth B is equal to twice the average well spacing. For example, given the borehole temperature data near a complex deep-buried tunnel, where the distance between the furthest temperature points is 30600 m, the search radius should be half of the distance (about 15300 m). When the azimuth interval is set to 22.5°, the confirmed direction angles are relatively dense in the range of 45° to 67.5°. In order to characterize the degree of mutation of the regionalized (45°~67.5°) variable at a small distance, reflecting the total variability of the variable in space, it is found from the nugget effect that the larger the abutment value, the greater the degree of data fluctuation and the greater the amplitude of parameter change [12]. When the nugget coefficients were ≤25%, 25 ~75% and >75%, respectively, the degree of variation was relatively weak, medium and strong, while the correlation in the opposite space was strong, medium and weak, respectively.

After multiple comparisons, the most appropriate azimuth angle and the best fitting model were established. The variofunction curve was fitted step by step through the cubic control variable method, and the parameters such as the number of the hysteresis distance, inclination angle and tolerance angle were obtained, which were listed in Table 1. Through the comparative analysis of the data in Table 1, the optimal array of the best nugget coefficient and the separation distance is 13000 m, that is, the hysteresis distance is $n = 25$, the hysteresis distance is 620 m, the azimuth angle is 45°, the inclination angle is 0°, and the tolerance angle is 15°.

Table 1 Related parameters and nugget effect

Azimuth angle n	Inclination angle α	Tolerance angle β	C_0	C_0+C	$C_0/(C_0+C)$
20	5°	15°	0.38	1.18	0.3230
25	5°	15°	0.163	1.33	0.1226
30	5°	15°	0.223	1.135	0.1965
25	0°	15°	0.146	1.657	0.0881
25	5°	15°	0.163	1.330	0.1226
25	10°	15°	0.164	1.156	0.1419
25	15°	15°	0.352	0.824	0.4272
25	5°	15°	0.146	1.657	0.0881
25	5°	20°	0.190	1.371	0.1386
25	5°	25°	0.205	1.484	0.1381

4 Three-Dimensional Modeling and Analysis of Highland Temperature Field in Complex Deep-Buried Tunnels

4.1 Three-Dimensional Modeling of Highland Temperature Field in Complex Deep-Buried Tunnel

The three-dimensional modeling of the highland temperature field in complex deep-buried tunnels has a lot of multi-type and multi-source data fusion work to be completed, considering the high-precision requirements required by scientific research, the high-precision multi-resolution voxel model is applied to the modeling of the expression of this special tunnel and surrounding environment, the integration of ground temperature data and terrain data, and after substituting SGeMS, a three-dimensional temperature field of complex deep buried tunnel based on the coordination effect of voxel model and Kriging algorithm can be constructed. The modeling process consists of four steps, namely, setting the bounding box and the appropriate size mesh, fitting the optimal variogram parameters and the semi-variation-variable deviation curve, setting the variogram and reasonable search ellipsoid parameters in the Estimation module, and assigning the appropriate color to identify the high temperature region.

The three-dimensional modeling method of highland temperature field in complex deep buried tunnel environment based on voxel model and Kriging algorithm makes up for the shortcomings of insufficient expression of single type of temperature data, improves the accuracy of three-dimensional highland temperature field model of complex deep buried tunnel, and considers the influence of spatial correlation, adaptive and accuracy of related parameters, and has broad application prospects in revealing the spatial distribution characteristics of high temperature heat.

Table 2 Cross validation for precision evaluation

Tolerance angle/°	*SEM*	*RMSSE*	*ASE*
10°	−0.1326	2.483	1.356
15°	0.153	2.746	3.652
20°	0.338	3.457	6.036
25°	0.346	3.589	6.329

4.2 Cross Validations

Through objective discussion on the setting of variance function parameters, the statistical analysis function of ArcGis, a mainstream commercial software, is cross-checked to cross-verify the existing variance function parameters. Table 2 array [13] is calculated from the data in Sect. 3.2. The analysis shows that when the tolerance Angle is 15°, the average standard error (ASE) is closest to zero, and the standardized root mean square error (RMSSE) and standard mean (SEM) are the smallest, with the minimum error of 0. Therefore, separation distance = 13000 m, nugget factor = 0.146 and the ground state value = 1.657 are the optimal parameter sets, indicating that multiple control variable tuning can fit the variance function with high spatial correlation.

4.3 Normal Test

It can be seen from Sect. 3.2 that data of Kriging algorithm requires a normal distribution. The trend of cumulative distribution function and probability density function of highland temperature field data can be tested and analyzed through Histogram and statistical value [13], as shown in Fig. 3. Where, the abscissa represents the histogram and normal *QQ* picture of the temperature data of this group, and the results show a normal distribution trend, and the fitting regression curve is $y = 0.583x + 3.101$.

4.4 Analysis Methods and Ideas

Through multi-source data fusion and feature point extraction of highland temperature data in the surrounding environment of the complex deep-buried tunnel, the above parameters are selected, and the interpolation model of ground temperature in the surrounding environment of the complex deep-buried tunnel is obtained after variational function fitting and reasonable search ellipsoid parameter setting. It shows that each parameter can be adjusted by using control variable method in the process of variational function adjustment [14]. The set of parameters with minimum nugget coefficient can be iteratively selected to obtain the variable function parameter set

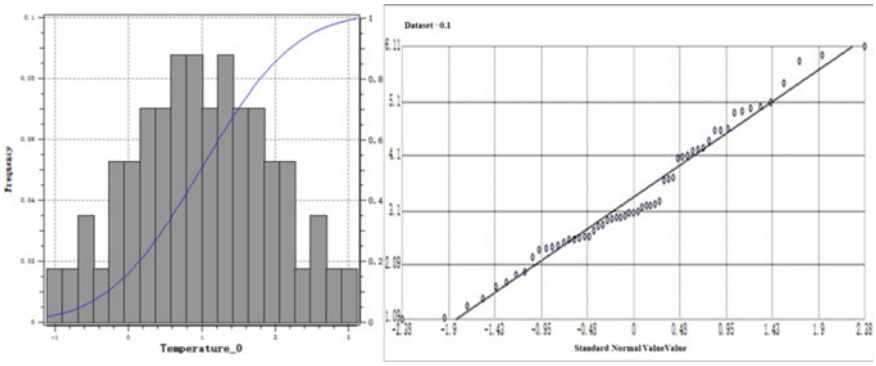

Fig. 3 Histogram and normal *QQ* plot of tunnel temperature characteristic points

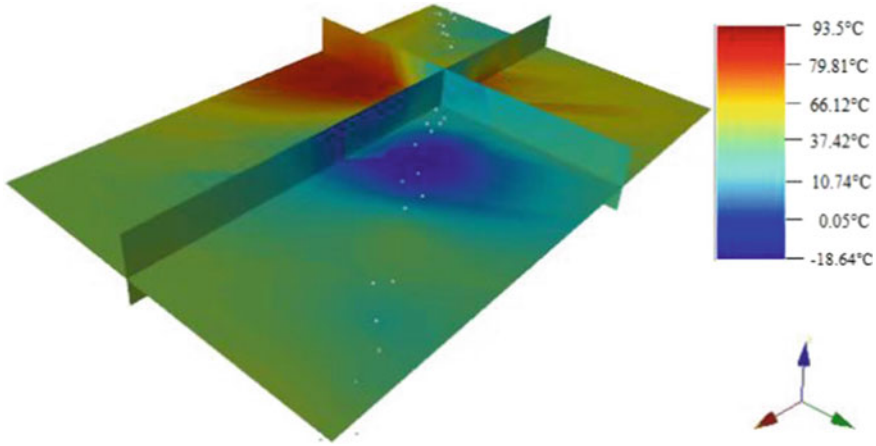

Fig. 4 Diagram of high geothermal field around complex deep buried tunnel environment

with the best spatial correlation, and the feasibility of the analysis method and idea is verified by cross validation and normalization detection.

In order to further analyze the feasibility of the 3D modeling method and analysis idea of highland temperature field in complex deep-buried tunnel environment based on voxel model and Kriging algorithm, the distribution of highland temperature field around complex deep-buried tunnel is obtained with the help of the proposed modeling method, as shown in Fig. 4. As can be seen from Fig. 4, the mileage increases step by step from bottom to top, and the temperature around the tunnel is as low as minus 18.64 °C and as high as 93.5 °C. In the low mileage area of the tunnel, the ambient temperature of some sections is greater than 26 °C, which has a slight heat damage effect. The ambient temperature near the high mileage is greater than 37 °C, and the northern part of the area is as high as 90 °C, with obvious high temperature heat source and serious heat damage. It is shown that

the three-dimensional modeling method and analysis idea of highland temperature field in complex deep-buried tunnel environment based on voxel model and Kriging algorithm are effective, and can describe the distribution of temperature characteristic points along the tunnel area.

5 Conclusions

(1) Taking the temperature field modeling around a tunnel as an example, the surface thermal infrared temperature and borehole temperature data were fused into consideration of terrain effects, and the selection of adaptive variogram parameters was discussed. Based on the multi-source fusion data, the three-dimensional model of the tunnel temperature field was established by using voxel model and Kriging algorithm, and the optimal variogram parameters could be selected by the multiple control variable method.
(2) Feature points of multi-source temperature data were extracted, and terrain factors were taken into account. Surface thermal infrared temperature data and borehole temperature data were fused, and reasonable voxel size was set to voxelize the modeling area.
(3) A set of fitting parameters were set, the multiple control variable method was used, the spatial correlation was taken into account, the key parameters in the variofunction were set adaptively, and the optimum parameters of inclination angle, tolerance angle and azimuth were selected. The accuracy analysis index and normal distribution were verified by cross-validation method, thus verifying the reliability of the optimal parameters. Finally, according to the temperature field model around the tunnel, and analyze the location of heat damage.
(4) The proposed three-dimensional modeling method and analysis of the highland temperature field in the complex deep-buried tunnel environment can provide theoretical basis and innovative ideas for the precise prevention and control of high geothermal disaster risk in the complex deep-buried tunnel environment, and has good practical significance and scientific value.

Acknowledgements The authors appreciate to anonymous reviewers whose constructive comments were helpful for the improvement of this paper. The present study had the financial support of the National Natural Science Foundation of China (Grant No. 41471320 and 41631174).

Conflicts of Interest The authors declare that they have no conflicts of interest.

References

1. Li Z, Zhang X, Clarke KC et al (2018) An automatic variogram modeling method with high reliability fitness and estimates. Comput Geosci 120:48–59
2. Gao Y, Geng JY, Jia C et al (2019) Temperature field law in cold region tunnels and insulation effect of air curtain. J Southwest Jiaotong Univ 54(5):1047–1054
3. Zhu S, Cheng J, Wang Z et al (2020) Physical simulation experiment of factors affecting temperature field of heat adjustment circle in rock surrounding mine roadway. Energy Sources Part A Recovery Utilization Environ Effects 1:1–18
4. Xu HH, Gao ML, Li ZH et al (2022) Comparison of accuracy of multi-source surface temperature estimation of near-surface temperature. Geomatics Inf Sci Wuhan Univ:1–24
5. Su PD, Zhang R, Du YB et al (2021) Non-coal tunnel gas prediction based on Kriging estimation method. J Undergr Space Eng 17(3):953–960
6. Li XJ, Wang CH, Zhu HH (2009) Application of Kriging interpolation method in formation model generation. Rock Soil Mech 30(1):157–162
7. Yan HW, Zhu GW, Xu ZY et al (2004) Volume rendering and 3D modeling of hydrogeologic layer based on Kriging algorithm. Geomatics Inf Sci Wuhan Univ 7:611–614
8. Shi C, Huang C, Nie F et al (2020) Using satellite thermal infrared images in land surface temperature inversion for identifying hidden faults: a case of Lishan piedmont fracture. Geotechn Invest Survey 48(3):45–50
9. Chen WH, Wang ZZ, Liu YT et al (2019) Multi-scale variation function estimation method in reservoir stochastic simulation. Oil Geophys Prospect 54(1):154–163, 174
10. Lei Y, Tong XC, Qu TT (2022) A scale-elastic discrete grid structure for voxel-based modeling and management of 3D data. Int J Appl Earth Obs Geoinf 113:103009
11. Zhang Q, Zhu HH (2018) Collaborative 3D geological modeling analysis based on multi-source data standard. Eng Geol 246:233–244
12. Zhang HQ, Liu JH, Wang JB et al (2018) Application of geostatistics in the simulation of vein-type ore bodies: a case study of Meiling-Hongshi copper deposit in Xinjiang. Geoscience 43(9):2980–2986
13. Wu HY, Zhu Q, Guo YX et al (2022) Multi-level voxel representations for digital twin models of tunnel geological environment. Int J Appl Earth Obs Geoinf 112:102887
14. An R, Kong LW, Zhang XW et al (2022) Effects of dry-wet cycles on three-dimensional pore structure and permeability characteristics of granite residual soil using X-ray micro computed tomography. J Rock Mech Geotechn Eng 14:851–860

Development of Truss Material Evaluation Software Using Application of AHP-Entropy and TOPSIS Method

Joe Robert Paul G. Lucena, Roselle L. Honorio, Franklyn F. Manggapis, Aaron Paul I. Carabbacan, Sanjie Dutt A. Kumar, Alfredo Mendoza Jr., and Orlean G. Dela Cruz

Abstract A truss member is an essential component for supporting roofs and bridge construction. While steel is the primary or most common material used, the industry faces various challenges today, such as product shortages and environmental concerns stemming from steel manufacturing. This research addresses these issues by identifying alternative materials for truss members using modern technology and software development. The study has four main objectives: first, to determine the necessary criteria for evaluating a truss member; second, to determine the weight of each criterion for truss member evaluation; third, to develop an evaluative framework software based on the principles of the Application of Hierarchy Process (AHP),

J. R. P. G. Lucena · A. P. I. Carabbacan
Civil Engineering Department, Colegio De Muntinlupa, 1770 Muntinlupa City, Metro Manila, Philippines
e-mail: lucenajoerobert@gmail.com

A. P. I. Carabbacan
e-mail: paulaaron120066@gmail.com

J. R. P. G. Lucena · F. F. Manggapis · A. P. I. Carabbacan · S. D. A. Kumar · O. G. Dela Cruz (✉)
Graduate School, Polytechnic University of the Philippines, Sta. Mesa, 1016 Metro Manila, Philippines
e-mail: ogdelacruz@pup.edu.ph

F. F. Manggapis
e-mail: fmanggapis.ce@tip.edu.ph

S. D. A. Kumar
e-mail: sanjiedutt_kumar@tup.edu.ph

R. L. Honorio · S. D. A. Kumar · A. Mendoza Jr.
Technological University of the Philippines Taguig, 1770 Taguig, Metro Manila, Philippines
e-mail: roselle_honorio@tup.edu.ph

A. Mendoza Jr.
e-mail: sir.apmendozajr@gmail.com

F. F. Manggapis
Civil Engineering Department, Technological Institute of the Philippines - Quezon City, 1109 Quezon City, Metro Manila, Philippines

H.-Y. Jeon (ed.), *Proceedings of the International Conference on Geosynthetics and Environmental Engineering*, Lecture Notes in Civil Engineering 374,
https://doi.org/10.1007/978-981-99-4229-9_19

the entropy method, and the Technique for Order of Preference by Similarity to an Ideal Solution (TOPSIS) method for truss member selection; and fourth and finally, to evaluate two or more alternative truss materials using the evaluative framework software. Data gathering was accomplished through surveys and literature reviews. The research team has developed software that can derive subjective criteria weights using the AHP method, non-subjective criteria weights using the entropy method, and combine the weights obtained from both methods using TOPSIS analysis.

Keywords Truss · AHP-entropy method · TOPSIS method · Truss material evaluation · Software application

1 Introduction

Truss structures have been essential in architectural and engineering design for many years. Steel has been the traditional material used in truss construction due to its durability and the strength-to-weight ratio [1]. However, with the increasing demand for sustainable and environmentally friendly construction materials, alternative materials for trusses are becoming increasingly popular [2–4]. Alternative materials, such as composite materials, engineered wood products, steel alternatives, and aluminum, offer durability and high strength while addressing some of the limitations of traditional steel trusses.

Steel production has so many flaws that it calls for exploring alternative materials. The first one is the large consumption of water. Manufacturing medium size iron mills may discharge 100 million gallons of water daily. The solid waste problem, producing more huge slag dumps, continues to build up near most steel mills. Overall, the production of steel still has adverse effects on the environment [5]. Another study presents the actual estimate of the effect of the steel mill in the Utah Valley. It shows that steel mills have the most significant air pollution in the said area [6].

Composite materials made of fiber-reinforced polymer (FRP) composites are a popular alternative to steel construction; these advantages include corrosion resistance, lightweight, and a high strength-to-weight ratio [7]. Engineered wood products, such as glued-laminated timber (glulam), laminated veneer lumber (LVL), and parallel strand lumber (PSL), offer high strength and stiffness compared to traditional wood products, it also improves performance and can reduce construction cost [8]. A study conducted by Sathre et al. (2014) found that engineered wood products have lower embodied energy and can provide a more sustainable solution for truss construction [9]. Steel alternatives, such as stainless steel, weathering steel, and high-strength low-alloy (HSLA) steel, can also be used in truss construction since it gives more resistance to fire leading to a safer solution for specific applications [10]. Finally, aluminum is another alternative material with a lower environmental impact and can provide more sustainable solutions or specific projects [11]. Numerous benefits allow replacing steel and traditional wood with alternative materials, demonstrating their

suitability. Experts can assess the choice of materials for truss construction through different methods based on the applications used.

Assessing alternative materials for truss construction is an essential step in ensuring the structural integrity and efficiency of a building or structure. Engineers and builders can make informed decisions when choosing a suitable material for their projects by using several methods to assess alternative materials. The paper in [12] presents some of the methods: (1) Material testing, which involves performing physical tests on the materials to determine the properties under different conditions; (2) computational analysis, which involves using computer simulations and models to study the materials; (3) cost analysis, which includes transportations, materials, and installation costs; and (4) environmental impact analysis.

2 Literature Review

Value Engineering/Analysis (VE/VA) is a systematic method used to improve the value of a product or service by analyzing its functions and identifying ways to improve its quality, reliability, and cost-effectiveness [13]. For example, in truss construction, VE is used to assess different materials used for trusses and determine which ones are the most cost-effective and efficient by presenting the VE job plan with careful analysis between the cost and performance [14]. However, despite its great benefits, VE/VA can be subject to biases that can negatively impact its outcome.

Biases significantly affect the results of value engineering, and this leads to sub-optimal solutions that do not fully address the needs of the projects [15]; Anchor bias arises when individuals rely too heavily on the first piece of information they receive, and they anchor their subsequent decisions to that first information [16]. Adopting a systematic and objective approach to value engineering that involves multiple stakeholders and relies on accurate and up-to-date data is essential to overcome these biases.

The AHP method is based on pairwise comparisons, determining each criterion's relative importance. Alternatives are then evaluated based on their performance on each criterion, and the researchers calculate a final score for each option. [17]. On the other hand, the TOPSIS method is a distance-based method that measures the similarity of each alternative to the ideal solution and the negative-ideal solution [18]. This systematic approach can achieve an optimal solution for selecting alternative materials.

One of the major concerns in the VA/VE approach is the slow-paced nature of the process; some of the reasons for this are: (1) manual procedure; (2) lack of standardization; and (3) lack of automation [19] To overcome these challenges, organizations need to adopt a more automated approach to value engineering, which can help to simplify the process, reduce manual effort, and ensure consistency and efficiency. The selection of truss materials is a critical task in engineering design as it impacts the final product's structural integrity, reliability, and cost-effectiveness. With the statement of the problem mentioned above, the main goal of this paper is

to present the development of a software application that utilizes Analytical Hierarchy Process (AHP), Entropy, and Technique for Order Performance by Similarity to Ideal Solution (TOPSIS) methodologies in selecting optimal truss materials which can provide a helpful tool for engineers and practitioners in the field. While the use of decision-making methods such as AHP-Entropy and TOPSIS has been widely applied in different areas [20–22], there remains a need for an automated system that can streamline the decision-making process and improve its efficiency.

3 Methodology

The researcher conceptualized the study as presented in Fig. 1. Evaluating alternative materials for truss members required several criteria. These criteria were determined by reviewing literature citing necessary information regarding mechanical properties used in truss analysis, economic aspects, and sustainability of truss member material.

The researchers establish the determination of criteria weights obtained from the literature review subjectively using the Analytic Hierarchy Process (AHP), termed in this paper as "*subjective weight*". The conduct of the survey opened the opportunity to gather subjective decisions from various civil engineers. Multiple respondents provided subjective decisions as input to generate subjective weights for various

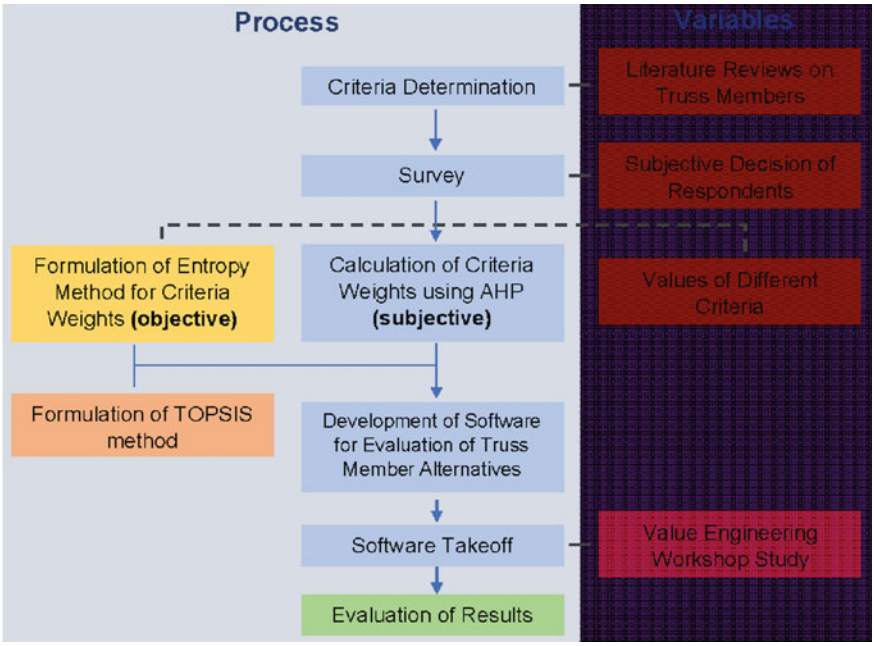

Fig. 1 Research conceptual framework

criteria. The formulation of the entropy method enabled the researcher to determine criteria weights based on the different values of each criterion. The researchers established the units for each criterion, and the corresponding value influenced the weight. This entropy method minimized the bias or personal decision of a user or an evaluator because the weights are entirely dependent on the criteria values that correspond to their units, termed in this paper as "*objective or non-subjective weights*".

The researchers process the subjective criteria weights using the software and then input the criteria values for the entropy method. It will also be capable of generating non-subjective weights. The software will generate the combined subjective and objective weights. The Technique for Order of Preference by Similarity to an Ideal Solution (TOPSIS) is added to the software to rank the evaluated materials. The software can assess various truss member alternatives by generating a report that ranks the best to least option.

3.1 Selection of Necessary Criteria

In finding and searching for suitable criteria for truss, the researchers rely on the Review of Related Literature and Studies. Following the Preferred Reporting Items for Systematic Reviews and Meta-Analysis (PRISMA) instruction [23] and the five steps systematic process introduced by Denyer and Tranfield [24], the researchers conducted a systematic literature review reporting. PRISMA will be a valuable tool for determining the criteria for a given topic by providing standardized checklists that ensures essential information is included in a systematic review [25] and has been used in the field of medicine [26], education [27], and engineering [28].

3.2 Conceptualization of Application of AHP-Entropy and TOPSIS Method to Truss Member

The researchers conceptualized AHP, Entropy, and TOPSIS method by categorizing it as (1) AHP or Analytical Hierarchy Process, which Thomas Saaty developed in the 1970s [29], it is a pairwise comparison matrix used as a subjective matter of the study and the software itself; (2) The Entropy method or the Shannon's Entropy Concept [30] is the decision comparison matrix used as the study's objective matter, Shannon's Entropy is a crucial element in information theory and is utilized as a universal indicator of uncertainty [31] and; (3) TOPSIS, or Technique for Order of Preference by Similarity to Ideal Solution, first introduced by Hwang and Yoon [32], combines the two methods mentioned above to produce an ideal ranking position for the software. The researchers used these three methods to produce evaluative software for truss members.

3.3 Develop and Execute a Survey and Collection of Data

After deciding on the necessary criteria for the study, the researchers developed a survey questionnaire using the pairwise comparison matrix; this method helps determine the relative importance of the criteria or alternatives. The researchers determined the sample size of the respondents needed in this study. To calculate the sample size n, the researchers get the total population size of the respondents required within the demographic to determine the sample size n of the respondents needed.

3.4 Calculation of Subjective Criteria Weights Using the AHP Method

The Analytic Hierarchy Process uses a pairwise comparison matrix (P) to analyze complex decisions. Constructing a pairwise comparison matrix to calculate the subjective criteria weights is necessary. The researchers used the calculated geometric mean to create a pairwise comparison matrix, input them in the correct element, and then get the sum of each column. The following we expressed in Eq. 1 as follows:

$$P = C_1 C_2 \cdots C_n C_1 C_2 \vdots C_m \begin{bmatrix} GM_{11} GM_{12} \cdots GM_{1n} GM_{21} GM_{22} \cdots GM_{2n} \\ \vdots \quad \ddots \quad \vdots \quad GM_{m1} GM_{m2} \cdots GM_{mn} \end{bmatrix}$$

$$Total = \sum_{i=1}^{m} GM_{m1} \sum_{i=1}^{m} GM_{m2} \cdots \sum_{i=1}^{m} GM_{mn} \tag{1}$$

Professionals with expertise in the field provided the subjective weights for the study. The AHP method calculated the main criteria and sub-criteria weights, which are subjective. The researchers ensured the accuracy of the sub-criteria weights. The researchers used the Consistency Index to measure consistency between pairwise comparison matrices in mathematical representation,

3.5 Calculation of Objective Criteria Weights Using the Entropy Method

A decision matrix is a tool to compare a group of choices to a set of criteria. The following can be expressed in Eq. 2 as follows:

$$D = C_1 C_2 \cdots C_n A_1 A_2 \vdots A_m \begin{bmatrix} d_{11} d_{12} \cdots d_{1n} d_{21} d_{22} \cdots d_{2n} \vdots \ddots \vdots d_{m1} d_{m2} \cdots d_{mn} \end{bmatrix} \tag{2}$$

Making utility preferences to have a standardized unit of measurement, the researchers normalized the data processed from the equation. The researchers then calculated the proportion value of the materials and criteria. The process was continued by calculating the information entropy, which is needed to calculate the information utility. The researchers used the information utility to determine the entropy weights of each sub-criteria.

3.6 Weight Combination of AHP and Entropy Method

The researchers calculated the weight combination of the main criteria weights and sub-criteria weights of the two methods. After the combined weight calculation of the main and sub-criteria, the researchers calculated the total sub-criteria combination weight by using Eq. 3.

$$w_{cj} = 1w_{ci} \times 2w_{cj} \tag{3}$$

3.7 Final Combined Weights Decision Matrix

Researchers divide the evaluation criteria of the TOPSIS method into cost and benefit criteria. A^- Represents the negative-ideal solution, and A^+ is the positive-ideal solution. TOPSIS can quantify the relative performance of each material based on which has the shortest and longest geometric distance from the PIS and NIS, respectively.

The researchers listed the materials in descending order based on their value concerning their relative proximity. Some materials have higher relative proximity values, indicating closer proximity to PIS. Therefore, the option with the highest proximity value was the most appropriate material.

To check if the created software was functional. The researchers added the last objective: "Evaluate two or more truss materials using the software". It will serve as the overall outcome of the project study. They examined the materials used to test the software in the VE Job Plan stage. In this testing stage, the researchers write down and debug all the unexpected difficulties. This trial-and-error stage makes the software the best version based on the researchers' work.

4 Results and Discussions

The researchers determined the following criteria for evaluating truss members by performing a systematic literature review. Figure 2 shows the different criteria determined from the review. The first level of the diagram shows the primary goal of the

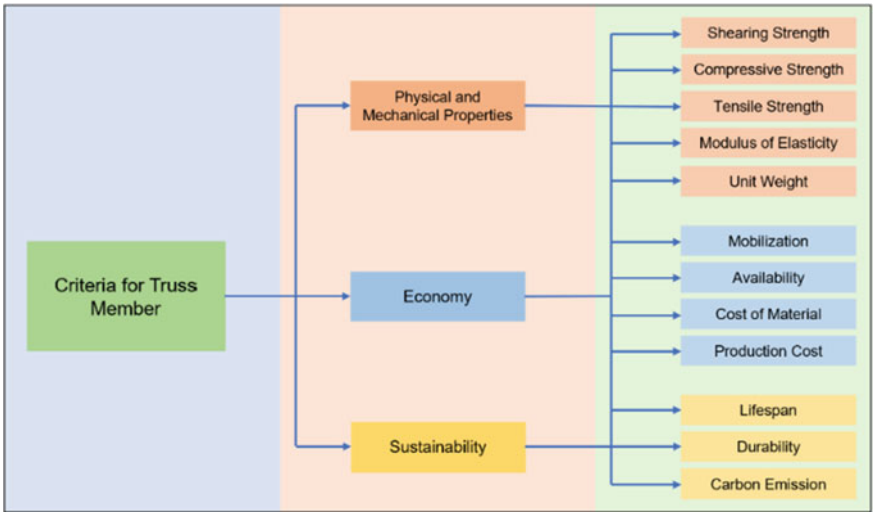

Fig. 2 Truss criteria diagram

review, which is to determine the criteria used for truss evaluation; the second level shows the three main criteria: Physical and Mechanical Properties, Economy, and Sustainability. Under these groups were the sub-criteria determined by the researcher from various literature.

The researcher aimed to determine the weights of the following criteria using the Analytic Hierarchy Process (AHP) from various civil and construction engineering professionals. The determination of sample size depends on the parameters set by the researchers and other reliable sources, such as the total population of civil engineers in the Philippines as of 2022.

4.1 Criteria Weights Derived from AHP Method

The AHP Method was utilized to determine the sub-criteria weights, as shown in Fig. 3. The data utilized in the weight determination process was gathered from a survey conducted by the researcher, given that AHP relies on the subjective judgments of each respondent. The results indicate that the sub-criterion "lifespan" holds the most weight among the other sub-criteria, with a value of 11.51%, while "compressive strength" has the least weight, with a value of 4.76%. Overall, the "Economy" main criterion was deemed the most significant, with a value of 37.92%.

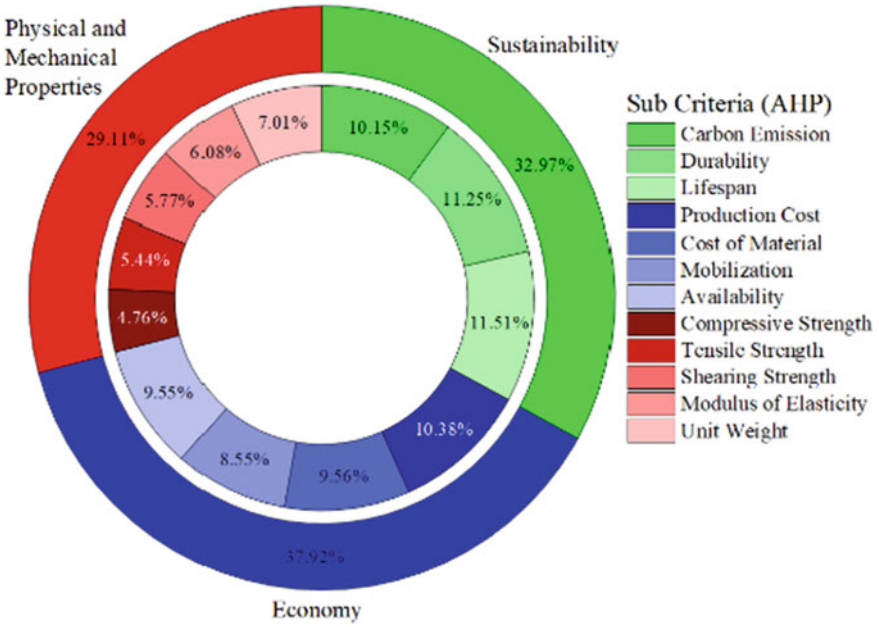

Fig. 3 Criteria weights determined using AHP Method

4.2 Development of Truss Member Evaluation Software

The software used in this study was developed using state-of-the-art technology, specifically Visual Basic.net 2010 and Microsoft Access 2016. The researcher also employed Microsoft Excel to carry out mathematical computations to validate the software's precision. The software is designed to enable users to input data gathered from the survey, which is subsequently processed using the pairwise comparison matrix method for twelve criteria. And to obtain criteria weights through AHP. Figure 4 presents the user interface for data entry, including the respondent's name.

In Fig. 5, the software's interface is presented, which grants users the ability to modify criteria for their analysis. The criteria can be placed within the software according to the criteria diagram, which provides a visual representation of their relationships. To facilitate further comprehension, users can assign each criterion with a unique Criteria ID, Criteria Code, and Criteria Description, allowing them to provide additional details or remarks regarding each criterion. This feature enhances the software's flexibility, making it an invaluable tool for conducting comprehensive analyses.

The software can calculate the geometric mean of data obtained from the pairwise comparison matrix of the respondents. The process allowed the determination of criteria weights using the AHP method. The software generated the pairwise comparison of each criterion using the geometric mean obtained from the 42 respondents, as

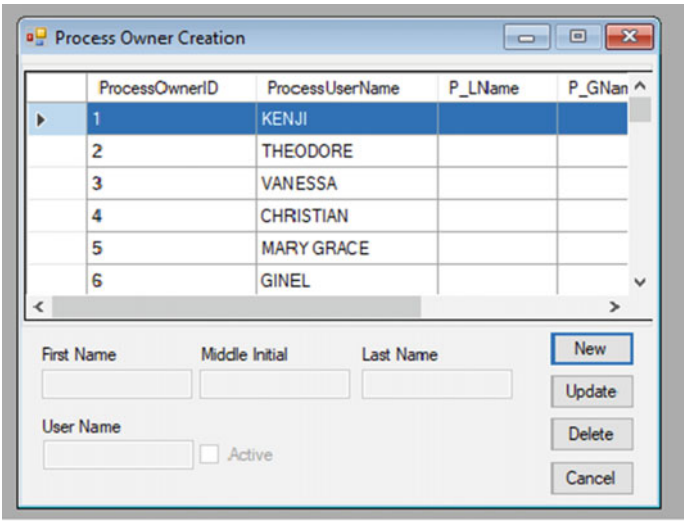

Fig. 4 Software interface for respondent's data

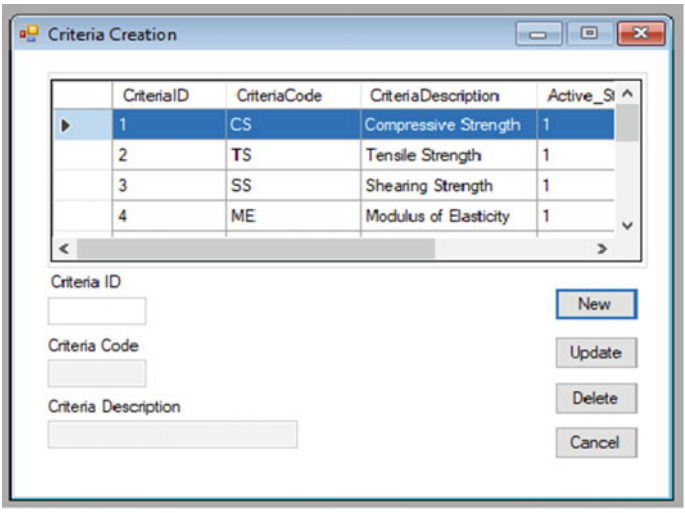

Fig. 5 Software interface for modification of criteria

shown in Fig. 6. The software is capable of calculating the criteria weights automatically based on the values of each criterion that the user inputs. To validate the software's accuracy, the researchers conducted a value engineering job plan, gathering criterion values from a literature review and market study of various construction materials.

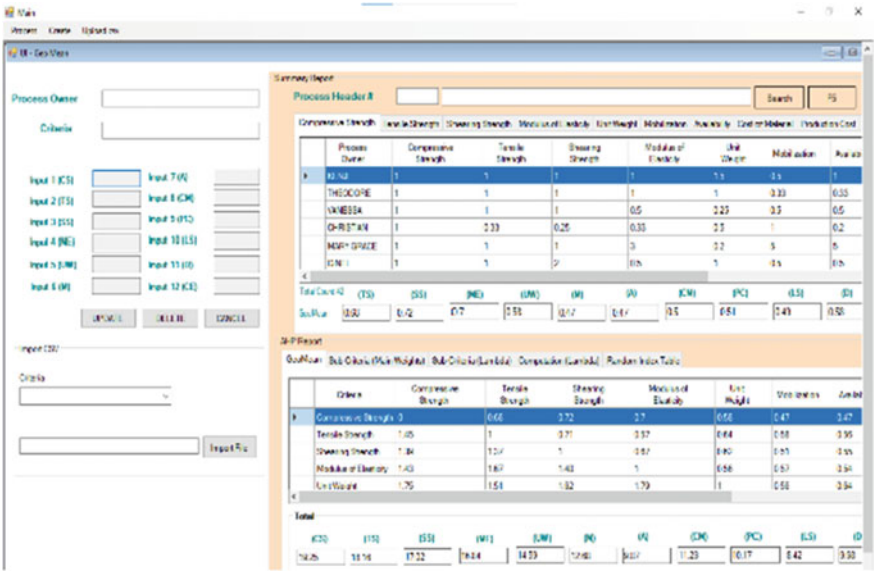

Fig. 6 Interface of software for criteria weights determination using the AHP Method

The software's validity was confirmed through the comparison of the obtained criterion weights and the weights determined by the software. Figure 7 displays the interface for computing criteria weights using the Entropy method. Moreover, the software is designed to recalculate criteria weights automatically in response to modifications made to the criteria values, thus enhancing its adaptability and functionality.The software utilized in this study facilitated the determination of sub-criteria weights based on criteria values obtained from literature reviews, which were inputted by the researchers. Analysis of the obtained results, as presented in Fig. 8, revealed that the sub-criterion "durability" holds the most substantial weight among all other sub-criteria, with a value of 20.60%, while "production cost" bears the least weight, with a value of 4.66%. The main criterion of "Physical and Mechanical Properties" was identified as the most significant, with a weight value of 41.55%.

The software can generate the combined weights from AHP and Entropy methods. Shown in Fig. 8 is the interface that shows the generation of criteria weights from combined AHP and Entropy criteria weights. The software also shows the summary where the user can see the weights of the criteria.

Upon generating combined weights, the software yielded results, shown in Fig. 9, indicating that the sub-criterion "durability" held the most significant weight among all other sub-criteria, with a value of 27.06%, while "tensile strength" had the least weight, with a value of 3.04%. Notably, the main criterion of "Sustainability" was identified as the most significant, with a weight value of 48.86%. These findings demonstrate the software's ability to perform complex computations and provide

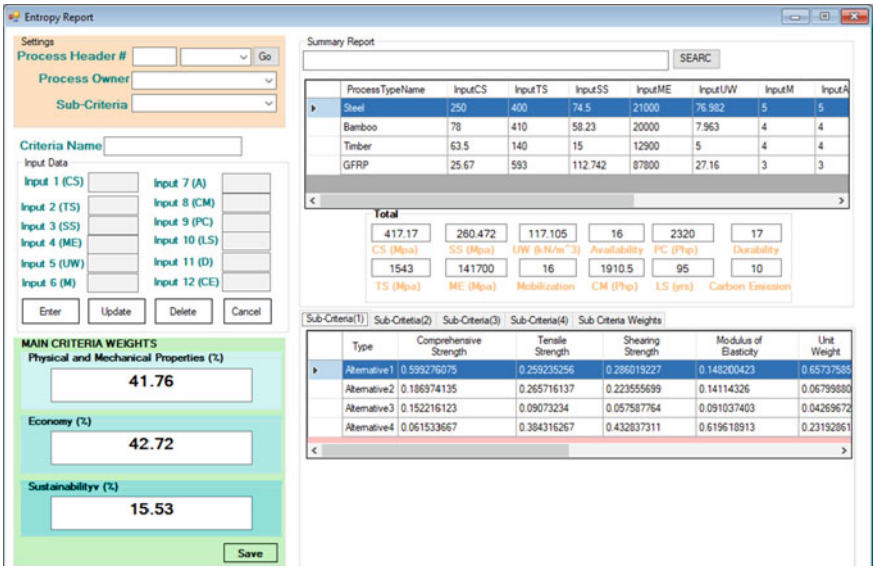

Fig. 7 Interface of software for criteria weights determination using the Entropy method

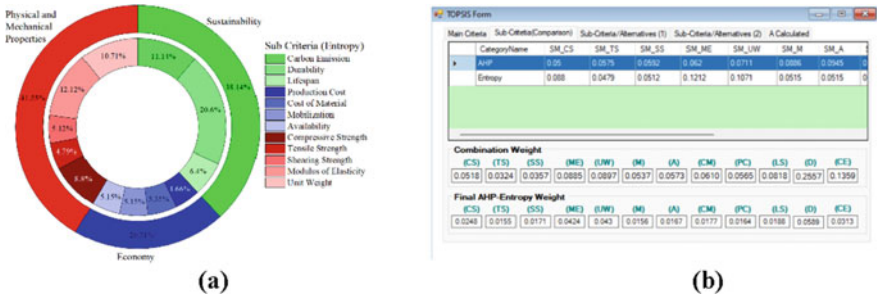

Fig. 8 Criteria weights generated by using Entropy method

valuable insights into the significance of various criteria and sub-criteria in the evaluation of materials, emphasizing the importance of considering sustainability in material selection.

Researchers can use the software to generate the *A* and *A*+ solutions for each alternative. The software, as shown in Fig. 10, can also provide the ranking of alternatives, with the best alternative having a rank of 1. For instance, the researcher conducted a simulation with four alternatives in the software, and the proximity index determined the ranking.

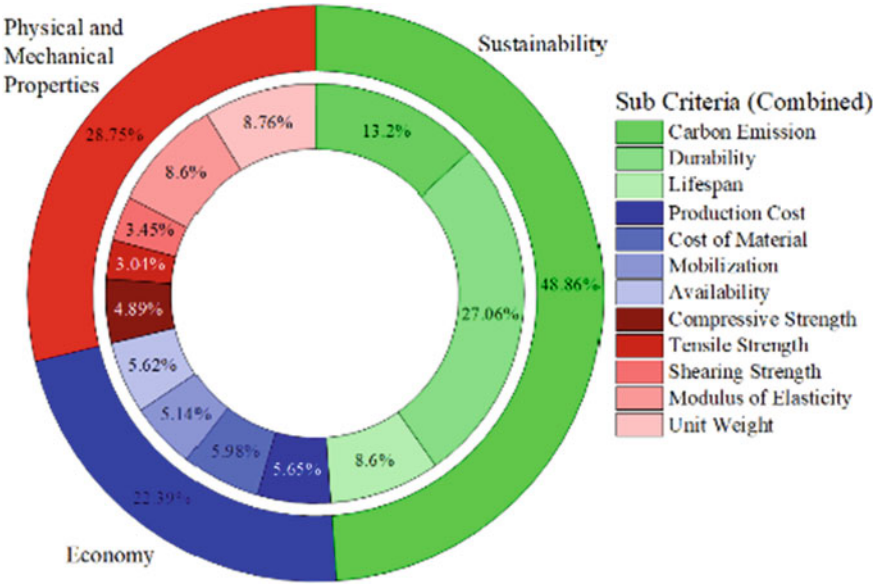

Fig. 9 Combined criteria weights from AHP and Entropy Method

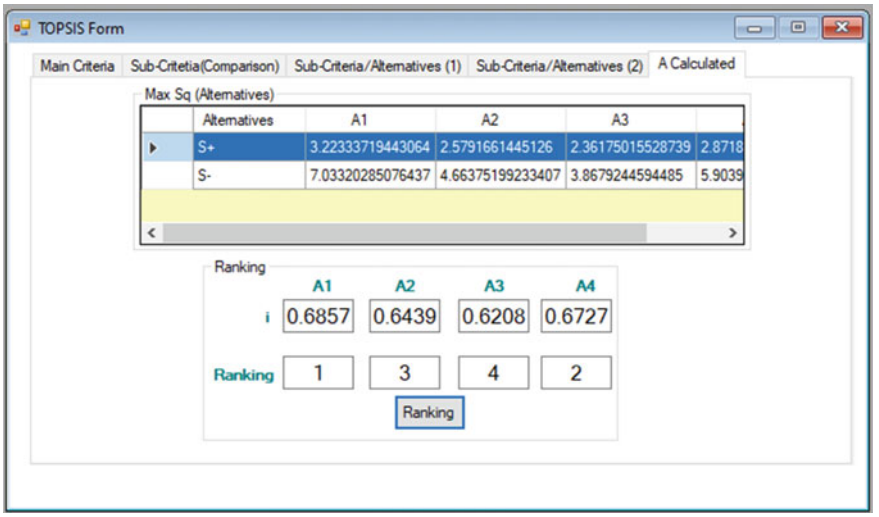

Fig. 10 Interface of software showing the ranking of different alternatives generated by software

5 Conclusions

There are twelve necessary criteria for truss members: compressive strength, tensile strength, shearing strength, unit weight, modulus of elasticity, availability, mobilization, cost of material, production cost, lifespan, durability, and carbon emission. The surveying setup of this project study comes with difficulties because of the situation while doing this study, which was the COVID-19 pandemic and the monkey fox disease. The scenario is mainly created online with very little face-to-face interaction.

Researchers notice that the Entropy and TOPSIS methods help the AHP method eliminate bias and secure consistency. The researchers use the AHP method for subjective traits in the comparison matrix and the Entropy method for objective traits in the comparison matrix. Additionally, the TOPSIS method aids the user in evaluating the truss member alternatives by ranking them from the most ideal to the least ideal alternative. Upon collecting information from licensed civil engineers and utilizing a variety of methodologies to evaluate the findings and conclusions, the researchers have arrived at several recommendations for future studies.

1. suggest that additional research be conducted to incorporate more relevant truss criteria to enhance the study. This would ensure that the study is more comprehensive and relevant to the current industry standards
2. recommend exploring various techniques for selecting appropriate criteria. This would help to ensure that the chosen criteria are relevant, accurate, and comprehensive enough to provide a thorough analysis
3. and suggest that future studies should be attempted in a more advanced program with additional features to enhance user-friendliness and convenience. This would allow participants to use the program with greater ease and efficiency, thereby improving the quality of the study.
4. Lastly, due to the impact of site construction health protocols on synchronous surveying, and strongly advise conducting face-to-face engagement for more accurate and in-depth results. In addition, future research should ideally be conducted face-to-face to allow participants to develop their ideas and perspectives.

Acknowledgements The researcher would like to acknowledge Guilberto Buendia, Rubielyn Cacabelos, Eulysis Diansig, Denver Lamusao, Joram Libarra, and Bernard Viaje for their technical knowledge and ideas that helped in the development of this paper.

References

1. Nazir A, Abate KM, Kumar A, Jeng JY (2019) A state-of-the-art review on types, design, optimization, and additive manufacturing of cellular structures. Int J Adv Manufact Technol 104(9–12):3489–3510. https://doi.org/10.1007/s00170-019-04085-3

2. Okoye FN (2017) Geopolymer binder: a veritable alternative to portland cement. Mater Today Proc 4(4):5599–5604. https://doi.org/10.1016/j.matpr.2017.06.017
3. Jeanjean A, Olives R, Py X (2013) Selection criteria of thermal mass materials for low-energy building construction applied to conventional and alternative materials. Energy Build 63:36–48. https://doi.org/10.1016/j.enbuild.2013.03.047
4. Elmessalami N, el Refai A, Abed F (2019) Fiber-reinforced polymers bars for compression reinforcement: a promising alternative to steel bars. Constr Build Mater 209:725–737. https://doi.org/10.1016/j.conbuildmat.2019.03.105
5. Bramer HC (1971) Pollution control in the steel industry. Environ Sci Technol 5(10):1004–1008. https://doi.org/10.1021/es60057a002
6. Ransom MR, Iii CAP (1995) External health costs of a steel mill. Contemp Econ Policy 13(2):86–97. https://doi.org/10.1111/j.1465-7287.1995.tb00745.x
7. Qureshi J (2022) A review of fibre reinforced polymer structures. Fibers 10(3):27. https://doi.org/10.3390/fib10030027
8. Lam F (2001) Modern structural wood products. Prog Struct Mat Eng 3(3):238–245. https://doi.org/10.1002/pse.79
9. Sathre R, González-García S (2014) Life cycle assessment (LCA) of wood-based building materials. In: Eco-efficient construction and building materials, Elsevier, pp 311–337. https://doi.org/10.1533/9780857097729.2.311.
10. Albrecht P, Coburn SK, Wattar FM, Tinklenberg GL, Gallagher WP (1989) Guidelines for the use of weathering steel in bridges. Transportation Research Board, Washington, D.C.
11. Rice JA, Foutch DA, LaFave JM, Valdovinos S (2012) Field testing and analysis of aluminum highway sign trusses. Eng Struct 34:173–186. https://doi.org/10.1016/j.engstruct.2011.09.021
12. Inyim P, Zhu Y, Orabi W (2016) Analysis of time, cost, and environmental impact relationships at the building-material level. J Manage Eng 32(4). https://doi.org/10.1061/(ASCE)ME.1943-5479.0000430
13. Chen WT, Chang P-Y, Huang Y-H (2010) Assessing the overall performance of value engineering workshops for construction projects. Int J Project Manage 28(5):514–527. https://doi.org/10.1016/j.ijproman.2009.08.005
14. Johnston J The value engineering (VE) process and job plan. U.S. Department of Transportation Federal Highway Administration
15. Smith ED, Terry Bahill A (2009) Attribute substitution in systems engineering. Syst Eng. https://doi.org/10.1002/sys.20138
16. Irias XJ (2011) Applying heuristics to civil engineering. Vulnerability Uncertainty Risk:493–500. https://doi.org/10.1061/41170(400)60
17. Li X, Wang C, Alashwal A (2021) Case Study on BIM and Value Engineering Integration for Construction Cost Control. Adv Civil Eng 2021:1–13. https://doi.org/10.1155/2021/8849303
18. Behzadian M, Khanmohammadi Otaghsara S, Yazdani M, Ignatius J (2012) A state-of the-art survey of TOPSIS applications. Expert Syst Appl 39(17):13051–13069. https://doi.org/10.1016/j.eswa.2012.05.056
19. Emami K, Emami T (2020) Value engineering: opportunities and challenges. Irrig Drain 69(2):307–313. https://doi.org/10.1002/ird.2410
20. Chen CH (2020) A novel multi-criteria decision-making model for building material supplier selection based on entropy-AHP weighted TOPSIS. Entropy 22(2):259. https://doi.org/10.3390/e22020259
21. Freeman J, Chen T (2015) Green supplier selection using an AHP-Entropy-TOPSIS framework. Supply Chain Manage Int J 20(3):327–340. https://doi.org/10.1108/SCM-04-2014-0142
22. Du Y-W, Gao K (2020) Ecological security evaluation of marine ranching with AHP-entropy-based TOPSIS: a case study of Yantai, China. Mar Policy 122:104223. https://doi.org/10.1016/j.marpol.2020.104223
23. Moher D, Liberati A, Tetzlaff J, Altman DG (2010) Preferred reporting items for systematic reviews and meta-analyses: the PRISMA statement. Int J Surg 8(5):336–341. https://doi.org/10.1016/j.ijsu.2010.02.007

24. Denyer D, Tranfield D (2009) Producing a systematic review. In: Buchanan DA, Bryman A (eds) The Sage handbook of organizational research methods, Bu Sage Publications Ltd, pp. 671–689
25. Page MJ et al (2021) The PRISMA 2020 statement: an updated guideline for reporting systematic reviews. Syst Rev 10(1):89. https://doi.org/10.1186/s13643-021-01626-4
26. Lisan Q, Rubin F, Werner A, Guiquerro S, Bonfils P, Laccourreye O (2019) Management of stylohyoid syndrome: a systematic review following PRISMA guidelines. Eur Ann Otorhinolaryngol Head Neck Dis 136(4):281–287. https://doi.org/10.1016/j.anorl.2019.05.002
27. Anil Yasin A, Abbas A (2021) Role of gamification in engineering education: a systematic literature review. In: 2021 IEEE global engineering education conference (EDUCON), pp 210–213. https://doi.org/10.1109/EDUCON46332.2021.9454038
28. Pérez J et al (2008) Integrating aspects in software architectures: PRISMA applied to robotic tele-operated systems. Inf Softw Technol 50(9–10):969–990. https://doi.org/10.1016/j.infsof.2007.08.007
29. Saaty TL (1980) The analytic hierarchy process. McGraw-Hill International, New York, NY
30. Shannon CE (1948) A mathematical theory of communication. Bell Syst Tech J 27(3):379–423. https://doi.org/10.1002/j.1538-7305.1948.tb01338.x
31. Lotfi FH, Fallahnejad R (2010) Imprecise Shannon's entropy and multi attribute decision making. Entropy 12(1):53–62. https://doi.org/10.3390/e12010053
32. Hwang CL, Yoon K (1981) Methods for multiple attribute decision making, pp 58–191. https://doi.org/10.1007/978-3-642-48318-9_3

Buried Industrial Wastes from Tyrnyauz Tungsten-Molybdenum Plant (North Caucasus): Assessment of the Negative Impact on the Ecosystems of Adjacent Territories and Problems of Their Complete Disposal

Alan Lolaev, Anatoly Gurbanov, Victor Gazeev, Aleksey Leksin, Aleksandr Dokuchaev, and Olga Gurbanova

Abstract There are large storages of industrial waste from the Tyrnyauz tungsten-molybdenum (TTMP), Sadon and Fiagdon polymetallic, Urup copper-pyrite-polymetallic and Lermontov uranium mining and processing plants (MPPs) in the North Caucasian Federal District of Russia, which can pose an environmental threat to the adjacent territories. On the other hand, the wastes of MPPs can be of significant practical interest if high concentrations of a number of valuable ore elements (Mo, W, Pb, Zn, Cu, Ag, etc.) are found in them with their significant reserves. Industrial wastes from TTMP is disposed of in two tailings. This publication presents the results of comprehensive studies of industrial waste TTMP with the identification of pollution sources and an assessment of the types and extent of their negative impact on the ecosystem of adjacent territories.

Keywords Industrial waste · Tailings · Sources of pollution · Ecological situation · Disposal

A. Lolaev (✉) · A. Gurbanov · V. Gazeev
Vladikavkaz Scientific Center of the Russian Academy of Sciences, Vladikavkaz, Russia
e-mail: abl-2010@mail.ru

A. Lolaev
North Ossetian State University Named by K. Khetagurov, Vladikavkaz, Russia

A. Gurbanov · V. Gazeev · A. Leksin · A. Dokuchaev
Institute of Geology of Ore Fields, Petrography, Mineralogy and Geochemistry of the Russian Academy of Sciences (IGEM RAS), Moscow, Russia

O. Gurbanova
Lomonosov Moscow State University, Moscow, Russia

H.-Y. Jeon (ed.), *Proceedings of the International Conference on Geosynthetics and Environmental Engineering*, Lecture Notes in Civil Engineering 374,
https://doi.org/10.1007/978-981-99-4229-9_20

1 Introduction

Toxic substances and elements are carried from the surface of tailing dumps by winds along the valleys of the Baksan, Urup and Ardon rivers to the adjacent natural pastures, farmlands and settlements (Bylym, Unal, Zintsar, Fiagdon, etc.), and heavy metals and their mineral forms accumulate in the lower horizons of the tailing dumps. A significant part of them can penetrate by infiltration into the underground hydrosphere with the formation of hydrochemical fields of toxic substances in aquifers confined to alluvial sediments, water from which is used for household needs and drinking water supply. Buried material can also be carried away by temporary watercourses, especially after heavy rains or intensive melting of snow cover, into rivers, polluting their water.

2 Case History

The Tyrnyauz Tungsten-Molybdenum Plant (TTMP) has been operating on the territory of the North Caucasian Federal District in the Kabardino-Balkarian Republic for more than 50 years. At present, the work on the extraction and processing of ores has been completely stopped. Ore was mined by underground and open-pit methods, and its concentration was carried out using flotation and chemical processes.

During the operation of TTMP, huge masses of industrial waste were dumped into storage facilities, two of which were reclaimed. As a result of his activities in the valleys of the Baksan and Gizhgit rivers (left tributary of the Baksan river), significant volumes (more than a hundred million m3) of industrial ore processing waste were formed and partially buried. In addition, for 15 km from the plant in Tyrnyauz and to the tailing dump No. 1 in the valley of the river Baksan wastes accumulated as a result of accidents in the slurry pipeline. The old tailing dump No. 2 functioned between 1959 and 1967, and the new dump No. 1 was laid down in 1967 and is being monitored (Fig. 1).

3 Results of Studies

Based on our previous research [1–5], we have obtained fundamentally new information:

I. Tailings ponds of TTMP are a complex technogenic deposit of metallic and non-metallic raw materials. The Geological Service of TTMP estimated reserves of the following metals in them: W ~ 213 thousand tons, Mo ~ 67 thousand tons, Cu ~ 15 thousand tons, Bi ~ 5 thousand tons, Au ~ 7 tons, Ag—the first tens of tons.

New geochemical data obtained by us [3, 6], in tailing dump No. 2 the average contents (in ppm) of Mo, Pb, Zn, W, and As (115, 31, 273, 511 and 111, respectively)

Fig. 1 Tyrnyauz tailing dumps №1 (43°25′53.84″N; 42°57′24.31″E) and №2 (43°27′41.77″N; 43° 0′31.03″E) of the Tyrnyauz Tungsten-Molybdenum Plant

are higher than in dump No. 1 (109, 19, 230, 314 and 58, respectively). These average grades are higher compared to the TTMP data, which may lead to an increase in the metal reserves estimated by TTMP. For the first time, data were obtained on the contents of ore elements in the material of various granulometric composition.

The reserves of mineral raw materials in the tailing dumps are estimated at millions of tons, and after extracting environmentally hazardous and economically valuable elements from them, they will be suitable for the production of various ecological clean types of building materials.

In 2014 the auger drilling of 2 wells was carried out at tailing dump No. 1 with a depth of 20 m and 2 wells—with a depth of 20 and 30 m, at tailing dump No. 2. Wells are documented with a lithological section. The core was sampled using the dotted furrow method every 1.5 m, from a drill auger. When processing the results of geochemical studies of 31 samples from the core of wells #3 and #4, obtained by X-ray structural analysis method, a clear trend of increasing W and Mo concentrations from the surface and to the base of the tailings dump No. 2 was revealed and that the clay fraction of waste, compared to the sand fraction, is characterized by higher Mo, W, Cu, As and Zn content.

W, Mo and Zn having higher content in the samples may be of practical value for extraction from the tailings. The tailings of the TTMP contain on average from 0.028 to 0.036% W and from 0.015 to 0.020% Mo [7]. As, Sb, Cu, Pb, Sn, Sr and others with elevated concentrations can hardly be of industrial interest and should be assessed from the environmental point of view, i.e. by comparing their contents with MPC values.

Detailed studies of buried waste, with huge reserves (108 million tons), made it possible to establish their mineral and geochemical composition and assess the degree of influence on the ecological safety of the environment [3]. The revealed mineral and geochemical characteristics of buried wastes predetermine both the nature of their impact on the environment and the geochemical features of their disposal by acid leaching. Environmental pollution is caused by a high concentration of a large complex of elements, significantly exceeding the MPC for soils and surface waters, especially in the small non-flowing “protective” lake of tailing dump No. 1 and in the

groundwater flowing from under its dam in the form of a series of streams. As a result of their complex impact, including constant runoff from a large "protective" lake through a drainage tunnel, the river is constantly polluted by these microcomponents Baksan river the main waterway of the Tyrnyauz region and neighboring regions [8, 9].

II. Soils of natural pastures and farmland. A significant degree of anthropogenic pollution of soils of natural pastures and farmlands (see Fig. 2) in the area of operation of TTMP and soils on the surface of the reclaimed tailing dump No. 2 has been established [1, 2, 10]. It has been proved that the degree of pollution of the territories adjacent to the tailing dumps is due to the following factors: the strength and speed of winds blowing up the valley in the morning and afternoon, and down the valley in the evening and at night; the dimension of non-reclaimed waste lying on the surface of tailing dumps, as well as exposed in natural gullies, in a number of workings at tailing dump No. 2 and from the beaches of tailing dump No. 1; direction and speed of movement of atmospheric air masses during massive explosions in open pits, produced on them during the operation of TTMP. in the latter case, dust with fine particles of a number of ore minerals was carried by constantly moving in the valley of the river Baksan by air flows for tens of kilometers.

A steady excess of MPC standards was established (for Zn—4–6 times, maximum 10 times; As—9–18 times, maximum 44 times; for Cu—9–15 times, maximum 33 times; Pb and Sb—2 times, maximum 7 times; P_2O_5—5–8 times, maximum 11 times; S—4–6 times, maximum 9 times; Ni—8–13 times, maximum 15 times) in the soil from the layer of recultivation of tailing dump No. 2.

III. Hydrosphere (surface streams and "protective" lakes). As a result of generalization of the obtained hydro-geochemical data, taking into account the physical and geographical features of this area, the main sources of environmental pollution were identified, represented by two groups—technogenic and natural.

The first group includes: (1) wastes buried in tailing dumps No. 1 and No. 2; (2) quarry dumps, which have accumulated 252 million tons of overburden; (3) aeolian pollution by "clouds" of finely dispersed dust arising from regular massive explosions in open pits during the period of TTMP activity (until November 2001). "Clouds" rose to a height of 1 km and were carried by winds over long distances; (4) surface waters in the "protective" lakes of tailing dumps and watercourses draining dumps of quarries and mines.

The second group is represented by streams: (1) draining the basal horizons of the Lower Jurassic conglomerates with sporadic U-Th mineralization; (2) arising from the underscarp of the Upper Jurassic (Tithonian)-Cretaceous limestones containing celestine (strontium) ore occurrences. The combination of man-made and natural factors has led to a high level of pollution of surface waters and soils in the area of operation of the TTMP. This is most clearly reflected in the level of water pollution in the river Baksan into which all these streams flow.

The data obtained show that the content of a large set of elements in the water of the r. Baksan, when it reaches the foothill plain, exceed from 3 to the first thousand times the MPC for drinking water: Bi—2.6; W—6.6; Mo—9; U—24; Fe—34; Sb—37; Cd—69; Rb—164; Li—400; Tl—1.16 and Be—1700. The main share of these

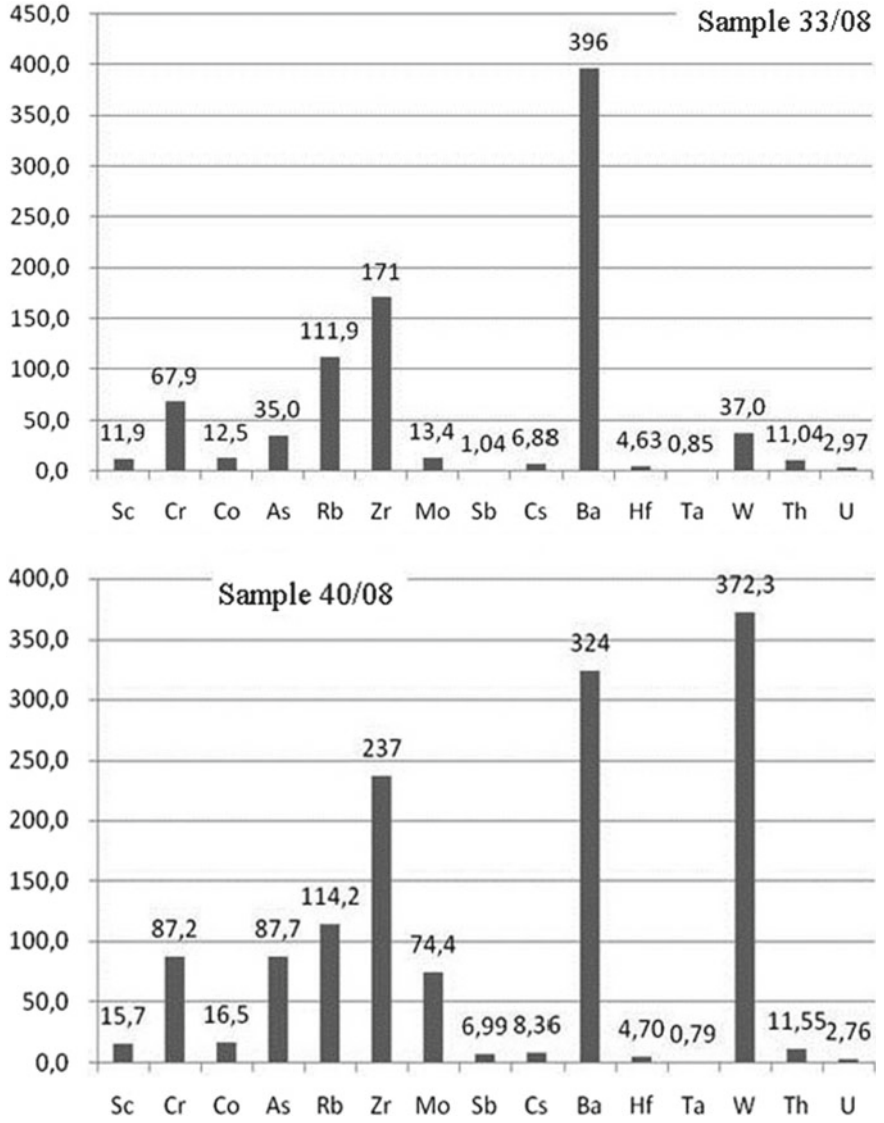

Fig. 2 The contents (ppm) of some elements in the soils of farmland in the village of Bylym, determined by the method of instrumental neutron activation analysis. *Note* Sample 33/08 (black fertile soil) was taken 0.4 km north of the outskirts of the village Bedyk, in the pasture. In it, in comparison with the background sample 30/08 (sample "BG") from a point located 1 km south of the village Zhanhoteko, increased contents of Cr, V, Ni, Ba, Pb, Sc, Sb, As, Mo, Zn (2 times) have been established; W (5 times). Sample 40/08—the soil was taken from a pasture on the left side of the Baksan river valley on the fourth above-floodplain terrace at 180 m N-E of the bulk dam of tailing dump No. 1. This soil has elevated contents of Na_2O, Fe_2O_3, MnO, Cu, Ba, Pb, Rb, Cr, V, Co in comparison with the "BG" Pb, Sc, Cs (1.5–2 times); As (3 times); Zn (4 times); Sn (7 times); Sb, Mo (~ 9.5 times); W (50 times)

elements is introduced: by the waters of the brook Big Mukulan (in its water, the concentrations of elements exceeding [several times] MPC for: Mn—84, Te—97, U—134, As—147, Fe—260, Bi—265, Sb—410, W—631, Rb—2446, Li—4921, Mo—10,687, Cd—12, Be—27.6 и Tl—32) draining the dumps of the quarries; and waters of "protective" lakes (in the western and eastern parts of the "Small" non-flowing lake, exceeding [several times] MPC in drinking water was established for: Al = 33; Si = 3.8; Ti = 2.4; Mn = 4.3; Fe = 24; As = 69; Li = 119; Be = 5085; Rb = 410; Nb = 52: Mo = 1193; Sb = 1906; Te = 30; W = 25,079; Tl = 2.28; Bi = 60; U = 13.

In the surface (1.2 m) layer of water from the northern and southern parts of the "Bolshoye", partly flowing [through the drainage tunnel] lake, concentrations have been established that exceed (several times) the MPC only for As = 1.8 and 1.66; and W = 1.6 and 1.4) flowing out: from the drainage tunnel (the concentrations of the following elements are established, exceeding [several times] MPC for: Al = 13; Fe = 23; P = 106; Li = 8.8; Be = 8.1; Rb = 4.1; Mo = 1.7; W = 1.6; U = 3.8 and dumped into the river Baksan; and in the form of streams flowing from the base of the fill dam (the concentrations of elements have been established that exceed [several times] MPC for: Si = 3.1–4.1–4.8 (respectively in samples No. 42, 43, 48); Fe = 3–3.2–0.9; As = 2.4–0.6–0.7; Li = 358–117-76.5; Rb = 61–52–41; Mo = 14,170–14,303-43,880; Sb = 944–1058–1095; W = 88,339–80,039–80,539) and flowing in r. Baksan.

These data must be taken into account in the construction of drinking water intakes and irrigation systems for farmland, i.e. to ensure the environmental safety of the population living along the valley of Baksan river, both in its mountainous part and on the plain. Two measures are being considered as measures to rehabilitate the area.

The first is the creation of an integrated processing technology of industrial waste, which will allow you to remove useful and harmful elements into the solution with the purification of the solid phase to an environmentally safe state. This will make it possible to: use the rock aluminosilicate component as building materials; and from a solution having a complex multicomplex composition, sequentially isolate valuable and harmful elements using various sorbents and other methods for subsequent implementation or disposal. It is important to note that there are no precedents for such a technology in the world and its creation is an extremely difficult task.

The second event is the construction of a water intake for the Bolshoi Mukulan stream (one of the main pollutants of the Baksan river) and a series of filters for purifying its waters from a complex of environmentally hazardous elements, in the form of ion-exchange columns of various types. This will significantly reduce their concentration in the water of the river Baksan and, accordingly, somewhat improve the ecological situation in the area.

IV. Disposal of buried waste is a complex scientific and technical problem, which involves the solution of two main tasks. The first includes a significant reduction in the concentration of the main complex of elements to obtain an environmentally friendly solid product that can be used as a raw material for the production of building materials. The second provides for the concentration of this complex of elements with the subsequent separation of a group of environmentally hazardous (As, Tl, etc.)

among them, requiring special disposal, and a group of economically valuable metals (W, Mo, Cu, Zn, Re, etc.), having a market value. Removing the latter separately can offset production costs, but isolating and isolating the former is of paramount importance.

Methods of acid leaching of waste with sequential sorption from a working solution of a geochemically heterogeneous complex of elements on different types of sorbents for their separation and concentration are most acceptable for its solution. This technology is widely used for the extraction and processing of uranium ores by heap and underground leaching [10, 11].

To solve this problem, the laboratory of IGEM RAS carried out 17 series of laboratory experiments on leaching waste from storage facilities No. 2 and No. 1 in different pH, Eh conditions and changing processing modes. Most of the experiments were carried out under favorable conditions for the process of acid leaching of the main complex of elements and included the treatment of waste samples weighing about 10 g with a solution of 1N H_2SO_4 or 1N HCl at a ratio of solid and liquid phases (S:L = 1: 5–10). The content of the main complex of elements (W, Mo, Cu, As, Zn, and Pb) was determined in the initial sample and in the dry sediment after leaching by X-ray fluorescence analysis (XRF) at the IGEM RAS laboratory, and the relative yield of elements into solution was estimated by the difference between them, contents taking into account the weight of dry sludge. Experiments on changing the pH of the pulp were carried out by adding oxidizing agents (H_2O_2 or HNO_3) to the working solution. Thus, the static and activation modes of acid leaching of wastes from storage facility No. 2 were experimentally studied.

Experiments on acid leaching of waste, carried out at temperatures up to 100 °C, showed the best results in experiments on hydrochloric and sulfuric acid treatment with the addition of H_2O_2 in the form of an oxidizing agent at a temperature of 60–80 °C for 2 h. For them, close values of the yield of basic metals into the working solution (rel.%) Were obtained: Mo—70–75, Cu—40–60, W and As—40–50, and Pb—20–60, i.e. the conditions for a sufficient level of acid leaching have been identified and patented [12]. These data can serve as a basis for the development of a technologically well-known and relatively low-cost method of sulfuric acid leaching of buried waste to obtain an ecologically safe solid product suitable for use in construction and a working solution with relatively high contents of basic elements as economically valuable (Mo, W, Cu, Zn) and environmentally hazardous elements (As, etc.), sufficient for sorption concentration and their subsequent separation.

Similar laboratory tests were carried out on waste samples with a carbonate content of about 15 rel.% from tailing dump No. 1 and, as expected, showed almost half the yield of basic elements into solution with a sharp increase in acid consumption, i.e. obvious lack of the necessary technological parameters. The performed experimental studies on small weighed portions (10 g) were the first step, followed by a similar experiment in the laboratory of Russian University of Chemical Technologies named by D.I. Mendeleev on a sample weighing 10 kg, i.e. with an increase in the mass of waste by 1000 times, which gave comparable results with laboratory experiments. This enlarged test was necessary not only for correcting laboratory experiments, but

also for obtaining a significant volume of working solution for priority experiments on sorption concentration and separation of a complex of elements on various sorbents.

In addition, the obtained data from the enlarged test can be used for a preliminary economic assessment of the technology for decontamination of buried waste of TTMP, and they will also be required for the subsequent compilation of R&D and the project of a pilot plant with a capacity of the first tons of waste per day. And only the data of industrial tests on this pilot plant can serve as the basis for the development of the main parameters, regulations and instrumentation of the industrial technology for decontamination of buried waste TTMP.

Acknowledgements The work was carried out according to the plan of the research work of the Vladikavkaz Scientific Center of the Russian Academy of Sciences—registration number: AAAA-A19-119040190054-8 and R&D on the tailings of Tyrnyauz tungsten-molybdenum plant was supported by the Russian Science Foundation under Agreement No. 14-17-00474.

Conflict of Interest The authors declare no conflict of interest.

References

1. Bogatikov OA, Bortnikov NS, Dokuchaev AY, Gurbanov AG, Karamurzov BS (2014) Technogenic mineral deposits: main aspects at the present stage (on the example of Tyrnyauz deposit). Doklady RAS Geochem 456(2):213–218 (In Russian)
2. Bortnikov NS, Bogatikov OA, Karamurzov BS, Gurbanov AG, Shazzo YK, Gazeev VM, Dokuchaev AY, Leksin AB, Shevchenko AV, Tsukanova LE (2014) Utilization of industrial waste storage facilities of Tyrnyauz tungsten-molybdenum processing plant is one of the necessary measures to solve environmental problems in Elbrus region (Kabardino-Balkarian Republic). Bull Vladikavkaz Sci Center 14(1):35–43 (In Russian)
3. Bortnikov NS, Bogatikov OA, Karamurzov BS, Gurbanov AG, Dokuchaev AY, Leksin AB, Gazeev VM, Shevchenko AV (2013) Buried industrial wastes of Tyrnyauz tungsten-molybdenum combinat composition, geochemical features and their disposal as solution of environmental and social problems in Kabardino-Balkarian Republic, Russia. Geoecol Eng Geol Hydrogeol Geocryology 3:231–245 (In Russian)
4. Bortnikov NS, Gurbanov AG, Bogatikov OA, Karamurzov BS, Dokuchaev AY, Leksin AB, Gazeev VM, Shevchenko AV (2013) Assessment of impact of buried industrial wastes of Tyrnyauz tungsten-molybdenum combine on ecological situation (soil and vegetation layer) of adjacent territories of Elbrus region (Kabardino-Balkar Republic, Russia). Geoecology Eng Geol Hydrogeol Geocryology 4:323–341 (In Russian)
5. Bortnikov NS, Gurbanov AG, Bogatikov OA, Karamurzov BS, Dokuchaev AY, Leksin AB, Gazeev VM, Shevchenko AV (2013) Assessment of impact of buried industrial wastes of Tyrnyauz tungsten-molybdenum combine on ecological situation (hydrosphere) of adjacent territories of Elbrus (Kabardino-Balkar Republic, Russia). Geoecol Eng Geol Hydrogeol Geocryology 5:405–416 (In Russian)
6. Gurbanov AG, Bogatikov OA, Karamurzov BS, Gazeev VM, Vinokurov SF, Leksin AB, Shevchenko AV, Dolov SM, Dudarov ZI, Bogotov NH, Lolaev AB, Oganesyan AKh, Dzeboev SO, Kozinkin AV, Kozakov AT, Tsukanova LE (2015) Problems of industrial waste disposal at Tyrnyau Tungsten-Molybdenum Combine (Kabardino-Balkarian Republic) in the light of new data. In: Proceedings of the Kabardino-Balkarian Scientific Centre of the Russian Academy of Sciences, Nalchik, No. 1 (63) (In Russian)

7. Laverov NP, Abdulmanov IG, Brovin KG et al (1999) Underground leaching of polyelement ores, 446 p. Academia of Mining Sciences Publisher, Moscow (In Russian)
8. Vinokurov SF, Gurbanov AG, Bogatikov OA et al (2016) Content, seasonal fluctuations and forms of migration of trace elements in surface waters of Tyrnyauz tungsten-molybdenum plant (Kabardino-Balkarian Republic) and measures to restore ecological environment. Dokl RAS 467(4):436–439 (In Russian)
9. Evdokimov SI, Evdokimov VS (2014) Extraction of metals from tungsten-molybdenum tailings from a tungsten-molybdenum concentrator. Vestnik of Vladikavkaz Scientific Center of RAS 14(2):46–52 (In Russian)
10. Turaev NS, Zherin II (2006) Chemistry and technology of uranium. Moscow Ore Metals, 396 (In Russian)
11. Reutova NV, Dreeva FR, Reutova TV, Shevchenko AA (2015) Study of genotoxic effects of the tailings of the mining and processing plant. Izvestiya Kabardino-Balkarian Scientific Center RAS, Nalchik, No 1 (63) (In Russian)
12. Vinokurov SF, Gurbanov AG, Shevchenko AV, Dudarov ZI (2017) Method of utilization of weak carbonate waste from flotation enrichment of tungsten-molybdenum ores//RU (11) 2 627 656(13) C1. Federal Service for Intellectual Property. 09.08.2017. Bulletin No. 22

Computation of Retaining Structures in Steep Slopes by Reducing M-C Strength Parameters to Failure

Jörg-Martin Hohberg

Abstract Parallel to a Benchmark problem for the FEM Strength Reduction Method by the German Geotechnical Society (DGGT), since 2015 a methodology for FEM analysis in steep slopes has been developed. It consists of three base practices, i.e., (1) finding a suitable primary stress state without excessive plastic zones; (2) simulating the erection of existing structures in the slope to derive the initial state 'as-built'; and (3) establishing a consistent concept for the analysis of deterioration, for checking ultimate limit states including seismic acceleration, and for designing rehabilitation measures in compliance with partial-safety design codes. The result is a numerical model which can serve as digital twin to study the effect of different rehabilitation measures, including prestressed ground anchors. While the application to soil-structure interaction of concrete retaining walls is demonstrated, it may be applied likewise to reinforced earth structures.

Keywords Ultimate limit state · FEM strength reduction · Steep slopes

1 Limit Equilibrium Methods Versus FEM Strength Reduction

According to common belief the *stability* of geotechnical structures is best investigated by limit equilibrium methods under varying the slip surface to find the smallest factor of safety. Comprehensive surveys of various formulations of limit equilibrium were presented 1996 by Duncan [1] and 2001 by Krahn [2]. The finite element method (FEM), in turn, is widely regarded as complementary technique to assess the *serviceability* state, e.g. ground settlements and deflection of supporting systems, that limit equilibrium methods cannot furnish. The application of FEM to embankments dates back to Clough and Woodward 1967 [3]. Also a computation of the stress distribution to improve the limit equilibrium analysis was proposed [4].

J.-M. Hohberg (✉)
IUB Engineering AG, 3007 Berne, Switzerland
e-mail: martin.hohberg@iub-ag.ch

H.-Y. Jeon (ed.), *Proceedings of the International Conference on Geosynthetics and Environmental Engineering*, Lecture Notes in Civil Engineering 374,
https://doi.org/10.1007/978-981-99-4229-9_21

Heibaum, in his dissertation from Darmstadt/Germany 1987, was probably the first to apply the FEM to anchored walls, assessing their safety against deep seated ground failure [5]. Parallel to this, the paper by Brinkgreve and Bakker [6] on the strength reduction method appeared, which most FEM codes nowadays have implemented. The German Geotechnical Society DGGT in its standing WG 1.6 [7] undertook in 2016–2018 a benchmark problem for comparison of several commercial FEM codes; they found that the results where more accurate than for limit equilibrium methods [8].

The method inevitably yields that failure mode with the lowest safety factor, but different failure modes may be triggered by varying the geological conditions, e.g., the depth of the bedrock (scenario thinking and sensitivity analysis). The stability of a slope is analyzed by reducing the strength envelope until convergence is lost and by taking the reduction factor as margin of safety with respect to either service or design level. For Mohr–Coulomb material this is known as the phi-c reduction method, but it works also for other constitutive models [9]. In the displacement-based FEM the numerical solution falls a little short of the lower bound theorem of plasticity due to the non-associated flow-rule for geomaterials, i.e., dilatancy angle $\psi < \varphi'$ [10].

2 Extension to Steep Slopes

It started in 2015 with the problem of how to analyze the widening of a mountain road in Switzerland, motivated by increasing traffic from tourist busses, SUVs and bikers on the same road. The underlying slope already exhibited signs of impending instability. Hence a numerical method for ultimate limit state analysis was needed for assessing alternative designs, e.g., the use of micro-piles in Fig. 1, as beneficial or detrimental compared to the current margin of safety against slope failure. All computations were performed with the structural & geotechnical software package ZSOIL.PC®, viz. https://zsoil.com.PC® has the unique feature that internal load functions can be applied to selected material parameters, allowing to model hardening or softening in load/time-stepping, using initial stiffness iteration.

2.1 Initial State

First of all a method of deriving a plausible initial stress state was needed. good results are achieved from the following sequence of steps, Fig. 2:

- Chose elevated values for cohesion, tensile strength and for the friction angle such that the FEM algorithm finds an initial stress state with no or small plastic zones
- Reduce first the tensile strength gradually to zero (upper left)
- In the second step reduce the friction angle and the cohesion (lower left) to realistic values, e.g. to 10 kPa and 20 kPa resp.

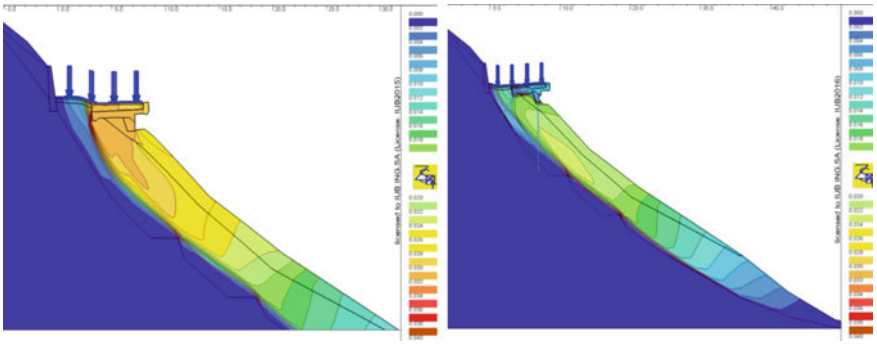

Fig. 1 Widening of a mountain road in potentially unstable slope [11], incremental absolute displacements with respect to the primary stress state [0…4 mm], without (left) and with micro-piles (right)

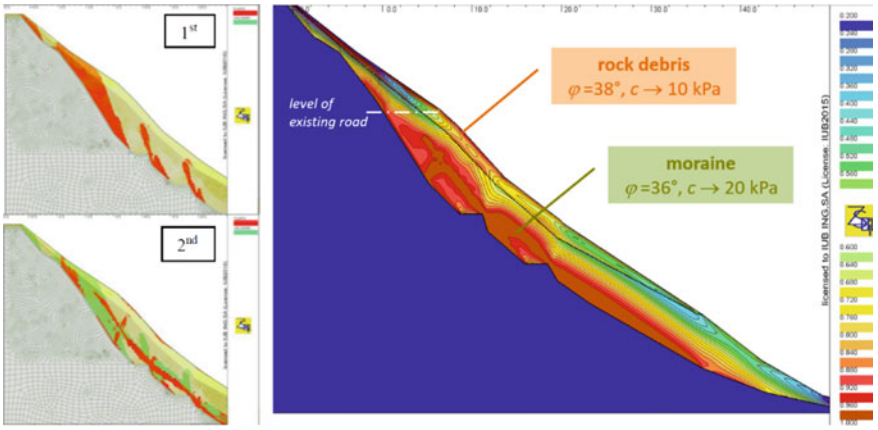

Fig. 2 Plastic zones after tension cut-off (1st step) and reduction of cohesion (2nd step, friction angle unaltered); at right strength utilization after reducing the cohesion to characteristic [0…100%]

In less critical situations it may suffice to adopt φ'_c and $f_t = 0$ from the start and work merely with artificial cohesion from the 'stiff' side.

As a second example, the case of a road tunnel is shown, traversing a gravel slope, Fig. 3. The challenge was to model the failure mode in the overlying gravel. If this problem was tackled in a naïve way by gravity turn-on, very strange phenomena may occur, such as buoyancy of the cavity in the gravel zone [12].

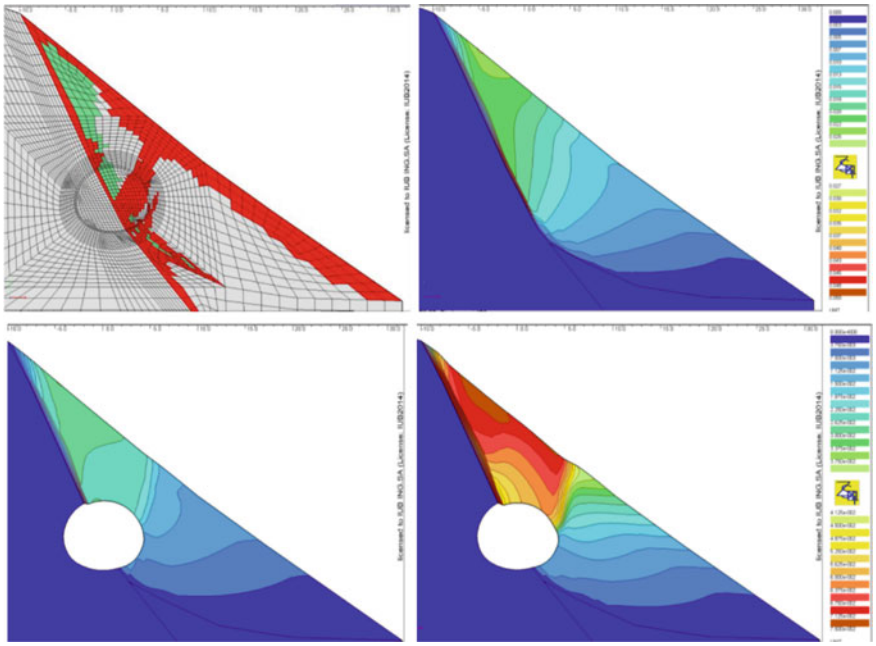

Fig. 3 Plastic zones and absolute displacements after $c'_{Gravel} \rightarrow 5$ kPa (top) [0…5 cm]; absolute displacements for unlined tunnel, $c'_{Gravel} = 10$ kPa (bottom left) $\rightarrow 5$ kPa (bottom right) [0…7.5 cm]

2.2 *Primary and Secondary Stress State*

In analyzing existing infrastructure for refurbishment it is not always necessary to revert to the 'undisturbed' state. Pre-existing artifacts like altered slopes, small footing walls and alike may be accepted as part of the initial computation, if the stress state is not affected in a complex manner. In general, however, it is useful to distinguish between the primary (near-natural) and the secondary stress state (as-built).

In the following example of a retaining wall built in the 1970s it was necessary to simulate the construction at least in an approximate fashion. Not uncommon when building a new bypass road, the preexisting hillside had to be cut back to gain construction space, keeping the backfill and the overall intervention as small as possible—for both environmental and financial reasons.

Temporary Restraints. One way is to model temporary ground anchors during excavation not in detail, but simply by introducing removable boundary conditions. Starting from the primary state, derived by c-reduction, the excavation contour is stabilized by horizontal restraints, which are temporarily applied roller supports, Fig. 4. The removal of the material in the cut is done by gradually releasing the equivalent boundary tractions via an unloading function.

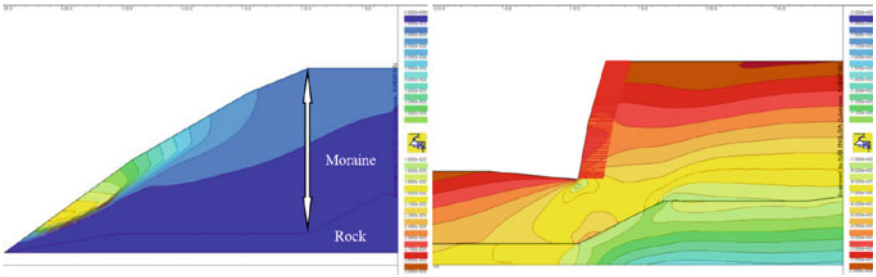

Fig. 4 Abs. displacements in undisturbed slope for $\varphi'_{Mo} = 33°$ and $c'_{Mo} \rightarrow 2$ kPa [0…3 mm] (left), vertical stress in cut slope with restraints representing temporary nailing after 40% stress release [0…−200 kPa] (right)

Figure 5 illustrates that this procedure results in a primary state with a realistic stress pattern in the ground, before the erection of the retaining wall is simulated. After complete backfilling the temporary restrains are removed and their forces released via an unloading function.

Note that the last few layers of backfill are sufficient to trigger slip lines in the backfill with accompanying slight rotation of the 8 m high retaining wall; upon removal of the restraints, both the rotation and the sagging of the backfill grow larger. With such plasticizing occurring in the backfill, either the thickness of the layers needs to be considerably reduced towards the top in order to assure numerical convergence, or a sub-incrementation on the gravity in the freshly placed layer must be applied to the backfill (Fig. 6).

The simple geometry with horizontal surface of the ground served as verification case for developing the methodology. By virtue of interface elements the friction coefficient between concrete and backfill is specified, also the contact stresses at the

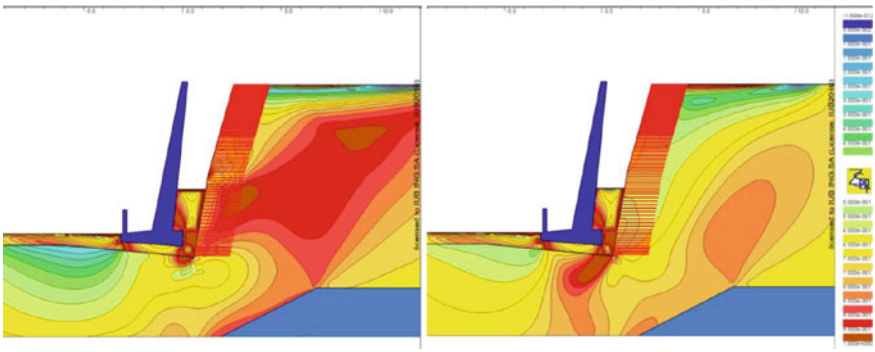

Fig. 5 Strength utilization in the ground with temporary restraints installed at 50% stress release (left), compared to gravity turn-on in the restraint state (right) [0…100%]

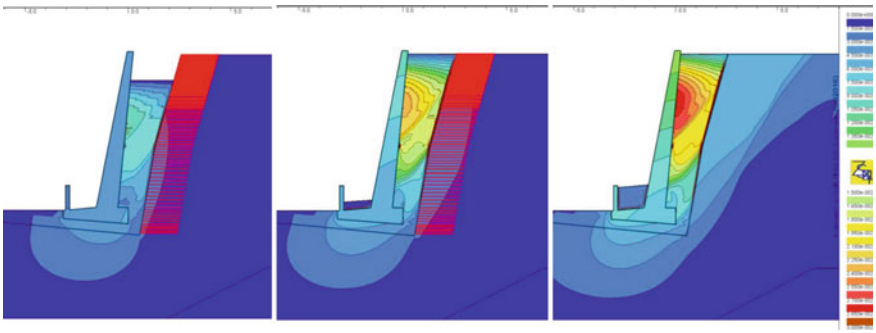

Fig. 6 Absolute displacements during backfilling (left and center) and after removing the restraints (right) [0…3 cm]

rear side of the wall and under the base slab can be recovered and compared to the analytical solution. No interface elements were used between backfill and Moraine.

Peak Strength. As an alternative to temporary restraints the construction sequence can be simulated by postulating a peak strength in the Moraine, which is subsequently released to the specified residual strength. This is demonstrated for the more complicated geometry of two angular retaining walls stacked upon each other. From core drillings behind the retaining wall the upper residual strength of the Moraine was specified as $\varphi'_{r,sup} = 39°$ and $c'_{r,sup} = 5$ kPa. The peak strength was chosen arbitrarily to $\varphi'_p = 45°$ and $c'_p = 8$ kPa [13]. Excavation in bays was assumed and accounted for by keeping 33% of the equivalent nodal forces from the excavated slope as support. After construction the peak strength is reduced to upper residual strength by means of an unloading function applied to them.

In conventional static analysis, there had been some unsatisfying guessing as to what the horizontal earth pressure—partially shielded by the base slab of the upper element—and the vertical pressure on the berm might be. With this construction simulation it became clear that most likely the berm started to shear off 35 years ago, that the two backfill spaces 'merge' and that the active wedge determining the horizontal pressure on the retaining wall is situated in the Moraine (Fig. 7).

3 Ultimate Limit State

From the secondary initial state, which is already highly nonlinear in the backfill, the ultimate limit state can be computed, finding the active wedge through strength reduction in the Mohr–Coulomb constitutive model. This is not a stability analysis, but again a softening effected through internal loading functions on the friction angle and the cohesion. After reduction to design values, the stress resultants in the retaining wall, to be compared with the factorized structural resistance, are recovered in the postprocessing (assuming elastic or inelastic concrete behavior) [14].

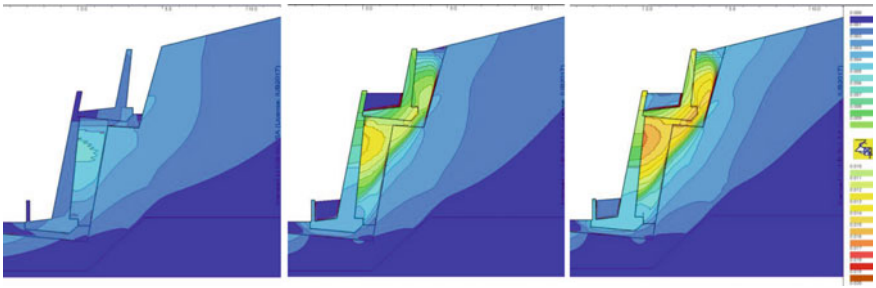

Fig. 7 Abs. displacements at peak (left and center) and upper residual strength (right) [0…3 cm]

3.1 Structural Capacity Before Strengthening

Monolithic Retaining Wall. Due to some ineffective drains, the drilling showed a soft consistency of the Moraine with low residual strength when wet. While the angle of friction ($\varphi'_{r,c} = 33°$) is not affected, the characteristic cohesion is expected to drop to zero ($c'_{r,c} = 2\,\text{kPa} \rightarrow c'_{r,inf} = 0\,\text{kPa}$). For validation of the FEM model one needs to verify, after strength reduction to these low values, whether the retaining wall stands up numerically as it does in reality. The monolithic, non-articulated section proves stable for the lowest residual strength with a safety factor $\gamma_\varphi = 1.1$, i.e. for $\varphi'_u = 30.5°$. As a second load scenario it withstands a horizontal acceleration $a_h = 8\%$ g in combination with the characteristic strength {33°; 2 kPa}, i.e. the partial safety factor on strength is 1.0 for the EQ load case. The failure mode is tilting (Fig. 8).

Stacked Retaining Wall. The articulated stacked element construction is more vulnerable and reaches the lower residual strength without additional safety margin. However, one must keep in mind, that in the numerical model the lower residual strength is applied everywhere along the slip surface and not just near the base plate in the wet zone with zero cohesion (conservative assumption).

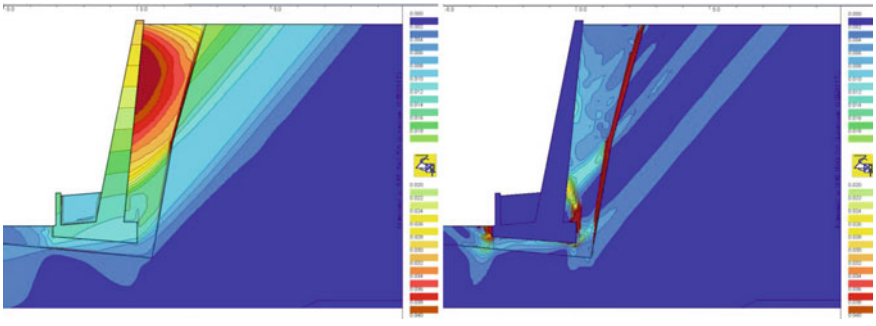

Fig. 8 ULS for the mono retaining wall at $\gamma_\varphi = 1.1$ ($c' = 0$), abs. displacements [0…4 cm] (left) and accumulated deviatoric strain [0…4%] (right)

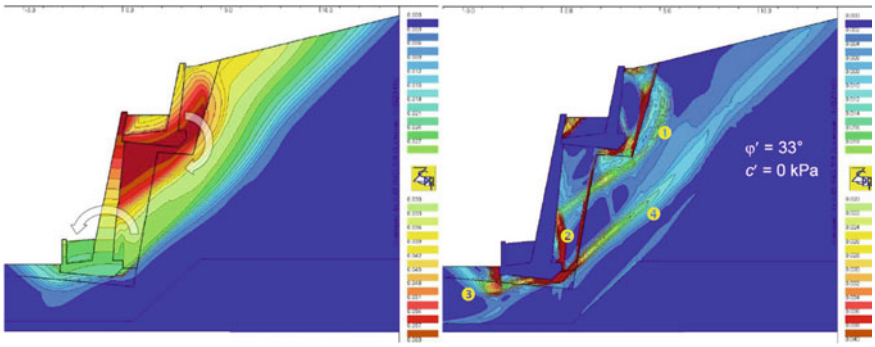

Fig. 9 ULS for the double retaining wall at $\gamma_{\varphi} = 1.0$ ($c' = 0$), abs. displacements [0…6 cm] (left) and accumulated deviatoric strain [0…4%] (right)

The failure mode is a combination of four mechanisms developing together, see Fig. 9 right:

① due to failure of the berm the upper element rotates clockwise, heel moving downwards
② the forward thrust of the upper base slab causes the lower element to rotate anticlockwise
③ this results in tilting of the lower element with a local punching of its toe
④ finally, the retaining wall ensemble shifts to the left as a whole due to slope failure.

This resembles an old man sitting on his sofa, who falls asleep and slumps down, with his knees moving forward (Fig. 9 left). Tho prevent this happening, simply his knees must be kept in place.

3.2 Effect of Prestressed Anchors

By placing a row of anchors directly under the articulation, where the upper base slab rests on the crest of the lower element, both rotations are equally blocked. Another effect of the anchoring is that the Moraine behind the retaining wall is compressed, restoring a multiaxial stress state, which raises the onset of plasticizing in the ground. Modelling the prestress as external line force allowed to assess the minimum required prestressing. This can be done by a horizontal line force (per m running), representing the group effect of discrete ground anchors at a certain spacing without discrete model of the individual anchors. As can be seen from Fig. 10, the prestressing line force leads to unloading of stress points by creating a 3D stress state in the plane-strain model. Subsequent reduction of the prestressing force reactivates the plastic zone.

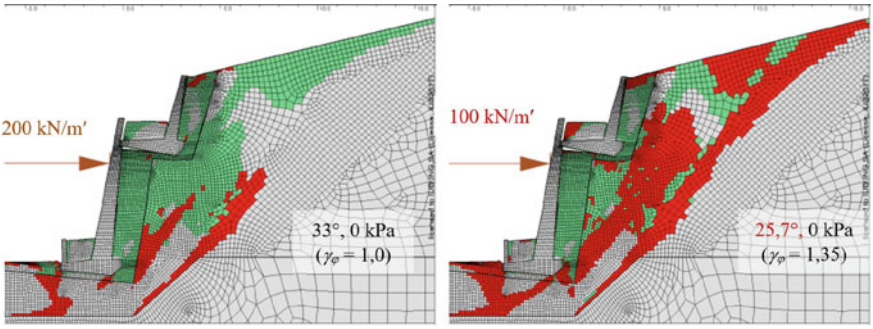

Fig. 10 Prestress at lower residual strength with unloaded plastic points in green (left); reactivation of plastic zones for 200 → 100 kN/m' prestress with the desired margin of safety (right)

Modelling of Anchors. The anchors are specified by their spacing, cross-section and prestressing force. The bond strength can be chosen to balance internal and external resistance. Ideally, the bonded length should be situated in the rock, but care needs to be taken that the resulting self-straining of the anchor due to slope failure can be accommodated within the anchor's yield strength.

Note that in the 2D plane-strain FEM model the ground can move across the free length of elongation between anchor head and the bonded end, since only the latter is affixed to the continuum. By adjusting the elastic penalty stiffness of the bond interface, the distribution of bond stresses can be regularized. Care must be taken to avoid a rigid connection to the ground, as this causes an over-stiff behavior (recognizable from the jump in prestressing force) and sliding of the retaining wall underneath the anchor head, Fig. 11 (left). Whereas the desired behavior is an elastically restrained translational displacement.

The anchor's internal yield limit and the external bond strength are not factorized by partial safety factors, as sometimes suggested. Rather, the nominal strength is allowed and checked with regard to the self-straining of anchors induced by the

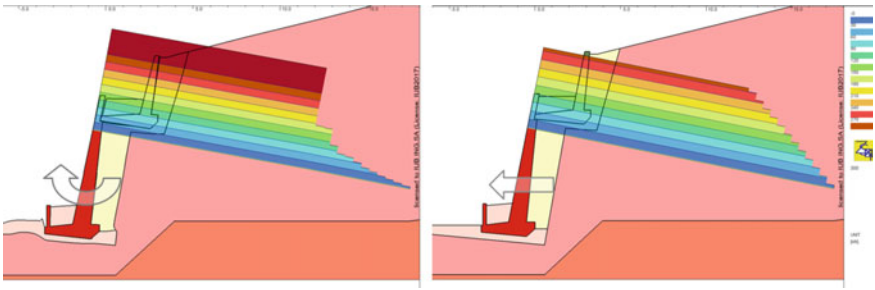

Fig. 11 Over-stiff behavior due to rigid link of the anchor to the ground (left) versus correct choice of stiffness to produce a linear bond stress distribution and soft restraint (right); note that this affects also the failure mode

sliding slope. Also the concrete retaining wall, which is modelled as ideally elastic, needs to be checked manually against punching shear failure under the anchor head.

3.3 Structural Capacity After Strengthening

Use as Digital Twin. If the base rock is not found during drilling, in variance with the design intent the bond lengths of certain anchors come perhaps to lie in the Moraine such that the entire anchor might move with the failing slope. Once the model is running, anchors can be easily adapted to the findings in the field during drilling, for instance necessitating a second row of anchors in the upper elements in case of a squat lower wall element directly founded on the out-cropping rock, Fig. 12. Allthough the longer additional anchors may not reach into the Moraine either, the stacked retaining wall is sufficiently stabilized.

Pseudo-Static Seismic loading. The horizontal acceleration is applied to both the structure and the Moraine above the base rock as volumetric load in the same way as for gravity. This is the equivalent to the well-known Mononobe-Okabe method. While the gravity acceleration remains constant, the seismic acceleration is gradually increased until failure occurs under characteristic strength parameters. By extending the anchors well behind the 'active wedge' and over-compressing the slip surface, the acceptable horizontal acceleration can be increased, even though a larger portion of the Moraine becomes involved.

Infinitely long slope. Provided the extension of the FEM mesh is long enough, the numerical method is able to solve situations in steep hillsides where the M–O formula does no longer find a solution. Also in static slope failure the angle of the slip surface may become too small to form an active wedge, which is then replaced by the failure mode of tensile stretching of overburden, cf. the small picture at the lower right in Fig. 13, showing the incremental displacement due to phi-c reduction. According to

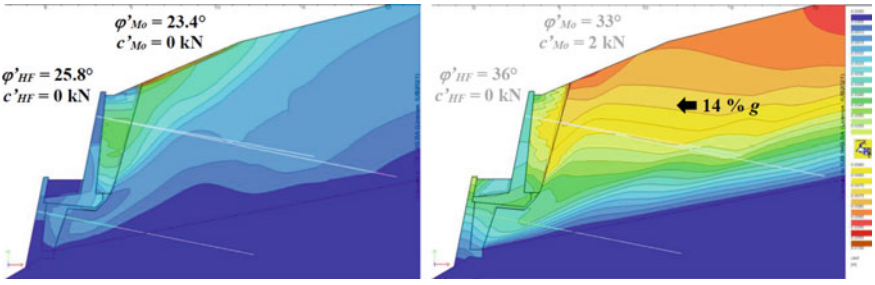

Fig. 12 Adaptation of an additional upper row of anchors to the situation in the field—abs. displacement of floating anchors under strength reduction (left) and horizontal acceleration (right) [0… 1 cm]

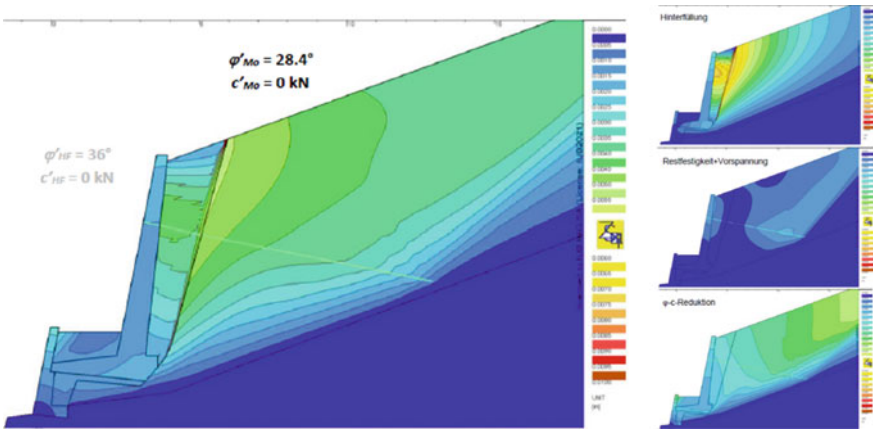

Fig. 13 Steep slope behavior of the abs. displacements (large picture) as composed from the contributions due to backfill (top right), effect of prestress during change to residual strength (center right), and further strength reduction to failure (lower right) [0…1 cm]

the theory of infinitely long slopes with a surface inclination of e.g., $\beta = 20°$, the angle of friction, where an active wedge can still form, is limited by $sin\ \varphi' = tan\ \beta$.

3.4 Aesthetic Consideration of Rehabilitation

Clearly, the peculiar geometry of this stacked retaining wall was the primary reason for applying the FEM strength reduction method. It was designed and dimensioned in the 1970s similar to a retaining wall with relief shelf, paying not much attention to the kinematics. The design had the aesthetic advantage to conceal high terrain cuts by growing plants in the trough formed by the recess of the upper wall elements. Also it could easily adapt to the ascending road, the rock outcrop, and the natural slope of the hillside above, with four different cross-sections over a length of only 140 m. From the point of buildability, the berm did not only reduce the cut-back of the slope but allowed re-use of formwork due to identical bevel of the lower and upper elements.

For the rehabilitation the same bevel ratio 5:1 was used as inclination of the prestressing bars with double corrosion protection. The flat washers of the anchor heads could thus be directly placed on the concrete surface with only an underlying Bentonite mat to prevent leakage from the injection grout. VSL thread-bars Ø 26 mm were chosen at short spacing (6 bars per 10 m element length) such that the punching resistance of the concrete elements was not exceeded. The avoidance of load-spreading walers contributes to the impression of a nonobtrusive preservation of

Fig. 14 The 45 years old retaining wall before and after modest rehabilitation

an efficient historical design, which could be implemented with a minimum of interference on the motorway (mobile platform for drilling and prestressing, scaffolding for cleaning) (Fig. 14).

4 Adaptation of the Method to Geosynthetics

The stability analysis of reinforced earth structures uses essentially the same approach of limit equilibrium analysis, which due to a-priori kinematic assumptions has the character of an upper-bound method [15]. Very often the geometry is too simple to justify elaborate FEM analysis, which may need to allow for large deformations necessary to activate the non-prestressed reinforcement. The continuous bond between the soil and the reinforcement, that functions in 2D models like a dense membrane, will prevent soil elements from moving across—unlike in the examples shown here with a free pre-tensioning length between anchor head and injection zone, or with an unbonded shaft in the case of micro-piles in Fig. 1.

Perhaps in combination with other features like precast front panels [16], or in case of more complicate geometry, the FEM strength reduction method may be attractive, serving as lower-bound method due to the displacement-based FEM formulation. Because reinforced earth walls are raised like embankments, the modelling will often be easier than shown here, with failure in or near the retaining structure, not distinguishing between primary and secondary stress states. Rather, the characteristic of the reinforcing elements will dominate the result.

5 Conclusion

While the stability analysis by strength reduction is known since 30+ years, the focus here is on special questions of steep slopes, an economic simulation of the secondary initial stress state needed for assessing the existing strength utilization, and—last but not least—on the demonstration of a versatile comprehensive approach to assessing global stability, deriving the contact pressure on structural elements, and the use as digital twin for dimensioning prestressed ground anchors in refurbishment.

It should be noted, however, that the algorithm employed is not that of global strength reduction. Rather, the software must allow to apply internal loading functions on strength parameters in order to derive a realistic primary stress in steep slopes, to account for both peak strength for construction simulation and softening to residual strength, as well as for applying safety factors in analyzing the ultimate limit state. As a nice extra feature, horizontal seismic acceleration can be accounted for in a straight forward manner, not limited to a certain ground surface inclination as with the classical Mononobe-Okabe formula. And it was shown that also the transition to an infinitely long slope can be handled in a sufficiently large domain, taken care that the sliding part is not held back in spurious tension from boundary effects.

Acknowledgements Thanks are due to Prof. Dr. Aurelio Muttoni at the EPF Lausanne, for pointing out the importance of the kinematics of the retaining wall, allowing this fully numerical analysis and design in a structural rehabilitation project.

References

1. Duncan JM (1996) State of the art—limit equilibrium and finite-element analysis of slopes. ASCE J Geotechn Eng 122(7):577–596
2. Krahn J (2003) The 2001 R.M. Hardy lecture—the limits of limit equilibrium methods. Can Geotechn J 40:643–666
3. Clough RW, Woodward RJ (1967) Analysis of embankment stresses and deformations. ASCE J Soil Mech Found Div 93(SM4):529–549
4. Fredlund DG, Scoular REG, Zakerzadeh N (1999) Using a finite-element stress analysis to compute the factor of safety. In: 52nd Canadian Geotechnical Conference Proceedings. BiTech Publ., Regina, Sask./Canada, pp 73–80
5. Heibaum MH (1993) Overall stability of anchored retaining wall. In: Internat. symp. limit state design in geotechnical engineering (ISLSD93), DGF-Bulletiner 10, Dansk Geoteknisk Forening, Copenhagen/Denmark
6. Brinkgreve RBJ, Bakker HL (1991) Non-linear finite element analysis of safety factors. In: 7th International conference on computer methods and advances in geomechanics, Proc. (Beer et al. Edts.). Balkema, Cairns/Australia, pp 1117–1122
7. DGGT section of soil mechanics, numerics in geotechnics. https://ak16.arbeitskreis-dggt.de/ Accessed 29 Mar 2023
8. Perau E (2019) Aktuelle Empfehlungen des Arbeitskreises Numerik zur Berechnung der Standsicherheit mit der FEM durch Reduzierung der Festigkeitsparameter. Koll. Numerik in der Geotechnik, Tagungsband. Bundesanstalt für Wasserbau (BAW), Karlsruhe/Germany pp 3–8

9. Potts DM, Zdravkowic L (2012) Accounting for partial material factors in numerical analysis. Géotechnique 62(12):1053–1065
10. Sloane SW (2013) Geotechnical stability analysis (51st Rankine Lecture). Géotechnique 63(7):531–571
11. Hohberg J-M (2015) Standsicherheitsnachweise für Lehnenviadukte und Stützmauern an Berghängen. Koll. Numerik in der Geotechnik, BAW-Mitteilungen 98. Bundesanstalt für Wasserbau (BAW), Karlsruhe/Germany, pp 17–31
12. Hohberg J-M (2016) Computational strategies for retaining structures in steep slopes. In: Zimmermann T, et al. (eds) Numerics in geotechnics and structures—30 years of ZSoil. PC 1985–2015. Rossolis & ZACE, pp 75–92. http://www.zsoil.com/publications/ZsoilDay2015_Book.pdf Accessed 29 Mar 2023
13. Hohberg J-M (2017) Vorgespannte Stabanker als Stützmauerverstärkung—Input-orientierte Nachweise mittels FEM. In: 32nd Cristian-Veder-Coll., Mitteilungshefte 58 (Gruppe Geotechnik Graz). Graz/Austria, pp 137–153
14. Hohberg J-M (2022) Rehabilitation of earth retaining wall for slope failure due to strength reduction and seismic acceleration, considering nonlinear soil-structure interaction. In: IABSE symp. challenges of existing and oncoming structures, report. Prague/Czech Republic, pp 766–773
15. Chehade HA, Dias D et al (2021) Pseudo-static analysis of reinforced earth retaining walls. Acta Geotech 16:2275–2289
16. Baig AA, Tiwary AK (2019) Behavior & stability analysis of geogrid reinforced earthwall—a case study in Vizianagaram (A.P). Int J Civil Eng Techn 10(4):1987–2000

Energy Saving Architecture: Multidisciplinary Improvement of Buildings Shape, Energy-Efficiency, Microclimate, Seismic-Resistance and Prevention Influences of Thermal Bridges and Mold Growth

Erkin Boronbaev

Abstract Based on the theoretical base and practice of energy-saving architecture proposed by the author, for the first time, the multidisciplinary task indicated in the title of this article was set and solved. This architecture allows harmonizing the daily, seasonal, and annual dynamics of the building's interaction with renewable energies of the environment (outside air, ground, wind, sky, surfaces facing the building) and incoming solar radiation. The thermodynamically ideal spherical building serves as a basis for comparative evaluation and improvement of real building's form. Based on the author's definition and classification of thermal bridges, an additional layer of external thermal insulation of architectural and structural thermal bridge zones was adopted. The required thickness of this layer is taken when the inner surface temperature of these zones becomes equal to the temperature on the main inner surface of the external enclosures. This investigation method was implemented by visual representation of isotherms and heat flux density in the enclosures coupling zone cross sections using the ArchiCAD20 software package. A design practice has been implemented that allows achieving, for an ordinary building in the form of a parallelepiped, the complex advantages of buildings in the form of a cylinder, the Kyrgyz National Yurt, and a sphere. Spherical buildings have significant comprehensive benefits, and the number of such buildings is increasing. The article provides practical recommendations.

Keywords Energy saving architecture · Building · Energy efficiency · Microclimate · Building shape · Thermal bridge · Mold growth · Isotherms

E. Boronbaev (✉)
Kyrgyz State Technical University named after I. Razzakov, 66, Ch. Aitmatov av, Bishkek 720044, Kyrgyz Republic
e-mail: boronbaev@elcat.kg

H.-Y. Jeon (ed.), *Proceedings of the International Conference on Geosynthetics and Environmental Engineering*, Lecture Notes in Civil Engineering 374,
https://doi.org/10.1007/978-981-99-4229-9_22

1 Introduction

In this article, for the first time, the multidisciplinary task of improving the shape of the building, energy efficiency, microclimate, seismic resistance, and preventing the influence of both thermal bridges and mold growth was set and solved.

Improving the architecture and thermal envelope of buildings to increase their energy efficiency is one of the ways to combat climate change [1].

From the position of solving such a significant problem, the author proposed the term, concept, theory, and practice of energy-saving architecture [1, 2]. Such architecture allows harmonizing the interaction dynamics of the thermal performance of the building with the renewable energies of the environment (of outside air, adjoining soil, wind, sky, surfaces facing the building) and incoming solar radiation.

The architectural and constructional parameters of the building affect [3] its thermal comfort and energy consumption. The unacceptable conditions of the internal microclimate cause moisture condensation and mold growth in buildings [4]. Moreover, architectural styles determine [5] the shape and thermal characteristics of building's thermal envelope. The author [6] for the first to put forward the concept and term of energy efficiency of the shape of a building, which serves as a theoretical basis for improving the shape of any building of a given volume relative to the performance of a theoretical building in the form of a sphere with the same volume.

The calculation formula, derived [1] by comparing the equations of thermal balances of a theoretical and any real building, makes it possible to quantify such a quality of the building as its shape. Such calculations make it possible to determine the theoretical potential for improving the shape of any building.

The building's shape's energy efficiency E_s is determined by comparing the outer surface area A_t, m^2 of thermal envelope of the spherical building of given volume, with the surface area A, m^2 of thermal envelope of a real building of the same volume. The E_s indicator is calculated [1] as the ratio of the difference between A and A_t by the value of A_t. For example, such potential of a building in the form of a cube E_s, which is equivalent to the theoretical potential for reducing thermal losses through its thermal envelope, is 24%.

For a two-story brick residential building (Fig. 1) having a less compact shape of the thermal envelope (with dimensions 12 × 8 m in plan), the indicated shape improvement potential is 31%.

Comparison of these indicators E_s shows the following: If, when designing a building in Fig. 1 takes its shape in the form of a cube, then its heat losses would be less by 7% due to such an improvement of its compactness.

The author proposed [7] a scientifically based definition and classification of thermal bridges as architectural, constructional, and operational. The latter occurs when the material of the enclosures is locally moistened (for example, by rainwater) or significant cracks appear in it.

With other equal parameters of the microclimate, relating to the room's air temperature, velocity, and relative humidity, the main parameter of a comfortable microclimate is the average temperature of the surfaces facing the room. For example,

Fig. 1 Two-story brick building with seismic-resistant reinforced concrete frame in Bishkek*. * All photos are taken by the author

the inner surface temperature of the external walls should differ from the room's air temperature by no more than 4 °C. Moreover, such a temperature should not allow, firstly, condensation of moisture; secondly, mold growth.

The building's seismic resistance is sufficient if during an earthquake the range of fluctuations of the upper point of the reinforced concrete seismic resistant frame is within acceptable limits.

The energy efficiency of the building must be not lower than a given energy efficiency certification class, for example, at least level B.

2 Methods and Results

In this article, the scientific postulate is adopted: «The thermal envelope of a spherical theoretical building does not have architectural thermal bridges». And a practically important task was set: «To obtain thermal microclimate indicators for an ordinary building in the form of a parallelepiped as for a spherical form theoretical building». To solve such a task [2, 8] the investigation method was implemented by visual representation of isotherms and heat flux density in the cross sections of thermal bridge zones using the ArchiCAD20 software package. Additional layers of external insulation on the zones of architectural and constructional thermal bridges were adopted. The required thickness of these layers is taken when the interior surface temperature on these zones becomes equal to the temperature on the interior main flat surface of the external enclosures.

The studies were carried out on the example of a typical residential building (Fig. 1) in Bishkek, Kyrgyzstan, with a cold, hot climate and a seismic load intensity of 9 points of the MSK 64 scale. It is made with a brick-filled monolithic reinforced concrete frame. Reinforced concrete elements of this frame cause intense heat losses.

Fig. 2 Mold growth on the internal corner zones of the walls: at the intersection of the exterior wall with the crossbar **a**; at the intersection of two exterior walls between themselves and at their intersection with crossbars **b**

Accordingly, the temperatures on their inner surfaces become low. Figure 2 shows the mold growth in the interior corner areas.

The mold growth shown in Fig. 2a was caused by the thermal bridges of the exterior wall intersections with the crossbar. Mold growth shown in Fig. 2b, is caused as a result of the complex influence of reinforced concrete structures of two crossbars and a corner column (Fig. 1).

Sharp corners of any bodies and building's enclosures heat up or cool down intensively. Therefore, «nature loves» smooth lines, not straight ones [1]. This idea could be the design basis for architects and the philosophy of energy saving architecture.

For a building with a cylindrical shape, there are no architectural thermal bridges, since the outer wall does not have corner zones. An example of such a case is the cylindrical outer wall of the Kyrgyz National Yurt (Fig. 3).

In this article a practically important task was set: to achieve the advantages of national Kyrgyz Yurt for widespread buildings in the form of a parallelepiped (see Fig. 1).

The authors of [2, 8] achieved the elimination of the influence of thermal bridges in the coupling zone of an external brick wall with a monolithic reinforced concrete inter-floor (Fig. 4a) and in the interior corner of the external walls (Fig. 4b).

To increase the temperature on the interior surface of the thermal bridge zone, realized: additional external layers of thermal insulation of this zone; rounding off the interior wall corners with cement-sand mortar (Fig. 4b). Isotherms in Fig. 4a [8, 9] show that with the additional external layers on the thermal bridge zones, the temperature on the corner interior surfaces at 17.9 °C is equal to the temperature on the interior main surface of the wall. The temperature on the corner (Fig. 4b) with the additional external layers and the 300 mm rounding radius is 17.1 °C. It has been calculated that when this rounding radius is increased up to approximately 305 mm,

Fig. 3 Restaurant buildings with the Kyrgyz National Yurt shape in Bishkek

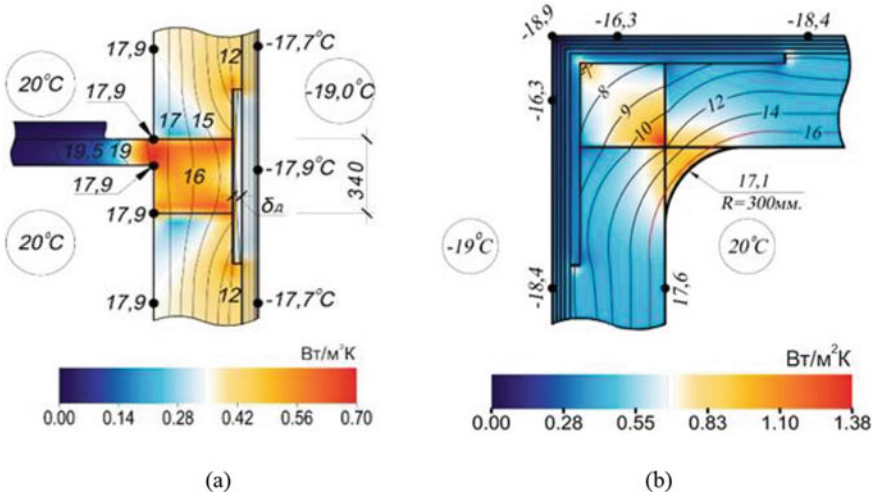

Fig. 4 Visual representations of isotherms and heat flux density on cross-sections of the zones: walls coupling with inter-floor monolithic construction **a**; walls' corner **b**

the indicated temperature rises to the temperature on the interior main surface of the wall at 17.6 °C.

In an ordinary building (Fig. 1), which has the shape of a parallelepiped, at the temperature regime shown in Fig. 4a, the inner microclimate is formed as in the cylindrical building and as in the building with the form of the Kyrgyz National Yurt (Fig. 3).

It should be noted that for the building in Fig. 1, as in [8, 9], the calculation for seismicity in Bishkek of 9 points on the scale MSK-64 was carried out using the Lira SAPR 2013 software package. The calculation results showed that the building

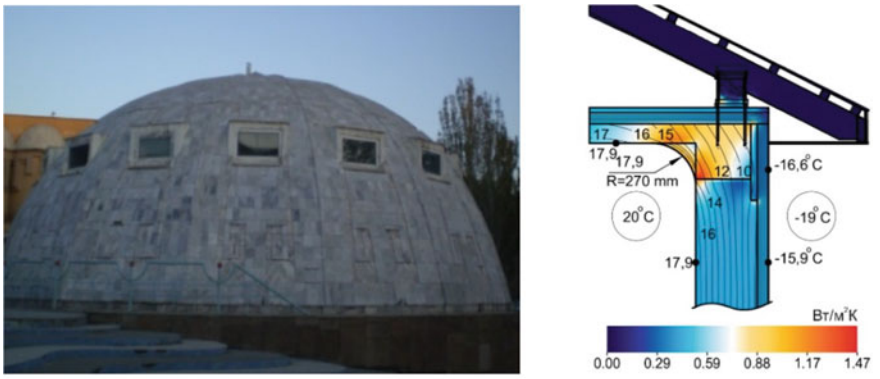

Fig. 5 Hemispherical swimming pool in Bishkek **a**; visual representations of isotherms and heat flux density on cross-sections of zone **b** walls coupling with upper floor monolithic construction

(Fig. 1) with a frame cross-section of 380 × 380 mm has a large seismic resistance margin. For this reason, the frame cross-section was reduced to 340 × 340 mm to have an additional 40 mm layer of mineral wool slabs of external thermal insulation of the frame (Fig. 4).

The hemispherical building (Fig. 5a) has minimal architectural thermal bridges.

For an ordinary building in the shape of a parallelepiped (Fig. 1), the elimination of the effect of thermal bridges in the coupling zone of an external brick wall with a reinforced monolithic concrete upper floor has been achieved. Visual representations of isotherms and heat flux density on cross-sections of zone walls coupling with upper floor monolithic construction represented on Fig. 5b. Isotherms in Fig. 5b as in [8, 9] show that with the additional external layers on the thermal bridge zones and the 270 mm rounding radius, the temperature on the corner interior surfaces is 17.9 °C. This temperature is equal to the temperature on the interior main surface of the wall.

For the building in the form of a sphere (Fig. 6a), the influences of thermal bridges of external enclosures of the building's lower zone that interact with the soil and outside air are minimal.

Scientific studies have established [2] that the provision of the required thermal insulation of the concrete foundation and its base (Fig. 6b) made it possible to increase the temperatures on the interior corner zones (17.8 °C) to the temperatures on the enclosure's main interior surfaces. Thus, it was possible to eliminate the influence of thermal bridges that interact with the outside air and soil.

The temperature results in Fig. 4 combined with the results in Fig. 5b and Fig. 6b provide the microclimate conditions of the ordinary building (Fig. 1) as in a building in the form of a sphere.

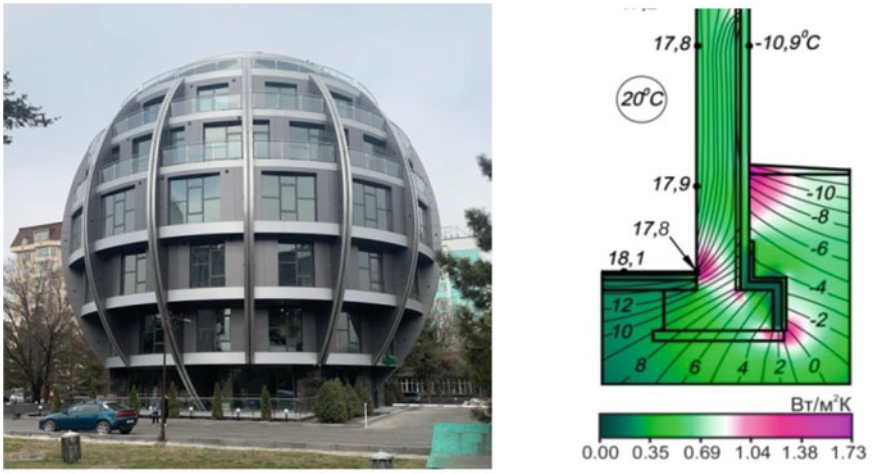

Fig. 6 Office spherical building in Bishkek **a**; visual representations of isotherms and heat flux density on the cross-section of coupling zone **b** of a concrete foundation and its base with a floor on the ground

3 Discussions

In this article, the quality of the microclimate in the building [10], its energy efficiency [11, 12] and geometric indicators [13], and reasons for mold growth on the interior surfaces of external enclosures [14] are taken as the basis for improving the thermal envelope of the building.

Multivariate computational investigations performed for the studies of two-dimensional heat flow through the thermal bridge zones, as in [15], made it possible to increase the temperatures on the interior surfaces of the enclosures due to an additional external layer of thermal insulation on these zones and rounding off the interior wall corners with cement-sand mortar. For the considered two-story house in Bishkek in the shape of a parallelepiped, such increased temperatures are set on the interior surfaces of the external enclosures, which are typical for buildings in the shape of a cylinder, the Kyrgyz National Yurt, and a sphere.

4 Conclusions

1. For the first time, a multidisciplinary improvement of the building's shape, energy efficiency, microclimate, seismic resistance, and prevention effects of thermal bridges and mold growth was set and solved. The design practice was tested on the example of a two-story brick residential building with a seismic resistant

reinforced concrete frame in Bishkek with seismicity of 9 points on the scale MSK-64.
2. The results of the research were achieved on the basis of the theory and practice of energy saving architecture to harmonize the daily, seasonal, and annual dynamics of the building's interaction with renewable energies of the environment (outside air, ground, wind, sky, surfaces facing the building) and incoming solar radiation.
3. The author proposed the basics of design practice and implemented them, which made it possible to achieve the complex advantages of buildings in the shape of a cylinder, the Kyrgyz National Yurt, and a sphere for an ordinary building in the form of a parallelepiped.
4. Buildings shaped like bodies of revolution improve multidisciplinary compactness, energy efficiency, microclimate, and seismic resistance, and prevention of the effects of thermal bridges and mold growth. From these positions, spherical buildings are more perfect.

References

1. Boronbaev E (2020) Energy saving architecture. Background, theory and practice in Kyrgyzstan. In: E3S 12th Nordic symposium on building physics 2020, NSB, vol 172, 19010, pp 1–8. Tallinn, Estonia
2. Boronbaev E, Unaspekov B, Abdyldaeva A, Tohlukova E, Holmatov K, Zhyrgalbaeva N (2022) Full-fledged use of semi-basement space by building seismic-resistance, energy-efficiency, microclimate and preventing influences of thermal bridges and mold growth. Civil Eng Arch (USA) 10(1):131–143
3. Alghamdi S, Tang W, Kanjanabootra S, Alterman D (2022) Effect of architectural building design parameters on thermal comfort and energy consumption in higher education buildings. Buildings 12(329):1–30
4. Kozdon B (2020) Microclimate conditions in rooms: their impact on mold development in buildings. Energies 13(17):4492, 1–18
5. Iranfar M, Al-Din SSM (2020) The cognition of the architectural styles role on thermal performance in houses of semi-arid climates: analysis of building envelope materials. Civil Eng Arch 8(5):929–941
6. Boronbaev E (2000) The concept of energy efficient form of buildings. Probl Control Auto 1(1):449–453
7. Boronbaev E (2013) Energy saving architecture and thermal bridges in building enclosures. Herald of the Kyrgyz State University of Construction, Transportation, and Architecture 3(41):130–136
8. Boronbaev E, Unaspekov B, Abdyldaeva A, Holmatov K, Zhyrgalbaeva N (2022) Buildings enclosures coupling by its energy efficiency, seismic resistance and microclimate. In: Akimov P, Vatin N (eds) Lecture notes in civil engineering 2021, FORM, vol 170. Springer, Basel, Switzerland, pp 495–503
9. Abdykalykov A, Boronbaev E, Begaluev U, Holmatov K, Zhyrgalbaeva N (2021) Building wall corner structures, its microclimate and seismic resistance. In: E3S 24th construction the formation of living environment 2021, FORM, vol 263, 04051, pp 1–8. Moscow, Russia
10. Lis A, Spodyniuk N (2019) The quality of the microclimate in educational buildings subjected to thermal modernization. In: E3S 12th Nordic symposium on building physics 2019, EKO-DOK, vol 100, 00048, pp. 1–12

11. Shandilya A, Hauer M, Streicher W (2020) Optimization of thermal behavior and energy efficiency of a residential house using energy retrofitting in different climates. Civil Eng Arch 8(3):335–349
12. Nikoofam M, Mobaraki A (2021) Improving passive solar housing design to achieve energy efficiency; case study: Famagusta, North Cyprus. Civil Eng Arch 9(4):1064–1074
13. Kistelegdi I, Horváth R, Storcz T, Ercsey Z (2022) Building geometry as a variable in energy, comfort, and environmental design optimization. A review from the perspective of architects. Buildings 12(1):1–42
14. Starakiewicz A, Miasik P, Krason J, Licholai L (2020) Methods of determining mold development and condensation on the surface of building barriers. Buildings 10(4):1–16
15. Hallik J, Kalamees T (2020) A new method to estimate point thermal transmittance based on combined two-dimensional heat flow calculation. In: E3S 12th Nordic symposium on building physics 2020, NSB, vol 172, 80050, pp 1–8

Investigations of Enclosures Conditions and Determination of Seasonal and Daily Work Schedules of the Mausoleum Shah-Fazil, Kyrgyzstan

Erkin Boronbaev, Aigul Abdyldaeva, Aizada Orozobekova, Nurbubu Zhyrgalbaeva, and Rishat Kozhonov

Abstract The scientific and practical task was set and solved to determine the seasonal and daily work schedules of the mausoleum, which does not have heating and ventilation systems. Perhaps in the eleventh century, when the structure was constructed, the fences were designed primarily for the strength and stability of the building, with less emphasis placed on the comfort and livability of the interior space for its inhabitants. For this reason, the enclosures in the upper zone of the museum are taken thin. Accordingly, the heat protecting performance of these enclosures is less. The measured low temperatures and high humidity on the wall's inner surfaces of the lower zones and the dome showed that the mausoleum has unacceptable microclimate conditions. The temperature, relative humidity, and internal air velocity are more dependent on weather conditions and are not comfortable for visitors. Based on comprehensive field studies of the year-round and daily state of the enclosures and the museum, the periods of winter conservation and the daily schedule of the museum were determined. The beginning and end of the conservation period should be taken when the average daily temperature of the outside air is not lower than 10 °C for five consecutive days. During the winter period, the museum will operate on a daily schedule from 11:00 to 17:00, provided that the air temperature inside the museum, 2 m above the floor level, is at least 13–15 °C, and the outside air temperature is at least 12–17 °C.

Keywords Museum building · Cold period · Enclosures condition · Measurements · Air temperature and humidity · Internal thermal condition · Winter conservation · Daily work schedule

E. Boronbaev (✉) · A. Abdyldaeva · A. Orozobekova · N. Zhyrgalbaeva
Kyrgyz State Technical University Named After I.Razzakov, 44, Ch. Aitmatov av, Bishkek 720044, Kyrgyzstan
e-mail: boronbaev@elcat.kg

R. Kozhonov
Limited Liability Company "Insolar-Climat Asia", 185, Chokmorov Str, Bishkek 720010, Kyrgyzstan

H.-Y. Jeon (ed.), *Proceedings of the International Conference on Geosynthetics and Environmental Engineering*, Lecture Notes in Civil Engineering 374,
https://doi.org/10.1007/978-981-99-4229-9_23

1 Introduction

A sharply continental and dry climate is observed throughout the territory of Kyrgyzstan. Its flat regions have relatively short and warm winters. The object of the investigation is the Shah-Fazil mausoleum, which is one of the eleventh century's surviving architectural monuments of Kyrgyzstan.

Currently, it is revered as a holy mausoleum and a place of pilgrimage for the local population and the peoples of Central Asia. The mausoleum is included in many tourist routes as a historical and architectural monument. It is located on a low rocky hill on the outskirts of the village of Safid-Bulan, Jalal-Abad region of Kyrgyzstan (Fig. 1).

The mausoleum has no heating and ventilation systems. Internal thermal conditions are characterized by air temperature, relative humidity, velocity, and temperature on the internal surfaces of the enclosures. These parameters are largely influenced by the prevailing climatic and weather conditions, making the building inextricably linked [1] with renewable energy sources such as incoming solar radiation and the surrounding environment. Thus, the environment has the thermal potential of the outdoor air, soil, wind, sky, and surfaces facing the mausoleum. These external influences have seasonal [2] and daily [1] changes. The influence of internal thermal effects, caused mainly by visitors, is insignificant [3]. The indicated internal thermal conditions, especially the temperatures on the inner surfaces of the enclosures [4], must not create a risk of visitors catching a cold. The main goal of the research is to determine the seasonal and daily work schedules of the mausoleum. Accordingly, the task of full-scale studies of the thermal state in the internal volume of the mausoleum was set.

Fig. 1 Location of the Shah-Fazil mausoleum (with coordinates 40°55' north latitude and 72°57' east longitude)

2 Methods and Results

The internal thermal conditions of the mausoleum depend on the characteristics of the architecture [1], the type and condition of the enclosure materials [5–7], the quality and orientation of the window and door openings. Figure 2 shows the appearance and schematic section of the mausoleum.

The base of the mausoleum is square in plan, with internal dimensions of 7.84 × 7.84 m and external dimensions of 11.12 × 11.16 m (Fig. 2b). The foundation and basement are made of limestone blocks laid on loess mortar. The height of the foundation is 0.6 m above ground level. On the northwestern (NW) facade of the mausoleum, there is a doorway with wooden shutters and two window openings with bars. A similar window opening is located on the southwestern (SW) facade. The walls of the structure are built using baked brick masonry with dimensions of 0.15 × 0.27 × 0.035 m.

The upper part of the mausoleum takes the form of an octahedron, which serves as the base of the dome. The total height of the structure is approximately 15 m. The interior of the mausoleum is adorned with ornamental patterns such as ribbon belts, borders, and rosettes (Fig. 2b). The thickness of the enclosing structures decreases with height: the lower brick wall has a thickness of 1.68 m, while the upper part of the dome is only 0.27 m thick.

During the coldest winter months, on some cloudy days, the outside air temperature can drop as low as −15 °C. As a result, the internal volume of the mausoleum experiences low temperatures during this cold period.

Based on field studies, it has been found that it is necessary to stop visitors from coming to the mausoleum during the coldest period of winter. The duration of this winter conservation period depends on seasonal weather conditions.

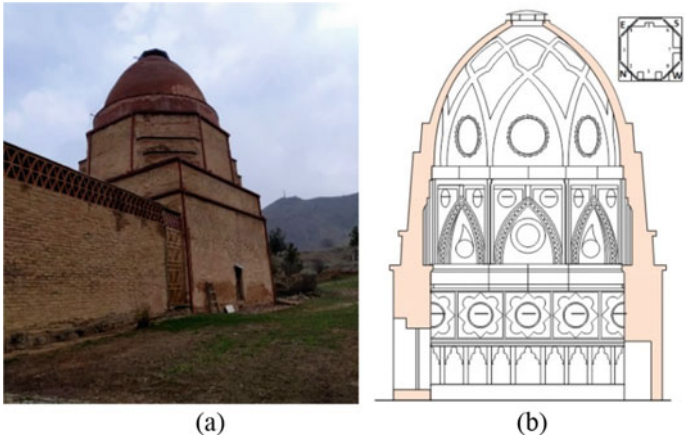

Fig. 2 External view **a** and sectional diagram **b** of the Shah-Fazil mausoleum [3]

It is recommended to begin and end the conservation period based on the days in autumn and spring where the average daily outdoor air temperature is at least 10 °C for five consecutive days. The average statistical results of long-term observations of weather conditions show that such a period is approximately from October 25 to April 1.

In Fig. 3, the conservation period is marked depending on the change in the average monthly temperatures of the outdoor air.

In this area, the average monthly temperatures during the cold period are not lower than −5 °C, and during the warm period they do not exceed 25 °C. The humidity of the outdoor air ranges from 48 to 70%. It has been found that the humidity of the materials of the enclosures greatly affects the internal thermal conditions of the mausoleum [8, 9]. Wetting of various zones of the dome, adjacent to its base, is observed during different seasons and times of the day due to atmospheric precipitation (Fig. 4).

During the research, it was observed that there is an increased humidity level in the lower zones of the southwestern (SW) wall (Fig. 5a) as a result of capillary diffusion of moisture along porous building materials.

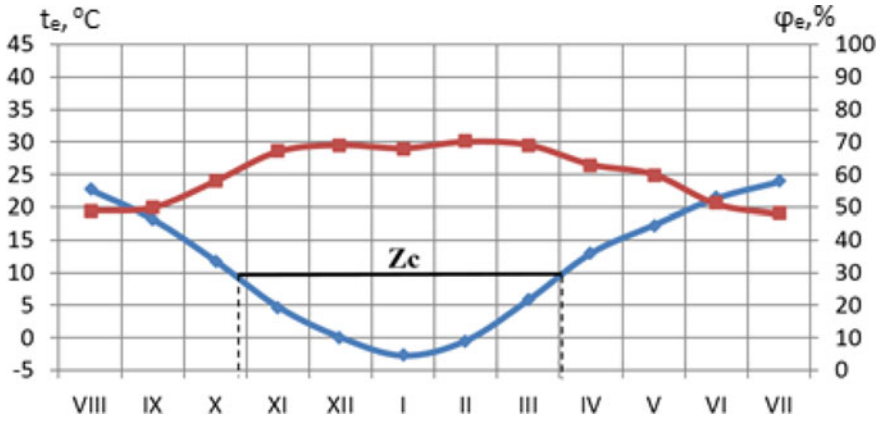

Fig. 3 Conservation period z_c of the mausoleum with average monthly temperatures and relative humidity of the outdoor air

Fig. 4 Dome areas with high humidity

Fig. 5 Zones with high humidity of the walls lower zones **a** and near the place of drainage of atmospheric precipitation **b**

Similar moistening is also found on the northwestern (NW) and northeastern (NE) walls. Additionally, increased humidity is observed in areas of the outer walls close to the point of precipitation removal (Fig. 5b). To improve the thermal condition of the enclosures [10, 11], it is necessary to ensure reliable coverage of the dome and proper drainage of precipitation water.

Temperature, relative humidity, and air velocity were measured using a Testo 425 device. The humidity of the upper layers of enclosure materials was measured using Testo 606–2 on their internal (Fig. 6a) and external (Fig. 6b) surfaces.

During the hot period, the microclimate conditions inside the mausoleum remain comfortable even in the hottest period of summer due to the high thermal mass of the mausoleum.

Fig. 6 Field measurements of temperature and humidity on the internal **a** and enclosures' external surfaces **b**

It has been found that the presence of visitors has a negligible impact on the variations in air temperature and humidity inside the building. These parameters are more dependent on the degree of opening of the doors and windows.

Field studies covered the annual period of change in the condition of the mausoleum enclosures.

Figure 7 shows the lines of change in the period from 11 am to 5 pm in temperatures and relative humidity of indoor air, as well as temperatures on the inner surface of the walls at a height of 2 m from the floor level, which are oriented to NW, NE, SE, and SW.

As shown in Fig. 7, from 11:00 am to 3:00 pm, the temperature of the indoor air at the indicated height gradually increases from 14 to 20 °C. The temperature on the inner surfaces of the enclosures is much lower than the internal air temperature. For the period under consideration, the relative humidity of the indoor air remained higher than that of the outdoor air. The same pattern of changes in these parameters shows that the parameters of the indoor air are formed depending on the incoming outdoor air. The temperature values on the inner surface of a wall oriented to the northwest are lower than such temperatures on the surfaces of walls of other orientations.

Figure 8 depicts the temperature measurements on the inner and outer surfaces of walls at a height of 2 m from the floor, with different orientations.

As shown, the temperature on the inner surfaces of walls raises by 3–4 °C at 3:00 pm (Fig. 8a). Under the influence of the total intensity of the incoming solar radiation, the temperature on the outer surfaces of the wall, oriented to the SE (at

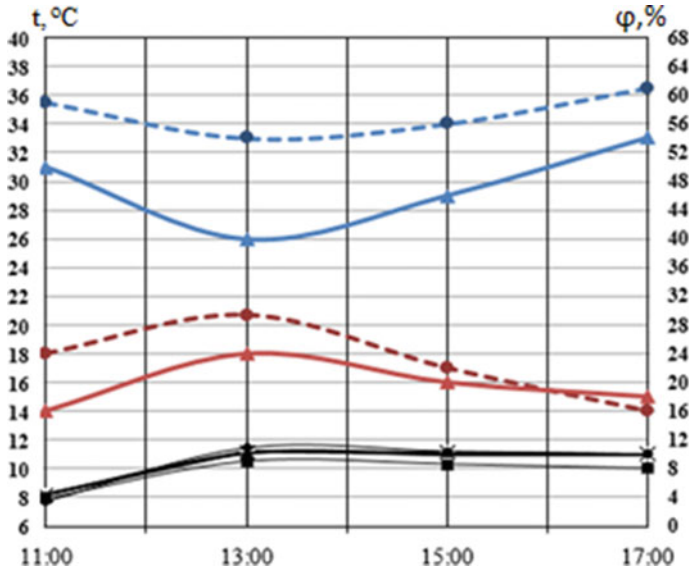

Fig. 7 Graphs of air temperatures: indoor; outdoor; of air relative humidity: indoor; outdoor; of internal surface temperatures of walls in the following orientations: southeast; southwest; northwest and northeast

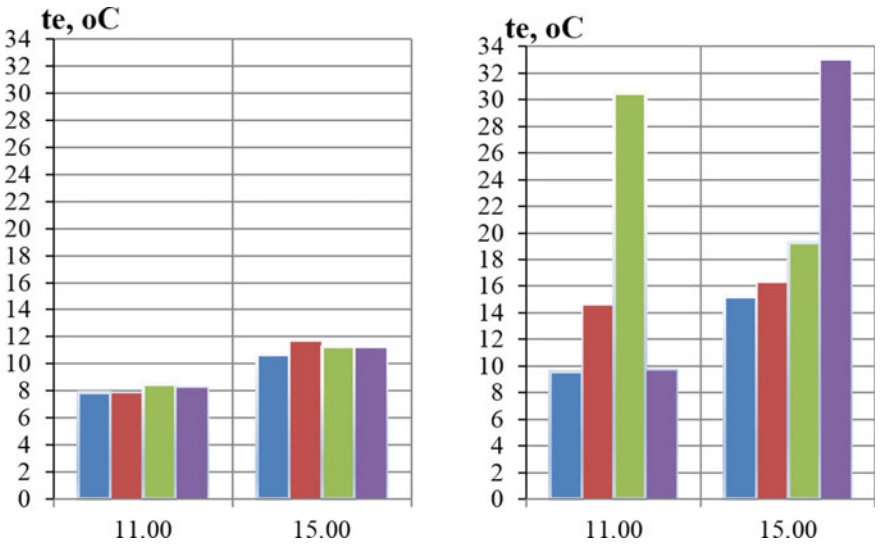

Fig. 8 Temperature values on the internal **a** and external **b** surfaces of the fences at a height of 2 m above the floor level in the following orientations: northwest, northeast, southeast, southwest

11:00) and SW (at 15:00), rises to 30–33 °C. The temperatures on the outer surfaces of the walls with the other three orientations are higher at 15:00 than at 11:00 due to the higher outside air temperature at that time.

3 Discussions

The outside air temperature, wind direction and speed, and incoming solar radiation not only affect the microclimate formation but also play a crucial role in the preservation of architectural monuments [12]. The authors of this article found that the parameters of the outside air affect the thermal state of the building envelope. As in [13, 14], the measurements showed that external climatic influences determine seasonal and daily fluctuations in the condition of the enclosures and the internal thermal conditions of the mausoleum. Other studies [15–17] similarly note the influence of architectural and planning indicators on the formation of indoor air parameters. Moreover, the temperature and humidity regimes of religious buildings also affect the state and thermo-physical parameters of the building envelope materials [16].

The absence of heating, ventilation, and air conditioning systems leads to unfavorable thermal conditions for the internal and external surfaces of the enclosures [18, 19]. Therefore, it is required to introduce a restriction on the period of operation of the mausoleum. Studies by other researchers [20, 21] on creating a suitable

microclimate and controlling indoor air parameters in similar structures support the need for full-scale measurements of microclimate parameters [22, 23]. The obtained data similarly can assist in making informed decisions depending on the temporal changes in parameter values during different seasons and times of the day.

4 Conclusions

Based on comprehensive field studies of the year-round and daily state of the enclosures and the internal volume of the museum, the periods of winter conservation and the daily schedule of the museum were determined.

The beginning and end of the conservation period should be determined by the average daily temperature of the outside air, which should not be lower than 10 °C for five consecutive days. The average statistical results of long-term observations of weather conditions show that such a period is approximately from October 25 to April 1.

The daily schedule of the museum during the winter period is set from 11:00 to 17:00, when the air temperature in the museum, at a height of 2 m from the floor level, is at least 13–15 °C and the outside air temperature is at least 12–17 °C.

References

1. Boronbaev E (2020) Energy saving architecture: background, theory and practice in Kyrgyzstan. In: E3S 12th Nordic symposium on building physics 2020, NSB, vol. 172, 19010. Tallinn, Estonia, pp 1–8
2. Boronbaev E (2004) Graphs of optimization of year-round modes of heat supply of the microclimate in the building. In: The news of Universities. Construction vol 10. Novosibirsk, Russia, pp 60–64
3. Boronbaev E, Abdyldaeva A, Abramov B, Mukhanova K, Polyakov Y (2017) Field experimental studies of the thermal regime of the Shah-Fazil Mausoleum. Sci New Technol Innov Kyrgyzstan 1:45–48
4. Boronbaev E (2011) Field studies of daily temperature changes on the outer and inner surfaces of the outer walls of the building. Indus Civil Const 2:57–58
5. Boronbaev E, Unaspekov B, Abdyldaeva A, Holmatov K, Zhyrgalbaeva N (2022) Buildings enclosures coupling by its energy efficiency, seismic resistance and microclimate. In: Akimov P, Vatin N (eds) Lecture notes in civil engineering 2021, FORM, vol 170. Springer, Basel, Switzerland, pp 495–503
6. Boronbaev E, Unaspekov B, Abdyldaeva A, Tohlukova E, Holmatov K, Zhyrgalbaeva N (2022) Full-fledged use of semi-basement space by building seismic-resistance, energy-efficiency, microclimate and preventing influences of thermal bridges and mold growth. Civil Eng Arch (USA) 10(1):131–143
7. Abdykalykov A, Boronbaev E, Begaluev U, Holmatov K, Zhyrgalbaeva N (2021) Building wall corner structures, its microclimate and seismic resistance. In: E3S 24th Construction the formation of living environment 2021, FORM, vol. 263, 04051. Moscow, Russia, pp 1–8
8. Gentile C, Gallino N (2008) Condition assessment and dynamic system identification of a historic suspension footbridge. Struct Control Health Monit 15:369–388

9. Pretelli M, Fabbri K (2018) Historic indoor microclimate. I:n Historic indoor microclimate of the heritage buildings. Springer, Berlin, Heidelberg, Germany, pp 73–83
10. Brimblecombe P (2013) Heritage climatology. In: Lefevre R-A, Sabbioni C (eds) Climate change and cultural heritage. Edipuglia, Bari, Italy, pp 57–64
11. Pavlogeorgatos G (2003) Environmental parameters in museums. Build Environ 38:1457–1462
12. Litti A, Audenaert G, Fabbri K (2017) Indoor microclimate quality (IMQ) certification in heritage and museum buildings: the case study of Vleeshuis Museum in Antwerp. Build Environ 124:478–491
13. Camuffo D (1998) Microclimate for cultural heritage. Elsevier, Amsterdam, The Netherlands
14. Hawkes D (2012) Architecture and climate. In: An envinronmental history of British architecture. Routledge, London, UK, New York, NY, USA
15. D'Agostino V, D'Ambrosio Alfano FR, Palella BI, Riccio G (2015) The museum environment: a protocol for evaluation of microclimatic conditions. Energy Build 95:124–129
16. Sizov B (1996) Evaluation of moisture content measurements in stone. In: Eighth international congress on deterioration and conservation of stone, vol 1. Berlin
17. La Gennusa M, Lascari G, Rizzo G, Scaccianoce G (2008) Conflicting needs of the thermal indoor environment of museums: in search of a practical compromise. J Cult Herit 9:125–134
18. Fabbri K, Pretelli M (2014) Heritage buildings and historic microclimate without HVAC technology, Malatestiana Library in Cesena, UNESCO Memory of the World. Energy Build 76:15–31. Italy
19. Ferdyn-Grygierek J (2016) Monitoring of indoor air parameters in large museum exhibition halls with and without air-conditioning systems. Build Environ 107:113–126
20. Pretelli M, Fabbri K (2016) New concept of historical indoor microclimate—learning from the past for a more sustainable future. Procedia Eng 161:2173–2217
21. Eibl M, Burmester A (2013) Learning from history. Historic indoor climate conditions and climate control strategies. In: Proceedings of the climate for collections, standards and uncertainties. Munich, Germany, pp 217–232
22. Aras FUAT, Krstevska L, Altay G, Tashkov L (2011) Experimental and numerical modal analyses of a historical Masonry palace. Constr Build Mater 25:81–91
23. Boscato G, Russo S, Ceravolo R, Fragonara LZ (2015) Global sensitivity-based model updating for heritage structures. Comp Aid Civil Infrastruct Eng 30:620–635

A Investigation of Coral Reef Sand Permeability and Factors Influencing Road Reconstruction and Expansion

Liu Shiquan, Li Yongquan, Ma Huili, Lü Chenwei, and Haoliang Wu

Abstract For road reconstruction and expansion, the application of coral reef sand is warranted to improve the permeability. The relationship between pore ratio, grade, max particle size, coarse–fine particle content, and permeability of coral reef sand blow-fill materials was examined with applied with an indoor normal head permeameter. The permeability of the same level of calcareous sand was examined at different pore ratios. This study investigates the effects of the inhomogeneity coefficient, curvature coefficient, maximum particle size, and coarse and fine particle content on coral reef sand permeability. According to the results, the permeability coefficient of coral reef sand blow-fill mixes decreases with increasing pore ratio. It increases with increasing inhomogeneity coefficient, curvature coefficient, maximum particle size, and coarse particle content. The coarse & fine material content in the specimen is closely related to permeability performance size. Through the analysis of the indoor test results, considering multiple factors, the model of coral reef sand permeability coefficient: $k_{20} = 2.38 \times 10^{-4} \times e^2 \cdot C_u \cdot C_c \cdot d^2{}_{10} \cdot D$ is proposed. The present study provides reef sand formation permeability assessment and hydrology & environmental geology data support for the expressway reconstruction and expansion of coral reefs.

L. Shiquan
Inner Mongolla Communications of Design & Research Co., Ltd, Hohhot 010020, China

L. Yongquan
Guangdong Road&Bridge Construction Development Co., Ltd, Guangzhou 510660, China

M. Huili
China Railway No.18 Bureau Group No.1 Engineering Co., Ltd., Baoding 071000, China

L. Chenwei
School of Transportation, Southeast University, Nanjing 211189, China

H. Wu (✉)
Sun Yat-sen University & Southern Marine Science and Engineering Guangdong Laboratory (Zhuhai), Zhuhai 519082, China
e-mail: wuhliang5@mail.sysu.edu.cn

H.-Y. Jeon (ed.), *Proceedings of the International Conference on Geosynthetics and Environmental Engineering*, Lecture Notes in Civil Engineering 374,
https://doi.org/10.1007/978-981-99-4229-9_24

Keywords Coral reef sands · Permeability · Inhomogeneity coefficient · Road reconstruction and expansion

1 Introduction

Reefs and islands are rare land resources in tropical oceans that are important for human habitation, the development of oil and gas resources, and the protection of their national maritime rights and interests [1, 2]. Coral reef sand produced by dredging harbor land and channel excavation is often used in large-scale infrastructure and island reef construction projects [3]. Considering the complex environment and the internal structure of coral bodies, the particles of coral reef sand are extremely irregular in shape, easily broken, loose and contain a large number of pores, fragmentation of the particle during stress–strain relationships, strength characteristics, shear swelling are different from ordinary land-based sand [4]. Several engineering problems have been caused by coral reef strata since the 1960s, including the construction of oil platforms in Bass Strait and the North Rankin "A" oil platform on the North West Shelf [5]. The permeability coefficients and permeability properties of coral reef sands are not analyzed and evaluated since they are directly used in engineering construction. It is possible to cause major engineering accidents if permeability parameters and other indicators are not properly selected, such as site flooding, dam seepage, reservoir failure, the sudden surge of foundation pits and failure of waterproofing curtains, resulting in incalculable losses. The effect of particle shape, coarse particle content, and satisfactory particle dosing on reef sand permeability has been studied little. Studies on coral reef sand permeability have focused on particle gradation, porosity, dry density, and biochemical means of improvement [6, 7].

This paper uses an indoor normal-head permeability test to study coral reef sand's permeability. Various influencing factors are controlled to study the influence of pore ratio, grading parameters, and coarse particle content on the permeability coefficient. Further, the permeability coefficient of coral reef sand can be calculated by considering various influencing factors so that the groundwater seepage on island reefs can be analyzed theoretically. This study also provides a scientific basis and data support for the assessment of the permeability of the island reef blow-fill layer and the hydrological and environmental geological analysis of the coral reef sand formation.

Table 1 Coral reef sand quality testing index

Test items	Coral reef/values	Coral sand/values
Bulk density, (kg/m^{-3})	980	1194
Void ratio, (%)	46	51
Porosity rate, (%)	23.4	8.6
Density, (kg/m^{-3})	2800	2794
Water absorption, (%)	7.73	3.64
Solidity, (%)	13.3	6.45
Barrel compression strength, (MPa)	2.13	–

2 Materials and Methods

2.1 Materials

The specimens were taken from loose coral debris strung and sucked from a sea area in the South China Sea. The physical and mechanical properties were determined according to "Light Aggregates and their Test Methods" (GB/T17431.1–2010), as shown in Table 1. The mineral composition of coral reef sand is mainly aragonite (mass fraction 33–47%) and high Mg calcite (mass fraction 53–67%), and the equivalent carbonate mass fraction reaches over 96%, and the chemical properties are incredibly stable under normal temperature and pressure [8–11]. Despite sedimentation, coral reef sands maintain some of their native morphological characteristics without long-distance transport. An irregularly shaped rock with sharply angular grains, relatively large pores, and irregularly shaped grains. Coral reef sands exhibit macroscopically distinctive properties from terrestrial sands (e.g., quartz sands) because they contain a large number of internal pores, which account for about 10% of all pores [5].

2.2 Materials

The test was carried out on coral reef sand with a grain size of 20 mm or less, using a TST-70 permeameter with a 40 cm high barrel and 10 cm diameter. In order to facilitate the integrity of the sample, all specimens are prepared with the same moisture content. In order to make the specimens fill the cylinder, they are loaded three times into the test cylinder and pressed tight with the mold on the jack. Before the test, the permeation meter with the specimen is connected to each device and left to stand under a certain water head. In order to avoid deformation and damage to the specimen due to excessive water head, a lower water head (15 cm) is used at the beginning. The feasible water head for the permeation test is determined through several groups of test trials, and the water head for the formal test is 25 cm.

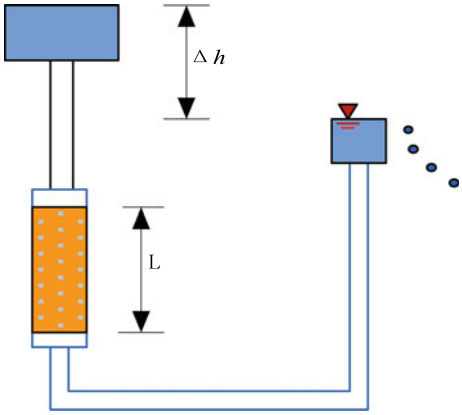

Fig. 1 Schematic diagram of the normal head test rig

During every 300 s of weighing the amount of water in the measuring cup, the water temperature needs to be measured with a thermometer at the beginning and end of the test. Finally, calculate the permeability coefficient according to the following formula (Fig. 1).

$$k_t = \frac{QL}{AHt}\frac{\eta_T}{\eta_{20}} \tag{1}$$

where: k_t is the permeability coefficient of the specimen at water temperature t°C, cm/s; Q is the amount of water permeated in time t seconds, cm^3; L is the permeation path, equal to the height of the specimen, cm; A is the specimen cross-sectional area, cm^2; H is the permeation head, cm; t is time, s; η_T is the dynamic viscosity coefficient of water at T°C, 10^{-6} kPa·s. H_{20} is the dynamic viscosity coefficient, 10^{-6} kPa·s.

3 Results and Discussion

3.1 Influence of Pore Ratio on Permeability

According to Taisakhi and Hazen's semi-theoretical and semi-empirical equations, pore ratios were squared and plotted in Fig. 2. The permeability coefficient increases with increasing pore ratios for the same gradation of specimens.

The permeability coefficient of the coral reef sand is concentrated around 10^{-3} cm/s, which is small compared to the permeability coefficient of terrestrial sands of the same grain size range. The linear correlation between the permeability coefficients k_{20} and e^2 are both high, and the fitted equation is $k_{20} = 5.29 \times 10{-}^2e^2$-$2.5 \times 10^{-2}$, which is a good linear relationship. The permeability characteristics of the pore medium are closely related to its pore ratio. As a result of the large density of

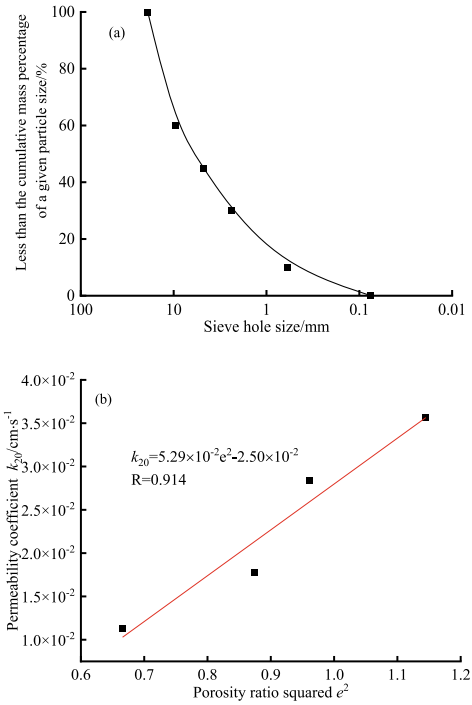

Fig. 2 **a** Experimental grading curves for permeability coefficients at different porosity ratios. **b** Relationship between permeability coefficient and pore ratio

a specimen, the particle contact force is relatively small. In the mixture, pores are not fully filled, resulting in a relatively loose skeleton. Therefore, a high permeability coefficient occurs when density is high. By reducing the pore ratio, the effective over-water area of the seepage channel is reduced, the seepage resistance and path are increased, and the permeability coefficient decreases.

3.2 Influence of Pore Ratio on Permeability

Permeability coefficient tests were carried out on coral reef sand-blown fill mixes with different inhomogeneity coefficients C_u. The curvature coefficients were fixed in the range of particle sizes studied. According to the different inhomogeneity coefficients, gradation curves were formulated for the mixes used to prepare the test samples, see Fig. 3.

The coefficient of inhomogeneity C_u is a parameter that reflects the degree of dispersion of the soil particle composition. The larger the $C_{u,}$ the more inhomogeneous the distribution of soil particles. For continuous graded mixes, the greater the unevenness factor C_u, the greater the variation between coarse and fine particles of different sizes in the mix. For C_u smaller compounds, the particle size interval is single, the pores cannot be fully filled, and larger pores are formed inside the

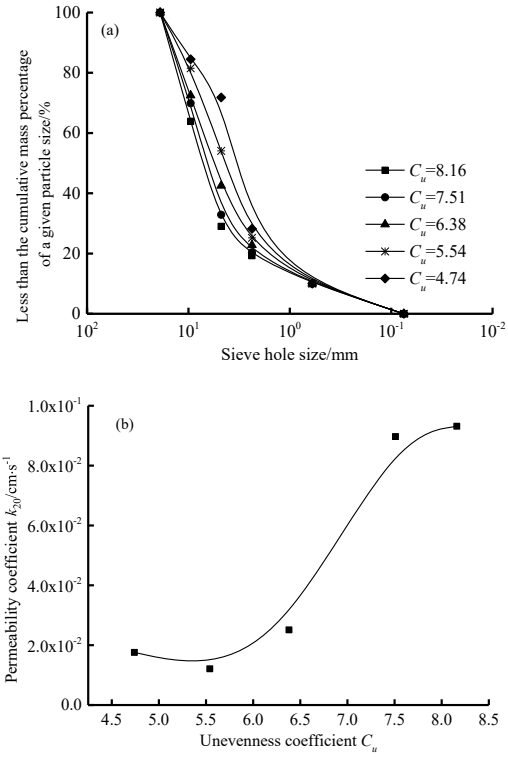

Fig. 3 **a** Test grading curves for different permeability coefficients of inhomogeneity. **b** Relationship between permeability coefficients and inhomogeneity coefficient

soil body. The test controls the specimen inhomogeneity coefficient from 4.74 to 8.16, and the pore ratio e, characteristic particle size d_{10} and curvature coefficient C_c are controlled to constant values. Further, the permeability coefficient k_{20} is positively correlated with the inhomogeneity coefficient C_u. Under a certain characteristic particle size d_{10}, the inhomogeneity coefficient increases with the increase of the control particle size. The content of the particle species between the characteristic particle size d_{10} and the control particle size d_{60} increases. As the inhomogeneity coefficient increases, the internal structure of the mix and the pore structure become more complex. By increasing the inhomogeneity coefficient, the coarse particle content increases, forming the skeletal structure and increasing permeability.

3.3 Influence of Maximum Particle Size

In order to determine the effect of maximum particle size on the permeability coefficient, the effect of coral reef sand on the permeability coefficient was studied in this experiment at different maximum particle sizes. As shown in Fig. 4, the permeability

coefficient increases with the maximum particle size increase. The permeability coefficient k_{20} is linearly correlated with the maximum particle size D. The fitted equation is $k_{20} = 1.09 \times 10{-}^{3}D{-}5.15 \times 10^{-3}$ and the correlation degree is 0.886. The pore size between the specimen particles increases with the increase of the maximum particle size. For the same pore ratio, the number of pores in the specimen decreases but the pore section size increases as the maximum particle size increases for the same volume of the mix. Through the increase in pore section size and the reduction in the number of pores, the water flow through the distance is shortened. With the same head pressure difference, there is relatively less head loss, and more seepage per unit of time. In the case of a certain pore ratio, increasing pore section size has a greater effect on permeability than increasing the pore number. The change in pore ratio has a tiny effect on permeability than the change in maximum particle size.

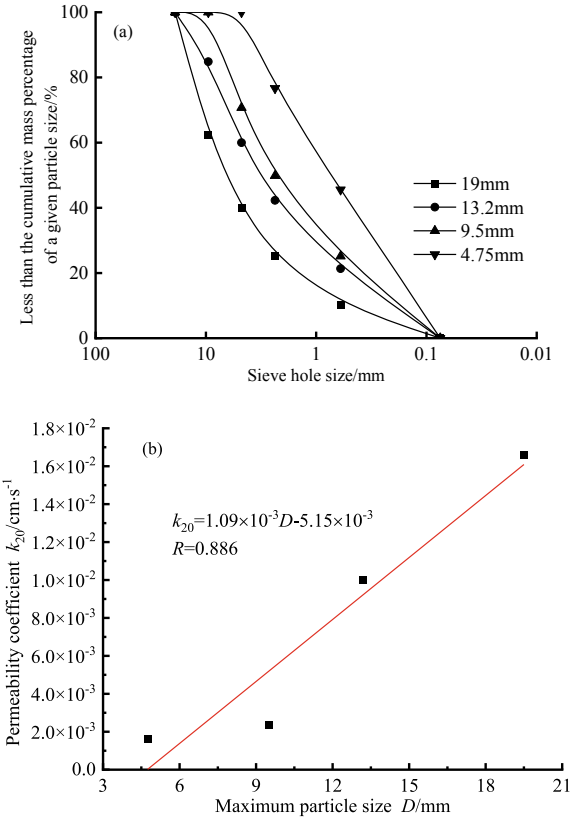

Fig. 4 **a** Test grading curves for different permeability coefficients for the largest particle sizes. **b** Permeability coefficient versus coefficients for the largest particle sizes Permeability coefficient modeling

3.4 Permeability Coefficient Model Building

According to the above analysis, the permeability coefficient of coral reef sand is positively correlated with the square of the pore ratio e; positively correlated with the inhomogeneity coefficient C_u; positively correlated with the curvature coefficient C_c; and positively correlated with the maximum grain size D, and is highly correlated with each factor. Research shows that the permeability coefficient k_{20} is related to the characteristic grain size d [12], and the control characteristic grain size d_{10} of this permeability test is a constant value, citing the research results of the cohesionless coarse-grained soil permeability coefficient Taishaki formula $K = 2d_{10}^2 \cdot e^2$ and A. Hazen's formula $K = \mathrm{C}d_{10}^2$ to collate the permeability coefficient model of coral reef sand.

$$k_{20} = R \cdot e^2 \cdot C_u \cdot C_c \cdot d_{10}^2 \cdot D \tag{2}$$

where: k_{20} is the permeability coefficient, cm/s; R is the coefficient related to other unknown influencing factors; e is the pore ratio, dimensionless; C_u is the inhomogeneity coefficient, dimensionless; C_c is the curvature coefficient, dimensionless; d_{10} is the effective particle size, mm; D is the maximum particle size, mm.

When R is taken as 2.38×10^{-4}, the ratio between the measured value and this paper is close to 1.0, which can calculate the permeability coefficient of coral reef sand better than Tai Shaji and Hazen's formula. In summary, the permeability coefficient of the coral reef sand is modeled as

$$k_{20} = 2.38 \times 10^{-4} \times e^2 \cdot C_u \cdot C_c \cdot d_{10}^2 \cdot D \tag{3}$$

This model can better predict the permeability coefficient of the coral reef sand by considering the effects of pore ratio, inhomogeneity coefficient, curvature coefficient and maximum grain size on the basis of the Taishaji and Hazen permeability models. From the comparison between the measured values of the permeability coefficient under different conditions and the calculated values of Taishaji, Hazen, and this study (see Table 2.). it can be seen that the permeability coefficient calculation model established in this test has greatly improved the calculation accuracy and the calculated and measured values are in better agreement. The maximum particle size of the permeability test is 19 mm. However, this model can theoretically be applied to cohesionless soils with a maximum particle size of 19 mm, and its applicability beyond this particle size requires further testing.

Table 2 Comparison of test results and calculations from permeation tests

Number	1	2	3	4	5	6	7
Maximum particle size D	19.0	19.0	19.0	19.0	19.0	19.0	19.0
d_{10}	0.6	0.6	0.6	0.6	0.6	0.6	0.6
Porosity ratio e^2	0.884	0.884	0.884	0.884	0.884	0.884	0.884
Unevenness factor C_u	6.38	5.54	4.74	7.9	7.9	7.9	7.9
Curvature factor C_c	2.00	2.00	2.00	0.7	1.0	1.2	1.3
Measured values	2.5×10^{-2}	1.2×10^{-2}	1.8×10^{-2}	9.5×10^{-3}	1.1×10^{-2}	1.2×10^{-2}	1.3×10^{-2}
Calculated values for Taishachi	6.3×10^{-1}	6.3×10^{-1}	6.3×10^{-1}	6.3×10^{-1}	6.3×10^{-1}	6.3×10^{-1}	6.3×10^{-1}
Hazen calculated values	3.6×10^{-1}	3.6×10^{-1}	3.6×10^{-1}	3.6×10^{-1}	3.6×10^{-1}	3.6×10^{-1}	3.6×10^{-1}
Calculated values in this paper	1.8×10^{-2}	1.6×10^{-2}	1.4×10^{-2}	7.4×10^{-2}	1.1×10^{-2}	1.3×10^{-2}	1.5×10^{-2}
Measured/taxa base values	0.039	0.019	0.028	0.015	0.018	0.019	0.020
Actual test/ Hazen	0.070	0.034	0.049	0.026	0.031	0.033	0.035
Measured/value in this paper	1.369	0.760	1.290	1.279	1.026	0.916	0.835
Number	8	9	10	11	12	13	14
Maximum particle size D	19.0	19.0	19.0	19.0	19.0	19.0	19.0
d_{10}	0.6	0.6	0.6	0.6	0.6	0.6	0.6
Porosity ratio e^2	0.94	0.94	0.94	1.07	0.98	0.935	0.816
Unevenness factor C_u	7.9	7.9	7.9	15.8	15.8	15.8	15.8
Curvature factor C_c	1.6	1.9	2.5	0.98	0.98	0.98	0.98
Measured values	1.9×10^{-2}	2.0×10^{-2}	2.0×10^{-2}	3.5×10^{-2}	2.8×10^{-2}	1.7×10^{-2}	1.1×10^{-2}
Calculated values for Taishachi	6.4×10^{-1}	6.3×10^{-1}	6.3×10^{-1}	8.2×10^{-1}	6.9×10^{-1}	6.3×10^{-1}	4.8×10^{-1}
Hazen calculated values	3.6×10^{-1}	3.6×10^{-1}	3.6×10^{-1}	3.6×10^{-1}	3.6×10^{-1}	3.6×10^{-1}	3.6×10^{-1}

(continued)

Table 2 (continued)

Number	1	2	3	4	5	6	7
Calculated values in this paper	1.8×10^{-2}	2.1×10^{-2}	2.8×10^{-2}	2.8×10^{-2}	2.4×10^{-2}	2.2×10^{-2}	1.6×10^{-2}
Measured/taxa base values	0.029	0.032	0.032	0.043	0.041	0.028	0.024
Actual test/ Hazen	0.052	0.056	0.056	0.099	0.079	0.049	0.031
Measured/value in this paper	0.996	0.919	0.715	1.236	1.175	0.807	0.676

Note C is taken as 1.0 in the Hazen formula

4 Summary

This study investigated the interrelationship between pore ratio, gradation, maximum particle size, coarse and fine particle content and permeability of coral reef sand blow-fill materials. The following conclusions can be drawn:

(1) The permeability coefficient of coral reef sand blown-fill mix decreases with increasing pore ratio and increases with increasing curvature coefficient of inhomogeneity, maximum particle size, and coarse grain content.
(2) The permeability coefficient of coral reef sand is lower than that of conventional terrestrial sands with the same grain size range, mostly at 10^{-3} cm/s. The permeability coefficient of coral reef sand with the same grain gradation increases with the increase of pore ratio, which also has a good linear correlation with e^2.
(3) According to the lab-scale experimental results, the effects of pore ratio, inhomogeneity coefficient, curvature coefficient and maximum particle size were considered, and the model of coral reef sand permeability coefficient was proposed after fitting four factors, namely $k_{20} = 2.38 \times 10^{-4} \times e^2 \cdot C_u \cdot C_c \cdot d_{10}^2 \cdot D$. This study provides that the reef sand formation permeability assessment and hydrology & environmental geology data support the expressway reconstruction and expansion of coral reef.

References

1. Li L (2012) Research on basic caracteristics of coral concrete. Ph.D thesis, Nanning: Guangxi University
2. Guo C (2017) Study on engineering properties of coral aggregate concrete in South China Sea. M.S thesis, Nanjing: Southeast University
3. He YX, Dong ZL, Yang HP, et al (2010) Study of packing compaction performance of reclamation of coral reef sand (gravel) used in coastal engineering. The Chinese and Foreign Road 30(6):34–37.(in Chinese)

4. Wang YQ, Hong Y, Guo Z et al (2018) Micro-and macro-mechanical behavior of crushable calcareous sand in South China Sea. Rock Soil Mech 39(1):199–215
5. Zhang JM (2004) Study on the fundamental mechanical characteristics of calcareous sand and the influence of particle breakage. Ph.D thesis, Beijing: Institute of Rock & Soil Mechanics, Chinese Academy of Sciences
6. Ren YB (2016) Experimental study on the permeability characteristics of calcareous sand in South China Sea . M.S thesis, Dalian: Dalian University of Technology
7. Qian K, Wang ZX, Chen JW, et al (2017) Experimental study on permeability of calcareous sand for islands in the South China Sea. Rock Soil Mech 38(6):1557–1572. (in Chinese)
8. Lü CW, Wu HL, Shi ML (2019) Laboratory tests of cement stabilized & solidified coral reef and sand for use of highway pavement. J Eng Geol 27(6):1440–1447
9. Lü CW (2016) The studyon pavement performance of cement-emulsified asphalt and reef sand solidification. M.S thesis, Nanjing: Southeast University
10. Mo HY (2015) Research on the mechanics characteristics of calcareous sand-limestone mixture. Southeast University, Nanjing
11. Zhu CH (2006) Study on the infiltration characteristics of coarse-grained soils. M.S thesis, Xi'an: Northwest Agriculture and Forestry University of Science and Technology
12. Huo YL (2021) Experimental study on the permeability of calcareous sand and its influencing factors M.S thesis, Guilin: Guilin University of Technology

Residual Clamping Force Assessment of Friction Type High-Strength Bolt in Steel Bridges

Gangnian Xu, Laiyong Wang, Zhongnan Tian, and Dayong Sun

Abstract Firstly, nine high-strength bolted gusset plates with different degrees of corrosion are selected from the upstream and downstream box girders of the steel bridge. Three corrosion nuts are selected for each gusset plate, Each corrosion nut is measured three times and the average value of its residual thickness is taken. Then, according to the empirical formula of equivalent radius and residual clamping force obtained from manual cutting nut test, the collected residual thickness of nuts is substituted into the formula to obtain the residual clamping force of 27 corroded nuts and high-strength bolts. The results show that: (1) the nuts outside the measured bolt box are seriously corroded, the bolt head in the box is not corroded, and the nuts are exposed to the outside all year round; (2) The measured residual radius loss ratio of corroded nut is 60%, and the maximum clamping force loss ratio of high-strength bolt is 59.62%; (3) The bolts of upstream GSW1 are seriously rusted compared with downstream GSW2, and the loss of effective clamping force is greater, which is related to the perennial wind direction; (4) When the residual radius loss ratio is more than 36.11%, and the clamping force loss ratio is more than 20%, it can be considered to replace the bolts with serious corrosion.

Keyword Steel bridge · High-strength bolt · Nut corrosion · Corroded thickness · Evaluation

G. Xu (✉)
School of Civil Engineering, Shandong Jiaotong University, Jinan 250357, China
e-mail: 204144@sdjtu.edu.cn

L. Wang
China Academy of Transportation Sciences, Beijing 100081, China

Z. Tian
Shandong Provincial Highway Detecting Center, Jining 272007, China

D. Sun
Jinan Urban-Rural Transportation Development Center, Jinan 250098, China

H.-Y. Jeon (ed.), *Proceedings of the International Conference on Geosynthetics and Environmental Engineering*, Lecture Notes in Civil Engineering 374,
https://doi.org/10.1007/978-981-99-4229-9_25

1 Introduction

As a permanent component of bridge member connection, the bolt preload of high-strength bolt has a vital impact on the reliability of connection [1]. The high-strength bolt is to tighten the nut and apply prestress to the bolt, so as to produce extrusion force between the connecting members, so as to produce great friction perpendicular to the screw direction. This kind of connection internal force is borne by the friction of the friction surface by clamping the members, which is the characteristic of high-strength bolt connection [2].

The investigation and study found that corrosion will first cause the reduction of the cross-section of the screw and nut of the steel box girder bridge connected by high-strength bolts, resulting in the reduction of the bearing capacity of the connecting joint, especially in the corrosive environment such as humid atmosphere and industrial atmosphere all year round, the connecting joint of the steel box girder bridge is also prone to corrosion [3]. Under the long-term service of the bridge, the water seepage at the internal section connection of the box girder is caused by design defects and other reasons, The diameter of individual nuts changed from the initial 36 to 27.6 mm. At present, corrosion is one of the main reasons for the slip of friction high-strength bolt connections, which brings great potential safety hazards to the normal use of steel structures, and seriously affects the service performance, operation and service quality of structures [4–7]. There are many factors affecting the corrosion of steel structure, mainly reflected in the effect of steel and surrounding environmental media [8, 9]. It is found that corrosion will first reduce the cross-section of screws and nuts of steel box girder bridges connected by high-strength bolts, resulting in the reduction of the bearing capacity of connecting joints. Especially in the corrosive environment of humid atmosphere and industrial atmosphere all year round, the connecting joints of steel box girder bridges are also prone to corrosion problems [10].

2 Project Overview

A Yellow River Bridge is located in the northeast of Kenli County in China. The bridge was completed in September 1987 and officially opened to traffic in June 1988. Up to now, the bridge has been in service for about 33 years. The north side of the bridge connects Beijing Tianjin area, Dongying port and Shengli oilfield oil area, and the south side connects Shengli Oilfield base, Jiqing expressway and Jiaodong area, which plays a vital role in the economic development of both sides of Dongying City. The total length of the bridge is 2817.46 m, which is composed of the main bridge and the North–South approach bridge. The total length of the bridge is 2817.46 m, which is composed of the main bridge and the North–South approach bridge. The bridge is 19.5 m wide with two-way four lanes. The main bridge is 682 m long, the span combination is (60.5 + 136.5 + 288 + 136.5 + 60.5) m, the main span

Fig. 1 Overview of main bridge

is 288 m, and the tower top elevation is 78.6 m. The overview of the main bridge is shown in Fig. 1.

The main bridge is a five hole continuous steel cable-stayed bridge with a span combination of (60.5 + 136.5 + 288 + 136.5 + 60.5) m and a split double box section. The steel beam has a total length of 681.5 m and is divided into 57 sections. Except for individual sections, most sections are 12 m; Each section of steel beam is divided into 6 pieces horizontally, including two East and West box girders and four orthotropic bridge decks in the middle, The transverse joints are connected by high-strength bolts; The longitudinal joint is connected by groove welding on site. The box girder is a two separated rectangular box girder with a height of 2.4 m and a width of 3.14~3.315 m. The top and bottom plates are U-shaped closed rib orthotropic plates, and the web plates are plate type open rib orthotropic plates, Except that the plate thickness of the web plate and bottom plate at the cable anchorage and attachment hole is 20 mm, the other top、bottom and web plates are 12 mm thick. The bridge deck is an orthotropic plate, with 4 pieces in each section and a width of 3.2 m each. The longitudinal rib is a U-shaped closed rib, and the transverse rib is a plate beam, with a spacing of 1.0~2.75 m, generally 2.75 m. The transverse joint of steel box girder is shown in Fig. 2.

3 Simulated Nut Corrosion Test of Manually Cutting Nut Section

In the simulated corrosion damage of manually cutting nut section, the change of bolt strain value includes: the strain change caused by applying clamping force and the strain change caused by manually cutting nut section. During the test, the bolt strain will be changed by cutting different nuts、the degree of cutting nut section and the depth of cutting section. At the same time, the number of the cut nut、the degree of the cut section and the depth of the cut section shall be continuously recorded until the manual cut nut damage test is completed. Finally, the residual clamping force

Fig. 2 Transverse joint of steel box girder

of the bolt is calculated according to the regression equation. During the test, the clamping force of the test bolt after final tightening (hereinafter referred to as "initial clamping force") is more than the design value of M20 high-strength bolt clamping force (155kN), which is about 1.1 times of the design value of clamping force.

The specific implementation steps of artificial cutting nut section simulation corrosion damage test are as follows: (1) unilateral cutting. Select the side convenient for cutting. When cutting, cut it four times along the thickness direction of the nut, and record the four cutting depths and the corresponding bolt strain values; (2) Bilateral cutting. Select the two sides convenient for cutting, first complete the cutting of one side at one time, then complete the cutting of the other side in four times along the thickness direction of the nut, and record the cutting depth of five times and the corresponding bolt strain value; (3) Three sided cutting. Select the three sides that are convenient for cutting, first complete the cutting of one side at one time, then complete the cutting of the other side at one time, finally complete the cutting of the third side four times along the thickness direction of the nut, and record the cutting depth and corresponding bolt strain value for six times.

This paper refers to the test results in the paper, considers the size, section damage shape and degree of the bolt, and evaluates it according to the regression curve of the test results of manually segmented damaged nut bolt connection. Equation (1) is the regression equations of the percentage of the equivalent radius of nut and the percentage of residual clamping force of high-strength bolt.

$$P_c = 0.3207 - 0.3305 \times \frac{D - D'}{D - d} - 0.0103 \times \left(\frac{D - D'}{D - d}\right)^2 \quad (1)$$

where, P_c represents the percentage of residual clamping force of the damaged nut in the section; D' represents the equivalent diameter of the nut after cutting; D represents the original diameter of the nut; d is the diameter of the screw.

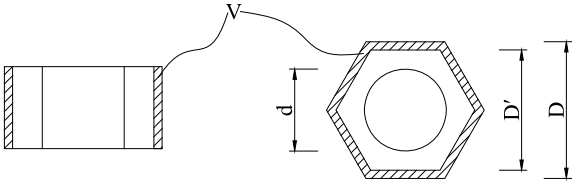

Fig. 3 Calculation sketch of equivalent radius method

Equation (1) is a suggested equation for evaluating the residual clamping force of connecting bolts, which is helpful for the quantitative evaluation of the clamping force of high-strength bolts in corrosive environment, and then puts forward remedial measures such as changing bolt connection or improving bolt clamping process. Figure 3 is the calculation sketch of equivalent radius method.

4 Analysis of Clamping Force Loss of High Strength Bolts in Corroded Joints

J1~J5 nodes represent 5 node numbers from west to east. The design value of preload corresponding to 22 mm high-strength bolt is 190KN. When calculating the preload loss, the average value of the remaining diameter of the nut measured for 3 times shall be adopted.

Figure 4(1~9) is drawn by calculating the nut thickness loss ratio and residual clamping force loss ratio according to the bolts selected from nodes J1~J5 in box girder section GW1 and GW 2. According to the analysis of Fig. 4, the loss ratio of residual clamping force is linear with the loss ratio of nut thickness, and the loss ratio of bolt residual clamping force increases with the increase of nut thickness loss ratio. Among them, the residual clamping force loss of J1 node bolt in GW1 is serious, and the overall residual clamping force loss of GW1 box girder section is more serious than that of GW2 box girder section.

At present, the existing inspection specifications do not specify how to evaluate the residual clamping force of high-strength bolts after corrosion. This evaluation is based on the relevant research results of our research (considering the size, section damage shape and degree of bolts, and according to the regression curve of the test results of manually segmented damaged nuts and bolts), which is only for reference. The clamping force loss ratio of individual high-strength bolts in the first section at the entrance of the west box is 51.2%. On the whole, the corrosion of GSW1 bolts is more serious than GSW2, and the loss of effective clamping force is more.

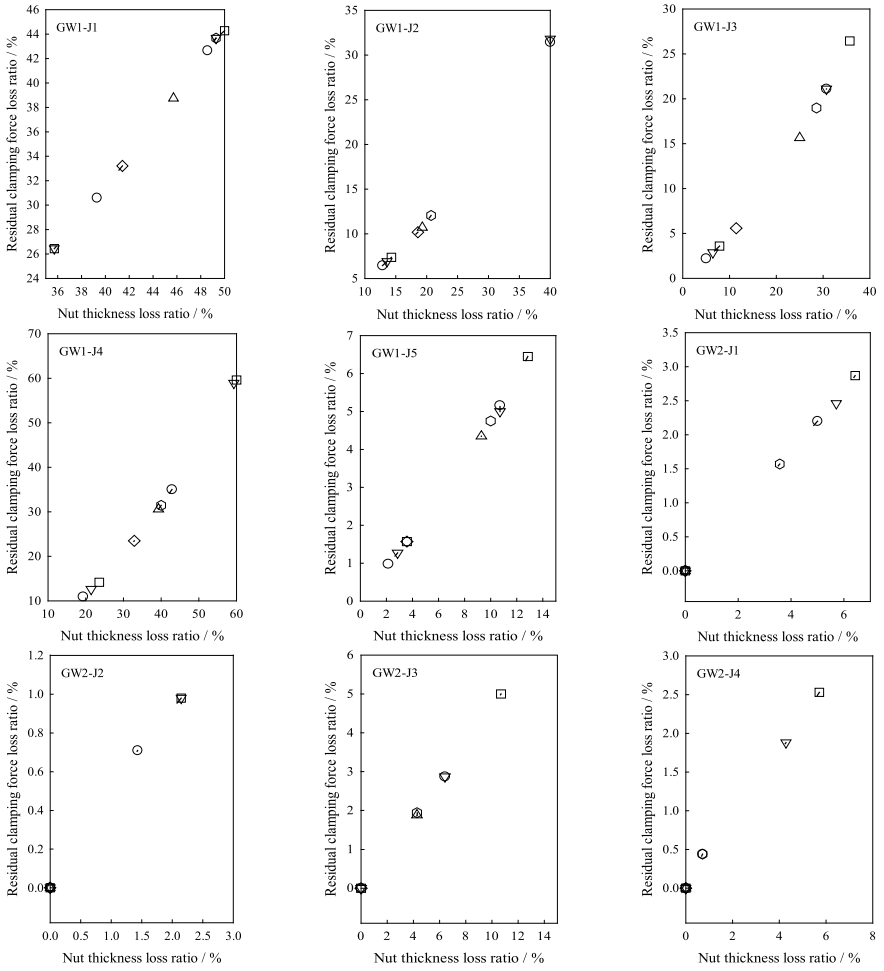

Fig. 4 Calculation

Acknowledgements This work is supported by the the Open Project of Key Laboratory of Transportation Industry (Beijing) for Old Bridge Detection and Reinforcement Technology (No. 2021-JQKFKT-3).

References

1. Xu GN (2019) Research on mechanical properties of variable section continuous girder bridge strengthened by a stay cable system. Shandong University
2. Zhao Q, Chen MZ, Chen YJ (2015) Investigation and analysis on the development status of continuous steel box girder bridges in China. Chinese Foreign Roads 35:98–102

3. Zhang BQ, Li Y, Fu H (2006) Anti corrosion method of steel structure bridge. World Bridge 67–70
4. Xiong L (2017) Analysis on mechanical properties of gusset plate with high strength friction bolt connection. Beijing Jiaotong University
5. Wang HL, Xia JG, Qing SF (2014) Corrosion fatigue life estimation model of high strength bolts and its application. J Dalian Maritime Univ 40:113–115+120
6. Hao L (2011) Fatigue life and service safety reliability evaluation of existing steel bridges. Chang'an University
7. Zhu YB (2018) Experimental study on fatigue performance of weather resistant steel bolted welded joints after corrosion. Zhejiang University
8. Du FQ, Liu XG, Zheng Y (2018) Experimental study on anti sliding coefficient of high strength bolt connection surface. Steel Const 33:126–130
9. Wu AM (2013) Study on corrosion and fatigue stress of bridge steel structure. Chang'an University
10. Zhan A (2008) Evaluation of corrosion fatigue life of existing steel bridges. Chang'an University

Jacking Construction Technology of Curved Steel Box Girder and Analysis of Its Mechanical Characteristics

Baoliang Ma, Hui Zhao, Qiang Xie, and Gangnian Xu

Abstract In this paper, taking Lasuo No. 2 Bridge as the construction background, the walking push construction method is selected, and the existing piers and temporary supports are used as the support platform for push construction to carry out push construction and high beam falling construction. The finite element analysis software is used to establish the simulation analysis program of the pushing process. The overall simulation analysis is made for each stage of the bridge's push construction, the deflection change of the beam end and the change of the push force are obtained, and the most unfavorable working conditions are determined for local analysis. In view of the characteristics of this project, a detailed comparative analysis was made on the mechanical parameters affecting the steel box girder, and the special requirements and relevant measures for launching were studied. It is proved theoretically that the construction method is safe and reliable, and meets the structural strength and local stability requirements during the jacking construction.

Keywords Steel box girder bridge · Jacking construction technology · Finite element analysis · Local analysis · Guide beam

1 Introduction

At present, domestic and foreign scholars have carried out a large number of tests and simulation studies on the stress characteristics analysis of the launching construction. Many scholars have used finite element analysis software to analyze the stress characteristics of the steel box girder launching construction process, discussed the stress situation of the launching platform from both structural deformation and combined stress, and simulated the stress and deformation of the box girder bridge during

B. Ma · H. Zhao · Q. Xie
Cccc Second Highway Engineering Co., Ltd, Hechi 547200, China

G. Xu (✉)
School of Civil Engineering, Shandong Jiaotong University, Jinan 250357, China
e-mail: 204144@sdjtu.edu.cn

H.-Y. Jeon (ed.), *Proceedings of the International Conference on Geosynthetics and Environmental Engineering*, Lecture Notes in Civil Engineering 374,
https://doi.org/10.1007/978-981-99-4229-9_26

the launching construction process [1–3]. Some scholars combined with the actual project, used the finite element analysis software to simulate the steel box girder, steel guide beam, launching platform and temporary pier constraints, analyzed the whole process of steel box girder launching construction, calculated the local stress and stability during the launching process, and proposed the key points and precautions for construction control and the corresponding measures to control beam cracking [4–11]. A small number of scholars used theoretical analysis and numerical simulation methods to analyze and verify the construction process, the key and difficult points in the construction process, and the overall stress of the structure at each important stage during the jacking construction process, and summarized how to optimize the local design parameters [12].

According to the characteristics of this project, this paper uses finite element software to establish the simulation analysis program of the pushing process. The overall simulation analysis is made for each stage of the bridge's push construction, the deflection change of the beam end and the change of the push force are obtained, and the most unfavorable working conditions are determined for local analysis. The stress of curved steel box girder in the stage of launching construction is compared and analyzed in detail, and the special requirements and relevant measures of launching are studied. It is proved theoretically that the construction method is safe and reliable, and meets the structural strength and local stability requirements during the jacking construction.

2 Project Overview

Lasuo Bridge 2 of Nandan Tian'e Xialao Expressway is located in Nandan County, Hechi City, Guangxi Zhuang Autonomous Region, with complex geological structure. No. 2 main bridge is (2 × 92) m two span continuous steel box girder, the main girder is full welded structure, the bridge deck width is 12.75 m, the beam height is 4.2 m, and the upper span is Weiming Railway Tunnel. The minimum horizontal distance from the expanded foundation edge of the support beside Lasuo Bridge 2 tunnel to the tunnel is 7 m, and the buried depth of the tunnel is 56 m. The main girder of the steel box girder is a fully welded steel box girder with a total width of 2 × 12.75 m, divided into 13 sections, composed of two independent left and right frames.

3 Pushing Construction Technology of Steel Box Girder

The left span of Lasuo No. 2 Bridge is installed by longitudinal pushing method and transverse sliding method, and the right span is installed by longitudinal pushing method. The following construction machinery and equipment are mainly used: 150

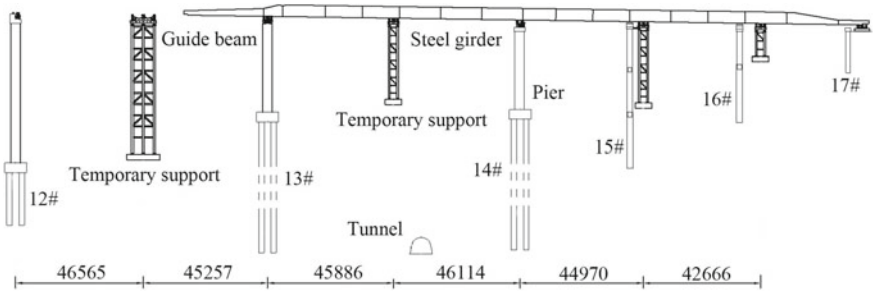

Fig. 1 Elevation of launching construction

ton crawler crane, 200 ton truck crane, 600 ton walking jack, three-dimensional jack, etc. The specific main steps of steel box girder launching construction include:

Step 1: The 200 ton truck crane is used to construct temporary supports, steel box girder assembly supports, and the walking type jacking system is arranged. Step 2: Use a 200t truck crane to install the front guide beam. Step 3: The 150t crawler crane is used to install segments 1–4. All components shall be blanking, plate unit manufacturing and section preassembly completed in the factory. After coating, they shall be delivered to the site to directly participate in the erection. All components shall be coated with primer, intermediate paint and first finishing coat in the factory. Step 4: Push forward after the welding is completed and the weld is tested as qualified. After one stroke of pushing is completed, all the push oil cylinders retract to the starting point of the next stroke, and then push can be carried out for the next stroke. Step 5: Repeat the above steps to continue the installation. Step 6: Push forward and install the rear guide beam after the welding is completed and the welding seam is qualified. The elevation of launching construction is shown in Fig. 1.

4 Force Characteristic Analysis

4.1 Overall Stress Analysis

The finite element software is used for analysis. The calculation model adopts beam element. Each working condition only changes the selection attribute and node coordinates of the beam element. Each working condition is calculated independently, so that the position and internal force of each jacking working condition can be reflected. When building the model, Lasuo No. 2 Bridge was divided into 17 working conditions. In this paper, two important working conditions are selected for finite element analysis. Q355 steel box girder and Q345 steel guide beam are used. The stress, displacement and reaction of the model under condition 2 and 8 are shown in Fig. 2. Figure 3 shows the detailed calculation results. The maximum stress of the bridge under all working conditions is less than the allowable stress value of 221 MPa.

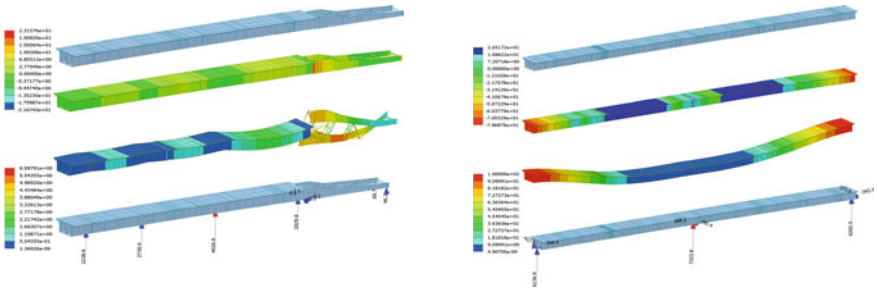

Fig. 2 Stress, displacement and reaction diagram of model under different working conditions

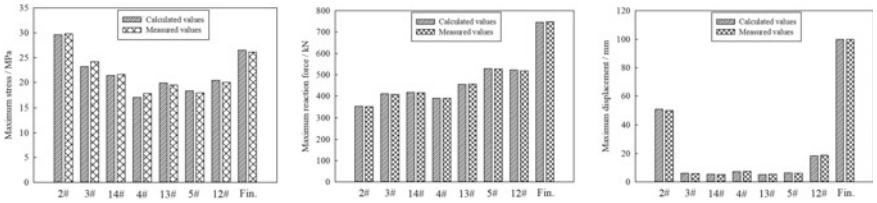

Fig. 3 Calculation results

Figure 3 shows the comparison between the calculated results of the finite element model and the measured results. Through the comparison of the results, the relative errors of the maximum stress, the maximum reaction force and the maximum deformation are 0.67–0.49%, 0.24–0.69% and 0.10–6.67% respectively, and the maximum error is only 6.67%. Therefore, it can be concluded that the difference between the calculated results of the model and the measured results is very small, and the finite element model simulation results are accurate.

4.2 Local Stress Analysis

Because the bridge is constructed by pushing curved steel box girder, and the span is large, in order to better prevent and control various problems arising in the process of pushing construction, local stress analysis of steel box girder is required. The jacking cushion beam and steel beam segment, cushion cushion beam and steel beam segment are sampled for modeling, and the local bearing checking stress and local bearing checking displacement are calculated respectively. The jacking pad beam and steel beam segment, the two ends of the steel beam are consolidated, and 350t load is applied at the contact position between the lower pad beam and the jack (calculated according to the most unfavorable working condition). Figure 4 shows the stress and displacement analysis diagram of jacking pad beam, cushion and steel beam. It

can be seen from Fig. 4 that the maximum local bearing stress of the steel beam is 102 MPa, and the measured value is 101.32 MPa, which is less than the allowable stress of 221 MPa. The maximum local bearing displacement of the steel beam is 1.02 mm, and the measured value is 0.99 mm. The pad beam and steel beam section shall be reinforced on both sides of the steel beam, and 150 t load shall be applied on the pad under the pad beam. The maximum local bearing stress is 110.4 MPa, and the measured value is 19.6 MPa, which is less than 153 MPa allowable stress. The maximum local bearing displacement is 1 mm, and the measured value is 0.98 mm. The maximum local bearing displacement of the steel beam is 1 mm. The deformation and stress of jacking pad beam and base pad beam are shown in Fig. 5.

The above results are the analysis results of the finite element analysis software on the overall force and two local forces of the established finite element model under eight working conditions. The stress, deflection and support reaction during the whole bridge launching construction process have been calculated and analyzed in detail, providing theoretical support and certain reference value for the entire launching construction process.

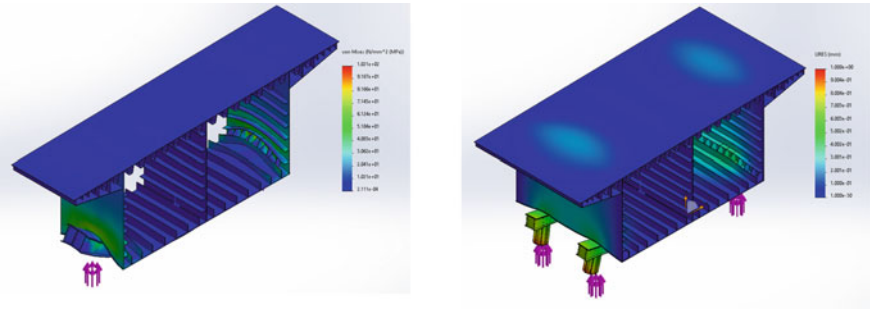

Fig. 4 Stress and displacement analysis of steel beam

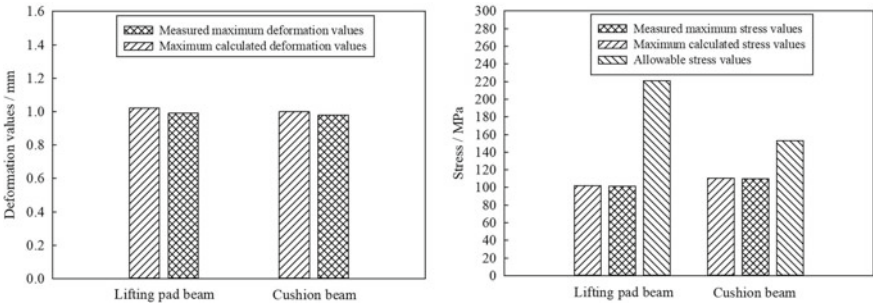

Fig. 5 Deformation and stress diagram of jacking pad beam and base pad beam

5 Conclusion

This paper systematically introduces the launching construction technology of the curved steel box girder of the project, uses the finite element software to build the model of the bridge, and analyzes the bearing pressure and displacement of the whole and local steel box girder under various conditions of the launching construction of the steel box girder, and draws the following conclusions:

(1) During the whole launching process, the maximum stress produced by the guide beam is 29.6 MPa, and the maximum stress of the steel box girder is less than the stress of the guide beam. The maximum reaction force and displacement occur after the completion of the bridge, and their values are 746.8 KN and 100 mm respectively.
(2) In the local stress analysis, the maximum local bearing stress of the steel beam is 102 MPa and the maximum displacement is 1.02 mm for the jacking pad beam and steel beam section. The maximum local bearing stress of cushion beam and steel beam section is 110.4 MPa, the maximum displacement is 1 mm, and the stress is less than the allowable stress.
(3) In this paper, two kinds of finite element software are used to model and analyze the whole and part of the steel box girder of the bridge. The stress and deformation calculation results are consistent with the measured values. The proposed finite element model can be used to analyze the mechanical characteristics of the steel box girder during the launching construction of the curved steel box girder.

References

1. Zhang Z (2021) Research on the key technology of walking-type incremental launching construction of long span steel box girder. HunanUniversity
2. Xu T (2011) Research on Big-span steel box girder mechanical characteristics and construction monitoring. Changsha University of Science & Technology
3. Zhao YF (2010) Numerical simulation technology research on steel-box girder incremental launching construction of Liangji canal bridge. Shandong University
4. Li HM (2014) Study on safety analysis of steel box girder during the incremental launching construction stage. Beijing Jiaotong University
5. Yang H (2010) A construction technology & mechanics characters of steel box girde which constructed by walking translation pushing method. Nanchang University
6. Cui QQ (2009) Calculation and analysis of incremental launching erection of prefabricated steel box girders having complicated geometry. Bridge Constr 06:50–53
7. Wang J (2009) Simulation and optimization for long-span changing curvature vertical curve steel-box girder bridge constructed by incremental launching method. Changsha University of Science & Technology
8. Ja HB (2019) Research on key technologies of steel box girder construction by step-up pushing method. Changan University
9. Yan YF (2014) Track thrusting technology for overpassing railway steel box girder construction. Railway Constr Technol 04:58–62

10. Che TC, Deng T, Wang W, Gong HW, Zhou YL (2021) Stability of transverse overturning of steel box girder bridge with small radius curve. J Water Resour Archit Eng 19(02):144–148
11. Jang X (2012) The steel box girder incremental launching construction local stability analysis of large span self-anchored suspension bridge. Changsha University of Science & Technology
12. Chen ZQ (2021) Force analysis and engineering application of long-span steel concrete curved bridge during incremental launching method. University of South China

Stress and Stability Analysis of Unequally Spaced Supports in Launching Construction of Curved Steel Box Girder Bridges

Baoliang Ma, Hui Zhao, Kun Zhu, and Gangnian Xu

Abstract In view of the problems of complex stress, great difficulty in analysis and high technical requirements for safety control of unequal support structure of curved continuous steel box girder bridge across railway tunnel, the mechanical performance and structural stability of three kinds of temporary supports with different structures, different heights and different spacing in the process of launching construction are analyzed by numerical simulation method. Then, the stress and deformation of the slideway beam are studied. By comparing with the measured data, the reliability and feasibility of the temporary support system for bridge erection are verified. Combined with theoretical analysis, the research results were successfully applied to the launching construction of curved continuous steel box girder bridge to ensure the safety of unequal spacing supports during the launching construction.

Keywords Curved steel box girder · Temporary supports and slideways · Launching construction · Numerical simulation · Stress performance · Stability analysis

1 Introduction

The jacking method construction is to set up an assembly site behind the abutment along the longitudinal axis of the bridge, assemble the steel box girder section by section, and connect the assembly section with the completed steel box girder body as a whole, then push the steel box girder body forward from the assembly site through the application of horizontal jacks, and then continue the assembly of the next section of steel box girder at the assembly site until the completion of the

B. Ma · H. Zhao · K. Zhu
Cccc Second Highway Engineering Co., Ltd, Hechi 547200, China

G. Xu (✉)
School of Civil Engineering, Shandong Jiaotong University, Jinan 250357, China
e-mail: 204144@sdjtu.edu.cn

H.-Y. Jeon (ed.), *Proceedings of the International Conference on Geosynthetics and Environmental Engineering*, Lecture Notes in Civil Engineering 374,
https://doi.org/10.1007/978-981-99-4229-9_27

construction. Jacking construction has the following advantages: 1. Long bridges are built with simple equipment, with low construction cost and stable construction. 2. The steel box girder is assembled in sections and operated continuously with good structural integrity. 3. The bridge sections shall be fixed and assembled at the same site to facilitate construction management, improve construction conditions and avoid aerial work.

At present, domestic and foreign scholars have carried out a large number of tests and simulation studies on the stability analysis of the launching construction. Many scholars have used finite element analysis software to analyze the stress and stability of the support system structure during the launching construction of steel box girders. Some scholars have shown that the most unfavorable conditions of displacement and stress are respectively under the condition of the guide beam reaching the front column and the condition of the maximum shear force at the root of the guide beam. Through scientific and reasonable design of the support system components, the stiffness, strength and stability of the support system structure can be guaranteed to meet the structural safety requirements during construction [1, 2]. Combined with the actual project, some scholars have introduced the construction scheme of launching and the construction technology of continuous steel box girder launching combined with support method in detail [3–5]. Among them, some scholars put forward the construction technology without support, and selected the tensioning temporary tie rod as the implementation plan, and introduced the working principle, construction steps and quality control measures of the floating jacking method in detail. In addition, some technologies use the steel tube bailey piece support to set up the jacking construction assembly platform, and replace the large steel box with bailey piece as the jacking slide, etc. [6–8]. A few scholars use the mechanical model of the steel pipe support and the truss beam-support separation model and coupling model established by the numerical simulation method to simulate the launching process, formulate the monitoring plan of the steel pipe support in the launching construction and propose a simulation method considering the support stiffness [9, 10].

To sum up, involving the crossing of tunnel lines and slope like complex terrain, and considering the impact of the dynamic load amount of jacking, the unequal height support structure has complex stress, great difficulty in analysis, and high technical requirements for safety control. To reveal the force transmission mechanism of unequal distance high pier support in the jacking stage of curved steel box girder, and propose the safety control index of temporary support structure is one of the problems that need to be solved urgently in the industry.

2 Project Overview

Lasuo No. 2 Bridge is located in Nandan County, Hechi City, Guangxi Zhuang Autonomous Region, with complex geological structure. No. 2 main bridge is (2×92) m two span continuous steel box girder, the main girder is full welded structure, the bridge deck width is 12.75 m, the beam height is 4.2 m, and the

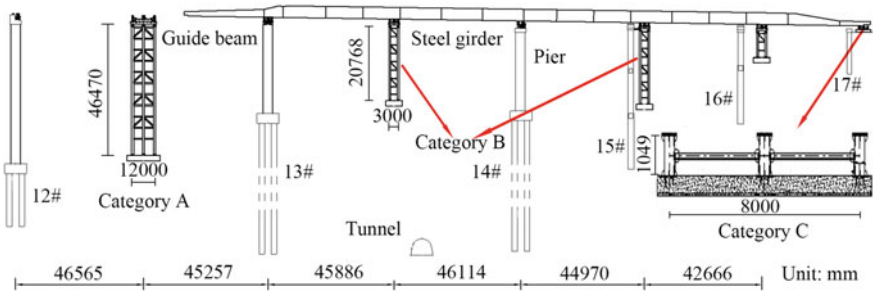

Fig. 1 Elevation of launching construction

upper span is Weiming Railway Tunnel. The minimum horizontal distance from the expanded foundation edge of the support beside Lasuo Bridge 2 tunnel to the tunnel is 7 m, and the buried depth of the tunnel is 56 m. The main girder of the steel box girder is a fully welded steel box girder with a total width of 2 × 12.75 m, consisting of two independent left and right frames. The main steel material of the main bridge is Q355D. The left span of Lasuo No. 2 Bridge is installed by pushing method and lateral sliding method, and the right span is installed by pushing method. The expanded foundation dimensions of Category A, Category B and Category C supports are (12 × 6 × 2) m, (6 × 6 × 1) m, (10.5 × 6 × 1)m, all of which are cast with C30 concrete, and the allowable values of compressive, tensile and splitting strength are 10.9 MPa, 1.10 MPa and 4.3 MPa, respectively. Elevation of launching construction is shown in Fig. 1.

3 Stress Analysis of Temporary Support Structure

During the launching construction of the steel box girder of Lasuo No. 2 Bridge, along with the launching construction, the position of the girder is changing all the time, and the structural system is also changing constantly. The temporary support must not only bear its own weight, but also be affected by pressure, wind load, horizontal load and friction between steel box girder and support. Therefore, the stress of the structure is complex, so it is necessary to analyze the mechanical properties of the temporary support structure.

3.1 Temporary Support

The temporary support consists of three types of support A, B and C, front and rear guide beams, runway beams and sliding system. There is 1 category A support in total; 3 category B supports; 2 category C supports. Steel pipes for temporary support

structures, distribution beams and connecting systems in the support system are all Q235B steel, and the values of tensile and yield strength are 420 MPa and 235 MPa, respectively.

Category A. The support column adopts steel pipe with diameter of 820 mm and pipe wall thickness of 10 mm, and the connection system adopts steel pipe with diameter of 820 mm and pipe wall thickness of 10 mm. The top and middle distribution beam is (900 × 600) mm, the lower distribution beam is (600 × 500) mm, and the lower part is an expanded foundation. There are 224 category A support column structure nodes and 506 beam elements. Carry out finite element analysis and modeling for category A support to check the force on the support, and apply dead weight, pressure, wind load and horizontal load. Horizontal load caused by longitudinal slope: According to the calculation, the maximum jacking reaction of the jacking support is 300t. The slope of beam section is 1.575%. Steel beam load is 300t. Wind load adopts steel beam wind load, support wind load. Dead weight is temporary support, and load combination adopts wind load, dead weight and horizontal force generated by longitudinal slope. Figure 2 shows the stress nephogram and support deformation diagram of the steel pipe of category A support, and the maximum stress is 130.6 MPa. Its value is less than the allowable stress of 153 MPa, The measured maximum stress is 127.5 MPa, the allowable deformation value is 46.47 mm, the calculated maximum deformation value is 34.87 mm, and the measured maximum deformation value is 28.4 mm.

Category B. The support column adopts steel pipe with diameter of 600 mm and pipe wall thickness of 14 mm, and the connection system adopts 16a channel steel. The upper distribution beam is (900 × 600) mm, the lower distribution beam is (600 × 500) mm, and the lower part is an expanded foundation. There are 39 category B support column structural nodes and 72 beam elements. Carry out finite element analysis and modeling for category B support to check the force on the support, and apply dead weight, pressure, wind load and horizontal load. Horizontal load

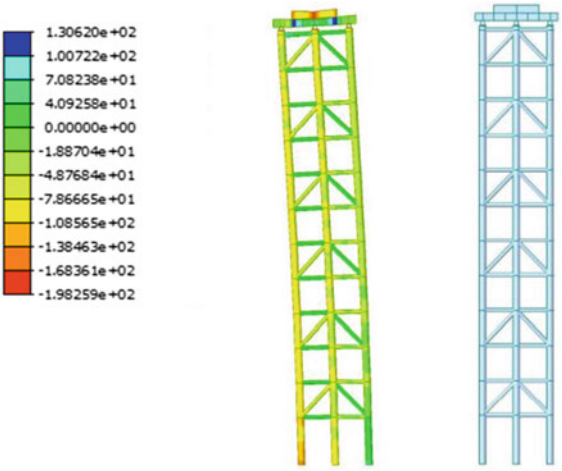

Fig. 2 Stress nephogram of category A support steel pipe and support deformation diagram

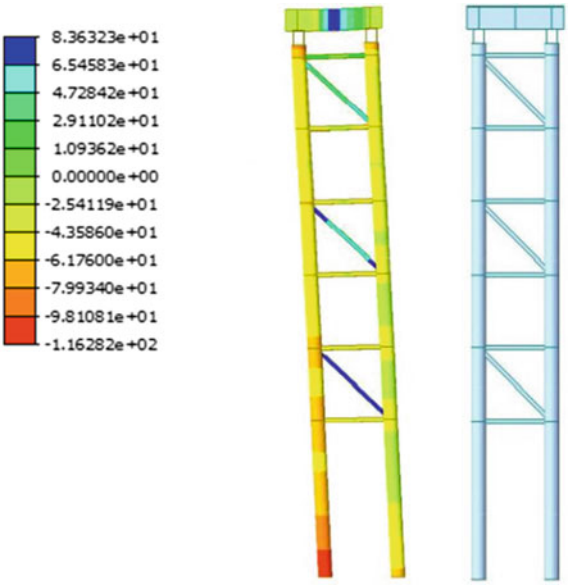

Fig. 3 Cloud chart of steel pipe stress and deformation of category B support

generated by longitudinal slope: according to the calculation, the maximum jacking reaction of the jacking support is 300t. The slope of beam section is 1.575%. Steel beam load is 300t; Wind load is composed of steel beam wind load and support wind load. The dead weight consists of temporary supports. The load combination consists of horizontal force generated by wind load, dead weight and longitudinal slope. Figure 3 shows the stress nephogram and support deformation diagram of the steel pipe for category B support.

The maximum stress is 89 MPa, which is less than the allowable stress of 153 MPa, the measured maximum stress is 82.3 MPa, the allowable deformation value is 20.768 mm, the calculated maximum deformation value is 17.86 mm, and the measured maximum deformation value is 15.4 mm.

Category C. The support column adopts steel pipe with diameter of 426 mm and wall thickness of 8 mm. The upper part is a double-welded 45a I-steel distribution beam, and the lower part is an expanded foundation. There are 40 nodes of category C support structure and 39 beam elements. Figure 4 shows the stress nephogram and support deformation diagram of the steel pipe for category C support.

The maximum stress is 99 MPa, which is less than the allowable stress of 153 MPa, the measured maximum stress is 89.4 MPa, the allowable deformation value is 1.049 mm, the calculated maximum deformation value is 0.9 mm, and the measured maximum deformation value is 0.75 mm. The stress and displacement calculation results of three types of temporary supports are shown in Fig. 5.

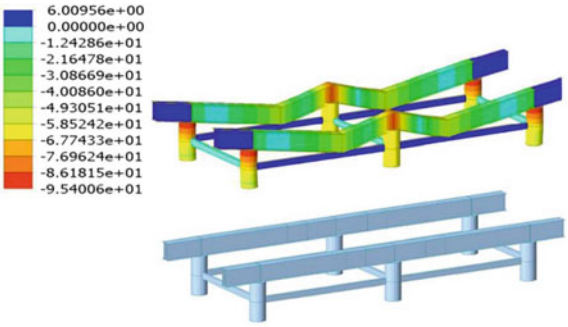

Fig. 4 Cloud chart of steel pipe stress and support deformation of category C support

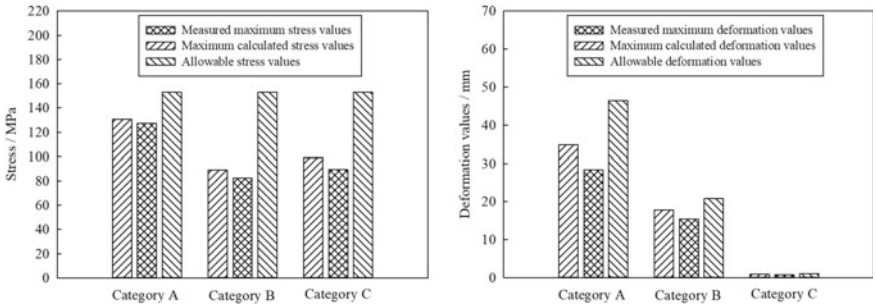

Fig. 5 Stress and displacement calculation results of three types of temporary supports

3.2 Runway Beam

The slideway system is composed of slideway beam, walking jack, jacking pad beam slider and pad stone. The slideway beam is made of Q355 material. The thickness of the top and bottom plates is 30 mm, the section height is 1000 mm, the thickness of the web plate is 20 mm, the width of the top plate is 900 mm, and the width of the bottom plate is 600 mm. It is calculated according to the most unfavorable layout of 13 # pier on the left side and 12 # pier on the right side. Midas is used to establish the finite element model of the slideway beam, and the lower part of the slideway beam is consolidated by the general support according to the actual position. The maximum reaction force of the standard runway beam is 677 tons, the spacing between the sliding blocks is 8 m, and the moving load is applied on the top of the runway beam. Figure 6 shows the model and stress nephogram of the runway beam. It can be seen from the figure that the maximum stress is 142 MPa, Its value is less than 355 MPa yield strength, which meets the strength requirements. In addition, the maximum displacement calculated is 0.3 mm, which is 15 mm less than the design value. The rigidity and strength of the slideway beam meet the requirements.

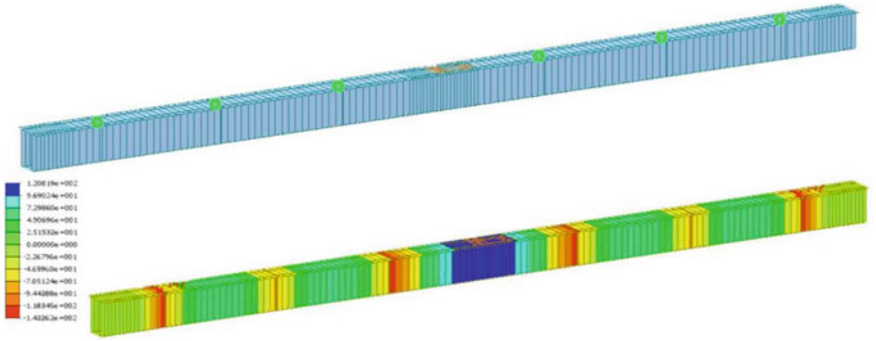

Fig. 6 Model and stress cloud chart of slideway beam

4 Stability Analysis of Temporary Support

Category A support. The finite element software is used to establish the calculation model, and the space beam element is used to simulate the vertical and horizontal connection of the support, analyze the stability of the temporary support structure, and fully consider the problems that may occur in each construction stage. The calculated loads include the dead weight of the structure, steel beam, wind load and the force generated on the support system during the jacking construction. Among them, the force generated by the dead weight of the support, steel beam and wind load is automatically applied in the program. Figure 7 shows the buckling analysis results of category A support. The buckling mode calculation results show that the critical load coefficient of the support structure is 66, and the structural stability meets the design requirements.

Category B support. Space beam element is used to simulate the longitudinal and transverse connection of category B support, analyze the stability of temporary support structure, and fully consider the problems that may occur in each stage of

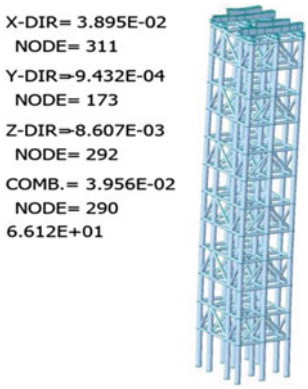

Fig. 7 Buckling analysis of category A support

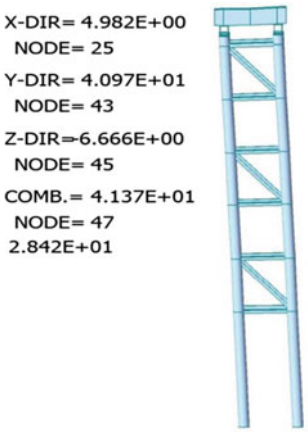

Fig. 8 Buckling analysis of category B support

construction. Figure 8 shows the buckling analysis results of category B support. The buckling mode calculation results show that the critical load coefficient of the support structure is 28, and the structural stability meets the design requirements.

5 Conclusion

In view of the problems of complex stress, great difficulty in analysis and high technical requirements for safety control of unequal support structures of curved continuous steel box girder bridges across railway tunnels, the stress performance and structural stability of three temporary supports with different structures, heights and spacing during the jacking construction process are analyzed by using numerical simulation method, and then the stress and deformation of the runway beam are studied, and the following conclusions are drawn:

(1) When the combination of wind load, dead weight and horizontal force generated by longitudinal slope is applied to the temporary support, the maximum stress generated is 130.6 MPa, which meets the strength requirements. The maximum stress generated by the slideway beam is 142 MPa, which is less than the yield strength.
(2) The research on the self weight, steel beam, wind load imposed by the support and the force generated by the support system during the jacking construction is carried out. Among them, the maximum critical load coefficient generated by the category C support is 329, and the structural stability also meets the design requirements.
(3) In this paper, Midas Civil is used to model the temporary support and slideway beam of Lasuo No. 2 Bridge and analyze their stress conditions, which can accurately simulate the stress conditions of the temporary support during construction.

References

1. Wang S, Yu ZR, Zhang HJ (2021) Design of temporary support structure for Incremental launching construction of urban curved' steel box girder. Qinghai Transp Sci Technol 33:92–99 +121
2. Wang H, Han F (2016) Technology research status review of long- span continuous rigid frame bridge deck pavement. J Chongqing Jiaotong Univ (Natural Science) 35(01):16–21
3. Chen SX, Chen KJ, Li R (2014) Study of design techniques of A- shape high-rise pier and long span concrete continuous rigid-frame bridge. Bridge Constr 44(01):63–68
4. Chen XQ, Li HL, Xian L (2007) A study on wind stability of cable supported bridges using CFRP cables. Highway 07:42–45
5. Chen ZM, Wang XQ, Zhang JD (2018) Incremental launching construction technology of long-span simply supported steel truss bridge. Constr Technol 47:643–646
6. Bajaber MA, Hakeem IY (2021) UPC evolution, development, and utilization in construction: a review. J Market Res 10:1058–1074
7. Dai J, Di J, Qin FJ (2013) Finite element analysis on incremental launching construction for steel box girder. Constr Urban Plan 2331:671–674
8. Wang J, Dai J, Qin FJ (2013) Parametric analysis on incrementally launched construction for concrete box girder. Adv Mater Res (838–841):838–841
9. Zhou DY (2018) An analysis of the mechanical behavior of the steel tube brackets in the course of jacking a concrete box girder. Traffic Eng Technol Natl Def 16:22–25
10. Ahmad S, Hakeem IY, Maslehuddin M (2016) Development of an optimum mixture of ultra-high performance concrete. Eur J Environ Civ Eng 20:1106–1126

Sensitivity Analysis of Impact Coefficient for Large Transport Vehicle Crossing Bridge

Laiyong Wang, Gangnian Xu, Yuzhi Wang, and Haoyu Li

Abstract When the vehicle speed is very low, it is generally believed that the impact coefficient of vehicle load can be ignored. However, under the conditions of uneven bridge deck and heavy cargo transportation, the impact coefficient of the bridge when the vehicle is running at low speed cannot be ignored. In order to study the sensitivity of the impact coefficient of large transport vehicles crossing the bridge, this paper first establishes the bridge structure model and vehicle model, and uses the range analysis method to influence the impact coefficient of 12 influencing factors, such as the unevenness of the bridge deck, the stiffness of the bridge structure, and the vehicle mass. The research results show that the method of neglecting the impact coefficient of vehicle load in the existing safety assessment of large transport bridges often makes the bridge structure in a state of potential safety hazard. The impact coefficient is affected differently by different factors. For mid span deflection and bending moment, the primary and secondary order of impact factor is: concrete elastic modulus > bridge deck flatness grade > vehicle speed > structural Rayleigh damping constant. For shear force, the primary and secondary order of influencing factors of impact coefficient is: vehicle speed > concrete elastic modulus > bridge deck flatness grade > structural Rayleigh damping constant.

Keywords Simply supported box girder bridge · Heavy cargo transportation · Impact coefficient · Sensitivity analysis · Orthogonal test method

L. Wang
China Academy of Transportation Sciences, Beijing 100088, China

G. Xu (✉) · H. Li
Shandong Jiaotong University, Jinan 250357, China
e-mail: 204144@sdjtu.edu.cn

Y. Wang
LiaoCheng City Highway Development Center ChiPing Highway Development Center, Liaocheng 252100, China

H.-Y. Jeon (ed.), *Proceedings of the International Conference on Geosynthetics and Environmental Engineering*, Lecture Notes in Civil Engineering 374,
https://doi.org/10.1007/978-981-99-4229-9_28

1 Introduction

Compared with ordinary vehicles, bulky transport vehicles are mainly characterized by large weight, long length, low driving speed, etc. When checking and evaluating the bridge undertaking heavy cargo transportation, it is generally believed that the impact coefficient of vehicle load can be ignored due to the low speed of vehicles. However, in the third chapter of this paper, the monitoring and numerical analysis of the real bridge show that if the bridge deck is uneven, the impact coefficient of heavy cargo transport vehicles running at low speed cannot be ignored. However, for the current situation of the bridge deck in China, the unevenness of the bridge deck is widespread. Similarly, Zhang et al. studied the dynamic impact coefficient of crescent shaped multi arch rib concrete filled steel tube truss arch bridge and found that when the vehicle speed is 10 km/h, the impact coefficient of arch rib deflection reaches about 0.35, and the impact coefficient of main beam deflection reaches about 0.30 [1]; Gui et al. studied the spatial dynamic impact effect of hollow slab bridge under the action of vehicle load. When the vehicle speed is 3.6 km/h, the impact coefficient of hollow slab still reaches about 0.15 [2]; Li et al. conducted a trolley walking test with a solid plate beam with a pit and groove, and found that when the vehicle speed was 0.5 m/s, the impact coefficient value of the solid plate beam still reached about 0.24 [3].

Due to the randomness of various vehicle loads acting on the bridge, such as the vehicle type, weight, speed and distance of passing vehicles, road roughness, as one of the main factors inducing vehicle bridge coupling vibration, is itself a random process, so the coupling vibration of vehicles and bridges must have a certain randomness. In 1988, Kawatani et al. assumed that the road roughness was a stationary random process, established a two degree of freedom vehicle model, and analyzed the non-stationary random response of the bridge under vehicle load using the random vibration theory [4]. Xiang et al. established the vehicle bridge interaction model by using the dynamic transfer matrix method in time domain and the d'Alembert principle, and carried out relevant research on the dynamic reliability of the vehicle bridge system by using the first-order reliability method [5]. Zhang et al. used the pseudo excitation method (PEM) to accurately transform the vertical random unevenness of the pavement into a series of vertical simple harmonic unevenness superposition, simulated the continuous changes of vehicle forces in the time domain and space domain using the precise integration method (PIM), and studied the non-stationary random vibration of the vehicle bridge coupling system [6]. Wang et al. studied the vehicle bridge coupling vibration of hyperbolic arch bridge under random traffic flow [7]. Sun et al. compiled the load spectrum of random traffic flow and analyzed the dynamic deflection and overall stiffness characteristics of T-beam bridge under random traffic flow [8]. Wu et al. established a Euler Bernoulli simply supported beam with non Gaussian material parameters by using spectral stochastic finite element method. Assuming that the road roughness is a Gaussian stochastic process, they analyzed the dynamic response of the bridge under vehicle load [9]. Ye et al. simplified the bridge as a Euler Bernoulli beam model simply supported at both

ends, considered the two degree of freedom vehicle moving system, and took the power spectral density function of the surface roughness of the bridge deck structure as the input, established a coupling mechanical analysis model of multiple mobile vehicle systems and bridges. Through the state space theory and the general theory of evolutionary random process, the method of solving the evolutionary random response of the whole vehicle bridge coupling system is given by using the modal analysis method. The theoretical formulas of the mean square value response of the bridge section displacement and section bending moment and the evolutionary power spectral density function are derived. The changing rules of the root mean square value response of the bridge midspan displacement under different bridge spans, different deck levels, and different vehicle moving speeds are discussed [10]. Kozar et al. established a vehicle bridge coupling vibration model based on the spectral method [11]. Zhang et al. established a space vehicle bridge coupling vibration model, taking vehicle speed, pavement conditions, etc. as random variables, and studied the fatigue reliability and residual life of existing bridges [12].

Under the condition of uneven bridge deck, the impact coefficient of the bridge can not be ignored when the vehicle is running at low speed. The systematic research on the impact coefficient of bridges under the action of low-speed heavy cargo transport vehicles is even more blank. In order to provide basis for the safety assessment of large transport bridges and eliminate potential safety hazards, this paper discusses the influence of various factors on the impact coefficient of bridges.

2 Bridge Structure Model

Taking the 20 m span fabricated prestressed concrete simply supported box girder (the width of the integral subgrade is 28 m, as shown in Fig. 1) in the general drawing of highway bridges as an example, the space girder method model is established. The change of structural stiffness is represented by different concrete strength grades. The corresponding elastic modulus of C45, C50 and C60 concrete is 33500 MPa, 34,500 MPa and 35,500 MPa, respectively.

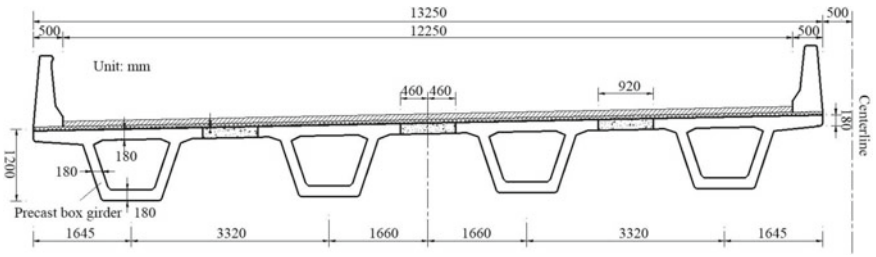

Fig. 1 Cross section of precast box girder. (Unit: mm)

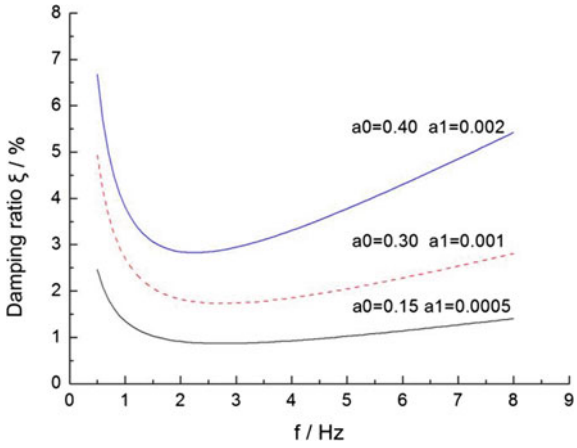

Fig. 2 Damping ratio

In the vibration problem of bridge structures, damping ratio is an important factor affecting the dynamic response of structures. In order to discuss the impact coefficient of damping ratio, this paper compares three Rayleigh damping in the empirical range, as shown in Fig. 2.

3 Vehicle Model

Take the low platform semi-trailer as an example to analyze the vehicle bridge coupling vibration. The basic parameters of the vehicle structure are: $L_1 = 2.5$ m, $L_2 = 0.5$ m, $L_3 = L_4 = 1$ m, $L_5 = 10$ m, $L_6 = 0.2$ m, $L_7 = 1.8$ m, $L_8 = 2$ m, $B = 1.8$ m, Except that the front axle tires are single wheels, the other wheels are multiple wheels. The relevant parameters of multiple wheels are twice that of single wheels. The mass of single wheel is 335 kg, the stiffness of single wheel is 2400 kN/m, the damping coefficient of single wheel is 6, the stiffness of single wheel suspension is 1200 kN/m, and the damping coefficient of single wheel suspension is 5; The head mass m_1 is 18000 kg, and the body mass m_2 is 88000 kg; The nose pitching moment of inertia is 30000, and the body pitching moment of inertia is 150000; The overall rolling moment of inertia of the vehicle is 45000.

Figure 3 shows the main vibration modes and frequencies of the low platform semi-trailer. The first vibration mode of the vehicle is the overall vertical translation of the vehicle; The second mode is the overall pitching motion of the vehicle, and the vibration of the vehicle head and body is in phase.

a) First order mode f=1.783 b) Second order mode f=2.392

Fig. 3 Main vibration modes and frequencies of low plate semi trailer

4 Sensitivity Analysis of Impact Coefficient

Figure 4 shows the dynamic response of prefabricated box girder under the action of low plate semi-trailer in numerical test 1. It can be seen from the figure that when the vehicle is driving in the middle, there will be two big peaks in the dynamic response curve of the prefabricated box girder, which is related to the longitudinal distribution of wheel force; The dynamic response of center beam is greater than that of side beam; The difference of bending moment between center beam and side beam is relatively small, and the difference of deflection is relatively large; Compared with the center beam, the supporting shear force of the side beam is smaller.

The range analysis method can be used to analyze the results of orthogonal test, which generally includes two steps: calculation and judgment, as shown in Fig. 5. K_{jm} in the figure is the sum of the test indexes corresponding to the level of factor m in column j, which is the average value. The optimal level of factor j and the horizontal combination of various factors can be determined by the size of K_{jm}, that is, the optimal combination. R_j is the range of the factors in column j, that is, the difference between the maximum and minimum average values of the indicators at each level of the factors in column j. R_j reflects the change range of the test index when the level of the factor in column j changes. The larger the index is, the greater the influence of the factor on the test index. Therefore, the more important it is, and the primary and secondary factors can be determined.

$$R_j = \max(\overline{K_{j1}}, \overline{K_{j2}}, \cdots, \overline{K_{jm}}) - \min(\overline{K_{j1}}, \overline{K_{j2}}, \cdots, \overline{K_{jm}}) \tag{1}$$

In addition, the horizontal variation curve of bending moment, deflection and shear impact coefficient with 12 influencing factors is shown in Fig. 6.

It can be seen from the figure that, in most cases, the deflection impact coefficient > the bending moment impact coefficient > the shear impact coefficient, and the deflection impact coefficient is close to the bending moment impact coefficient, with the same change trend; With the increase of the elastic modulus of the structure, that is, the stiffness of the bridge superstructure, the impact coefficient increases.

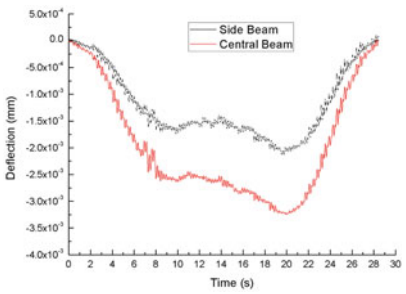

a) Mid span deflection time history curve

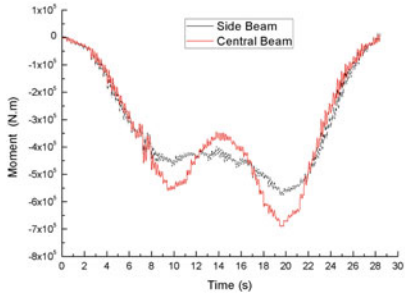

b) Mid span bending moment time history curve

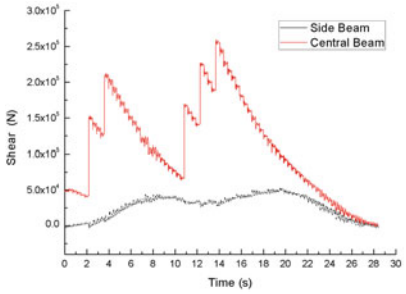

c) Shear time history curve of left fulcrum

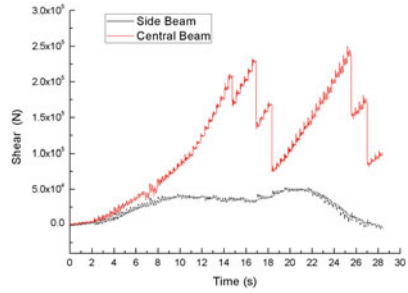

d) Shear time history curve of right fulcrum

Fig. 4 Dynamic response of precast box girder under the action of low plate semi trailer

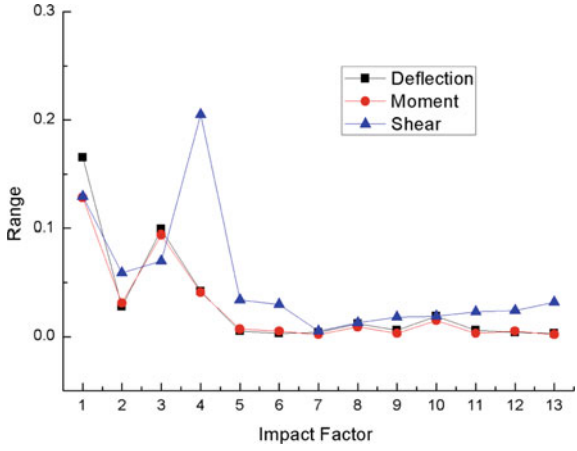

Fig. 5 Range analysis chart of influencing factors

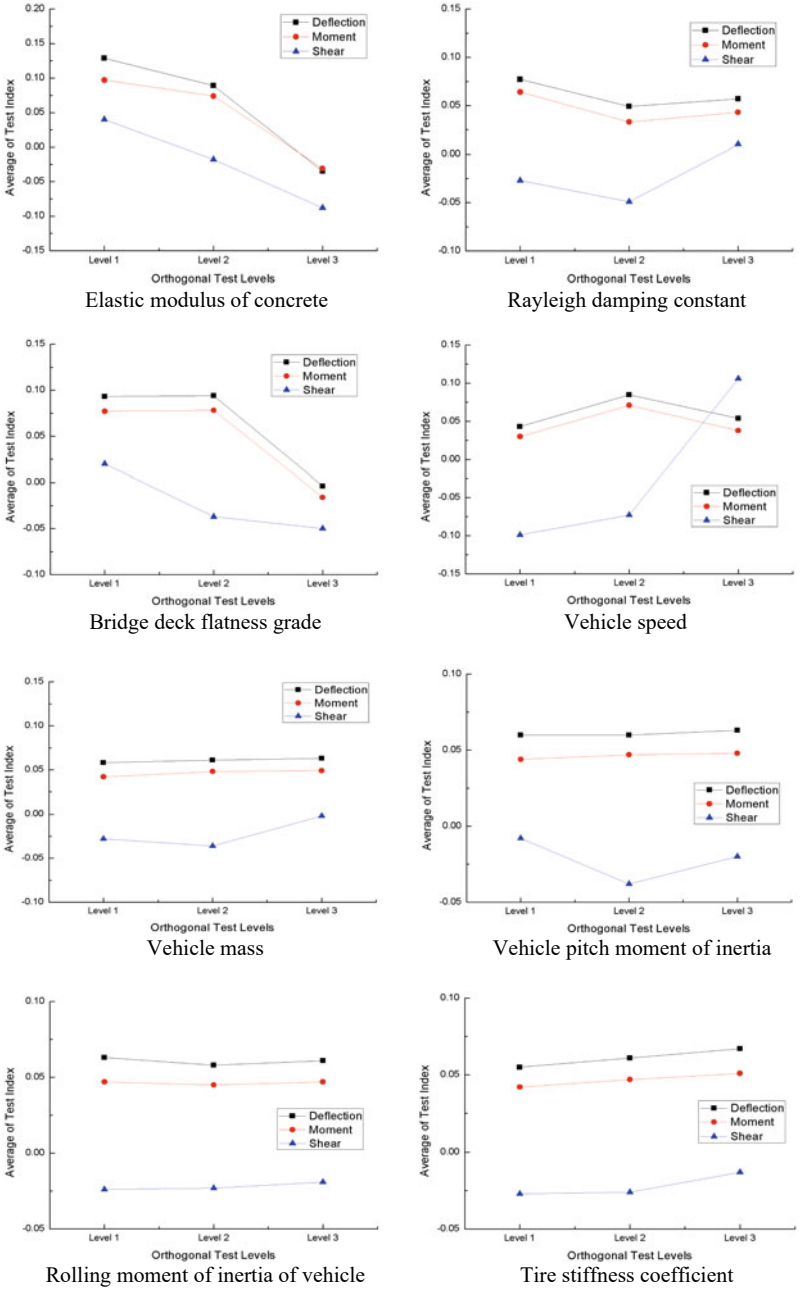

Fig. 6 Curve of impact coefficient changing with influencing factors

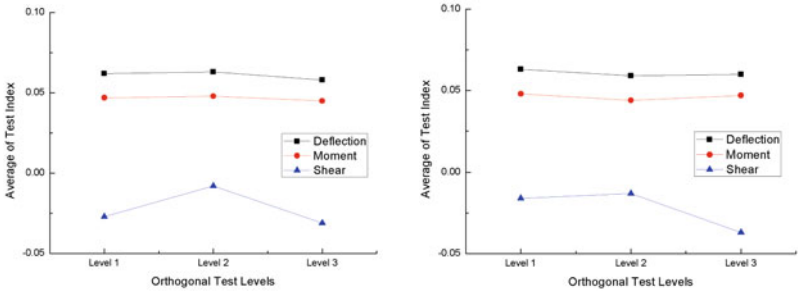

Fig. 6 (continued)

5 Conclusion

When large transport vehicles are traveling across the bridge at low speed, the impact coefficient calculated after considering the factors such as the unevenness of the bridge deck, the stiffness of the bridge structure, and the vehicle mass cannot be ignored. In the existing safety assessment of large transport bridges, the practice of ignoring the impact coefficient of vehicle load often makes the bridge structure in a state of potential safety hazard.

The impact coefficient is affected differently by different factors. For mid span deflection and bending moment, the primary and secondary order of impact coefficient influencing factors is: concrete elastic modulus > bridge deck flatness grade > vehicle speed > structural Rayleigh damping constant, and other factors have weak influence. For shear force, the primary and secondary order of influencing factors of impact coefficient is: vehicle speed > elastic modulus of concrete > bridge deck flatness grade > structural Rayleigh damping constant, and other factors have weak influence.

Acknowledgements This work is supported by the the Open Project of Key Laboratory of Transportation Industry (Beijing) for Old Bridge Detection and Reinforcement Technology (No. 2021-JQKFKT-3).

References

1. Mitsuo K, Sadao k (1988) Nonstationary random response of highway bridges under a series of moving vehicles. Struct Eng Earthq Eng JSCE 5(2):285–292
2. Xiang TY, Zhao RD, Xu TF (2007) Reliability evaluation of vehicle–bridge dynamic interaction. J Struct Eng ASCE 133(8):1092–1099
3. Zhang ZC, Zhang YH, Zhao Y et al (2009) PEM-PIM algorithm for non-stationary random vibration of vehicle bridge system. J Comput Mech 26(1):26–32
4. Wang D, Liu Y, Huang PM (2009) Research on vehicle bridge coupling vibration of hyperbolic arch bridge under random traffic flow. J China Highw Eng 22(6):67–73

5. Sun SJ, Xu JW, Han WS (2010) Overall stiffness characteristics of T-beam bridge under random traffic flow. J Transp Eng 10(5):23–29
6. Wu SQ, Law SS (2011) Dynamic analysis of bridge with non-Gaussian uncertainties under a moving vehicle. Probab Eng Mech 26(2):281–293
7. Ye M, Tan P, Ren M (2010) Random vibration analysis of bridge evolution under multiple vehicle loads. J Vib Eng 23(3):269–274
8. Kozar I, Malic NT (2013) Spectral method in realistic modelling of bridges under moving vehicles. Eng Struct 50:149–157
9. Zhang W, Cai CS (2012) Fatigue reliability assessment for existing bridges considering vehicle speed and road surface conditions. J Bridge Eng ASCE 17(3):443–453
10. JTG D60–2004 (2004) General code for design of highway bridges and culverts. People's Communications Press, Beijing
11. JTG D62–2004 (2004) Code for design of highway reinforced concrete and prestressed concrete bridges and culverts. People's Communications Press, Beijing
12. Guo T, Li AQ, Bian CD (2005) State assessment of long span bridges based on Monte Carlo Numerical Simulation. J Highw Transp Res Dev 22(8):26–30

Study on Microstructure of Malan Loess by SEM

Xiaojun Yin and Lanmin Wang

Abstract The structure is the main factor of loess collapsibility. Whether the collapsible deformation of loess can occur completely depends on whether the structural strength can be lost and the degree of loss. The microstructure of Malan loess was analyzed by scanning electron microscope, and the images with magnification of 500 and 1000 were obtained from three different angles. Through analysis, it is concluded that the structure of the loess soil sample is granular. The mechanism of microstructure changes of Malan loess after encountering water was revealed. The particles are mostly plate-like, long-columnar, sub-angular, partially sub-circular, mostly single-particle structure, with a small number of particles. The contact between particles is mainly point-to-point contact, point-angle contact, and a small number of point-to-point contacts. Macroscopically, the soil becomes dense. Microscopically, the point-to-point contact with relatively large friction between particles has changed into the face-to-surface contact with less friction.

Keywords Malan loess · SEM · Loess collapsible · Microstructure

1 First Section

1.1 A Subsection Sample

The shape of loess particles often contains the origin of loess and the source of loess. It is generally believed that the loess plateau is formed by the accumulation of wind dust in the northwest desert region. However, some experts believe that there are large areas of thick loess of different ages distributed in the southeast of the loess

X. Yin (✉)
Jiaying University, Meizhou 514015, China
e-mail: yinxiaojun800@126.com

L. Wang
Institute of Lanzhou Earthquake, China Earthquake Administration, Lanzhou 730000, China

H.-Y. Jeon (ed.), *Proceedings of the International Conference on Geosynthetics and Environmental Engineering*, Lecture Notes in Civil Engineering 374,
https://doi.org/10.1007/978-981-99-4229-9_29

plateau. After study, it is believed that the formation of these loess may be different from that of the loess plateau. The particle morphology can reflect the deposition rate, the formation process and the later stress state. Therefore, the study of particle morphology in microstructure photos is helpful to understand the origin of soil and related physical and mechanical properties.

Structure [1–4] is the main factor of loess collapsibility. Whether loess collapsible deformation can occur depends entirely on whether the structural strength can be lost and the degree of loss. Before structural failure, the compressibility of undisturbed loess is very small. After the structure is damaged, the compressibility increases significantly.

The structure of loess in northern China has been classified and studied [5–8] by scanning electron microscope, and the relationship between microstructure category and collapsibility coefficient has been summarized. The mercury intrusion method has been used to reveal the distribution characteristics of loess pores, the relationship between pore size distribution and collapsibility.

The type of microstructure is directly related to the magnitude of seismic subsidence deformation [9–11]. The anisotropy and strength difference of dynamic deformation caused by different types of microstructure are different. The author believes that for the constitutive problem of structural soil, the problem of deformation strength difference caused by different microstructure of soil should be solved first. The deep reasons that affect the residual deformation of soil samples are found from the microscopic aerial pore level of soil, and the theory of graininess and gas–solid two-phase is introduced, and the microscopic method of soil research is proposed. Xie [12] found the following phenomena in the dynamic elastic modulus test: loess with low water content is different from ordinary saturated clay or sand, and its influence range under dynamic load is gradually developing from the top of the sample. In the test [9], the dense accumulation of particles can be clearly observed, and the macroscopic performance is that the upper soil layer becomes dense while the lower soil layer at a certain depth is basically unchanged. This phenomenon is caused by the graininess of loess [13–19]. According to the particle theory, when the dynamic stress of soil particles is very small, the deformation of soil samples can only occur at a certain height. The underlying soil layer has no particle conduction, the particles arch and block, and the energy terminates. The macroscopic phenomenon is similar to “elasticity”. That is, the propagation of force by soil particles is layered, and each layer has a maximum value of critical deformation under a certain dynamic stress.

In this study, the morphology and structure of Malan loess particles were analyzed by scanning electron microscope, and its microstructure mechanism was studied.

Fig. 1 SEM

2 SEM Test of Malan Loess

2.1 SEM Test

The loess sample was taken from a natural loess slope in Shanzidun Village, Lanzhou New District as the prototype, the soil belongs to Malan loess, that is Q_3 loess.

Scanning electron microscope MX2600FE, experimental apparatus is shown in Fig. 1.

The main technical indicators of SEM:
VP variable pressure mode resolution:
5.0 nm guarantee index;
Magnification range: 15x ~ 30000x;
Acceleration voltage: 0.5 kV ~ 30 kV;
Maximum sample size diameter: 60 mm;
Range of electric moving image: ± 10 μm ~ $\pm$ 40 μm;

2.2 Loess Sample of Test

The test site is located in a certain area of Shanzidun, Lanzhou New Area, belonging to the natural slope of Class III terrace on the south bank of the Yellow River. The soil layer is relatively thick, belonging to weathered Q_3 loess, and the loess layer is silt and silty clay. The natural height of the slope is 25 m. No underground water is found within the depth of 20 m underground. The soil samples used were taken from a depth of 6.5 m in the slope, and the natural dry density of the test sample was about 1.33 g/cm^3. In order to control different suction, adjust the water content to 20%.

3 Results of the Test

3.1 SEM Results with Magnification of 500 Radius

Figure 2 shows the electron microscope image of the loess sample at a magnification of 500 times. It can be more clearly seen in the electron microscope image of the loess that the internal porosity of the loess can be seen, and the morphology of the loess particles is mainly composed of two types of structures, namely, agglomerate and granular—agglomerate, and the contact of the skeleton particles can be seen. At this magnification, it can be clearly seen that the soil particles with the size of clay particles are mainly filled between the skeleton particles, and a small part adhere to the surface of the skeleton particles. It can be seen that the microscopic type of loess is mainly skeleton structure.

3.2 SEM Results with Magnification of 1000 Radius

The above image shows the electron microscope image of loess at a magnification of 1000 times. At this magnification, most particles can be seen in the image. Obviously, the main constituent minerals of the powder are still rock-forming minerals such as quartz, feldspar and mica. These minerals have good crystalline morphology, which are mostly flaky, massive and granular, and have certain symmetry (Fig. 3).

Under this magnification, it can be clearly seen that the contact between the coarse particles of loess, the contact relationship between the coarse particles and the fine particles, as well as the support pores and some embedded pores formed between them can also be identified and analyzed. The loess structural information that can be reflected has a good overall structure.

3.3 Calculation of Experimental Results

A. **Resolution**

The smallest distance between two points that can be distinguished.

$$R = \frac{0.61\lambda}{n\sin\alpha} \tag{1}$$

where, λ is wavelength; n is index of refraction; R is aperture radius (Table 1).

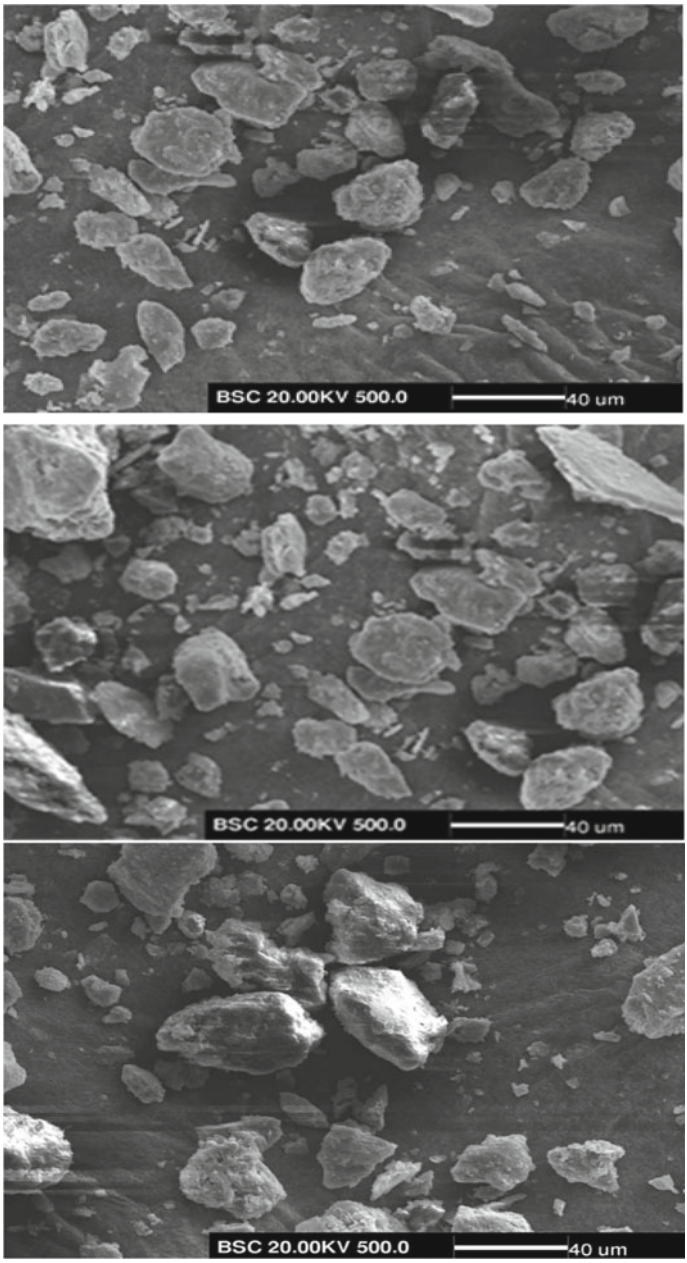

Fig. 2 Magnification of 500 radius

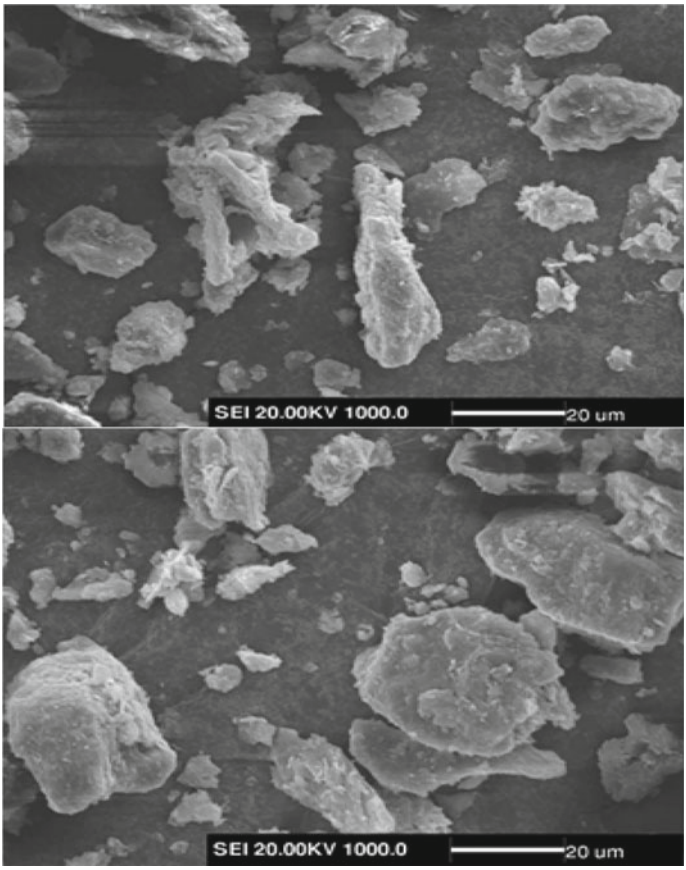

Fig. 3 Magnification of 1000 radius

Table 1 Wavelength of different tests

	λ	Actual resolution
LM	400 nm	200 nm
SEM	0.007 nm	1.0 nm
TEM	0.0025 nm	0.2 nm

B. **Depth of Focus**

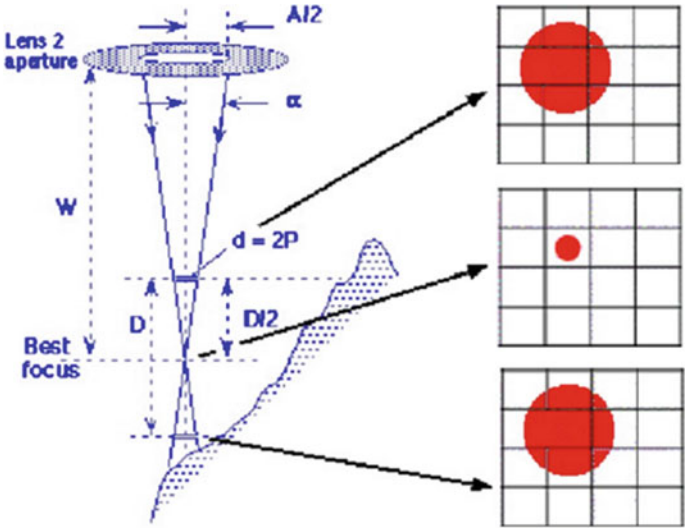

$$\Delta f = \left(\frac{0.2}{M} - d\right)\frac{D}{a} \tag{2}$$

where D is the working distance; A is the aperture of the objective diaphragm, M is the magnification, and d is the diameter of the electron beam. Large depth of field images can be obtained with long working distance, small objective aperture and low magnification.

4 Discussion

From the above two sets of scanning pictures, it can be seen that the Malan loess is in granular structure: the particles are mostly tabular, long columnar and sub-angular, some are sub-circular, most are single-particle structure, and a few particles are concentrated. The contact between particles is mainly point-to-point contact, point-to-point contact, and a few point-to-point contacts. The particles have clear edges and corners, and the friction between them is large. It is easy to support each other to form a support overhead structure, and the pores between particles are clearly visible.

Under the action of dynamic load, the overhead structure of Malan loess support was damaged, and smaller soil particles were squeezed into the pores, while the macropore structure further changed into microporous structure. The contact mode between particles has also changed from point-to-point contact and point-rigid contact to edge-to-surface contact and surface-to-surface contact. Macroscopically, the soil becomes dense; Microscopically, the point-to-point contact with relatively large friction between particles has changed into the face-to-surface contact with less friction.

5 Conclusions

The surface characteristics and arrangement of the loess particles, the microstructure of the loess, the structure of the pores, and the contact of the loess skeleton particles were observed with the scanning electron microscope under different magnification. The following conclusions are drawn.

Two sets of scanning pictures show that the Malan loess is in granular structure.

The particles are mostly plate-like, long-columnar, sub-angular, partially sub-circular, mostly single-particle structure, with a small number of particles. The contact between particles is mainly point-to-point contact, point-angle contact, and a small number of point-to-point contacts.

Macroscopically, the soil becomes dense; Microscopically, the point-to-point contact with relatively large friction between particles has changed into the face-to-surface contact with less friction.

Acknowledgements The research was financially supported by the Fundamental Research Funds for the Jiaying Universities (Project no. 2022JYU02), National Natural Science Foundation of China (Project no. U1939209).

References

1. Ding-yi XIE (2001) Exploration of some new tendencies in research of loess soil mechanics. Chin J Geotech Eng 23(1):3–13
2. Fu-sheng ZHA, Song-yu LIU, Yan-jun DU et al (2010) Quantitative assessment on change in microstructure of loess during collapsing using electrical resistivity measurement. Rock Soil Mech 31(6):1692–1698
3. Jin-qian DANG, Jing LI (2001) The structural strength and shear strength of unsaturated loess. J Hydraul Eng 7, 79–83, 90
4. Hai-song LIU, Wan-kui NI, Bin YAN et al (2008) Discussion on relationship between structural strength and collapsibility of loess. Rock Soil Mech 29(3):722–726
5. Yongyan W, Zaiguan L (1990) Research on the structure and phys-ico -mechanical properties of loess[M]. Science press, Beijing
6. Xiangy L (1989) i Research on relation between the types of loess micro-structure and physico-mechanical indexes. Acta Geologica Sini-ca 63(2):182–190

7. Guoru G (1990) i The structural theory for research of loess collapse de-formation. Chin J Geotech Eng 12(1):1–9
8. Weibin CAI (2014) Study on interaction between loess skeleton particles. Chang'an University, Xi'an
9. Jin DENG, Lanmin WANG, Zhijian WU (2013) Establishment and analysis of elasto-plastic loess microstructure and dynamic deformation model. Chin J Rock Mech Eng 32(S2):3995–4001
10. Jin DENG, Lanmin WANG, Zhenzhong ZHANG (2007) Microstructure characteristics and seismic subsidence of loess. Chin J Geotech Eng 29(4):542–548
11. Lanmin WANG (2003) Loess dynamics. Earthquake Press, Beijing, pp 12–82
12. Dingyi XIE (1998) Preliminary research on dynamic characteristics of the undisturbed loess. Science Press, Beijing, pp 60–100
13. Quanyi ZHANG, Zheng PENG, Run HE et al (2007) The drag force experienced by a projectile in granular medium under gravity. Acta Physica Sinica 58(8):4708–4712
14. Yong-fu XU, Si-hong LIU, Ping DONG (2001) Microstructural model for granular soils. Rock Soil Mech 22(3):366–372
15. Jiu-sheng REN (1995) The theoretical and experimental research on the mechanical characteristic of collapsible loess. Lanzhou University, Lanzhou
16. Zai-qiang HU, Zhu-jiang SHEN, Ding-yi XIE (2000) Research on structural behavior of unsaturated loess. Chin J Rock Mech Eng 19(6):775–779
17. Osipov VI, Sokolov VN (1995) Factors and mechanism of loess collapsibility. Genesis and properties of collapsible soils. Kluwer Academic Publishers, Netherlands
18. Feda J (1995) Mechanisms of collapse of soil structure. Genesis and properties of collapsible soils. Kluwer Academic Publishers, Netherlands
19. YIN XJ (2020) Study on stability of loess slope under the coupling effect of rainfall and earthquake. Institute of Engineering Mechanics, China Earthquake Administration, Harbin

"L" Shaped Short Bench Excavation Method with Small Step Spacing

Bo Wang, Gang Hao, Juwei Hou, and Defeng Zhang

Abstract This paper takes the Nanjing Hengjiang Avenue construction project as the background and the finite element ABAQUS software as the platform. The 3D digital model of foundation pit excavation is established, and the influence of step construction method and L shape short step construction method on the deformation of foundation pit supporting structure and concrete supporting axial force is calculated and analyzed. After comprehensive analysis of mechanical construction efficiency, operating space and safety, the final selection of "L" shaped short step short distance construction method. The influence of erection time on supporting structure is analyzed, and the final determination is within 10 h. Finally, by comparing the simulation of foundation pit with the measured value, it is concluded that the deformation considering creep is close to the measured value, which is very important for the study of foundation pit deformation.

Keywords Step type · "L" shaped short step distance · ABAQUS · Erection time · Deformation · Supporting axial force

1 Introduction

Deep foundation pit engineering involves supporting structure and soil deformation analysis, supporting structure soil and water pressure calculation, foundation pit overall stability analysis, deformation and protection of surrounding buildings and other aspects of surface settlement and deformation of supporting structure are the key to the success of deep foundation pit engineering construction [1–3]. At present, the deep foundation pit is developing towards the direction of larger scale, deeper depth, more complex surrounding environment and more strict excavation

B. Wang (✉)
Beijing Guodaotong Highway Design and Research Institute Co., Ltd., Beijing, China
e-mail: 2551082197@qq.com

G. Hao · J. Hou · D. Zhang
Beijing Municipal Road and Bridge Co., Ltd., Beijing, China

H.-Y. Jeon (ed.), *Proceedings of the International Conference on Geosynthetics and Environmental Engineering*, Lecture Notes in Civil Engineering 374,
https://doi.org/10.1007/978-981-99-4229-9_30

deformation control. Strict control of the surface settlement around the excavation of deep foundation pit and the deformation of supporting structure is the key to the success of deep foundation pit construction [4, 5]. This paper takes the foundation pit engineering of an existing project in Nanjing as the background, combined with the unique characteristics of the silty soil layer in this area (the silty soil generally has "three high and three low" characteristics: high water content, low permeability, high sensitivity, low strength, high compressibility and low density) [3]. Its special engineering mechanical properties also bring difficulty to the design and construction of support, dewatering and excavation of foundation pit engineering in silty soil area [5]. The alternating deposition of silt or clay and silty soil forms the interlayer of clay and silty soil or the microbedding structure with multiple thin silty sand layers only 1–2 mm thick in the thick cohesive soil, among which the silty cohesive soil layers in the floodplain area of the Yangtze River are the most typical [6].

In the excavation of large excavation excavation, it is necessary to consider the temporal and spatial effects of soil mass, such as "center island method" and "basin excavation method" [7–15]. However, there is a lack of relevant literature reports in the silty soil layer. According to the characteristics of the existing foundation pit, based on the theory of "spatio-temporal effect", the foundation pit excavation method of slope layer, section and block is formed, which is widely used because of its good deformation control effect. But at the same time, the construction of foundation pit is very practical, and there are many factors affecting the excavation and support of earth, including subjective management factors and objective weather and technology factors. Under various factors, it is easy to cause the unsupported exposure of the enclosure structure for a long time, and the actual deformation of foundation pit is usually much larger than the theoretical requirements (14). Therefore, how to reduce unsupported exposure time during block excavation through optimization of earthwork excavation process is the key to deformation control.

The excavation process of silt foundation pit has obvious spatio-temporal effect [16], so it is necessary to study the deformation characteristics of foundation pit supporting structure under different earthwork excavation methods, so as to determine the earthwork excavation method suitable for large-span silt foundation pit [17]. The excavation of foundation pit mainly adopts the step excavation method of stratified section. However, in the process of excavation of silt foundation pit, the construction time of step excavation method is longer, and the mechanical running back and forth will increase the disturbance times to the enclosure structure and soil mass, and the soil mass creep deformation is larger. At the same time, for the foundation pit with limited operating space, the step excavation will obviously affect the mechanical operation. In view of the silt soil foundation pit with strong creep, it is in urgent need of an excavation method with fast construction and high safety performance. Therefore, it is of practical social and economic significance to develop an efficient excavation method.

2 Rsearch Method

The foundation pit with the largest depth and width (270 m*63 m) in this project is selected as the research object, and two excavation methods of step type and "L" shaped short step construction are adopted respectively. The deformation characteristics of foundation pit supporting structure under different excavation conditions are studied by numerical simulation method and compared and optimized.

The foundation pit excavation model is established for calculation. The upper and lower layers of internal support are adopted, the first layer is concrete support, and the lower layer is steel pipe support. The foundation pit model is shown in Fig. 1.

2.1 Step Excavation

As shown in Fig. 2, the foundation pit is divided into a 30 m section with a total of 8 construction sections. Numerical simulation calculation of the stepped excavation method is carried out. The specific sequence of excavation methods is shown in Table 1.

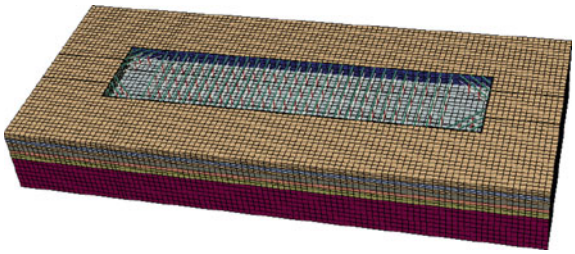

Fig. 1 Foundation pit model

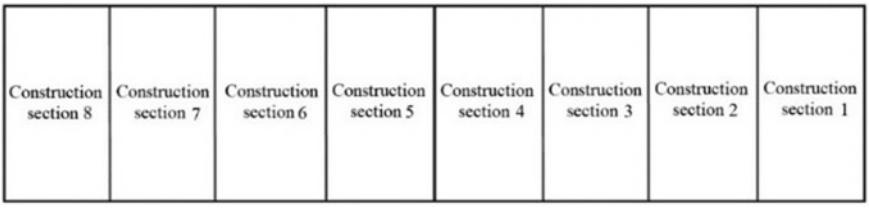

Fig. 2 Division of construction section

Table 1 Step excavation sequence

Working condition	Excavation condition
1	Construction Sect. 1 was excavated to 5 m and steel support was erected
2	Construction Sect. 2 was excavated to 5 m and steel support was erected
3	Construction Sect. 1 was excavated to the basement
4	Construction Sect. 2 was excavated to the basement

2.2 "L" Shape Short Step Distance Construction Technology

The process principle of "L" shaped short step small step construction technology is as follows. In Fig. 3, the A-A profile of the foundation pit adopts slope excavation, and when excavating to a depth of 5 m, a 3 m wide working platform is set for the excavator to operate. The B-B profile adopts a slope with a relatively small slope for grading and excavation. At the same time as the A-A profile is excavated, the B-B profile is excavated in advance, and the steel support is erected when the foot of the base slope is excavated to the lower part of the steel support. After the steel support is erected, the back cover work is carried out.

The A-A profile of the foundation pit adopts PC320 model excavator to excavate vertically down the excavation surface, and PC400 model excavator to excavate on one side. Initially, two excavators pour the soil into the muck truck at the same time, and after excavating to a depth of 3 m, the PC320 excavator pours the soil to the PC400 excavator, and the PC400 excavator pours the soil into the muck truck. After the excavation of the foundation pit to 5 m, a 3 m wide working platform is set up, and the bottom of the foundation pit is transported to the excavator on the step by PC320 excavator, and then transferred to the excavator in the upper part of the foundation pit, and the upper excavator is poured into the muck truck, and the three excavators are pushed forward at the same time, the specific construction steps are shown in Fig. 4.

Profile B-B in Fig. 3 adopts slope with relatively small slope for slope excavation, and the excavation depth is 5 m. At the beginning of the excavation, PC320 excavator was used to excavate vertically down the working face, and PC400 was used for slope lowering. After the excavation depth was 5 m, two excavators were used to promote

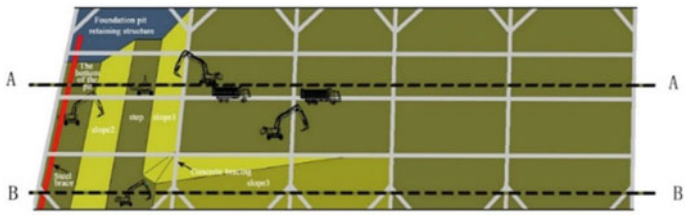

Fig. 3 The plan of the foundation pit excavation

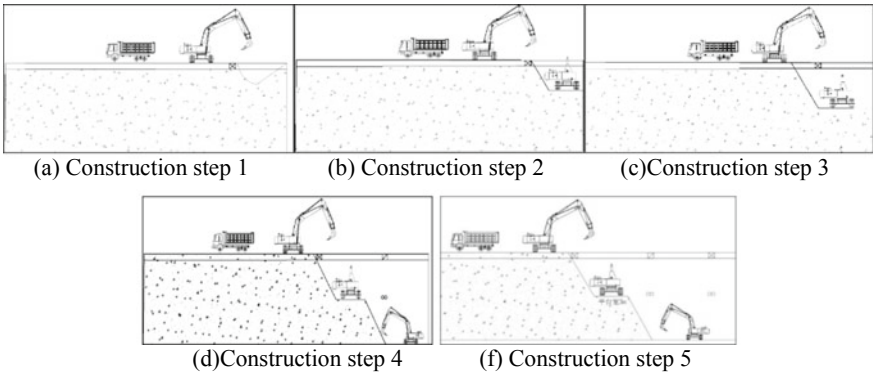

Fig. 4 Long distance direction slope excavation process of foundation pit

the excavation horizontally. A step 3 m wide is reserved for the construction of the 5 m deep foundation pit, and the same slope as A-A profile is used to excavate the foundation pit below 5 m. The excavation sequence of B-B profile is shown in Fig. 5.

The A-A profile and B-B profile shall be excavated along the long distance direction at the same time. When the excavation reaches the pit corner the Angle shall be closed by the excavation on both sides. The specific construction procedure as shown in Fig. 6.

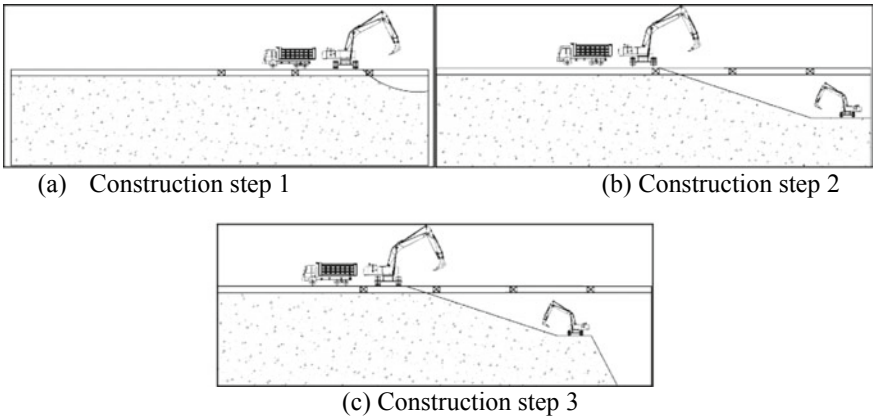

Fig. 5 Excavation steps of B-B section

(a) Construction step 1 (b) Construction step 2 (c) Construction step 3

Fig. 6 Construction method of "L" shaped short step spacing

3 Results and Discussion

3.1 Step Excavation

According to the simulation results in Figs. 7 and 8, when the stepped excavation method is adopted, the deformation of the foundation pit is relatively stable during the whole excavation process. When the construction Sect. 2 is excavated to the bottom of the foundation pit, the deformation of the supporting structure is 33.95 mm and the maximum axial force is 742.3 kN. Overall, the deformation of supporting structure is within the safe range.

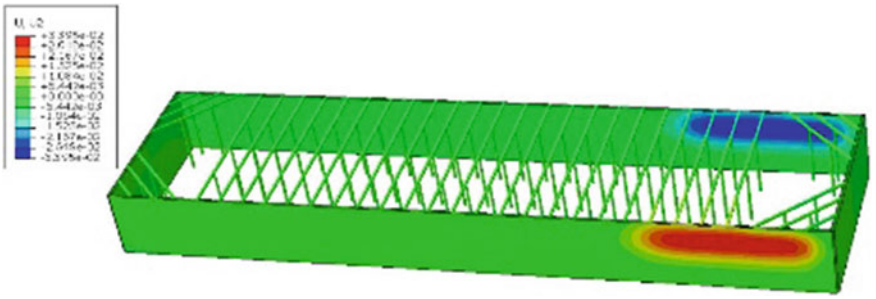

Fig. 7 Deformation of stepped excavation retaining pile

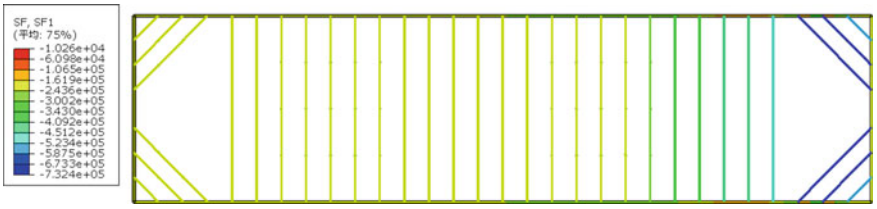

Fig. 8 Step excavation concrete supports axial force

3.2 "L" Shape Short Step Distance Construction Technology

The reinforcement depth of the strips is taken as 3 m, and the width of the soil strips between the strips is taken as 3.35 m. The influence of the reinforcement width on the deformation of the foundation pit is studied.

3.3 "L" Shape Short Step Distance Construction Technology

According to Fig. 7, 8, 9 and 10 and Table 2, by comparing the maximum deformation of the supporting structure and the maximum axial force of the concrete support with the two excavation methods, it can be seen that the construction method of "L" shaped short step is slightly larger than that of the step excavation. The reason is that the support construction method of "L" shaped short step is set up later and the soil creep deformation is more obvious. According to the requirements of Technical Regulations DGJ32/J189-2015 for the Monitoring of Building Foundation Pit Engineering in Nanjing Area, the early warning value of concrete support axial force is determined to be 800 kN based on the specific situation of this project and the experience of similar projects. The two excavation methods do not exceed the safe value range. However, considering the mechanical construction efficiency, operating space and safety, the construction method of "L" shaped short step is suitable for the excavation of silt long distance foundation pit.

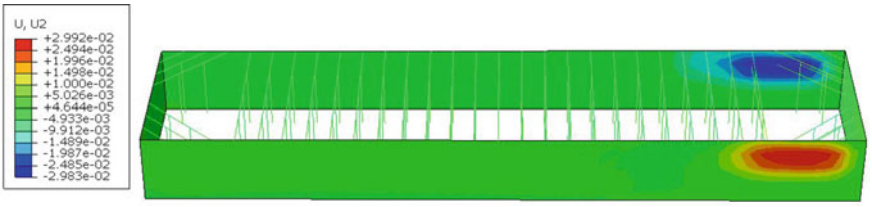

Fig. 9 Construction method of "L" shape short step and short distance excavation deformation

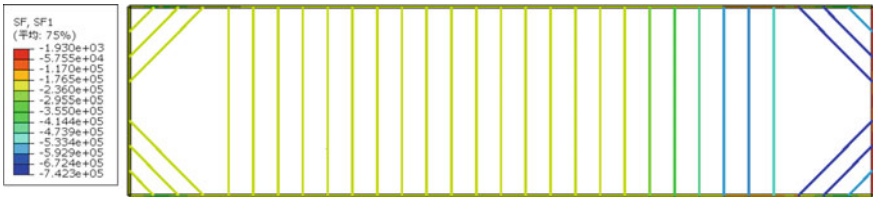

Fig. 10 The construction method of "L" shaped short step and short distance excavation axial force

Table 2 Comparison of two excavation methods

Excavation method	Maximum deformation of supporting structure (mm)	Maximum axial force of concrete support (kN)
Step type	33.95	742.3
Construction method of "L" shaped short step spacing	34.69	766.5

4 Influence of Erection Completion Time on Supporting Structure

In the construction process, the foundation reinforcement, SMW construction pile and concrete support are all completed before the excavation. In the construction process, the two-layer steel support is set up when the base slope foot is excavated to the lower part of the steel support. The erection time of the support is an important factor affecting the deformation and stability of the foundation pit. Determining the erection time of the support can not only improve the overall safety of the foundation pit, but also improve the construction efficiency, so the erection time of the support is explored and analyzed. Based on the construction method of "L" shaped short step and small distance, the simulation calculation is carried out in seven cases: steel support is erected immediately when the foundation pit bottom slope is excavated to the lower part of the steel support, and steel support is erected 2 h, 4 h, 6 h, 8 h, 10 h and 12 h after the excavation to the bottom slope.

The calculation results of Table 3 are analyzed in combination with Fig. 11. When the support erection time is not considered, the displacement and axial force of the foundation pit are both smaller than the values considering the erection time, indicating that time has a great influence on the displacement and deformation of the foundation pit. The axial force and displacement of concrete support for foundation pit gradually increase with the increase of erection time, and the increase rate gradually decreases. Therefore, the creep deformation is mainly concentrated in the early stage after the completion of excavation. Erection in time can effectively reduce the influence of creep deformation on foundation pit deformation. According to Technical Regulations DGJ32/J189-2015 for Construction Foundation Pit Engineering Monitoring in Nanjing Area, the horizontal displacement of the foundation pit is within the safe range, and according to the regulations of GB50497-2019 for Construction Foundation Pit Engineering Monitoring and similar engineering experience, it can be known that the warning value of concrete support axial force is 800 kN. When the steel support is erected 12 h after the foundation pit excavation to the foot of the slope, the supporting axial force exceeds 800 kN, and the steel support is still within the safe range after the erection 10 h. Therefore, the completion time of steel support erection should be controlled within 10 h for the construction method of "L" shaped short steps.

Table 3 Calculation result

Number	Time for erection of support	Maximum horizontal displacement of retaining pile (mm)	Maximum axial force of concrete support (kN)
1	Erection immediately after excavation to the foot of slope	34.69	766.5
2	Set up 2 h after excavation to the foot of slope	35.84	784.1
3	Set up 4 h after excavation to the foot of slope	36.13	789.3
4	Set up 6 h after excavation to the foot of slope	36.29	793.5
5	Set up 8 h after excavation to the foot of slope	36.40	796.4
6	Set up 10 h after excavation to the foot of slope	36.49	799.1
7	Set up 12 h after excavation to the foot of slope	36.56	801.6

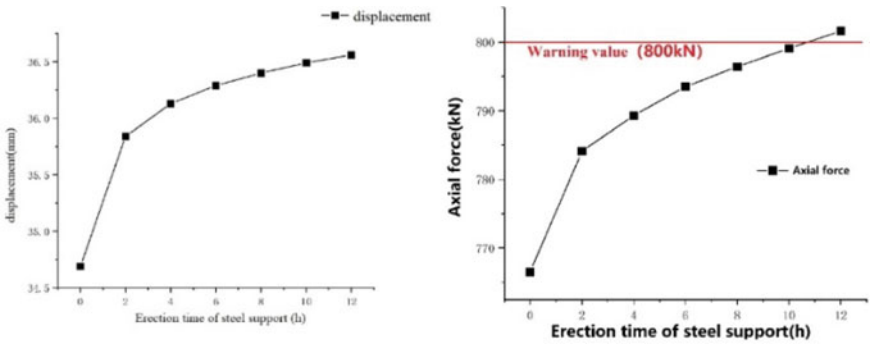

Fig. 11 The displacement axial force of foundation pit varies with the time interval of erection

5 Comparison between Simulation and Measured Values of Foundation Pit

According to the construction method of "L" shaped short step and short distance, the erection time of steel support is 10 h. The overall deformation of A, B and C foundation pit after excavation is studied (Fig. 12 and Table 4).

Figures 14 and 15 are the comparison of simulated and measured results of horizontal displacement and surrounding settlement deformation of foundation pit A, B and C respectively. The location of measuring points is shown in Fig. 13. From the

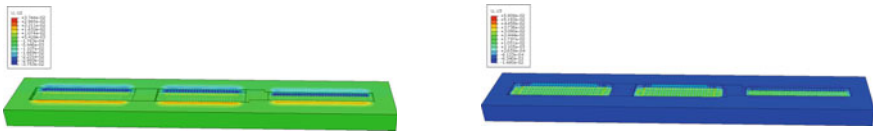

(a) Excavation displacement (b) Vertical displacement of foundation pit excavation

Fig. 12 Excavation of foundation pit deformation

Table 4 Calculation result

Number	Excavation length (m)	Maximum horizontal displacement of retaining pile (mm)	Maximum settlement (mm)	Basal uplift (mm)
A	275	36.31	14.17	57.62
B	240	37.53	14.80	58.08
C	280	35.62	14.02	56.41

whole simulation, the displacement of foundation pit matches the simulation. It can be seen from the contrast curve of surrounding settlement that the variation trend of the simulation results is basically consistent with the measured values, and the maximum settlement value is 5–10 m. At the same time, the measured values are close to the deformation after considering creep. Therefore, considering creep has a very important role in the study of foundation pit deformation.

When creep is considered in foundation pit A, B and C, deep horizontal displacement and surrounding settlement increase, while the maximum displacement points of deep horizontal displacement and surrounding settlement do not change. When creep is considered, the displacement increases obviously above the basement, while the horizontal displacement decreases obviously after reaching the basement. The surrounding settlement is the most obvious at the position 10 m away from the pit edge, and the influence of creep is also the most obvious. After the completion of excavation of A, B and C foundation pits, the displacement and supporting axial force of the foundation pits do not exceed the warning value, and the supporting structure and excavation method of the foundation pits meet the requirements of excavation.

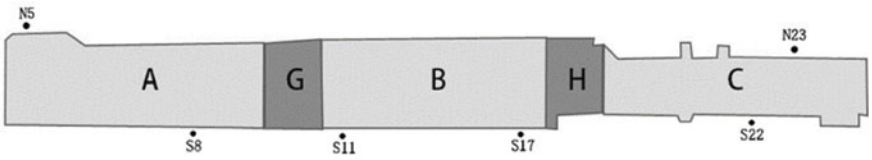

Fig. 13 A, B, C foundation pit measuring point location

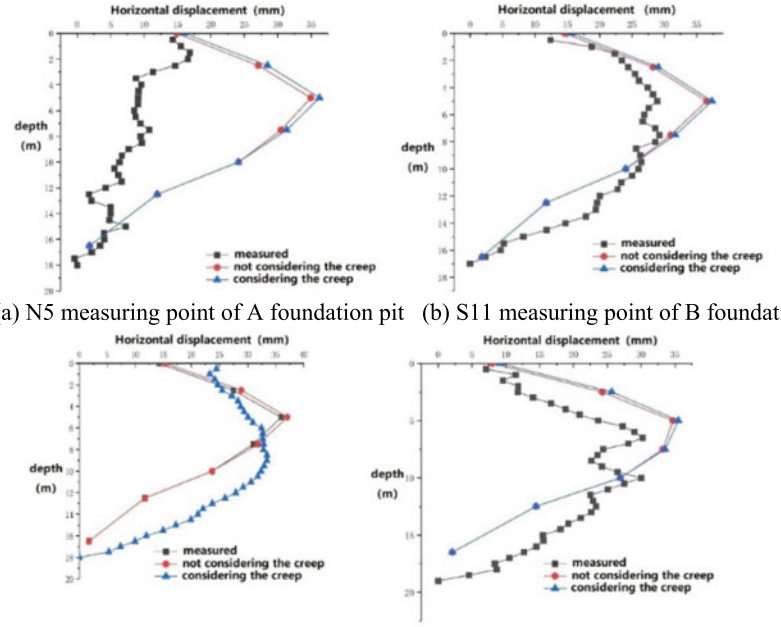

(a) N5 measuring point of A foundation pit (b) S11 measuring point of B foundation pit

(c) S13 measuring point of B foundation pit (d) N23 measuring point of C foundation pit

Fig. 14 Horizontal displacement simulation—measured comparison curve

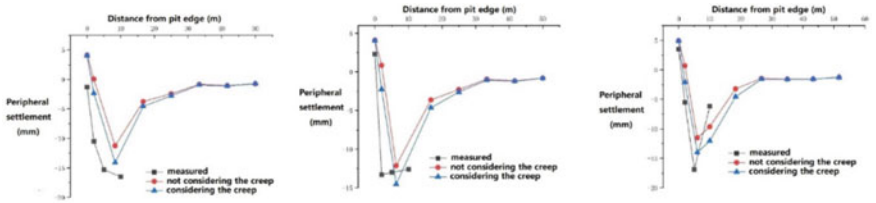

(a) S8 measuring point of A foundation pit
(b) S11 measuring point of B foundation pit
(c) S22 measuring point of C foundation pit

Fig. 15 Comparison curve between simulated and measured peripheral settlement

6 Conclusion

By studying the excavation method of the foundation pit, comparing the proposed construction method of "L" shaped short steps with the step method, comprehensively considering the safety and economy of the foundation pit, the following conclusions are drawn:

(1) The construction method of "L" shaped short steps and small steps can effectively avoid the disturbance of the enclosure structure and soil mass caused by the mechanical running back and forth, and has advantages over the step excavation in mechanical operation and excavation, which can significantly reduce the construction time and also meet the requirements of the excavation specification.
(2) In view of the erection time of steel support in the construction method of "L" shaped short step, it is determined that the erection time of steel support should not exceed 10 h, and the supporting axial force and structural displacement gradually increase with the erection time.
(3) By comparing the simulation results with the measured values, the deformation after considering creep is close to the measured values. Considering creep has a very important role in the study of foundation pit deformation.

References

1. Jiuchun S, Yanhui B (2021) Research and application of small scale basin excavation method for deep foundation pit in soft soil. J Undergr Space Eng
2. Xian L (2019) Summary and research on soft soil deep foundation pit construction cooperation in emergency. Urban Express Rail Transit 2:7
3. Yuechen J, Quanmei G, Yu, Zhao et al (2021) Energy method for horizontal deformation of underground diaphragm wall caused by soft soil excavation. J Undergr Space Eng 17(6):13
4. Dapeng L, Changhong Y, Shuai Z (2018) Research progress on the influence of deep foundation pit excavation on surrounding environment. J Wuhan Univ Eng Ed 51(8):10
5. Yibin L, Wei D, Wangbing (2017) Monitoring and deformation characteristics analysis of deep foundation pit in soft soil area. Surv Mapp Notif (S2):6
6. Huizhong Z, Mingjian L (2005) "Microconfined water" in Shanghai soft soil and foundation pit engineering. J Geotech Eng 08:95–98
7. Xiaonan G (1999) Design and construction manual of deep foundation pit engineering. Design and construction manual of deep foundation pit engineering
8. Shunqun L, Yinghong W, Gang Z (2011) Study on the influence of backpressed soil on embedment depth of cantilever support structure
9. Xunfan B, Li Z, Peilin L (2006) Research on reserved width of soil platform in Center Island method construction of large soft soil foundation pit. J Geotech Eng 28(10):1208-12
10. Jing Y, Xiaomi F (2014) Review of calculation method of backcompacting soil in front of supporting structure and a new simplified analysis method. Rock Soil Mech 35(1):8
11. Shengbin Y (2016) Study on the simplified analysis method of reserved foundation pit. Rock Soil Mech 37(2):13
12. Yangbo S, Yuan J, Xihong Z (2006) Study on the width of reserved soil shoulder in reverse basin excavation. J Undergr Space Eng 2(5):4
13. Meihua W, Fang J (2005) Discussion on construction technique of superlarge area deep foundation pit with reverse method. J Undergr Space Eng 4:5
14. Shijia L, Changping Z, Weiran H (2015) Deformation law and countermeasure of deep silt layer foundation pit excavation in East China. Guangdong Civil Eng Architect 4:4

15. Xuanxiang W (2009) Discussion on application of reserved soil embankment in construction of wide foundation pit of subway. Railway Constr 2:4
16. Chen P (2021) Research on monitoring deformation of deep foundation pit excavation construction based on spatiotemporal effect. Heilongjiang Transp Sci Technol 011:044
17. Bo W, Peng Y, Meng G (2020) Measured analysis of spatiotemporal effect of deep foundation pit excavation construction in soft soil area of Ningbo. J Railw Sci Eng 17(1):13

Study on the Effect of Surface-Base Bond State on the Mechanical Response of Cement Concrete Pavement

Leqiang Shen, Chunzhen Chang, Renliang Guo, and Hao Han

Abstract To study the influence of the surface-base bond state on the mechanical response of cement concrete pavement, a pavement structure model was established, and the bond coefficients were set between the cement concrete surface and the poor cement concrete base for stress and strain analysis. The research results show that: (1) The horizontal tensile stress and shear stress at the bottom of the surface layer both significantly decreased with an increase in the surface-base bonding coefficient, whereas the horizontal tensile stress at the bottom of the base layer increased overall and the shear stress dropped. (2) After the surface-base bonding coefficient increases to 6.0, the stresses reach a steady state and the surface-base bonding state is nearly completely continuous. In the actual project, the concrete slab can be poured directly before the initial setting of the poor cement concrete base, so that the best combination between the surface-base can be achieved, thus prolonging the pavement's service life.

Keywords Cement concrete · Poor cement concrete base · Surface-base bond state · Mechanical response

1 Introduction

Poor cement concrete substrates are rigid substrates with advantages such as high strength, good integrity and stability. It is widely used in cement concrete pavement structures for heavy traffic because it can support the surface concrete slab well and transfer the load between slabs. Experimental studies have been conducted to show that the cement concrete surface layer is semi-bonded with the poor concrete base

L. Shen · C. Chang (✉) · R. Guo · H. Han
Shandong High Speed Engineering Construction Group Co., The Sixth Engineering Company, Jinan, China
e-mail: 1477623937@qq.com

L. Shen
e-mail: 120404340@qq.com

H.-Y. Jeon (ed.), *Proceedings of the International Conference on Geosynthetics and Environmental Engineering*, Lecture Notes in Civil Engineering 374,
https://doi.org/10.1007/978-981-99-4229-9_31

and is not ideally bonded or separated [1]. Different interface treatment methods can produce large differences in the bonding state of the surface and subgrade, affecting the structural forces of the pavement [2, 3], mainly in the interface shear strength [4]. Hu et al. [5] and Zhang et al. [6] found that the interlaminar bond state has a significant impact on the stress at the base of the face layer, but the change law of stress in different face-base bond states is not clearly proposed. To this end, this research builds a finite element model of the pavement structure, and different bonding coefficients are assigned between the cement concrete surface layer and the poor cement concrete base layer to analyze the stress variation law of each structural layer with the bonding coefficient and provide a theoretical foundation for the design of cement concrete pavement with poor cement concrete as the base layer.

2 Finite Element Model of Cement Concrete Pavement

2.1 Model Building

In this paper, an elastic laminated half-space foundation model is used to simulate the pavement structure, which is 3.5 m wide and 5.0 m long. Since most heavy-duty pavement structures will have a subgrade, to reduce the difficulty of the model analysis, the subgrade and roadbed are converted to an equivalent roadbed with a modulus of 200 MPa. Table 1 shows the thickness and material characteristics of each structural layer.

2.2 Grid Division

The accuracy of the computation results and the rate of convergence are directly impacted by the grid division quality. In this paper, the grid division of the base and foundation is the same as the surface layer in the plane, and the division size is 0.05×0.05 m, so that the nodes correspond to each other to improve the calculation accuracy.

Table 1 Material parameters and each structural layer's thickness

Structural layers	Thickness (h/mm)	Elastic modulus (E/MPa)	Poisson ratio (μ)
Cement concrete surface layer	280	31,000	0.15
Poor cement concrete base	200	14,000	0.15
Equivalent road base	2000	200	0.35

2.3 The Setting of Interlayer Contact

In this paper, interlayer contact is set between cement concrete panel and poor concrete subgrade, and different bonding coefficients are used to simulate the bonding state between surface and subgrade, which are set to a completely continuous state, completely separated state, and semi-bonded state. The completely continuous state is represented by a binding coefficient of $+\infty$, the completely separated state is represented by a binding coefficient of 0, and the semi-bonded state uses seven binding coefficients of 0.5, 1.0, 1.5, 2.0, 4.0, 6.0, and 10.0.

2.4 Define Boundary Conditions and Apply Loads

In this paper, when imposing the boundary conditions of the finite element model, all the degrees of freedom at the bottom surface of the soil base are constrained, and the degrees of freedom normal to the face and around the following layers are constrained. Wheel loads are generally assumed to be circular uniform loads with an axle weight of 100 KN, and the wheel loads are equated to 25 nodes [7], as depicted in Fig. 1 (Table 2).

To study the effect of the surface-base bond state on the mechanical response of the cement concrete pavement structure, the travel load is applied to the middle of the longitudinal joint edge of the cement concrete panel in this paper. The geometric relationship between the location of the load action and the pavement panel is shown in Fig. 2, with the shaded part of the figure showing the wheel marks. z indicates the direction of travel and x indicates the direction of road width.

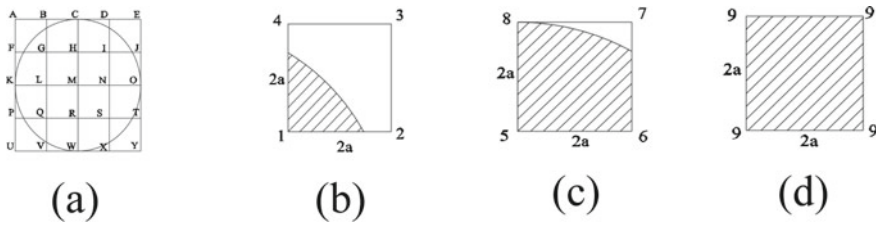

Fig. 1 Nodal force calculation schematic

Table 2 Displays the outcomes of the nodal force superposition

Loading location	AEUY	BDFJPTVX	CKOW	GIQS	HLNR	M
Node stacking method	3	4 + 7	8 + 8	1 + 6 + 6 + 9	9 + 5 + 5 + 9	4 × 9
Loads (N)	68	641	1038	1661	1750	1752

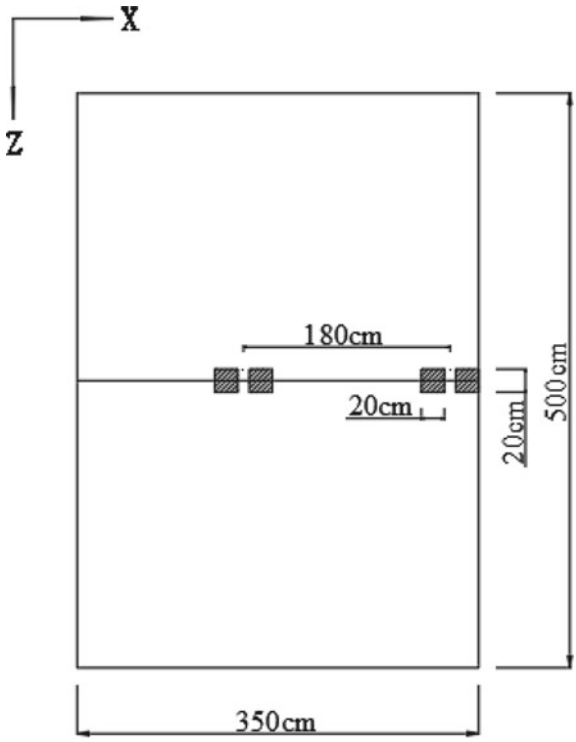

Fig. 2 Schematic diagram of the location of the load action

3 Influence of Surface-Base Bond State on Pavement Mechanical Properties

3.1 Horizontal Tensile Stress at the Bottom of the Surface Layer and the Bottom of the Base Layer

The tensile stress at the bottom of cement concrete pavement structure is one of the main factors to be considered in pavement design. The significance of the effect of the surface-base bonding state on horizontal and vertical stresses is related to the way of stress transfer. Both the interlayer smooth model and the contact model assume that vertical stresses can be transferred continuously in the vertical direction, so the surface-base bonding state has almost no effect on vertical stresses. In this paper, we only analyze the horizontal tensile stresses under different surface-base bonding states, and obtain the horizontal tensile stresses at the bottom of the surface layer and the bottom of the base layer along the middle of the road longitudinal joints under different surface-base bonding coefficients by finite element simulation, as shown in Table 3.

Table 3 Horizontal tensile stresses in the bottom of the surface layer and the bottom of the base layer at the middle of the edge of the longitudinal joints with different surface-base bonding coefficients (Pa)

Combination coefficient		0	0.5	1.0	1.5	2.0	4.0	6.0	10.0	+∞
X-direction tensile stress	Surface layer bottom	402,853	292,457	215,710	171,890	147,180	105,708	89,762	87,680	83,778
	Base layer bottom	42,590	54,620	65,043	74,689	81,513	87,870	82,426	81,649	82,796
Z-direction tensile stress	Surface layer bottom	808,407	662,762	524,923	420,464	354,583	251,568	230,280	227,377	172,920
	Base layer bottom	104,335	102,040	99,894	99,573	102,179	125,174	139,049	140,577	142,820

It can be seen from Table 3 that the surface-base bond coefficient has a great influence on the horizontal stress at the bottom of the surface plies. Since the bending and tensile stresses in concrete pavement panels are precisely the control index for cement concrete pavement design, the surface-base bond condition needs to be considered when performing cement concrete pavement design. The horizontal tensile stress at the base of the subgrade plies does not always increase with the increase of the surface-base bond coefficient. The maximum value of tensile stress was found when the surface-base bonding coefficient was 4.0.

The tensile stresses in the x- and z-direction at the bottom of the surface layer are lowering with an increase in the surface-base bonding coefficient, therefore increasing this bonding coefficient will be advantageous. When the surface-base bonding coefficient is in the range of 0–2.0, the tensile stress value decreases faster, and decreases gradually in the range of 2.0–6.0. When the surface-base bonding coefficient is greater than 6.0, the horizontal tensile stress is basically stable and unchanged. With the increase of the surface-base bonding coefficient, the horizontal tensile stress at the bottom of the base layer tends to rise in general, and the change of the stress value is much smaller than that of the tensile stress at the bottom of the surface layer. When the surface-base bonding coefficient reaches 6.0, the horizontal stresses in the x-direction and z-direction are basically stable.

From this, it can be seen that the tensile stress at the bottom of the surface plies generally tends to decrease with the increase of the surface-base bonding coefficient, while the horizontal tensile stress at the bottom of the subgrade plies generally increases slightly. The influence of surface-base bonding coefficient on the tensile stress at the bottom of the face layer is larger, and the influence on the bottom of the base layer is smaller. When the surface-base bonding coefficient is greater than 6.0, the horizontal tensile stresses at the bottom of both the surface layer and the bottom of the base layer tend to be stable, and the difference in stress values is not large. Liu [8] and Zhang et al. [9] found that concrete slabs poured directly on the subgrade could achieve a combined surface-base friction coefficient of 6.0 and the interface bond between the surface and the substrate base was maximum. Liu et al. [10] found that the bending and tensile stress at the bottom of the layer were the smallest when the base was formed in one pour, and the bending and tensile stress at the bottom of the layer were the largest when the layer was formed in two pours with contamination and damage between the layers, resulting in loosening and separation. Therefore, in the poor cement concrete road project, the concrete slab can be poured directly after the construction of the poor cement concrete base layer is just completed, so that the surface-base bonding coefficient reaches 6.0 or more to ensure that both the surface layer bottom and the base layer bottom tensile stress is small.

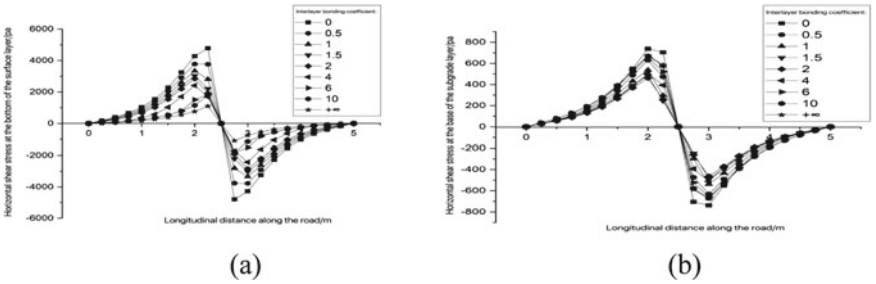

Fig. 3 Horizontal shear stress at the surface layer's bottom

3.2 Maximum Horizontal Shear Stress of the Bottom of the Surface Layer and the Bottom of the Base Layer

The large horizontal shear stress between layers of cement concrete pavement structure may lead to slip damage of the structure. The horizontal shear stresses at the bottom of the surface layer and the bottom of the base layer along the edge of the road longitudinal joints were obtained by finite element simulation with different surface-base bonding coefficients, as shown in Fig. 3.

Through Fig. 3, it can be seen that the changes of horizontal shear stress and horizontal tensile stress at the base layer's bottom and the surface layer's bottom are similar, and the horizontal shear stress at the surface layer's bottom is more influenced by the surface layer-subgrade bonding coefficient. The largest horizontal shear stress at the surface layer's bottom is much larger than that at the base layer's bottom, indicating that the worse the surface-base bonding condition is, the larger the horizontal shear stress is.

With the rise of the surface-ground bonding coefficient, the largest horizontal shear stress at the surface layer's bottom tends to decrease, decreasing sharply in the range of the bonding coefficient of 0–2.0, decreasing in the range of 2.0–6.0, and a stable state after reaching 6.0. The largest horizontal shear stress at the base of the subgrade layer does not vary much in general, and the largest horizontal shear stress is almost unchanged when the bonding factor is greater than 6.0.

4 Results and Discussions

By analyzing the horizontal tensile and shear stresses at the surface bottom and base layer bottom of the base layer road surface of poorly cemented concrete, we found that the maximum horizontal shear stress at the surface bottom tends to decrease with increasing surface layer adhesion coefficient, while the largest horizontal shear stress at the base layer bottom does not change significantly overall, which is and base layer z tensile stresses, which is basically consistent with the law of variation

of the surface layer bottom and base layer z tensile stresses. When coefficient of surface-base bonding increases, the horizontal tensile stress and shear stress at the surface layer's bottom decrease significantly, while the horizontal tensile stress at the bottom of the base layer increases slightly and the horizontal shear stress remains basically unchanged, indicating that the larger the surface-base bonding coefficient is, the stronger the interlayer bonding effect is, and the more beneficial to the transfer of stress. The stresses at a surface-based bond coefficient of 6.0 are nearly equal to the stresses in the fully continuous state, showing that the poor cement concrete ground and the slab of cement-concrete are in a roughly fully continuous state.

In this paper, only the variation law of mechanical response of pavement structures with different surface-base bond coefficients is investigated, but the stresses of pavements during normal use are not only related to the surface-base bond state and loads, but also to temperature [11]. Under the effect of positive temperature gradients, cement concrete panels will develop temperature warpage stresses, which will lead to structural fatigue damage [12]. More research can be done on the mechanical behavior of cement concrete pavement systems at various temperatures or when multiple elements are coupled together.

5 Conclusion

In this paper, finite element software is used to establish a three-dimensional pavement structure model, define different surface-base bonding coefficients and conduct stress and deformation analysis, and through analysis and the following study findings are attained through analysis and discussion.

(1) The horizontal tensile stress at the base of the subgrade layer has an overall increasing trend, while the horizontal shear stress has an overall decreasing trend. As the surface-base bonding coefficient increases, the horizontal tensile stress and shear stress at the bottom of the surface layer of poor cement concrete base pavements decrease more, and the stress at the bottom of the surface layer is more affected by the bonding coefficient.
(2) When the surface-base bonding coefficient increases to 6.0, the horizontal stress at the base layer's bottom and the surface layer's bottom reaches a stable state, and at the same time, the surface-base bonding state approaches a completely continuous state. During the construction of poor cement concrete base pavement, the concrete slab can be poured directly after the construction of poor cement concrete base is completed, so that the surface-base bonding coefficient reaches 6.0 and the best bonding state is achieved between the surface and base, thus extending the service life of the pavement.

References

1. Zhao W, Xu Z, Huang W (2003) Effect of interlayer action between the concrete surface and poor concrete subgrade on load stress and bending settlement. China J Highw Transp (04):10–16
2. Wu X, Zhang Q, Jin B, Li X (2008) Effect of isolation layer on structural mechanical properties of cement concrete pavement with poor concrete base. Highway (07):127–130
3. Chun S, Kim K, Greene J et al (2015) Evaluation of interlayer bonding condition on structural response characteristics of asphalt pavement using finite element analysis and full-scale field tests 96:307–318
4. Yu S (2009) Stress analysis and structural design of cement concrete pavement subgrade with interlayer functional layer. Chang'an University
5. Hu P, Cheng Y, Wang B (2021) Study on the rational structure of rigid pavement with poor cement concrete base. Highway 66(04):1–5
6. Zhang Y, Zhao D, Liu S, Shen J (2014) Effect of subgrade parameters on the mechanical properties of cement pavements when considering interlayer contact. J Chongqing Jiaotong Univ (Natl Sci Ed) 33(02):49–52+67
7. Zhou Z (2003) Nonlinear analysis of highway asphalt pavement structure. Chang'an University
8. Liu P (2013) Analysis of the influence of interlayer bonding state of cement concrete pavement on panel stress. Chang'an University
9. Zhang H, Zhou Z, Chen X, Yin H, Zhang Q (2005) Study on interface characteristics between cement concrete surface and lean concrete base. Trans Changsha Commun Coll 04:27–31
10. Liu Y, Chen J, Huang Z (2011) Analysis of mechanical properties of cement stabilized macadam base under different interlayer contact conditions. J Guilin Univ Technol 31(03):372–375
11. Wu G, Yao L, Yi Z (2003) The formation mechanism of early cracks in cement concrete pavement. J Southwest Jiaotong Univ (03):304–308
12. Liu X, Liu Y (2001) Reason analysis of rigid pavement damage. J Beihua Univ (Natl Sci Ed) 01:89–92

Research on the Preparation Process and Modification Method of Cotton Straw Fiber Based on Road Performance

Chunzhen Chang, Leqiang Shen, Renliang Guo, and Hao Han

Abstract For better application of modified cotton straw fibers in asphalt pavements, Preparation of cotton straw fibers using the "mechanical-shear" method, Modification of cotton straw fibers by preparation of NaOH solutions of different mass fractions, Comprehensive evaluation of the modification effect of cotton straw fibers by oil absorption and heat resistance, Optimal modification process for cotton straw fibers; he roadworthiness of the modified cotton straw fiber was then analysesd by means of pH, oil absorption, heat resistance, ash content and absorbency tests. The results show that the best modification process for cotton straw fibers is infiltration in NaOH with a mass fraction of 5% for 30min; Modified cotton straw fibers are weakly alkaline, and have increased adhesion to bitumen, 20.7% increase in oil absorption compared to unmodified cotton straw fiber, Improved heat resistance, Slight reduction in tensile strength, 4% increase in absorbency compared to unmodified cotton straw fiber, better compatibility with asphalt.

Keywords Cotton straw fiber · Preparation process · Modification methods · Roadworthiness

1 Introduction

In China, straw burning is a key contributor to haze during the crop harvest season [1]. In recent years, cotton straw fibers have gradually been used in asphalt pavements [2, 3], it has properties such as oil absorption, heat resistance and high toughness. In asphalt mixes can play a reinforcing and toughening, improve the high and low temperature stability of the pavement, reduce road reflection cracks, etc. [4]. However, the fiber preparation process is complex and the natural straw fiber itself is hydrophilic, which is not conducive to the compatibility of the fiber with asphalt

C. Chang · L. Shen (✉) · R. Guo · H. Han
Shandong High Speed Engineering Construction Group Co., The Sixth Engineering Company, Jinan, China
e-mail: 1477623937@qq.com

H.-Y. Jeon (ed.), *Proceedings of the International Conference on Geosynthetics and Environmental Engineering*, Lecture Notes in Civil Engineering 374,
https://doi.org/10.1007/978-981-99-4229-9_32

and affects the application of the fiber in asphalt pavements, so the straw fiber needs to be modified for processing.

Alkali treatment is now commonly used to reduce the hydrophilicity of the fibers [5, 6]. Italso improves the cleanliness and roughness of the fiber surface [7, 8]. Increasing the specific surface area [9, 10]. This improves the compatibility of the fibers with the asphalt. Ahad et al. [11] used acid and alkali to chemically modify coconut shell, banana stem and bagasse fibers respectively and found that alkali treatment was more suitable for natural fibers and the tensile strength of the fibers increased after alkali treatment. Rachchh et al. [12] Sodium hydroxide was used for the surface alkali treatment of bagasse fibers and it was found that the alkali treatment not only removed wax and oil from the fiber surface but also increased the surface roughness of the fibers. However, the tensile strength values of different types of natural fibers can vary even in the same medium, at the same immersion time and at the same immersion concentration, because each fiber has its own unique surface morphology, which determines the bonding of the fibers and thus affects their mechanical or physical properties.

In order to study the preparation process and modification method of cotton straw fiber and improve its performance in asphalt pavement, this paper first explores the preparation process of cotton straw fiber, and then conducts microstructure analysis to reveal the interaction mechanism between fiber and asphalt; Secondly, the sieved straw fibers were soaked in different concentrations of NaOH for different times to study the best modification method; Finally, the properties of cotton straw fiber, modified cotton straw fiber and lignin fiber are compared and the feasibility of the processing and modification methods are analysed.

2 Cotton Straw Fiber Production

Cotton straw is composed of main stem, branch stem, root stem and other parts, where the main stem includes the outer bark and xylem, the outer bark is mainly composed of bast fibers and the xylem is mainly composed of wood fibers [13], both fibers have the advantages of toughness and good mechanical properties.

2.1 Straw Fiber Preparation

Existing methods of fiber production include steam blasting [14], “Mechanical-shear” method, etc. This paper uses the “mechanical-shear” method for fiber production. Direct crushing of dry cotton straw results in a powdered fiber that does not have the basic fiber [15]. In this paper, the cotton straw was prepared by wet method by removing the roots, leaves and collars, soaked for 7 days and then cut into small sections of about 10 mm, crushed for 3 min using a multifunctional crusher with a speed of 30,000 r/min and dried to obtain cotton straw fiber.

2.2 Straw Fiber Sieving

In order to control the fiber length to meet the requirements of *Lignin fibers for asphalt pavements* (JT/T 533–2004), a laboratory standard square hole sieve with apertures of 0.15mm, 0.3mm, 0.6mm and 1.18mm was used for sieving, and 50 fibers were selected from each stage of the sieve after sieving. The results of the measurements are shown in Table 1.

According to Table 1, the length of cotton straw fibers on the 1.18 mm square hole sieve generally exceeded 6mm. Not within the length range specified in *Lignin fibers for Asphalt Pavements* (JT/T 533–2004). The length of the fibers on the 0.15mm square hole sieve is mainly in the range of 1.0–1.5 mm and the fibers are almost powder-like, so the fibers on the 1.18 mm and 0.15 mm sieves are discarded. The average length of the fibers on the 0.6 mm square hole sieve was 4.16 mm and the average length of the fibers on the 0.3 mm square hole sieve was 2.44 mm. The maximum length of the cotton straw fibers on the 0.3 mm and 0.6 mm square hole sieves was in the range of 4.5–5.0 mm, which shows that the fibers on the 0.3 mm and 0.6 mm square hole sieves were within the specification and remained fibrous, so it was determined that the straw fibers on the 0.3 mm and 0.6 mm sieves were identified as usable fibers with an average length of <4 mm and a maximum length of <6 mm.

3 Straw Fiber Microstructure

The morphology of the fibers plays a dominant role in the bonding effect of the fibers to the bitumen. Microscopic analysis of the fiber morphology was carried out with the aid of a scanning electron microscope and the cotton straw fiber morphology is shown in Fig. 1.

According to Fig. 1, under the 100 × field of view, the cotton straw fibers are in good shape and well dispersed, and the fibers can maintain a certain straight shape; Under the 500 × field of view, it can be clearly observed that the single fiber surface presents uniform and straight grooves along the longitudinal direction, and is bonded with bitumen and mineral powder, etc. Some of the grooves have been completely filled with bitumen, and it is found from the figure that the bitumen is very closely bonded to the fibers, and the bitumen film is gradually destroyed under the action of external force; Under the 1000 × field of view, it can be seen that the cotton straw fibers have a cavity structure, when the asphalt fills the cavity structure of the fibers to a certain extent, it can greatly enhance the mechanical locking effect of the fibers and the asphalt, thus showing that there is a tight adhesion between the asphalt and the fibers, but when preparing the straw fiber asphalt mastic, the asphalt has fluidity, so that the embedded locking effect of the straw fibers and the asphalt is not stable, affecting the straw fiber asphalt the mechanical properties of the mastic. For this reason, how to improve the straw fiber and asphalt interface properties, enhance

Table 1 Distribution of fiber length on sieves with different aperture sizes of square hole sieves

Aperture/mm	0.5–1.0	1.0–1.5	1.5–2.0	2.0–2.5	2.5–3.0	3.0–3.5	3.5–4.0	4.0–4.5	4.5–5.0	5.0–5.5	5.5–6.0	6.0–6.5	6.5–7.0	7.0–7.5	7.5–8.0	8.0–8.5	Average length
1.18	–	–	–	–	–	–	–	–	6	–	–	9	10	10	13	2	6.78
0.6	–	–	–	–	5	8	15	13	6	3	–	–	–	–	–	–	4.16
0.3	–	10	5	21	10	3	1	–	–	–	–	–	–	–	–	–	2.44
0.15	18	13	13	2	4	–	–	–	–	–	–	–	–	–	–	–	1.41

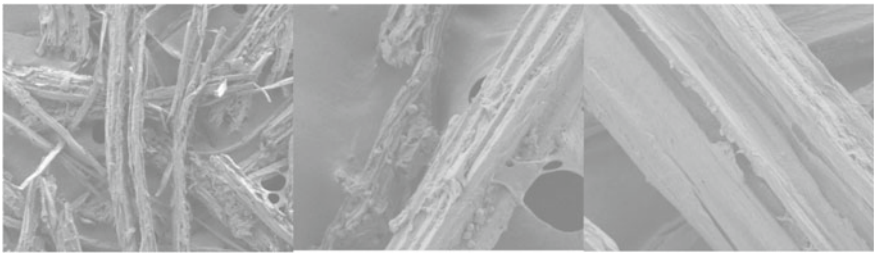

a) 100x field of view b) 500x field of view c) 1000x field of view

Fig. 1 Microscopic morphology of cotton straw fibers

the interlocking force between the two, become the most important to improve the mechanical properties of straw fiber asphalt mastic.

4 Straw Fiber Modification Process and Performance Study

In order to improve the performance of the straw fiber-asphalt interface, researchers usually achieve the effect of enhancing its adhesion by means of fiber surface modification, but the interface modification should be moderate; excessive modification can cause the opposite effect. Excessive modification of the fibers can lead to a reduction in the strength of the fibers themselves, affecting the mechanical properties of the fiber asphalt mastic and reducing the fiber reinforcement effect [16]. Therefore, it is crucial to choose the right type and concentration of modifier to modify the surface of the fibers in order to enhance the bonding effect between the fibers and the asphalt interface. In this paper, NaOH was chosen as the chemical modification reagent to modify cotton straw fibers under different NaOH concentrations and different infiltration times to arrive at the optimum modification process.

4.1 Straw Fiber Surface Modification Process

The cotton straw fibers were immersed in NaOH solutions with mass fractions of 1%, 3%, 5%, 7% and 9% for 15 min, 30 min, 45 min and 60 min respectively. two indicators of oil absorption and heat resistance were used in this paper as the basis for determining the performance of modified cotton straw fibers, and the best modification process for cotton straw fibers was selected from the above modification schemes. Oil absorption has a direct impact on the ability of the fibers to adsorb asphalt. The higher the oil absorption multiple of the fibers, the more asphalt will be adsorbed and transformed into structural asphalt, thus reducing summer oil flooding and improving the temperature stability of asphalt pavements. According to《the

Specification for Testing Asphalt and Asphalt Mixtures for Highway Engineering》 (JTG E20-2011), the mixing temperature of hot mix asphalt mixes is around 160°C. Polymer modified asphalt fiber mixes can even reach 175°C. Therefore, the fibers are required to have certain heat resistance.

Oil absorbency. The surface properties of cotton straw fibers are modified by NaOH and their oil absorption capacity is changed. This article refers to《fibers for Asphalt Pavements》(JT/T 533–2020), Oil absorption test on modified cotton straw fibers. By the Eq. 1 Calculating the oil absorption rate of fibers X_1, the results of the calculations are shown in Fig. 2.

$$X_1=(m_3-m_2-m_1)/m_1 \tag{1}$$

in the Eq. 1, m_1 is the quality of the modified straw fiber after drying; m_2 is the sample sieve mass; m_3 is the total mass of the sample sieve and the absorbed fiber.

According to Fig. 2, it can be seen that the trend of oil absorption of modified cotton straw fibers varies with infiltration time at different concentrations. At 1% and 3% NaOH concentration, the oil absorption rate of the fibers tended to increase with the increase of infiltration time, and the maximum oil absorption rate was 7.13 and 7.46 at 60 min infiltration, respectively; The oil absorption rate at a concentration of 5% tended to increase and then decrease with the increase of infiltration time, and the maximum oil absorption rate was 7.63 at 30 min of infiltration; The oil absorption rate decreases with the increase of infiltration time, and the maximum oil absorption rate of modified straw fiber is 7.49 and 7.30 when infiltrated for 10 min. According to the above comparison of the oil absorption rate of fiber under different modification process, it can be found that the oil absorption rate of modified straw fiber is maximum when the concentration of NaOH is 5% and infiltration time is 30 min.

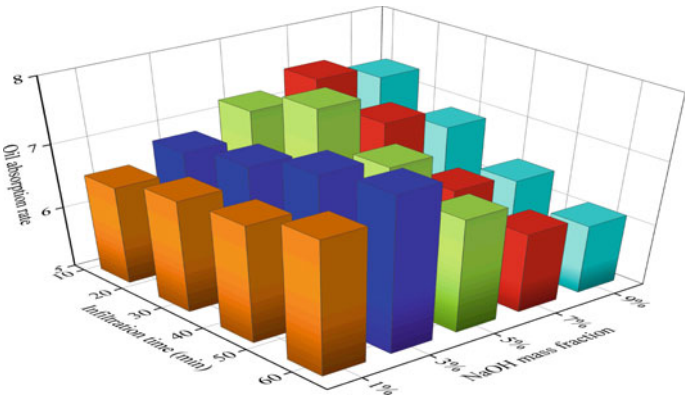

Fig. 2 Modified cotton straw fiber oil absorption

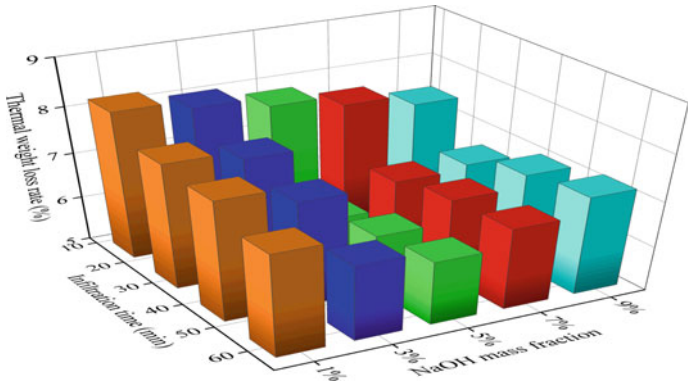

Fig. 3 Modified cotton straw fiber heat loss rate

Heat resistance. In the case of cotton straw fibers, their heat resistance determines whether they can be used as road fibers in asphalt mixes. The heat resistance of fibers is expressed in terms of heat loss rate. By the Eq. 2 Calculating thermal weight loss X_2, the results of the calculation are shown in Fig. 3.

$$X_2=(m_4 - m_5)/m_4 \times 100\% \tag{2}$$

In the Eq. 2, m_4 is the quality of the modified straw fiber after drying; m_5 is the mass of the fiber after being held for 2h in an infrared blast dryer.

According to Fig. 3, the heat loss rate of modified cotton straw fibers tends to decrease gradually with the increase of infiltration time when the concentration of NaOH is 1% and 3%; The concentration of 5% tends to decrease and then grow slowly with the increase of infiltration time; The concentration of 7% and 9% does not change much, and the heat loss rate tends to decrease and then grow with the increase of infiltration time. The smaller the heat loss rate, the better the heat resistance of the modified cotton straw fibers, so the modifier concentration of 5% and infiltration time of 30 min had the best effect.

The modification effect of cotton straw fibers was evaluated by oil absorption and heat resistance, and the best modification process for cotton straw fibers was: infiltration in a 5% mass fraction NaOH solution for 30 min.

4.2 Comparative Microscopic Morphological Analysis of Cotton Straw Fibers Before and After Modification

To analysess the changes in the surface morphology of cotton straw fibers after the above modification process, scanning electron microscopy was used to observe the changes at 100 × and 1000 × fields of view, as shown in Fig. 4.

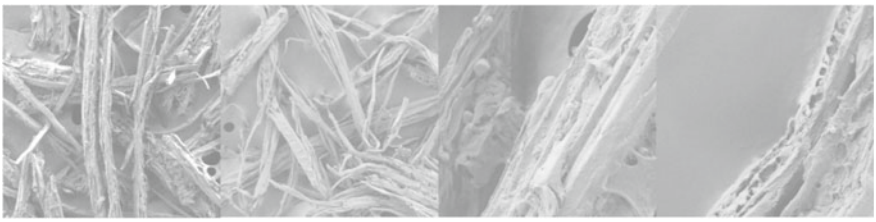

a) Unmodified at 100x field of view | b) Modified at 100x field of view | c) Unmodified at 1000x field of view | d) Modified at 1000x field of view

Fig. 4 Microscopic morphology of cotton straw fibers before and after modification

According to Fig. 4 can be seen in the 100 × field of view, the original straight cotton straw fiber modified slightly curved, a small number of single fiber curl obvious, this is because the mechanically broken cotton straw fiber slightly thicker, single fiber bundle is larger, NaOH solution modification can only make the straw fiber microfibril rotation angle reduced, can make the whole fiber curl angle smaller, so the modified cotton straw fiber curl is not obvious. After the modification of cotton straw fibers, impurity molecules such as pectin and hemicellulose in cotton straw were dissolved by NaOH solution, which could induce the fiber bundles to disperse into smaller units of fiber bundles and even form cotton straw monofilament fibers. Under a 1000 × field of view, it can be seen that the modified cotton straw fibers show pits of varying sizes, a small number of collapsed lumen structures, a larger exposed area inside the lumen, the fiber surface becomes rougher and the specific surface area increases, increasing oil absorption and embedding locking with the bitumen.

4.3 Comparative Analysis of the Performance of Modified Cotton Straw Fiber for Road Use

In order to evaluate the performance of modified cotton straw fibers for road use, PH value, oil absorption, heat resistance, ash content and absorbency tests were conducted and compared with lignin fibers and common cotton straw fibers to analyses the changes in straw fiber performance before and after modification and to investigate the feasibility of replacing lignin fibers with modified cotton straw fibers. Three sets of parallel tests were set up for each test, and the results and comparative analysis are as follows.

The PH value of cotton straw fiber is 6.47, which is weakly acidic, while the PH values of modified cotton straw fiber and lignin fiber are 7.86 and 8.2 respectively, both of which are weakly basic. Asphalt presents acidity, asphaltic acid and asphaltic anhydride in asphalt can form a sticky interface with the alkaline interface by establishing a chemical bond, weakly alkaline lignin fibers and asphalt show good

adhesion, modified cotton straw fibers and lignin fibers are close in nature, so the adhesion between modified cotton straw fibers and asphalt is better.

The oil absorbency of unmodified and modified cotton straw fibers was 6.32 and 7.63 respectively. The oil absorbency of modified cotton straw fibers was 20.7% higher than that of unmodified cotton straw fibers, which was mainly due to the increased specific surface area of straw fibers after modification by NaOH. While the lignin fiber oil absorption rate of 7.96, straw fiber modified, oil absorption is still slightly lower than the lignin fiber, this is due to the modified straw fiber surface roughness increased, but the fineness is still less than the lignin fiber, the specific surface area is relatively small.

The heat loss rate of cotton straw fiber and modified cotton straw fiber were 8.7% and 5.5% respectively, the heat loss rate of modified straw fiber was significantly reduced, indicating that the heat resistance of modified straw fiber was improved, mainly due to the attachment of NaOH solution to the fiber surface and the removal of pectin, fat and other components that lead to the lack of heat stability of straw fiber. The heat loss rate of lignin fiber is 5.4%, the heat loss rate of modified cotton straw fiber is similar to that of lignin fiber, which means that its heat resistance is as good as that of lignin, which ensures that the modified cotton straw fiber can meet the temperature requirements of the common asphalt mix mixing and paving process.

The ash content mainly characteristic the content of inorganic salts and trace elements in fibers after combustion, which can significantly affect the strength of fibers, with studies showing that the lower the ash content, the better the fiber breaking strength and elasticity. The ash content of unmodified and modified cotton straw fiber is 4.6% and 4.9% respectively, while the ash content of lignin fiber is as high as 17.6%. The ash content of unmodified and modified cotton straw fiber is much lower than the ash content of lignin fiber, indicating that the tensile properties of unmodified and modified cotton straw fiber are better. The ash content of modified straw fibers is higher than that of unmodified straw fibers, indicating that the mechanical properties of the fibers themselves have decreased after modification, but the decrease is not significant and the ash content is still much lower than that of lignin fibers, whose mechanical properties are better than those of lignin fibers.

The absorption rate of cotton straw fiber and modified cotton straw fiber were 1304 and 1362 respectively, the absorption rate of modified cotton straw fiber was 4% higher than that of unmodified cotton straw fiber, the main reason for this is that the impurities on the fiber surface were removed after the straw fiber was modified by NaOH solution, the surface of the straw fiber was rougher, the specific surface area increased and the contact area with the bitumen increased, making the absorption rate of modified straw fiber and bitumen increased and the modified straw fiber had better compatibility with the bitumen.

5 Conclusion

This paper explores the preparation process of cotton straw fibers, investigates the control method of fiber length, makes microstructural observations on the fibers, uses NaOH solution for fiber modification and conducts experimental analysis on the road-use properties of the modified fibers, and obtains the following conclusions:

(1) The cotton straw is pre-treated by root, leaf and collar removal, soaked, sheared and crushed, dried and sieved to obtain the required straw fiber; The fiber length is controlled by a laboratory standard square-hole sieve, with 0.3mm and 0.6mm square-hole sieves for usable fiber.
(2) The presence of a cavity structure in the cotton straw fibers was observed using scanning electron microscopy and the mechanical locking of the fibers to the bitumen was enhanced when the bitumen filled the cavity structure to a certain extent; NaOH solution modification increases the roughness of the fiber surface and increases the specific surface area, which enhances the locking effect of the straw fibers with the bitumen.
(3) The optimum modification process for straw fibers is infiltration in a 5% mass fraction NaOH solution for 30min. The modified cotton straw fibers are weakly alkaline and have increased adhesion to asphalt, significantly improved oil absorption and heat resistance, slightly reduced tensile strength and significantly improved compatibility with asphalt. The overall improved properties of the modified cotton straw fibers, which are similar to those of lignin fibers, indicate that the process and modification method is effective.

References

1. Zhou Y, Zhang Y, Xing X et al (2022) Impacts of emissions from crop residue open burning in Hebei on the air quality of the Beijing-Tianjin-Hebei region. J Beijing Univ Technol 48(10):1056–1068
2. Lei T, Li Z, Liu K et al (2016) Road performance of cotton straw fiber asphalt mixture. Highway 61(07):59–63
3. Wang P (2018) Experimental study on high and low temperature properties of cotton straw fiber asphalt mortar. J China Foreign Highway 38(5):231–234
4. Chen Z, Yi J, Chen Z, Feng D (2019) Properties of asphalt binder modified by corn stalk fiber. Constr Build Mater 212(JUL.10):225–235
5. Narendar R, Dasan KP (2014) Chemical treatments of coir pith: morphology, chemical composition, thermal and water retention behavior. Compos B Eng 56(2):770–779
6. Ashori A, Ornelas M, Sheshmani S, Cordeiro N (2012) Influence of mild alkaline treatment on the cellulosic surfaces active sites. Carbohydrate Polymers 88(4):1293–1298
7. Hashim MY, Amin AM, Marwah OMF et al (2017) The effect of alkali treatment under various conditions on physical properties of kenaf fiber. J Phys Conf Ser 914:012030
8. Anggono J, Habibi NR, Sugondo S (2014) Alkali treatment on sugarcane bagasse to improve properties of green composites of sugarcane bagasse fibers-polypropylene. mechanical engineering department—faculty of industrial technology Petra Christian University Jalan

Siwalankerto 121–131 Surabaya 60236 Indonesia; Mechanical Engineering Department—Faculty of Industrial Technology Petra Christian University Jalan Siwal
9. Chen JH, Xu JK, Huang PL et al (2016) Effect of alkaline pretreatment on the preparation of regenerated lignocellulose fibers from bamboo stem. Cellulose 23(4):1–13
10. Boynard CA, Monteiro SN, D'Almeida JRM (2010) Aspects of alkali treatment of sponge gourd (Luffa cylindrica) fibers on the flexural properties of polyester matrix composites. J Appl Polym Sci 87(12):1927–1932
11. Ahad NA, Mohamad Rosdi MHH, Yaacob N, Che Fauzi NHN, Zakaria S (2020) The effect of chemical treatments on tensile strength and absorption ability of epoxy/natural fibers composites. IOP conference series earth and environmental science 476(1)
12. Rachchh NV, Trivedi DN (2018) Mechanical characterization and vibration analysis of hybrid E-glass/bagasse fiber polyester composites. Mater Today Pro 5(2):7692–7700
13. Xin G (2013) Experimental study of mechanical properties of corn stalks. Huazhong Agricultural University
14. Han G, Deng J, Zhang S et al (2010) Effect of steam explosion treatment on characteristics of wheat straw. Ind Crops Prod 31(1):28–33
15. Li Z, Chen Y, Zhou J et al (2019) Analysis of road performance and fiber mechanism for corn stalk fiber asphalt mixture. China J Highway Transp 32(02):47–58
16. Mohd Edeerozey AM, Akil HMd, Azhar AB, Zainal Ariffin MI (2006) Chemical modification of kenaf fibers. Mater Lett 61(10)

Study of the Mechanical Properties of Coral Reef Sand Mixes Using Large-Scale Triaxial Shear Tests

Lü Chenwei, Zhang Dingwen, Haoliang Wu, Shi Minglei, and Chai Li

Abstract In order to reveal the macro-mechanical characteristics of coral reef sand mixes, triaxial tests were conducted on graded coral reef sand mix specimens using a large dynamic triaxial instrument. Under different circumferential pressures, the specimens' stress–strain relationship curves showed a typical hyperbolic curve. Upon reaching peak stress, the specimens continued to develop axial strain with little change in principal stress difference. After damage, the radial strain-axial strain curve becomes straight. Under different peritectic pressures, all specimens experienced shear contraction followed by shear expansion. The strength of the coral reef sand is mainly derived from the combined effect of reef sand strength, inter-particle friction and occlusion, without the effect of cohesion. The initial particle filling determines the deformation and strength characteristics of the material in the test, while shear expansion (shear contraction), particle fragmentation and rearrangement, and volume changes influenced by the surrounding pressure are all manifestations of the changing interparticle filling relationship.

Keywords Coral reef sand · Large triaxial shear test · Mechanical characteristics · Deformation characteristics · Shear strength

L. Chenwei · Z. Dingwen (✉) · S. Minglei
School of Transportation, Southeast University, Nanjing 211189, China
e-mail: zhang@seu.edu.cn

H. Wu
Sun Yat-Sen University & Southern Marine Science and Engineering Guangdong Laboratory (Zhuhai), Zhuhai 519082, China

C. Li
Inner Mongolia Research Institute of Transportation Science Development, Hohhot 010050, China

H.-Y. Jeon (ed.), *Proceedings of the International Conference on Geosynthetics and Environmental Engineering*, Lecture Notes in Civil Engineering 374,
https://doi.org/10.1007/978-981-99-4229-9_33

1 Introduction

Increasing development of high earth and rock dams in marine reef areas, highways and railways, and rock throwing projects to protect harbor shores has led to a need for engineering research on coral reef sand mixes [1–3], which can replace some construction aggregates, under high pressure, complex stress states and cyclic loading has become a priority. Coral reef sands are clastic materials deposited in situ or deposited by near-source transport from the remains of reef-forming coral communities that have been compacted and lithified over time [4]. Due to the complex marine environment and the special internal structure characteristics of coral bodies, coral reef sand particles present characteristics of low strength, easy fracture, loose and containing a large number of internal pores, and the coral reef sand mix is significantly different from that of rubble and other rock piles in terms of stress–strain relationships, deformation characteristics and shear strength [5]. Since the 1960s, engineering problems caused by coral reef strata in the exploration of marine resources development. For example, during the construction of the Lavan oil platform in Iran, a 1 m diameter immersed pile sank nearly 15 m under its own weight after passing through a coral reef formation about 8 m thick; the 1.83 m diameter pile of the North Rankin "A" oil platform on the northwest shelf of Australia did not reach the designed bearing capacity and penetration in the coral reef formation. The pile body of the North Rankin "A" oil platform with a diameter of 1.83 m in the coral reef strata in Australia did not reach the designed bearing capacity and penetration degree, and the remedial measures had no effect. At present, previous researchers have completely investigated the conventional triaxial test research of coral sand, in-depth research on the engineering properties of coral sand under the action of high pressure, complex stress state and cyclic loading [1, 5, 6], the research results show that: the engineering properties of coral sand have complex relationships with grain size gradation, particle shape, pore ratio, effective stress state, effective stress path and particle fragmentation. With increasing peritectic pressure, coral sand's strength index decreases, particle fragmentation gradually decreases after a certain level of particle fragmentation, and mechanical properties tend to remain stable as a result. However, in view of the complex characteristics of coral reef sand mixes, it is necessary to carry out an in-depth study to reveal the strength-deformation properties and the intrinsic mechanism of the mixes in the real state, so as to provide a strong basis for solving the problems encountered in practical engineering. Therefore, the shear strength parameters of coral reef sand mixes were determined through large triaxial shear tests. Further, the stress–strain relationship and deformation characteristics of the specimens were investigated to analyse the factors affecting the shear strength and deformation characteristics. This investigation will provide a necessary scientific basis for the geotechnical construction of island reef development.

2 Materials and Methods

2.1 Materials

The test material is taken from the loose coral debris strung from a sea area in the South China Sea, which can be mainly divided into coral sand and coral reef rock after being rinsed with pure water, dried and first sieved. The coral sand was mostly deposited on the surface of the coral reef rock, forming a special coral reef rock soil structure with coral sand on top and coral reef rock on the bottom. The diffraction peak areas of different minerals were used to semi-quantitatively calculate the proportion of each phase in the coral reef sand, and the analysis of diffraction patterns shows that the mineral composition of coral reef sand is mainly biotite (mass fraction 33–47%) and high-Mg calcite (mass fraction 53–67%), and quartz minerals are interspersed, the content of other components (mass fraction) is relatively small, and the equivalent carbonate mass fraction reaches 96% above [7, 8], as shown in Table 1.

Coral reef sand is formed in sedimentation without long distance transport and retains some of its native biomorphology, with irregularly shaped, sharp-edged particles, which bite into each other and have relatively large pores. The pore ratio of the coral sand is much greater than that of the quartz sand, both in its loosest and densest state. Scanning electron microscopy of coral reef sand particles and surface structure characteristics as shown in Fig. 1, coral reef sand is rich in internal pores, pores are rounded, the face pore structure of the particles are mostly determined by the structure of the organisms themselves. Studies have shown that the internal pores of coral sands account for about 10% of all pores, and more than 98% of the internal pores are equiaxed or unequiaxed pores, with equiaxed pores standing for more than half of the total number of pores. The presence of a large number of internal pores is the fundamental reason why coral sands exhibit macroscopically distinctive properties from terrestrial sands (e.g. quartz sands) [9].

Table 1 Oxide chemistry of coral reef sand

Oxide chemistry	Mass fraction (%)
Calcium oxide (CaO)	47.10
Magnesium oxide (MgO)	2.48
Strontium oxide (SrO)	0.63
Sulfur trioxide (SO_3)	0.47
Silicon oxide (SiO_2)	0.13
Aluminium oxide (Al_2O_3)	0.06
Phosphorus pentoxide (P_2O_5)	0.06
Potassium oxide (K_2O)	0.0082
Cl	0.026
Burning loss	48.7

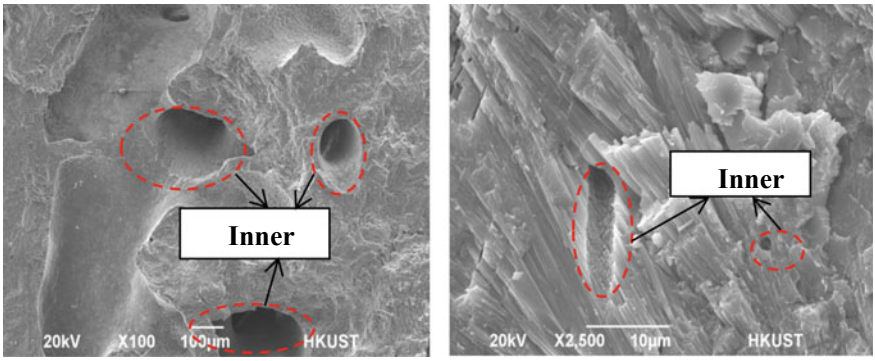

Fig. 1 Particle and surface structure characteristics of coral reef sand particles under high magnification

Table 2 Coral reef sand quality testing index

Test items	Coral reef/values	Coral sand/values
Bulk density, (kg/m^{-3})	980	1194
Void ratio, (%)	46	51
Porosity rate, (%)	23.4	8.6
Density, (kg/m^{-3})	2800	2794
Water absorption, (%)	7.73	3.64
Solidity, (%)	13.3	6.45
Barrel compression strength, (MPa)	2.13	–

The physical and mechanical properties of the coral reef sand were determined according to "Light Aggregates and Their Test Methods" as shown in Table 2. The average saturated uniaxial compressive strength of coral reef rock is 6.35 MPa (COV $\leq$ 3%), which is much smaller than the saturated uniaxial compressive strength of Yanshan III granite with different degrees of weathering (73.01 MPa for weakly weathered granite; 22.68 MPa for strongly weathered granite), as determined by the Rock Testing Procedure for Highway Engineering [7].

2.2 Testing Methods

The test was conducted using a large triaxial shear apparatus specimen diameter of 300 mm, and the stranded loose coral debris in the greater than 60 mm particle content is less, subject to the maximum size of the indoor test material is limited, the need to exceed the test allowable maximum particle size of the grain material for the necessary scale reduction process, through the scale of the test material after the test

to determine the mechanical properties of the actual graded material. At present, there are three common methods of coarse grain size reduction: the equivalent substitution method, the similar gradation method and the hybrid method. The test is carried out on a mixture that exceeds the permitted particle size of the test apparatus by the equivalent substitution method. Equivalent substitution method that is according to the instrument allows all the coarse material (from the particle size of 5 mm to the maximum particle size between the coarse material) in proportion to the quality of the replacement of oversized particles content. The calculation formula is:

$$p_{\mathrm{i}} = \frac{100 - p_m}{p_m - p_5}(p_{oi} - p_5) + p_{oi} \tag{1}$$

where: p_{i} indicates the percentage passage of a particle size after substitution, %; p_5 indicates the percentage passage of a particle size of 5 mm in the original grading, %; p_{m} indicates the percentage passage of a particle size of 60 mm in the original grading, %; p_{oi} indicates the percentage passage of a particle size in the original grading, %.

The test was carried out using a 1500 KN electro-hydraulic servo dynamic and static triaxial testing machine (large size dynamic and static triaxial), the size of the test piece was $\varphi 300 \times 620$ mm, the maximum vertical pressure under static load conditions was 1500 KN, the enclosing pressure was 5 MPa; the maximum vertical pressure under dynamic load conditions was 350 KN, the enclosing pressure was 2 MPa, the form of vibration load was sine wave, triangle wave, square wave and random wave, the vibration, the frequency is 0.01–10 Hz. The test processes were all carried out in strict accordance with the Geotechnical Test Methods Standard (GB/T50123-2019) and the Coarse-grained Soil Test Procedure (T/CHES-2019). The specimens were 30 cm in diameter and 60 cm in height, and the specimens were filled in 6 layers. The natural moisture content of the granular material at all levels is determined during the test and the amount of water addition required to fill each layer of the test material is calculated. When mixing, water should be added to the granular material with a particle size greater than 0.5 mm and mixed fully, mixed with fine particles until well blended, covered tightly with plastic film to be used. The pressure chamber sample base plus cover plate, tied rubber film, installed molding cylinder, layer by layer into the test material, each layer first with a fine steel braze pounding, and then vibrating compaction method to make the test material dense. Loosen the surface and install the second and final layer. Install the pressure chamber, fill the pressure chamber with water, tighten the water hole nut, place the pressure chamber on the shear tester base and leave it for 24 h to allow the test piece to be fully infiltrated with water. After the start of shear, the test piece every 1.0 mm of vertical deformation measured axial pressure, axial deformation, radial deformation and volume change. When the axial force meter percentage reading no longer rise or have a significant reduction, indicating that there has been a peak, need to continue to measure the reading 1–2 times. If there is no peak, the stress difference between the two adjacent levels is less than 5 kPa.

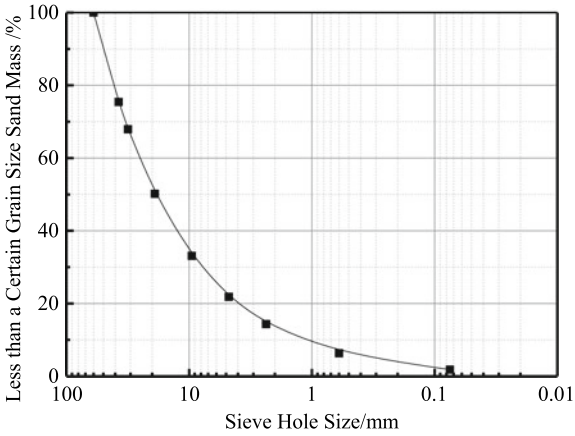

Fig. 2 Initial grading curve grading of large triaxial shear test specimens

The coral reef sand gradation curve after equal sample substitution is shown in Fig. 2. The coral reef sand blowing material inhomogeneity coefficient Cu is 37.9, which is typical for poorly graded sand.

3 Results and Discussion

3.1 Stress–Strain Relationships

The tests were carried out on sized triaxial shear tests on reduced reef sands under unsaturated, unconsolidated and undrained conditions. Figure 3 shows a schematic diagram of the stress and strain states of the coral reef sand specimens, and Fig. 4 shows the stress–strain relationship graphs for the same graded specimens at three different envelope pressures. From the figure, it can be seen that the difference in peak principal stresses ($\sigma_1 - \sigma_3$) of the three sets of specimens increases with the increase of the enclosing pressure, while the peak principal stress ratio (σ_1/σ_3) decreases with the increase of the enclosing pressure. The stress–strain relationship curves for the specimens at each envelope pressure have no obvious peaks and show a typical hyperbolic curve. The stress–strain relationship can be represented by the hyperbolic model of Duncan-Zhang (Kondner. Zalasko 1963) [10]. The stress–strain relationship curve at different envelope pressures is similar to the test curve at high envelope pressures in the triaxial test, where shear exhibits shear-compression properties, which are associated with high envelope pressures inhibiting shear expansion of the specimen and causing particle fragmentation [6, 9]. The degree of linearity and tangential slope of the initial section of the stress–strain curve increased with increasing envelope pressure, showing a more pronounced quasi-elastic nature. After reaching the peak, the specimens continued to develop axial strain with little change in the principal stress difference, which is plastic damage. The test results show that:

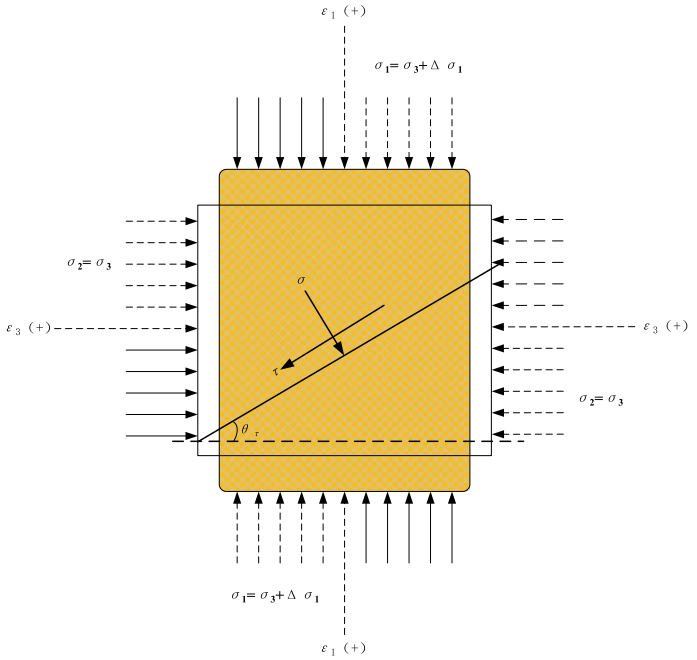

Fig. 3 Schematic diagram of the stress and strain state of the specimen

the coral reef sand specimens had an axial strain of 6–12% during damage, which did not reach an axial strain of more than 15% during damage of fine-grained soils [11]. The strain softening in the coral reef sand is not significant and can still be subjected to higher stresses after the peak occurs. With the increase of the principal stress σ_1, the coral reef sand specimens began to break, and the larger grains bearing the role of skeleton were broken first, the specimen gradation changed, the content of smaller grains increased, the specimen structure gradually changed from skeleton type to dense type, and the shear strength of the specimen showed a decreasing trend. On the other hand, with the increase of the surrounding pressure σ_3, the shear damage limit value of the specimen increased in different magnitudes. It can be seen that, the same proportion of increase in circumferential pressure, the proportion of increase in damage shear damage limit value gradually decreased.

3.2 Deformation Characteristics

Figure 5 shows the radial strain-axial strain ($\varepsilon_3 - \varepsilon_1$) curve and the volumetric strain-axial strain ($\varepsilon_v - \varepsilon_1$) curve of the coral reef sand specimen. As can be seen from the figure, the radial strain-axial strain ($\varepsilon_3 - \varepsilon_1$) curves of the coral reef sand specimens are highly linear at the initial stage, but become linear after entering the damage stage,

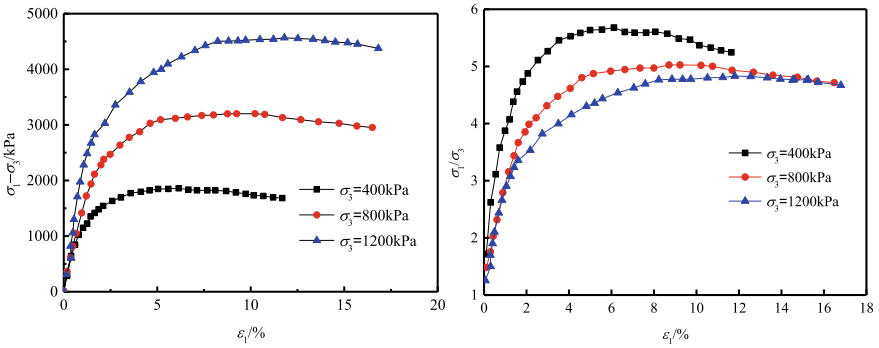

Fig. 4 Stress–strain relationship curves for specimens at different envelope pressures

and the slope of the straight line tends to be around 0.4 at different envelope pressures. The coral reef sand specimens exhibit shear shrinkage followed by shear expansion under different envelope pressures. The specimens are loose in their initial state and, under partial stress, the particles move with each other, fill each other's pores, and fit together closely, resulting in a certain volume compression. As the specimens are under the action of continuously increasing partial stress, the specimens experience the peak of shear shrinkage and then begin to shear expansion, and the volume of the specimens grows slightly but the shear expansion rate is very small, which is related to the mutual extrusion and crushing of the particles and the rearrangement of the granular particles [9, 10]. With the increase of the surrounding pressure, the shear swelling of the specimen shows a decreasing trend, and the shear swelling of the specimen gradually tends to stabilize after destruction. This shows that the deformation of coral reef sand is jointly determined by particle deformation, particle crushing, relative interparticle dislocation and rearrangement, and the deformation includes elastic deformation such as interparticle contact and plastic deformation resulting from relative interparticle dislocation and crushing [11].

3.3 Shear Strength

The strength of the coral reef sand is mainly derived from the combined effect of reef sand strength, inter-particle friction and occlusion effect, and there is no effect of cohesion c as show in Fig. 6. Neither the shear strength nor the normal stress of reef sand is constant, nor is the Mohr circular envelope a straight line, but varies with surrounding pressure. When the envelope pressure is small, the value of φ is relatively large, and as the envelope pressure increases, the value of φ gradually decreases, and the strength envelope is non-linear within a certain range. This law is more obvious at low envelope pressures, and tends to be more linear at high envelope pressures. The shearing and swelling effect at low envelope pressures leads to an increase in

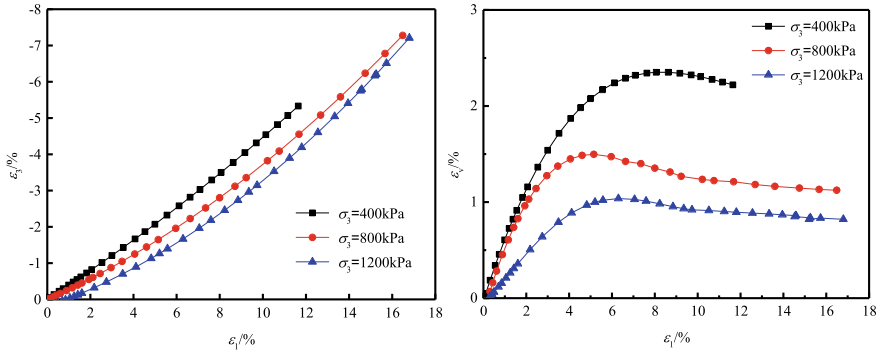

Fig. 5 Radial strain-axial strain curves and volumetric strain-axial strain curves for specimens under different circumferential pressures

strength, while at medium and high envelope pressures the shearing and swelling effect decreases and the particles break down and rearrange themselves to reduce strength. When the enclosing pressure increases to the so-called crushing stress, the particles break so that the pores of the specimen are fully filled and dense and the shear strength line curvature disappears. As the curvature of the strength envelope is not taken into account when using a best-fitting straight line instead of the strength envelope, cohesion is present, which is not present in the test. The internal friction angle of the coral reef sand specimen under the large triaxial shear test was 39.9°, which is closer to the parameters of the actual engineering of coral reef sand, such as the internal friction angle φ value of 40.17° for the calcareous sand by Mo Hongyun [9] and 42° for the calcareous sand by Zhang Jiaming [12], and the underwater rest angle φ value of 39°. While coral reef sand remains highly compressible under high stress, attention should be paid to the design and construction of high-weight foundation elements in natural sedimentary reef sand deposits.

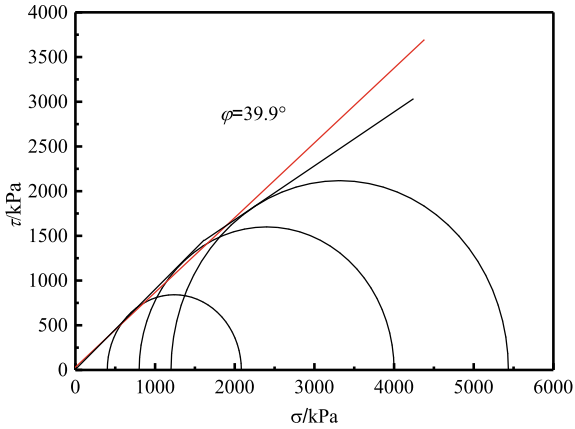

Fig. 6 Strength envelope of coral reef sand specimens for large triaxial shear test

4 Summary

The following conclusions can be drawn:

(1) The stress–strain relationship curves of the specimens at different envelope pressures have no obvious peaks and show a typical hyperbolic curve. In response to increasing pressure, the linearity of the initial section of the stress–strain curve and the slope of the tangent line increase significantly, indicating a quasi-elastic nature. While the main stress difference does not change much after reaching the peak, the axial strain continues to develop.

(2) The radial strain-axial strain curves of the coral reef sand specimens were linear at the initial stage, but became straight after entering the damage stage. The shear contraction followed by shear expansion was observed for the specimens under different circumferential pressures. As the coral reef sand is filled with particles of different sizes, the initial filling of the particles determines the deformation strength characteristics in the test. The shear expansion (shear shrinkage), particle fragmentation and rearrangement, volume changes and other test data influenced by the surrounding pressure.

(3) The strength of coral reef sand is mainly derived from the combined effect of reef sand strength, inter-particle friction and occlusion effect, and there is no role of cohesion c. The proportional relationship between shear strength and normal stress is not a constant, and the internal friction angle of the coral reef sand specimen under the large triaxial shear test is 39.9°.

References

1. Wang G, Ye QG, Zha JJ (2018) Experimental study on mechanical behavior and particle crushing of coral sand-gravel fill. Chin J Geotech Eng 40(5):802–810
2. Yodsudjai W, Otsuki N, Nishida T et al (2003) Study on strength and durability of concrete using low quality coarse aggregate from Circum-Pacific region. In: Fourth regional symposium on infrastructure development in civil engineering (RSID4). Bangkok, Thailand, pp 1–10
3. Lade PV, Liggio CD Jr, Nam J (2009) Strain rate, creep, and stress drop-creep experiments on crushed coral sand. J Geotech Geoenviron Eng 135(7):941–953
4. Lü CW (2016) The study on pavement performance of cement-emulsified asphalt and reef sand solidification. MS thesis, Southeast University, Nanjing
5. Wang YQ, Hong Y, Guo Z et al (2018) Micro-and macro-mechanical behavior of crushable calcareous sand in South China Sea. Rock Soil Mech 39(1):199–215
6. Qian CJ, Li ZP, Tan FL et al (2018) Experimental study on the strength characteristics of coral sand fillers. Highw Transp Technol (Appl Technol) 14(1):133–136
7. Lü CW, Wu HL, Shi ML (2019) Laboratory tests of cement stabilized and solidified coral reef and sand for use of highway pavement. J Eng Geol 27(6):1440–1447
8. Lü CW, Zhang DW, Wu HL, Shi ML (2022) Gradation design method of coral reef and sand filling materials based on maximum density curve theory. J Southeast Univ (Natl Sci Ed) 52(6):1095–1103
9. Mo HY (2015) Research on the mechanics characteristics of calcareous sand-limestone mixture. MS thesis, Southeast University, Nanjing

10. Zhang ZY, Zhang XA, Xuan FH (2013) Weathering characteristics of Yanshan-age granite in Zhuhai and its influence on its uniaxial compressive strength. J Postgrad Stud Sun Yat-sen Univ (Natl Sci, Med Ed) 34(4):42–51
11. Li GX et al (2016) Advanced geotechnics, 2nd edn. China Tsinghua University Press, Beijing, pp 21–24
12. Zhang JM (2004) Study on the fundamental mechanical characteristics of calcareous sand and the influence of particle breakage. PhD thesis, Institute of Rock & Soil Mechanics, Chinese Academy of Sciences; Li L (2012) Research on basic characteristics of coral concrete. PhD thesis, Guangxi University, Nanning

Mechatronic Spring Drives for Rod Borehole Pumps

Wen Zhao, Sen Li, and Milana Zhavner

Abstract The work is committed to the development of novel types of drives for rod borehole pumps, specifically mechatronic spring drives with energy recovery. These drives have the potential to reduce the size, weight, and energy costs by several orders of magnitude. The central concept is to design an oscillatory system as a spring drive with energy recovery, wherein the potential energy of the springs is transformed into the kinetic energy of the rod, and subsequently, the kinetic energy of the rod is converted back into the potential energy of the springs. Various linear motor designs are utilized to counterbalance dissipative losses. The paper examines the utilization of load balanced drive variants and the simultaneous operation of two drive variants operating in reverse phase to ensure the mutual balance of rod mass. It is demonstrated that in the case of weight balancing, the mass of power springs is twice as large as compared to drives that operate synchronously, while performing the same operation with the same number of cycles per minute and the same masses of the rods. The power consumption necessary to compensate for dissipative losses is also evaluated. It has been established that in this case, the amount of energy consumed during the load balancing will be twice as much. In addition, the study shows that autonomous power supply is achievable through the utilization of solar panels and wind generators.

Keywords Energy saving · Mechatronic drive · Spring drive · Energy recovery · Cyclic operation · Rod borehole pumps · Inertial forces · Balancing devices · Performance · Speed

W. Zhao (✉)
Northeast Forestry University, Harbin, China
e-mail: wenfly2015@yandex.ru

S. Li · M. Zhavner
Peter the Great St. Petersburg Polytechnic University, Sankt-Petersburg, Russia

H.-Y. Jeon (ed.), *Proceedings of the International Conference on Geosynthetics and Environmental Engineering*, Lecture Notes in Civil Engineering 374,
https://doi.org/10.1007/978-981-99-4229-9_34

1 Introduction

In contemporary society, reducing energy costs in industry is widely recognized as a critical undertaking. One of the key factors that impact energy costs is the weight of equipment, which is determined by several factors including the mass of its moving parts, overall dimensions, drive system, and installed power. A comparative analysis of different types of technological equipment with the same functional purpose has revealed that these characteristics, linked to a unit of production, are vital criteria for assessing energy efficiency [1–9].

Energy costs related to the overcoming of gravity and inertia represent a substantial portion of the energy expenditure in numerous technological processes. Particularly, in work operations involving reciprocating and reciprocating rotational movements of the working masses, the energy costs are mainly determined by these operations. As reported in [9], a productivity increase of twice the original amount can result in a four-fold increase in energy costs and an eight-fold increase in the required power.

The utilization of mechatronic spring drives, featuring energy recovery, in work processes pertaining to the linear movement of products on a horizontal plane, can potentially reduce energy costs up to ninefold when compared to electric, hydraulic, and pneumatic drives [9]. It is noteworthy to mention the invention documented in the German patent, "Electromechanical device for obtaining oscillatory motion", by L. Szilard and A. Einstein, introduced the first-ever spring accumulator powered by a helical spring, which was utilized to drive a refrigeration compressor [10].

The paper aims to examine the feasibility of utilizing mechatronic spring drives, with an emphasis on energy recovery, for vertical product movement, as exemplified by the drive mechanism for rod borehole pumps. The work operations in question require the overcoming of both inertia and gravity forces.

The authors acknowledge that the API standard [11] does not currently propose mechatronic spring drives for sucker rod borehole pumps. However, it is worth noting that two patents have been issued for such drives in Russia [12, 13]. The authors are optimistic that, in due course, they will also be incorporated into the American standard. It is worth noting that modern rod borehole pump drives often utilize some form of rod weight balancing.

When designing drives for rod borehole pumps with the goal of reducing energy consumption, developers have three primary approaches at their disposal.

1. Reduce inertial loads (without changing performance) by reducing the mass of moving elements.
2. Reduce the mass of moving elements that operate vertically, thereby reducing gravitational loads.
3. Utilizing mechatronic spring drives with energy recovery offers the lowest energy costs compared to all other types of drives and demonstrates the best performance in terms of power density [9].

Simultaneously, mechatronic spring drives exhibit several advantageous characteristics:

1. Enhanced reliability;
2. Prolonged service life;
3. Reduced noise levels;
4. Explosion prevention and fire safety;
5. Insensitivity to temperature changes;
6. Favorable dynamic regimes.

Theoretical studies on mechatronic spring drives with energy recovery for industrial robots have been summarized in the papers [5, 6]. It is worth noting that industrial robots are significant energy consumers. This is primarily due to the transfer of products along complex trajectories that require precise movement and large manipulation systems. To reduce the workload of industrial robot drive systems, spring balancing devices have been widely implemented [6].

A variety of have been employed in the development of the aforementioned drives. In this paper, the authors utilize the term "mechatronic spring drive with energy recovery", which provides a clear definition of the drive's fundamental characteristics.

1. The primary engine, a spring accumulator, functions by utilizing stored energy to accelerate working masses and subsequently decelerate them, thereby accumulating potential energy;
2. Accounting for dissipation loss, the engine's power is determined by the value of dissipation loss, which remains notably lower than the power of a spring accumulator;
3. Equipped with a control system, the engine enables compensation for dissipative losses through activation and deactivation, while also facilitating the regulation of clamps to ensure technological pauses.

The paper [14] presents a comparative analysis of electromechanical, pneumatic, hydraulic, and spring drives with energy recovery that are designed for work operations involving the reciprocating movement of working masses.

Linear spring drives with energy regeneration exhibit a smaller linear envelope in the direction of travel when compared to actuators, pneumatic and hydraulic cylinders. Moreover, their performance is comparable to that of linear motion modules with electrically-driven sliding tables.

The objective of this thesis is to establish a technical ideology for the development of mechatronic spring drives that enable the movement of working bodies in a vertical plane, with a maximum displacement of 2 m and a maximum moving mass of 8000 kg. The number of rod downhole pumps worldwide that operate under such specifications exceeds 10,000.

The operational modes of a rod borehole pump should be taken into consideration. It is worth noting that the working movements typically occur in a vertical plane, within a range of 2 m and with a maximum load mass of 8000 kg. The frequency of cycles is approximately 15 per minute. The movement in a rod borehole pump takes place in a vertical plane, and the primary loads experienced are those of gravity and inertia.

A classic version of a rod borehole pump drive involves an output link that executes a reciprocating motion. On one end of this link, a block segment with a flexible element is fixed, which is then connected to the pump rod. On the other end, the output link is connected to the counterweight. In recent years, alternative types of rod borehole pump drives have emerged, which can be categorized into the following types:

1. Drives with pneumatic balancing systems;
2. Drives employing hydraulic cylinders without a balancing system;
3. Drives with electric drive and load balancing;
4. Drives with linear electric motors with weight balancing [15].

The mechatronic spring drive, incorporating an energy recovery system, comprises a spring accumulator, a motor responsible for compensating dissipative losses, a balancing mechanism, and a control system equipped with measuring and informational components.

Standard engines that generate reciprocating motion can be utilized to compensate for dissipative losses. However, this paper proposes a linear motor with a reciprocating rotor for this purpose, as outlined in Ref. [15].

The energy expenses in mechatronic spring drives primarily result from internal friction of the springs, which are roughly five times lower compared to those incurred by standard classical drives. Hence, for preliminary computations, the effort expended on combating dissipative losses can be assumed to be 20% of the spring accumulator's maximum potential energy.

When developing mechatronic spring drives, standard tension or compression helical coil springs are employed.

This study examines the properties of spring drivers with a central position relative to the wellhead.

Figure 1 shows a schematic diagram of a spring actuator with a center rod.

The spring drive comprises two spring accumulators, with each accumulator consisting of a rod 1 placed between two compression springs 2. The lower springs rest against base 3, whereas the upper springs rest against flange 4. Guides 5 ensure the transverse stability of the springs. Rod 6 is secured to traverse 7, which is linked to the rods 1 of the spring accumulators. Traverse 7 contains apertures that facilitate the connection with balancing devices.

The stiffness of each spring is determined from the equation:

$$c = \frac{\pi^2}{t^2} \cdot m_{rod}/4 \tag{1}$$

t time to move from one extreme position to another;
m_{rod} rod mass.

The maximum force of the spring is:

$$F_{max} = Lc \tag{2}$$

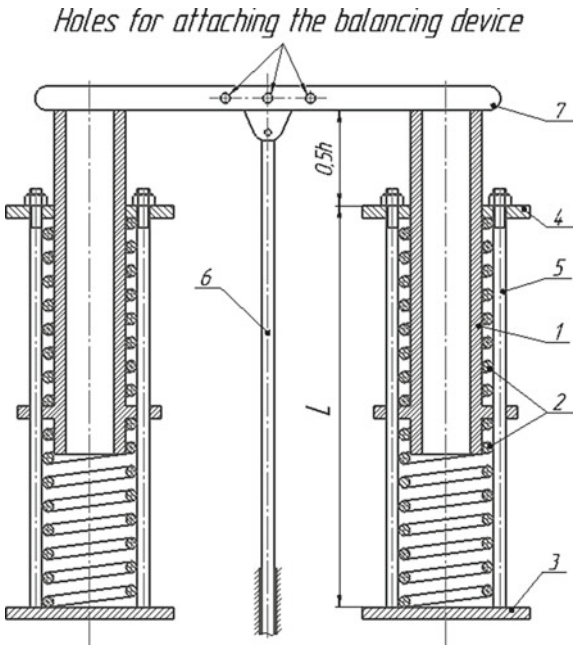

Fig. 1 Diagram of a mechatronic spring drives with a center rod: 1—output link, 2—springs, 3—base, 4—plate, 5—couplers, 6—rod, 7—traverse

L working stroke of the spring.

The time length for moving from one extreme position to another depends on the number of strokes of the rod per minute.

As depicted in Fig. 2, the mechatronic spring drive with energy recovery comprises two compression springs, 1 and 1a, which are interconnected through a flexible element 2. This, in conjunction with two deflecting blocks 4 mounted on the rod, forms a reverse chain hoist. One end of the spring is secured to traverse 6, while the other end is in contact with a disk to which flexible element 2 is attached, located inside the spring. Two sets of deflecting blocks, 3 and 3a, aligned parallel to the rod, define the configuration of the spring drive. In this mechanism, the operational stroke of the springs is twice as low as the maximum stroke of the rod, which is equal to $2z_{max}$.

The spring accumulator comprises two compression springs situated on opposite sides of the rod, with their operational elongation equivalent to half of the maximum stroke of the rod:

$$L_{spring} = z_{max} \tag{3}$$

For this scheme, the stiffness of each spring is:

$$c = \frac{\pi^2}{t^2} \cdot m_{rod}/2 \tag{4}$$

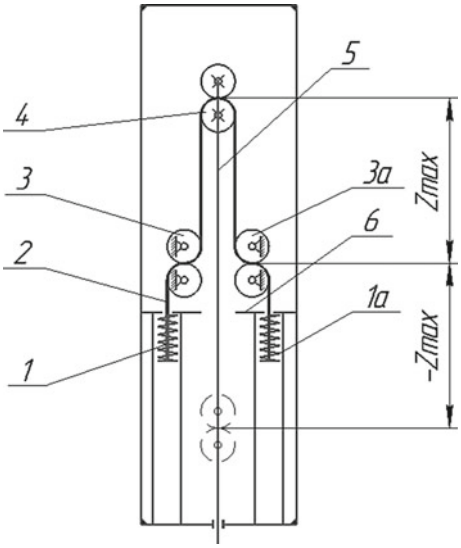

Fig. 2 Diagram of a mechatronic spring drive: 1.1a—springs; 2—flexible element; 3,3a—blocks fixed on the base; 4—blocks fixed on the rod; 5—rod; 6—traverse

$$F_{max} = 2z_{max}c. \tag{5}$$

The working stroke of the spring is more than half of the working stroke of the rod.

The time length for moving the rod from one extreme position to another is determined from the expression:

$$t = \pi\sqrt{\frac{m_{rod} + \frac{2}{3}m_{spring}}{2c}}, \tag{6}$$

m_{spring} spring mass.

The optimal solution for minimizing energy costs involves utilizing both options in a balanced manner, with consideration given to the mass of the rods in two drives, particularly for wells operating at small offsets [16]. Specifically, this involves the use of one linear electromagnetic drive to offset the dissipative losses in two rod spring drives (Fig. 3).

Assuming that downhole installations 1 and 2 (Fig. 3) are connected by gear 3 and are operating in antiphase, the mass of each spring is determined to be 5 kg.

The mechatronic spring drives with energy recovery, as introduced in the paper, offer numerous advantages compared to classic balancer drives used for rod borehole pumps. First of all, these drives offer a substantial reduction in mass and size of equipment, as well as decreased electricity consumption. In addition, they have the potential for development of autonomous drives that can be powered by solar panels

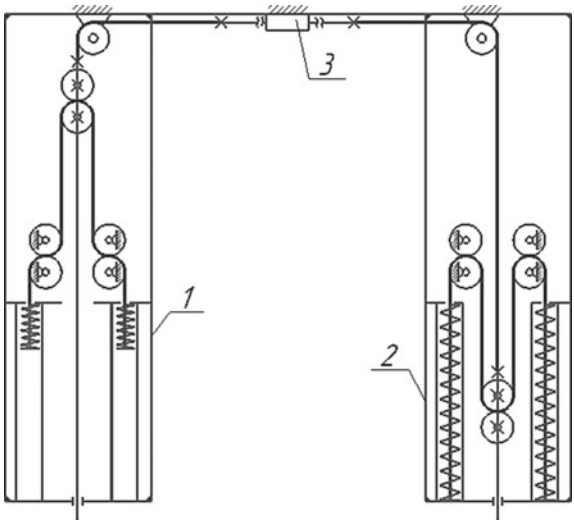

Fig. 3 Scheme of synchronously operating in antiphase spring drives

and wind turbines. In certain circumstances, it may even be possible to transport these drives in fully assembled form within a sea container.

Balancing systems are commonly employed in many downhole rod borehole pump drives, with weight balancing representing the most straightforward and cost-effective solution. Additionally, it is possible to use the suspension of rod borehole pumps located in close proximity and connected through a kinematic connection as a counterweight [16]. In instances where mutual balancing of a constant static load is not possible, traditional weight balancing or balancing spring devices may be employed as an alternative.

The implementation of a spring balancing device entails a serial connection between a crank-slider mechanism and a crank-rocker mechanism, with the crank serving as the common component. The length of the crank is equivalent to the length of the connecting rod and the distance between the axes of the swivel joints of the rocker mechanism with the base, as outlined in [9]. Figure 4 displays the schematic of the spring balancing device, which features a flexible element that loops around two blocks. One block is situated on the axis of the crank, while the other is located on the base, with the distance between the axis of the block and the axis of connection of the crank with the base equivalent to the length of the crank (Fig. 4).

The stiffness of each balancing spring is equal to:

$$c = \frac{m_{rod} \cdot g}{4l} \tag{7}$$

The maximum force of the spring is:

$$F_{max} = 2lc \tag{8}$$

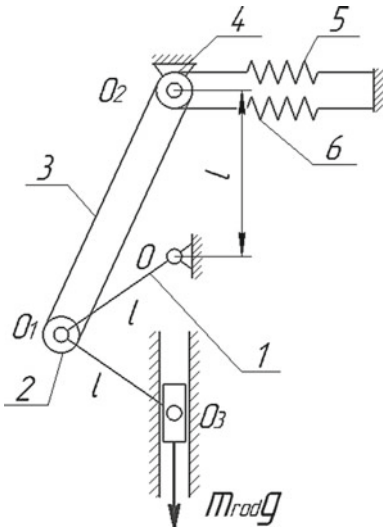

Fig. 4 Scheme of a balancing device based on tension springs for driving rod borehole pumps: 1—crank, 2—block, 3—flexible element, 4—double block fixed on the base, 5.6—springs

Figure 5 shows a scheme for balancing the rod based on compression springs.

The mass of the rod, denoted as m_{rod} , dictates the upper limit of force the spring can sustain, as well as the computed displacement of the rod, which is equivalent to 4*l*. This displacement value can be utilized to compute the mass of the spring, contingent upon the chosen dimensions of the equilibrium apparatus. The spring's maximal displacement is 2*l*, but for the purpose of augmenting its longevity, it is advisable to adopt a lesser displacement value of L_{spring}.

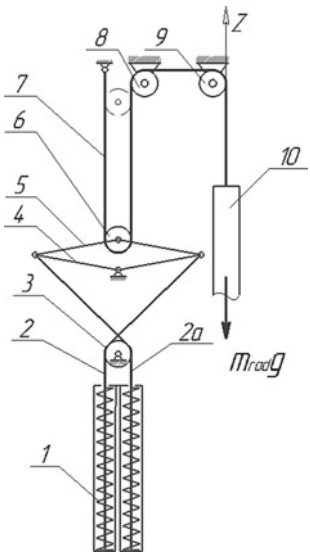

Fig. 5 Balancing scheme of the rod based on compression springs: 1—spring drive; 2.2a—flexible elements; 3—double block; 4—rotary link; 5—connecting rod; 6—flexible element; 7.8—blocks; 9—rod

Consider the range of balancing masses—1200, 2000, 3000 and 4000 kg (although the operational range of masses is substantially wider). For balancing masses of m = 8000 kg, a pair of balancing devices (Fig. 5) should be utilized, positioning them on opposing sides of the balancing mass.

The maximal spring forces for this set of balanced masses are 5,000 N, 10,000 N, 15,000 N, and 20,000 N, correspondingly. The lengths of the pendulum arms are selected arbitrarily.

Table 1 displays the primary attributes of the springs utilized in the balancing apparatus.

When the balancing mass equals 2000 kg, the aggregate mass of the springs amounts to 66 kg.

When the balancing mass is 4000 kg, according to GOST 13776-86 standard, the spring No. 68 with a maximum force of 20,000 N is recommended. Thus, it is prudent to transition to the modular method of constructing balancing devices. Firstly, the minimum interval for altering the balanced mass, denoted as m_{rod}*, must be established. In this situation, a geometric sequence of springs with a ratio of 2 can be formed, taking on the subsequent configuration: $2m_{rod}$*, $4m_{rod}$*, $8m_{rod}$*, $16m_{rod}$*. With the maximum balanced mass equivalent to 8000 kg, m_{rod}* = 500 kg, thereby resulting in the following sequence: 1000, 2000, and 4000 kg.

Following the study, the characteristics of spring accumulators have been ascertained. These characteristics may be utilized in diverse combinations to develop balancing mechanisms for rod borehole pumps. This, in turn, facilitates the design of oil production equipment that operates with considerably lower energy expenditure and installed power.

The mechatronic spring drives with energy recovery, as described in the article, offer considerable advantages over traditional balancer drives for rod borehole pumps. Foremost among these benefits are the substantial reductions in size and weight, electricity consumption, and the potential to develop drives powered independently by solar panels and wind turbines. In certain cases, these drives may be delivered pre-assembled within a shipping container.

Table 1 Main characteristics of balancing device springs

The value of the balanced mass m_{rod} (kg)	Swing arm length l (mm)	Spring rate *c* (N/m)	Maximum spring force (N)	Mass of two springs (kg)	Working stroke L_{spring} (mm)
4000	1500	6700	20,000	194	2500
3000	1250	6000	15,000	116	2000
2000	1000	5000	10,000	66	1500
1200	1000	3000	5000	37	1500

References

1. Levin AI (1978) Mathematical modeling in research and design of machine tools. Engineering, 184 pp
2. Ishii T, Simoyama I, Inoue H et al (1988) Mechatronics: Per. from Japanese, p 318
3. . Babitsky VI, Kotlyachkov AA, Salamander BL, Checherov VA, Shipilov AV, Panin VN (1990) Resonant drive. Patent R.F. 1544550, № 7
4. Akinfiev TS (1983) Resonant handling systems with electric drive. Eng Sci 6:18–23
5. Korendyasev AI, Salamander BL, Tyves LI (2006) Theoretical foundations of robotics. In: 2 book. Science
6. Korendyasev AI, Salamander BL, Tyves LI et al (1989) Manipulation systems of robots. Mechanical Engineering, pp 279–286
7. Pelupessi DS, Zhavner MV (2016) Spring accumulators with an output rotary link for step movements. News of higher educational institutions. Engineering 10(679):9–17
8. Nadezhdin IV (2015) Executive mechanisms of cyclic automatic machines and mechatronic systems. In: Nadezhdin IV (ed) LAP LAMBERT Academic Publishing, Deutschland, 280 pp
9. Zhavner VL, Belogur VP, Zhavner MV, Zhao W (2020) Development and research of mechatronic spring drives with energy recovery for rod depth pumps. In: Advances in mechanical engineering: selected contributions from the conference "Modern Engineering: Science and Education", pp 38–51
10. Patentschrift № 562040 Dr. Leo Szilard und Dr. Albert Einstein. Elertromagnetische Vorrichtung zur Erztugung einer oszillierenden Bewegungen. 1933 Prioritatsdatum 1.Juni 1928
11. API SPEC 11E, 20th Edition, October 2022 –Pumping Units
12. Patent No. 2741187 RU. Downhole rod pump drive. In: Belogur VP, Zhavner VL, Zhavner MV, Zhao W. Appl. No. 2020135561 from 29.10.2020; publ. 22.01.2021, Bul. No. 3
13. Patent No. 2777174 RU. Spring drive downhole pump. In: Belogur VP, Zhavner VL, Zhavner MV, Zhao W. Appl. No. 2021125841 from 01.09.2021; publ. 01.08.2022, Bul. No. 22
14. Zhavner VL, Matsko ON, Zhavner MV (2018) Mechatronic drives for reciprocal motion. Int Rev Mech Eng Comp Anal (IREME) 12(9):784–789
15. CN2284867U Y, 1998.06.24/ Linear motor driven beam-pumping unit Shen Fengquan, Sun Ping, Wang Tongbin
16. Patent No. 2770704 RU. The method of oil production using a SRP pumping unit and the design of the latter for the implementation of this method. Denikin EI. Appl. No. 2021111429 from 20.04.2021; publ. 21.04.2022, Bul. No. 12

Numerical Modeling for Long-Period Waves in a Harbor Basin

Zhibo Xue, WenKai Wang, Yuanchao Liu, and Ruisai Zhou

Abstract A breakwater is a mechanism designed for the protection of a harbor basin, it becomes difficult for it to perform its sheltering functions when long-period waves propagate into the harbor, which leads to poor conditions for the body of water. In this paper, a BW numerical model was verified via a harbor wave-filling simulation, which yielded results that matched quite well with the physical model. The impact of boundary dimensions, angle of wave incidence, seabed friction, and water depth on the harbor's long-period wave oscillation were studied. With these long-period waves, height will first increase, then decrease slightly and keep steady while the wave frequency stays constant when the model's boundary dimensions increase. The angle of incident waves' impact on the long-period wave height had a slight influence. Additionally, the seabed friction and water depth are inversely proportional to long-period wave height and oscillations.

Keywords Long-period waves · Numerical model · Boundary dimension · Angle of incidence · Seabed friction · Water depth

1 Introduction

In port construction, it is generally necessary to build hydraulic architecture such as breakwaters to prevent the invasion of the harbor basin by waves and currents from outside the harbor. A breakwater, which is effective in reducing the height of short-period waves, provides insufficient resistance against long-period waves, i.e.

Z. Xue · W. Wang (✉)
China Waterborne Transport Research Institute, Beijing 100088, China
e-mail: wangwenkai@wti.ac.cn

Y. Liu
China Harbour Engineering Company LTD., Beijing 100027, China

R. Zhou
Tianjin Maritime Safety Administration, Tianjin 300211, China

H.-Y. Jeon (ed.), *Proceedings of the International Conference on Geosynthetics and Environmental Engineering*, Lecture Notes in Civil Engineering 374,
https://doi.org/10.1007/978-981-99-4229-9_35

those with a longer wavelength. In areas with heavy swells, long-period waves can easily directly invade a harbor, worsening the operation conditions in the harbor. When the incident waves' frequency is close to the natural frequency in the harbor, the amplitude of the water in the harbor can reach several times that of the incident waves due to forced vibration, leading to a harbor oscillation [1]. Being extremely unfavorable to steady mooring conditions, a harbor oscillation seriously endangers the normal docking and operation of ships in the harbor. For this reason modeling for long-period waves in harbor basins is a critical subject in port planning and design.

According to literature, in the 1950s, a seiche in Table Bay Harbour, Cape Town caused destructive accidents for ships in the harbor [2]. Through using an acoustic doppler current profiler in Wellington Harbour, New Zealand, Abraham [3] discovered that there were oscillations with periods of 15.8 and 14.7 min in the harbor. Miles and Munk [4] studied the oscillation of a rectangular harbor basin connected to a body of open water and the expression of the amplification factor when the oscillation occurred via the application of Green's function. Based on a linear hypothesis, Wang [5] delivered an analytic expression of a narrow and long rectangular harbor's longitudinal oscillation, and obtained an analytic solution of the oscillation of a harbor with varying water depth based on the weakly dispersive Boussinesq equation. Shi and Pan [6] analyzed long-period waves' generation factors and reduction measures based on an overall wave model test. Shi et al. [7], Xu [8] adopted the Boussinesq wave numerical model to calculate wave heights in a harbor with different incident wave periods of the harbor basin under an ideal terrain, predicted the occurrence of a harbor oscillation, and then proposed preventive measures. Yin [9] simulated the oscillation energy change process in a slender harbor, a circular harbor, a double-circular harbor, and an irregular harbor via the Boussinesq wave numerical model. Although countless domestic and foreign scholars have conducted research on long-period waves, numerous studies are still based on ideal harbor basin conditions. Therefore, this paper took an actual harbor basin as the subject to carry out research on long-period wave numerical modeling.

2 Model Verification

2.1 Introduction to the Model

Developed by the Danish Hydraulic Institute, the BW wave numerical model of MIKE21 is based on the Boussinesq equation proposed by Madsen and Sørensen [10, 11] to improve the frequency dispersion relationship and shoaling performance, and adopts the alternating direction implicit scheme (ADI) for a solution in the time domain. After long-term development, the BW model can accurately describe the refraction, deflection, reflection and nonlinear wave interactions that occur during wave propagation in coastal waters. Its control equation and numerical calculation method can be found in the literature [10, 11].

2.2 Model Verification

In this paper, this numerical model's rationality was firstly verified based on a physical model test. See Fig. 1 for the physical model's layout, Fig. 2 for the layout of measuring points, and Table 1 for wave elements. Among them, the physical model test was carried out in a 40 m × 60 m × 1.5 m wave harbor basin. Wave elimination settings were installed around the harbor basin to eliminate secondary reflected waves, and a DJ 800 was used for wave collection. The southeast (SE) and south-southeast (SSE) directions are shown in Fig. 1; a scale of 1:80 was adopted for the test. The test accurately simulated the harbor basin; the bottom elevation of the harbor basin was set to −9 m, and the outer elevation of the harbor basin was −11 m.

This numerical model is arranged exactly in accordance with the physical model. After the layout in the physical model test and the tested harbor basin were enlarged proportionally according to a scale of 1:80, a numerical model map of the harbor basin's terrain was obtained. The calculation range of the wave mathematical model was 1,600 m × 5,000 m, the terrain setting was exactly the same as that in the physical model, and the model's space interval was 10 m. For the purpose of absorbing long-period waves, the thickness of the open-boundary sponge layer in the model was set to 100 layers, that is, the thickness of the sponge layer reached 1,000 m.

Since this paper focuses on the verification and study of long-period waves, the period and wave height of long-period waves in the MIKE21 BW harbor basin model were verified, respectively. In wave height verification, the wave time series of the measuring points were separated. Additionally, the wave height at the measuring

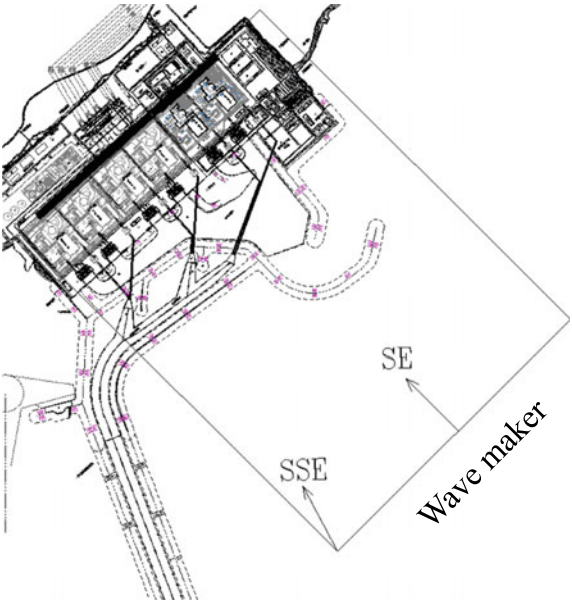

Fig. 1 Model layout diagram

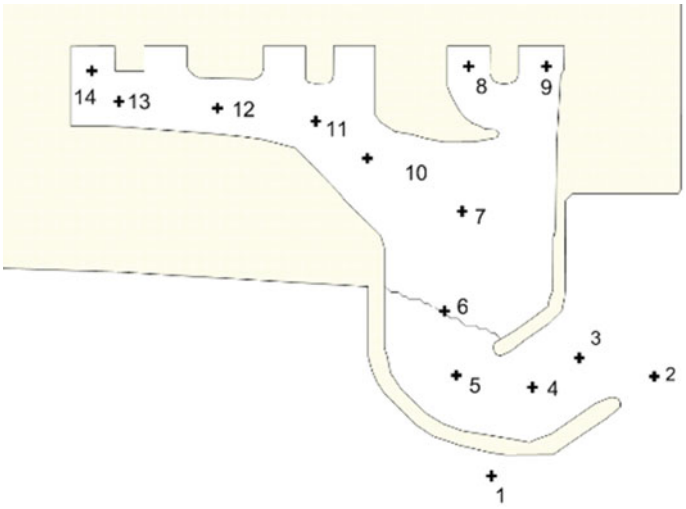

Fig. 2 Measuring point layout diagram

Table 1 Test waves' elements

D (m)	Hs (m)	T (s)	Direction	Recurrence period
5.90	5.47	10.2	SE	100 years
	5.47	10.2	SSE	100 years
3.91	5.15	10.2	SE	100 years
	5.15	10.2	SSE	100 years

points and the separated long-period wave height were verified. In the verification of period, the period of the long-period wave series (wave period longer than 30 s) was verified.

Wave Height Verification The Fourier transform was utilized to separate the long-period wave series, the effective wave height of the long-period waves was compared with that in the physical model test, and a comparison chart of wave height of between the numerical model and the physical model at different measuring points under the action of waves from the SE and SSE directions was obtained (as shown in Fig. 3). It can be seen from the numerical simulation results and the physical model test that the trend and law of the total wave height at each measuring point and the wave height of the long-period waves are relatively consistent, and the degree of agreement in the results is satisfactory.

Wave Period Verification With the Fourier transform, wave filtering was conducted to separate the long-period waves longer than 30 s at each measuring point, and amplitude and frequency diagrams of the long-period waves were drawn. In this paper, two typical measuring points, Nos. 8 and 13, were selected for long-period wave

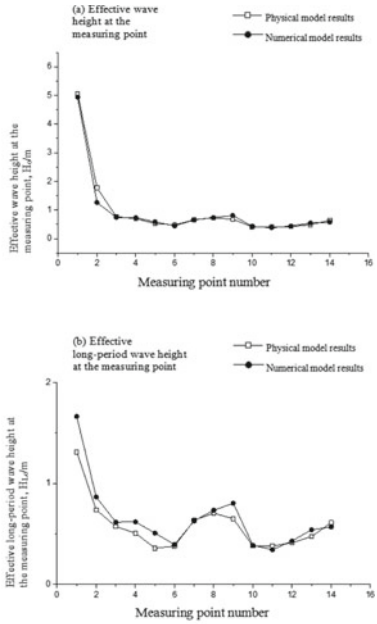

(1) Incident waves from the SE, HS=5.15 m

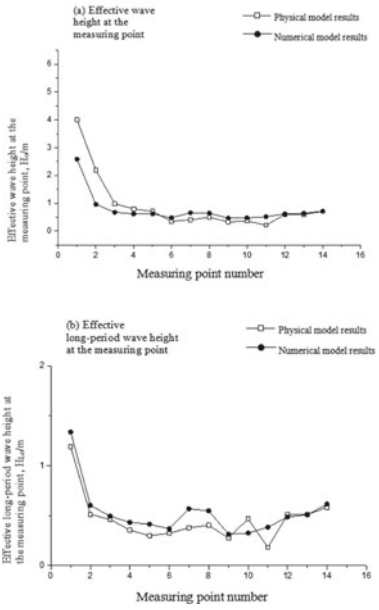

(2) Incident waves from the SSE, HS=5.47 m

Fig. 3 Comparison of wave height between the numerical model and the physical model

amplitude and frequency comparison, thus yielding the amplitude and frequency comparison chart, as shown in Fig. 4. As can be learned from the figure, the numerical simulation results of the long-period waves' period at the measuring points in the harbor and the physical model test results tend to be consistent, which demonstrates a high degree of coincidence. In other words, this numerical model can more accurately simulate the long-period waves' propagation in the harbor.

3 Impact of External Conditions on Long-Period Waves in the Harbor Basin

3.1 Impact of the Model's Boundary Dimensions

The numerical model in this paper was arranged exactly with reference to the physical model, with its horizontal dimension being 1,600 m and vertical dimension being 5,000 m. Through wave filtering, the resulting long-period waves' oscillation period reached that of a few hundred seconds, corresponding wavelength could reach several thousand meters, making it truly necessary to discuss the model boundaries' impact on the calculation results of long-period waves.

In the calculation, the boundaries of the model were gradually extended, and then 13 groups were set on the model's horizontal dimension. The vertical dimension of the model remained unchanged, and a sponge layer with a thickness of 1,000 m was set for absorbing long-period waves. Through making a comparison of the calculation results at different model dimensions (see Figs. 5 and 6), it was found that when the horizontal dimension of the model's boundary expands from 1,550 to 1,930 m, the wave height of the long-period waves in the harbor basin increases sharply; when the model scale continued to expand, the long-period wave height at each measuring point decreased slightly; and the subsequent values remained basically the same. The movement of boundaries would bring changes to the amplitude of the long-period waves' oscillation of the harbor at each frequency, while the long-period waves' oscillation frequency in the harbor would not change as a result, which clarified that the boundary dimension change basically had little impact on the long-period waves' oscillation frequency.

In long-period wave oscillation, the water body outside the harbor formed a composite vibrating body with that in the harbor, and the increase of the boundary dimensions would cause the increase of the water body outside the harbor. For long-period wave oscillation in the harbor, the oscillation frequency of the harbor was 0.002 Hz, and the corresponding wavelength could reach several kilometers. When the distance from the harbor's exterior boundaries to the interior boundaries of the harbor's inlet was short, the oscillation of the body of water between the two boundaries was not complete enough, and its corresponding amplitude was relatively small. With the expansion of the exterior boundaries, when the distance from the harbor's

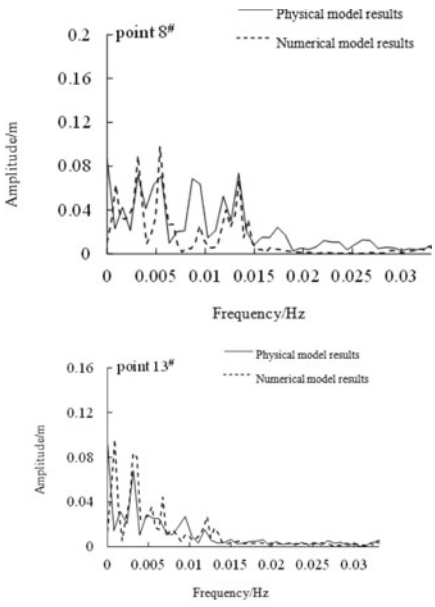

(a) Incident waves from the SE, HS=5.47 m

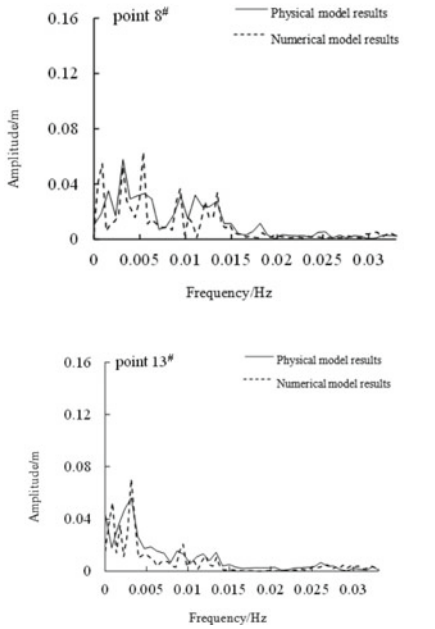

(b) Incident waves from the SSE, HS=5.47 m

Fig. 4 Comparison of the long-period waves' amplitude and frequency between the numerical model and the physical model

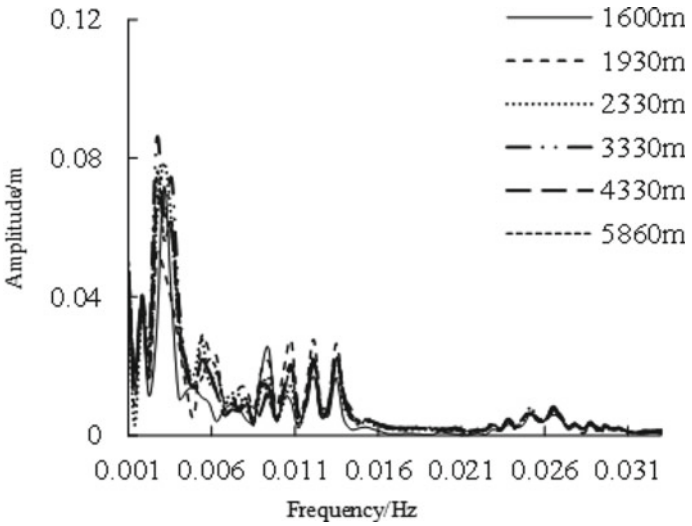

Fig. 5 Comparison of the long-period waves' amplitude and frequency under different boundary dimensions

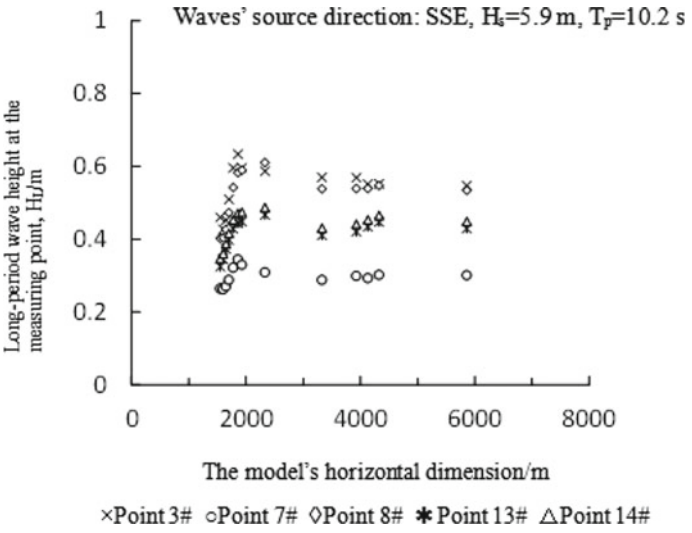

Fig. 6 Comparison of the long-period waves' height under different boundary dimensions

exterior boundaries to the interior boundaries of the harbor's inlet was increased, the water bodies inside and outside the harbor were more likely to form a joint oscillating body whose oscillation amplitude increased with its gradual expansion. With the further expansion of the model range, the impact of the harbor's exterior boundaries on the harbor's long-period wave oscillation began to decrease. When a

relatively complete long-period wave oscillation was able to take place in the water body of the harbor, the model's boundaries could no longer impose restrictions to the long-period wave oscillation, and the corresponding wavelength of the long-period wave oscillation of the harbor would not change due to boundary expansion. Hence, with the further expansion of the model's boundaries, the long-period wave oscillation of the harbor started to weaken slightly, but the overall change was not obvious.

However, in a natural coast, there are no boundaries in numerical operations as with physical model experiments, which also suggests that the larger the exterior boundary range of a numerical model, the closer the phenomenon to that of natural waves invading the harbor, especially in the discussion of the phenomenon of long-period wave oscillation, the larger the external boundary range, the greater impact of the exterior boundaries on the oscillation of the water body in the harbor can be eliminated. Thus, in order to better demonstrate the long-period wave oscillation in an actual harbor, the horizontal dimension of the model should be greater than 3,000 m.

3.2 Impact of Incident Waves' Source Direction

In order to analyze the impact of the incident waves' source direction on the wave height in the harbor, this study merely changed the incident waves' source direction instead of changing the layout of the harbor basin to calculate the wave height in the harbor under waves from different directions. In this study, the angle α between the end axis of the breakwater and the source direction of the incident waves was used as a reference (as shown in Fig. 7), and 6 sets of different operation conditions were set by changing the source direction of the incident waves. Meanwhile, the same wave element was used in different operation conditions.

As the angle α between the incident waves' source direction and the axis of the end of the breakwater gradually increased (the incident waves' direction gradually shifted towards the harbor), the wave height of the short waves at the measuring points in the harbor gradually increased as well. In contrast, the changes in wave height of a long-period waves were relatively minor, but on the whole, there was a tendency to increase with the increase of the angle α between the incident waves' source direction and the breakwater. The calculation results can be found in Fig. 8. The changes in the incident waves' source direction led to an enhancement in the response of incoming short-period waves received in the harbor, while long-period waves were not highly sensitive to the incident waves' source direction.

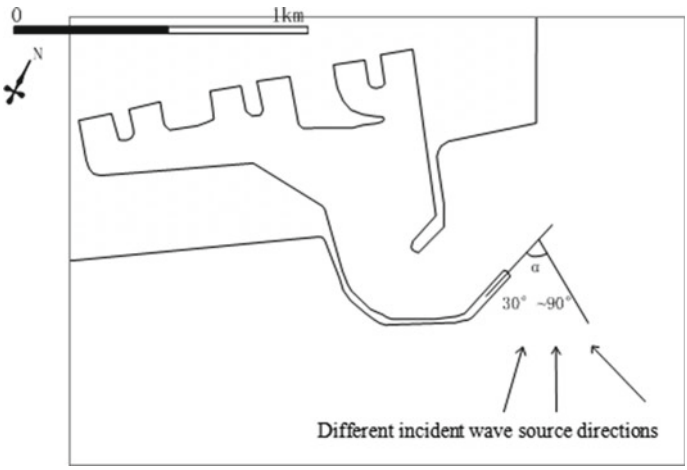

Fig. 7 Changes in the angle between the incident waves' source direction and the axis of the end of the breakwater

3.3 Impact of Seabed Friction

During the wave propagation process, seabed friction will reduce the wave energy. The seabed friction can be expressed through the Chézy coefficient or Manning coefficient. This section studied the law of variation of the long-period wave height with the Chézy coefficient in the harbor.

The wave heights of the short-period waves and long-period waves at each measuring point in the harbor under different seabed friction are shown in Fig. 9. With the gradual increase of the Chézy coefficient, the short-period wave height at each measuring point in the harbor basically remained unchanged, while the long-period wave height gradually increased. Since the seabed friction is inversely proportional to the Chézy coefficient, that is, when the Chézy coefficient increases, the seabed friction decreases, the long-period wave height in the harbor then increased. The wavelength of long-period waves was much larger than the water depth, and long-period waves were greatly affected by the seabed during their propagation and oscillation. Specifically, the increase in the seabed friction could effectively weaken the long-period waves in the harbor, while the short-period waves were relatively weakly affected by the seabed due to their shorter wavelengths. When the water was deeper, the propagation of the short-period waves was weakly affected by the seabed. Therefore, changes in the seabed friction had little impact on the short-period wave height.

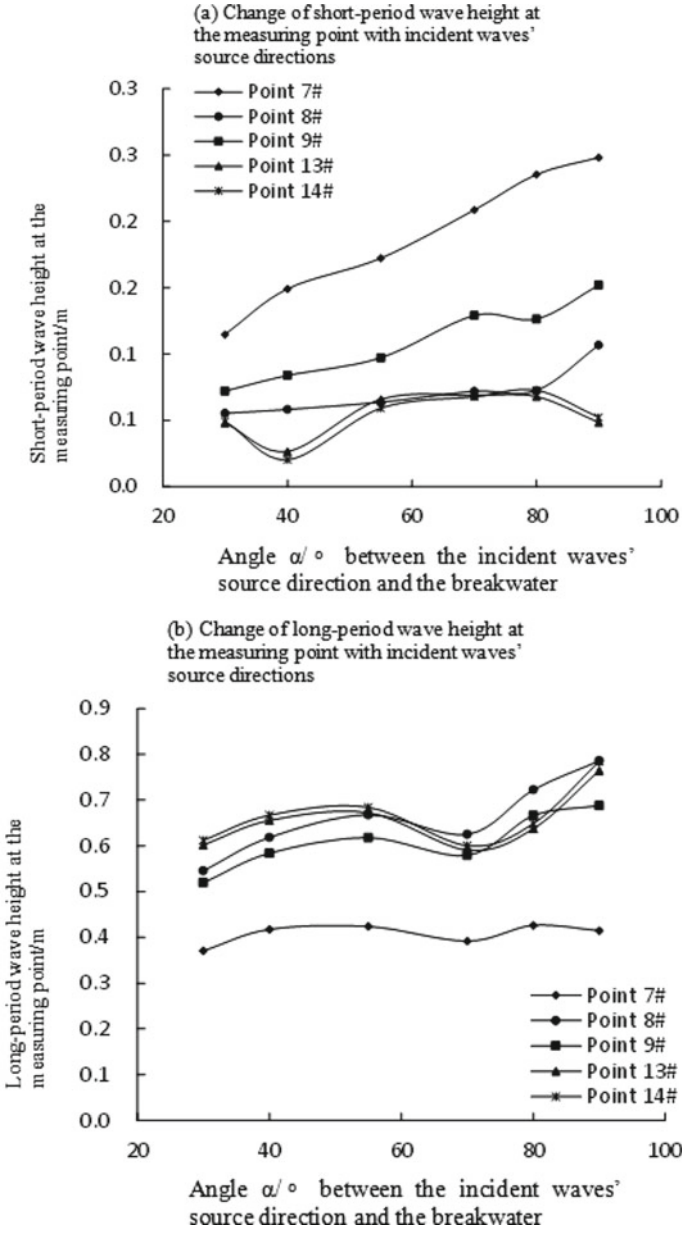

Fig. 8 The impact of the incident waves' source direction on the wave height in the harbor

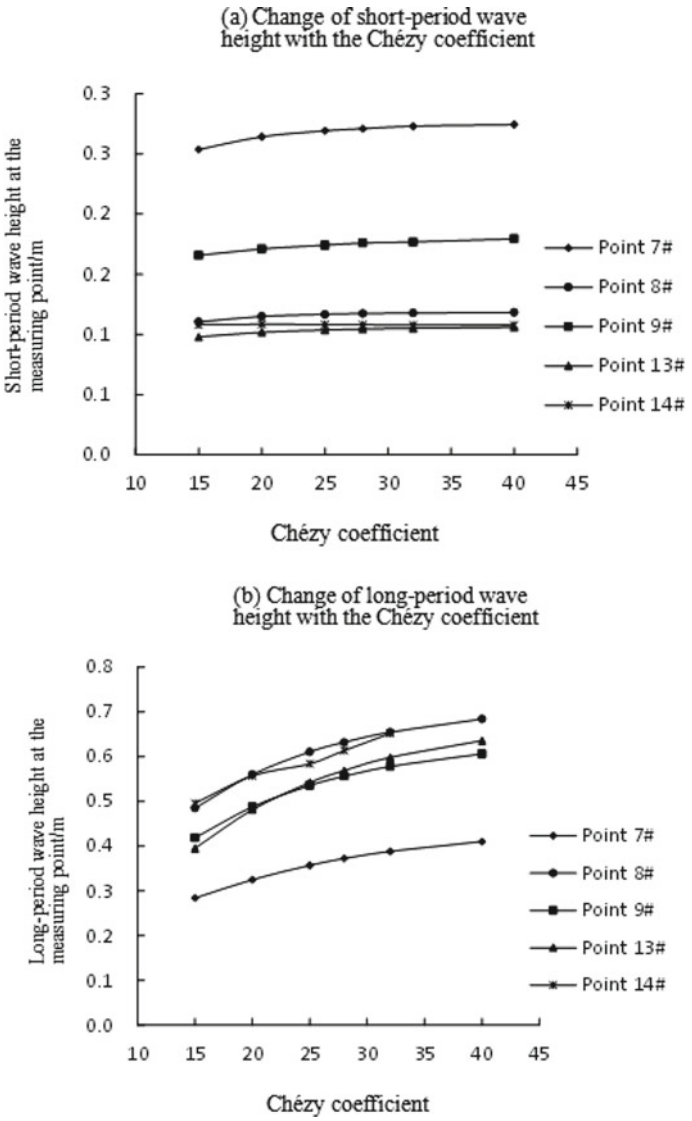

Fig. 9 Seabed friction's impact on the wave height in the harbor

3.4 Impact of Water Depth

In the process of wave propagation to the inshore, due to the shallowness of the water, the seabed has a direct effect on the waves, bringing about shallow water deformation of the waves. Accordingly, the propagation of the waves is also affected by water depth. Hence, this section counted the change of long-period wave height

and short-period wave height with water depth, respectively, and yielded the results shown in Fig. 10. With the gradual increase of water depth, the short-period wave heights at various measuring points in the harbor also gradually increased, and their growth trend and slope were basically the same. Nevertheless, the opposite of such a law was manifested in the long-period wave height. Consequently, water depth had a significant impact on the propagation and oscillation of long-period waves.

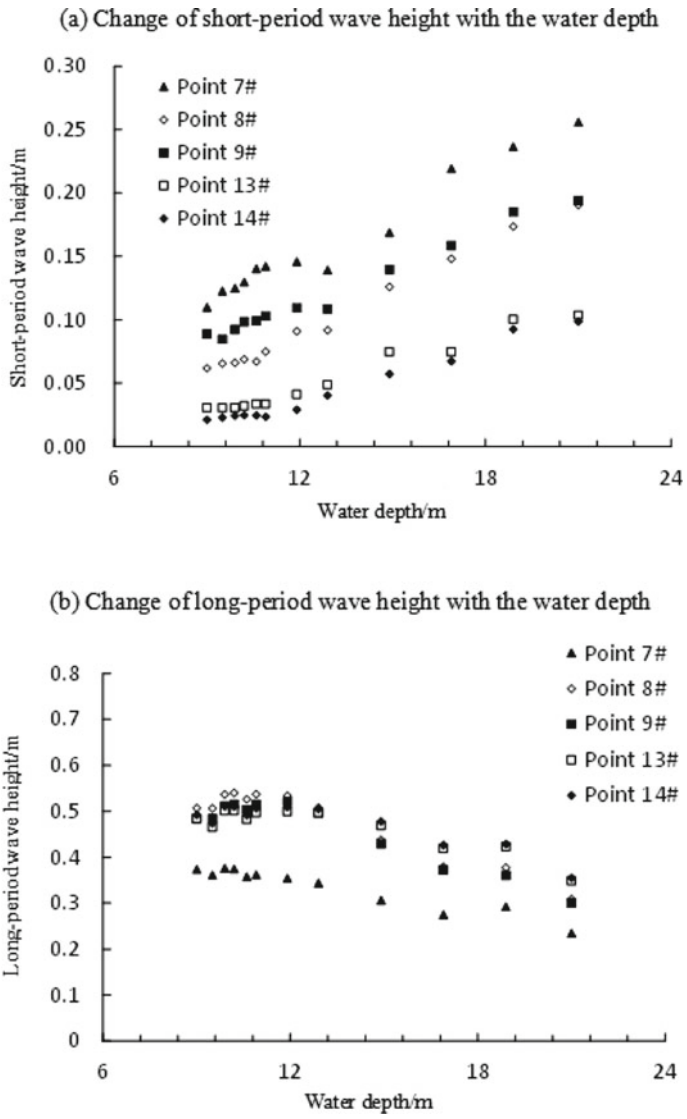

Fig. 10 Water depth's impact on the wave height in the harbor

4 Summary

In this paper, the BW numerical model's rationality was verified based on the test results from a harbor physical model project. On this basis, the impact of boundary dimensions, angle of wave incidence, seabed friction, and water depth on the long-period wave oscillation were studied. The specific conclusions are as follows:

(1) This study calculated the disturbance and distribution of long-period waves in the harbor based on the MIKE21-BW model, and compared and analyzed them with the test results in the overall physical model. The two types of results were in ideal agreement, which verified the rationality of the BW model in calculating the waves in the harbor.
(2) The long-period wave height will first increase, then decrease slightly and maintain steady when the model's boundary dimensions increase. The movement of boundaries would bring changes to the amplitude of the long-period waves' oscillation of the harbor at each frequency, while the long-period waves' oscillation frequency in the harbor under various boundary dimensions would not change as a result. Thus, in order to better demonstrate the long-period wave oscillation in an actual harbor, the horizontal dimension of the model should be greater than 3,000 m.
(3) The impact of the incident waves' source direction on the long-period wave height in the harbor was weak. Seabed friction and water depth, by contrast, have a significant impact on the long-period wave oscillation, in which the greater the seabed friction, the smaller the long-period waves in the harbor. As the water depth gradually increases, the long-period wave oscillation of the harbor gradually weakens.

References

1. Gu JL (1984) Research on oscillation in harbor basins. Port Waterw Eng 12:1–10
2. Wilson BW (2010) Table Bay as an oscillating basin. Coastal Eng 201–212
3. Abraham ERC (1997) Seiche modes of Weilington harbour. N Z J Marine Freshw Res 31:191–200
4. Miles J, Munk W (1961) Harbour paradox. J Waterw Harb Div 87:111–132
5. Wang G (2010) Research on harbor oscillation caused by different power factors. Dalian University of Technology, Dalian
6. Shi LS, Pan JN (2009) The phenomenon of long-period wave fluctuations and its reduction in the water intake channel of Binhai nuclear power plant. J Hydraul Eng 40(02):201–207+213
7. Shi HD, Xu GD, Sun LL (2011) Research on harbor oscillation of rectangular harbors. Coastal Eng 30(02):14–21
8. Xu GD (2011) Research on the characteristics and preventive measures of harbor oscillation. Ocean University of China, Qingdao
9. Yin XC (2014) Research on the energy evolution of harbor oscillation. Dalian University of Technology, Dalian

10. Madsen PA, Murray R, Sørensen OR (1991) A New form of the Boussineq equations with improved linear dispersion characteristics. Coastal Eng 15:371–388
11. Madsen PA, Sørensen OR (1992) A new form of the Boussineq equations with improved linear dispersion characteristics. Part 2. A slowly-varying bathymetry. Coastal Eng 18:183–204

The Effect of Multi-Wall Carbon Nanotubes on the Flexural and Compressive Strength of Cement-Based Composites

Fani Gkountakou, Maria Falara, Athanasia Thomoglou, and Anaxagoras Elenas

Abstract Nanoparticles are characterized as the most frequently used materials for embellishing the nanomodified specimens' multifunctional characteristics. The combination of cementitious composites with nanomaterials is important for enhancing the microstructural characteristics of cement-based materials and filling voids in the cement pastes. Recently, many studies on incorporating carbon nanotubes in cement paste showed an improvement in the engineering field. In this research, many three-point bending tests into prismatic samples that were cast into molds conducted to examine the multi-wall carbon nanotubes' (MWCNTs) mechanical characteristics. More specifically, for creating cement paste enhanced with MWCNTs, three different amounts of MWCNTs, such as 0.1 wt.% MWCNTs, 0.2 wt.% MWCNTs, and 1.0 wt.% MWCNTs of cement were applied. Sonication energy and surfactants were applied in order to disperse the MWCNTs into the aqueous solution. By evaluating the results, it was concluded that the amount of 0.1 wt.% MWCNTs revealed the best mechanical properties, such as 55.5 MPa 28-day compressive strength and 6.9 MPa flexural strength compared to the other samples. Thus, MWCNTs are capable of creating cement-based materials with multiple structural functions.

Keywords Nanomaterials · Multi-wall carbon nanotubes (MWCNTs) · Compressive Strength · Flexural Strength · Ultrasonic energy · Cement-based composites

F. Gkountakou (✉) · M. Falara · A. Thomoglou · A. Elenas
Department of Civil Engineering, Democritus University of Thrace, Xanthi, Greece
e-mail: fgkounta@civil.duth.gr

M. Falara
e-mail: mfalara@civil.duth.gr

A. Thomoglou
e-mail: athomogl@civil.duth.gr

A. Elenas
e-mail: elenas@civil.duth.gr

H.-Y. Jeon (ed.), *Proceedings of the International Conference on Geosynthetics and Environmental Engineering*, Lecture Notes in Civil Engineering 374,
https://doi.org/10.1007/978-981-99-4229-9_36

1 Introduction

Cement-based materials are considered as an important factor in building construction. Their enhanced mechanical properties and high durability make them the most commonly applied materials for developing high construction behavior. Nevertheless, many researchers were interested in studying their quasi-brittle performance. For embellishing the mechanical capabilities of cement-basted materials and avoid concrete's ductility, multi-wall carbon nanotubes (MWCNTs) can be applied.

The incorporation of MWCNTs into cement paste gained the interest of many researchers since they provide high mechanical performance [1]. For example, it was reported that by adding 0.1 wt.% and 0.2 wt.% MWCNTs [2], the flexural strength of cementitious samples improved by 65% and 26.9%, respectively, in contrast to the reference specimen at 28 days of hydration. Also, the proportions of 0.01 wt.% MWCNTs, 0.02 wt.% MWCNTs and 0.03 wt.% MWCNTs were dispersed using silica fume as a surfactant agent [3]. It was concluded that the sample containing 0.01 wt.% MWCNTs improved the compressive strength by 12.4% at 7 days of hydration, and the sample of 0.02 wt.% MWCNTs had 6.8% higher compressive strength on the aforementioned days. Similarly, the proportion of 0.03 wt.% MWCNTs revealed a 4.1% increase in compressive strength on the same days. In addition, it was studied the impact of many lengths and proportions of MWCNTs on the compressive and flexural strength of nano-modified materials [4]. It was concluded that the proportion of 0.048 wt.% MWCNTs enhanced by 25% the flexural performance. Similar behavior was also observed for the specimen containing 0.08 wt.% MWCNTs. Particularly, a compressive strength improvement of cement-based materials reinforced with MWCNTs was also demonstrated. It was mentioned that the incorporation of MWCNTs in the amount of 0.01 wt.% into cement improved by 1.6% the compressive strength at 28 days and 4.1% for 90 days, in contrast to the reference specimen [5]. The specimens containing 0.015 wt.% MWCNTs also exhibited higher results as the increment of the compressive strength was 3.0% and 4.7% at 28 and 90 days, respectively. It was also studied the incorporation of 0.038 wt.% and 0.075 wt.% MWCNTs to cement matrix [6]. In order to disperse MWCNTs, superplasticizer was used as a surfactant and ultrasonic energy was applied in the solution. Interestingly, the flexural strength yielded an improvement in their values. Likewise, Hunashyal et al. [7], by adding 0.75 wt.% MWCNTs assumed that the mechanical properties were enhanced by about 33.66% the compressive and 20.55% the flexural strength.

The dispersion of nanoinclusions is a necessary process for embellishing their performance in the cement matrix. Many surfactants can be applied to enhance the dispersion of CNTs [8, 9]. For example, five surfactants were applied to enhance the incorporation of MWCNTs to cement matrix. It was concluded that the SDBS along with TX10 exhibited an increase in both mechanical and electrical properties. Likewise, gum arabic (GA) was used [10] in dispersing process of the proportion of 1.5 wt.% and 3 wt.% MWCNTs and the results revealed nanofluid stability. In addition, it was investigated that the application of sodium dodecyl benzene sulfonate

Table 1 The mechanical characteristics of MWCNTs

Fiber Type	Diameter mm	Length μm	Purity (%)	Density (gr/cm^3)	Aspect Ratio	Fiber count
MWCNTs	9.5	1.5	>90	1.66	158	2.04×10^{13}

(SDBS) combined with polyvinylpyrrolidone (PVP) yielded the highest performance in the dispersion process [11].

In this paper, in order to create cement pastes enhanced with MWCNTs, three different amounts of MWCNTs by the mass of cement, namely 0.1 wt.% MWCNTs, 0.2 wt.% MWCNTs, and 1.0 wt.% MWCNTs were incorporated into the cement matrix. Three-point bending procedures were carried out for each specimen for determining the mechanical properties of nanomodified materials at a hydration age of 28 days. By evaluating the results, it was concluded that cement paste reinforced with 0.1 wt.% MWCNTs yielded an increase in the mechanical characteristics, optimizing the cement-based material's properties.

2 Application Section

2.1 Specimens' Preparation

For casting the samples enhanced with multi-wall carbon nanotubes, general purpose Portland cement 42.5 R was applied, supplied by the company named TITAN HELLAS. The characteristic parameters of MWCNTs, which are in powder form and were purchased from Nanocyl, are shown in Table 1. Carbon nanotubes have to be dispersed in order to incorporate them into the matrix of cement paste effectively [12]. A successful dispersion process provides an increase in the mechanical characteristics of cement pastes and the optimization of their performance. In the present research, for improving the dispersion process of MWCNTs, a surfactant named sodium dodecylbenzene sulfonate (SDBS), which was purchased from Aldrich and Tri-n-butyl phosphate (TBP) were added to the aqueous solutions [13].

The method that was used for breaking up the agglomerates that appeared in the solution was 60 min of ultrasonic energy with an ultra-sonic processor that emitted a 500 W ultrasonic wave [14]. Then, the CNT/SDBS solutions were applied to the Ordinary Portland cement for preparing the specimens.

2.2 Testing Procedure

For estimating the mechanical characteristics of reinforced cement composites, a series of three-point bending procedures were carried out into prismatic specimens,

which were cast into molds. The machine that was used for assessing the flexural strength is a servo-hydraulic 25 kN MTS with displacement rate 0.1 mm/min.

Upon completing the flexural test process, the halves of every specimen were subjected to a 2000 kN machine for evaluating the compressive strength under force control. The displacement rate was 0.5 kN/s.

3 Results

As already mentioned, multi-wall carbon nanotubes (MWCNTs) were applied at the proportions of 0.1 wt.% MWCNTs, 0.2 wt.% MWCNTs, and 1.0 wt.% MWCNTs for evaluating the mechanical properties of cement-based materials enhanced with MWCNTs. Figure 1a) represents the results of flexural strength of nanomodified specimens. It is demonstrated that the amount of 0.1 wt.% MWCNTs yielded the best ultimate flexural strength results at the hydration age of 28 days, which improved by 17% in comparison with the reference sample. Such behavior was also noticed for the specimen in the amount of 0.2 wt.% MWCNTs that its flexural strength was increased by 3.5%. On the other hand, a higher proportion of MWCNTs, such as 1.0 wt.%, decreased the flexural behavior of cement paste nanocomposites. This can be related to the fact that higher proportions of MWCNTs cannot be dispersed effectively, leading to an inaccurate flexural behavior of specimens.

Figure 1b) illustrates the outputs of the compressive strength of cement pastes incorporated with MWCNTs. It is shown that the specimen contained 0.1 wt.% MWCNTs increased by 5.9% the compressive strength for 28 days of hydration related to the plain cement paste [4, 15–17]. Similarly, the specimen containing 0.2 wt.% MWCNTs also exhibited higher results as the increment of the 28-day compressive strength was almost 1%. Conversely, the proportion of 1.0 wt.% MWCNTs caused a decrease compared to the plain specimen. The decrease may be attributed to the inadequate MWCNTs' distribution into the cementitious matrix.

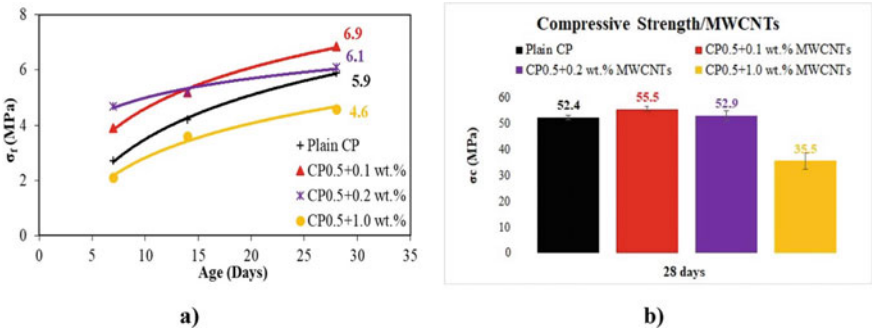

Fig. 1 Results in **a** flexural strength and **b** compressive strength of different proportions of MWCNTs

Table 2 Experimental outputs of different proportions of MWCNTs at 28 days

	σ_f [MPa]	σ_c [MPa]
Plain CP	5.9	52.4
0.1 wt.% MWCNTs	6.9	55.5
0.2 wt.% MWCNTs	6.1	52.9
1.0 wt.% MWCNTs	4.6	35.5

The aforementioned experimental outputs are listed in the following Table 2.

4 Conclusions

This research examines the impact of different MWCNTs proportions on nanomodified specimens' mechanical properties. More specifically, three different amounts of MWCNTs by the cement mass, such as 0.1 wt.% MWCNTs, 0.2 wt.% MWCNTs, and 1.0 wt.% MWCNTs were incorporated to enhance the matrix of cement pastes. For a better dispersion process, sodium dodecylbenzene sulfonate (SDBS) and Tri-n-butyl phosphate (TBP) were applied to the mixture, and the solution was subjected for 60 min with ultrasonic energy. Afterwards, a series of bending tests were carried out to estimate each specimen's mechanical characteristics. The results revealed that the proportion of 0.1 wt.% MWCNTs yielded the best mechanical results at a hydration age of 28 days. On the other hand, a higher amount of MWCNTs, such as 1.0 wt.% MWCNTs caused a decrease in the mechanical properties as bigger proportions of MWCNTs cannot be dispersed successfully.

To sum up, the incorporation of multi-wall carbon nanotubes (MWCNTs) in the proportion of 0.1 wt.% MWCNTs into cementitious materials proved to be the most effective proportion. This demonstrates that MWCNTs can enhance cement-based materials with multiple structural functions.

Authors' Background

Your Name	Title*	Research Field	Personal website
Fani Gkountakou	Ph.D. Candidate	Mechanical and Structural Engineering science, Construction materials	https://www.researchgate.net/profile/Fani-Gkountakou
Maria Falara	Post-Doc Researcher	Nanocomposites, Material and Structural Engineering science, Nanotechnology in construction materials	https://www.researchgate.net/profile/Maria-Falara/research
Athanasia Thomoglou	Post-Doc Researcher	Nanotechnology, Composite Materials, Mechanical and Structural Engineering science, building construction	https://www.researchgate.net/profile/Athanasia-Thomoglou/research

(continued)

(continued)

Your Name	Title*	Research Field	Personal website
Anaxagoras Elenas	Full Professor	Statics and Dynamics of Structures, Finite Element Methods	https://civil.duth.gr/author/elenas/

Acknowledgements The financially supported organizations of this study are the European Union and Greek national funds under the Operational Program Competitiveness, Entrepreneurship, and Innovation, through the call RESEARCH-CREATE-INNOVATE (HICOTEG-T1EDK-03482).

References

1. Hu Y, Luo D, Li P, Li Q, Sun G (2014) Fracture toughness enhancement of cement paste with multi-walled carbon nanotubes. Constr Build Mater 70:332–338
2. Al-Rub RKA, Ashour AI, Tyson BM (2012) On the aspect ratio effect of multi-walled carbon nanotube reinforcements on the mechanical properties of cementitious nanocomposites. Constr Build Mater 35:647–655
3. Naqi A, Abbas N, Zahra N, Hussain A, Shabbir SQ (2019) Effect of multi-walled carbon nanotubes (MWCNTs) on the strength development of cementitious materials. J Market Res 8(1):1203–1211
4. Konsta-Gdoutos MS, Metaxa ZS, Shah SP (2010) Highly dispersed carbon nanotube reinforced cement based materials. Cem Concr Res 40(7):1052–1059
5. Cerro-Prada E, Pacheco-Torres R, Varela F (2021) Effect of multi-walled carbon nanotubes on strength and electrical properties of cement mortar. Materials 14(1):79
6. Zou B, Chen SJ, Korayem AH, Collins F, Wang CM, Duan WH (2015) Effect of ultrasonication energy on engineering properties of carbon nanotube reinforced cement pastes. Carbon 85:212–220
7. Hunashyal A, Banapurmath N, Jain A, Quadri S, Shettar A (2014) Experimental investigation on the effect of multiwalled carbon nanotubes and nano-SiO_2 addition on mechanical properties of hardened cement paste. Adv Mater 3(5):45–51
8. Borode AO, Ahmed NA, Olubambi PA (2019) Surfactant-aided dispersion of carbon nanomaterials in aqueous solution. Phys Fluids 31(7):071301
9. Luo J, Duan Z, Li H (2009) The influence of surfactants on the processing of multi-walled carbon nanotubes in reinforced cement matrix composites. Physica Status Solidi (a) 206(12):2783–2790
10. Glory J, Bonetti M, Helezen M, Mayne-L'Hermite M, Reynaud C (2008) Thermal and electrical conductivities of water-based nanofluids prepared with long multiwalled carbon nanotubes. J Appl Phys 103(9):094309
11. Tang QY, Shafiq I, Chan YC, Wong NB, Cheung R (2010) Study of the dispersion and electrical properties of carbon nanotubes treated by surfactants in dimethylacetamide. J Nanosci Nanotechnol 10(8):4967–4974
12. Shi T, Li Z, Guo J, Gong H, Gu C (2019) Research progress on CNTs/CNFs-modified cement-based composites–a review. Constr Build Mater 202:290–307
13. Maria F, Athanasia T, Fani G, Anaxagoras E (2022) Carbon nanotubes' amount and type: crucial parameters in mechanical performance enhancement on cement paste nanocomposites. In: Journal of physics: conference 2022, vol 2321, pp 012003. IOP Publishing (2022)
14. Thomoglou AK, Falara MG, Gkountakou FI, Elenas A, Chalioris CE (2022) Influence of different surfactants on carbon fiber dispersion and the mechanical performance of smart piezoresistive cementitious composites. Fibers 10(6):49

15. Siddique R, Mehta A (2014) Effect of carbon nanotubes on properties of cement mortars. Constr Build Mater 50:116–129
16. Yazdani N, Mohanam V (2014) Carbon nano-tube and nano-fiber in cement mortar: effect of dosage rate and water-cement ratio. Int J Mater Sci 4(2):45
17. Metaxa ZS, Konsta-Gdoutos MS, Shah SP (2013) Carbon nanofiber cementitious composites: effect of debulking procedure on dispersion and reinforcing efficiency. Cement Concr Compos 36:25–32

Effect of Polyformaldehyde Fibers on Durability of Concrete

Xiang Li, Pengjin Wu, Maoyi Liu, Yunhao Wang, Daifeng Wu, Zhiqiang Wang, and Xin Bi

Abstract The influence of polyformaldehyde (POM) fiber on durability of concrete was discussed through experiments. The strength, pore structure, impermeability, chloride ion corrosion resistance and frost resistance of concrete specimens with 5 mix proportions were tested. The findings demonstrate that POM fiber can enhance concrete's cube compressive strength and splitting tensile strength, reduce the average pore diameter, most integrable aperture, and porosity of concrete, and increase concrete's compactness. As POM fiber improves the compactness of concrete, it can be used to increase the durability of concrete, including impermeability, sulfate corrosion resistance and frost resistance.

Keywords POM fiber concrete · Pore structure · Concrete durability · Concrete strength

1 Introduction

Fiber concrete is formed by adding various fibers to concrete, which increases the durability and concrete's compressive and tensile strength [1–3]. At present, commonly used fiber types include polypropylene fiber, steel fiber, basalt fiber and glass fiber [4]. Researchers have conducted a great deal of study on the performance changes of these fibers on concrete, with a lot of positive outcomes. Polyformaldehyde (POM) fiber is a recently discovered and utilized high-performance fiber. POM fiber has excellent characteristics such as high strength, high modulus, corrosion

X. Li · P. Wu · Y. Wang
School of Civil Engineering, Chongqing University, Chongqing 400045, China

M. Liu · D. Wu · Z. Wang
Chongqing Urban Investment Infrastructure Construction Co., Ltd., Chongqing 400045, China

X. Bi (✉)
Department of Civil Engineering, Xi'an Jiaotong-Liverpool University, Suzhou 215123, China
e-mail: cqu2022@126.com

H.-Y. Jeon (ed.), *Proceedings of the International Conference on Geosynthetics and Environmental Engineering*, Lecture Notes in Civil Engineering 374,
https://doi.org/10.1007/978-981-99-4229-9_37

resistance and good dispersion in the composite matrix [5, 6]. Existing studies have shown that adding POM fibers to concrete will reduce the workability of concrete, but it can increase the strength of concrete [7, 8], lessen the shrinkage of concrete, and increase its resistance to cracking and high temperatures [6]. These studies show that POM has a good application prospect in concrete, but there are still few studies on the durability of POM fiber concrete, which cannot meet the needs of further popularization and application of POM fiber concrete. Therefore, this paper launched research work on the durability of POM fiber concrete.

2 Experimental Setups

2.1 Materials

Like other fibers, there is an optimal dosage of POM fiber for concrete. Referring to past related research results, this study selected 1.1 kg/m^3 as a fixed dosage. Research work has been carried out on concrete's durability, including impermeability, sulfate dry–wet cycle resistance, and freeze–thaw cycle resistance. A total of 5 water-binder ratios were designed in the study, and a benchmark group (JZ) and a POM fiber group (POM) were set for each water-binder ratio. The concrete mix proportion is shown in Table 1.

Table 1 Concrete mix proportion (kg/m^3)

No	Water-binder ratio	Water	POM fiber	Water reducer (%)	Cement	Fly ash	Sand	Gravel
JZ/POM	0.45	190.1	0/1.1	0	330.1	88.5	750	1050
JZ/POM	0.40	176.9	0/1.1	0.1	350.5	93.5	745	1035
JZ/POM	0.35	168.8	0/1.1	0.2	380.5	103	730	1025
JZ/POM	0.30	160.3	0/1.1	0.3	400.2	126	720	1000
JZ/POM	0.25	140.5	0/1.1	0.5	425.0	135	718	985

Among them:
JZ-Benchmark group;
POM-Polyformaldehyde fiber group;
Cement: Standard Portland cement P.O 42.5, fineness 0.6%;
Water: Ordinary tap water;
POM: Density 1.41 g/cm^3, average fiber length 19 mm, melting point 175 °C, tensile strength 750 MPa;
Fly ash: Chongqing Luohuang grade II, fineness 21%, water requirement ratio 103%, activity 70% (28 days);
Water reducer: FND retarded water reducer, water reducing rate 24%;
Sand: Fineness modulus 2.6, mud content less than 2%;
Gravel: The particle size range 5–20 mm, mud content 0.7%

2.2 Mechanical Properties of Concrete

The compressive and splitting tensile strength of concrete cubes at 28 days involved in this research were tested in accordance with the Standard for Test Methods of Mechanical Properties of Ordinary Concrete (GB/T50081).

2.3 Test on Impermeability, Sulfate Resistance and Freeze–thaw Resistance of Concrete

The impermeability, sulfate resistance and freeze–thaw cycle resistance of the concrete involved in this research were tested in accordance with the Standard for Test Methods of Long Term Performance and Durability of Ordinary Concrete (GB/T50082).

The impermeability of concrete is tested by the method of seepage height. The specimen is a 150 mm high cone, with the upper bottom diameter of 175 mm and the lower bottom diameter of 185 mm. 6 specimens are prepared for each group.

The specimen used for sulfate resistance dry–wet cycle of concrete is 100 mm × 100 mm × 100 mm cube, 6 specimens for each group. The circulation system is: soak in 5% sodium sulfate solution for 15 h, air dry for 1 h, then dry for 6 h, and finally cool for 2 h. The research carried out 150 cycles, and after 30, 90 and 150 cycles, the specimens' compressive strengths were tested to determine the concrete's sulfate corrosion resistance.

The freeze–thaw cycle performance of concrete is tested by quick freezing method, and the specimen is a cuboid of 100 mm × 100 mm × 400 mm. The circulation system is: the single cycle time is controlled within 2–4 h, and the melting of the specimens is controlled at no less than a quarter of the entire cycle time. When freezing and thawing, control the minimum temperature of the center of the specimens at -18 ± 2 °C, the maximum temperature at 5 ± 2 °C, and the minimum and maximum temperatures in the box at -20 ± 2 °C and 15 ± 2 °C. Taking the completion of 25 cycles as a full cycle, use the DT-20 dynamic elastic mold machine to measure the specimens' dynamic elastic modulus.

2.4 Concrete Pore Structure Testing

The main variable studied was the addition of POM fibers. Therefore, the test under single water-binder ratio has been able to reflect the influence of POM fiber on the concrete pore structure in general. Therefore, the study exclusively examined the concrete's pore structure of specimens under a 0.35 water-binder ratio. The specimens used to test the concrete pore structure were subjected to the same curing conditions as those used to test the durability performance. When the test condition is reached,

the concrete to be tested need to be crushed, after which concrete particles with a size between 2.5 mm and 5 mm are selected with a sieve. Next, the concrete is dehydrated with acetone and the specimens are dried with a vacuum dryer. Finally, the pore structure inside the concrete is tested using an Auto IV9510 automatic mercury porosimeter.

3 Results and Discussion

3.1 Compressive and Tensile Strength of Concrete

Figure 1 shows the comparison of the compressive and tensile strength of the JZ concrete and POM concrete at 28 days under different water-binder ratios. Figure 1 illustrates that under various conditions of water-binder ratios, the compressive and tensile strength of concrete have increased after adding POM fibers. According to different water-binder ratios, the compressive strength increases by 4.7–8.3%, and the tensile strength increases by 15.4–22%.

Due to the good physical, chemical and dispersion properties of POM fiber itself, when added to concrete, POM fiber can be dispersed equally in concrete and forms a strong bond with it. When the concrete is under load, these uniformly distributed POM fibers can effectively block the development of fractures in the concrete, consuming a certain energy which leads to concrete failure. Therefore, the use of POM fibers can boost the concrete's compressive and tensile strength to some extent.

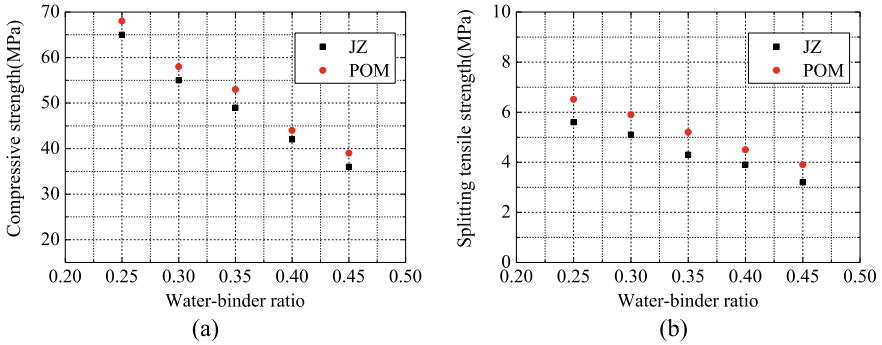

Fig. 1 Influence of POM fiber on the strength of concrete: **a** cubic compressive strength; **b** splitting tensile strength

3.2 Concrete Impermeability

Figure 2 shows the comparison of the impermeability performance of JZ concrete and POM concrete under different water-binder ratios. It indicated that as concrete water-binder ratios decline, concrete impermeability increases. Simultaneously, the addition of POM fibers to concrete can effectively enhance the its impermeability.

Table 2 shows the pore structure of the 0.35 mix proportion concrete specimens. It indicated that after adding POM fibers to concrete, the porosity of concrete dropped from 21.7% to 17.2%, the most integrable aperture of concrete dropped from 85.7 nm to 47.6 nm, and the average pore diameter dropped from 25.4 nm to 23.5 nm. These show that adding POM fibers can improve the compactness of concrete.

The compactness of the concrete directly affects its impermeability. For the same type of concrete (JZ and POM groups), the internal compactness of the concrete rises as the water-binder ratio falls. Consequently, the impermeability of concrete rises as the water-binder ratio falls. For POM fiber concrete, POM fiber fills the pores in the concrete, preventing micro-cracks' development within the concrete, improving concrete's compactness concurrently. Moreover, fibers can enhance concrete's resistance to water pressure. Therefore, adding POM fiber can enhance concrete's impermeability.

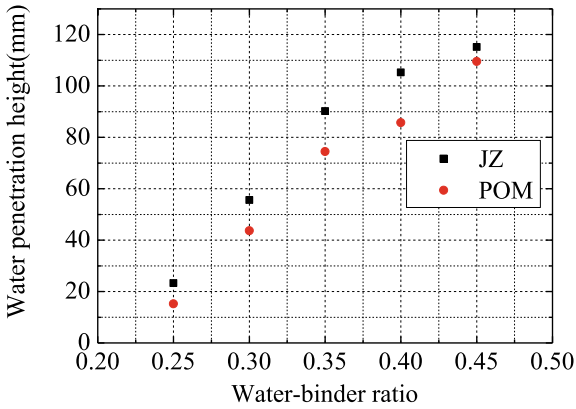

Fig. 2 Impermeability of concrete

Table 2 Pore structure of concrete

	Average pore size (nm)	Most integrable aperture (nm)	Porosity (%)
JZ	25.4	85.7	21.7
POM	23.5	47.6	17.2

3.3 *Concrete Resistance to Sulfate Dry–wet Cycle Performance*

Figure 3 and Table 3 are the comparison between concrete's strength after sulfate dry–wet cycle and concrete's strength with standard-cured, and changes of concrete's strength after the sulfate dry–wet cycle. These results indicate that when sulfate dry–wet cycle index increases, the concrete's strength initially increases and eventually falls. After 30 and 90 cycles, compared with the strength of concrete cured simultaneously, the strength of concrete corroded by sulfate is greater. When the cycle index reaches 150, the erosion effect of sulfates on the concrete's strength begins to appear, and compared with the strength of concrete cured simultaneously, the corroded concrete's strength is lower.

When sulfates erode concrete, the etching solution's sulfate ions will react with the concrete's calcium hydroxide and calcium aluminate hydrate to generate gypsum and ettringite. At the early stage of erosion, the gypsum and ettringite produced by the erosion filled the pores and micro-cracks inside the concrete (as shown in Table 4), and the expansion caused by the filling did not exceed the tensile limit of the concrete. The concrete's compressive strength increases as its internal density increases. Therefore, at this stage, the strength of concrete eroded by sulfates are higher than that of concrete cured at the same time. With the further erosion of sulfates, the reactants generated by the erosion increase, which makes the expansion exceed concrete's ultimate tensile strength and damage its internal structural integrity, thus reducing concrete's compressive strength.

We can also find that when the POM fibers were added to the concrete, after 30 and 90 cycles, the rate of strength growth in concrete increased. Meanwhile, after 150 cycles and the degradation effect of sulfates on concrete performance appeared, the decrease rate of compressive strength of concrete added with POM fiber was lower than that of the JZ concrete. It shows that POM fiber improves the sulfate erosion resistance of concrete. The main reason for this phenomenon is that POM fibers fill the pores and micro-cracks inside the concrete, making it more difficult for sulfates to penetrate into the concrete.

Concrete's erosion resistance coefficient can more clearly indicate its capacity to withstand sulfate, which is calculated according to the Standard for Test Methods of Long-term Performance and Durability of Ordinary Concrete (GB/T50082). It can be seen from Fig. 4 that after 30, 90 and 150 cycles, the corrosion resistance coefficients of the concrete added with POM fibers are all higher than those of the JZ concrete. It was determined that the incorporation of POM fibers can enhance concrete's sulfate resistance.

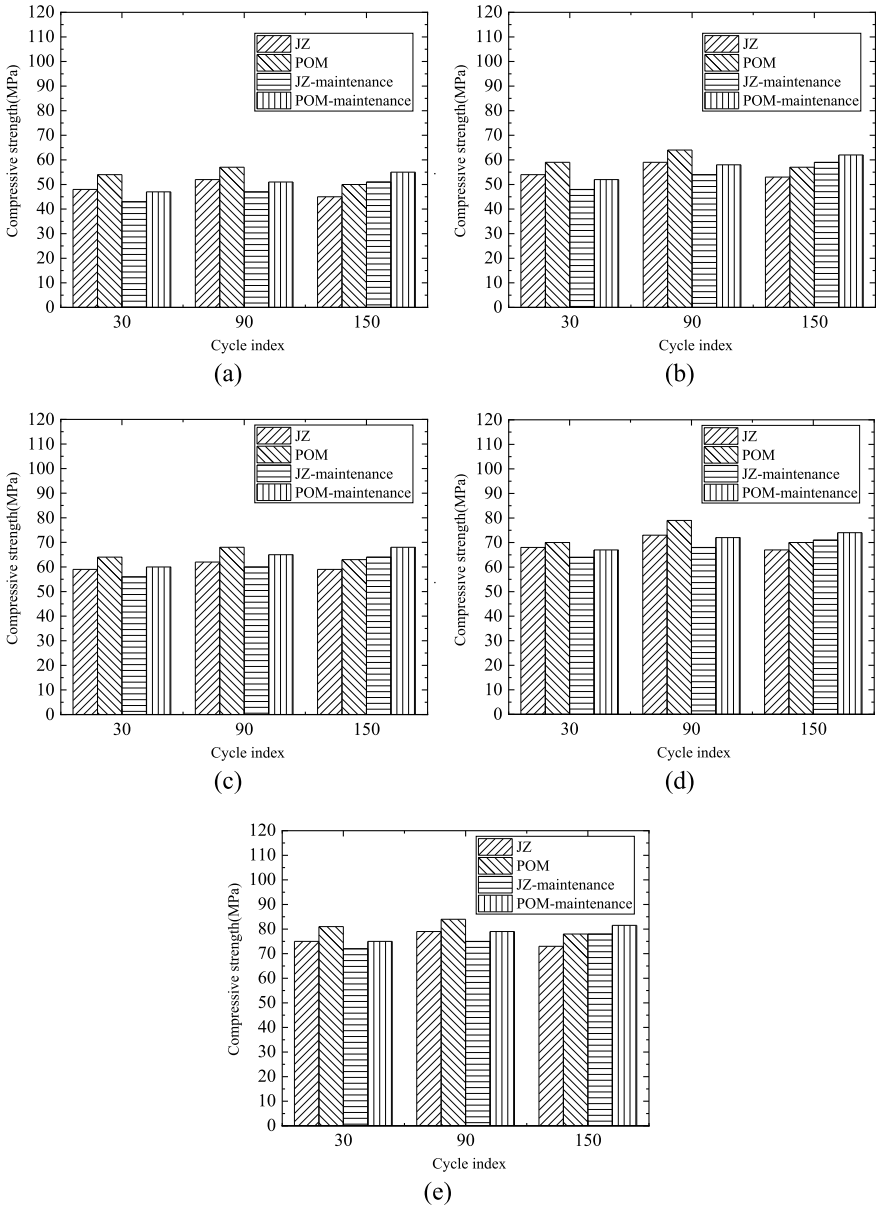

Fig. 3 Comparison between compressive strength of concrete after dry–wet cycle of sulfate and that of standard curing concrete: **a** 0.45 **b** 0.4 **c** 0.35 **d** 0.3 **e** 0.25

Table 3 Changes of concrete strength after sulfate dry–wet cycle

Water-binder ratio (%)		Cycle index		
		30	90	150
0.25	JZ	4.17	5.33	−6.41
	POM	8.00	6.33	−4.29
0.3	JZ	6.25	7.35	−5.63
	POM	4.48	9.72	−5.41
0.35	JZ	5.36	3.33	−7.81
	POM	6.67	4.62	−7.35
0.4	JZ	12.50	9.26	−10.17
	POM	13.46	10.34	−8.06
0.45	JZ	11.63	10.64	−11.76
	POM	14.89	11.76	−9.09

3.4 Freeze–thaw Cycle Resistance of Concrete

Table 5 and Fig. 5 show the relative dynamic modulus of elasticity of concrete after freeze–thaw cycles. Table 5 demonstrates that as freeze–thaw cycles increases, the relative dynamic elastic modulus of concrete gradually falls. In the meantime, after each cycle, the relative dynamic elastic modulus of the concrete filled with POM fiber was higher than JZ concrete, which indicated that POM fiber can enhance the concrete's frost resistance.

POM fiber's enhancement in concrete frost resistance is mainly related to the filling effect of POM fiber on pores and micro-cracks in concrete. Table 6 shows the concrete pore structure after several cycles. It indicated that POM concrete's pore structure is significantly lower than JZ concrete after freeze–thaw cycles. The mechanism underlying concrete freeze–thaw destruction is that the water in concrete pores and micro-cracks repeatedly freezes and expands, constantly increasing the concrete's intrinsic flaws, thus reducing concrete's performance. POM fiber can efficiently lessen the amount of water in concrete which produces icing phenomenon, hence enhancing concrete's freeze–thaw performance. Moreover, POM fiber can also play a role in the development of concrete cracks and inhibit the development of cracks.

4 Conclusions

(1) POM fiber can play a tie effect on concrete and inhibit the crack development of concrete when it is loaded. Studies have shown that adding 1.1 kg/m^3 POM fibers can improve concrete's cubic compressive strength and splitting tensile strength when water-binder ratio is in 0.25–0.45. The strength of concrete under

Table 4 Pore structure of concrete after sulfate dry–wet cycle

	30			90			150		
	Average pore size (nm)	Most integrable aperture (nm)	Porosity (%)	Average pore size (nm)	Most integrable aperture (nm)	Porosity (%)	Average pore size (nm)	Most integrable aperture (nm)	Porosity (%)
JZ	31.5	65.5	20.6	27.6	44.1	18.5	37.2	90.5	23.5
POM	20.6	27.5	19.5	19.1	37.7	15.8[2]	29.7	80.1	22.1

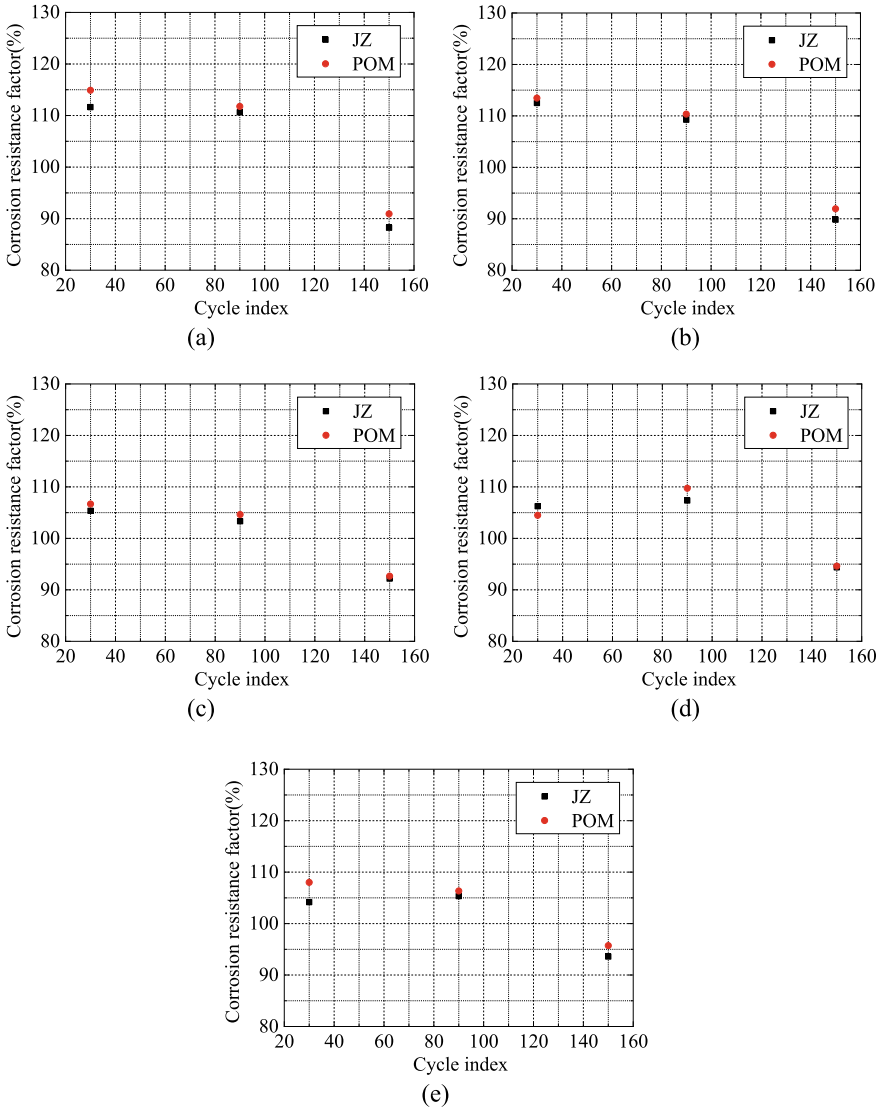

Fig. 4 Concrete's erosion resistance coefficient under different water-binder ratios: **a** 0.45 **b** 0.4 **c** 0.3 **d** 0.25 **e** 0.2

varying water-binder ratios increases in distinct ranges: the compressive strength increases by 4.7%–8.3%, and the tensile strength increases by 15.4%–22%;

(2) For the same type of concrete (JZ and POM groups), as the concrete water-binder ratio decreases, the impermeability of the concrete increases; Sulfate erosion will raise the concrete's compressive strength until the expansion caused by

Table 5 Concrete's relative dynamic elastic modulus after freeze–thaw cycle (%)

Cycle index	0.25		0.3		0.35		0.4		0.45	
	JZ	POM	JZ	POM	JZ	POM	JZ	POM	JZ	POM
25	97.4	99.2	97.1	99.5	93.5	97.8	95.4	96.3	93.4	95.4
50	90.6	95.6	87.2	93.7	87.7	92.2	87.6	92.6	86.5	93.2
75	84.2	90.5	79.9	83.2	73.2	79.4	71.4	80.5	69.4	78.6
100	72.1	75.5	71.4	75.5	66.8	72.4	65.3	69.4	52.1	65.5

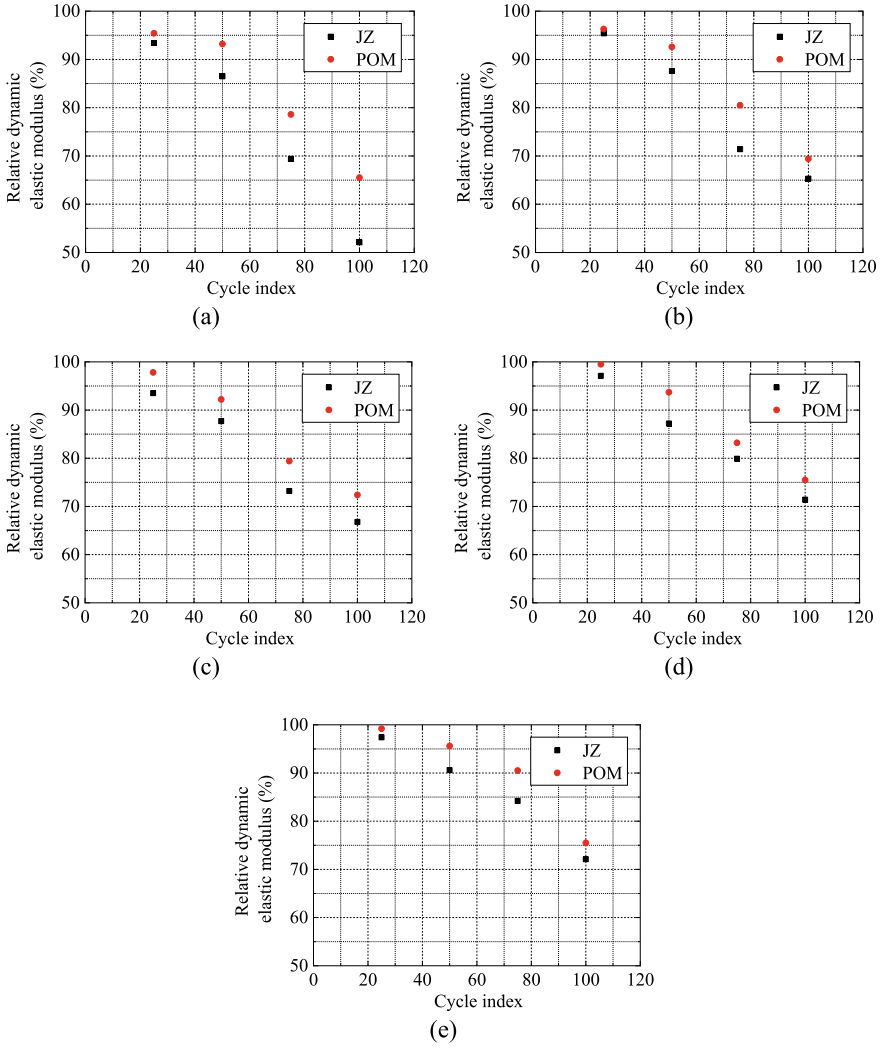

Fig. 5 Concrete's relative dynamic elastic modulus under different water-binder ratios: **a** 0.45 **b** 0.4 **c** 0.35 **d** 0.3 **e** 0.25

Table 6 Concrete's pore structure after freeze–thaw cycle

Cycle index	Parameter	JZ	POM
25	Average pore size (nm)	21.3	17.5
	Most integrable aperture (nm)	56.2	25.3
	Porosity (%)	20.1	17.6
50	Average pore size (nm)	24.6	19.6
	Most integrable aperture (nm)	70.4	29.6
	Porosity (%)	21.33	19.65
75	Average pore size (nm)	31.9	23.6
	Most integrable aperture (nm)	86.8	55.3
	Porosity (%)	24.53	22.8
100	Average pore size (nm)	34.4	32.6
	Most integrable aperture (nm)	92.68	88.1
	Porosity (%)	26.1	25.3

sulfate erosion surpasses the concrete's ultimate tensile strength; as freeze–thaw cycle index rises, the relative dynamic elastic modulus of concrete falls gradually, and the frost resistance performance decreases;

(3) Due to the good dispersion and filling performance of POM fibers, adding POM fibers to concrete can enhance concrete's compactness and lessen the pore structure parameters of concrete including average pore size, most integrable aperture and porosity. It is precisely because POM fibers increase the compactness of concrete, so adding POM fibers to concrete can enhance concrete's durability including water permeability, sulfate corrosion resistance and frost resistance.

References

1. Chen L et al. (2023) Green construction for low-carbon cities: a review. Environ Chem Lett
2. Chen L et al (2022) Strategies to achieve a carbon neutral society: a review. Environ Chem Lett 20(4):2277–2310
3. Chen L, Yang M (2021) The impact of the use of new environmentally friendly materials on the management of construction projects: taking straw fiber materials as an example. J Phys Conf Ser 2011(1):012019
4. Wang Z et al (2022) Study on flexural fatigue properties of POM fiber airport pavement concrete. Polymers 14(15):2979
5. Guo L et al (2022) Dynamic compression mechanical properties of polyoxymethylene-fiber-reinforced concrete. Materials 15(21):7784
6. Rui Y et al (2022) Comparative study on the effect of steel and polyoxymethylene fibers on the characteristics of Ultra-High Performance Concrete (UHPC). Cement Concr Compos 127:104418
7. He J et al (2021) Mechanical properties of high strength POM-FRCC and its performance under elevated temperatures. Constr Build Mater 290:123177
8. Ravichandran D et al (2022) Influence of fibers on fresh and hardened properties of Ultra High Performance Concrete (UHPC)—a review. J Build Eng 57:104922

Experimental Research of Concrete Shrinkage Under Constraint Based on Capillary Tension Theory

Maoyi Liu, Daifeng Wu, Songxiao Huang, Zhiqiang Wang, and Pengjin Wu

Abstract In this work, a method based on the capillary tension theory is suggested for figuring out how much concrete will shrink while it is held in place by steel plates and studs. When concrete examples were restrained by steel plates of various thicknesses and materials with variations in their diameters, heights, and stud counts, the pore structure and shrinkage strain of the plates were examined. The findings demonstrate that steel plates and studs have a considerable impact on the pore structure of the specimens, and that as the plates and studs exert more constraint on the samples, the values of the pore structure parameters of the samples will grow linearly. Additionally, the coordinated deformation between the constrained parts that results from the decrease of capillary stress in the concrete would lessen specimen deformation and shrinkage. The purpose of this research is to provide recommendations for predicting shrinkage stresses in concrete that is supported by steel plates and studs.

Keywords Capillary tension theory · Steel plates · Studs · Concrete shrinkage prediction

1 Introduction

Shrinkage results in a continuous decrease in the volume of the concrete in the absence of external stresses. Tensile stresses are created by the restraining body as it prevents the concrete from shrinking; they are referred to as restraining tensile stresses. Concrete cracking may be prevented in part by the restricting tensile stress. Concrete cracking may be handled in one of two ways: (1) To look into how the restrained body affects concrete shrinkage; (2) To forecast the strain that concrete would experience during shrinkage in the restrained body.

M. Liu · D. Wu · Z. Wang
Chongqing Urban Investment Infrastructure Construction Co., Ltd., Chongqing 400045, China

S. Huang · P. Wu (✉)
School of Civil Engineering, Chongqing University, Chongqing 400045, China
e-mail: wendy2028@126.com

H.-Y. Jeon (ed.), *Proceedings of the International Conference on Geosynthetics and Environmental Engineering*, Lecture Notes in Civil Engineering 374,
https://doi.org/10.1007/978-981-99-4229-9_38

The effects of reinforcing on shrinkage have been the subject of earlier studies on concrete shrinkage [1]. Steel-plate-reinforced concrete composite shear walls (abbreviated as SPRWs), often referred to as composite shear walls made of steel plate reinforced concrete, are frequently employed in high-rise and super high-rise buildings. These walls generally have a high strength concrete construction and excellent mechanical properties. High-strength concrete shrinks more than conventional concrete does, and its initial tensile strength is rather low [2]. On the other hand, SPRWs are restricted by the combined action of steel plates, studs, and reinforcement in reinforced concrete shear walls that are solely restrained by steel reinforcement. SPRW has a propensity to break because of its rapid shrinkage and intricate restriction.

The effect of studs and plates has rarely been studied in current research into concrete shrinkage. Yousef et al. [3] investigated the effect of specifications of stud on concrete by tests. Chen et al. [4] investigated concrete shrinkage effect with different components re-strained to protect structures against aggressive environment challenges. Due to the lack of research in this area, our structural codes for SPRW crack control are based on the existing reinforcement literature. These terms and conditions are sometimes valid, but in most cases they are not applicable. As a result, many SPRWs experienced massive cracking during construction.

Concrete shrinks as a result of capillary strains being created on the pore walls as a result of water being consumed within the concrete [5]. The capillary tension hypothesis allows for the prediction of common concrete's shrinkage [6]. Due to this limitation, this article examines the pore structure, shrinkage strain, and mechanical characteristics of concrete [7, 8]. A technique that can forecast the shrinking strain is suggested in light of the test findings. The findings of this research demonstrate that there is excellent agreement between measured and anticipated concrete shrinkage values under restricted body limitations.

2 Theoretical Model

This work develops a concrete model with limited steel plates and studs. The model's overall length is L, its stud diameter is d, and its length is n (Fig. 1). Shear stresses will be created between the steel plate, studs, and concrete when the capillary tension causes the concrete to shrink since the constraint bodies will not be deformed. Shear tension travels in the opposite direction to concrete shrinkage. The constrained part will experience a compressive stress as a result of the shear stress.

According to the capillary tension hypothesis, when the water inside the concrete is consumed, the capillary stress (σ_{ca}) which is the main factor causing shrinkage of the concrete, is generated in the pore wall. This can be expressed by the following equation:

$$\Delta P = \frac{2\gamma cos\theta}{r}\sigma_{ca} \tag{1}$$

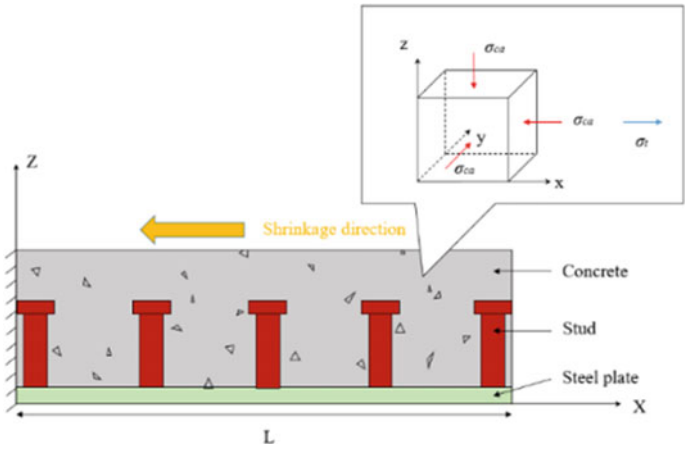

Fig. 1 Analytical model

wherein γ is the capillary pore wall tension (7.28×10^{-2} N/m at 20 °C), θ is the liquid–solid interface contact angle, and r is the critical diameter.

As the studs are not arranged continuously, the restrained concrete contains two typical section: Sect. 1, steel plate, concrete and studs; Sect. 2, steel plate and concrete (Fig. 2). The total length of the first part is nd and the total length of the second part is L-nd. Simplifying the stud head, the stud head diameter is equal to the stud diameter and the cross-sectional area of the stud is its projected area. In addition to this, in Sect. 1, the cross-sectional area of the studs is expressed by their projected area.

According to the mechanics of materials, the strains in the x-direction for the Sects. 1 and 2 specimens can have the following expressions:

$$\begin{aligned}\varepsilon_{c-i} &= \frac{1}{E_s}\left[\sigma_x - \mu\left(\sigma_y + \sigma_z\right)\right] = \frac{1}{E_s}\left[\left(\sigma_{ca} - \sigma_{t-i}\right) - \mu\left(\sigma_{ca} + \sigma_{ca}\right)\right] \\ &= \frac{1-2\mu}{E_s}\sigma_{ca} - \frac{1}{E_s}\sigma_{t-i}\end{aligned} \tag{2}$$

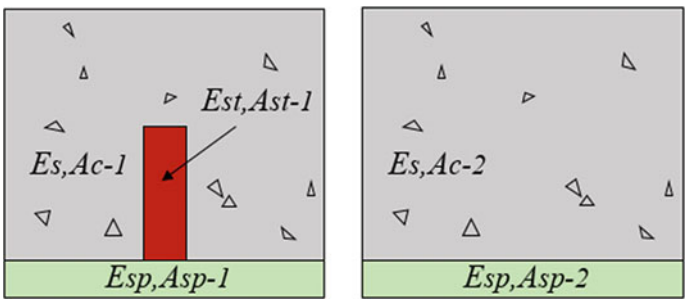

Fig. 2 Two sections in concrete

The restricted tensile stress on the concrete in section i (i = 1, 2), $\sigma_{t\text{-}i}$ is the Poisson's ratio, and $\varepsilon_{c\text{-}i}$ is the concrete strain in section i (i = 1, 2). E_s is the elastic modulus (EM) of the critical matrix around the capillary pore.

ΔL stands for the specimen's overall displacement. shrinkage stress may be characterized as follows:

$$L = \varepsilon_{c-1} nd + \varepsilon_{c-2}(L - nd) \tag{3}$$

wherein $\varepsilon_{c\text{-}i}$ is the concrete strains in the section.

Thus the total strain of the whole modal can be expressed as:

$$\varepsilon_{c-\text{total}} = \frac{\Delta L}{L} = \frac{\varepsilon_{c-1} nd + \varepsilon_{c-2}(L - nd)}{L} \tag{4}$$

wherein $\varepsilon_{c\text{-}total}$ is the total strain in the restrained concrete.

According to the equilibrium of forces, the studs and steel plates are in pressure and the concrete is in tension during shrinkage. The sections satisfy the following equations:

$$\sigma_{t-1} A_{c-1} = \sigma_{sp-1} A_{sp-1} + \sigma_{st-1} A_{st-1} \tag{5}$$

$$\sigma_{t-2} A_{c-2} = \sigma_{sp-2} A_{sp-2} \tag{6}$$

$\sigma_{t\text{-}i}$ is the concrete's confining tensile stress in section i (i = 1, 2), and $\sigma_{sp\text{-}i}$ is the steel plate's compressive stress in section i. The cross-sectional areas of the concrete, steel plate, and studs in section i (i = 1, 2) are $A_{c\text{-}i}$, $A_{sp\text{-}i}$, and $A_{st\text{-}i}$.

Where $\sigma_{sp\text{-}1}$ is the compressive stress in Sect. 1 of the steel plate and $\sigma_{sp\text{-}2}$ is the compressive stress in Sect. 2 of the steel plate, where $\sigma_{t\text{-}1}$ is the confined tensile stress in part 1 of the concrete, $\sigma_{t\text{-}2}$ is the confined tensile stress in Sect. 2 of the concrete, and $\sigma_{t\text{-}1}$ is the compressive stress in Sect. 1 of the steel plate. The cross-sectional area of the first portion of the concrete is denoted by the letter $A_{c\text{-}i}$, the first part of the steel plate by the letter $A_{sp\text{-}i}$, and the first part of the studs by the letter $A_{st\text{-}i}$.

Thus, the confining tensile stresses of each section can be expressed by the following equation:

$$\sigma_{t-1} = \frac{A_{sp-1}}{A_{c-1}} \sigma_{sp-1} + \frac{A_{st-1}}{A_{c-1}} \sigma_{st-1} \tag{7}$$

$$\sigma_{t-2} = \frac{A_{sp-2}}{A_{c-2}} \sigma_{sp-2} \tag{8}$$

In addition, the strains of studs and steel plates under confining compressive stresses in Sect. 1 are represented by Eqs. (9) and (10). The strains of the steel plates under the confining compressive stresses in Sect. 2 are represented by Eq. (11):

$$\varepsilon_{sp-1} = \frac{\sigma_{sp-1}}{E_{sp}} \tag{9}$$

$$\varepsilon_{st-1} = \frac{\sigma_{st-1}}{E_{st}} \tag{10}$$

$$\varepsilon_{sp-2} = \frac{\sigma_{sp-2}}{E_{sp}} \tag{11}$$

wherein E_{sp} is the modulus of elasticity of the steel plate and E_{st} is the modulus of elasticity of the stud; $\varepsilon_{sp\text{-}i}$ is the strain in the section i (i = 1, 2) of the steel plate under the action of the confining compressive stress; $\varepsilon_{st\text{-}i}$ is the strain in the section i (i = 1, 2) of the stud.

In Sect. 1, an arbitrary length of the concrete under restraint is considered I. The displacements of concrete, studs and plates under capillary stresses in Sect. 1 are the same according to the requirement of coordination of deformations:

$$\delta_{c-1} = \delta_{sp-1} = \delta_{st-1} \tag{12}$$

wherein $\delta_{c\text{-}1}$, $\delta_{sp\text{-}1}$, and $\delta_{st\text{-}1}$ represent, respectively, the displacements of steel plates, concrete, and studs under capillary stresses in Sect. 1.

Therefore,

$$\frac{\delta_{c-1}}{1} = \frac{\delta_{sp-1}}{1} = \frac{\delta_{st-1}}{1} = \varepsilon_{c-1} = \varepsilon_{sp-1} = \varepsilon_{st-1} \tag{13}$$

Similar to the equation in Sect. 2:

$$\varepsilon_{c-2} = \varepsilon_{sp-2} \tag{14}$$

Substituting the Eqs. (9), (10) and (13) into the Eq. (7) yields the Eqs. (15), and the (11) and (14) into the Eq. (8) yields the Eq. (16):

$$\sigma_{t-1} = \frac{A_{sp-1}}{A_{c-1}}\varepsilon_{c-1}E_{sp} + \frac{A_{st-1}}{A_{c-1}}\varepsilon_{c-1}E_{st} \tag{15}$$

$$\sigma_{t-2} = \frac{A_{sp-2}}{A_{c-2}}\varepsilon_{c-2}E_{sp} \tag{16}$$

Substituting the Eqs. (15) and (16) into the Eq. (2) yields the following equation:

$$\&\varepsilon_{c-1} = \frac{(1-2\mu)}{\left(E_s + \frac{A_{sp-1}}{A_{c-1}}E_{sp} + \frac{A_{s+1}}{A_{c-1}}E_{st}\right)}\frac{2\gamma}{r} \tag{17}$$

$$\&\varepsilon_{c-2} = \frac{(1-2\mu)}{\left(E_s + \frac{A_{sp-2}}{A_{c-2}}E_{sp}\right)}\frac{2\gamma}{r} \tag{18}$$

Table 1 Concrete mixing ratios (kg/m^3)

Mix	Water-binder ratio	Cement	Water	Fly ash	Sand	CA	Polycarboxylate superplasticizer (PS)
C40	0.31	410	160	100	720	1000	10.5

The shrinkage strain of concrete under the constraint is calculated by substituting Eqs. (17) and (18) into Eq. (4) and setting $\rho = nd/L$:

$$\varepsilon_{c-\text{ total}} = \frac{2\gamma(1-2\mu)}{r}\left[\rho\frac{1}{E_s + \frac{A_{sp-1}}{A_{c-1}}E_{sp} + \frac{A_{t+1-1}}{A_{c-1}}E_{st}} + (1-\rho)\frac{1}{E_s + \frac{A_{sp-2}}{A_{c-2}}E_{sp}}\right] \tag{19}$$

3 Experimental Procedure

3.1 Materials

The concrete mixes are shown in the Table 1. The cementitious material is fly ash and silicate cement (PO42.5R). Quartz sand is used for the fine aggregate. The modulus of fineness is 3.0. The coarse aggregate is limestone with a maximum nominal grain size of 20 mm.

3.2 Measuring Shrinkage

Prepare two specimens with different constraints to measure shrinkage: (1) specimens under steel plate restraint and (2) specimens under stud and steel plate restraint. The specimens were fabricated using Plexiglas molds that could be assembled from all four sides, with dimensions of 150 × 150 × 1000 mm. Component parts of each specimen are given in Table 2, and the material properties of constrained components are described in Table 3.

To measure the deformation of each specimen, a linear variation transformer (LVDT) with an accuracy of 1 mm and a measuring range of 2 mm is put in the middle of the cross section at either end of the specimen. At the time of the measurement, the outside temperature was maintained at 20 ± 1 °C. The relative humidity was kept at 60 ± 5 percent.

Table 2 List of tests

No	Thickness of steel plates (mm)	Diameter of studs (mm)	Height of studs (mm)	Number of studs (mm)	Restraining material (studs/steel plates/)
P	–	–	–	–	–
Sp-1	3	–	–	–	Q345A/–
Sp-2	5	–	–	-	Q345A/–
Sp-3	8	–	–	–	Q345A/–
Sp-4	8	–	–	–	Q500–7A/–
St-1	3	13	60	24	Q345A/ML15AL–
St-2	3	13	120	24	Q345A/ML15AL
St-3	3	13	120	30	Q345A/ML15AL
St-4	3	19	60	24	Q345A/ML15AL
St-5	3	19	120	24	Q345A/ML15AL
St-6	3	28	60	24	Q345A/ML15AL
St-7	3	28	120	24	Q345A/ML15AL

Table 3 Characteristics of constraint components

	Material	EM ($\times 10^4$ Mpa)	Yield strength (Mpa)	Ultimate strength (Mpa)
Steel plate	Q345A	20.6	390.0	555.0
	Q500-7	15.4	320.0	500.0
Stud	ML15AL	19.0	419.0	520.3

3.3 Concrete Porosity

Concrete porosity tests were carried out by casting distinct specimens, much as the experiments used to measure shrinkage strain in concrete, to determine the porosity of concrete. Samples were taken from the specimens at 3, 7, and 28 days into the test period. Concrete particles between 2.5 mm and 5 mm in size were extracted from the samples by first crushing and then sieving them. Acetone was then used to stop the concrete from hydrating, and the samples were dried using a vacuum desiccator. An automated IV9510 mercury porosimeter was used to evaluate the concrete's pore structure.

3.4 Mechanical Properties

The cubic compressive strength, splitting tensile strength (STS), EM, and Poisson's ratio of the concrete were evaluated to ascertain the results (shown in Table 4).

Table 4 Physical characteristics of concrete

Age(days)	Physical properties			
	Cubic compressive strength (Mpa)	STS (Mpa)	EM ($\times 10^4$Mpa)	Poisson's ratio
3	33.5	2.1	2.97	0.17
7	38.6	2.9	3.44	0.172
28	41.2	3.2	3.76	0.175

4 Results and Analysis

4.1 Concrete Pore Structure

Table 5 shows the pore structure parameters at all ages for concrete confined by steel plates only.

The pore structure characteristics for concrete constrained by studs and steel plates are shown in Table 6 for all ages.

The pore structure parameters decrease with increasing curing time. The pore structure parameters for normal concrete specimens (P) at 3 d (39.76 nm, 19.53%, 19.48 nm and 52.01 nm, respectively) were greater than each value at 28 d (16.46 nm, 13.74%, 12.44 nm and 27.73 nm, respectively).

Table 5 Pore characteristics of samples held in place by steel plates

Age (days)		Critical capillary diameter (nm)	Porosity (%)	Median pore diameter (nm)	Median pore diameter (nm)
P	3	39.76	19.53%	19.48	52.01
	7	26.58	17.08%	15.74	40.29
	28	16.46	13.74%	12.44	27.73
Sp-1	3	37.78	24.22%	22.96	55.30
	7	29.68	15.84%	17.35	45.82
	28	18.03	14.83%	11.67	33.15
Sp-2	3	53.81	25.88%	24.90	60.07
	7	41.57	22.07%	21.18	52.61
	28	25.65	18.24%	15.96	37.01
Sp-3	3	72.29	29.60%	27.54	81.22
	7	48.13	26.39%	25.96	69.16
	28	31.91	20.71%	18.75	47.19
Sp-4	3	63.84	27.25%	25.49	70.54
	7	45.07	23.79%	21.19	55.41
	28	30.41	18.52%	17.84	42.52

Table 6 Pore-related characteristics of the specimens are held in place by steel plates and studs

Age (days)		Critical capillary diameter (nm)	Porosity (%)	Median pore diameter (nm)	Median pore diameter (nm)
St-1	3	51.99	22.90%	24.25	60.64
	7	33.47	18.88%	20.16	47.91
	28	23.47	16.08%	14.87	39.20
St-2	3	54.41	25.01%	23.39	62.94
	7	36.98	20.59%	19.21	44.85
	28	25.49	17.86%	13.05	42.08
St-3	3	56.74	25.11%	22.20	63.03
	7	41.40	21.60%	20.99	52.06
	28	27.03	18.31%	16.83	41.26
St-4	3	60.96	26.80%	25.50	70.10
	7	42.61	22.30%	20.90	50.25
	28	29.31	19.09%	17.33	44.00
St-5	3	65.55	27.79%	25.70	72.99
	7	47.15	23.97%	20.76	53.46
	28	31.68	21.23%	19.70	46.72
St-6	3	68.88	29.17%	27.19	75.26
	7	48.13	25.63%	23.66	57.09
	28	33.97	22.47%	18.36	49.65
St-7	3	73.87	30.52%	28.46	79.01
	7	52.48	29.33%	25.26	62.39
	28	35.65	23.68%	24.06	51.07

There are two main reasons why the pore structure of concrete gradually decreases with increasing age: (1) During the increasing age of concrete, the hydration of cement continues, and its hydration products continuously fill all the pores and cracks in concrete, thus decreasing the concrete pore structure. (2) During the hydration of cement, the water in the pores of concrete is continuously consumed, thus generating capillary stresses in the walls of the concrete pores. In addition to making pore structure gradually decrease with the increasing age, these two causes also lead to a decrease of concrete pore structure parameters.

The size of the concrete's pores is significantly influenced by the steel plate. With increasing steel plate thickness, the pore size steadily became larger. After 28 days of curing, Sp-3's critical capillary diameter was 31.91 nm, its porosity was 20.71%, its average pore size was 18.75 nm, and its median pore size was 47.19 nm. Sp-3 was constrained by steel plates that were 10 mm thick. The difference between this and Sp-2 constrained by 6 mm thick steel plates was 6.26 nm, 1.76%, 2.79 nm, and 10.18 nm, or 18.24%, 15.96 nm, and 37.01 nm, respectively. 6.26 nm, 1.76%, 2.79 nm, and 10.18 nm are greater than the Sp-1 limit of 18.03 nm, 14.83%, 11.67 nm,

and 33.15 nm, which is imposed by a 4 mm thick steel plate, by 13.88 nm, 5.17%, 7.08 nm, and 14.04 nm. The pore size of the concrete is affected by both the thickness of the steel plate and the EM of the plate, with the pore structure of the concrete progressively becoming larger as the EM of the plate rises. Sp-3 has a greater EM than Sp-4 (20.6×10^4 MPa > 15.4×10^4 MPa). At all ages, Sp-3's pore structure characteristics were greater than those of Sp-4.

There are three parameters involved in relation to studs, diameter, height and number. The stud heights used in this paper are all 3 mm, so it is possible to study the effect of the third on the concrete pore size when two of the three parameters are held constant.

Contrary to typical concrete specimens, constrained concrete is exposed to both capillary stresses and restricting tensile forces that are directed in the opposite direction of the capillary stresses. The restricted specimen's concrete has a less porous structure due to the combined effects of capillary tension, confining tensile stress, and cement hydration product filling.

$$\overline{\sigma}_{c-\text{total}} = E_s \times \frac{2\gamma(1-2\mu)}{r}\left[\rho\frac{1}{E_s + \frac{A_{sp-1}}{A_{c-1}}E_{sp} + \frac{A_{t-1}}{c_{c-1}}E_{st}} + (1-\rho)\frac{1}{E_s + \frac{A_{sp-2}}{c_{c-2}}E_{sp}}\right] \tag{20}$$

wherein $\overline{\sigma}_{c-\text{total}}$ is expressed as the average combined force on the concrete under the combined action of the stud and steel plate on the hole wall.

A new parameter restraint factor (λ) is proposed to gauge the restraint effect of the restraining components on the concrete.

$$\lambda = \frac{1}{(1-2\mu)\left[\rho\frac{1}{E_s+\frac{A_{sp-1}}{A_{c-1}}E_{sp}+\frac{A_{st-1}}{A_{c-1}}E_{st}} + (1-\rho)\frac{1}{E_s+\frac{A_{sp-2}}{A_{c-2}}E_{sp}}\right]} \tag{21}$$

According to Eq. (21), the confinement coefficient steadily rises with increasing steel plate thickness and EM, as well as height, diameter, and stud count at the same age (μ and E_s stay constant), with constant cross-sectional specimen dimensions.

Substituting λ into Eq. (20), the equation is given as follows:

$$\tilde{\sigma}_{c-\text{ total}} = \frac{1}{\lambda}E_s\frac{2\gamma}{r} \tag{22}$$

The Eq. (22) and Table 7 show that The confining capacity of the constraining body is inversely proportional to the combined force of the concrete specimen pore wall and the reduction of the pore structure. The similar thickness of the steel plate material gradually increases from Sp-1 to Sp-3. The thicker the steel plate the higher the restraining effect, so the combined force of the pore walls in the concrete specimens is significantly reduced. Therefore the pore structure gradually decreases from Sp-1 to Sp-3. For the same reason, the experimentally observed changes in the EM and stud parameters of the steel plates lead to changes in the pore structure of the specimens.

Table 7 Constraint coefficient λ of constraint components ($\times 10^4$ Mpa)

	3 days	7 days	28 days
Sp-1	0.89	0.98	1.04
Sp-2	1.08	1.17	1.23
Sp-3	1.38	1.47	1.52
Sp-4	1.19	1.27	1.33
St-1	1.00	1.09	1.15
St-2	1.07	1.16	1.22
St-3	1.12	1.22	1.28
St-4	1.19	1.29	1.35
St-5	1.25	1.36	1.41
St-6	1.41	1.52	1.52
St-7	1.74	1.87	1.94

The impact of the constraint coefficient on the various pore structure characteristics in the constrained specimens is shown in Fig. 3. The graphic shows that these parameters grow linearly as the constraint coefficient rises.

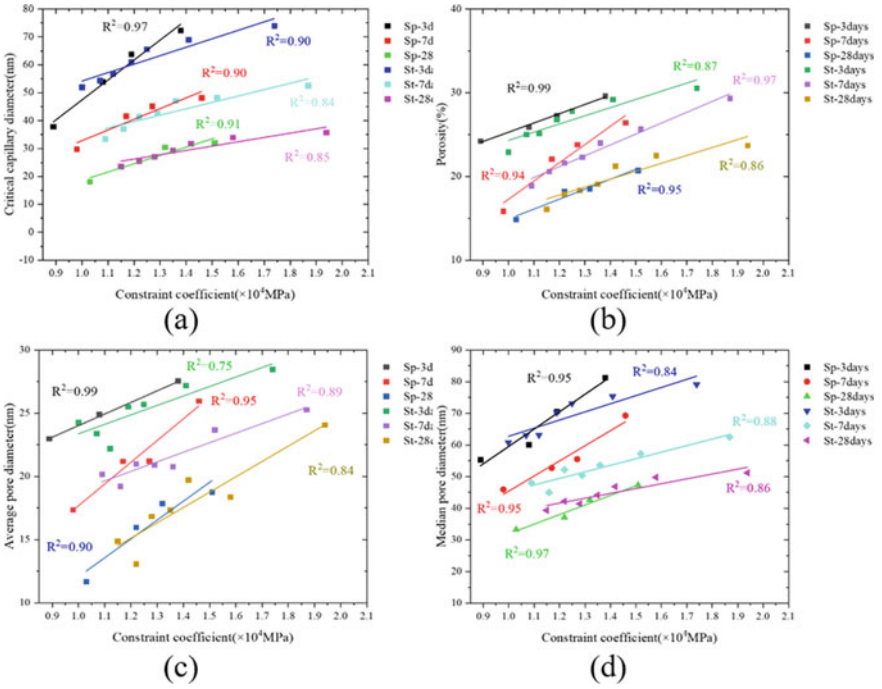

Fig. 3 Influence of constraint coefficient on various concrete pore structure characteristics: **a** Critical capillary diameter, **b** Porosity, **c** Average pore diameter, **d** Median pore diameter

4.2 Concrete Shrinkage

The shrinkage curves for the various specimens at 0 to 28 days are shown in Fig. 4. The concrete shrinkage curves of sample are separated into three phases: The first phase, lasting from 0 to 5 days, sees the concrete shrinkage occur quickly while the relative humidity drops quickly (Fig. 4a); the second phase, lasting from 6 to 14 days, sees the concrete shrinkage slow down; and the third phase, lasting from 15 to 28 days, sees the concrete shrinkage decrease and reach a relatively stable value.

The shrinkage of concrete specimens restrained by steel plates only was affected by the thickness of the plates and EM (Fig. 4b): (1) the thicker the plate, the smaller the shrinkage of concrete when the plate material was the same; (2) the larger the plate EM, the smaller the shrinkage of concrete when the plate thickness was the same. These findings are in high concordance with the results given by Eqs. (19) and (22) (the thicker the steel plate, the larger the EM, and the higher the constraint coefficient at the same age).

The stud specifications had an impact on the shrinkage of the concrete sample that was being held in place by constraint bodies (Fig. 4c). Concrete shrinkage statistics for St-1, St-4, and St-6 make it clear that shrinkage goes down as stud diameter goes up. Additionally, as stud height and stud count increase, concrete shrinkage reduces. The restraint coefficient is significantly impacted by the variation in stud parameters. The shrinkage of specimens constrained by constraint bodies reduced with increasing restraint coefficient, same as that of specimens restrained exclusively by steel plates.

The primary cause of concrete's shrinkage deformation is capillary strains. Table 8 provides the capillary tensions for each sample at all ages. Equation (1) shows that the capillary stresses in the concrete were reduced as a result of the improved pore structure of the stud and plate restrained sample. As a consequence, the three deformations were coordinated, and the capillary stress was reduced, which decreased the shrinkage of the restrained concrete.

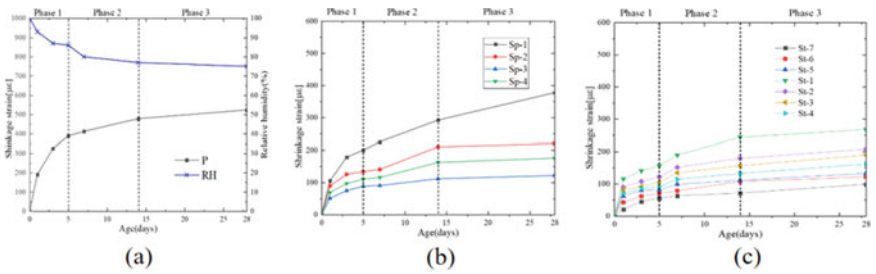

Fig. 4 Shrinkage of concrete: **a** Normal specimens, **b** Specimens restrained only by steel plates, and **c** Specimens restrained by studs and steel plates

Table 8 Capillary stress on concrete at three ages (MPa)

	3 days	7 days	28 days
P	3.66	5.48	8.85
Sp-1	3.85	4.91	8.07
Sp-2	2.71	3.50	5.68
Sp-3	2.01	3.02	4.56
Sp-4	2.28	3.23	4.79
St-1	2.80	4.35	6.20
St-2	2.68	3.94	5.71
St-3	2.57	3.52	5.39
St-4	2.39	3.42	4.97
St-5	2.22	3.09	4.60
St-6	2.11	3.03	4.29
St-7	1.97	2.77	4.08

Table 9 Testing and computed values comparison

	3 days			7 days			28 days		
	Test value (με)	Calculated value (με)	Relative error (%)	Test value (με)	Calculated value (με)	Relative error (%)	Test value (με)	Calculated value (με)	Relative error (%)
Sp-1	178	189	6.0%	225	215	4.4%	377	329	12.7%
Sp-2	125	109	12.8%	140	129	8.1%	320	196	11.0%
Sp-3	74	64	14.0%	90	89	1.4%	121	127	4.9%
Sp-4	96	84	12.7%	115	109	5.1%	175	152	12.9%
St-1	140	122	12.9%	189	171	9.4%	267	228	14.6%
St-2	107	109	2.1%	151	146	3.6%	207	197	4.7%
St-3	91	100	9.5%	134	124	7.5%	189	178	6.0%
St-4	85	94	10.9%	114	123	7.6%	161	167	3.8%
St-5	79	84	6.6%	98	106	8.5%	132	148	12.2%
St-6	61	65	6.9%	78	89	10.1%	121	115	5.0%
St-7	45	49	9.6%	63	64	1.5%	98	89	9.3%

4.3 Shrinkage Prediction

To determine the likelihood of concrete cracking, constrained concrete shrinkage prediction is crucial. Equation (19) was used to forecast the shrinkage of concrete under steel plate and stud constraint based on the capillary tension theory.

The results of the test were compared with the predicted values of Eq. (19) (Table 9). According to the data in Table 9, the average prediction error at days 3, 7 and 28 was 12.75%. Therefore, Eq. (19) is valid for predicting the shrinkage.

A thicker steel plate with a greater height, a bigger diameter, and more studs can lessen the shrinkage deformation of concrete, according to both experimental and anticipated results. The greater the strain on the concrete under the confining tension, for the same kind of concrete (the same concrete free shrinkage), the smaller the shrinkage strain. The stress–strain relationship states that concrete with less shrinkage is subjected to greater tensile stresses, and when the tensile stresses are greater than the concrete's tensile strength, the concrete will break. However, because to the limitations of related research, it is still difficult to accurately calculate the tensile stress of concrete and anticipate when it will break. Engineers can assist to lessen the problem of concrete cracking due to shrinkage by using thinner steel plates with lower height, smaller diameter, and fewer studs in order to fulfill the load-bearing capability of the structure.

5 Conclusion

In this study, the capillary tension theory was used to build a model for predicting concrete shrinkage contained by steel plates and studs. The impact of various stud and steel plate properties on concrete shrinkage and pore structure was investigated by measuring the pore structure and shrinkage strain of concrete specimens enclosed by various studs and steel plates. The following are the main deductions:

(1) Due to capillary stress and the filling impact of the hydration products created by cement hydration, the pore structure of concrete deteriorates with time.
(2) Constraint bodies have a larger restraint effect when the restraint factor is higher. The restraint strain coefficient steadily rises as height, diameter, and stud count increase along with steel plate thickness and elastic modulus.
(3) The use of constraint bodies changed the structure of the concrete pores. With the increase of the constraint coefficient, the concrete pore structure parameters such as porosity, mean pore size, median, and critical pore size gradually increased.
(4) With an increase in the constraint factor, the concrete's shrinkage strain reduces. Concrete shrinks as a result of capillary stresses and forces, thus it stands to reason that reducing these stresses and forces would also minimize the strain caused by concrete's shrinkage. Additionally, the coordination of deformation between the steel plates and the studs will lessen the strain caused by concrete's shrinkage.
(5) To forecast concrete shrinkage while being held in place by steel plates and studs, utilize Eq. (19). It is shown in this study that Eq. (19) is useful for estimating the shrinkage of concrete when restrained by studs and steel plates since the projected values match the observed values well.

References

1. Yoo D-Y et al (2014) Influence of reinforcing bar type on autogenous shrinkage stress and bond behavior of ultra high performance fiber reinforced concrete. Cement Concr Compos 48:150–161
2. Shen W et al (2016) Experimental investigation on shrinkage and water desorption of the paste in high performance concrete. Constr Build Mater 114:618–624
3. Yousef RF, Muteb HH, Ibrahim AA (2023) Studying the effect of embedded length strength of concrete and diameter of anchor on shear performance between old and new concrete. Curved and Layered Struct 10(1)
4. Xu C et al. (2022) Shrinkage effect and mechanical performance of steel-ultra-high performance concrete composite deck under negative bending action. Eng Struct, 273
5. Li Y, Li J (2014) Capillary tension theory for prediction of early autogenous shrinkage of self-consolidating concrete. Constr Build Mater 53:511–516
6. Di Bella C, Wyrzykowski M, Lura P (2016) Evaluation of the ultimate drying shrinkage of cement-based mortars with poroelastic models. Mater Struct 50(1):52
7. Hua J et al (2020) Influence of reinforcement bars on concrete pore structure and compressive strength 13(3):658
8. Hua J et al (2020) Prediction on the shrinkage of concrete under the restraints of steel plates and studs based on the capillary tension theory. Constr Build Mater 258:119499

Research on Resource Utilization and Zero Loss Utilization of Construction Waste

Zhiqiang Lai and Yuancai Chen

Abstract The most common way 10 of handling construction waste currently is by outdoor dumping or direct landfilling, which wastes a lot of land resources and causes soil and water pollution. Research has found that the resource utilization of construction waste has high economic and environmental values. The main approach is to sort and classify the construction waste and dispose of different categories of construction waste into different facilities, producing environmentally-friendly recycled aggregates that meet construction requirements. Then, these recycled aggregates are mixed with other materials such as recycled powder to produce new green building materials that can be used, which can theoretically achieve zero loss.

Keywords Construction waste · Resource utilization · Zero loss

1 Research Background and Significance

The construction accumulation is a common problem in the whole world [1], In the process of continuous development of urbanization in the countries, the amount of construction, decoration and demolition waste generated is increasing day by day. Studies have shown that the amount of construction waste emissions in most cities in the country is very high. For example, in first-tier cities in China such as Shenzhen, Guangzhou, Beijing, and Shanghai, the annual production of construction waste in Shenzhen almost reaches 100 million cubic meters, and the production level will remain consistent over the next decade. Guangzhou has produced about 70 million cubic meters of construction waste in recent years, and if calculated based on 3 acres of land per 5 m high for every 10,000 cubic meters of construction waste, the amount

Z. Lai · Y. Chen (✉)
School of Environment and Energy, Guangdong Provincial, Key Laboratory of Solid Wastes Pollutiong Control and Recycling, South China University of Technology, Guangzhou, Guangdong 510006, P.R. China
e-mail: 105936799@qq.com

H.-Y. Jeon (ed.), *Proceedings of the International Conference on Geosynthetics and Environmental Engineering*, Lecture Notes in Civil Engineering 374,
https://doi.org/10.1007/978-981-99-4229-9_39

of construction waste produced in Guangzhou each year can occupy up to 20,000 acres of land.

This article mainly analyzes the current situation of resource utilization, and then classifies construction waste into five categories: engineering soil, engineering sludge, engineering waste, demolition waste, and decoration waste. It explores the resource utilization methods, recyclable utilization rates, and application ranges for each category of construction waste.

2 The Current Status of Resource Utilization of Construction Waste

2.1 Abroad

Since the 1990s, many countries around the world, especially developed countries, have regarded the reduction and resource utilization of urban building waste as one of their environmental protection and sustainable development strategies. Currently, it is widely recognized that building waste is a recyclable resource. In particular, the United Statesand has made great efforts in promoting resource utilization since 1976. Japan issued its first legal provision on the disposal of building waste in 1970, and has since then introduced several policies to promote the resource utilization of building waste. Some studies have shown that Japan's resource utilization rate can reach 98%. As the country with the highest building waste resource utilization rate in the world, the Netherlands has independently developed multiple high-tech sorting equipment, This type of equipment can perform multi-level control in synchronization and ensure sorting efficiency.

2.2 Domestic

Since the 1990s, many countries around the world, especially developed countries, have regarded the reduction and resource utilization of urban building waste as one of their environmental protection and sustainable development strategies. Currently, it is widely recognized that building waste is a recyclable resource. In particular, the United States has had relevant laws and regulations on resource recycling since 1976 and has made great efforts in promoting resource utilization. Japan issued its first legal provision on the disposal of building waste in 1970, and has since then introduced several policies to promote the resource utilization of building waste. Some studies have shown that Japan's resource utilization rate can reach 98%. As the country with the highest building waste resource utilization rate in the world, the Netherlands has independently developed multiple high-tech sorting equipment, including 3D sorting drum screens, wind selectors, and optical sorters. The Netherlands' 3D sorting drum

screen equipment can sort out light waste with a diameter greater than 210 microns and use it as fuel, while adsorbing iron-metallic substances and sorting out light waste with a diameter less than 210 microns [2]. At the same time, the screening machine is activated to screen particles less than 10 microns in diameter. This type of equipment can perform multi-level control in synchronization and ensure sorting efficiency.

3 Various Types of Processing Methods and Application Scopes for Resource Utilization of Construction Waste

The main components of construction waste are a mixture of waste materials such as earth, broken stones, waste mortar, brick and tile fragments, concrete blocks, asphalt blocks, waste plastics, waste metal materials, waste bamboo and wood. However, the overall processing approach is to screen and classify on-site, transport to the processing site, re-sort, and then process and utilize different types of waste using different equipment and technologies.

The following table lists the proportion of construction waste and the amount of waste generated per unit building area for new buildings of different structural types (Table 1).

According to their different generation methods, they can be divided into the following categories:

Table 1 Typical Composition of Construction Waste from Newly Built Buildings

Composition	Proportion (%)		
	Brick concrete structure	Frame structure	Frame-Shear wall structure
Broken bricks (broken blocks)	30–50	15–30	10–20
Mortar	8–15	10–20	10–20
Concrete	8–15	15–30	15–35
Pile head	–	8–15	8–20
Packaging materials	5–15	5–20	10–15
Roofing materials	2–5	2–5	2–5
Steel	1–5	2–8	2–8
Wood	1–5	1–5	1–5
Others	10–20	10–20	10–20
Total	100	100	100
Building area generation Construction waste volume(kg/m^2)	50–200	45–150	40–150

3.1 Construction Waste of Engineering Soil

Engineering soil construction waste refers to the waste soil (stone) generated during the excavation process of various construction projects, structures, and pipelines, including loess, clay, windblown sand, yellow soil, humus soil, mudstone, peat soil, etc. It accounts for more than 60% of the total construction waste. There are three types of resource utilization methods for engineering soil: coarse screening and backfilling, unburned sintering with admixtures to make bricks, and adding solidifying agents to form solidified soil.

Coarse screening and backfilling refers to the direct utilization of uniformly sized and well-graded aggregates selected after coarse screening through landfilling, leveling, watering, rolling, and curing. This can be used for mining backfill, road base backfill, sponge city construction, or as building materials. Relevant policies issued by cities such as Shanghai suggest that owner units and construction enterprises should use engineering soil to create green landscapes in conjunction with design plans, maintaining the original state of the soil and covering it with climbing plants to form small local landscapes. It can also be designed as a micro-topography in green spaces to embellish the overall landscape.

Unburned sintering with admixtures to make bricks involves coarse screening, secondary crushing and screening, adding sand, stone and admixtures, and solidifying and mixing to form bricks.

Adding solidifying agents to form solidified soil means using solidifying agents to enhance the anti-seepage characteristics of soil, increase the application width and breadth of engineering soil, and effectively improve the resource utilization rate of engineering soil. Research shows that there are successful cases of solidified soil application in cities such as Hebei, Shandong, and Xi'an. The main raw material is engineering soil, and an appropriate proportion of solidifying agent is added. The addition time interval for the admixture is set, and a new type of backfill material can be made. It is transported to the operation site for filling and maintenance under certain transportation conditions, effectively improving the quality of solidified soil and ensuring construction results (Fig. 1).

3.2 Engineering Slurry Type Construction Waste

Engineering slurry is a type of construction waste with a relatively high water content in the category of engineering debris. Different waste slurry contains different trace elements, and the performance characteristics of slurry such as viscosity vary greatly. For example, the waste slurry left by pile foundation slurry, shield slurry, and drilling

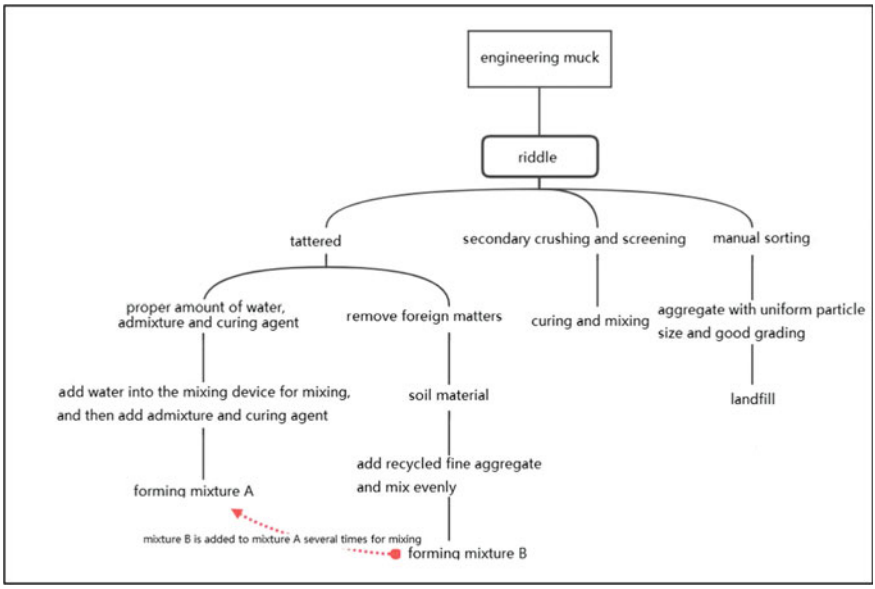

Fig. 1 English translation: flowchart of resource utilization of construction waste

slurry are all different. Ma Qiang et al. discussed and studied seven resource utilization methods for different types of waste engineering slurry, including land cultivation, precipitation, chemical solidification, direct discharge, injection into safe formations or annular space, MTC conversion technology, and water gel solidification of waste engineering slurry [3] (Fig. 2).

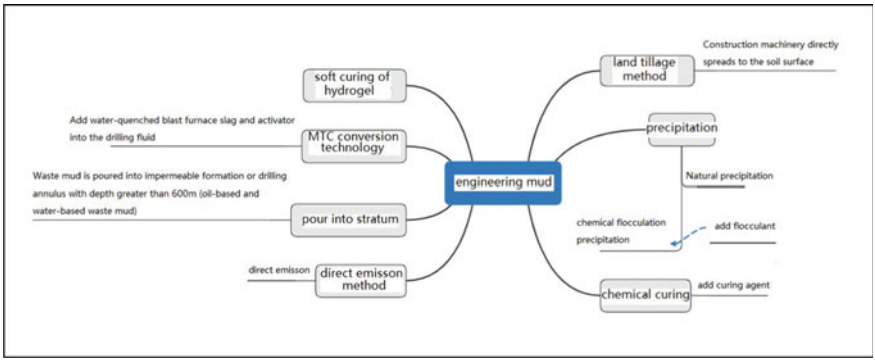

Fig. 2 Resource utilization process flowchart of engineering slurry

3.3 Construction Waste from Engineering Construction Projects

Construction waste from engineering construction refers to the various waste generated during the construction process of different structural types of buildings. It mainly includes scattered mortar and concrete, bricks and concrete debris produced by excavation, steel reinforced concrete pile heads cut from pile driving, waste metal materials, bamboo and wood, and various packaging materials. The following are the most commonly used materials for resource utilization: waste concrete, bricks, and waste asphalt, for which resource utilization methods will be explored.

Waste concrete and bricks are often used to produce recycled aggregate through processes such as sorting, crushing, metering, mixing, vibration molding, curing, and factory inspection. The production facilities involved are mostly mobile crushing systems, screening systems, conveying systems, non-fired brick and block production systems, road material preparation systems, composite material production systems, and environmental protection drainage production systems. In addition to the resource utilization equipment, the quality of the aggregate can be improved through techniques such as heating crushing, mechanical crushing, and gravity concentration. The use of fast brick making methods can also solve problems such as excessive crushing and high recycling costs during the processing [4].

The disposal of waste concrete is the most comprehensive and highest recycling rate method. In the authors' opinion, usually concrete waste is used as a material for building temporary roads, for secondary backfilling and in terrain planning [5–7], that will lose valuable recyclable materials. Countries such as the United States, Sweden, and Japan have advanced disposal equipment for waste concrete, such as rotary push grinding devices and eccentric rotating crushers, which can handle waste concrete with particle sizes ranging from 25–500 mm and produce recycled aggregates and recycled fine powder. In the later stage, methods such as sintering hardening, cold hardening, steam curing hardening, and carbonization hardening can be used to increase the strength of the aggregates and expand their application range.

There is a research theory for rapid brick-making that uses crushed waste bricks and stones as aggregate, fills them into a mold, connects the mold to a filling device, injects a certain amount of bonding agent for a certain period of time, while also insulating the mold surface. The resulting molded bricks can serve as lightweight brick aggregates, and old bricks can also be made into floor tile materials, non-fired cement raw materials, cement mixtures, or used in road subgrade engineering by adding lime to the crushed clay bricks.

The treatment of waste asphalt often requires re-mixing with rejuvenators, new aggregates, and other materials in appropriate proportions. This process is divided into plant-mixed hot recycling, on-site hot recycling, plant-mixed cold recycling, and on-site cold recycling. The waste asphalt materials from roofing contain cellulose structures that can replace some of the aggregates in cold-mix and hot-mix asphalt, thus improving the performance of the asphalt [8] (Fig. 3).

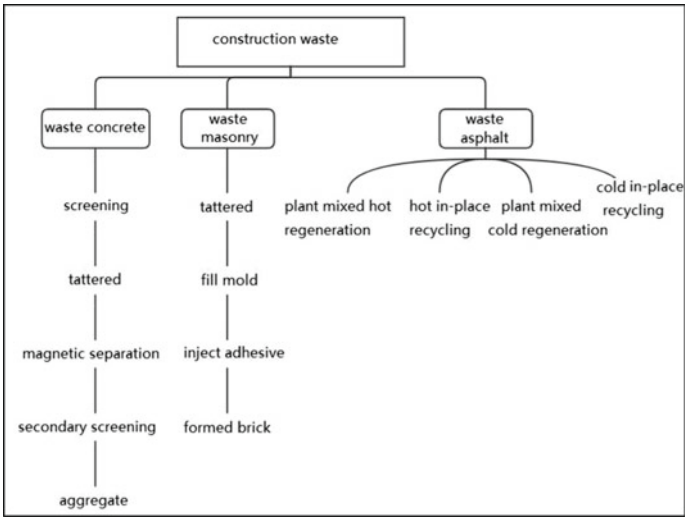

Fig. 3 Flowchart of engineering waste resource utilization (Concrete, Brick and Asphalt)

3.4 Demolition Waste from Buildings

In recent years, the area and quantity of the old city reconstruction projects were vast, resulting in more construction waste generated compared to other engineering projects. The main types of construction waste generated were bricks, tiles, concrete, scrap steel, scrap rebar, and other metal waste materials. The handling of bricks and concrete is consistent with the methods used for handling construction waste, while the reuse of scrap steel, rebar, other waste metal materials, and waste tiles needs further exploration and research.

The recycling of scrap rebar and steel is the most scientific and straightforward approach. In addition to direct reuse, the magnetic characteristics of steel are utilized by separating the metal using electromagnetic or permanent magnetic separation equipment, and the remaining scrap steel is recycled through furnace smelting. Common permanent magnetic equipment includes the CTN-type permanent magnetic cylinder magnetic separator.

The amount of waste tiles generated in demolition is relatively small and can be directly used in landscaping, such as on the surface of buildings or as individual decorative landscapes [9] (Fig. 4).

3.5 Renovation Building Waste

In building construction waste, the proportion of decoration waste is relatively small, but the composition is more complex, and it contains certain toxic and harmful

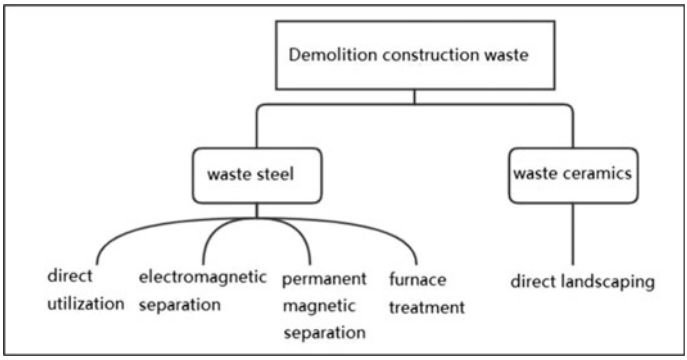

Fig. 4 Flow chart of recycling of demolition construction waste

substances such as waste paint, coatings, and adhesives. In addition to the commonly used concrete, bricks, slag, and steel, the research on the resource utilization of waste wood, waste glass, and waste plastic in decoration waste is mainly studied.

Similar to waste steel bars, some waste wood can be directly used for rebuilding buildings and landscape decoration. For waste wood that cannot be used directly, the first step is to use wind selection technology or hydraulic flotation technology for separation. The separated small particle size materials can be used as coverings for erosion protection projects, fuel stack materials, and papermaking. The larger particle size materials can be added to clay and cement to form composite materials, which can be used as insulation materials.

Engineering waste plastics can be sorted, cleaned, directly granulated, or modified for reuse through physical methods. Alternatively, they can be thermally decomposed at high temperatures under the action of catalysts or degraded by chemical solvents or monomer copolymerization (Fig. 5).

4 Recycling Rate

Through the study and discussion of the resource utilization of various types of construction waste generated by different types of engineering, it is clearly and explicitly shown that, except for hazardous substances, all types of construction waste can be recycled and reused through resource regeneration, with a utilization rate of up to 100%. Especially important recyclable materials are concrete, bricks, and slag, accounting for over 60%, and the finished products produced are used in the green building industry, with the entire process covering nearly 98% of the types of construction waste. This study aims to promote the advanced disposal methods of construction waste to cities nationwide, introduce advanced disposal facilities and equipment from domestic and foreign sources, and draw on relevant policies issued at home and abroad, to explore and demonstrate the possibility of zero waste.

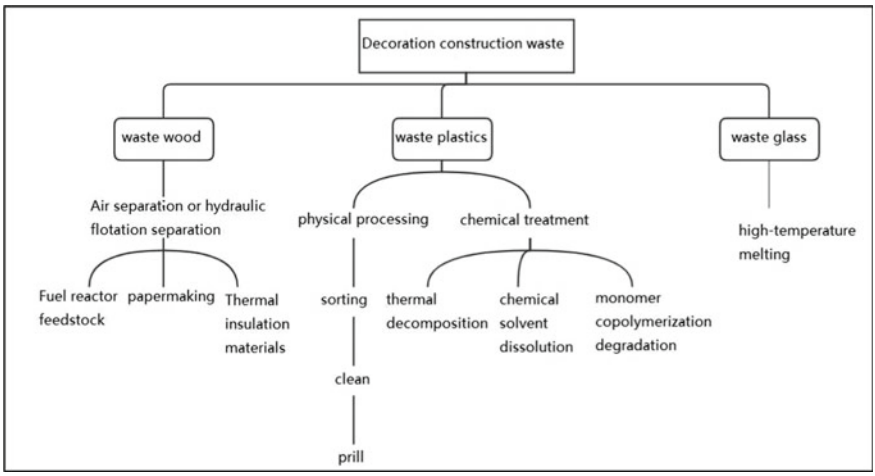

Fig. 5 Flow chart of recycling of decoration construction wastee

5 Production Volume Prediction (Taking Guangzhou as an Example)

At present, the building area estimation method is the mainstream method for predicting the amount of construction waste generated. It can comprehensively consider the various stages of construction waste generation from the perspectives of construction, demolition, decoration, etc., and the prediction accuracy error is less than 10%, which is relatively accurate. Therefore, based on the research direction of this article, the production volume of construction waste from new construction projects, demolition waste from old buildings, and house decoration waste is predicted [10].

5.1 Prediction of the Amount of Construction Waste Generated in New Construction Projects

Based on the experience, construction waste can be disposed of at a rate of $1m^3 = 1.6$ ton conversion; According to the related materials, the work goal is to achieve a maximum discharge of 300 tons of construction waste (excluding engineering waste and engineering mud) per 10,000 m^2 at new construction sites, Therefore, the amount of construction waste (engineering waste) generated during the construction of new buildings in this plan is 187.5 m^3/ 10,000 m^2 Estimate and calculate the amount of construction waste generated in new construction projects. The prediction model is:

$$Q_n = 0.01875 \times S_{con}$$

Q_n—the amount of construction waste generated during the construction of new buildings, unit (10,000 m^3);

S_{con}—Construction area of new buildings, unit (10,000 m^2).

5.2 Prediction of Waste Production from Demolition of Old Buildings

Based on the experience of the Chinese construction industry and the actual situation in Guangzhou, approximately 0.81 cubic meters of construction waste are generated per square meter of demolished buildings. Therefore, based on the annual renewal and renovation of the building area, the annual output of waste from the demolition of old buildings can be calculated. The prediction model is:

$$Q_0 = 0.81 \times S_{dem}$$

Q_o—the amount of waste generated from the demolition of old buildings, unit (10,000 m^3);

S_{dem}—Construction area of old building demolition, unit (10,000 m^2).

5.3 Prediction of the Generation of House Decoration Waste

According to the actual discharge of residual mud and soil in Guangzhou, the amount of house decoration waste can be estimated as 7 cubic meters of decoration waste generated by each house decoration project. The prediction model is (Table 2).

Table 2 Production volume prediction

Serial Number	Name	Formula	Forecast of waste generation from 2021 to 2025 (10,000 m^3)
First	Construction waste from new construction projects	Yield = 0.01875 × Construction building area	4000
Second	Old building demolition waste	Yield = 0.81 × Construction building area	14,500
Third	House decoration waste	Yield = 7×10^{-4} × (Number of newly built houses + 0.1) × Number of newly built houses)	2700

$$Q_d = 7 \times 10^{-4}(N_n + 0.1 \times N_n)$$

Q_d—the amount of house decoration waste generated, unit (10,000 m^3);
N_n—Number of newly built houses.

6 Conclusion

More and more people are gradually realizing the importance of resource utilization of construction waste, and the value, benefits, and cost savings that construction waste can bring. It is equivalent to hidden minerals in the city, and how to better utilize them to maximize their recycling value is crucial in the following urbanization development. For construction waste with different material characteristics, it is important to establish classification and disposal standards, and refer to the resource utilization rate mechanism set in the construction plan in the United States. A strategy of combining economic penalties and financial support should be adopted to fine non-compliant units and improve financial support policies. Japan promotes utilization rates from legal and technical management perspectives, optimizing the technical path, management strategy, and utilization and disposal of waste. Theoretically, achieving the goal of zero waste from construction waste will have a positive and profound impact on regional economy, market employment, energy conservation and emission reduction, and environmental protection.

The research was financially supported by grants from National Key Research and Development Program (2022YFF0607201), National Natural Science Foundation of China (22,276,061, 41,977,316), and the Guangdong Science and Technology Program (2020B121201003).

References

1. Hussin JM, Rahman IA, Memon AH (2013) The way forward in sustainable construction: issues and challenges. IJAAS 2(1):15–24
2. Cui X, Shi X (2022) Research on the problem of building waste recycling under the background of dual carbon [1]. Constr Technol 32–35
3. Ma Q, Men B (2023) Research on the treatment method of solidified waste mud by water gel [1]. Shanxi Archit 49(2):29–33
4. Shi M, Lin Z (2019) Overview of manufacturing and maintenance technology of artificial bone material [1]. National Natural Sci Foundation 9:56–61
5. Gasilov VV, Kryuchkova IV (2012) FES: finance. Economics 11:5–8
6. Kashevskaya EV, Kostenko KK, Kostenko AK (2004) Science and technology in the road industry 2(29):30–33
7. Kanayev AYu (2011) Science and the Present 11:254–257
8. Jiang X, Ma H, Chen M, Su X (2021) Hasimaimaiti: analysis of the recycling and reuse of waste asphalt mixture [1]. Research on technology for recycling and reuse of asphalt pavement milling materials, pp 243–246

9. Peng H, Tang L (2022) Research on the reuse of waste ceramics in modern landscape design [1]. Learning Exploration 14:152–154
10. Layout Plan for Construction Waste Disposal Facilities in Guangzhou (2021–2035), 31–39

Research on the Application of Geophysical Exploration in Tunnel Survey

Yong Hai He and Hong Qiang Zhang

Abstract The accuracy of geological survey plays an important role in the cost and safety of tunnel construction. In recent years, with the development of expressway from plain to mountain, the geological conditions of highway tunnels are becoming more and more complex. The interpretation results of geophysical exploration can well present the geological conditions of the tunnel in the form of surface. The geophysical exploration technology used varies with the burial depth of the tunnel. High density resistivity method has high resolution in shallow layer, which can accurately and quickly detect karst caves, faults and other geological structures in the shallow buried section of tunnel portal. The results will play a guiding role in the prevention and treatment of geological disasters such as tunnel portal landslide, collapse and roof fall. The magnetotelluric method is used to measure the depth of tens to 3000 m, which can be used to detect the fault, water content and other geological conditions in the deep buried section of the tunnel. The comprehensive geophysical exploration method combining high-density resistivity method and magnetotelluric method is adopted for highway tunnels in mountainous areas, which can provide relatively accurate geological survey reports, effectively reduce geological diseases during construction and operation, reduce project cost, and ensure the safety of traffic after operation. This method is worth using for reference.

Keywords High density resistivity method · Magnetotelluric method · Tunnel survey · Cost and safety

Y. H. He (✉) · H. Q. Zhang
Hebei Provincial Communications Planning, Design and Research Institute Co., LTD, Shi Jia Zhuang 050011, China
e-mail: 27837343@qq.com

H.-Y. Jeon (ed.), *Proceedings of the International Conference on Geosynthetics and Environmental Engineering*, Lecture Notes in Civil Engineering 374,
https://doi.org/10.1007/978-981-99-4229-9_40

1 Introduction

Taking the Hebei section of Xiaolongmen Tunnel of National Highway G109 New Line Expressway as the engineering background, this paper explains the application of high-density resistivity method and magnetotelluric method in tunnel exploration.

2 Technology and Principle of the Geophysical Prospecting Methods

2.1 High Density Resistivity Method

The instrument uses the DUK-2A high-density resistivity measurement system produced by Chongqing Geological Instrument Factory of Zhongzhuang Group. The system is characterized by large storage capacity, accurate and fast measurement, convenient operation, etc. Its main functions include automatic signal acquisition, automatic storage, real-time curve display, two-way data communication, etc. The multi-channel electrode converter is connected to 120 electrodes at most, and the system is equipped with domestic advanced high-density resistivity method forward and inversion interpretation software, It greatly improves the accuracy and efficiency of geophysical interpretation [1–3].

2.2 Magnetotelluric Method

The instrument uses the STRATAGEM EH-4 magnetotelluric sounding instrument (continuous conductivity tester) produced by GEOMETR Company of the United States. This instrument can detect the depth of several meters to more than one kilometer underground by using natural and artificial electromagnetic sources, and measure point by point to obtain the electrical structure under the measuring point. The magnetotelluric sounding instrument obtains the surface impedance by simultaneously measuring a series of local electric and magnetic field fluctuations, These impedance data are stored in energy spectrum after Fourier transform. The surface impedance calculated from the energy spectrum value is a complex frequency function. In this frequency function, the high-frequency data is affected by shallow or nearby geological bodies, while the low-frequency data is affected by deep or distant geological bodies. In this work, we only observe the high-frequency band, the detection depth can reach 300–500 m, and the distance between observation points is 20 m, Playback the original data observed in the field to the computer, use IMAGEM special software for data and processing, generate resistivity profile (lattice map), use ground elevation data, convert the interpretation depth to absolute elevation, and then

use surfer8 software for post-processing to generate color profile, which is intuitive and easy for geological interpretation [4, 5].

2.3 Instrument Performance Control and Self-Inspection

Before the field work, the instrument was self checked and checked for quality according to the Specifications for Geophysical Prospecting of Highway Engineering (JTG/T C22-2009) and the Specifications for Physical Prospecting of Highway Engineering (TB10013-2004), and the results showed that the instrument had good performance and the error of check points met the specifications. Before the high-density resistivity measurement, the loose layer and weeds on the surface of each electrode are removed. In dry places, the grounding resistance is minimized by watering. Before the measurement, the grounding resistance of each electrode is checked by using the automatic detection function of the instrument. When the grounding conditions are met, the formal measurement is conducted to ensure the measurement quality. Before EH4 measurement, the parallel test of the instrument shall be carried out to show that the instrument operates well.

3 Project Overview

The Hebei section of Xiaolongmen Tunnel of National Highway G109 New Line Expressway is 2151.775 m long on the left and 2022.208 m long on the right. A ventilation shaft is set on the right side of K1 + 348 on the right.

4 Engineering Geological Conditions

4.1 Physical and Geographical

The Xiaolongmen Tunnel of the proposed new line expressway is located in the mountainous area of Taihang Mountains. The terrain of the tunnel area is undulating. The orifice elevation in the tunnel area is 830.00–967.75 m. The region is located in the warm temperate semi humid continental monsoon climate, with an average annual rainfall of 408.7 mm, an average maximum temperature of 22.0 °C in July, an average minimum temperature of −11.0 °C in January, and a seasonal frozen soil depth of 1.01 m. The tunnel area is only connected by mountain roads, so the traffic is not convenient.

4.2 Geological Structure

The tunnel area is located in the transition zone between the Xinhuaxia uplift of Taihang Mountain and the Xinhuaxia subsidence zone of Hebei Plain. The structural state is relatively complex. The geological structure that has an impact on the stability of the tunnel area is mainly the Sunzhuangzi Wulonggou fault. The fault extends from Laiyuan Futuyu in the northern section of Taihang Mountains to Huangqi from Wulonggou, Zhuolu Dahan, Xiaohenan, Xiejiapu, Kongjian, Zhifangkou, Sun Zhuangzi, Chicheng, Fengning to the north, and extends into Inner Mongolia. The overall trend is 20–400 northeast, with a length of about 115 km, and a crushing belt width of about 100 m. The fault zone is composed of cataclastic rock and mylonite, filled with veins in the structural zone, and then cut off by the structure, reflecting multiple activities.

5 Geophysical Characteristics of the Survey Area

The stratum in the tunnel area is Yanshanian granodiorite; The lithology is relatively simple, mostly coarse grained, mainly massive structure–mosaic cataclastic structure, completely weathered as loose, uneven weathering.

According to previous data, there are obvious electrical differences between the Quaternary loose layer and the underlying bedrock, and there are also electrical differences between different geological lithology. If there are fault structures and rock fracture zones, the rocks within the fault structure zone are broken, and there are electrical differences with complete rocks, which provides a geophysical premise for the application of high-density resistivity method and magnetotelluric method.

6 Data Interpretation and Result Analysis

6.1 Analysis of Results of High Density Resistivity Method

K2 + 911 ~ K2 + 961 vertical section: the bedrock of the section is exposed, the lithology is Yanshanian granodiorite, with obvious stratification, little difference in weathering degree of rock mass, and the strongly weathered layer is thin, mainly moderately weathered rock mass, with apparent resistivity more than 1000 Ω·m; No other obvious abnormality is found.

K3 + 030 cross section: the bedrock of the section is exposed, and the lithology is Yanshanian granodiorite. The stratification is obvious, and the weathering degree of the rock mass is not different. The strongly weathered layer is thin, and most of the rocks are moderately weathered. The apparent resistivity of the right side is low,

which is the Quaternary overburden. The apparent resistivity of other locations is more than 1000 Ω·m; No other obvious abnormality is found.

6.2 Analysis of Magnetotelluric Method Results

K0 + 900 ~ K1 + 000 vertical section: the lithology of this section is Yanshanian granodiorite; The resistivity of geophysical exploration is poor in stratification, and the distribution of high and low resistances is uneven; The low resistance section is connected from top to bottom, and the apparent resistivity at the tunnel excavation is relatively low–low, so it is speculated that the rock mass is broken– relatively broken.

K1 + 000 ~ K1 + 200 vertical section: the lithology of this section is Yanshanian granodiorite, with good stratification of geophysical resistivity and uneven distribution of high and low resistances; The apparent resistivity at the tunnel excavation is high, so it is speculated that the rock mass is relatively broken–complete.

K1 + 200 ~ K1 + 350 vertical section: the lithology of this section is Yanshanian granodiorite, with poor stratification of geophysical resistivity and uneven distribution of high and low resistivity; The low resistance section is connected from top to bottom, and the apparent resistivity value at the tunnel excavation is relatively low to low. It is speculated that the rock mass is broken to relatively broken, and the water bearing property of the rock mass is good.

K1 + 380 ~ K1 + 550 vertical section: the lithology of this section is Yanshanian granodiorite with thin overburden; The resistivity of geophysical exploration is poor in stratification, and the distribution of high and low resistances is uneven; The apparent resistivity at the tunnel excavation is high, so it is speculated that the rock mass is relatively broken–complete.

K1 + 550 ~ K1 + 700 vertical section: the lithology of this section is Yanshanian granodiorite, the physical exploration resistivity is generally layered, and the high and low resistances are evenly distributed; The low resistance section is enclosed in a ring and located above the tunnel. The apparent resistivity value at the tunnel excavation is relatively low to low. It is speculated that the rock mass is broken to relatively broken, and the water bearing capacity of the rock mass is good.

K1 + 700 ~ K1 + 950 vertical section: the lithology of this section is Yanshanian granodiorite, with good stratification of geophysical resistivity and uniform distribution of high and low resistances; The apparent resistivity value at the tunnel excavation is relatively high, so it is speculated that the rock mass is relatively broken–complete.

K1 + 950 ~ K2 + 400 vertical section: the lithology of this section is Yanshanian granodiorite, with poor stratification of geophysical resistivity and uneven distribution of high and low resistances; The low resistance section is connected from top to bottom, and the apparent resistivity value at the tunnel excavation is relatively low to low. It is speculated that the rock mass is broken to relatively broken, and the water bearing property of the rock mass is good.

K2 + 400 ~ K2 + 700 vertical section: the lithology of this section is Yanshanian granodiorite, with good layering property of physical exploration resistivity and uniform distribution of high and low resistances; The apparent resistivity value at the tunnel excavation is relatively high, so it is speculated that the rock mass is relatively broken–complete.

K2 + 700 ~ K2 + 900 vertical section: the lithology of this section is Yanshanian granodiorite, with poor stratification of geophysical resistivity and uneven distribution of high and low resistances; The low resistance section is connected from top to bottom, and the apparent resistivity value at the tunnel excavation is relatively low to low. It is speculated that the rock mass is broken to relatively broken, and the water bearing property of the rock mass is good.

7 Conclusion and Evaluation

The tunnel adopts high-density resistivity method and magnetotelluric sounding method. The technical method is reasonable and the resistivity characteristics are obvious, which can better reflect the actual geological conditions.

According to the high-density resistivity method, the surrounding rock at the tunnel portal is classified as Class V, and the span is more than 5 m without self stability; When the span of Grade IV surrounding rock is 6–9 m, it generally has no self stabilization ability and is prone to small or medium–large collapse; When the span of Grade III surrounding rock is 7–14 m, it has a certain self stability; Corresponding support treatment shall be carried out during excavation.

According to the EH4 geophysical exploration results, the Class IV surrounding rock section of the Project is mostly developed with tensile fractures, which have strong water permeability and water content. The probability of water gushing out during excavation is high. For fissure water and fissure water of rock vein structure, the dynamic reserves shall be the main, and the influence of seasonal change on water yield shall be considered.

References

1. Jian Y, Wei L, Yongshen L (2015) Application of high-frequency magnetotelluric in deep tunnel detection. Water Resour Planning Design 9:12–13
2. Huiming L, Hui W (2009) Application of comprehensive exploration technology in expressway along the yangtze river. Eng Constr 6:803–805
3. Li Y, Fei L, Xiaonian H (2018) Application and research of comprehensive geophysical exploration technology in permafrost survey of northeast highway engineering. Sci Disaster 33(S1):25–29
4. Yongjin C, Shanpu T, Guanglong P (2018) Application of comprehensive geophysical method in high altitude buried tunnel survey. Subgrade Eng 5:175–179

5. Shu L, Yong P, Yangfei L (2018) Applicability analysis and application of high density electrical method and audio frequency magnetotelluric method in highway tunnel investigation. West-China Exploration Eng 4:164–167

Effect of Capillary Tension Theory on Early Shrinkage of Reinforcement-Constrained Concrete

Ruixiang Shun, Junlong Jin, Bo Chen, Shenlin Hu, Yang Li, and Sheng Zhang

Abstract In this research, we propose a technique to predict the early contraction of reinforced concrete based on the theory of capillary tension and the microscopic pore structure of concrete. The results of the study showed that reinforcement alters the pore structure of concrete. We prepared concrete specimens with two different strength classes and three different reinforcement rates to study the contraction and physical properties of concrete at the ages of 3, 7, and 28 days. Additionally, as the reinforcement rate is increased, the size of the concrete's pore structure grows linearly. Due to the joint deformation of the concrete and reinforcement and the restriction of capillary stresses, the contraction of reinforced concrete is reduced. The predicted and tested concrete contraction values that are restrained by reinforcement show better agreement.

Keywords Restrained contraction · Concrete pore structure · Contraction prediction · Capillary tension theory

1 Introduction

The reinforcement will restrain the deformation of the concrete, which in turn will be subjected to restraint tensile stresses. When the confining tensile stresses exceed the tensile strength of concrete, the concrete will crack. Statistically, confining tensile stresses are the main factor causing concrete structures to crack, and this is especially true during construction. In the absence of external loads, the concrete's volume is further reduced following hardening, which is the contraction of concrete. Currently, the contraction of concrete used in engineering practice (especially high-strength

R. Shun · J. Jin
School of Civil Engineering, Chongqing University, Chongqing 400045, China

B. Chen · S. Hu · Y. Li · S. Zhang (✉)
Chengdu First Construction Engineering of CDCEG, No. 123 Yusha Street, Chengdu 610017, Sichuan Province, China
e-mail: albert0411@163.com

H.-Y. Jeon (ed.), *Proceedings of the International Conference on Geosynthetics and Environmental Engineering*, Lecture Notes in Civil Engineering 374,
https://doi.org/10.1007/978-981-99-4229-9_41

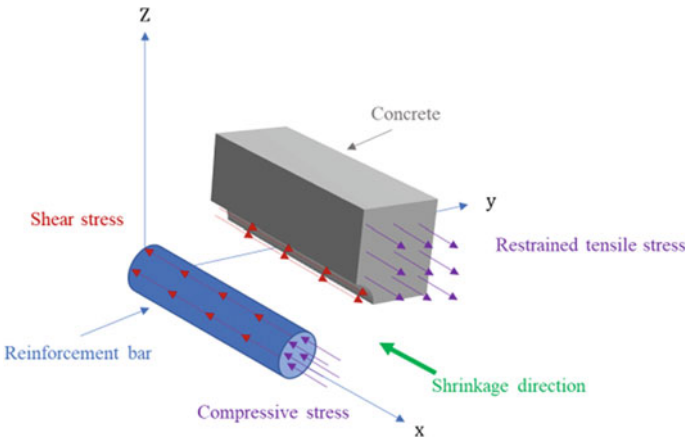

Fig. 1 Reinforcement bars prevent concrete from shrinking

concrete), especially in the early stages (construction period), demonstrates a substantial rise, which causes more severe structural cracking issues during the construction phase [1, 2] (see Fig. 1).

In order to reduce the cracking problem of concrete structures, the contraction behavior of concrete restrained by reinforcing needs to be studied. In earlier investigations, the effects of reinforcement diameter, surface, material and member type on the contraction of concrete have been investigated and some useful results have been obtained [3–5]. However, there are few studies about the assessment of concrete's ability to withstand contraction under the influence of reinforcing. Even though the mechanical model of reinforcement-constrained concrete is not complex, is not ideal to use it directly to predict the contraction of reinforcement-constrained concrete. Therefore, after several experiments, researchers finally derived empirical formulas to forecast the contraction of concrete when restrained by reinforcement. However, the empirical formula has limitations, so the scope of application is relatively small. To calculate the restraint tensile stress and assess the possibility of concrete cracking, the value of contraction strain of concrete subjected to reinforcement restraint is critical. It can effectively help the designer to take measures to inhibit the concrete cracking phenomenon. Therefore, the study of accurate prediction of contraction of restrained concrete is important.

The capillary tension theory shows that after the pores have absorbed water, the capillary force in the concrete pore wall will further shrink the concrete. Changes in pore structure cause changes in capillary pressure, which further affects the contraction characteristics of concrete [6, 7]. Previous research has shown that reinforcement can limit the volume reduction (contraction) of concrete and alter the pore structure and restrain the concrete's contraction properties. Therefore, the capillary tension theory is reasonable. However, the specific effects have not been elucidated.

The capillary tension theory can describe and foresee the contraction of concrete, where a crucial factor in determining contraction is the concrete's pore structure [8, 9].

In this research, an approach was developed to forecast contraction of reinforcement-constrained concrete according to the hypothesis of capillary tension. Then, using two strength grades (C20 and C50) and three reinforcement ratios (0, 1.14 and 3.24%) of concrete, the mercury-pressure approach was used to further examine the pore architectures of the six distinct specimens. We also examined the concrete's contraction and its physical characteristics, including its splitting tensile strength, cubic compressive strength, elastic modulus, and Poisson's ratio. The study's goals included assessing the impact of reinforcement on the pore structure of concrete and predicting, using the capillary tension theory, the contraction strain of concrete restricted by reinforcement. The test results were ideal.

2 Contraction Prediction Method for Reinforcement-Constrained Concrete

When the concrete shrinks, shear stresses are generated between the concrete and the reinforcement. The shear stress causes a normal stress between the reinforcement and the concrete. Compressive stress, which tightens the reinforcement and encourages shrinking, is the typical stress for steel that is being reinforced. In addition, the typical stress in concrete is known as the confining tensile stress, which is runs counter to concrete contraction.

Figure 2 shows a concrete specimen considering confinement. As stated by the theory of capillary tension, the capillary stress promotes the contraction of concrete with a value equal to the pressure difference between the liquid and gas phases of water in the pore space with a value equal to the pressure differential between the liquid and gas phases of water in the pore space, the capillary stress promotes the contraction of concrete. And the Laplace equation could be used to compute the pressure differential (DP). Consequently, the capillary stress (σ_{ca}) may be written as:

$$\sigma_{ca} = \Delta P = \frac{2\gamma \cos\theta}{r} \tag{1}$$

where γ is the capillary's inner wall's surface tension, which at 20 °C has a value of 7.28×10^{-2} N/m. θ represents the angle of contact at the liquid–solid interface (for concrete, $\theta = 0$ °C). r represents the pore space's critical diameter.

In the specimen's length direction (x direction), the concrete is subjected to capillary and confining tensile stresses. In this study, in the length direction (x), the reinforcement is more restrained, so it is assumed that the concrete members are subjected to only capillary stresses in the directions of breadth (y) and height (z). According to the mechanics of materials, the strain in the x-direction of concrete (ε_{sh-x}) is expressed as

$$\varepsilon_{sh-x} = \frac{1}{E_s}\left[\sigma_x - \mu\left(\sigma_y + \sigma_z\right)\right] = \frac{1}{E_s}[(\sigma_{ca} - \sigma_t) - \mu(\sigma_{ca} + \sigma_{ca})]$$

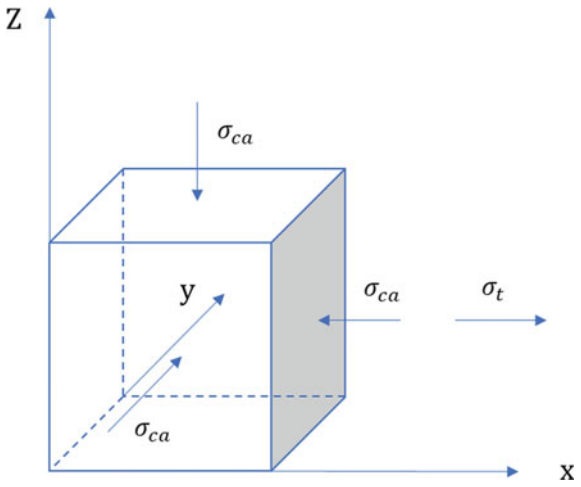

Fig. 2 Concrete element in restrained specimens

$$= \frac{1-2\mu}{E_s}\sigma_{ca} - \frac{1}{E_s}\sigma_t \tag{2}$$

where σ_t denotes the concrete's restricted tensile stress. μ refers to the concrete's Poisson's ratio. E_s indicates the elastic modulus of the capillary's micro-matrix.

The concrete's shear stress leads to a limiting the tensile tension inside the concrete and also leads to a compression tension (σ_{re}) inside the reinforcement. Based on the balance of forces, the following expressions are derived.

$$A_c\sigma_t = A_{re}\sigma_{re} \tag{3}$$

where, A_{re} denotes the reinforcement's cross-sectional area. A_c stands for the concrete's cross-sectional area.

Therefore, One way to represent the restrained tensile tension is as follows:

$$\sigma_t = \frac{A_s}{A_c}\sigma_{re} = \rho\sigma_{re} \tag{4}$$

where, ρ is the reinforcement rate.

The reinforcement is subjected to compressive stresses only. Therefore, in the x-direction, the strain in the reinforcement (ε_{re-x}) can be expressed as

$$\varepsilon_{re-x} = \frac{\sigma_{re}}{E_{re}} \tag{5}$$

E_{re} is the reinforcement's modulus of elasticity.

Due to the displacement of the reinforcement and concrete being the same in the specimen. Therefore

$$\delta_{sh-x} = \delta_{re-x} \tag{6}$$

where δ_{sh-x} represents the concrete's displacement and δ_{re-x} represents the reinforcement's displacement.

We assume that the concrete and reinforcement lengths (L) are the same. Therefore

$$\frac{\delta_{sh-x}}{L} = \frac{\delta_{re-x}}{L} = \varepsilon_{sh-x} = \varepsilon_{re-x} \tag{7}$$

Substituting Eqs. (1), (4), (5) and (7) into Eq. (2), the contraction of reinforcement-constrained concrete can be calculated as follows.

$$\varepsilon_{sh-x} = \frac{(1-2\mu)}{E_s+E_{re}\rho} \cdot \frac{2\gamma}{r} \tag{8}$$

A conclusion can be drawn from Eq. (8). That is, for the concrete under study, Poisson's ratio, pore structure, elastic modulus of concrete and reinforcement, and reinforcement rate all have an effect on its contraction strain. To further verify the accuracy of Eq. (8), experiments were carried out to investigate the precise impact of reinforcing on the pore structure of concrete.

3 Experiments and Methods

3.1 Materials and Mix Ratio

The concrete mixes used in this study are shown in Table 1. The cementitious materials consisted of Portland cement and fly ash. Quartz sand with a fineness modulus of 3.0 served as the fine aggregate, while crushed limestone with a maximum nominal size of 20 mm served as the coarse aggregate.

3.2 Pore Structure Measurement

Regarding the pore structure test, the specimen molds were made of Plexiglas with internal dimensions of 200 mm × 200 mm × 1000 mm and removable on all sides.

The detachable Plexiglas plate was relocated and a Teflon plate with a thickness of 1 mm was placed on the mold's bottom after the concrete had had time to solidify

Table 1 Mixing ratio of concrete (kg/m^3)

Concrete	Ratio water/binder	Cement	Water	Fly ash	Sand	Coarse aggregate	Polycarboxylate superplasticizer
C20	0.43	320	175	90	840	930	8.2
C50	0.30	350	150	150	700	1100	12.2

initially. It was important to make sure that the reinforcement was the sole means by which the specimens were bound.

Six specimens were cast using two different concrete strength classes (C20 and C50) and three different reinforcement rates ($\rho = 0$, 1.14 and 3.24%). Table 2 provides information about the specimens. In order to achieve the criteria for the reinforcement rate, four reinforcement bars were inserted on each of the four sides of the cross section of the restrained specimens (Fig. 3). The specimens were created and kept in certain environments. (20 ± 2 °C, 65 ± 5% RH).

At each test age (3, 7 and 28 days), holes were drilled in the specimens to collect concrete material from them. The concrete was then broken up and screened to remove any particles larger than 2.5 mm. In order to avoid hydration, acetone was utilized, and a vacuum desiccator was used to dry the samples. Finally, a fully automated Auto IV9510 mercury press was used to measure the interior pore structure of the concrete.

Table 2 Details of the specimens

No.	Strength grades	Reinforcement				
		Reinforcement ratio (%)	Reinforcement bar diameter (mm)	Elastic modulus ($\times 10^4$ MPa)	Yield strength (MPa)	Ultimate strength (MPa)
C20-P	C20	0	–	–	–	–
C20-R1		1.14	12	20.6	400	580
C20-R3		3.24	20	20.6	400	580
C50-P	C50	0	–	–	–	–
C50-R1		1.14	12	20.6	400	580
C50-R3		3.24	20	20.6	400	580

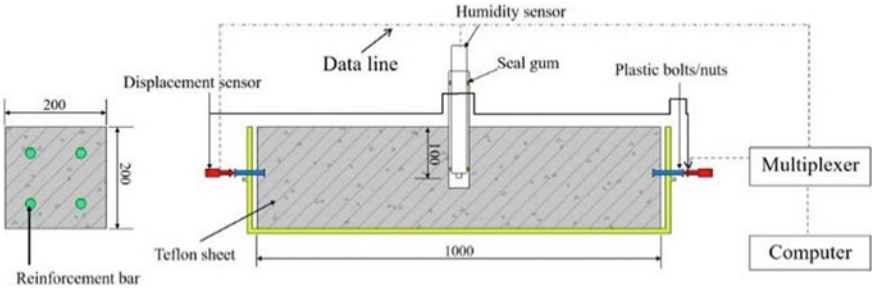

Fig. 3 Pore structure, contraction, and physical characteristics testing apparatus (size unit: mm)

3.3 Contraction Measurement

Due to the difference in strength class and reinforcement rate of concrete for different specimens, different types of contraction test specimens were ready and maintained similarly to the pore structure test specimens. The contraction of the specimens was measured using a linear variable differential transducer (LVDT) with a measuring range and precision of 2 mm and 1 μm, respectively. The measurement sites were positioned in the middle of the specimen cross-section, and the LVDTs were situated at both ends of the specimens (Fig. 3). This is done by waiting for the first concrete set and removing the mold for Plexiglas placed on the specimen's side so that the LVDT is in direct contact with the bolt. The nuts were inserted into the bolts and prefabricated in to specimens. Thermocouples are already placed in the specimen to monitor how temperature changes during the test affect the concrete. And then the computer equipment automatically records the measured values.

3.4 Physical Property Measurements

The findings of measuring the concrete's cubic compressive strength, splitting tensile strength, elastic modulus, and Poisson's ratio at 3, 7, and 28 days of age are shown in Table 3.

Table 3 Concrete's physical characteristics

	Age (days)	Physical characteristics			
		Cube compressive strength (MPa)	Splitting tensile strength (MPa)	Elastic modulus ($\times 10^4$ MPa)	Poisson's ratio
C20	3	13.5	1.2	2.05	0.155
	7	18.5	1.8	2.77	0.158
	28	21.5	2.2	3.11	0.161
C50	3	27.4	1.7	2.74	0.164
	7	41.0	3.9	3.35	0.166
	28	52.1	4.2	3.54	0.169

4 Consequence and Discussion

4.1 Pore Structure of Concrete

Table 4 shows the pore characteristics parameters for each specimens in various stages of cure. Different pore sizes have different effects on the concrete properties. The pores that mainly affect the contraction properties of concrete are gel pores (diameter < 10 nm) and transition pores (diameter, 10–100 nm).

As can be seen from Table 4, the size of concrete's pore structure decreases with increasing curing age for specimens with the same reinforcing rate and concrete strength class. For instance, the mean pore size, median pore size, critical pore size, and porosity of the C20-P specimen with an age of 3 days were 37.55 nm, 79.54 nm, 40.61 nm, and 22.65%, respectively. They were 20.03, 38.32, 25.06 nm, and 7.2% higher than those with age 28 days. The percentage of pores and gel pores with diameters of 10–50 nm increased significantly on day 28 compared to day 3, while the percentage of pores with diameters greater than 50 nm decreased compared to day 3. The main reason for this trend is the infiltration of the hydration products into the

Table 4 Pore characteristic parameters of specimens

	Age (days)	Reinforcement ratio (%)	Porosity (%)	Average pore diameter (nm)	Median pore diameter (nm)	Critical diameter of capillary (nm)
C20-P	3	0	22.65	37.55	79.54	40.61
	7	0	19.32	28.54	70.45	31.65
	28	0	15.45	17.52	41.22	15.55
C20-R1	3	1.14	30.11	40.54	95.32	51.36
	14	1.14	25.35	35.32	80.14	37.56
	28	1.14	20.14	24.11	51.23	27.55
C20-R3	3	3.24	36.12	47.66	110.20	67.86
	14	3.24	32.22	41.25	98.55	58.55
	28	3.24	28.64	33.65	66.45	35.22
C50-P	3	0	17.65	26.45	67.88	36.54
	7	0	14.55	19.74	54.23	24.33
	28	0	12.10	13.87	32.47	16.13
C50-R1	3	1.14	22.35	29.56	79.14	48.54
	7	1.14	19.45	25.00	65.33	30.21
	28	1.14	17.55	22.58	42.13	24.55
C50-R3	3	3.24	32.22	39.41	90.25	60.25
	7	3.24	28.54	33.11	82.44	45.54
	28	3.24	26.54	27.89	60.13	30.41

pores of the concrete, which, together with the capillary stress, causes the distance between the various pore walls and the microcracks in the concrete to shrink.

It is also found that the size of the specimens' pore structure increases with an increase in the rate of reinforcing at the same level of concrete strength. For example, at 28 days, the critical diameter of concrete in the non-contraction specimen C20-P ($\rho = 0\%$) was 15.55 nm, which was 12.00 nm and 19.67 nm lower than that of C20-R1 ($\rho = 1.14\%$) and C20-R3 ($\rho = 3.24\%$), respectively. Similar tendencies were seen in specimens with actual strengths of C50 and other pore characterization metrics.

The characteristics of the concrete pore structure and reinforcement rate are reflected in Fig. 4 (mean pore size, median pore size, capillary critical diameter and porosity). The relationship between them can be expressed as follows.

$$a_\rho = a_0 + k\rho \tag{9}$$

where a_ρ denotes the reinforcement-constrained concrete's pore structure parameter. a_0 denotes the unconfined concrete's pore structure parameter. ρ denotes the reinforcement ratio. k is a positive coefficient.

It should be noted that Eq. (9) applies when the concrete's pore structure is not destroyed. The confining tensile stress in the specimen, which was determined by

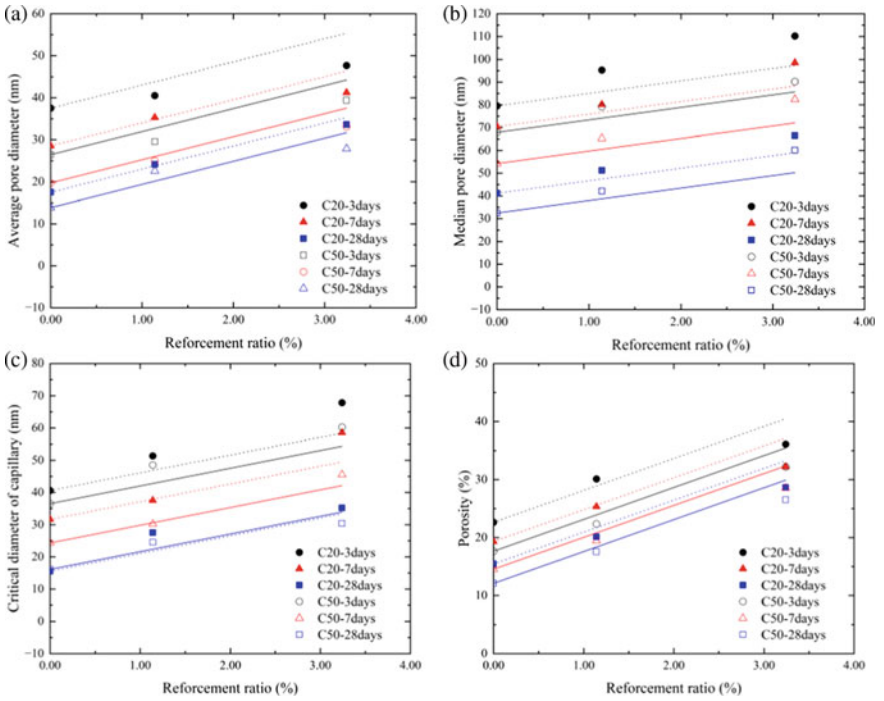

Fig. 4 A connection between pore structure parameters and reinforcement rate: **a** average pore diameter, **b** median pore diameter, **c** critical diameter of capillary, **d** porosity

Table 5 Values of k for various pore parameters

	Average pore diameter (nm)	Median pore diameter (nm)	Critical diameter of capillary (nm)
k	550	550	550

testing, may be represented as follows using the previously introduced process for reinforcement-constrained concrete:

$$\sigma_t = \frac{A_s}{A_c}\sigma_{re} = \rho\sigma_{re} = \rho E_{re}\varepsilon_e \tag{10}$$

where ε_e is the contraction strain obtained experimentally.

In this research, In specimens without contraction (C20-P and C50-P), a_0 was found. k values were found by regressing the outcomes of the experiment and their values are shown in Table 5.

In non-contraction specimens, The size of the pore structure is decreased by the capillary stresses on the concrete pore walls. But in the confined specimens, both capillary and confining tensile stresses impact the pore walls. According to Eq. (8) as well as (9), the synthetic stress (σ_{sh-x}) acting on the concrete in the confined specimen can be expressed as

$$\sigma_{sh-x} = \frac{E_s(1-2\mu)}{E_s+E_{re}\rho} \cdot \frac{2\gamma}{a_0+k\rho} \tag{11}$$

It can be found that the higher the reinforcement ratio, the better the restraint effect of the reinforcement. This in turn leads to a decrease in the synthetic stress put on the concrete pore wall. This indicates that as the reinforcement ratio increases, the concrete's pore size decreases to a lesser extent due to the capillary stresses. This is consistent with the experimental results.

4.2 Concrete Contraction

In the contraction test, the specimens are prepared and cured similarly to the test specimens for pore structure. There are three phases to the contraction's development for all specimens: Stage 1—Rapid Rise Stage (roughly 0–5 days), Stage 2—Slow Rise Stage (approximately 6–10 days) and Stage 3—Relative Stability Stage (after 10 days). When the pores in the concrete absorb water, the capillary stresses applied to the pore walls cause contraction of the concrete. In the early stage, the concrete absorbs water quickly due to the strong cement hydration, which can lead to a quickly rising in contraction. Secondly, the water absorption rate decreases with the decrease of cement hydration rate. Therefore, the contraction will gradually decrease and its value will eventually be relatively stable.

Table 6 Capillary stress of different concrete (MPa)

	C20-P	C20-R1	C20-R3	C50-P	C50-R1	C50-R3
3 days	3.59	2.83	2.15	3.98	3.00	2.42
7 days	4.60	3.88	2.49	5.98	4.82	3.20
28 days	9.36	5.28	4.13	9.03	5.93	4.79

Among all concrete specimens of curing age, the highest contraction strain was observed in the non-contraction specimens. For instance, in the C20 concrete specimens. The maximum contraction strain obtained in the C20-P ($\rho = 0\%$) specimen at 28 days was 620 le. This value was 310 le and 462 le higher than the values obtained in specimens C20-R1 ($\rho = 1.14\%$) and C20-R3 ($\rho = 3.24\%$), respectively. This indicates that, when concrete is restrained by reinforcement, its contraction strain reduces as the reinforcement ratio rises.

The capillary stresses are also affected by the size of the concrete's pore structure. The capillary stresses in concrete were calculated by Eq. (1) and the results are shown in Table 6. In the specimen, it can be seen that the reinforcement has an effect on the size of the pore structure, and that when the reinforcement rate is increased, the capillary stress decreases. Therefore, we found that the contraction of the restrained specimens decreases with increasing reinforcement rate, not just because of the joint deformation between the concrete and the reinforcement, but also because the capillary stress, which is what causes the contraction of the concrete, is constrained.

4.3 Concrete Contraction Calculation

To verify the validity of Eq. (8), the experimental values are compared with the calculated values. E_s can be get from E_c. The ratio between the modulus of elasticity E_c and E_s of concrete is adjustable between 2.5 and 3.5 as the strength of concrete increases. In this study, the ratios were 3.0 and 3.2 for C20 concrete and C50 concrete, respectively. Poisson's ratio and modulus of elasticity of concrete at each age are given in Table 2, and the critical diameters of concrete capillaries are listed in Table 4.

In Table 7, the results of the contraction test are compared to those that were anticipated using Eq. (8). It can be observed that the relative errors are less than 15% for all age specimens. This suggests that when concrete is constrained by reinforcement, Eq. (8) in may accurately predict the contraction of the concrete.

In this study, because there are no research on surface tension-induced contraction, internal water movement and separation pressure, we assumed that the concrete contraction was owing to capillary tension. Therefore, the results in Table 7 indicate that the calculated results differ from the experimental results. Therefore, further studies are needed.

Table 7 Comparison of experimental and calculated results

	3 days			7 days			28 days		
	Test value (με)	Calculated value (με)	Relative error (%)	Test value (με)	Calculated value (με)	Relative error (%)	Test value (με)	Calculated value (με)	Relative error (%)
C20-P	330.00	362	−9.71	364.00	341	6.38	620.00	612	1.23
C20-R1	190.00	213	−12.13	221.00	229	−3.59	310.00	282	9.09
C20-R3	99.00	110	−10.71	115.00	107	7.02	158.00	164	−4.10
C50-P	345	303	12.19	425	382	10.15	566	540	4.56
C50-R1	210	185	12.03	288	251	12.78	335	293	12.61
C50-R3	119	107	10.44	135	125	7.72	188	179	4.95

5 Conclusions

In this study, based on the capillary tension theory, a forecasting model for the early contraction of reinforcement-constrained concrete was developed, and after that, it was looked at how reinforcing affected the pore structure of concrete. In this study, The contraction strain and pore structure of specimens with various concrete strength classes and reinforcing ratios at various ages were measured. Investigations were also done on concrete's physical characteristics.

The findings of the experiment led to the following deductions.

(1) Due to hydration products and capillary forces, the pore size of concrete for concrete specimens (C20 and C50) continually decreases with age.
(2) The confining action of reinforcement causes the size of the pore structure in concrete to expand with increasing reinforcing rate. The average, median, capillary critical diameter, and porosity characteristics of the pore structure are directly linked to the reinforcing rate.
(3) As the reinforcement rate increases, the contraction of the restrained specimens decreases, not just because of the joint deformation between the concrete and the reinforcement, but also because the capillary stress, the force behind concrete contraction, is constrained.
(4) The calculated results from Eq. (8) are more in line with the experimental results, suggesting that Eq. (8) can accurately predict how much concrete will contract when it is restrained by reinforcement.

References

1. Deboodt T, Fu T, Ideker JH (2016) Evaluation of FLWA and SRAs on autogenous deformation and long-term drying shrinkage of high performance concrete. Constr Build Mater 119:53–60
2. Soliman AM, Nehdi ML (2011) Effect of drying conditions on autogenous shrinkage in ultra-high performance concrete at early-age. Mater Struct 44(5):879–899
3. Yoo D-Y et al (2014) Influence of reinforcing bar type on autogenous shrinkage stress and bond behavior of ultra high performance fiber reinforced concrete. Cement Concr Compos 48:150–161
4. Huang L et al (2017) Influence of reinforcement configuration on the shrinkage and cracking potential of high-performance concrete. Constr Build Mater 140:20–30
5. Yoo D-Y et al (2013) Early age setting, shrinkage and tensile characteristics of ultra high performance fiber reinforced concrete. Constr Build Mater 41:427–438
6. Li Y, Bao J, Guo Y (2010) The relationship between autogenous shrinkage and pore structure of cement paste with mineral admixtures. Constr Build Mater 24(10):1855–1860
7. Meddah MS, Tagnit-Hamou A (2009) Pore structure of concrete with mineral admixtures and its effect on self-desiccation shrinkage. ACI Mater J 106(3):241
8. Li Y, Li J (2014) Capillary tension theory for prediction of early autogenous shrinkage of self-consolidating concrete. Constr Build Mater 53:511–516
9. Garboczi EJ, Bentz DP (1997) Analytical formulas for interfacial transition zone properties. Adv Cem Based Mater 6(3–4):99–108

Experimental Study of Pore Structure and Compressive Strength of Reinforced Concrete

Ruiyi Wang, Maoyi Liu, Jian Kang, Daifeng Wu, Zhiqiang Wang, and Xingyang Zhou

Abstract Experimental research on how reinforcing bars affect the pore structure and compressive strength of concrete was studied in this work. The samples used in the tests were from concrete with 2 mix ratios and 9 reinforcement ratios. At three, seven, and twenty-eight days old, respectively, the concrete compressive strength and the structure of pores were examined. The pore structure of the concrete was discovered to alter as a result of the reinforcing bars. The size of the pore structure of concrete grew larger together with the reinforcement ratio. As the reinforcement ratio rose, the samples of reinforced concrete of the same age lost compressive strength. The formula for calculating the compressive strength of reinforced concrete samples was developed based on the known strength of plain concrete.

Keywords Pore structure · Reinforcing bar · Concrete compressive strength · Prediction of compressive strength

1 Introduction

Due to concrete being made of cement, concrete's strength can be impacted by a variety of factors, such as pores and microcracks, particularly when it is subjected to thermal stress. The link between the structure of the pores and compressive strength of concrete has been the subject of numerous academic studies. In a bid to investigate the association between the pore structure and concrete strength, Li et al. [1] developed a mathematical model of effective strength of concrete, and analyzed and

R. Wang · J. Kang
School of Civil Engineering, Chongqing University, Chongqing 400045, China

M. Liu · D. Wu · Z. Wang
Chongqing Urban Investment Infrastructure Construction Co., Ltd., Chongqing 400045, China

X. Zhou (✉)
Department of Civil Engineering, Xi'an Jiaotong-Liverpool University, Suzhou 215123, China
e-mail: egbert2023@163.com

H.-Y. Jeon (ed.), *Proceedings of the International Conference on Geosynthetics and Environmental Engineering*, Lecture Notes in Civil Engineering 374,
https://doi.org/10.1007/978-981-99-4229-9_42

discussed the influence of porosity and pore structure on the strength of compression as well as tensile. In addition, some researchers also conducted proportional and static compression tests on a series of concrete mix ratios with various pore structures to determine the relationship between the strength and pore structure of hardened concrete [2]. Lian et al. [3] has researched the link between concrete's compressive strength and the structure of the pores. Depending on the GRE principle, Zhang et al. [4] proposed the quantitative relationship between the concrete pore structure and compressive strength. In general, it was discovered that the concrete's strength increased with increasing pore structure density [5].

Concrete and steel reinforcement are typically used to create reinforced concrete structures in practical engineering [6, 7]. It has been demonstrated that there exist interface transition zones (ITZs) between the reinforcing bar and the concrete in reinforced concrete structures. As a result of the concrete's increased porosity in ITZ areas compared to non-ITZ areas, a number of properties changed, including the concrete strength, particularly under the horizontal reinforcement and in areas where the reinforcing rate is quite large, and more effective vibrating of the concrete is not feasible. In these regions, ITZ's porosity increases even more, severely lowering the performance of the concrete. At once, as the cement hydration gradually consumes water and the concrete becomes dry, the capillary force created in the concrete pores will gradually shorten the distance between the concrete particles, which causes a macroscopic reduction in the volume of concrete (this phenomenon is known as shrinkage). Inside the concrete, the restraint stress shrinks in the opposite direction when it is restrained by the reinforcement bars, reducing concrete shrinkage. The concrete pore structure is subject to corresponding changes due to its deformation. Previous studies [8] have demonstrated that various pore structure parameters (porosity and average pore size) of laterally constrained concrete are significantly lower than those of non laterally constrained concrete. Nevertheless, the influence of constrained concrete volume diminution (such as shrinkage) on concrete pore structure is still not known.

At the beginning of construction, scaffolding is required to support the load owing to the low strength of concrete. As required by Chinese standards, whether the scaffold can be removed during construction is mainly based on the concrete compressive strength. When the concrete compressive strength of ordinary members alongside other significant members individually achieves 75 and 100% of the design strength, scaffolding allowed to be removed. Subject to certain limitations of engineering practice, tests on concrete blocks without reinforcement bars are used to determine whether the compressive strength of concrete can achieve the requirements. As a result, some impacts of reinforcing bars on the concrete pore structure and strength are not taken into account. If a study shows that reinforcement bars can cause changes of concrete pore structure, and subsequently lessen its compressive strength throughout shrinkage, then the concrete strength evaluation methods that already has been implemented at the construction site have the potential to increase the likelihood of structural failure of the building during the construction period.

To learn how reinforcing bars affect the structure of the pores and compressive strength of concrete, experiments were carried out. Nine reinforcement ratios (0–6.56%) and two mix rates for concrete specimens were presented. Concrete specimens with 2 mix rates and reinforcement ratios of 0, 1.14, 3.24, and 6.52% were tested for pore structure at different ages (3, 7, and 28 days) using the mercury intrusion method. Furthermore, compressive strength tests were performed on all types of specimens. The samples were placed in closed containers for accelerated tests and their volumetric water content and porosity were measured. All samples were completely vibrated prior to the test. By comparing the pore structure and compressive strength of concrete with various reinforcing rates, the structure of the pores and compressive strength of concrete after reinforcement were investigated.

2 Experiments

2.1 Methods and Materials

In this investigation, two various concrete mixtures were employed (Table 1). The proportional contents of sand, coarse aggregates and water were different. The cementitious materials chosen were cement and fly ash, and quartz sand which has a particle size distribution 0.2–4 mm, specific gravity 2.8 g/cm^3 and a fineness modulus 3.0, was selected as the fine aggregate. The crushed limestone has a specific gravity of 2.8 g/cm^3 and an average particle width distribution of 5–20 mm, making it suitable as coarse aggregate. A polycarboxylate superplasticizer with a water reduction ratio of 30–35% is the one that is employed. Table 2 displays details about the reinforcement bars that were employed in the study.

In this study, a mold was made of Teflon material (as shown in Fig. 1) to create concrete samples that were 200 mm × 200 mm × 500 mm in size. After the initial setting of the concrete, first remove all sides of the mold (orange in Fig. 1). The concrete specimens after taking the above measures are restrained only by the reinforcement bars.

Table 1 Mixture ratio

Mixture	Cement	Water	Fly ash	Sand	Coarse aggregate	Superplasticizer
C40	300	155	110	840	930	8.2
C70	380	120	150	700	1100	12.2

Table 2 Reinforcement bar performance

Constraint	Elastic modulus (× 10^4 MPa)	Yield strength (MPa)	Ultimate strength (MPa)
Reinforcing bar	20.6	400	580

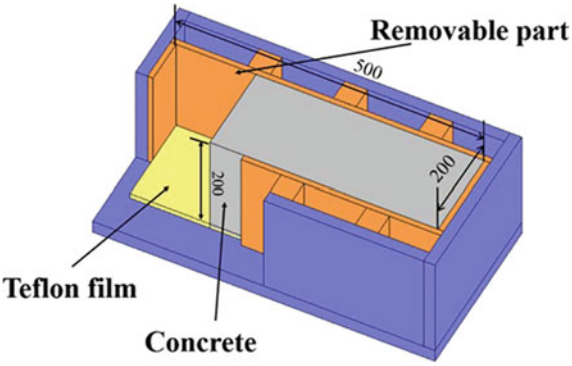

Fig. 1 Teflon specimen-forming mold (all dimensions are in mm)

In total, 18 concrete specimens with 2 mix ratios and 9 reinforcement rates were used in the investigation, and the reinforcement rates were % = 0, 1.14, 1.56, 2.05, 2.61, 3.24, 3.95, 5.16 and 6.52% (Table 3), and the test results were analyzed. The reinforcement bars of different diameters are uniformly placed at each corners of the concrete cross-sectional area (see Fig. 2). Three samples of each form of concrete were made in order to assess its compressive strength at 3 various ages. The curing and testing of all samples took place in an unchanging environment of 20 ± 2 °C and 65 ± 5% relative humidity.

After 3, 7 and 28 days, three cylindrical specimens with dimensions equal to 100 mm in diameter and 200 mm in height (height/diameter = 2) were individually cut out of every form of sample to determine the concrete's compressive strength (in accordance with JGJ/T384 standard). The concrete strength test procedure is in accordance with GB/T50081, a national standard for China.

2.2 Concrete Pore Structure Specimens Test

The pore structures of concrete (C40-R0, C40-R1, C40-R5, C40-R8 and C70-R0, C70-R1, C70-R5 and C70-R8) with reinforcement ratios of 0, 1.14, 3.24 and 6.52% were studied experimentally. Concrete porosity tests were performed on residual samples after drilling that were utilized as test specimens. To obtain concrete particles with a particle size range of 2.5–5 mm, the specimens of concrete were crushed initially and afterwards sifted using a screen. Acetone was used to inhibit the concrete's polymerization, and the samples were dried by a vacuum desiccator. Lastly, a fully automated mercury porosimeter with a resolution of 69 kPa, a pressure ranging of 0–345 kPa for low pressure assessment, and a ranging of 101.325–414,000 kPa for high pressure analysis was used to examine the concrete's pore structure.

Table 3 Specimens information

Number	Strength	Reinforcing rate (%)	Reinforcing bars diameter (mm)
C40-R0	C40	0	–
C40-R1		1.14	12
C40-R2		1.56	14
C40-R3		2.05	16
C40-R4		2.61	18
C40-R5		3.24	20
C40-R6		3.95	22
C40-R7		5.16	25
C40-R8		6.52	28
C70-R0	C70	0	–
C70-R1		1.14	12
C70-R2		1.56	14
C70-R3		2.05	16
C70-R4		2.61	18
C70-R5		3.24	20
C70-R6		3.95	22
C70-R7		5.16	25
C70-R8		6.52	28

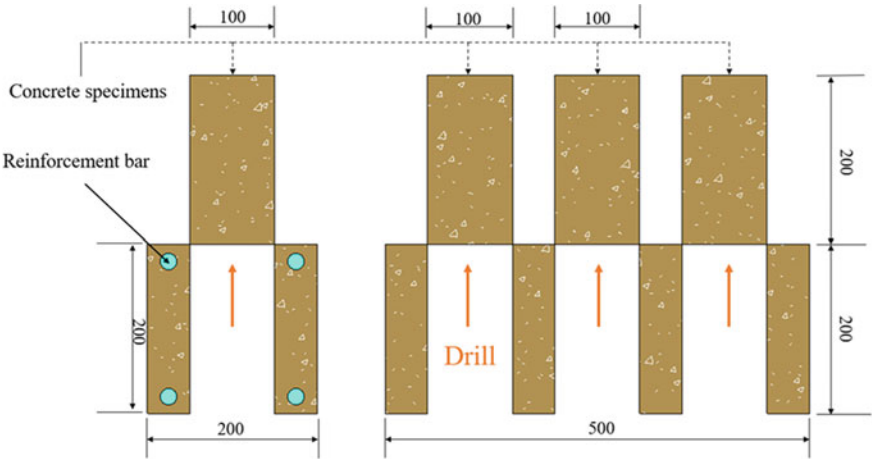

Fig. 2 Concrete specimens for testing its compressive strength and pore structure

3 Results and Discussion

3.1 Alterations to Pore Structure

Table 4 displays the pore structure characteristics for concrete samples at various ages with reinforcing ratios of 0, 1.14, 3.24, and 6.52%, and for the same mixing ratios and reinforcing ratios, the size of the concrete structure of the pores steadily shrank over the curing time. In addition, the percentage of pores with diameters just under 50 nm at 28 days was significantly larger for C40-R0 concrete than at 3 days. Further samples revealed an identical pattern. Concrete pore structure size with the growth of the curing age and gradually become smaller, mainly for two reasons, one is the hydration products filled with pores, the second is due to the role of capillary stress, concrete between the various types of pore walls and microcrack size reduction.

Besides, it was found that the arrangement of reinforcing bars significantly altered the pore structure of concrete, and the size of its structure of the pores significantly grew as the reinforcement rate rose. For instance, the C40-R8 concrete specimens with 6.52% reinforcement rate had a critical diameter at 28 days of 42.50 nm, which is larger than the specimens of C70-R5 (3.24%), C70-R1 (1.14%), and C70-R0 (0%) (31.09 nm, 21.54 nm and 16.28 nm, respectively).

Figure 3 depicts the association between pore structure variables such porosity, average and median pore size, critical diameter and the concrete reinforcing rate. The size of the concrete pore structure and the reinforcement rate are shown to be correlated linearly. Therefore, the following equation can be used to describe how reinforcing bars alter the structure of the pores of concrete:

$$S_\rho = S_0 + n\rho \tag{1}$$

In this formula, S_ρ is the reinforcing rate ρ corresponding to the concrete pore structure parameters; S_0 denotes the concrete pore structure parameters matching to a reinforcing rate of 0%. The rise in the pore structure parameter generated by a raise in the unit reinforcing rate is denoted by n.

The obtained test data were regressed to obtain n values (Table 5). Figure 3 represents the error of the concrete pore structure parameters computed from Eq. (1) relative to the measured data, and it can be seen that there is an agreement between the calculated and measured values.

Porousness characterizes concrete. With the consumption of hydration and the drying effect within the pores of concrete, capillary stress is formed on the sidewalls of concrete pores, causing the concrete to shrink. Due to reinforcement bars prevented the concrete from shrinking freely, the shear tension was created at the joint where the concrete and reinforcing bars met. This caused the concrete to be subjected to normal stress (called constraint stress) in an opposite manner to the shrinkage induced by capillary stress. The constraint stress can be calculated using the equation shown below:

Table 4 Concrete pore factors at various ages

No.		Reinforcement ratio (%)	Average pore diameter (nm)	Median pore diameter (nm)	Critical diameter (nm)	Porosity (%)
C40-R0	3	0	40.40	81.90	42.20	25.37
	14	0	29.31	71.29	33.65	22.19
	28	0	19.90	44.08	18.09	15.94
C40-R1	3	1.14	43.16	97.72	52.35	30.90
	14	1.14	37.86	83.11	37.62	27.36
	28	1.14	24.93	52.19	22.14	22.03
C40-R5	3	3.24	47.92	108.41	60.65	36.46
	14	3.24	43.40	100.32	52.41	33.78
	28	3.24	34.77	58.52	32.55	30.60
C40-R8	3	6.52	50.14	120.11	70.40	40.74
	14	6.52	46.61	105.54	60.25	36.88
	28	6.52	40.23	70.30	42.50	35.45
C70-R0	3	0	28.54	69.18	38.72	17.78
	7	0	21.97	56.26	26.33	15.54
	28	0	14.38	32.81	16.28	14.95
C70-R1	3	1.14	31.49	81.09	45.55	23.02
	7	1.14	27.45	67.01	32.51	22.34
	28	1.14	24.95	42.41	21.54	17.56
C70-R5	3	3.24	41.08	92.03	61.67	33.94
	7	3.24	33.78	74.03	46.41	30.85
	28	3.24	29.92	52.36	31.09	27.76
C70-R8	3	6.52	48.98	104.50	65.55	40.51
	7	6.52	40.24	96.50	50.46	36.54
	28	6.52	35.66	60.53	42.11	31.55

$$\sigma_t = \frac{\varepsilon_{sh} \cdot E_c}{1 + \frac{E_c}{\rho E_s}} \tag{2}$$

In the formula, E_c and E_s represent the respective elastic moduli of concrete and reinforcing bars; Concrete's free shrinkage is denoted by the symbol ε_{sh}.

According to Eq. (2), the restraint stress increased as the reinforcement rate rose, thus lessening the concrete's pore structure as a result of capillary stresses. As a result, the test findings show that the pore structure of concrete grew larger as the reinforcement rate rose.

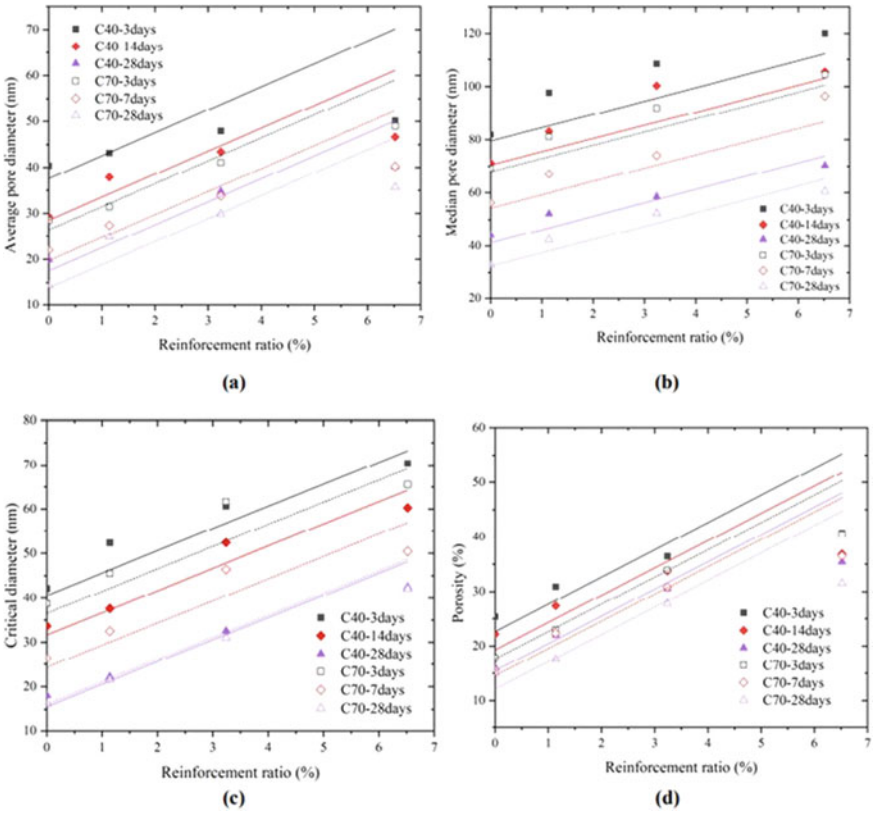

Fig. 3 Relations between the reinforcing rate and the pore structure of concrete: **a** average pore diameter, **b** median pore diameter, **c** critical diameter of capillary, **d** porosity

Table 5 n of various pore parameters

Coefficient	Average pore diameter (nm)	Median pore diameter (nm)	Critical diameter (nm)	Porosity
n	500	500	500	500

3.2 Concrete Compressive Strength

Table 6 provides the compressive strength of the concrete at every stage of age. It should be noted that as the age of cure grew, each specimen's compressive strength of concrete rose. After 3 days, every group of concrete compressive strength achieved 56–65% of that after 28 days; after 7 days, the concrete compressive strength reached 79–91% of that after 28 days. Obviously, the strength of concrete had the characteristic of rapid growth at the initial periods (3–7 days), and then the growth rate gradually decreased.

Table 6 Concrete strength test results (MPa)

Number	Strength (standard deviation)			Number	Strength (standard deviation)		
	3 days	7 days	28 days		3 days	7 days	28 days
C40-R0	29.7	35.64	42.36	C70-R0	55.1	68.5	74.4
C40-R1	28.1	34.5	41.5	C70-R1	54.1	67.4	73.5
C40-R2	29.2	33.4	38.7	C70-R2	53.5	66.5	72.1
C40-R3	26.5	31.2	36.5	C70-R3	51.4	64.2	70.1
C40-R4	25.4	30.3	37.1	C70-R4	49.8	62.2	69.4
C40-R5	24.8	28.7	34.5	C70-R5	47.7	60.4	67.5
C40-R6	23.5	27.5	33.6	C70-R6	45.6	59.6	66.4
C40-R7	22.0	25.5	32.1	C70-R7	43.3	60.2	64.3
C40-R8	22.4	26.7	30.23	C70-R8	42.3	58.8	61.1

However, as the reinforcement ratio rose, the specimen's compressive strength decreased, and the strength was the same while the reinforcement ratio was not consistent. For the same strength grade specimens, the specimen with 0% reinforcement ratio has the greatest compressive strength. For instance, at 28 days, the compressive strength of C40-R8 (% = 6.52%) concrete was 30.23 MPa, which was lower than that of C40-R7 (% = 5.16%), C40-R6 (% = 3.95%), C40-R5 (% = 3.24%), C40-R4 (% = 2.61%), C40-R3 (% = 2.05%), C40-R2 (% = 1.56%), C40-R1 (% = 1.14%), and C40-R0 (% = 0%) (32.1, 33.6, 34.5, 37.1, 36.5, 38.7, 41.5, and 42.36 MPa, respectively).

The link between strength and pore structure factors for samples with reinforcing ratios of 0%, 1.14%, 3.24%, and 6.52% are shown in Fig. 4, respectively. The notion that the denser the pore structure is, the greater the concrete strength is supported by the fact that for concrete samples that have the identical strength level, the compressive strength generally declined with the increase of pore structure characteristics. Because the capillary pore stress in restricted samples decreased as a result of restricted tensile tension, the pore structure of restricted samples was greater than that of ordinary concrete samples. The higher the reinforcement rate of the restrained specimens the greater the restraint impact and the larger the concrete pore structure. Therefore, it was discovered through the experiment that the strength of the concrete dropped while the reinforcement ratio rose.

The correlation between concrete pore structure (primarily porosity) and compressive strength can be ideally expressed in the form of linear, exponential or polynomial. Figure 4d depicts a linear model that was used to fit the relation between concrete porosity and compressive strength. This illustrates that the linear fit is better for concrete with the same strength grade, while for concrete with similar porosity, the strength of concrete of each strength grade changed greatly. For example, when the porosity was 25.37%, the compressive strength of the C40 concrete samples was 29.7 MPa, whereas the C70 concrete specimen had a compressive strength of

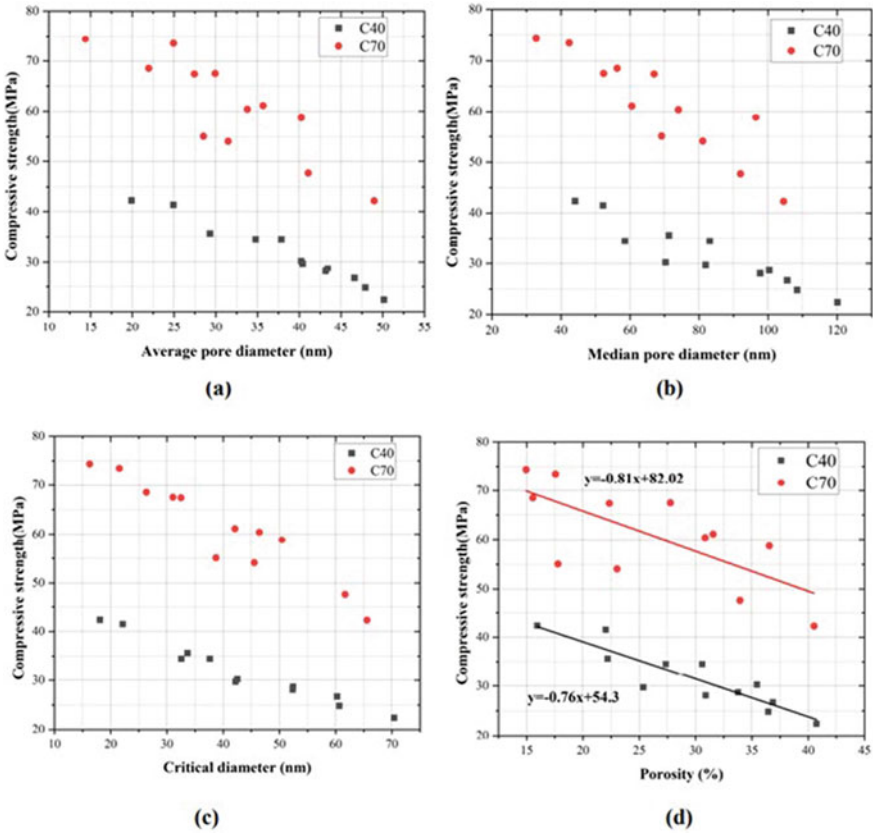

Fig. 4 Link between compressive strength and the following pore structure factors: **a** average pore diameter, **b** median pore diameter, **c** critical diameter, **d** porosity

54.1 MPa at a porosity of 23.02%, which was 24.4 MPa higher than that of the C40 specimens. Similarities have been found in the past in studies by Li et al.

The content of each pore is reflected in the porosity of concrete, and varied pore size distributions also result in the same or nearly the same porosity. At the same time, previous studies have also shown that the compressive strength of concrete would increase when the proportion of small and medium-sized pores in concrete is larger, which results in that when the experimental porosity was close, but the C40 and C70 strengths were different.

3.3 *Link Between Concrete Compressive Strength and Reinforcing Rate*

This research demonstrates that reinforcing bars will lessen capillary strains, causing a reduction in the pore structure of concrete, resulting in a lower compressive strength of reinforced specimens than unreinforced specimens. The compressive strength of concrete progressively declined since the reinforcing rate grew. If the scaffold can be removed depending on the compression strength of unreinforced concrete in the actual project construction, the accident risk may increase.

At the construction site, direct testing of concrete pore structure parameters is difficult. Hence, in order to assess the reinforced concrete's strength when the strength of plain concrete is known, Eq. (3) established a link between the reinforcing rate and the compressive strength of concrete.

$$f_{c\rho} = f_{c0} \exp^{b\rho} \tag{3}$$

In this formula, b is a calculation parameter that in this research is equivalent to -5. $f_{c\rho}$ and f_{c0} represent, respectively, the compressive strength of concrete when its reinforcing rate is ρ and 0.

Figure 5 gives the concrete compressive strength estimated by Formula (3) for different reinforcement ratios. The predicted results shown in Fig. 5 were consistent with the practical test values. It's important to note that parameter b also be influenced by other factors probably, for instance an additive agent used in concrete, exterior environment and the age of concrete. Further experiments are needed to explore this issue in the future.

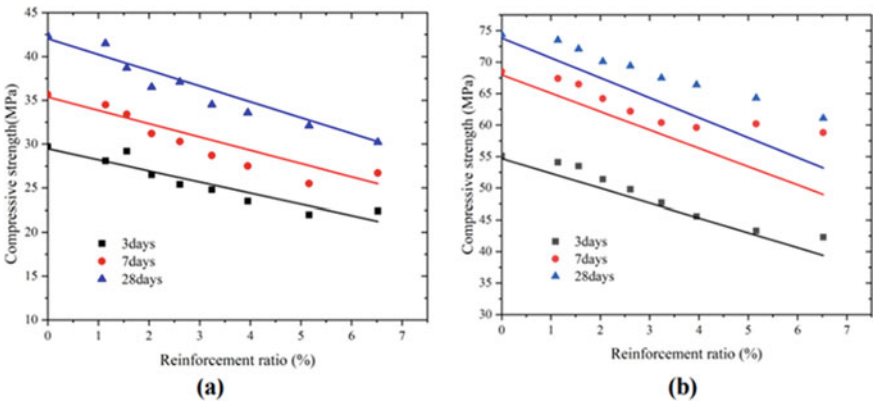

Fig. 5 Comparison between predicted and measured results: **a** C40, **b** C70

4 Conclusions

Utilizing an experimental approach, the effect of different reinforcing ratios on concrete pore structure and compressive strength was studied, and three age concrete specimens were tested in this research. The following are the main findings:

(1) The size of concrete pore structure steadily becomes smaller due to the absorption of hydration products and the action of capillary stress during the cement hydration process. The porosity proportion with diameters in the range of 0–50 nm rose, while the percentage of pores with diameters greater than 50 nm dropped significantly.
(2) The size of concrete pore structure became progressively larger as the reinforcing rate rose. The pore structure characteristics (porosity, average and medium pore diameter and critical pore diameter) have a linear relation with the reinforcing rate.
(3) Reinforced concrete specimens had lower compressive strengths than unreinforced concrete specimens at the same age, and the strength steadily dropped as the reinforcing ratio rose.
(4) If the compressive strength of unreinforced concrete is used to decide whether a scaffold can be removed in actual engineering construction, accidents may occur more frequently.

Thus, in light of the given compressive strength of unreinforced concrete, this paper developed a equation for predicting reinforced concrete strength, and the predicted value can match well with the actual value.

References

1. Li D et al (2018) A predictive model of the effective tensile and compressive strengths of concrete considering porosity and pore size. Constr Build Mater 170:520–526
2. Bu J, Tian Z (2016) Relationship between pore structure and compressive strength of concrete: experiments and statistical modeling. Sādhanā 41(3):337–344
3. Lian C, Zhuge Y, Beecham S (2011) The relationship between porosity and strength for porous concrete. Constr Build Mater 25(11):4294–4298
4. Zhang M et al (2021) Study of concrete strength and pore structure model based on grey relation entropy. Materials 14(2):432
5. Gao H, Zhang X, Zhang Y (2015) Effect of the entrained air void on strength and interfacial transition zone of air-entrained mortar. J Wuhan Univ Technol-Mater Sci Ed 30(5):1020–1028
6. Rui Y et al (2022) Comparative study on the effect of steel and polyoxymethylene fibers on the characteristics of ultra-high performance concrete (UHPC). Cement Concr Compos 127:104418
7. Li Y, Li J (2014) Capillary tension theory for prediction of early autogenous shrinkage of self-consolidating concrete. Constr Build Mater 53:511–516
8. Zhao H et al (2020) Effects of CaO-based and MgO-based expansion agent, curing temperature and restraint degree on pore structure of early-age mortar. Constr Build Mater 257:119572

Study on Sliding Construction Technology of Complex Steel Structure Roof System: A Case Study of Xiamen, China

Ping Zeng, Pengjin Wu, Yunhao Wang, Muhuo Lai, Ruiyi Wang, Jingzhen Chen, and Meitong Lin

Abstract The construction of a steel structure roof is typically an exceedingly intricate system engineering, with exceedingly elevated technical and managerial demands throughout the course of construction. The insufficiency of engineering proficiency frequently hampers the construction timeline, resulting in substantial monetary losses and amplifying the likelihood of safety incidents. Therefore, predicated on the roof construction project of Exhibition Hall 3 of Xiamen New Convention and Exhibition Center, this paper introduces a two-stage planning and analysis technique for technical solutions. In the initial planning stage of the technical proposal, the pros and cons of the installation approaches for large span intricate steel structure roofs were scrutinized, and after comparative analysis from five dimensions, the "sliding assembly jig frame method" was ascertained as the technical proposal for the project. During the implementation and planning stage of the technical proposal, the construction procedure and approach were clarified, the lifting structure was split, and the type of lifting equipment was selected. Finally, critical construction steps were analyzed through MIDAS/GEN simulation to authenticate the safety of the technical proposal. The research outcomes indicate that the two-stage planning and analysis technique for technical solutions posited in this paper can markedly abridge the construction timeline, save expenses, ameliorate construction quality, and diminish construction safety hazards.

Keywords Steel structure roof · Sliding construction · Bed-jig · Technical proposal planning

P. Zeng · M. Lai · J. Chen
China Construction Fourth Engineering Bureau Co., Ltd., No. 220 Weihai Road, Panyu District, Guangzhou 511497, Guangdong Province, China

P. Wu · Y. Wang · R. Wang
School of Civil Engineering, Chongqing University, Chongqing 400045, China

M. Lin (✉)
Department of Civil Engineering, Xi'an Jiaotong-Liverpool University, Suzhou 215123, China
e-mail: ldachan@163.com

H.-Y. Jeon (ed.), *Proceedings of the International Conference on Geosynthetics and Environmental Engineering*, Lecture Notes in Civil Engineering 374,
https://doi.org/10.1007/978-981-99-4229-9_43

1 Introduction

In recent times, with technological advancements, a growing number of projects have been executed using sliding technology, predominantly for large-span steel roof structures [1], such as airport terminals, vast gymnasiums, and exhibition centers. Currently, numerous researchers have conducted studies on the sliding construction process. Some researchers employed finite element simulation analysis to determine the safety and construction monitoring early warning values of the structure during the sliding construction process, and proposed a method to monitor the structural safety, stability, and sliding synchronization during the construction of large span steel structures [2]. Others analyzed the influence of high and low track designs on reducing wind loads during steel structure sliding construction at high altitude [3]. With respect to a mixed-purpose bridge, certain studies proposed that the steel truss beam in the side span cable area of a highway railway dual-purpose bridge be constructed using a walking-type jacking slip scheme [4]. The mechanical properties of the large tonnage steel truss beam during the jacking slip construction under two working conditions were analyzed using MIDAS Civil [5]. Further, some scholars analyzed the construction scheme of four sliding jig frames in the construction of steel box girders and, combined with the engineering construction scheme, elaborated on the jacking construction technology in detail [6]. Moreover, certain studies compared the overall sliding construction technology of using block hoisting in place, high altitude in-situ bulk loading, and using hydraulic crawlers as the primary driving equipment, relying on computer control to regulate the hydraulic pressure [7, 8].

In conclusion, the use of sliding construction in steel structure roof systems has significant advantages in project progress. However, the technology of roof sliding construction is relatively complex, and different engineering projects possess their unique characteristics, which limit the reference experience available. Furthermore, most scholarly research on roof system sliding still concentrates on the technical level without sorting out the technical planning process. Based on the project background of complex steel structure roof construction in large exhibition centers, this paper performs a comprehensive and systematic analysis of the sliding construction process, summarizes and extracts crucial technical points, which can provide guidance for the construction of similar engineering projects.

2 Case Study

2.1 Project Background

The installation project for the steel structure roof of Exhibition Hall 3 at Xiamen New Convention and Exhibition Center comprises two parts, namely, the upper part, which is a pipe truss steel roof, and the lower part, which is a steel frame structure system. The north–south overhanging part is a welded ball spatial grid structure, and

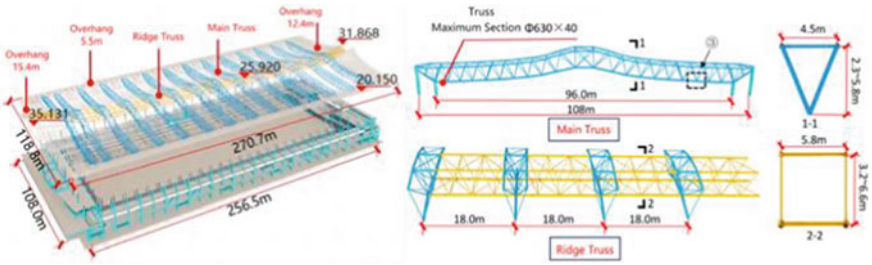

Fig. 1 Overview of steel structure of exhibition hall

the roof comprises of 14 inverted triangular main trusses, 1 trapezoidal ridge truss, and 48 segment secondary trusses. The maximum span of the roof is 96 m, and the overall steel consumption of a single exhibition hall is approximately 94,600 tons, as depicted in Fig. 1.

The project site is located in a subtropical marine monsoon climate zone, characterized by mild and rainy weather, with an annual average temperature of around 21°. The average annual rainfall is approximately 1200 mm, with the heaviest rainfall occurring between May and August each year. The wind force in the area is usually 3–4°, and the dominant wind force is the northeast wind. The terrain around the project site is open and flat, with convenient transportation.

2.2 Preliminary Planning and Analysis of Technical Proposal

Project Analysis

Based on the characteristics of the project, several challenges need to be addressed during the installation of the steel structure roof system of Exhibition Hall 3. These include the large number of components, nodes, and branch members, the complexity of curved pipe components, and the difficulty in controlling welding quality due to dense welding seams and large welding deformation. Therefore, choosing the right installation method is crucial to ensure installation accuracy and quality. The comparative analysis of various installation methods for large span complex steel structure roofs is summarized in Table 1.

To conclude, the extensive span of the steel structure roof system in the exhibition hall, coupled with the demanding workload of on-site assembly and the constrained construction timeline, renders the high altitude assembly method unsuitable. The roof structure, a multifarious multi-layer steel truss structure with a considerable lifting weight, requires high-performance lifting equipment and presents difficulties in analyzing and controlling the safety of the lifting structure. Additionally, the site's flat terrain and the building structure's regular shape further corroborate this. Thus, given these circumstances, the sliding construction method is the most appropriate

Table 1 Analysis and summary of installation methods for large span complex steel structure roof

	High altitude assembly method	Lifting construction method	Sliding construction method
Definition	The method of assembling components directly at the design position by erecting a support jig	The construction method of gradually lifting a structure on the ground or floor to a predetermined position using a lifting device	A method for completing the overall installation of a roof by sliding a divided unit or jig frame on a previously set slide rail
Advantage	• Effectively reduce the lifting requirements of components • High installation accuracy	• Less temporary measures • Less equipment investment • Safe and reliable construction • Short occupation time of construction site	• Low quantity of assembled jig frame • Less occupation of working surface • Short construction period
Limiting condition	• Additional support systems require a large amount of material • Long occupation time of construction site with support • Long construction period	• It is required that the lifted structure should have greater stiffness and the substructure should have better support conditions • During the lifting process, it is necessary to control the influence of relative displacement difference between lifting points	• Many factors, such as the erection of the support jig, the setting of the guide rails, and the irregularity of the structural form, will limit its application

installation method for this project, and it has become the preferred technical solution for the steel structure roof system of the exhibition hall.

Comparison and Selection of Technical Proposals

Based on the object being slid, sliding construction methods can be categorized into three types: main structure sliding method, cumulative sliding method, and jig frame sliding method. The main structure sliding method involves sliding a single structure into place at one time, and then sliding the subsequent single structure until the entire large-span structure construction is completed. This method is used when a jig frame cannot be erected at the lower part of the large-span structure or the crane cannot be moved. However, this method is not suitable for this project due to the large roof span and the availability of support under the roof for jig frame erection.

On the other hand, the cumulative sliding method, illustrated in Fig. 2, involves constructing a strip unit by sliding it for a distance, connecting it to the second unit, sliding them together for a distance, and then connecting the third unit. This process continues until the last unit is connected, after which the support is fixed, the track is cut, and the roof panel is constructed.

Fig. 2 Construction diagram of "cumulative sliding of structure"

Fig. 3 Construction diagram of "sliding assembly jig frame"

As there is no connecting beam between the supports at both ends of the large-span roof structure and only a single column fulcrum bears the load, it is impractical to install a slide rail. In such a case, the jig frame sliding method requires the installation of a slide rail at the lower part of the assembled jig frame, followed by the assembly of the striping unit at the designated position. Subsequently, the assembly fulcrum is lowered, and the assembled jig frame is slid one by one to complete the overall structure installation, as illustrated in Fig. 3.

Table 2 compares and analyzes two sliding construction schemes for the steel structure roof system: the cumulative sliding technology scheme and the sliding assembly tire frame technology scheme. The comparison is based on five aspects, which are: construction safety, construction efficiency, installation accuracy, construction cost, and applicability.

After conducting a comprehensive analysis of multiple factors such as construction period, quality, safety, large machinery, and temporary measures, it is evident that the sliding assembly tire frame technology scheme presents significant advantages in the aforementioned aspects. As a result, the sliding assembly tire frame technology scheme has been chosen as the final technical solution for the project implementation.

Table 2 Summary of analysis of the slip method for steel roof systems

Project objectives	Cumulative sliding technology scheme	Technical proposal for sliding assembly tire frame
Construction period	229 days (after calculation)	174 days (after calculation)
Quality	• Generally controllable quality • Complex structural stress • Difficulty in unloading analysis	• Controllable quality • The structural stress during construction is basically consistent with the original design • Small structural deformation
Safety	The roof system is temporarily fixed before unloading, posing a risk in typhoon areas	Roof system installed in situ, safe and controllable
Large machinery	Large usage of large machinery	
Temporary measure	The amount of sliding measures exceeds 800 tons	The amount of sliding measures is less than 200 tons

2.3 Implementation Planning and Analysis of Technical Proposal

Construction Sequence

The construction of the roof truss is segmented into three distinct areas, and their construction sequence is shown in Fig. 4. The construction commences from the central area, utilizing a movable jig frame for the installation process. Once the central area is halfway constructed, the construction for the lifting areas on both ends will commence. The installation sequence involves installing the main truss, followed by the secondary truss, supplementing the web members partially, and finally installing the cantilever truss.

The demonstration of the construction sequence is illustrated in Fig. 5, and the specific steps are delineated below:

(a) Unit assembly process 1: Establish a sliding track and assemble a jig frame. The primary lifting equipment employed is a 320 ton crawler crane, as depicted in Fig. 5a.
(b) Unit assembly process 2: Utilize a 320 ton crawler crane to hoist the first main truss segment in the area of the movable jig frame, as shown in Fig. 5b.
(c) Unit assembly process 3: Persist in utilizing a 320 ton crawler crane to hoist the initial trusses of the main truss on the opposite side of the movable tire frame area in sections, as illustrated in Fig. 5c.
(d) Unit assembly process 4: Continue to employ a 320 ton crawler crane to elevate the middle section of the first main truss in the movable jig frame area, as demonstrated in Fig. 5d.
(e) Unit assembly process 5: Use a 320 ton crawler crane to raise the two sides of the second main truss in the movable jig frame area, as portrayed in Fig. 5e.

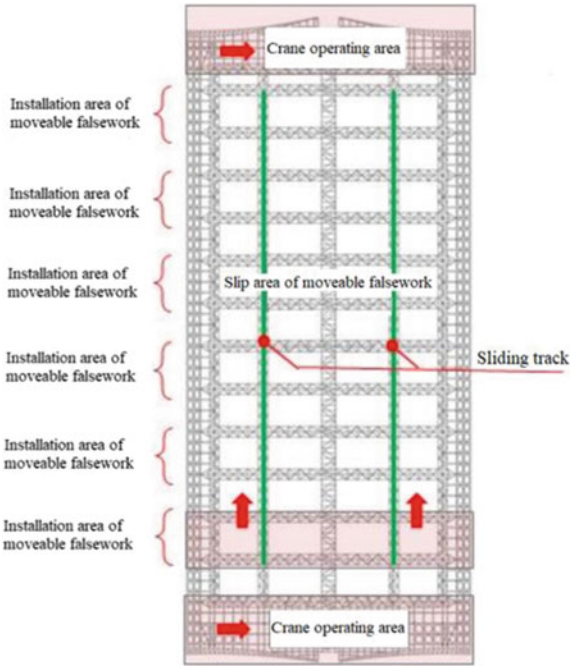

Fig. 4 Construction sequence plan

(f) Unit assembly process 6: Sustain the use of a 320 ton crawler crane to lift the middle section of the second main truss in the movable jig frame area, as exemplified in Fig. 5f.
(g) Unit assembly process 7: Elevate the ridge truss between the two main trusses, and utilize an 80 ton truck crane to lift the secondary truss and purlins, as presented in Fig. 5g.
(h) Unit assembly process 8: Discharge the roof of the movable jig area and relocate the movable jig northward for 36 m, as evinced in Fig. 5h.
(i) Unit assembly process 9: Likewise, adhere to the aforementioned steps to finalize the installation of the roof in the movable jig frame area, as revealed in Fig. 5i.
(j) Unit assembly process 10: Unload the roof of the movable jig area and relocate the movable jig northward for 36 m. Concurrently, use a 100 ton truck crane and an 80 ton truck crane to insert and restore the ridge truss, the sub truss, and the east and west overhanging trusses amid the roofs of the two movable jig frame installation areas, as demonstrated in Fig. 5j.

Zoning and Segmentation of Hoisting Structure

The hoisting of the roof truss is performed using the method of ground sectional assembly and movable jig frame installation. To ensure the quality of construction while maintaining economic and rational lifting operations, it is recommended to

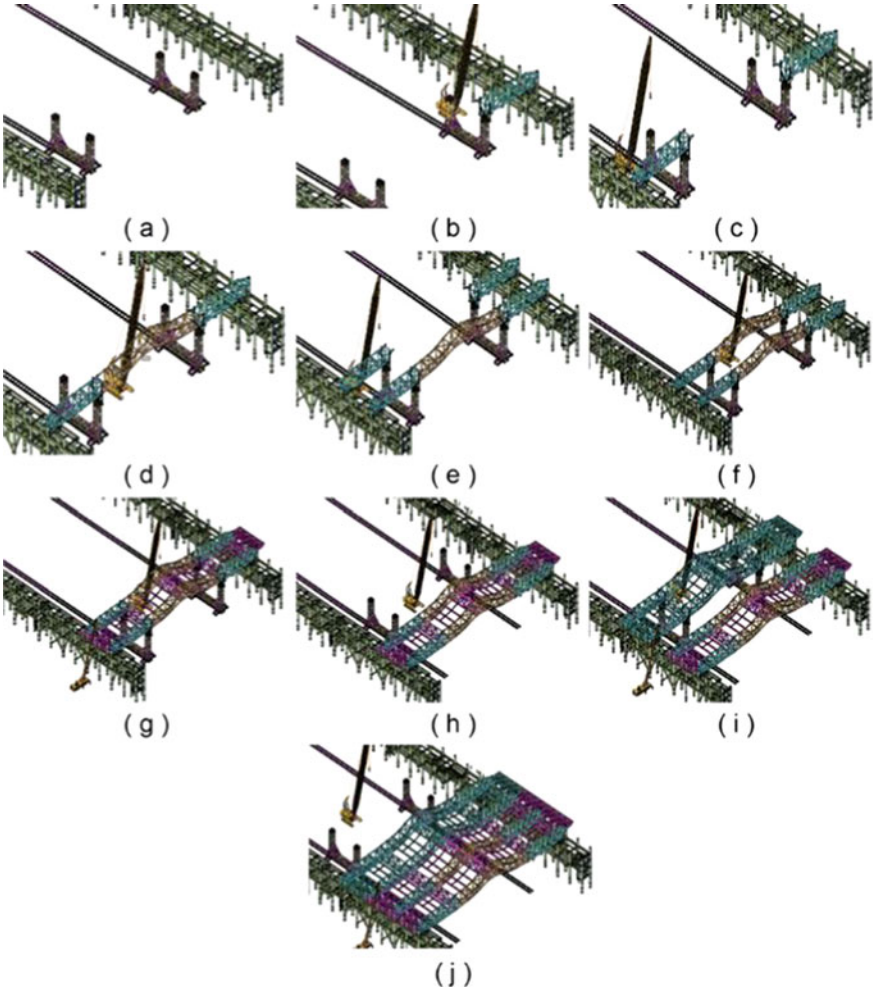

Fig. 5 Construction sequence BIM demonstration diagram

utilize medium and large lifting equipment as much as possible, thereby reducing the number of lifts and the amount of overhead splicing. In addition, light lifting equipment can be used in conjunction with medium and large lifting equipment to transport materials and lift parts of structures. This combination not only saves costs but also provides flexibility in operations. Heavy lifting equipment should be avoided as much as possible to save costs and overcome site use restrictions. Based on the formal characteristics of the roof structure, the lifting process is logically divided into three sections, as shown in Fig. 6. The main truss, which is divided into three sections, consists of 42 main truss sections. The ridge truss and sub truss segments are interrupted at the main truss and comprise a total of 14 ridge trusses and 28 sub

trusses. The north and south overhanging grid structures are divided into 16 blocks, with a total of 32 blocks. The east and west overhanging trusses are divided into 12 sections, with a total of 24 lifting sections. The heaviest section among all sections of the main truss weighs 103 tons, and with the hook weighing 3.5 tons, and the steel wire rope and shackle weighing 2.5 tons in total, the total weight is 109 tons. Assuming a safety factor of 1.2, which takes into account the wind load, the heaviest segment to be lifted weighs 130.8 tons. The installation position of the highest section is at a height of 30.2 m.

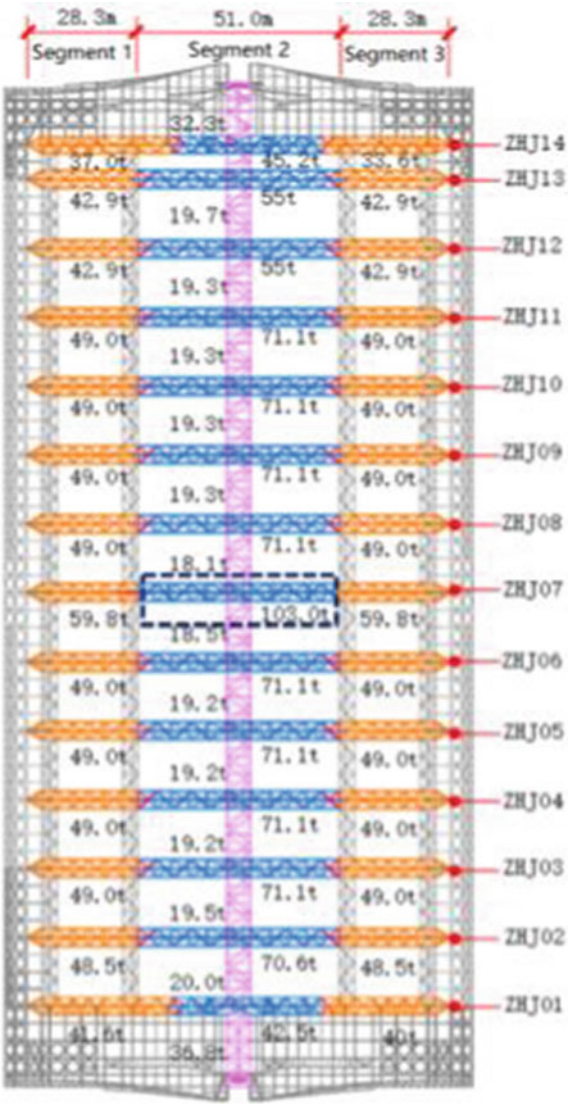

Fig. 6 Main truss section and schematic diagram

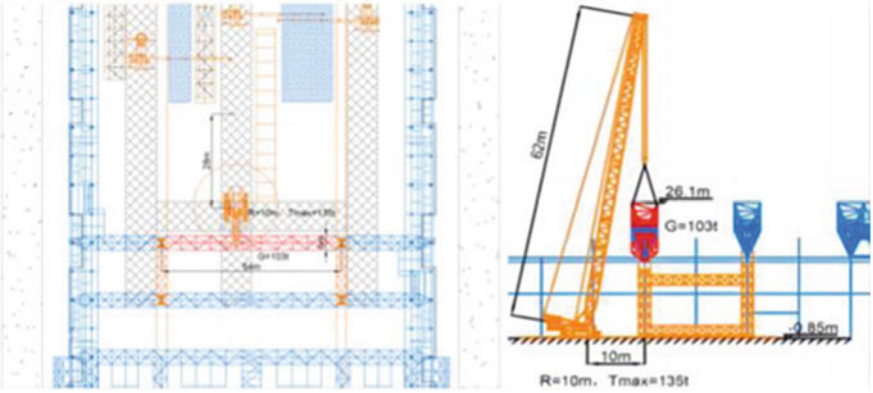

Fig. 7 Analysis diagram of the most unfavorable working conditions of the main truss

Hoisting Condition Analysis and Equipment Selection

Based on the segmentation results of the main truss, it is determined that the weight of the main truss in the section II area is the heaviest. To select the appropriate lifting equipment, it is necessary to consider not only the weight of the heaviest section, but also the location of the lifting equipment and the installation location. Considering the site limitations of large lifting equipment and the relatively fixed driving routes, it is important to analyze the working conditions and rely on experience to select the most suitable equipment. Also, according to the analysis in the previous section, the heaviest section load of the main truss is 130.8 t, and the highest section installation position is 30.2 m. In order to meet the hoisting requirements, a 320 tons crawler crane is selected for lifting, with a lifting radius of R = 10 m and a main boom length of 62 m, as shown in Fig. 7. At this configuration, the rated lifting capacity of the crawler crane is T = 135 t, which exceeds the heaviest section weight, ensuring safe and efficient lifting operations.

Likewise, the heftiest cross-sectional weight of the suspended grid positioned on both the northern and southern sides is the third segment located on the southern side, tipping the scales at 40.8 tons. Accompanied by a hook weighing 1.5 tons and 1 tons steel wire ropes and shackles, the total weight adds up to 43.3 tons. Assuming a safety factor of 1.2, the maximum weight of the segment to be lifted is calculated to be 43.3 tons $\times$ 1.2 = 52 tons. In light of this, a 150 tons crawler crane, featuring a main boom length of 56 m and a hoisting radius of R = 10 m, is selected for the task at hand. At present, the rated lifting capacity of the crane stands at T = 54.2 tons, exceeding the required hoisting capacity of 52.0 tons, thereby satisfying the lifting requirements.

Moreover, the heaviest section weight of the ridge truss measures 20 tons, with the hook weighing 1 tons and the steel wire rope and shackle accounting for approximately 0.5 tons, resulting in a total of 21.5 tons. Assuming a safety factor of 1.2, the maximum weight of the segment to be hoisted is 21.5 tons $\times$ 1.2 = 25.8 tons.

Fig. 8 Overall model

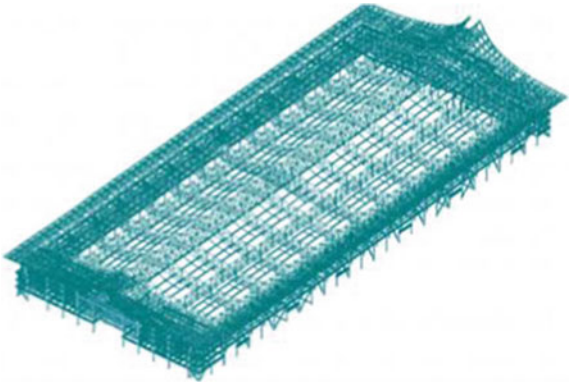

A 100 tons truck crane is chosen to accomplish the task, featuring a main boom length of 48.5 m and a hoisting radius of R = 10 m. At this moment, the rated lifting capacity of the crane stands at T = 29 tons, surpassing the required hoisting capacity of 25.8 tons, hence satisfying the lifting requirements.

2.4 Numerical Simulation Analysis of Jig Frame Sliding Construction Stage

This paper employs MIDAS/GEN for simulating the construction stage. The analysis model is a comprehensive model that groups structural components, support constraints, and load cases according to construction steps and defines the construction stage. The simulation program is conducted based on control data, and the calculation model is built entirely based on the structural construction drawings, with all components' cross sections and materials in line with the structural construction drawings. The comprehensive model is presented in Fig. 8.

The simulation analysis results of diverse unfavorable working conditions have been verified below. The maximum combined displacement during the entire construction process is 69.19 mm, which is less than L/400 = 112.5 mm (calculated based on the truss span where the maximum displacement occurs), meeting the usage requirements of the specification. The position of the maximum displacement occurs at the middle of the main truss, as illustrated in Fig. 9a. This is related to the unloading of certain sections of the main truss. During the process of continuously installing the secondary truss and other loose parts, the displacement will persistently increase, indicating that as the structure is integrated, the stress on the main truss will also increase. After the installation of the entire structure, the local members of the roof structure reach the maximum displacement. The maximum stress of roof structural members is compressive stress, reaching 124.26 MPa, which is less than f = 295 MPa, satisfying the specification requirements. The maximum displacement occurs at the connection between the end of the main truss and the main structure,

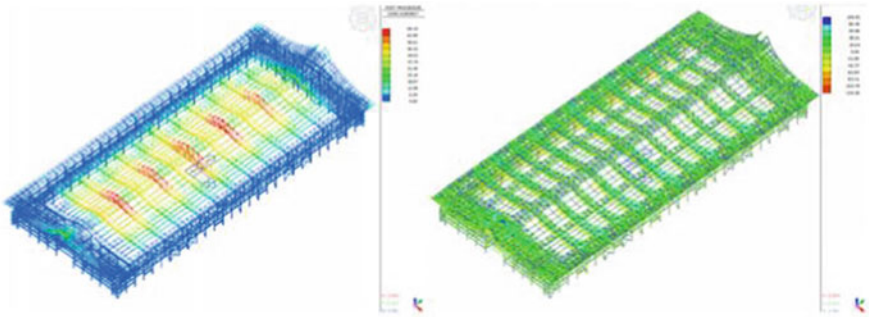

Fig. 9 Figure of numerical simulation analysis results

as depicted in Fig. 9b. This indicates that with the overall formation of the structure, the stress on the main truss will continue to rise. After the installation of the entire structure, the local members of the roof structure will experience the maximum stress.

Furthermore, this paper also simulates the hoisting of roof truss structures, the usage of jig frames, and their displacement, stress, and stability. Additionally, the foundation supported by the jig frame and the track beam of the mobile jig frame are also scrutinized and calculated. The simulation results demonstrate that the technical scheme proposed in this paper is highly secure. In summary, the two-stage planning analysis method proposed in this article can considerably shorten the construction period, reduce costs, enhance construction quality, and mitigate construction safety hazards.

3 Conclusions

This study presents a technical proposal for the construction of the Exhibition Hall 3 roof project at the Xiamen New Convention and Exhibition Center, along with a two-stage planning and analysis method for the technical plan. The first stage involves the preliminary planning of the technical proposal, which includes a comparative analysis of two installation methods, namely the "structural cumulative sliding method" and the "sliding assembly jig frame method," based on five dimensions, such as construction period, quality, safety, construction measures, and comprehensive analysis of large machinery. The "sliding assembly jig frame method" was ultimately selected for construction. The second stage involves the implementation planning of the technical proposal, which includes the analysis and determination of specific and reasonable construction procedures and methods. The lifting structure was divided based on the analysis of lifting conditions, and the selection of lifting equipment was determined based on the maximum weight of the lifting structure and the level and

height difference distance between the installation position and the lifting position. The safety of the lifting construction was verified through numerical simulation analysis of important construction steps using MIDAS/GEN. The proposed two-stage planning and analysis method for the technical proposal can significantly reduce the construction period, improve construction quality and safety, and enhance the economic benefits of the project.

References

1. Shi J, Kong D (2021) Floor heave mechanism and anti-slide piles control technology in deep and large-span chamber. 11(10):4576
2. Sun J et al (2020) Investigation and finite element simulation analysis on collapse accident of Heyuan Dongjiang Bridge. Eng Fail Anal 115:104655
3. Zhou X, Zhang X (2019) Thoughts on the development of bridge technology in China. Engineering 5(6):1120–1130
4. Tao M-X, Fan J-S, Nie J-G (2013) Seismic behavior of steel reinforced concrete column–steel truss beam hybrid joints. Eng Struct 56:1557–1569
5. Grabow MJJDTC, TUoHH (2004) Construction stage analysis of cable-stayed bridges. Environmental Engineering, Germany
6. Niu Z et al (2020) A new method for predicting ground settlement induced by pipe jacking construction. Math Probl Eng 2020:1681347
7. Schoessler P, et al (2015) Kinetic blocks: actuated constructive assembly for interaction and display. In: Proceedings of the 28th annual ACM symposium on user interface software and technology. Association for Computing Machinery, Charlotte, NC, USA, p 341–349
8. Cheng X et al (2020) A new construction technology suitable for frame partitioned infill walls with sliding nodes and large openings: test results. Constr Build Mater 258:119644

Research on Temporary Support Unloading During Construction of Long Cantilevered Steel Structure Roof System: A Case Study in Xiamen, China

Jinbing Wang, Yunhao Wang, Jingzhen Chen, Ruiyi Wang, Pengjin Wu, Mingsi Jiang, Fenbin Lin, and Xingyang Zhou

Abstract When simulating the unloading process of a steel structure roof construction, it is commonly assumed that the working condition is synchronous unloading, but this is challenging to achieve in actual construction and can pose safety risks. Upon examining various unloading methods for structural analysis, it was determined that their computational workload is substantial. To address this issue, this paper proposes a combined unloading method based on the structural characteristics of the southern cantilever grid structure of the roof cover of No. 3 exhibition hall of Xiamen New Convention and Exhibition Center. The reliability of this method is confirmed through finite element simulation analysis and on-site monitoring tests. The research findings demonstrate that this method can optimize the construction unloading sequence, significantly reduce the amount of structural calculation and analysis, and improve the safety of the steel roof construction process.

Keywords Steel structure roof · Temporary support · Structural unloading · Finite element analysis · Construction monitoring

J. Wang · J. Chen · F. Lin
China Construction Fourth Engineering Bureau Co., Ltd., No.220 Weihai Road, Panyu District, Guangzhou 511497, Guangdong Province, China

Y. Wang · R. Wang · P. Wu · M. Jiang
School of Civil Engineering, Chongqing University, Chongqing 400045, China

X. Zhou (✉)
Department of Civil Engineering, Xi'an Jiaotong-Liverpool University, Suzhou 215123, China
e-mail: egbert2023@163.com

H.-Y. Jeon (ed.), *Proceedings of the International Conference on Geosynthetics and Environmental Engineering*, Lecture Notes in Civil Engineering 374,
https://doi.org/10.1007/978-981-99-4229-9_44

1 Introduction

The large span steel joist structure offers many advantages, including a high degree of industrialization and assembly, short construction period, and reasonable comprehensive cost [1]. This type of structure is widely used in the roofing systems of buildings such as stadiums, industrial plants, and exhibition halls [2]. However, due to variations in construction plans and environmental conditions [3, 4], the analysis conditions for construction are often not available during the structural design process. As a result, the secondary internal forces generated by the structure during the implementation of the construction plan and the impact of temporary and short-term internal forces caused by the construction process on structural safety are not typically considered. Nevertheless, the structural system is gradually improved and established during the entire construction process [5], and its internal force redistribution is bound to exist during this period. Some studies have shown that if the structural system is not fully established, the local instability of the structure is more likely to occur during the construction process [6]. Therefore, temporary support should be set up before the overall completion of the structure, particularly for structures such as large-span steel trusses and spatial grids, to ensure the stability of the structure itself during construction and to ensure construction safety.

In the installation of steel structures, a temporary support called a tire frame is commonly utilized to uphold the load and maintain the structure's stability during the entire construction process. The tire frame is removed once the task is finished, and this removal process is referred to as the unloading of the supporting tire frame, which is a complex construction process. The unloading of the tire frame leads to a change in the structure's internal forces, resulting in the redistribution of internal forces. If the internal force or local deformation becomes too great and exceeds the standard limit, safety accidents during the construction process become more likely [7]. Therefore, the safety, stability, and stress state of the main structure depend greatly on the unloading process of the tire frame. If the internal force characteristics of each member under different unloading modes and processes are fully described in a comprehensive construction plan, it will result in a massive database. In addition, some researchers use finite element analysis software to conduct individual analysis and manual intervention to find the optimal solution, but the workload is also extremely large [8].

To summarize, analyzing the unloading process of steel structure roof systems for construction is a challenging task due to the various possibilities of support unloading. The primary goal is to optimize the process with a focus on rationality and safety. This study examines the installation project of the steel structure roof of Exhibition Hall 3 at Xiamen New Convention and Exhibition Center, specifically the southern overhanging section of the roof system. To address the project's complexity and specificity, a combined unloading method based on structural characteristics is proposed to optimize the structural unloading scheme. The method's reliability is verified through finite element simulation analysis and on-site monitoring tests.

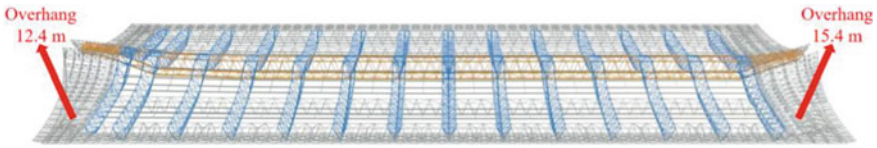

Fig. 1 Axonometric drawing of the roof of exhibition hall 3

2 Case Analysis

2.1 Project Background

The Exhibition Hall 3 of Xiamen New Convention and Exhibition Center has an overall structure consisting of a steel frame and pipe truss system, with a space pipe truss steel roof serving as the upper structure and a building height of 38 m. The cantilever trusses on the east and west sides are composed of circular tube-shaped components with circular cross-sections, while the north and south sides are cantilever grid structures, with the southern side having a maximum overhang of 15.4 m. The entire exhibition hall requires approximately 94,600 tons of steel (see Fig. 1). This case study specifically focuses on the construction and unloading of the southern cantilever grid, which is more complex than the other structures in the building.

2.2 Tire Frame Support Arrangement of the Overhanging Net Frame

During the construction process of the steel structure roof system, the cantilever grid is supported by temporary tire frames, which are placed based on the structural stress characteristics. In the case of the southern cantilever grid, 14 support points were set up using circular tube and profiling work support methods, with positions that are nearly uniformly distributed, as depicted in Fig. 2.

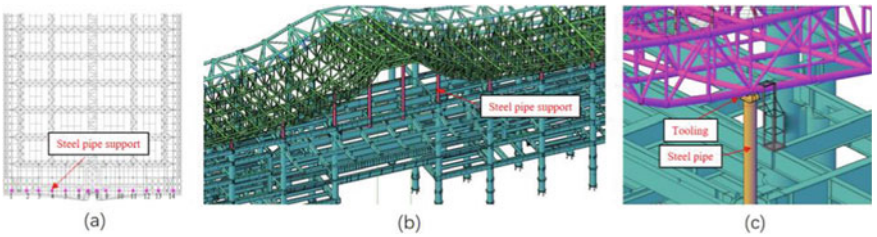

Fig. 2 Support tire frame layout

2.3 Unloading Construction Plan

The principles for unloading the steel structure roof system are presented in Table 1. Specifically, the steel pipe support of the southern cantilever grid will undergo the flame cutting method during unloading, and the most preferable unloading sequence is a synchronous unloading of the entire southern cantilever area. This technique closely resembles the original design and ensures better force distribution, but it proves difficult to accomplish the synchronization of a substantial number of support frames during construction. Therefore, during the construction of spatial grid structures, the support only carries the self-weight and partial construction load, and the load type is simple. However, during the overall formation of the structural model, temporary supports are positioned and removed, leading to significant changes in the constraints and overall stiffness characteristics of the structure, presenting time-varying characteristics as the construction progresses. The overall mechanical characteristics of the structure exhibit significant nonlinearity, while the unit stiffness characteristics of the components remain generally linear. Consequently, the support position of the tire frame becomes a key factor leading to changes in the structural system, and the unloading construction process becomes more susceptible to safety issues.

A dependable construction plan involves utilizing commercial finite element analysis software, implementing traversal algorithms, and conducting automatic static calculations and elastic buckling analyses on all states of the temporary structural system with supports under various working conditions, including addition and disassembly, based on the construction progress. This is done in order to obtain the fundamental internal force and deformation distribution of all states during the construction process. The analysis results serve as the foundation for technical personnel to select a relatively optimal construction plan. However, the more temporary supports are used, the greater the number of uninstallation combinations, making it challenging to complete the analysis tasks with high-performance computers in the short term. Therefore, it is especially crucial to resolve how to optimize the construction unloading method of temporary tire frame support.

2.4 Optimization of Structural Unloading Plan

In order to optimize the unloading process of the southern overhanging grid, it is important to consider the force characteristics of the structural system. Specifically, the process can be viewed as the removal of support bearings from a multi-span continuous beam, with the aim of controlling the larger support reaction force. To determine the best unloading method, it is necessary to study the force characteristics of the support bearings using different unloading methods. By identifying a safe and effective unloading method, the structural unloading scheme can be quickly optimized. The structure in question, as shown in Fig. 3, is a six-span continuous

Table 1 Unloading construction principles

No.	Unloading principles	Specific description
1	Conditions to be met	• The force on adjacent supports during unloading should not undergo significant changes • The deformation of the bars of the structural system shall not exceed the specified allowable range to avoid damage caused by changes in the internal force of the temporarily supported structure or excessive deformation of the bars of the structural system • The force transformation of the structural system is reliable and steadily formed
2	Centered around controlling deformation	• Due to the varying strength and stiffness of each part of the spatial structure, and the varying deformation of each part during the unloading process, it is necessary to ensure the control of the force on the structure itself and temporary supports during the unloading process, as well as the final deformation of the structure
3	Measurement control as a means	• The unloading process of this project is a gradual process, and strict construction monitoring must be carried out during the unloading process to ensure that the unloading is carried out according to the predetermined goals and prevent accidents caused by local deformation due to operational errors or other factors
4	Aiming for a smooth transition	• Due to the fact that the unloading process is also the formation process of the structural system, the selection of unloading plans must aim at a smooth transition to ensure the reliable transformation of the structural stress system

beam with equally spaced supports, subjected only to a uniform load of assumed size 1 kN/m. The flexural stiffness of the beam is infinite, and the supports are rigid.

Through a systematic dismantling and combination of the characteristic supports in a multi-span continuous beam, different reaction diagrams of the supports were obtained, as illustrated in Fig. 4. Figure 4a displays the reaction characteristics of

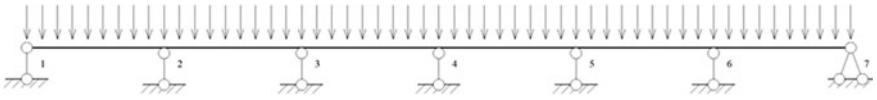

Fig. 3 Multi-span continuous beam

the remaining supports after they are sequentially removed from one end. From the figure, it can be inferred that this approach is the least desirable since the remaining supports that are on the verge of being removed will have to share most of the load on the eliminated beam segment, thereby increasing their support reaction force. Therefore, this method of dismantling should be avoided. Conversely, Fig. 4b suggests that dismantling the support from the middle of the structural beam, i.e., using a symmetrical dismantling method, is more advantageous. After the bearing is removed, the bearing that will be taken off next will experience less reaction force amongst the remaining bearings, while a greater reaction force will arise in the adjacent bearing that is closer to the edge of the structure. Figure 4c displays the reaction force characteristics of the remaining bearing after the simultaneous removal of two adjacent bearings. When two adjacent bearings are removed simultaneously, the neighboring bearing that has not been removed will generate a larger reaction force. The closer the removal position is to the middle of the structure, the smaller the reaction force of the remaining bearing will be. If the two bearings are removed symmetrically, the adjacent unremoved bearing will experience less bearing reaction force than the asymmetrical removal method, but the bearing reaction force will be the largest for the bearing adjacent to the cantilever end after the removal of the bearing. If two bearings are removed at the same time, the symmetric removal from the middle of the structure is the preferred choice, and the reaction force of the remaining unremoved bearings is smaller. Finally, Fig. 4d demonstrates the continuous removal of the bearing rod, and it is apparent that the more bearings are removed continuously, the higher the reaction force of the adjacent unremoved bearings. Similarly, the more symmetrical the structure is after the removal of the bearing, the smaller the reaction force of the remaining bearing will be.

To sum up, the fundamental stress characteristics of a multi-span continuous beam structure system dictate that removing supports symmetrically leads to smaller reaction forces in the remaining supports. Similarly, when multiple supports are removed, symmetric removal from the middle produces less reaction force in the remaining supports. It is important to avoid continuously removing too many supports, which can generate significant reaction forces in adjacent undemolished supports. If symmetrical removal of a bearing is not possible, it is advisable to avoid removing the cantilever end bearing.

In the case of the unloading process of the southern cantilever grid structure, it is similar to that of a multi-span continuous beam, and the support removal process is akin to that of the tire frame support unloading. Hence, this article proposes an optimal unloading plan based on the engineering structural system's characteristics by employing a combination unloading method. The first synchronous unloading is to unload the support of tire frame 3, 5, 7, 8, 10, and 12; the second synchronous unloading is to unload the supports of tire frame 2, 6, 9, and 13; and the third synchronous unloading is to unload the supports of tire frame 1, 4, 11, and 14.

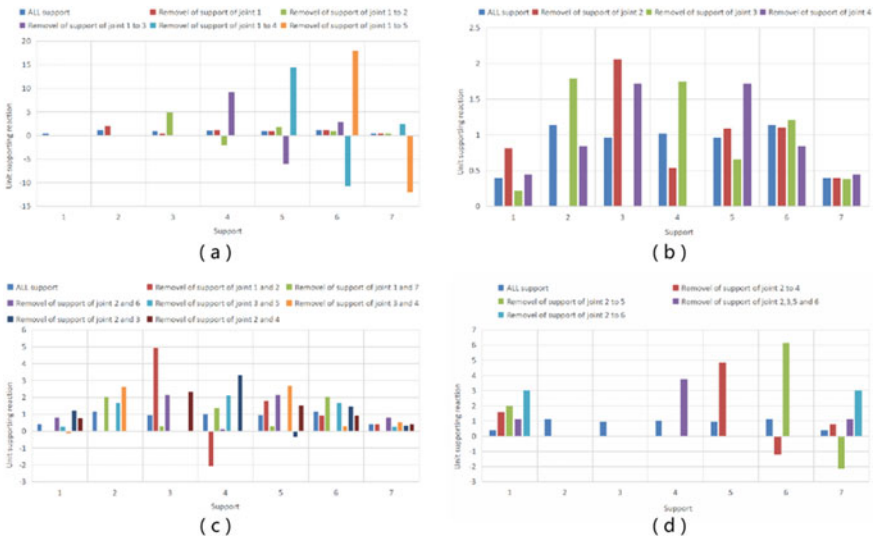

Fig. 4 Support reaction force diagram corresponding to different removal methods of multi-span continuous beam support

2.5 Numerical Simulation Analysis of Structural Unloading Optimization Scheme

The MIDAS/GEN software is utilized to conduct a simulation analysis of the construction unloading process, specifically for the southern overhanging grid of the steel roof system. The optimized construction unloading steps from the previous section are utilized to divide the structural components, support constraints, and load conditions into groups, and separate stages of construction unloading are defined. The program is ultimately analyzed based on control data. The creation of the calculation model is carried out in accordance with the structural construction drawings, with the cross-section and material of all components consistent with those in the drawings. Figure 5 displays the calculation model.

Initially, the operational conditions of various combinations of construction unloading underwent analysis. Subsequently, the most elevated steel pipe support uprights, with a length of 7 m, were subjected to testing. The maximum deflection of the neutral pole is computed as 0.17 mm by deducting 4.91 mm from 5.08 mm.

Fig. 5 Calculation model diagram of side cantilever grid frame

The allowable deflection value, as per the "Code for Design of Steel Structures" GB50017 [9], is determined to be l/1000, which equates to 7 mm since l, the length of the steel pipe support upright, is 7000 mm. This value surpasses the recorded deflection and complies with the regulations. The peak stress of the neutral pole is measured to be 17.38 MPa. According to GB50017 and the "Code for Design of Steel Structures," the compressive yield strength of Q235B steel should be above 205 MPa, which exceeds 17.38 MPa when the plate thickness is between 16 and 40 mm. Consequently, the steel pipe support upright meets the standards of the code. Furthermore, the compressive stability coefficient of the upright pole, which is $\varphi x = \varphi y = \varphi = 0.353$, along with the strength stress of the upright pole, calculated as N/A = 18.485 MPa $\leq f$, meet the requirements of the specification. The computed outcomes demonstrate that the stable stress around the X or Y axis is N/φ·A = 52.311, MPa $\leq f$, fulfilling the specification prerequisites. The ratio of the outer diameter to wall thickness is determined to be 24.917, satisfying the requirements of the specification and not necessitating further horizontal support.

2.6 Deformation Monitoring

During the construction and unloading process of the cantilever grid on the southern side of the steel roof system, the total station was employed to monitor the structural displacement, record the plane coordinates of each measurement control point, and finally determine whether the structure was displaced or deformed through the coordinate increment. Throughout the construction process, seven deformation and displacement observation points were arranged, respectively at the ends and intermediate nodes of the two truss segments. The layout of the monitoring points is depicted in Fig. 6. The monitoring cycle was once a day, using a total station (RTS-862R10A) with an accuracy class of II. The allowable maximum deformation value was 70 mm. After monitoring, it was observed that the measured deformation at most of the measurement points was smaller than the theoretical deformation, and the trend was consistent, with a deviation within a reasonable range. Hence, the structural stiffness of the southern cantilever grid structure is excellent, and the construction quality is commendable.

3 Conclusions

This study presents a case study on the construction and unloading process of the southern cantilever grid structure of Exhibition Hall 3 of Xiamen New Convention and Exhibition Center. Through theoretical research and experimental testing results, it has been discovered that a large number of tire supports are difficult to achieve synchronous unloading, which can cause internal force redistribution in the structural system, and different construction unloading methods can easily lead to safety

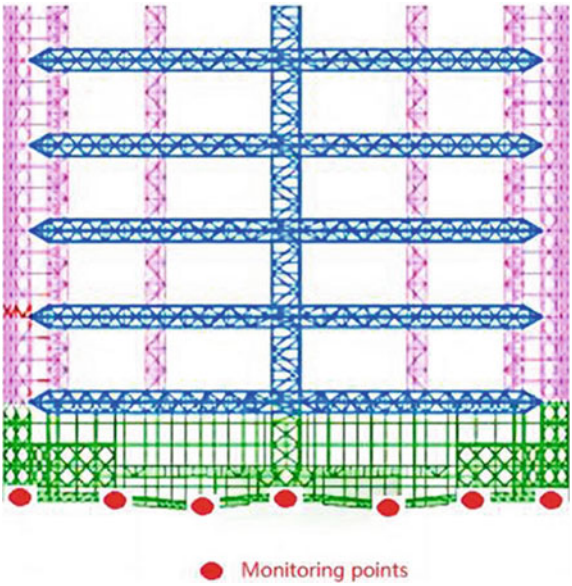

Fig. 6 Layout plan of monitoring points

issues. Additionally, with an increase in the number of tire supports, the combination methods of unloading also increase, which makes exhaustive calculation unfeasible.

To ensure construction safety, this study proposes a combined unloading method based on structural characteristics. The research results show that the stress characteristics of the entire construction unloading process of the cantilever grid structure are similar to those of multi-span continuous beams. Based on this, the study summarized the law of construction unloading by analyzing the process of removing supports from multi-span continuous beams and applied it to the construction unloading of cantilever grid structures to optimize the construction unloading sequence.

Further, numerical simulation analysis of important construction steps and on-site monitoring tests were conducted using MIDAS/GEN software, which verified the safety of this method. As a result, this method can significantly reduce the calculation amount of structural engineering, expedite the construction progress, and ensure the safety of the steel roof construction process.

References

1. Eckelman MJ et al (2018) Life cycle energy and environmental benefits of novel design-for-deconstruction structural systems in steel buildings. Build Environ 143:421–430
2. Han J, Lu L, Yang H (2009) Investigation on the thermal performance of different lightweight roofing structures and its effect on space cooling load. Appl Therm Eng 29(11):2491–2499
3. Keane P, Sertyesilisik B, Ross AD (2010) Variations and change orders on construction projects. 2(2):89–96

4. Chen L et al (2022) Strategies to achieve a carbon neutral society: a review. Environ Chem Lett 20(4):2277–2310
5. Shafei B, Zareian F, Lignos DG (2011) A simplified method for collapse capacity assessment of moment-resisting frame and shear wall structural systems. Eng Struct 33(4):1107–1116
6. Bachmann R, Inkpen AC (2011) Understanding institutional-based trust building processes in inter-organizational relationships. 32(2):281–301
7. Paik JK, Thayamballi AK (2003) Ultimate limit state design of steel-plated structures. Wiley
8. Ellobody E, Feng R, Young B (2013) Finite element analysis and design of metal structures. Elsevier
9. Li T-J et al (2016) Behavior of Q690 high-strength steel columns: part 1: experimental investigation. J Constr Steel Res 123:18–30